Antonio Vizán Idoipe
Juan Carlos García Prada *Editors*

Proceedings of the XV Ibero-American Congress of Mechanical Engineering

CIBIM 22 / CIBEM 22

OPEN ACCESS

Springer

Proceedings of the XV Ibero-American Congress
of Mechanical Engineering

Antonio Vizán Idoipe · Juan Carlos García Prada
Editors

Proceedings of the XV Ibero-American Congress of Mechanical Engineering

CIBIM 22 / CIBEM 22

Springer

Editors
Antonio Vizán Idoipe
Departamento Ingeniería Mecánica
Universidad Politécnica de Madrid
Madrid, Spain

Juan Carlos García Prada
Departamento Mecánica
E.T.S. de Ingenieros Industriales - UNED
Madrid, Spain

Preface

This volume entitled "Advances in Mechanical Engineering" aims to present a selection of the works submitted at the XV Congreso Iberoamericano de Ingeniería Mecánica / XV Congresso Iberoamericano Engenharia Mecânica (CIBIM 2022). These works represent a significant sample of the research and development that is currently carried out in the field of Mechanical Engineering in Ibero-America.

Mechanical Engineering is a broad discipline that comprises different areas of work, which by themselves have also a wide scope. The networking and exchange of ideas among researchers and academics from different areas can be enriching for the future development of each one of them. For this reason, some of the objectives of the Congress are to provide an attractive forum of discussion, to serve as a meeting place for experts and to promote mutual knowledge that may open the possibility of future collaborations.

The selected works are grouped into five thematic areas: mechanics, vehicle engineering, energy and thermal engineering, manufacturing engineering, and automaton and artificial intelligence. Each area comprises different papers, which cover a wide range of themes.

The selection was made taking into consideration the opinion of the reviewers of the submissions and the chairpersons of the sessions, where 360 works were presented.

From all the topics covered in the Congress, it is observed that the topics related to energy, biomechanics, and additive manufacturing have a special interest, as they form a large group of submissions and attracted the interest of many researchers. Some of these works are collected in this volume.

As it is widely known, the organization of an event of this magnitude with 500 attendees, especially after the COVID epidemic, requires the contribution of numerous people, who from this preface are recognized for their valuable work and to whom we would like to express our most sincere gratitude.

We hope this volume serves as a medium to disseminate knowledge and encourage further developments within and outside the Ibero-American Mechanical Engineering community, and we look forward to meeting you at the next XVI Ibero-American Congress of Mechanical Engineering (CIBIM 2024) in Concepción, Chile.

March 2023

Antonio Vizán Idoipe
Juan Carlos García Prada

Organization

Scientific Committee

Baldo, Crhistian Raffaelo	Universidad Federal do ABC, Brazil
Borja Borja, Mario Gastón	Universidad Nacional de Ingeniería, Perú
Coronado Marin, John Jairo	Universidad del Valle, Colombia
Diez Cifuentes, Eduardo	Universidad de la Frontera, Chile
Félez Mindán, Jesús	Universidad Politécnica Madrid, España
Fosca Pastor, Carlos	Pontificia Universidad Católica de Perú, Perú
Gamboa Ritto, Thiago	Universidad Federal do Rio de Janeiro, Brazil
González-Estrada, Octavio Andrés	Universidad Industrial de Santander, Colombia
Hernández-Guerrero, Abel	Universidad de Guanajuato, México
Hernández Frías, Alfonso	Universidad del Pais Vasco, España
Hidalgo Diaz, Victor Hugo	Escuela Politécnica Nacional, Ecuador
López Martínez, José María	Universidad Politécnica Madrid, España
Martins da Silva, Maira	Universidad de São Paulo, Brazil
Mayo Núñez, Juana María	Universidad de Sevilla, España
Meruane Naranjo, Viviana Isabel	Universidad de Chile
Moraga Benavides, Nelson	Universidad de la Serena, Chile
Natal Jorge, Renato	Universidad do Porto, Portugal
Navas, Helena	Universidad Nova de Lisboa, Portugal
Ochoa Villa, Alvaro Antonio	Instituto Federal de Pernambuco, Brazil
Peón Escalante, Ricardo	Universidad Autónoma de Yucatán, Mexico
Pucheta, Martín Alejo	Universidad Tecnológica Nacional, Córdoba
Ramos Grez, Jorge	Pontificia Universidad Católica de Chile
Rogelio Lorenzo, Hecker	Universidad Nacional de la Pampa, Argentina
Romeu Garbi, Jordi	Universidad Politécnica Catalunyia, España
Rui Huerta, Leopoldo	Universidad Nacional Autónoma de México, México
Soriano Idrovo, Guillermo	Escuela Superior Politécnica del Litoral, Ecuador
Suell Dutra, Max	Universidad Federal do Rio de Janeiro, Brazil
Teixeira, Senhorinha	Universidad do Minho, Portugal
Tulio Piován, Marcelo	Universidad Tecnológica Nacional Bahía Blanca, Argentina

Organizing Committee

Vizán Idoipe, Antonio (President)	Universidad Politécnica Madrid, España
Alcalá Fazio, Enrique	Universidad Politécnica Madrid, España
Arenas Ramírez, Blanca Del Valle	Universidad Politécnica Madrid, España
De Arcas Castro, Guillermo	Universidad Politécnica Madrid, España
Chacón Tanarro, Enrique	Universidad Politécnica Madrid, España
Clavijo Jiménez, Miguel	Universidad Politécnica Madrid, España
Díaz Lantada, Andrés	Universidad Politécnica Madrid, España
Echávarri Otero, Javier	Universidad Politécnica Madrid, España
Félez Mindán, Jesús	Universidad Politécnica Madrid, España
Guzmán Bautista, Álvaro	Universidad Politécnica Madrid, España
Hernández Matías, Juan Carlos	Universidad Politécnica Madrid, España
Jiménez Alonso, Felipe	Universidad Politécnica Madrid, España
López Martínez, José María	Universidad Politécnica Madrid, España
Márquez Sevillano, Juan de Juanes	Universidad Politécnica Madrid, España
Martínez Muneta, María Luisa	Universidad Politécnica Madrid, España
Martínez Sáez, Luis	Universidad Politécnica Madrid, España
Muñoz Guijosa, Juan Manuel	Universidad Politécnica Madrid, España
Muñoz Sanz, José Luis	Universidad Politécnica Madrid, España
Páez Ayuso, Francisco Javier	Universidad Politécnica Madrid, España
Pavón García, Ignacio	Universidad Politécnica Madrid, España
Ríos Chueco, Jose	Universidad Politécnica Madrid, España
Romero Olleros, Ignacio	Universidad Politécnica Madrid, España

Executive Committee

Vizán Idoipe, Antonio (President)	Universidad Politécnica Madrid, España
Chacón Tanarro, Enrique	Universidad Politécnica Madrid, España
De Arcas Castro, Guillermo	Universidad Politécnica Madrid, España
Jiménez Alonso, Felipe	Universidad Politécnica Madrid, España
López Martínez, José María	Universidad Politécnica Madrid, España
Martínez Muneta, María Luisa	Universidad Politécnica Madrid, España
Muñoz Guijosa, Juan Manuel	Universidad Politécnica Madrid, España
Muñoz Sanz, José Luis	Universidad Politécnica Madrid, España
Romero Olleros, Ignacio	Universidad Politécnica Madrid, España

Contents

Vehicle Engineering

Energy and Thermal Engineering

Manufacturing Engineering

Automation and Artificial Intelligence

Mechanics

Bayesian Inversion of a Non-linear Dynamic Model for Stockbridge Dampers

Damián Campos[1] , Andrés Ajras[1] , Lucas Goytiño[1] , and Marcelo Piovan[2(✉)]

[1] Laboratorio de Ensayo de Conductores, Departamento de Mecánica Aplicada, Facultad de Ingeniería, Univ. Nacional del Comahue, Neuquen, Argentina
damian.campos@fain.uncoma.edu.ar

[2] Centro de Investigaciones en Mecánica Teórica y Aplicada, Univ. Tecnológica Nacional Facultad Regional Bahía Blanca - CONICET, Bahia Blanca, Argentina

Abstract. Stockbridge dampers are the most widely used in wind induced vibration control of overhead power transmission lines. This dynamic absorber comprises a carrier cable with a mass at each end and a bolted clamp that can be attached to a conductor or a guard wire, with the purpose of supplementing the energy dissipated by the cable related to its self-damping. The maximum response of this type of absorber is associated with the frequencies of its different oscillation modes. The masses are designed in such a way to obtain moments of inertia and location of their center of gravity such that, with the vibration of the clamp, their various characteristic bending and torsional modes are excited. In this work, the calibration of a nonlinear finite element model using Bayesian inference is presented to evaluate the dynamic behavior of the damper for all excitation frequencies and displacement amplitudes. To this end, an inverse problem was posed in which the probability distributions of the parameters of interest are obtained from backward uncertainty propagation of experimental measurements performed in laboratory tests. Finally, the uncertainty of the calibrated model was propagated and contrasted with the experimental data. The developed model is a powerful tool when defining the quantity and distribution of dampers in the span of a line.

Keywords: Aeolian vibrations · Stockbridge damper · Bayesian calibration · Inverse Problems · Uncertainty Propagation

1 Introduction

During the operation of overhead power lines for electric transmission, the conductors as well as the guard filaments are subjected to several classes of mechanical vibrations such as: galloping, Aeolian, and subspan oscillations [1] for bundled conductors. The so-called Aeolian vibrations (generated by von Karman vortex shedding [2]), are the most dangerous because they cause fatigue failures in cable filaments and support accessories. Such failures are observed in the supporting clamps or dampers clamps because of high alternative bending stresses.

Due to the high capital investments involved in the line projects, it is necessary to pay special attention to the potential failures that vibrations can cause on the cables. The Stockbridge type damper has been used successfully to reduce of wind vibrations. Figure 1 shows an installation of the Stockbridge on a guard wire (Fig. 1(a)) and a scheme for experimental tests (Fig. 1(b)). The employment of appropriate mathematical models to analyze this type of problems is quite relevant. Since the dynamic response of the Stockbridge is non-linear and hysteretic (due to internal friction in the cable wires), various models of increasing complexity have been proposed [3].
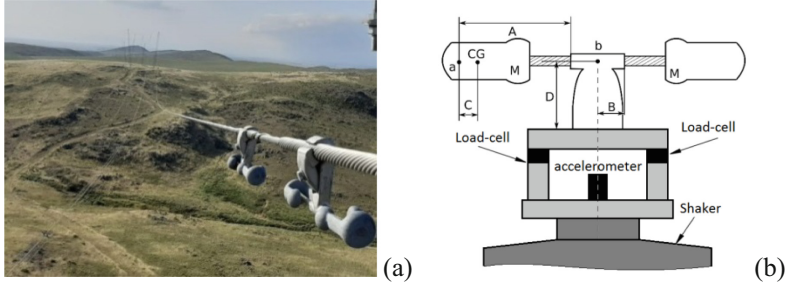
Fig. 1. (a) Detail of an installation of Stockbridge-type damper in a guard wire. (b) Test-rig set-up for the identification procedure of the Stockbridge.

In order to analyze the system cable-damper, Barry [4] developed a simple analytic model in which the cable is conceived as a beam subjected to axial loads and the damper is reduced to a lumped mass-spring-dashpot approach. Subsequent models [5] considered a coupled double beam where the cable is the main beam and the Stockbridge is modeled as a beam with a rigid mass attached to each end. A geometrically non-linear conception and viscous structural damping of the messenger cable have been incorporated into the model; moreover, experiments have been conducted to validate the approach and equivalent values of the parameters (e.g. damping coefficient, natural frequencies of the cable with and without the damping system, etc.) have been calculated as well. Although the non-linear model is evidently time-demanding, it gives quite good predictions of the dynamics. In other studies, non-linear finite elements were involved by considering the hysteresis phenomenon [6].

In the present article, a computational approach of a given Stockbridge is constructed and aimed to identify parameters with the final objective to study the uncertainty propagation in its dynamics. The Stockbridge is conceived as a non-linear finite element beam model subjected to movement in a plane. The intrinsic hysteretic non-linearity of the messenger cable as well as the structural viscous damping, are incorporated. A Bayesian inversion technique is employed to identify parameters of the model, which are quite difficult to measure directly (e.g. cable stiffness, bending moments of individual filaments, etc.). The procedure is explained in the second section. As the parameters of the Stockbridge can have variability due to many circumstances (approaches to identify and calculate the dynamics, constructive gaps or assembly discrepancy under service, etc.) and given that Bayesian Inversion is time-consuming, a study of the uncertainty propagation of the parameters is performed as well.

2 Methodology

As mentioned before several parameters of a Stockbridge model are difficult to be identified by direct experimental tests, consequently, a Bayesian inversion method is employed. This approach, based on Bayes' theorem, requires an appropriate predictive deterministic model, a physical system to extract experimental values and a probabilistic approach. Figure 2(a) shows a diagram of the Bayesian inference procedure to estimate parameters of a model. Figure 2(b) shows the structure of the whole procedure of this article, i.e. first an identification process and then the uncertainty propagation; μ, ε, δ, and λ are the parameters to be identified (see Sect. 2.3).
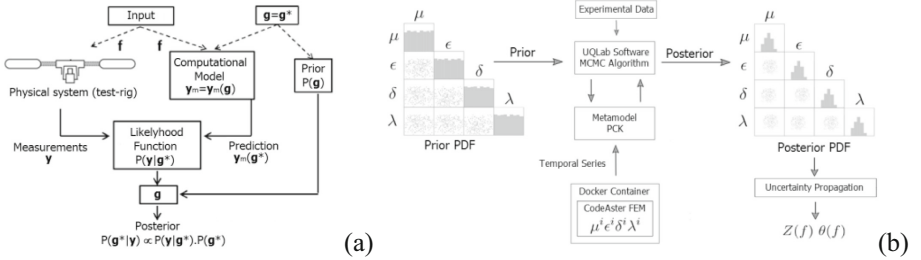
Fig. 2. (a) General scheme of the Bayesian inference approach. (b) Present computational scheme based in the UQLab procedures.

In Fig. 2(a), $\mathbf{y}$ is the vector of experiments (under test frequency $\mathbf{f}$); $\mathbf{g}$ is the vector of parameters in the predictive model $\mathbf{y}_m(\mathbf{g})$; $\mathbf{g}^*$ is a vector of proposed parameters, P($\mathbf{y}$) is the probability density function (PDF) of $\mathbf{y}$, P($\mathbf{g}$) is the PDF of the parameters, P($\mathbf{y}|\mathbf{g}^*$) is the PDF (or likelihood function) of $\mathbf{y}$ given $\mathbf{g}^*$.

2.1 Experimental Test-Rig

The Stockbridge was subjected to the vibratory loads of an electro-dynamical shaker according to the International Standard IEC 61897 [7]. This standard requires a frequency sweep with constant speed. The mechanical Impedance (Z) of the Stockbridge is measured; the force in the damper clamp (F) and the excitation speed ($\dot{x}$) are measured as well. In Eq. (1) one can see expressions of the Impedance and phase angle (θ).

$$Z = \frac{F}{\dot{x}}, \quad \theta = arg(Z) \tag{1}$$

According to Fig. 1(b), the force in the clamp is measured by means of two load cells (type HBM U9C). The speed of the clamp is measured with an accelerometer (Brüel & Kjaer Delta Tron 4507 B004) by integrating the signal. This measuring configuration avoids spurious moments and shearing displacements, allowing absolute direct data which is registered in the Acquisition System HBM QuantumX. The frequency sweep is carried out in discrete steps and the experimental signals are processed with Fourier transformation by means of an "ad-hoc" routine developed by the authors for this particular study.

2.2 Brief Description of the Predictive Deterministic Model

In the present article, the non-linear dynamics of the Stockbridge is computed by means of non-linear beam finite element of the open-source software CodeAster [8], that the authors modified and adapted in order to incorporate the variation of the stiffness along the beam. This is done by coupling several types of beam elements. The messenger cable is modeled by a linear elastic beam element coupled to other beam elements that have an ideal elastoplastic behavior. This conception is aimed to take into account the stick-slip of inner filaments [9]. The bending stiffness (EI) of the messenger cable is an important parameter for the dynamical response and its behavior is related to the curvature (κ). The bending stiffness varies between EI_{min} (where filaments can slip freely and only the stiffness of each filament with respect to its local neutral axis is taken into account) and EI_{max} (where all filaments are stuck as a solid body). The bending moment (M_f) can be approximated by Eq. (2), where the bending stiffness is calculated according to the stick-slip variation along the beam with Eq. (3).

$$M_f \approx EI\kappa, \forall EI = fnc(\kappa) \tag{2}$$

$$EI = EI_{max} = EI_{\min} + EI_{stick} \quad or \quad EI = EI_{\min} + EI_{slip} \tag{3}$$

It has to be mentioned that under a cyclic load one can observe the hysteretic behavior that is responsible for the energy dissipation in the system. The Newmark-beta method is used to integrate the finite element equation $M\ddot{U} + D\dot{U} + KU = F$, where M, D and K are the global matrices of mass, damping and stiffness, respectively; whereas F is the vector of forces and U the vector of kinematic variables. Due to space restrictions, the mathematical formalism of the beam finite element model cannot be expressed, however, the interested readers are invited to look into [8, 9].

2.3 Brief Description of the Stochastic Approach

As explained in Sect. 2.1, in order to infer the input parameters $\mathbf{g}$ of the structural system, the experimental data $\mathbf{y} \in R^N$ (N is the number of independent tests) are such that $\mathbf{y} = \mathbf{y}_m(\mathbf{g}) + \varphi$,where $\mathbf{y}_m(\mathbf{g})$ is the mathematical representation of the system (or predictive model) and the term φ represents the discrepancy between experimental data and the predictive model [10]. The Bayesian Inference requires the proposal of prior PDFs of the parameters to be identified. This can be done by applying the Maximum Entropy Principle based on given information about the physics of the problem. In the present study, the following parameters are considered stochastic: μ (bending stiffness of external filaments), ε (eccentricity of the lumped mass), δ (bending stiffness of the messenger cable core), λ (limit bending moment of the external filaments).

    The Bayesian Inversion procedure employed in this article appeals to a Markov-Chain Monte Carlo simulation through the Metropolis-Hastings algorithm implemented with the software UQLab [11]. The direct use of this procedure requires a lot of realizations of the deterministic predictive model for the aleatory input parameters. In order to reduce the computational cost, a meta-model was implemented (by means

of the predictive deterministic model) to evaluate the dynamic response of the Stock-bridge. Among all the available platforms to construct the meta-model, in this article the Polynomial-Chaos-Kriging (PCK) approach is employed [12].

Finally, once the parameters are identified (and consequently their posterior PDFs), the propagation of uncertainty is carried out by means of realizations of the predictive model whose sampling is performed in the frame of the Latin Hypercube method.

3   Casuistic Study and Results

In this section, a particular Stockbridge as the one sketched in Fig. 1(b) is evaluated. Since some data is not available from the manufacturer, A, B, C, D and M have been gathered from a 3D solid model employing the measuring tools of the CAD software Solidworks™. The following values were obtained: A = 0.138 m, B = 0.030 m, C = 0.020 m, D = 0.088 m, M = 0.640 kg. With these values, it is possible to calculate realizations in the predictive deterministic model and/or the PCK meta-model. The calibration of the PCK meta-model was carried out from 81 evaluations of the numerical deterministic model at 32 frequencies of interest (from 5 Hz to 37 Hz).
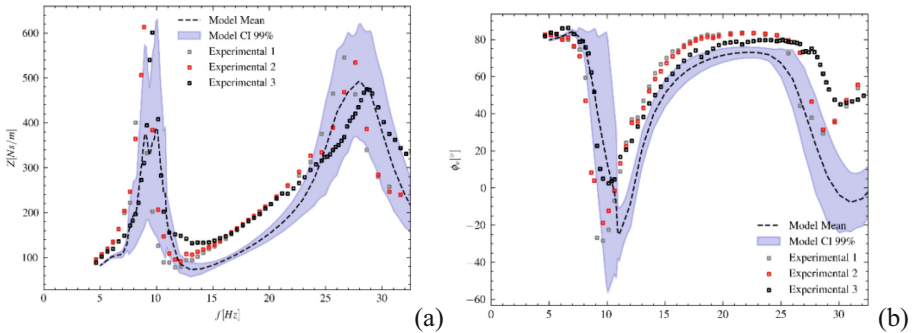
Fig. 3. Experimental results and uncertainty propagation (a) Mechanical impedance. (b) Phase angle of the impedance.

Figure 3(a) and Fig. 3(b) show the uncertainty propagation of the Impedance and its phase angle, respectively; for the calibrated numerical model contrasted with the experimental data. A good fit of the predictive model with the experimental info of the damper in the frequency range of interest is evidenced. In this sense, it should be noted that the resonance frequencies of the model, both flexional (first mode) and torsional (second mode), correspond satisfactorily with the experimental observations. The uncertainty propagation of the angle phase fits adequately the experimental data in most of the frequency range. However, discrepancies appear in higher frequencies, after the second resonance mode. Notice that after 25 Hz, there is divergence.

4 Conclusions

The proposed methodology allows modeling the non-linear dynamic behavior of the Stockbridge considering the variability of the design nominal parameters. By applying the PCK meta-model, the computational cost associated with the evaluation of the inverse problem (and/or parameter identification) is significantly reduced. The quantification of the uncertainty allows evaluating the variability of the Stockbridge response.

Finally, the computational tool developed will allow the assembly of the Stockbridge model in a global system of finite elements of increasing complexity, such as the cable-damper assembly, in order to analyze the vibrational behavior against wind actions of a stochastic nature. In particular, it is proposed to evaluate in future works the reliability of the damping system of the line from the application of numerical optimization techniques. Moreover, other stochastic methods (such as Non-parametric Probabilistic Approach) and enriched beam non-linear formulations are being evaluated to extend the analysis of the Stockbridge, but this is part of a forthcoming paper.

References

1. Chan, J.: Updating the EPRI transmission line reference book: Wind-induced conductor motion ('The Orange Book'). EPRI, 3(3) (2005)
2. Hagedorn, P.: On the computation of damped wind-excited vibrations of overhead transmissions lines. J. Sound Vib. **83**, 253–271 (1982)
3. Wang, Z., Li, H.N., Song, G.: Aeolian vibration control of power transmission line using stockbridge type dampers - a review. Int. J. Struct. Stab. Dyn. **21**(1), 1–29 (2021)
4. Barry, O.R.: Vibration Modeling and Analysis of a Single Conductor with Stockbridge Dampers. University of Toronto (2014)
5. Barry, O.R., Zu, J.W., Oguamanam, D.C.D.: Nonlinear dynamics of stockbridge dampers. J. Dyn. Syst., Meas. Control (ASME) **137**(6), 1–7 (2015)
6. Langlois, S., Legeron, F.: Prediction of aeolian vibration on transmission-line conductors using a nonlinear time history model - part I: Damper model. IEEE Trans. Power Delivery **29**(3), 1168–1175 (2014)
7. International Electrotechnical Commission. IEC 61897: Overhead lines - Requirements and tests for Aeolian vibration. IEC (2020)
8. Électricité de France: Analysis of Structures and Thermomechanics for Studies and Research, Code ASTER home page https://www.code-aster.org/. Last accessed 10 May 2022
9. Papailiou, K.O.: On the bending stiffness of transmission line conductors. IEEE Trans. Power Delivery **12**(4), 1576–1583 (1997)
10. Aster, R., Borchers, B., Thurber, C.: Parameter Estimation and Inverse Problems, Elsevier (2019)
11. Marelli, S., Sudret, B.: UQLAB: a framework for uncertainty quantification in matlab. In: Proceedings 2nd International Conference on Vulnerability, Risk Analysis and Management, ICVRAM2014, Liverpool, United Kingdom (2014)
12. Schöbi, R., Sudret, B., Wiart, J.: Polynomial-chaos-based kriging. Int. J. Uncertain. Quantif. **5**, 71 (2015)

Study and Optimization of a Numerical Algorithm for Hydrodynamic Lubrication Problems with Cavitation

Pedro Gómez Molina[1]($\boxtimes$), Jaime Carpio Huertas[2], and Luis Sanz Lorenzo[1]

[1] Departamento de Matemática Aplicada a La Ingeniería Industrial, Universidad Politécnica de Madrid, Madrid, Spain
pedro.gomezm@alumnos.upm.es, luis.sanz@upm.es

[2] Departamento de Ingeniería Energética, Universidad Politécnica de Madrid, Madrid, Spain
jaime.carpio@upm.es

Abstract. We present a study of a method to solve numerically stationary problems of hydrodynamic lubrication with cavitation in bearings using the finite element method and the method of characteristics. The problem is based on the Elrod-Adams mathematic model for the lubricant fluid behavior. To achieve realistic pressure solutions, cavitation must be considered. However, this leads to a non-linear system of equations including a multivalued operator. To solve this problem, we use the Bermúdez-Moreno algorithm combining its ideas with a mesh intersection technique, known as supermesh, to compute certain integrals exactly, and with other strategies to improve the performance of the iterative method. We have studied the solutions, the precision in mass conservation and the speed of convergence of the method trying to improve it. Results of the simulations are presented and analyzed.

Keywords: Hydrodynamic lubrication · Method of Characteristics · Supermesh technique · FEM

1 Introduction

Tribology is the science that studies the interaction between surfaces. One of its main fields of study is the minimization of friction and wear, and one of the most common solutions to reduce these phenomena is lubrication. The lubricant can be considered a third body that is placed between two surfaces to prevent contact between them and facilitate their relative movement [1].

One of the most common applications of lubrication lies in hydrodynamic bearings. These consist of a static element named hub with a cylindrical hollow in which a shaft is housed. For their study, starting from the basic equations of fluid mechanics and accepting certain fundamental hypotheses, we reach the most common starting point, the Reynolds equation. This, for the case of incompressible fluid in bearings is:

$$\frac{\partial}{\partial\theta}\left(\frac{h^3}{R^2\eta}\frac{\partial p}{\partial\theta}\right) + \frac{\partial}{\partial z}\left(\frac{h^3}{\eta}\frac{\partial p}{\partial z}\right) = 6\omega\frac{\partial h}{\partial\theta}, \tag{1}$$

where θ is the angular coordinate, z is the axial coordinate, η is the dynamic viscosity, ω is the rotational speed and h is the film thickness, for which an analytical expression is known,

$$h = C + e\cdot\cos(\theta) = C(1 + \epsilon\cdot\cos(\theta)), \tag{2}$$

where C is the difference of radii between hub and shaft, e is the distance between centers, called eccentricity, and ϵ is the eccentricity coefficient.

From (1) it is possible to approximate analytical solutions for the pressure distribution when either L $\gg$ D or L $\ll$ D is satisfied, L being the axial length of the bearing and D its diameter. However, in bearings one usually has L $\approx$ D, so it becomes necessary to solve numerically the two-dimensional Reynolds equation. To reach realistic solutions, cavitation of the fluid must be considered in the model.

The model used in this work, known as the Elrod-Adams model, is complemented by the Floberg condition on the boundary between the cavitation and non-cavitation regions [2]. The boundary between these regions is not known at the beginning of the problem and must be found, meaning this is a free boundary problem. The approach involves introducing an additional variable, denoted by γ, which is the mass fraction of liquid lubricant.

The value of γ is equal to one in the non-cavitation zone ($p > p_v$), and $0 \leq \gamma < 1$ is satisfied in the cavitation region ($p = p_v$). The relation between the pressure p and γ is given through the so-called maximal monotonic operator, H, which is multivalued and introduces into the problem a nonlinear relation, $\gamma \in H(p)$.

Let Ω be the domain $[0,2\pi] \times [0,L/R]$ resulting from the nondimensionalization of the variables θ and z. This can be seen in Fig. 1. The dimensionless pressure function, $\bar{p}$ must satisfy the Reynolds equation in the region where there is no cavitation. In the cavitation zone, denoted by Ω_C, this equation does not model the fluid behaviour.
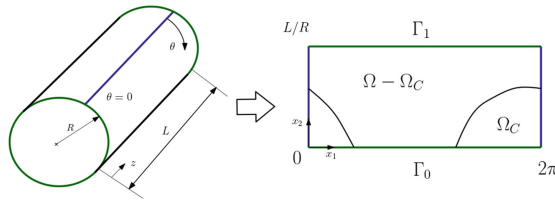
Fig. 1. Non-dimensional domain of the problem. Source: own elaboration

These ideas lead to the Elrod-Adams mathematical model. In papers such as [2, 3] and [4] the existence and uniqueness of solution of the Elrod-Adams model is proved. It is also obtained that the associated weak problem is:

Find $(\bar{p}, \gamma) \in K \times L^\infty(\Omega)$ so that:

$$
\begin{cases}
\int\limits_{\Omega} \bar{h}^3 \nabla \bar{p} \cdot \nabla \varphi + \int\limits_{\Omega} \frac{\partial(\bar{h}\gamma)}{\partial x_1} \cdot \varphi = 0, \ \forall \varphi \in K_0 \\
\gamma \in H(\bar{p}) \\
p(x=0, y) = p(x = 2\pi, y); p(x, y = 0) = 0; p\left(x, y = \frac{L}{R}\right) = \Delta p
\end{cases}
\tag{3}
$$

2 Methodology

In order to solve this problem numerically, a strategy based on the ideas of [2] and [3] will be used, which makes use of the method of characteristics and the Bermudez-Moreno algorithm [5].

2.1 Method of Characteristics

First, the problem is transformed into an evolution one, so that the solution sought is the stationary state of the problem. An artificial time dependence t is introduced in all the functions of the problem and denoted by " ~ ". Using an artificial velocity field $\vec{V}(x_1, x_2) = (1, 0)$, the derivative in the problem is expressed as a material derivative.

We denote by $X^k(x)$ the position at instant t-k of a particle that reaches at instant t the position x when convected by the velocity field. The material derivative operator in this case can be discretized with time step k and, following the ideas of [2], one can formulate the weak problem as a fixed-point iteration problem.

Given $\tilde{\gamma}^n$, find $\tilde{p}^{n+1}$ y $\tilde{\gamma}^{n+1}$ such that:

$$
\begin{cases}
k \int\limits_{\Omega} \tilde{h}^3 \nabla \tilde{p}^{n+1} \cdot \nabla \varphi + \int\limits_{\Omega} \tilde{h}\tilde{\gamma}^{n+1}\varphi = \int\limits_{\Omega}\left(\left(\tilde{h}\tilde{\gamma}^n\right) \circ X^k\right)\varphi \forall \varphi \in K_0 \\
\tilde{\gamma}^{n+1} \in H\left(\tilde{p}^{n+1}\right)
\end{cases}
\tag{4}
$$

If this iteration converges it will converge to the solution of the weak problem, $(\tilde{p}, \tilde{\gamma})$.

2.2 Bermúdez-Moreno Algorithm

This algorithm introduces the variable $\beta^{n+1} = \gamma^{n+1} - \omega p^{n+1}$ in the problem and applies certain transformations to convert the problem into one with univalued operators. The goal is to apply the Yosida regularization, H_λ^ω [5] and use the property that if one employs suitable ω and λ, then

$$
\beta \in (H - \omega I)(p) \Leftrightarrow \beta = H_\lambda^\omega(p + \lambda\beta)
\tag{5}
$$

The advantage of H_λ^ω is that it is univalued. This means that it is possible to find β^{n+1} as the solution of the fixed-point problem $\beta^{n+1} = H_\lambda^\omega\left(p^{n+1} + \lambda\beta^{n+1}\right)$. Thus, we must introduce a second fixed-point iteration, in j, where the problem to be solved is:

Given β_j^{n+1}, find $\tilde{p}_j^{n+1}$ y β_{j+1}^{n+1} such that:

$$
\begin{cases}
k \int\limits_\Omega \tilde{h}^3 \nabla \tilde{p}_j^{n+1} \cdot \nabla \varphi + \omega \int\limits_\Omega \tilde{h} \tilde{p}_j^{n+1} \varphi = \int\limits_\Omega \left(\left(\tilde{h} \tilde{\gamma}^n \right) \circ X^k \right) \varphi - \int\limits_\Omega \tilde{h} \beta_j^{n+1} \varphi \, \forall \varphi \in K_0 \\
\beta_j^{n+1} = H_\lambda^\omega \left(\tilde{p}_j^{n+1} + \lambda \beta_j^{n+1} \right)
\end{cases}
\tag{6}
$$

We now have a double fixed-point iteration. Within each iteration in n, in order to obtain the solutions ($\tilde{p}^{n+1}$, $\tilde{\gamma}^{n+1}$), the convergence of the Bermudez-Moreno iterations must be reached in j, which provides new values $\tilde{p}^{n+1}$ and β^{n+1} which will be used to update the value of $\tilde{\gamma}^{n+1}$.

Upon reaching convergence of the iterations in n, the values of $\tilde{p}$ and $\tilde{\gamma}$ obtained are the solution of the weak problem (4). This convergence is guaranteed by [6] provided that the chosen method parameters satisfy $\lambda \cdot \omega = 0.5$. A spatial discretization based on the finite element method (FEM) is employed to solve this problem.

2.3 Mass Conservation

The equations of the lubrication problem guarantee that the fluid mass in the domain must be conserved upon convergence of the iterative method. The use of the FEM guarantees the mass conservation if the integrals that appear in the weak formulation are calculated exactly. However, when applying the FEM, the presence of X^k in the terms implies that some integrals are not computed exactly when using the conventional approach, which results in an error in mass conservation.

One option to keep the mass error small is to use a large number of quadrature points to find a good approximation [7], and another option to achieve an accurate machine error calculation in these terms, is to use mesh intersection methods such as the supermesh technique [8]. In this work, both approaches have been employed to compare their results. The construction of the supermesh is performed with a local approach according to the algorithm explained in [8].

3 Results

3.1 Model Validation

The numerical model should provide solutions similar to the analytical ones in the cases where these are valid. In addition, the parameter values obtained with the numerical model in the area where L $\approx$ D, must present a coherent and smooth evolution in relation to those predicted by the analytical solutions in their area of application.

To verify this behaviour, a study of the evolution of the Sommerfeld number as a function of L/D is carried out. The results in Fig. 2 show the expected evolution.
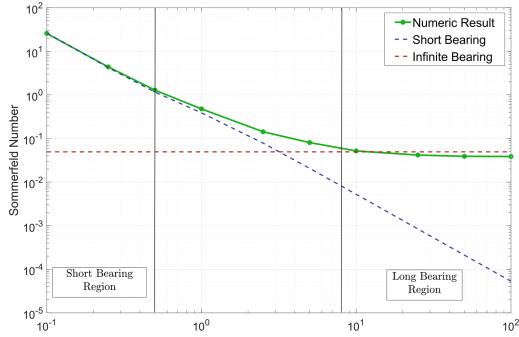
Fig. 2. Evolution of Sommerfeld number as a function of bearing axial length. Comparison with analytical solutions. Source: own elaboration.

3.2 Convergence Study

It is known that the convergence speed of the Bermudez-Moreno algorithm depends largely on the choice of the parameter ω [5]. A study, particularized to the lubrication problem, of the optimal value of ω, i.e., the one that provides the minimum number of iterations until convergence, has been carried out, checking the influence on this optimal value of the rest of the input parameters of the model.

The total number of iterations of the Bermudez-Moreno algorithm, at index j, is analysed for 80 iterations in n, after verifying that for this number of iterations in n the process can be considered to have reached convergence. The influence of physical and numerical parameters of the model on the value of the optimal ω is analysed.

The results show a dependence of the optimal ω as a function of other parameters of the model. Some input variables, such as the mesh size, keep the optimum at a practically constant value, but others make the optimum value of ω vary significantly.

3.3 Mass Conservation Study

In the problem, the lubricant mass in the domain must remain constant at the steady state, i.e., when $n \rightarrow \infty$. Mass errors appear only for numerical reasons. A study of the mass error is carried out varying the iterative method tolerance and the integration technique for integrals where X^k is present.

The graphs in Fig. 3 show the results. As expected, the accuracy improves as the stopping tolerance of the iterative method is reduced. It is also found that the use of the supermesh technique can achieve results up to 5 orders of magnitude more accurate when combined with a small tolerance. This study also shows that in certain cases the supermesh achieves lower computational cost than the conventional approach.
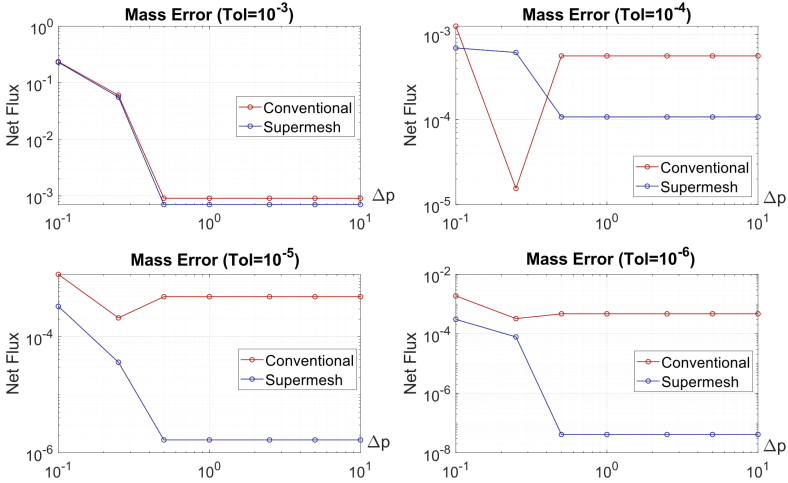
Fig. 3. Flow errors for different stopping tolerances using conventional L^2 projection and Supermesh technique for the calculation of terms composed with X^k. Source: own elaboration.

4   Conclusions

This work starts with the Elrod-Adams model for hydrodynamic bearings. The model leads to a free boundary problem as the limits of the zones with and without cavitation are not known. To deal with it, the variable γ is introduced.

In the associated weak problem, a nonlinear relationship between the unknowns of the problem appears through a multivalued operator. To solve the problem, the method of characteristics and the iterative algorithm of Bermudez-Moreno [5] are introduced, obtaining a double fixed-point iteration that is solved using the finite element method for spatial discretization.

The proposed algorithm has been implemented in the C programming language to perform the simulations. In addition, the functions of the supermesh technique have been incorporated in order to calculate exactly certain integrals that appear when applying the method of the characteristics.

A study was executed comparing the numerical solutions with the analytical solutions in the cases where these are accepted, which allowed the model to be validated.

Finally, we have conducted a study of the performance of the algorithm and of the mass error. In this aspect, although the use of the supermesh technique considerably improves the mass conservation accuracy, the truncation error inherent to the Bermudez-Moreno method makes it difficult to achieve a mass error at the machine error level, as it is the case when applying this technique to pure convection problems [8].

References

1. Ghosh, M.K., Majumdar, B.C., Sarangi, Y.M.: Theory of Lubrication, Tata McGraw Hill (2013)
2. Bermúdez, A., Durany, Y.J.: Numerical solution of cavitation problems in lubrication. Comput. Methods in Appl. Mech. Eng. **75**, 457–466 (1989)

3. Calvo, N., Durany, J., Vázquez, Y.C.: Comparación de Algoritmos Numéricos en Problemas de Lubricación Hidrodinámica con Cavitación en Dimensión Uno, Revista Internacional de Métodos Numéricos para Cálculo y Diseño en Ingeniería **13**, 2 185–209 (1997)
4. Durany, J., Vazquez, C., Calvo, Y.N.: Comparación de algoritmos numéricos en problemas de lubricación hidrodinámica con cavitación en dimensión uno. Revista Internacional de Métodos Numéricos para Cálculo y Diseño en Ingeniería **13** 2, 185–209 (1997)
5. Bermúdez, A., Moreno, Y.C.: Duality methods for solving variational inequalities. Comput. Math. Appl. **7**, 43–58 (1979)
6. Parés, C., Castro, M., Macías, Y.J.: On the convergence of the Bermúdez-Moreno algorithm with constant parameters. Numer. Math. **92**(1), 113–128 (2002). https://doi.org/10.1007/s002110100352
7. Bermejo, R., Carpio, J., Saavedra, L.: New error estimates of Lagrange-Galerkin methods for the advection equation. Submitted (2022)
8. Gómez-Molina, P., Carpio, J., Sanz-Lorenzo, L.: A stable conservative Lagrange-Galerkin scheme to pure convection equations with mesh intersection, Submitted to Journal of Computational Physics (2022)

Wake Interactions in an Asymmetric Binary Cylinder System in the Subcritical – Supercritical Regime

Joseph Rozas Rozas[1,2(✉)] and Rodrigo Hernández Pellicer[1]

[1] Laboratorio de Estudios Avanzados en Fenómenos no Lineales LEAF-NL, Departamento de Ingeniería Mecánica, Universidad de Chile, Santiago, Chile
joseph.rozas@ug.uchile.cl

[2] Centro de Investigación y Desarrollo en Ciencias Aeroespaciales (CIDCA), Fuerza Aérea de Chile, Casilla, 8020744 Santiago, Chile

Abstract. Experimental results on the interaction between the wakes of a formed by two cylinders (binary) of different diameters are presented. The binary system is introduced into a pond with water and coupled to a system with linear displacement, causing the development of a Bérnard von Kármán (BvK) stability through the relative movement between the body and the fluid. The dynamics of the wakes are characterized through a PIV (Particle Image Velocimetry) algorithm using a CCD sensor coupled to the solidarity movement of the system. On the other hand, the visualization is done using the hydrogen bubble technique. The measurements of the velocity profiles allowed us to analyze characterize the dynamic behavior od the wakes in the subcritical-supercritical rage of the Reynolds number. The result of the analysis with PIV allows for obtaining profiles of average speed. In addition, it allowed determining the vortex emission frequency of the system in the wakes of both cylinders at beginning of the von Kármán instability.

Keywords: Wake · binary system · PIV · BvK instability

1 Introduction

The study of wake dynamics, which originated from the interaction between a body and a fluid stream, has been an important field of research. On the one hand, this type of research is developed with the interest of studying the effect on structural engineering components that can be affected by dynamics loads originated by the interaction with a fluid: heat exchange lines, marine structures, chimneys, bridges, energy recovery system, among other [1, 2]. On the other hand, in many of these applications, vortex shedding emits acoustic noise and flow-induced vibrations [3]. In this context, researches on the modification of wakes to attenuate and/or control vortex emission have been relevant for developing passive and active devices considered in engineering systems [4–6].

On the other hand, cylinders introduced in a fluid stream are used as a "test bed" to explore the wake instability in open flows [7]. For a stationary system composed

of a cylinder, the Reynolds number is an important indicator for the formation of a non-stationary wake. This condition is obtained when a critical Reynolds number is reached [8], initiating the well-known Bérnard von Kármán (BvK) street. Under the critical Reynolds, the wake is stationary, forming a symmetric pair of vortices attached to the body's surface called a recirculation bubble. The bubble growth is linear as the Reynolds number increases [9]. The interaction of wakes developed by a binary cylinder system could activate or deactivate the shedding of vortices in the vicinity of critical Reynolds; in this sense, the present work seeks to study the interaction around considering a two-dimensional flow regime (see Fig. 1).

2 Methodology
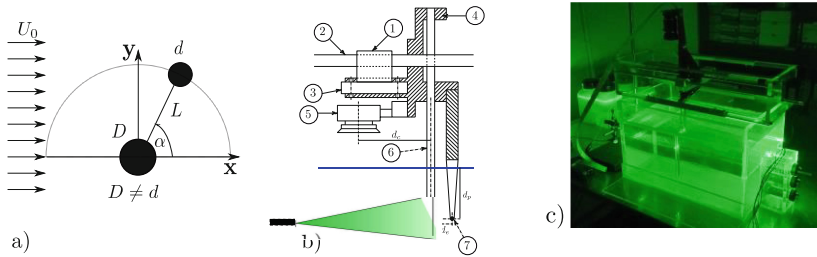
Fig. 1. a) Schematic of a binary system using cylinders in different positions (D: diameter of the main cylinder, d: diameter of the secondary cylinder, L: distance between centers, alpha: position angle, Uo velocity of the linear movement of the carriage). b) Schematic of the system coupling 1) linear bearing; 2) rail; 3) connection platform with bearings; 4) mounting structure for the camera, electrode, and cylinders; 5) CCD sensor; 6) cylinders; 7) electrode. c) Illumination for PIV. The MATLAB PIVLab algorithm is used [10]

2.1 Water Tank

The binary system is introduced into the tank and coupled to a carriage with linear motion. Since the Reynolds number involved is low (of the order of the critical Reynolds), the BvK instability develops through the relative movement between the binary system and the water initially at rest.

On the other hand, hydrogen bubbles are used to visualize the vortex structures downstream of the cylinder system [11]. A 50 µm diameter platinum wire is used as the cathode, while imaging is performed by a Sony IMX477 camera (CCD sensor) which is activated by a Raspberry. For the PIV analysis, tracer particles are incorporated in the water pond (Sphericel 110P8) of 11.7 µm diameter. The sampling frequency of the camera was adjusted to 30 fps to comply with the Nyquist principle [12].

2.2 Wind Tunnel

The velocity profiles measured with PIV were compared with measurements in a closed-loop subsonic wind tunnel with two test sections for high and low velocity [13]. The measuring instrument is a hot wire anemometer located downstream of the system. The digital signal is prepared through a low-pass filter (Hz), an offset adjustment, and an amplifier of the filtered signal.

3 Results

3.1 Single Cylinder
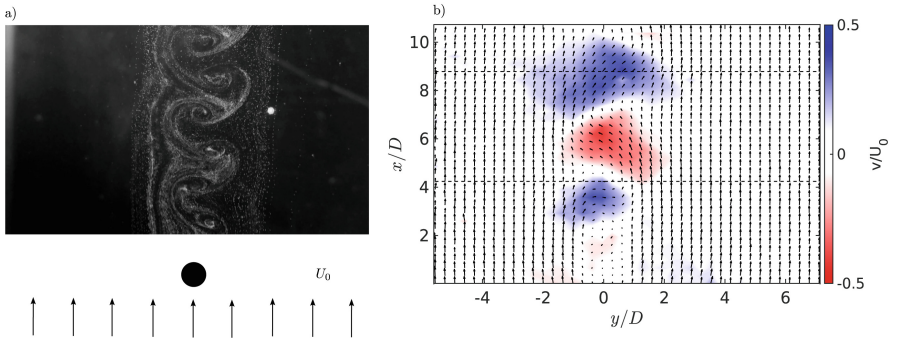
Fig. 2. Measurement and visualization system in a tank with water: D = 6.4 mm, Re = 67. a) Visualization of the Bérnard von Kármán Instability using hydrogen bubbles. b) Measure the transverse component of velocity dimensionless with the free stream velocity.

The Bernard von Kárman instability is visualized in Fig. 2-a) through the hydrogen bubble technique, showing the advection of vortices downstream of the cylinder (relative motion). In Fig. 2-b), the transverse velocity field dimensionless with the free stream velocity, obtained through PIV. Two segmented lines (x/D = 4.2 and x/D = 8.8) are drawn to measure the profile of velocities averaged downstream of the cylinder position.

3.2 Binary System Wakes Measured in Water

$\alpha = 90°$ In Fig. 3-a), the wakes and the activation of the instability of the secondary cylinder by the wake of the main cylinder can be seen. On the other hand, Fig. 3-b) presents the transverse component of the velocity field whose alternation of the main cylinder wake is coupled with the instability activation of the secondary cylinder wake. The averaged velocity profile is presented in Fig. 4, and the asymmetric shape of the profile can be visualized from an asymmetric configuration of the binary system.

$\alpha = 75°$ The results of the visualization and velocity field are presented in Fig. 5. It is observed that both wakes develop with vortex emission downstream of the system. Qualitatively, it is observed that the development of the wakes is closer to each other

because the "y" component of the distance between cylinder centers decreases due to the inclination of the secondary cylinder. This condition impacts the increase in the size of the vortices generated downstream of the secondary cylinder compared to the position of the secondary cylinder.
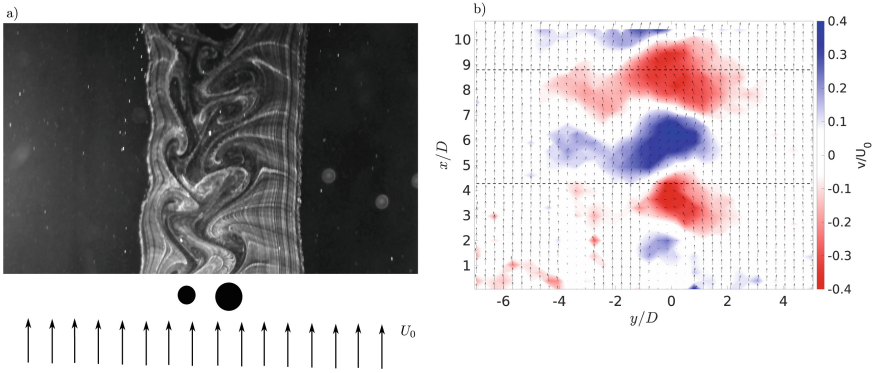
Fig. 3. A binary system under a configuration of $\alpha = 90°$. $D = 6.4$ mm, $d = 3.9$ mm, $L = 20$ mm, $Re_D = 67$, $Re_d = 42$. a) Visualization with HB. b) Field of the transverse component of velocities using PIV technique.
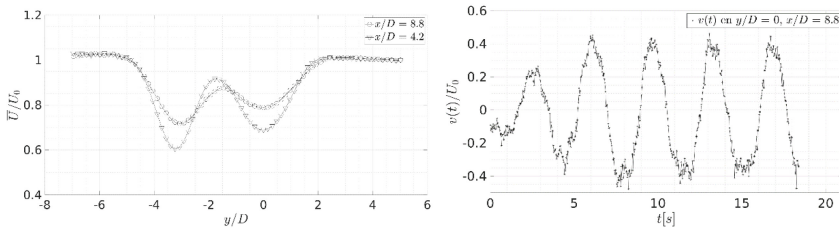
Fig. 4. $\alpha = 90°$. Average velocity profile and time evolution of the transverse component of the velocity.

Figure 6 shows the averaged velocity profile for the asymmetric configuration of $\alpha = 75°$. It can be seen that for positions closer to the binary system (decrease of "x"), the shape of the profile takes a symmetric condition, whose average velocity perturbation of the main cylinder is of the same order as the average perturbation of the secondary cylinder. A decrease in the intensity of the transverse velocity component is observed compared to the values presented for the condition of $\alpha = 90°$. However, a longer transient region reappears than the previous configuration but is lower than that of the single cylinder.

3.3 Binary System Wakes Measured in Wind Tunnel

The Fig. 7 shows the profile of averaged velocities measured through hot wire anemometry in a wind tunnel, the shape of average velocities can be seen for $\alpha = 75°$, finding a
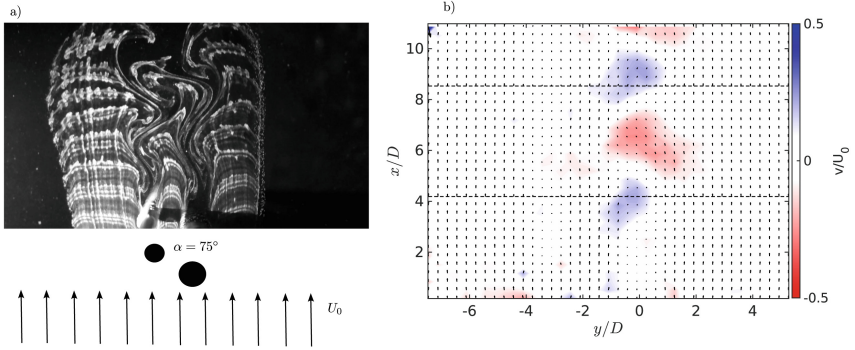
Fig. 5. $\alpha = 75°$, D = 6.4 mm, d = 3.9 mm, L = 20 mm, Re_D = 67, Re_d = 42. a) visualization with HB. B) Field of the transverse component of velocities using PIV technique.
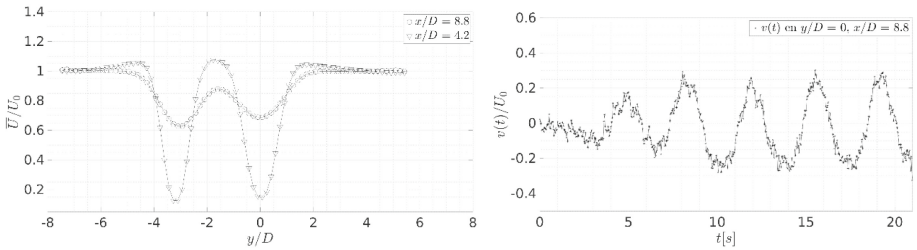
Fig. 6. $\alpha = 75°$. Average velocity profile and time evolution of the transverse component of the velocity

great symmetry analogous to that measured in the tank with water. This effect is interesting because the system that generates the disturbance in the flow is entirely asymmetric (position and size), so there is a strong interaction between the two wakes. The vortex emission frequency is altered under the condition of $\alpha = 75°$. Only one fundamental frequency of the velocity magnitude measured with the anemometer is presented, whose value corresponds to $f_{2c\_75} = 15.8$ Hz.
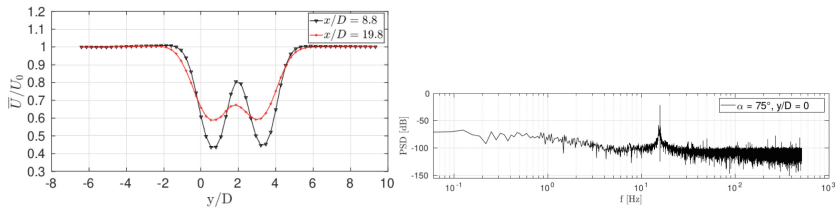
Fig. 7. Average velocity profile measured in a wind tunnel and PSD from x/D = 8.8.

4 Conclusions

Using a secondary cylinder as a passive controller modifies the onset of the system instability, varying the frequency of vortex shedding due to the perturbative interaction between the wakes.

According to the visualizations and velocity field measurements presented, it is inferred that under specific configurations, both cylinders emit vortices, so the emission of the main cylinder excites the wake of the secondary cylinder.

The feedback interactions of both wakes generate a symmetric averaged velocity profile under a completely asymmetric geometrical condition (different diameters and forward position of the secondary cylinder).

For future work, other positions and sizes of the second cylinder will be studied, mainly for the description of the asymmetric region, applying other measurement techniques such as Laser Doppler anemometry to measure the effect of the interaction between wakes.

References

1. Bernitsas, M.M., Raghavan, K., Ben-Simon, Y., Garcia, E.M.H.: VIVACE (vortex induced vibration aquatic clean energy): a new concept in generation of clean and renewable energy from fluid flow. J. Offshore Mech. Arct. Eng. **130**(4), 041101 (2008)
2. Blevins, R.D.: Flow-Induced Vibration (2001)
3. Zhou, Y., Alam, Y.M.: Wake of two interacting circular cylinders: a review. Int. J. Heat Fluid **62**, 510–537 (2016)
4. Zdravkovich, M.M.: Review and classification of various aerodynamic and hydrodynamic means for suppressing vortex shedding. J. Wind Eng. Ind. Aerodyn. **7**, 145–189 (1981)
5. Bhattacharya, Gregory, J.W.: Effect of three dimensional plasma actuation on the wake of a circular cy-linder. AIAA J. **53**, 958–967 (2015)
6. Yang: Revisiting coherent structures in low-speed turbulent boundary layer. Appl. Math. Mech. **39**, 1–11 (2018)
7. Cantwell, C.D., Barkley, D.: Computational study of subcritical response in flow past a circular cylinder. Phys. Rev. E **82**(2), 1–13 (2010)
8. Mathis, C., Boyer, L.: Benard-von Karman instability: transient and forced regimes. J. Fluid Mech. **182**, 1–22 (1987)
9. Nishioka, M., Sato, H.: Mechanism of determination of the shedding frequency of vortices behind a cylinder at low reynolds numbers. J. Fluid Mech. **89**(1), 49–60 (1978)
10. Thielicke, W., Sonntag, R.: Velocimetría de imágenes de partículas para MATLAB: precisión y algoritmos mejorados en PIVlab. J. Open Res. Softw. **9**, 12 (2021). https://doi.org/10.5334/jors.334
11. Smits, A.J.: .Flow visualization: techniques and examples2.aed. World Scientific (2010)

12. Oppenheim, A., Schafer, R.: Tratamiento de señales entiempo discreto3.aed. (Pearson Educación) (2011)
13. Hernández, H., Sánchez, M.: Localized Bénard-von Karman vortex wake packets. Europhys. Lett. **58**, 222–228 (2002)

Contribution to Mathematical Modeling and Numerical Simulation of Welding Processes

Mario Freire-Torres(✉) [ID] and Jaime Carpio [ID]

Departamento de Ingeniería Energética, E.T.S. Ingenieros Industriales, Universidad Politécnica de Madrid, 28006 Madrid, Spain
mario.freire.torres@alumnos.upm.es

Abstract. The present work describes a mathematical model for the numerical simulation of the welding process. Initially, the domain Ω is solid to which the heat is released in certain areas. This heat increases the temperature of the solid, and when the fusion temperature is reached, the phase change occurs. At the fusion temperature, there is a mixture between liquid and solid (modelled as a porous medium); above this temperature mentioned; we will find only liquid. Natural convection currents can occur in the liquid due to buoyancy induced by the gravitational field. In order to reproduce all the phenomenology described, the mathematical model will be based on the energy conservation equation, expressed in terms of enthalpy, together with the mass and momentum conservation equations to determine the velocity of the fluid. The numerical resolution of the equations will be carried out with a Lagrange-Galerkin formulation in a finite element framework, where a temporal discretization BDF2 scheme will be used.

Keywords: Welding Problems · Numerical Simulation · Lagrange-Galerkin scheme · BDF2 scheme

1 Introduction

1.1 Welding Problem

Welding is one of the most critical manufacturing processes in the world of metallurgy; it is present in the industry due to its versatility when joining parts of complex structures, providing economic and technological advantages. With the development of computational techniques, the welding and metallurgy industry has opted for the mathematical modeling of the physical processes that characterize the phenomenon and allow us to understand the thermomechanical behavior of the physical variables involved in the manufacturing process [1].

In this work, the scheme of Fig. 1 will be considered to analyze the welding process. A heat source travels through a solid and communicates a heat power that increases its temperature. When the melting temperature of the material T_F is reached, the solid begins to melt, passing some areas to a liquid part. In the fusion zone, the temperature is kept constant, and the heat is used in the phase change, appearing a mixing zone

(called 'mushy region'), where the liquid and solid phases coexist. When all the solid has melted locally, the resulting liquid can continue to increase its temperature when it receives heat (or, conversely, the liquid solidifies if it gives up heat to other parts of the solid or the environment). When the molten zone increases its temperature $T > T_F$, and in the presence of the gravitational field, it generates convection currents due to the buoyancy induced by gravity.
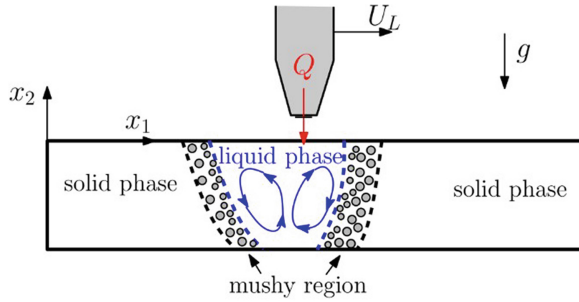
Fig. 1. Diagram of the welding process considered in this work.

Joint modeling of the three zones appearing in the domain (solid phase, liquid phase, and mixing zone) will be carried out to study this phenomenon. To do this, the energy conservation equation written in terms of enthalpy is proposed, together with mass and momentum conservation equations to determine the velocity of the fluid when it appears. It is noted that most of the models presented in the literature formulate the energy equation solely in terms of temperature. An approach that is erroneous if one wants to realistically describe the melting zone in pure materials that are kept at a constant temperature while the phase change occurs.

Numerous numerical methods are used to numerically solve problems of a metallurgical nature, such as the Galerkin method for free elements [2], the Petrov-Galerkin method [3], the finite volume method [4] and the finite element method [5]. In this work, a Lagrange-Galerkin scheme in a finite element framework [6–9] has been used to solve the mathematical model.

2 Mathematical Modeling

2.1 Equations of Conservation of Mass and Momentum

In the first place, the equations of conservation of mass and momentum are presented to calculate the velocity field of the liquid phase. To simplify the model, it will be considered that the density of the solid and the liquid is the same, a constant value that does not depend on the temperature or the stress state of the solid.

For the momentum equation, we assume that the liquid behaves as a Newtonian fluid with constant viscosity and the density variation due to temperature changes are only retained in the buoyancy term according to the Boussinesq model in the molten zone. On the other hand, to model the flow of fluid through porous media, the Darcy model [10] has also been considered.

2.2   Equation of Energy Conservation

For the description of welding problems, the enthalpy h, is revealed as the most appropriate state variable to describe the mixed zone, where the solid and liquid phases coexist. Leaving all the equations as the dimensionless form in the following way:

$$
\begin{cases}
\nabla^* \cdot \mathbf{v}^* = 0, \\[2mm]
\frac{\partial \mathbf{v}^*}{\partial t^*} + (\mathbf{v}^* \cdot \nabla^*)\mathbf{v}^* = -\nabla^* p^* + \frac{1}{Re}\Delta^* \mathbf{v}^* + \frac{Gr}{Re^2}(\theta - 1)\mathbf{e}_{x_2} - \frac{1}{ReDa}\frac{(1-Y_L)^2}{Y_L^3}\mathbf{v}^*, \quad (1) \\[2mm]
\frac{\partial h^*}{\partial t^*} + \nabla^* \cdot (\mathbf{v}^* h^*) = \frac{1}{Pe}\nabla^*(\lambda \nabla^* \theta) + Q^*
\end{cases}
$$

where, the dimensionless variables are: $\mathbf{v}^*$ is the velocity field, p^* is the pressure, θ is the temperature, Y_L is the liquid fraction, h^* is the enthalpy, Q^* is the heat source. On the other hand, we consider the following dimensionless numbers as: Re is the Reynolds Number, Gr is the Grashof Number, Da is the Darcy Number, Pe is the Peclet Number.

3   Numerical Method

For the numerical resolution of the proposed mathematical model, the conservative formulation of the Lagrange-Galerkin scheme will be used. After this, the temporal and spatial discretization will proceed, which will lead us to the matrix problem to be solved. The unknown variables of the problem will be $\mathbf{v}^*$, p^* and h^*; moreover θ, Y_L and $du^* = \lambda d\theta$ will be auxiliar variables which can be expressed as a function of h^*. For a temporal discretization BDF2 scheme will be used. For this purpose, we develop a Newton-type algorithm to solve the energy conservation equation, given its non-linear nature as can be seen in Fig. 2.

Algorithm   Algorithm of Newton to solve the energy equation

Data: $\overline{h}^{n-1}, \overline{h}^{n-2}, \text{Tol}_N$
Result: $\overline{h}^n, \overline{\theta}^n, \overline{u}^n$
initialize $\overline{h}^n_{0)} = \overline{h}^{n-1}$, $\text{error}_N = 1$, $k = 0$;
evaluate $\theta^n_{0)i} = \theta(h^n_{0)i})$, $u^n_{0)i} = u(\theta^n_{0)i})$;
while $\text{error}_N > \text{Tol}_N$ **do**
    calculate $\overline{dh}^n_{k+1)}$, solving: $\overline{\overline{J}}^n_{k)}\ \overline{dh}^n_{k+1)} = -\overline{F}^n_{k)}$;
    calculate $\text{error}_N = \|\overline{h}^n_{k+1)} - \overline{h}^n_{k)}\|_2$;
    increase $k = k + 1$;
    update $\overline{h}^n_{k+1)} = \overline{h}^n_{k)} + \overline{dh}^n_{k+1)}$;
    update $\theta^n_{k)i} = \theta(h^n_{k)i})$, $u^n_{k)i} = u(\theta^n_{k)i})$;
end
calculate $\overline{h}^n = \overline{h}^n_{k)}$, $\theta^n_i = \theta(h^n_i)$, $u^n_i = u(\theta^n_i)$

Fig. 2. A Newton-type algorithm for solving equation of energy conservation.

4 Results

In Figs. 3 and 4 we can see a graphical representation of the solution of our problem in several instants of time. The isolines that mark the border between the solid and liquid area are represented in the lower part of the figures, together with blue current lines that indicate where there is fluid movement. In the upper panel, a section is represented by the line $x_2 = -0.5$ of the domain, to observe the profiles of the thermodynamic variables of the problem and of the vertical component of the velocity field v_{x_2}.

Specifically, Fig. 3, represents the solution in the first moments of time t $\leq$ 1.0 in which the heat source acts. It can be seen that from t $\approx$ 0.25 the heat supplied has managed to warm the solid up to the melting temperature $\theta = 1.0$, and the phase mixing zone begins to appear, called the 'mushy region'. The source in its movement continues to provide heat and at t $\approx$ 0.5 the first zone of pure liquid is observed at temperatures higher than those of fusion. It is from that moment, when the buoyancy terms are no longer zero and the movement of the fluid begins. For longer times, a coexistence of the 3 regions is observed (solid zone, liquid zone, and mixing zone). In the front zone (where the heat source is reaching) the fusion of the solid takes place and presents relatively smooth gradients in the variable enthalpy h. However, in the rear part (where the heat source is away from) the resolidification of the liquid formed takes place, and very marked fronts are formed in the variable enthalpy h around the lines that mark the mixing zone and that causes the area where the phases coexist to shrink.

Once the source is turned off, the phenomenon of cooling and homogenization of the temperature will begin, an effect that can be observed in detail in Fig. 4. In a few instants of time, the area where the phase mixture exists begins to drastically reduce, as a result of resolidification of the material. This disappearance of the mixing zone can be seen very well on the sides and in the upper zone where the movement of the fluid is slower. However, in the lower zone is where the mixing zone is maintained until the last moments of time. On the other hand, as time progresses, the complete disappearance of the mixing zone is observed, leaving only the solid phase and the liquid phase, separated by a zone of discontinuity, which gradually reduces in size due to the heat that is being lost.

But the heat only flows at the edges of the interface, because inside, where the liquid is at a temperature $\theta = 1.0$, there is no heat conduction.
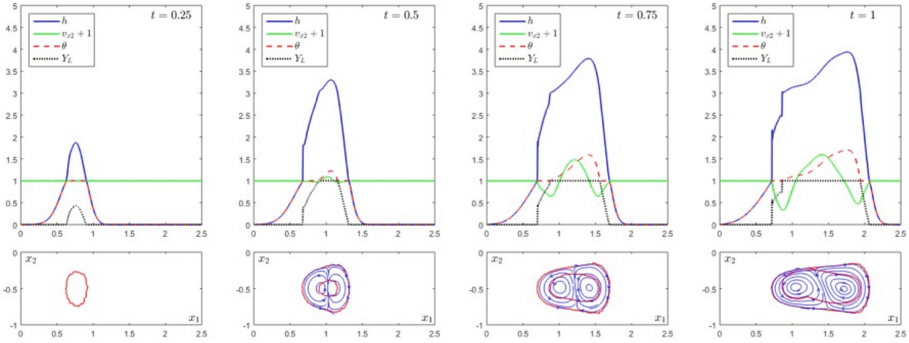
Fig. 3. Solutions obtained in the first moments of time t ≤ 1.0, in which the external heat source Q is acting.
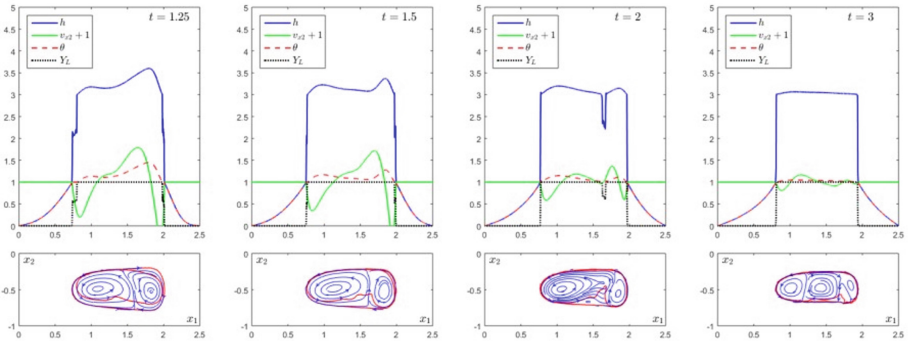
Fig. 4. Solutions obtained in the final moments of time t > 1.0, in which the external heat source Q off.

5 Conclusions

This paper presents a numerical method based on the Lagrange-Galerkin methodology to solve a welding problem. The mathematical model is formulated to correctly define the solid, liquid zone and the mixed or soft zone, which appear in the problem.

The energy equation is written conservatively in the enthalpy variable and Newton's algorithm is used to obtain the value of enthalpy h. The advantage of using the enthalpy state variable h is that the rest of the thermodynamic variables can be written in a monotonic and single-valued way as a function of it. The good properties of Newton's algorithm have been verified in terms of convergence speed, the fact that it does not require additional parameters, and the cheap computational cost to perform the matrix assembly in each iteration.

To describe the velocity field **v**, the laws of conservation of mass and momentum are used, which are valid in all three areas of the material. It is considered an incompressible fluid, except in the buoyancy terms given by the Boussinesq model. The phase mixing zone is considered a porous medium where Darcy's law is considered. To numerically

solve the Stokes problem that is formed, the Uzawa-type conjugate gradient algorithm is used.

Finally, the finite element method with anisotropic mesh adaptation techniques was used to carry out the numerical simulations. This substantially improves the calculation times and the precision obtained.

References

1. Karkhin, V.: Engineering Materials Thermal Processes in Welding. 1st edn. Springer (2019)
2. Álvarez-Hostos, J.C., Bencomo, A.D., Puchi-Cabrera, E.S., Fachinotti, V.D., Tourn, B., Salazar-Bove, J.C.: Implementation of a standard stream-upwind stabilization scheme in the element-free Galerkin based solution of advection-dominated heat transfer problems during solidification in direct chill casting processes. Eng. Anal. Bound. Elem. **106**, 170–181 (2019)
3. Shibahara, M., Atluri, S.N.: The meshless local Petrov-Galerkin method for the analysis of heat conduction due to a moving heat source, in welding. Int. J. Thermal Sci. **50**, 984–992 (2011)
4. Piekarska, W., Kubiak, M.: Three-dimensional model for numerical analysis of thermal phenomena in laser-arc hybrid welding process. Int. J. Heat Mass Transf. **2011**, 4966–4974 (2011)
5. Anca, A., Cardona, A., Risso, J., Fachinotti, V.D.: Finite element modeling of welding processes. Appl. Math. Model. **35**, 688–707 (2011)
6. Bermejo, R., Galán Del Sastre, P., Saavedra, L.: A second order in time modified Lagrange-Galerkin finite element method for the incompressible Navier-Stokes equations. SIAM J. Numer. Anal. **50**, 3084–3109 (2012)
7. Bermejo, R., Saavedra, L.: Finite elements, High Reynolds numbers, Lagrange-Galerkin, Local projection stabilization, Navier-Stokes. Comput. Math. Appl. **72**, 820–845 (2016)
8. Carpio, J., Prieto, J.L.: An anisotropic, fully adaptive algorithm for the solution of convection-dominated equations with semi-Lagrangian schemes. Comput. Methods Appl. Mech. Eng. **273**, 77–99 (2014)
9. Carpio, J., Prieto, J.L., Vera, M.: A local anisotropic adaptive algorithm for the solution of low-Mach transient combustion problems. J. Comput. Phys. **306**, 19–42 (2016)
10. Cho, J.H., Na, S.J.: Three-dimensional analysis of molten pool in GMA-laser hybrid welding. Weld. J. (Miami, Fla) **88**, 35–43 (2009)

Dimensionless Coefficients for Validation and Evaluation of a CFD Methodology Applied to a H-Darrieus Vertical Axis Wind Turbine

Celso Antonio Bittencourt Sales Junior[1] , Angie Lizeth Espinosa Sarmiento[1(✉)] , and Francesco Balduzzi[2]

[1] Federal University of Itajubá, Itajubá, MG 37500-903, Brazil
{celsosalesjunior,angieespinosa}@unifei.edu.br
[2] University of Florence, 50121 Florence, FI, Italy
francesco.balduzzi@unifi.it

Abstract. Small-scale wind turbines can play an important role in the energy transition by providing distributed generation in urban and rural areas. They can help decrease the reliance on traditional forms of energy generation, such as fossil fuels, which can have negative environmental impacts. Thereby, this study aims to implement and complement a computational fluid dynamics (CFD) methodology for predicting the aerodynamic performance of a H-Darrieus Vertical Axis Wind Turbine (VAWT). The analysis of dimensionless numbers, such as Grid-reduced Vorticity (GRV) and Reference Courant Number (Co*), is used to indicate the suitability of spatial and temporal discretizations. Results for Power Coefficient (Cp) agreed with data from the literature and were associated with corresponding GRV and Co* values. It was also identified that incorporating the evaluation and analysis of dimensionless numbers as simulation parameters can guide methodology settings and significantly reduce simulation time compared to conventional methods such as mesh independence studies.

Keywords: VAWT CFD · Dimensionless Coefficients · H-Darrieus simulation

1 Introduction

Small-scale wind power systems are increasingly focused on Vertical Axis Wind Turbines (VAWT) due to their improved performance in turbulent conditions compared to Horizontal Axis Wind Turbines (HAWT). Particularly, the H-Darrieus VAWT solution has received significant attention due to benefits such as low wind speed and omni-directional operation. Equations 1 and 2 express the most common operational and performance parameters of this type of turbomachinery, Tip Speed Ratio (TSR) and Power Coefficient (Cp).

$$Cp = \frac{T\omega}{\frac{1}{2}\rho A U_\infty^3} \tag{1}$$

$$TSR = \frac{\omega R}{U_\infty} \tag{2}$$

where T is the torque generated by the turbine, ω is the angular velocity, ρ the specific mass of the air, A the frontal area swept by the rotor, U_∞ the undisturbed wind speed and R the radius of the rotor.

Computational fluid dynamics (CFD) simulations are valuable tools for predicting wind turbine performance. It reduces the need for physical testing, but sometimes the computational cost can be high or even prohibitive [1, 2]. Regarding H-Darrieus VAWT, 2D simulations are reliable but require solving an unsteady flow, which increases computational cost. Proper simulation setup is crucial for balancing accuracy and computational time. This study proposes a simplifying methodology for a CFD simulation of a three-bladed H-Darrieus VAWT by using dimensionless numbers to assess discretization and simulation stability.

2 Methodology

Simulations were run on a workstation with Intel Xeon E-2236 6-core processors. The model set up followed article [3], where authors carried H-Darrieus VAWT simulation using ANSYS Fluent ®. Convergence criteria was based on Cp variability during turbine rotation and the total cpu-clock time was recorded. Aerodynamic performance results were associated to dimensionless numbers Grid-Reduced Vorticity and Reference Courante Number Co* [4] which indicating mesh and time step suitability, respectively.

Equation 3 represents the dimensionless Courant number (Co):

$$Co = V \frac{\Delta t}{\Delta x} \tag{3}$$

where V is the necessary velocity for a particle to cross an element of size Δx, and Δt is the time-step adopted in the simulation. For Co*, Δx must represent the perimeter of the rotor blade divided by the number of elements that the discrete and V the peripheral velocity of the blade. According to [3, 4], the recommended value of Co* for turbomachinery should be less than 10.

Equation 4 represents the dimensionless number GRV:

$$GRV = \frac{\omega_v}{V_0/L_0} \tag{4}$$

where ω_v represents the vorticity, V_0 the local velocity and L_0 the representative length or local element size. Authors of [4] recommends GRV values of up to 0.01 in the critical regions of the flow, such as near the blades and in areas of vortex shedding.

2.1 Computational Domain

Figure 1 shows the computational domain, including auxiliary lines, boundary conditions, and their locations. The rotor has an 850 mm radius (R_{turb}) and 246 mm chord length (c) of cambered NACA0018. The domain comprises a rectangular stationary zone (SZ) which surrounding a circular rotating zone (RZ). Blade position along its circular path is represented by azimuthal angle (θ).
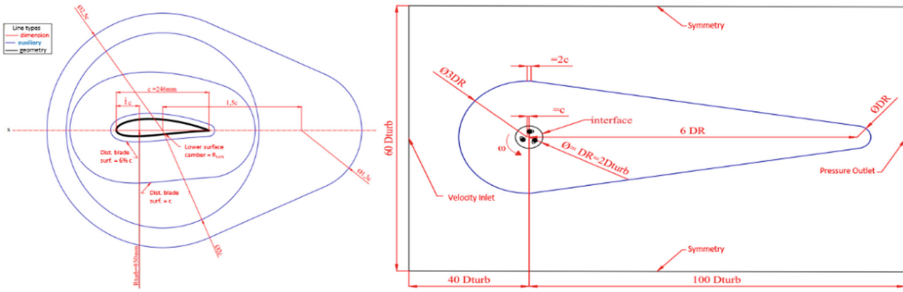
Fig. 1. Computational Domain and boundary conditions locations.

2.2 Spatial Discretization

Non-structured triangular elements mesh was generated, except for the use of quadrilateral elements in the near-wall regions of blade surfaces. Sizing controls tools were utilized on auxiliary lines to regulate element size, ensuring Skewness and Orthogonal Quality mesh metrics were maximum 0.6 and minimum 0.5 respectively. Figure 2 displays mesh details.
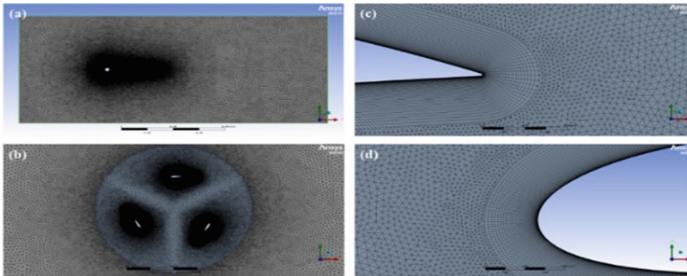
Fig. 2. Grid details. (a) SZ, (b) RZ, (c) trailing edge, (d) leading edge.

2.3 Modelling setup

The ANSYS Fluent® solver software was configured with a 2nd order upwind scheme for spatial discretization and a bounded 2nd order implicit scheme for temporal discretization. The k-ω SST turbulence model, which requires a y^+ value close to 1, was found to be the best performer for the case. This is supported by references [5–7], which demonstrate satisfactory results obtained by using this model for turbomachinery. Moreover, pressure-based solver type, coupled solution algorithm, and 30 iterations per time step were used. The boundary conditions included a velocity inlet of 8 m/s in the x-axis direction, a pressure outlet of 0 Pa (gauge), symmetry on the side edges, a sliding interface between the SZ and RZ, and a wall on the blades with a no-slip condition and stationary in relation to the RZ.

3   Results and Discussion

The authors of [3] suggest using a convergence criterion of 0.1% deviation in Cp value over two subsequent rotor revolutions. In this study, the criterion was met prematurely and produced unrealistic Cp values, leading to a revision requiring at least three consecutive revolutions with four decimal place precision. Table 1 displays Cp results for five operating points along with relative percentage error compared to [3], number of revolutions required for convergence, and simulation time.

Table 1. Cp error in relation to reference [3] results.

TSR	Cp	Error (CFD)	Error (Exper.)	#revs. to conv	time (hours)
1.1	0.0636	8.7%	>100%	15	100
2	0.2245	4.5%	12%	82	430
2.225	0.2928	5.4%	33%	100	360
2.6	0.2378	6.61%	8%	115	350
3.3	0.0822	6.9%	>100%	127	360

Comparing with CFD data from reference [3], errors were below 10%, considered sufficient for methodology validation. Total simulation time using one reference workstation was estimated at 1600 h, and with a mesh sensitivity study, it would be at least three times longer.

Concerning spatial discretization, it's worth mentioning that y^+ results, not included here for conciseness, indicated reliability of the k-ω SST turbulence model. The GRV number showed similar magnitudes and behaviors throughout a complete rotor revolution. Figure 3 displays a variation between 0.022 and 0.032 in maximum values.
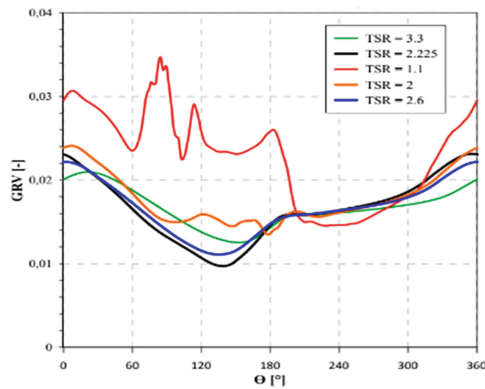
Fig. 3. GRV along a complete rotor's revolution at different operating points.

Comparing Fig. 3 with Table 1, it can be observed that at TSR of 1.1 (operating point with highest prediction errors), the GRV behavior is more chaotic and has a larger amplitude between minimum and maximum values. Conversely, at other operating points, the amplitude is smaller, and behavior is more uniform.

Table 2 shows that Co* is below the recommended upper limit of 10 in temporal discretization, indicating potential to increase the time-step, resulting in decreased simulation convergence time. Like GRV, Co* does not significantly vary after a few rotor revolutions, allowing evaluation of the time-step without waiting for convergeen.

Table 2. Maximum value of Co* during one complete revolution at different operating points.

TSR	Δx	Δt	Co*
1.1	0.000981 mm	0.0002276 s	2.04
2	0.000981 mm	0.0002504 s	4.08
2.225	0.000981 mm	0.0002250 s	4.08
2.6	0.000981 mm	0.0001926 s	4.08
3.3	0.000981 mm	0.0002276 s	6.12

4   Conclusions

The CFD methodology applied to a small Darrieus H TEEV in reference [3] was successfully replicated in this study. Results in Table 1 showed small errors compared to reference methodology, demonstrating its validity. However, modifications and adaptations were necessary, such as the adaptation of the simulation convergence criterion. It is recommended to consider the simulation converged after Cp does not vary for three consecutive rotor revolutions at four decimal place precision.

The high computational demands of the simulation (1600 h for five operating points) emphasize the significant resources required for predicting aerodynamic performance of H-Darrieus VAWT. Monitoring GRV from the start of the simulation allows for early assessment of spatial discretization adequacy, avoiding the need to wait for Cp convergence and simplifying methodologies requiring multiple simulations, such as optimization, by eliminating mesh sensitivity studies. Results in Fig. 3 suggest that GRV values up to 0.022 indicate adequate mesh and reliable Cp results for the three-bladed H-Darrieus VAWT.

Finally, after establishing an appropriate GRV number, the time-step should be adjusted to result in Co* < 10. Like GRV, Co* stabilizes in the early revolutions, making it useful for determining the time-step. Setting limits on GRV and Co* can be beneficial in cases of limited computational resources or tasks requiring many simulations.

References

1. Yepes, D., et al.: Biomass gasification in downdraft dual stage reactor by experimental analysis and simulation with CFD tools. In: European Biomass Conference and Exhibition Proceedings, vol. 25, pp. 808–816 (2017). ISSN 22825819
2. Sarmiento, A., Yepes, D., Chejne, F., Lora, E.: Gasification of agro-industrial wastes for electricity cogeneration. In: ASME Turbo Expo 2015: Turbine Technical Conference and Exposition, vol. 3, paper No: GT2015–43410, V003T03A008 (2015). https://doi.org/10.1115/GT2015-43410
3. Balduzzi, F., Bianchini, A., Maleci, R., Ferrara, G., Ferrari, L.: Critical issues in the CFD simulation of Darrieus wind turbines. Renew. Energy **85**, 419–435 (2016). https://doi.org/10.1016/J.RENENE.2015.06.048
4. Balduzzi, F., Bianchini, A., Ferrara, G., Ferrari, L.: Dimensionless numbers for the assessment of mesh and timestep requirements in CFD simulations of Darrieus wind turbines. Energy **97**, 246–261 (2016). https://doi.org/10.1016/J.ENERGY.2015.12.111
5. Sarmiento, A.L.E., Camacho, R.G.R., de Oliveira, W., Velásquez, E.I.G., Murthi, M., Diaz Gautier, N.J.: Design and off-design performance improvement of a radial-inflow turbine for ORC applications using metamodels and genetic algorithm optimization. Appl. Thermal Eng. **183**, 116197 (2021). https://doi.org/10.1016/j.applthermaleng.2020.116197
6. Espinosa Sarmiento, A.L., Ramirez Camacho, R.G., de Oliveira, W.: Performance analysis of radial-inflow turbine of ORC: new combined approach of preliminary design and 3D CFD study. J. Mech. Sci. Technol. **34**(6), 2403–2422 (2020). https://doi.org/10.1007/s12206-020-0517-5
7. Sarmiento, A.L.E., de Oliveira, W., Camacho, R.G.R.: Influence of the vortex design method in the performance characteristics of reversible axial rotors. J. Braz. Soc. Mech. Sci. Eng. **39**(5), 1575–1588 (2016). https://doi.org/10.1007/s40430-016-0680-x

Changes in Hardness and Volume of Polymers in Contact with Lubricants Used in Electric Vehicle Transmissions

Alejandro García Tuero[1]([✉]) [ID], Guillermo Díez-Valbuena[1] [ID], Noelia Rivera[2] [ID], Rubén González[2] [ID], and Antolín Hernández Battez[1] [ID]

[1] Department of Construction and Manufacturing Engineering, University of Oviedo, Gijón, Asturias, Spain
garciatalejandro@uniovi.es

[2] Department of Marine Science and Technology, University of Oviedo, Gijón, Asturias, Spain

Abstract. The location of the electric motor (EM) within the transmission in an electric vehicle requires the compatibility of automatic transmission fluids (ATF) with the EM and transmission materials. This work studies the compatibility of four conventional ATF with three structural polymers (PEEK, PTFE and PA66) and three elastomers (FKM, EPDM and silicone). Changes in volume and hardness of the materials after a period of aging in ATFs were measured. Complementary tests were carried out to explain the results. All four ATFs showed good compatibility with all materials except EPDM. This low compatibility was related to changes in the composition and crystalline structure of the elastomer. PA66, despite its good results, showed a certain hardening due to an increase in the degree of crystallinity after aging, so it is necessary to monitor its results in resistance tests.

Keywords: Electric vehicle · Automatic transmission fluid (ATF) · Polymers compatibility

1 Introduction

Electric vehicles (EV) are one of the main solutions developed to reduce greenhouse gas emissions and thus mitigate the effects of climate change. Certain EV configurations have the EM within the transmission case. In these circumstances, the EM is contact with the ATF, which makes it necessary for the ATF to present a series of additional properties to the usual ones for this type of fluid: electrical, magnetic and materials compatibility, protection against corrosion and resistance to the formation of foams, a part from reducing friction and wear and improving the EM cooling.

The aim of this work is to analyze the compatibility of four conventional ATFs with three structural polymers (Polyether Ether Ketone – PEEK, Polytetrafluoroethylene – PTFE and Polyamide 66 – PA66), used in supports and moorings, and three elastomers (Fluorocarbon – FKM, Monomer of Ethyl – Propyl – Diene – EPDM and Vinylmethylsil-icone Rubber – silicone), used in seals and joints, as well as in the insulation of electrical cables [1]. For this, the variations in volume and hardness after a period of aging of the materials in the ATFs will be analyzed.

2   Materials y Methods

2.1   Materials

Four conventional automatic transmission fluids (ATFs), commonly used by many auto-
mobile manufacturers in their current models, were selected for materials compatibility
testing. The composition of the ATFs is shown in Table 1. The specimens used in the
compatibility tests were extracted from sheets of each material with the dimensions
specified (type V) in the ASTM D638 standard.

Table 1. ATFs composition.

ATF	Base oils (wt%)	Additive package (wt%)
A	Group I, 4.9 cSt/100 °C (77.7)	11.7
	Group I, 2.7 cSt/100 °C (10.6)	
B	Group III, 3.0 cSt/100 °C (38.3)	11.0
	Group III, 6.5 cSt/100 °C (50.7)	
C	Group III, 3.0 cSt/100 °C (45.0)	17.0
	Group III, 6.5 cSt/100 °C (38.5)	
D	Group III, 3.0 cSt/100 °C (36.5)	27.0
	Group III, 4.2 cSt/100 °C (36.5)	

2.2   Aging of Materials

According to the recommendations of the ASTM D7216-15 standard [2], the variations
in the volume and hardness of the materials after aging were studied. The test samples
of the materials were immersed in the ATFs at 100 °C in a MEMMERT Universal Oven
(Model U, precision: ±0.5 °C) for 168 h. In addition, other material samples were aged
for longer periods (336, 504 and 672 h). The specimens were cleaned after the machining
process with a damp cloth, immersed in ethanol and dried with paper and hot air. After
removing the specimens from the oven, they were cleaned with blotting paper to drain
the oil. Subsequently, ethanol was used to ensure complete cleaning and excess ethanol
was removed with blotting paper to prevent its evaporation on the surface of the samples.

2.3   Materials Characterization

Volume and hardness variations were also measured according to ASTM D7216-15 [2].
Volume changes were determined using an analytical balance (readability: 0.1 mg). The
hardness of three specimens of each material was measured with a SAUTER HBD 100
durometer (structural polymers) and with a SAUTER HBA 100 (elastomers), before
and after the aging process, in four different positions. The mean value of these four
measurements was considered as the result to be compared.

2.4 Complementary Tests

X-Ray Diffraction (XRD) experiments were performed to calculate the degree of crystallinity of the polymers before and after aging in the different oils using a PHILIPS X'PERT PRO diffractometer in a range of 2θ between 5° and 80°, with a step angle of 0.0167°. Fourier transform infrared spectroscopy (FTIR) measurements were performed on the structural polymers and elastomers on a Varian 670-IR FTIR spectrometer with a Golden Gate ATR device to verify possible variations in their composition after the aging process. Aditionally, the elastomers underwent a thermal characterization using thermo-gravimetric analysis (TGA) to analyze how the aging process could affect the structure of the elastomers and their thermal stability. The same SDT Q600 thermal analyzer (TA Instruments) was used. A nitrogen atmosphere was used. The samples were heated from room temperature to 800 °C at a heating rate of 10 °C/min.

3 Results

3.1 Volume Variation

The compatibility of the structural polymers and the elastomers with the ATF was first verified in terms of the variation in volume, according to the ageing time specified in the ASTM D7216-15 standard (168 h) [2]. In the case of structural polymers, the volume changes depended more on the type of material than on the oil used (Table 2). The three structural materials (PEEK, PTFE and PA66) experienced a slight reduction in volume. Although there are no specifications on the compatibility of these materials with ATFs, the measured volume variations, which are around -0.5%, indicate that these ATFs and materials are compatible. For longer times (more than 168 h), only PTFE showed some variability, although it could be concluded that all structural materials underwent negligible volume changes.

Regarding the elastomers, there are compatibility specifications set by transmission manufacturers [3]. Table 2 shows the volume variations of them after the aging process. The silicone perfectly complied with the maximum recommended limit values (ΔV + 20%). On the other hand, the FKM constitutes a special case, since the volume of the samples was reduced between 2.5 and 3.5%, with which they would be out of specification (ΔV between −2% and +5%). Therefore, the tested oils are not compatible with FKM in terms of volume change. The EPDM experienced a considerable increase in volume, obtaining the maximum values with oil A. Despite the lack of reference, the results obtained allow us to conclude that these oils are not compatible with EPDM. On the other hand, the long-term results (more than 168 h) showed that both FKM and EPDM worsened their results, while silicone remained stable.

3.2 Hardness Variation

There are also no specifications for hardness changes of ATF-aged structural polymers. The hardness variation after the first 168 h in the three materials was small (Table 3). On the one hand, in PEEK and PTFE it decreased around 3 points (Shore D). On the other hand, the hardness increased slightly in PA66 after the aging period. The changes

Table 2. Volume variation of the materials after ageing.

Structural polymer	ATF	ΔV (%) 168 h	ΔV (%) 672 h	Elastomer	ATF	ΔV (%) 168 h	ΔV (%) 672 h
PEEK	A	−0.48	−0.36	FKM	A	−3.19	−3.80
	B	−0.43	−0.27		B	−2.62	−3.30
	C	−0.27	−0.37		C	−3.13	−4.98
	D	−0.39	−0.48		D	−3.3	−3.80
PTFE	A	−0.64	−0.39	EPDM	A	85.05	115.51
	B	−0.50	−0.67		B	66.18	93.20
	C	−0.65	−0.45		C	68.31	97.79
	D	−0.49	−0.32		D	69.51	101.79
PA66	A	−0.44	−0.46	Silicone	A	16.26	17.64
	B	−0.62	−0.56		B	14.79	15.90
	C	−0.30	−0.65		C	17.46	17.26
	D	−0.81	−0.65		D	19.09	21

in the hardness of each material did not depend on the oil used. In the long-term tests, the hardness values remained stable in all cases, which allows us to conclude that these materials are compatible with the ATF in this study.

Table 3. Hardness variation of the materials.

Structural polymer	ATF	ShD 0 h	ShD 168 h	ShD 672 h	Elasto-mer	ATF	ShA 0 h	ShA 168 h	ShA 672 h
PEEK	A	90	87	88	FKM	A	78	78	84
	B	90	87	88		B	78	77	83
	C	90	88	88		C	78	77	85
	D	90	87	88		D	78	78	84
PTFE	A	60	58	56	EPDM	A	70	46	37
	B	60	59	58		B	70	47	40
	C	60	58	58		C	70	47	38
	D	60	57	57		D	70	47	33
PA66	A	80	82	82	Silico-ne	A	65	56	54
	B	80	83	82		B	65	56	54
	C	80	82	82		C	65	53	54
	D	80	82	82		D	65	54	52

Regarding the evolution of the hardness of the different elastomers during the aging process. The FKM showed small changes in hardness in the first 168 h, confirming what was reported by Drobny [4]. On the other hand, EPDM and silicone showed a great reduction in hardness, although in the case of silicone it complies with the values recommended by manufacturers (-15 ShA), which confirms what has been found in the literature [5]. There is no bibliographical reference on the behavior of EPDM in oils, but its loss of hardness is the greatest of the three elastomers. The studies by Nakamura et al. [6] and de Souza [7] confirm this trend and that it is due to immersion in fluids, although EPDM would not be affected by high temperatures. These results did not vary according to the oil used (Table 3).

3.3 Complementary Tests

Hardness increases with the degree of crystallinity, so XRD results can be correlated with experimentally measured hardness and volume variation results. The spectra obtained in the case of structural polymers did not show notable changes in the proportion of crystalline and amorphous areas, which confirms the small variations measured in volume and hardness for these materials. The analysis of these values showed that the measured changes in hardness are explained by the significant changes in the percentage of crystallinity showed in Table 4.

Table 4. Percentage of crystallinity of elastomers FKM and Silicone by ATF and ageing time.

	ATF	0 h	168 h	672 h		ATF	0 h	168 h	672 h
FKM	-	21.29	-	-	Silicone	-	65.50	-	-
	A	-	13.47	13.50		A	-	26.20	34.76
	B	-	13.55	19.22		B	-	23.47	34.51
	C	-	20.33	18.64		C	-	18.73	17.35
	D	-	13.96	12.45		D	-	16.60	18.24

In FTIR spectra, qualitative differences (peak positions) in the same material were almost negligible for structural polymers. For this reason, a principal component analysis (PCA) [8] was performed and the results suggested that, in the case of PEEK, time affects to a greater extent than the type of oil. This would explain, in general, the similarity of results in the hardness and volume tests of PEEK after aging in the different ATFs. The other two structural polymers were analyzed in a similar way and the results showed that on PTFE, contrary to PEEK and PA66, the type of oil had more influence than the aging time.

The TGA showed that the mass loss of the fresh FKM below the T_{Onset} was higher than that of the aged samples probably due to the volatile components presence in the material [9], which is not present in the aged samples. Meanwhile, the EPDM [10] and the Silicone [11] showed the higher mass loss due to loss of the oil previously absorbed, which explains the huge volume increase shown (Table 2) along with the huge reduction in hardness (Table 3).

4   Conclusions

The compatibility between four conventional ATFs, three structural polymers (PEEK, PTFE and PA66) and three elastomers (FKM, EPDM and silicone) which can be used in electrified transmissions was researched by determining volume and hardness variations after ageing the materials separately immersed in the ATFs. The main conclusions obtained were: (a) PEEK and PTFE showed short and long term compatibility according to volume and hardness variations; (b) PA66 experienced an increase in hardness due to the increase in crystallinity during aging, (c) ATFs A and C increased excessively EPDM volume witch made the no compatible. The remaining elastomers endured well all ATFs, (d) XRD test denote a significate reduction in the crystalline structure of silicone aged in ATF C. The variation in FKM was not remarkable and no test where run on EPDM due to its semi-crystalline structure; and (e) due to oil absorption, verified by TGA test on EPDM and silicone, a volume increase occurred which led to a hardness reduction. FKN did not absorbed oil, but volatile components evaporation in the fresh rubber provoked a volume decrease and a hardness increase.

References

1. Haghshenas, N., Nejat, A., Seyedmehdi, S.A., et al.: Adhesion aspects of silicone rubber coatings for high voltage insulators: a critical review. Rev. Adhes. Adhes. **9**, 434–480 (2021)
2. ASTM D7216-15 Standard Test Method for Determining Automotive Engine Oil Compatibility with Typical Seal Elastomers (2015)
3. Afton Specification Handbook. Afton Chemical, Richmond, VA (2019)
4. Drobny, J.G.: Compounds for Automotive Power Train Systems. In: Fluoroelastomers Handbook, pp. 483–490. Elsevier (2016)
5. Kusuhara, S., Yoshimura, K., Kunieda, K., et al.: Experimental investigation on the influence of engine oil additives on silicone rubber. SAE Int. J. Fuels Lubr. **10**, 461–468 (2017)
6. Nakamura, T., Chaikumpollert, O., Yamamoto, Y., et al.: Degradation of EPDM seal used for water supplying system. Polym. Degrad. Stab. **96**, 1236–1241 (2011)
7. de Souza, E.L., de Souza, Z.M., de Paiva, K.V., et al.: Evaluation of the aging of elastomeric acrylonitrile-butadiene rubber and ethylene-propylene-diene monomer gaskets used to seal plates heat exchanger. Polym. Eng. Sci. **61**, 3001–3016 (2021)
8. Jackson, J.E.: A User's Guide to Principal Components. Wiley-Interscience (2003)
9. Kader, M.A., Lyu, M.Y., Nah, C.: A study on melt processing and thermal properties of fluoroelastomer nanocomposites. Compos. Sci. Technol. **66**, 1431–1443 (2006)
10. Rojas Rodríguez, F.I., d'Almeida, J.R.M., Marinkovic, B.A.: Natural aging of ethylene-propylene-diene rubber under actual operation conditions of electrical submersible pump cables. Materials **14**(19), 5520 (2021)
11. Bouguedad, D., Mekhaldi, A., Jbara, O., et al.: Physico-chemical study of thermally aged EPDM used in power cables insulation. IEEE Trans. Dielectr. Electr. Insul. **22**, 3207–3215 (2015)

Calculation of Williams-Landel Ferry Shift Factors via Probe Tack Testing for Uncured Prepreg Materials

Guillermo Retuerta del Rey[1] , Andrea Fernández Gorgojo[1,2] ,
Juan Pedro Fernández Blázquez[2] , and Enrique Chacón Tanarro[3(✉)]

[1] Grupo de Investigación en Ingeniería de Fabricación. Departamento Ingeniería Mecánica,
Universidad Politécnica de Madrid, Madrid, Spain
guillermo.retuertadel.rey@alumnos.upm.es
[2] IMDEA Materials Institute, Madrid, Spain
[3] GI-IM, Departamento Ingeniería Mecánica, Universidad Politécnica de Madrid, Madrid, Spain
e.chacon@upm.es

Abstract. Knowledge of the viscoelastic properties of the resin present in uncured pre-impregnated composites is essential for the development and optimization of current automated manufacturing processes for composite parts (AFP, ATL, FPP…). Time-temperature superposition applied to the tack force between the prepreg and the tool allows to optimize production times without influencing the viscoelastic behavior of the material by simply varying the temperature. The application of this time-temperature superposition principle requires the calculation of two parameters that depend on the matrix of the composite and that are usually calculated by rheological tests with pure resin samples. In this work, a novel method to obtain these parameters directly from the pre-impregnated composite material using adhesion tests is presented.

Keywords: Composite material · Prepreg · Tack · Time-temperature superposition

1 Introduction

Pre-impregnated composite materials are of special interest in the composite parts manufacturing industry because the great stability of the automatic pre-impregnation process, compared to wet lay-up process, allows laminates with higher and more uniform fiber to resin ratio, which means better mechanical properties of the manufactured parts.

Processing of pre-impregnated composite materials is usually performed via manual lamination, requiring skilled technicians and an elevated number of working hours. This is the reason why, in recent years, numerous techniques have been developed to automate the lamination of materials [1]. Knowing the adhesive behavior of uncured composites when they come into contact with the different tooling systems is essential to optimize their quality and productivity [2–5].

Crossley et al. demonstrated that the Williams, Landel and Ferry (WLF) model for time-temperature superposition can be applied to the calculation of the maximum tack force (F_T) between the pre-impregnated material and any surface [6].

$$F_T(T, t) = F_T(T_0, ta_T) \tag{1}$$

$$\log_{10} a_T = \frac{-C_1(T - T_0)}{C_2 + (T - T_0)} \tag{2}$$

where T is the temperature; t, the contact time; and C_1 and C_2, the WLF shift factors that depend on the resin and the reference temperature (T_0). These constants are usually obtained by rheological tests. However, such a test, although possible, is complex to perform with pre-impregnated materials due to the influence of the reinforcement fibers.

In this work, an experimental method that allows the obtention of the constants defined by Williams, Landel and Ferry without the need to perform a rheological test is proposed. Using a differential mechanical analysis (DMA) machine, the tack force of the pre-impregnated material to the tooling (F_T) is measured at different temperatures and with different contact times under pressure. Using these values in the solution of Eqs. (1) and (2) for different points of the F_T curves, the WLF constants of this work can be obtained.

2 Method

2.1 Materials

For the realization of this work, a non-commercial pre-impregnated material manufactured by the authors is used. This composite material is manufactured from a twill (2 × 2) carbon fiber TC203T manufactured by Teijin Group with an areal weight of 200 g/m², and a 200 g/m² epoxy resin film MTFA500 from SHD Composites. For the fabrication of the pre-impregnated material the stack of fabric and resin is subjected to temperature and pressure for a period of 10 min in a hot plate press at 60 °C and 0.4 MPa. With these values, a correct resin transfer is observed, obtaining a uniform composite material from which to obtain the samples necessary for the adhesion tests described below.

2.2 Differential Scanning Calorimetry

Differential scanning calorimetry (DSC) tests are performed to the samples for rheology, the prepreg material and the virgin resin to know the degree of curing suffered during the processing of the resin, and to verify that there are no significant differences between the samples for rheology and the samples for the adhesion tests.

2.3 Rheology

Small amplitude oscillatory shear tests (SAOS) are performed in which isothermal frequency sweeps in a range between 0.5 and 200 rad/s, and temperatures from 30 °C to

60 °C. From these tests, the values of the storage modulus (G') and losses (G'') can be obtained and, hence, the WLF shifting factor (C_1 and C_2) at 30 °C and 45 °C.

For the rheology tests carried out during this work, resin specimens of 25 mm diameter and 1 mm thickness are manufactured by stacking several layers of film until the target thickness is obtained. The resin stack is compacted at 60 °C for 10 min for homogenization.

2.4 Adhesion Tests

For the measurement of tack force, a TA Instruments Q800 DMA equipped which a tooling specifically designed for this type of test is used.
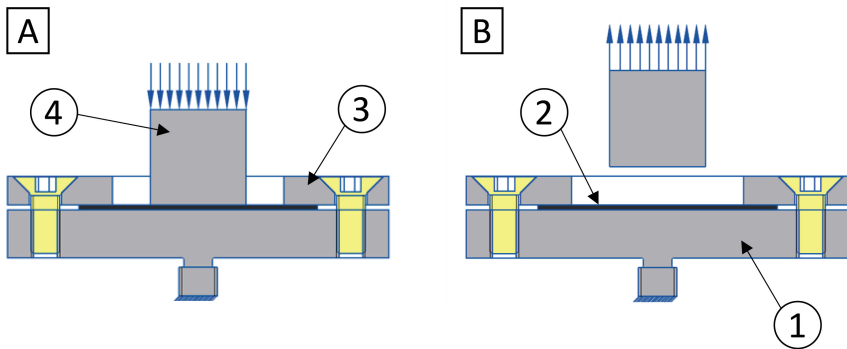
Fig. 1. Tooling during the compression stage. (b) Tooling during the debonding stage

The moving part of the tooling consists of a 10 mm diameter cylinder (4) which is lowered to apply a controlled force for a fixed time (Fig. 1A) and then ramps upward until the adhesion force at the resin-steel interface is exceeded (Fig. 1B). The sequence of the test is as described below:

1. The composite material sample (2) is placed with the side with more resin facing upwards on the 40 mm disc (1) and is fixed using the locking ring (3).
2. The machine's furnace is closed and brought to the test temperature.
3. A 5 min isothermal holding is performed to ensure that both the tooling and the pre-impregnated composite sample reach the target temperature.
4. The test starts by lowering the 10 mm diameter cylinder (4) until it contacts the sample of composite material and applies a compressive force of 3 N.
5. The contact force is maintained for the test time and then, the force is released.
6. The tensile force is increased at a rate of 9 N/min until debonding occurs.
7. The sample is removed and both surfaces are cleaned with acetone for the next test.

Figure 2 shows a typical curve obtained in this type of test in which the three phases of the experiment can be clearly distinguished:

1. Isothermal holding phase at the test temperature.

2. Compression phase.
3. Debonding phase.
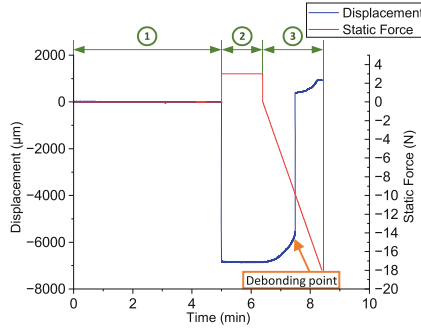
Fig. 2. Characteristic curve of an adhesion test

   It is during the debonding phase that the failure occurs. This point, indicated on the displacement curve in Fig. 2, can be identified as the highest velocity point. The force value measured at that instant of time corresponds to the maximum tack force. This procedure is repeated for temperatures ranging from 20 °C to 50 °C and contact times from 0.10 min to 10 min.

   With the maximum adhesion force values (F_T) obtained for each one of the tests mentioned above, it is possible to construct a master curve at the chosen reference temperature (T_0). To construct this master curve, it is necessary to horizontally shift the curves obtained using Eqs. (1) and (2). The experimental values are subjected to an optimization algorithm in which the WLF constants C_1 and C_2 are searched for. This algorithm fits the shifted data to a curve of the form $F_T(t, T_0) = a \cdot t^b$ and searches for the values of C_1 and C_2 for which the coefficient of determination (R^2) is maximized. This fitting procedure is performed, as in the rheology tests, at two reference temperatures: 30 °C and 45 °C.

3   Results

3.1   DSC

Table 1 shows a summary of the most important values obtained from the DSC tests performed for each sample. Assuming a degree of cure (DOC) of 0% for the virgin resin, it can be observed that the samples obtained after the process of impregnation of the fibers and after the manufacturing of the rheology specimens have reached a degree of cure of 11% and 2%, respectively. In both cases, low degrees of cure are observed. However, this difference in the degree of cure may affect the values obtained for the WLF constants.

Table 1. Summary of DSC results

Sample	Enthalpy (J/g)	Tg (°C)	DOC
Virgin resin	350	3,7	0%
Pre-impregnated material	310	2,9	11%
Stacking for rheology	343	2,8	2%

3.2 Rheology

Values for the storage modulus (G') and loss modulus (G'') when exposing a resin speci-
men to isothermal frequency sweeps with 0.5% strain amplitude are obtained. Applying
the time-temperature superposition principle, the obtained curves are horizontally shifted
to a reference temperature (T_0). Table 2 shows the values of the WLF constants for 2
reference temperatures (30 °C and 45 °C) calculated from the data obtained from testing
two resin specimens under the described test conditions.

Table 2. Values of the shift factors C_1 and C_2 *at 30 °C and 45 °C* calculated from rheological
tests on pure resin samples.

	30 °C		45 °C	
Test	C_1 (-)	C_2 (°C)	C_1 (-)	C_2 (°C)
1	1.37	6.89	0.41	21.14
2	1.35	9.15	0.47	23.14
Mean	1.36	8.02	0.44	22.15
Standard deviation	0.019	1.60	0.043	1.41

3.3 Adhesion Tests

Figure 3A shows the results obtained in the adhesion tests described in Sect. 2.4 of this
work. It can be observed that, in general, the tack force between the pre-impregnated
composite material and the steel surface of the moving cylinder increases with decreasing
temperatures and increasing contact time under pressure.

Figure 3B and 3C show the values of F_T shifted to the reference temperatures
$T_0 = 30$ °C and $T_0 = 45$ °C, respectively, using the WLF displacement factors given
in Table 3. A high degree of fit can be observed in these curves, especially in the points
displaced from the high temperature results.
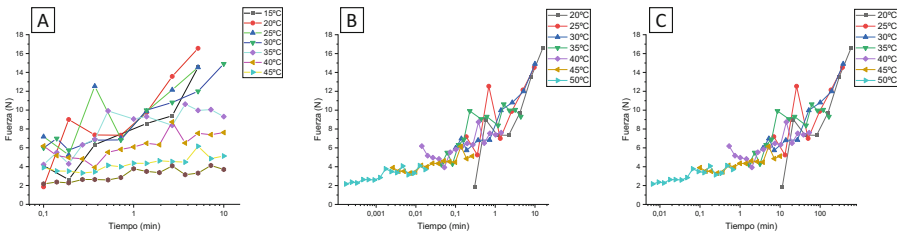
Fig. 3. (A) Tack force (F_T) between prepreg and steel as a function of contact time under pressure (t) and test temperature (T). (B) Tack force curves (F_T) shifted at $T_0 = 30\ °C$. (C) Tack force curves (F_T) shifted at $T_0 = 45\ °C$.

Table 3. Values of the shift factors *at 30 °C and 45 °C* calculated from adhesion tests.

30 °C		45 °C	
C_1 (-)	C_2 (°C)	C_1 (-)	C_2 (°C)
2.21	36.01	3.78	21.01

4 Conclusions

In this work, the need to develop an alternative technique to rheology for obtaining the Williams-Landel-Ferry constants in pre-impregnated composite materials is justified. For this purpose, the authors develop a method based on probe tack testing that allows to obtain these values directly from composite material samples.

Using a differential mechanical analysis (DMA) machine, probe tack tests at different temperatures and with different contact times under pressure are performed. Using these values in solving the WLF the WLF constants are obtained.

Isothermal frequency sweeps are performed on samples of the same resin using a rheometer. The results obtained from these tests allow to calculate, by state-of-the-art methods, the WLF constants to validate those obtained by the new methodology.

The methodology proposed in this work yields values of the WLF constants in the expected orders of magnitude. These values allow the construction of master curves with an excellent fit at various temperatures. However, it is observed that the values obtained for these constants do not match those obtained by rheology, which opens the door to an improvement of the proposed methodology.

References

1. Lukaszewicz, D.H.J.A., Ward, C., Potter, K.D.: The engineering aspects of automated prepreg layup: history, present and future. Compos. B Eng. **43**(3), 997–1009 (2012). https://doi.org/10.1016/j.compositesb.2011.12.003
2. Budelmann, D., Detampel, H., Schmidt, C., Meiners, D.: Interaction of process parameters and material properties with regard to prepreg tack in automated lay-up and draping processes. Compos. Part A Appl. Sci. Manuf. **117**, 308–316 (2019). https://doi.org/10.1016/j.compositesa.2018.12.001

3. Budelmann, D., Schmidt, C., Meiners, D.: Prepreg tack: a review of mechanisms, measurement, and manufacturing implication. Polym. Compos. **41**(9), 3440–3458 (2020). https://doi.org/10.1002/pc.25642
4. Matveev, M.Y., Schubel, P.J., Long, A.C., Jones, I.A.: Understanding the buckling behaviour of steered tows in Automated Dry Fibre Placement (ADFP). Compos. Part A Appl. Sci. Manuf. **90**, 451–456 (2016). https://doi.org/10.1016/J.COMPOSITESA.2016.08.014
5. Bakhshi, N., Hojjati, M.: Time-dependent wrinkle formation during tow steering in automated fiber placement. Compos. B Eng. **165**, 586–593 (2019). https://doi.org/10.1016/J.COMPOSITESB.2019.02.034
6. Crossley, R.J., Schubel, P.J., de Focatiis, D.S.A.: Time-temperature equivalence in the tack and dynamic stiffness of polymer prepreg and its application to automated composites manufacturing. Compos. Part A Appl. Sci. Manuf. **52**, 126–133 (2013). https://doi.org/10.1016/j.compositesa.2013.05.002

Modal Analysis of a 2R Flexible Platform Using Screw Theory

Martín Pucheta[(✉)] and Alejandro Gallardo

Research Center in Informatics for Engineering (CIII) and National Scientific and Technical
Research Council (CONICET), Córdoba Regional Faculty, National University of Technology
(FRC-UTN), X5016ZAA Cordoba, Argentina
{mpucheta,agallardo}@frc.utn.edu.ar

Abstract. Compliant mechanisms perform precision movements generated by
the elastic deformation of their flexible elements. For most applications, reso-
nance frequencies must be bounded by a defined range of values. Therefore, a
modal analysis of the mechanisms is required at the initial stage of design. In this
work, a novel flexible platform with 2 degrees of rotational freedom restricted
by beam-type flexure elements is analyzed. The Screw Theory description of the
movement of the mechanism is used for the rigid and the flexible elements. Using
this formalism, the stiffness and mass matrices for a two-node beam element are
derived and can be assembled using a standard finite-element-like procedure to
perform the modal analysis of the mechanism. Starting from the desired move-
ments, the mechanism is synthesized using screws and a hybrid (series/parallel)
solution is proposed. The analytical results for the modal analysis obtained by
Screw Theory are compared with the results of finite element analysis. Due to the
computational efficiency, the analytical equations are chosen to be applied in the
optimization of the designs.

Keywords: 3D compliant mechanisms · 2R flexible platform · Beam Theory ·
Screw Theory · modal analysis

1 Introduction

Compliant mechanisms have wide applications in the field of precision engineering,
medical devices, and optical instrumentation, among others [1, 2]. In the initial stage of
design and optimization, a modal analysis of the mechanisms must be carried out [2–4]
to satisfy requirements on the resonant frequencies.

For parallel and series flexible mechanisms constrained by plate and beam-type
elements there are well-established methods for their linear static analysis applying
Screw Theory [5]. Using screws, the kinematics of rigid bodies linked by clamped-
clamped flexible elements is determined by a 6×6 flexibility matrix (and its inverse,
the 6×6 stiffness matrix) [4, 6, 7]. Hopkins et al. [6] derive the stiffness matrix of
hybrid topologies considering relative screw displacements starting from the ground of

the structure. Wu et al. [7] firstly determines the potential energy of the structure using the 6×6 flexibility matrices for each flexure element; subsequently, they determine the minimum state of the energy and obtains the stiffness matrix of the complete mechanism.

In this work, the Screw Theory formalism by Ding and Selig [8, 9] is applied to obtain the stiffness and mass matrices of a two-node beam element that is assembled applying the standard techniques of the finite element method [10] to build the stiffness and mass matrices of the complete flexible mechanism required to perform its modal analysis. This enables analysts to consider more than one beam element per flexure element, increasing the accuracy in the modal analysis. As an application example, a flexible platform with a hybrid structure and 2 rotational degrees of freedom (RR) restricted with beam-type flexure elements is analyzed. This kind of platform is mainly used in optical applications for guiding light or laser beams through mirrors of several scales [2]. The analytical results obtained through the Screw Theory are compared with the results of finite element analysis.

2 Beam Element Derivation Using Screw Theory

The beam element that will be developed in this work is a slender beam with a straight centroidal axis, with a constant cross section, and subjected to external loads applied only at its end nodes, see Fig. 1(a).
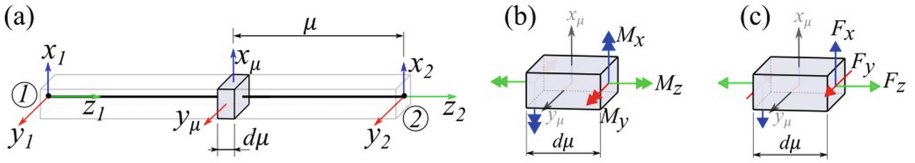
Fig. 1. Notation for a two-node beam element

A differential segment of the beam element is selected, see Fig. 1(a). This segment will be analyzed as a beam of length $d\mu$ with a reference system located in the center of the segment. When a moment is applied at one of the ends of the beam of length $d\mu$, on the other end there must be a moment with equal direction and magnitude, but in the opposite sense to enforce static equilibrium, see Fig. 1(b). Equations (1)–(3) are the constitutive relationships for the moments of a Euler-Bernoulli beam [10]

$$M_z = GI_p \frac{d\theta_z}{d\mu} \rightarrow d\theta_z(\mu) = \frac{d\mu}{GI_p} M_z \tag{1}$$

$$M_y = EI_y \frac{d\theta_y}{d\mu} \rightarrow d\theta_y(\mu) = \frac{d\mu}{EI_y} M_y \tag{2}$$

$$M_x = EI_x \frac{d\theta_x}{d\mu} \rightarrow d\theta_x(\mu) = \frac{d\mu}{EI_x} M_x \tag{3}$$

where E is the longitudinal elasticity modulus, G is the transversal elasticity modulus, I_x (I_y) is the moment of inertia of the section with respect to the $x(y)$ axis, and I_p is

the polar moment of inertia of the section. Throughout the differential segment the internal moment forces are constant. Therefore, the variation of rotations between the extreme sections can be obtained from the constitutive relations given by Eqns. (1)–(3). The same differential beam segment is analyzed for the applied forces at its ends, see Fig. 1(c). The forces transversal to the beam axis generate distortions and bending moments. If $d\mu \to 0$, then the moments produced by these forces will tend to zero. In addition, in the Euler-Bernoulli beam hypotheses, the deformations due to distortions are negligible. Therefore, F_z is the only force that generates an appreciable deformation and its constitutive relationship is expressed as

$$F_z = EA\frac{d\delta_z}{d\mu} \to d\delta_z(\mu) = \frac{d\mu}{EA}F_z \tag{4}$$

Equations (1)–(4) can be expressed in compact form

$$dt = c.Q.w$$

$$\begin{bmatrix} d\theta_x \\ d\theta_y \\ d\theta_z \\ d\delta_x \\ d\delta_y \\ d\delta_z \end{bmatrix} = \begin{bmatrix} d\mu/EI_x & 0 & 0 & & & \\ & d\mu/EI_y & 0 & & \mathbf{0}_{3\times3} & \\ & & d\mu/GI_p & & & \\ & & & 0\,0 & 0 & \\ & sym. & & 0 & 0 & \\ & & & & & d\mu/EA \end{bmatrix} \boxed{Q} \begin{bmatrix} F_x \\ F_y \\ F_z \\ M_x \\ M_y \\ M_z \end{bmatrix} \tag{5}$$

where dt is the differential deflection screw, c is called the flexibility density matrix, Q is an exchange matrix, and w is the wrench [8, 9].

A possible boundary condition of the beam element shown in Fig. 1(a) is clamped at node 1 and free at node 2, where a wrench is applied. The displacement twist at the free end can be obtained by integrating Eq. (5). To integrate the differential deflection screw dt of each cross section, they must be expressed in a common reference frame [8], for example, in a frame located at node 2 as

$$\int_{-L}^{0} dt_2 = \left(\int_{-L}^{0} H_{2\mu}cQH_{2\mu}^{-1}\right)w_2 \to t_2 = C_{22}w_2$$
$$w_2 = k_{22}t_2 \tag{6}$$

where L is the beam length, dt_2 is the differential deflection screw of the differential element $d\mu$ expressed in the reference system of node 2, w_2 is the wrench applied on node 2, and $H_{2\mu}$ is the matrix that changes the coordinates (a passive translation in μ) from the system located at coordinate μ to a system located at the node 2.

The reactions at the clamped end of the beam must ensure equilibrium

$$(w_1)_2 = -w_2 \tag{7}$$

where $(w_1)_2$ is the wrench applied on node 1 expressed in the reference system of node 2. Taking the expression of w_2 from Eq. (6), then using Eq. (7) and applying to $(w_1)_2$ a change of coordinates H_{21} from a node 2 to a node 1 frame, the stiffness matrix that

relates the twist of node 2 with the wrench applied on node 1 can be computed as

$$(w_1)_2 = -k_{22}t_2$$
$$w_1 = \left(-H_{21}^{-1}k_{22}\right) \cdot t_2 \tag{8}$$
$$w_1 = k_{12} \cdot t_2$$

where w_1 is the wrench at node 1 expressed in the reference frame of node 1.

By clamping the node 2 and applying a wrench on node 1, the same procedure as above is used to get the stiffness matrices k_{11} and k_{21}. Finally, the wrench – deflection screw relationship for the beam element can be put in compact form as

$$\begin{bmatrix} w_1 \\ w_2 \end{bmatrix} = \begin{bmatrix} k_{11} & k_{12} \\ k_{21} & k_{22} \end{bmatrix} \begin{bmatrix} t_1 \\ t_2 \end{bmatrix} = K_e \begin{bmatrix} t_1 \\ t_2 \end{bmatrix} \tag{9}$$

The stiffness matrix K_e obtained in Eq. (9) is equal to that obtained by classical methods for structural analysis, like the Direct Stiffness Method and the Finite Element Method, where bending, torsion, and tension are analyzed in a decoupled way [10]. To compute the total stiffness matrix of a flexible mechanism, the stiffness matrix of each flexible element must be assembled in the same way as is done in the finite element method. Thus, before performing the assembly, each local stiffness matrix K_e must be expressed in a single global reference system, usually located in the moving platform.

In this work, a concentrated mass matrix [10] is adopted, where it is not necessary to assume and/or to know the internal displacements of the beam. By assuming the node 1 of the element as clamped and applying forces at node 2, the Second Newton's Law is expressed as $w_2 = m\,Q\,\ddot{t}_2$ where the mass matrix is defined as

$$m_{6\times6} = \rho \cdot A \cdot L \cdot diag\left(\frac{1}{2}, \frac{1}{2}, \frac{1}{2}, \alpha L^2, \alpha L^2, \frac{I_P}{2A}\right) \tag{10}$$

ρ is the density of the beam material, and α is a non-negative parameter between 0 and 1/50; here $\alpha = 1/100$ is adopted. The same procedure as above is developed for a clamped node 2 and a wrench applied on node 1. Then, by combining this result with that of node 2, the local mass matrix of the beam element is obtained

$$\begin{bmatrix} w_1 \\ w_2 \end{bmatrix} = \begin{bmatrix} m \cdot Q & 0_{3\times3} \\ 0_{3\times3} & m \cdot Q \end{bmatrix} \begin{bmatrix} \ddot{t}_1 \\ \ddot{t}_2 \end{bmatrix} = M_e \begin{bmatrix} \ddot{t}_1 \\ \ddot{t}_2 \end{bmatrix} \tag{11}$$

3 Modal Analysis

The dynamic equation of undamped flexible mechanisms without external excitation is $M \cdot \ddot{T} + K \cdot T = 0$, where T is a column vector containing the deflection screws of each node of the structure, M and K, are respectively, the global mass and stiffness matrices of the entire mechanism. For small oscillations, harmonic motions are assumed [4, 9, 10] and this equation is transformed into a generalized eigenvalue problem $\left(-\omega^2 M + K\right) \cdot T = 0$, where the solutions for ω are the natural frequencies.

The 2R flexible mechanism shown in Fig. 2(a) has two rotational degrees of freedom around two concurrent axes of rotation, x and y. It was designed as two parallel sub-mechanisms in series: An intermediate platform is linked to the moving one by the flexure elements shown in Fig. 2 (b) that allow rotation around the x axis. Then, flexure elements that link the foundation and the intermediate platform are added, allowing the rotation around the y axis; see Fig. 2 (c). The material of the mechanism is aluminum with a density of $\rho = 7700$ kg/m^3, a longitudinal elasticity modulus $E = 2.1 \cdot 10^{11}$ N/m^2 and transversal modulus $G = 8 \cdot 10^{10}$ N/m^2. The flexible elements are 30 mm long and have a cross section with 0.2 mm thick and 5 mm wide.
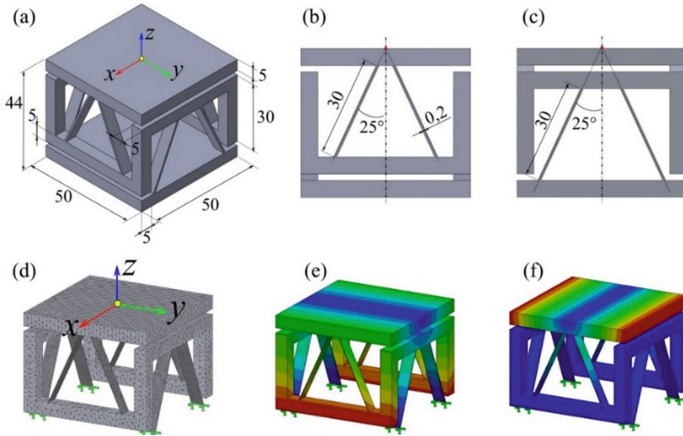
Fig. 2. Dimensions (in mm) of the 2R mechanism (a, b, c) and FEM simulation (d, e, f).

All flexure elements are modeled with the proposed beam for three cases of modal analysis: Considering 1 beam element for each flexure element, (i) including the mass of the beam (ii) and ignoring the mass of the beam, respectively, and (iii) by considering 2 beam elements for each flexure element where the mass of the beam is taken into account, otherwise the mass matrix would be singular.

The values obtained for the first 6 vibration modes are very similar to each other and are shown in Table 1. The results obtained with the proposed method are compared with results that were obtained by the finite element method shown in the 2nd column of Table 1. In Fig. 2(d) the mesh of high-order quadratic tetrahedral elements consisting of 100630 nodes is shown. Figures 2(e) and 2(f) show the results for the first two natural frequencies corresponding to the two desired rotational degrees of freedom. It should be noted that using 2 beam elements per flexure element has less error in the 6th mode compared to using 1 element per flexure element. The execution times to calculate the natural frequencies with the proposed analytical method are 100 orders less if they are compared to results obtained through the finite element method.

Table 1. Natural frequencies (in Hz) of the 2R flexible mechanism

Mode	FEM	(i) With beam mass 1 Element	(ii) W/O beam mass 1 Element	(iii) With beam mass 2 Elements
1st	141.21	140.33	141.82	140.33
2nd	169.52	165.28	165.42	165.28
3rd	2041.2	2101.61	2109.19	2101.61
4th	2422.2	2528.11	2532.47	2528.11
5th	4741.1	5255.80	5279.7	5244.43
6th	7432.3	9742.33	9771.67	7325.57

4 Conclusions

In this work, the modal analysis of flexible platforms with application to precision devices with small displacements and deformations was presented. A stiffness matrix for a Euler-Bernoulli beam was derived by applying the Screw Theory formalism. This matrix allows to be assembled in a simple and direct way to carry out static analysis of flexible mechanisms and, together with a mass matrix of concentrated parameters, it also allows to carry out the modal analysis of flexible mechanisms. Using the proposed beam, the flexure elements of a flexible mechanism with two rotational degrees of freedom were modeled to analyze their vibration modes. The results of the modal analysis obtained with the proposed analytical method were validated with the finite element method and its accuracy was acceptable and had faster execution than the FEM, highlighting that the number of beam elements per flexure element is important to capture the correct physics of the modal analysis.

References

1. Howell, L.L., Magleby, S.P., Olsen, B.M.: Handbook of Compliant Mechanisms. John Wiley & Sons, New York (2013)
2. Song, Y., Panas, R.M., Hopkins, J.B.: A review of micromirror arrays. Precis. Eng. **51**, 729–761 (2018)
3. Hopkins, J.B., Song, Y.P., Wang, S.Y., Behbahani, A.H., Josefson, I.: Optimal actuation of dynamically driven serial and hybrid flexure systems. In: Proceedings of the ASME IDETC/CIE 2014, pp. DETC2014-35181, Buffalo, NY, USA (2014)
4. Li, Z., Kota, S.: Dynamic Analysis of Compliant Mechanisms. Volume 5: 27th Biennial Mechanisms and Robotics Conference (2002)
5. Pucheta, M.A., Gallardo, A.G.: Synthesis of hybrid flexible mechanisms using beams and spatial design constraints. In: Pucheta, M., Cardona, A., Preidikman, S., Hecker, R. (eds.) MuSMe 2021. MMS, vol. 94, pp. 47–56. Springer, Cham (2021). https://doi.org/10.1007/978-3-030-60372-4_6
6. Hopkins, J.B., Lange, K.J., Spadaccini, C.M.: Designing microstructural architectures with thermally actuated properties using freedom, actuation, and constraint topologies. ASME J. Mech. Des. **135**(6), 061004 (2013)

7. Wu, S.L., Shao, Z.X., et al.: An energy-based approach for kinetostatic modeling of general compliant mechanisms. Mech. Mach. Theory **142**, 103588 (2019)
8. Selig, J.M., Ding, X.: A screw theory of static beams. In: IEEE International Conference on Intelligent Robots and Systems, Maui, Hawaii, pp. 2544–2550 (2001)
9. Ding, X.L., Selig, J.M.: Screw theoretic view on dynamics of spatially compliant beam. Appl. Math. Mech. **31**(9), 1173–1188 (2010)
10. Géradin, M., Rixen, J.D.: Mechanical Vibrations: Theory and Application to Structural Dynamics, 3rd edn. John Wiley & Sons, UK (2015)

OpenBeam: Off-Line and On-Line Tools to Solve Static Analysis of Mechanical Structures

José Luis Blanco-Claraco[1](✉) [iD], Javier López-Martínez[2],
Francisco Javier Garrido-Jiménez[2], Pedro Gómez-Calvache[2],
and José Manuel García-Manrique-Ocaña[3]

[1] Engineering Department, Agrifood Campus of International Excellence (ceiA3), University of Almería, Almería, Spain
jlblanco@ual.es

[2] Engineering Department, University of Almería, Almería, Spain

[3] Civil Engineering, Materials, and Fabrication Department, University of Málaga, Málaga, Spain

Abstract. The direct stiffness matrix method for static calculation of structures represents one of the most precise and efficient paradigms to address the analysis of the structures most typically used in construction. The present work intends to fill a niche in open-source software in the field of computational mechanics in relation to said matrix methods, providing a C++ programming library and a set of associated tools that allow an easy approach to structural analysis. This new project, named *OpenBeam*, presents a design that emphasizes didactic applications with, among other features: an easy parameterization of structures, the presentation of diagram graphs, and the creation of animations of the deformed structures. In addition, an interactive version of the software is offered as a freely accessible online tool for use on any desktop or mobile device without the need for installations since it runs directly on the web browser. The application is accessible from https://open-beam.github.io/openbeam/.

Keywords: Stiffness matrix method · finite elements · educative innovation · web applications

1 Introduction

Matrix methods are widely known and used today for static calculation of structures typically used in construction [1, 2] and, through the finite element method, of arbitrary pieces in two or three dimensions [7]. With this work we intend to fill a niche in the open-source software of the field of computational mechanics in relation to said matrix methods, providing a C++ library and a set of associated tools to ease computational structural analysis. The software is design emphasizing a didactic aiming by means of, among other features, parameterization of structures, the presentation of force diagrams, and the creation of animations of the deformed structures.

The availability of versatile, open-source and universally free matrix calculation tools for structures would have multiple applications. Firstly, as a reusable block (programming language library) in the creation of static analysis tools for engineering projects. In the educational field, it would allow the automation of tasks such as the creation of graphics and animations of different structures, including the parametric generation of structures and the automatic calculation of static solutions (reactions, deformations, and stresses), thus facilitating the creation of teaching material, including randomized exercises and exams. Carrying all this out online, from a web browser, minimizes the access threshold to the tool.

At present there are numerous software for structural calculation using the matrix method and/or by the finite element method, but most are proprietary software. This work presents an open-source software that, in addition, in its offline form is compatible with all major operating systems (Windows, Mac, and GNU/Linux), and in its online form works from any computer or modern mobile device. Another of its noteworthy feature is its ability to define nodal coordinates not concordant with the global coordinate axis [10], allowing the definition of sliders with arbitrary orientations.

The presented software is written in C++ 17 [11] and makes use of the well-known Eigen3 library [3] for calculations with dense and sparse matrices. Documentation and online tools are available on the project website [4] and the Git repository[1].

The rest of this article is organized as follows. Section 2 exposes the materials and methods, Sect. 3 presents the results of the work, and finally the conclusions are summarized in Sect. 4.

2 Methods

2.1 Direct Stiffness Matrix Method

This matrix method is not limited by the type of structure as other classical calculation methods are, by means of organizing all the information about the structure in the form of matrices. In addition, a greater number of unknowns can be solved compared to classic resolution methods in Strength of Materials [5] and with the benefit of being able to automate it. To be able to apply it to a continuous structure, it is necessary to model it through a discrete and finite set of variables. There is some freedom on the part of the engineer when choosing: (i) the way in which continuous bodies are divided into a discrete series of elements, and (ii) how many degrees of freedom (dof) each of these elements will have at the joints (or nodes). It should be noted that the use of the stiffness method is motivated by the greater ease of automation, allowing to define a library of predefined elements with stiffness matrices with known expressions from an earlier theoretical analysis [1, 7, 10].

2.2 Distributed Loads

The study of discretized problems implies that: (i) results are obtained only for the state vector dof, and (ii) only point loads can be defined. Therefore, any distributed

---

[1] URL: https://github.com/open-beam/openbeam.

loads must be converted into equivalent concentrated loads, for which the well-known methods in matrix calculus [10] are used using the Strength of Materials equations [5, 8, 9]. Regarding the axial, shear, bending and torsion moments, in our work we have opted to mesh the structures in sufficiently small elements, so that, by calculating the stresses at the ends of each element in a rigorous manner, linear piecewise stress diagrams are obtained. The following distributed loads have been implemented: uniform, trapezoidal, temperature variation, and non-nodal point.

2.3 Meshing

Meshing is the step in which a continuous solid is divided into a multitude of finite elements [7]. In our work, only basic meshing of linear elements (rods or beams) into smaller, also linear elements has been necessary, so the connectivity between elements after meshing is trivial as it is purely linear. There are two noteworthy aspects: (i) An element of a particular type (see Fig. 1), when meshed, can be converted into several elements of different types according to the degrees of freedom defined at its ends (e.g. when meshing a bi-articulated bar, an articulated-rigid element, several rigid-rigid elements, and finally a rigid-articulated element will be obtained), and (ii) distributed loads along a beam or bar must also be "meshed" to be distributed among the finite elements, which are the ones that are finally calculated.

2.4 Eigen3 Library

Eigen (version 3) is one of the most widely used C++ libraries in multiple engineering fields to represent and manipulate matrices, vectors, and tensors [3]. It allows two representation modes for matrices: dense and sparse. The formers are used in our work to represent the stiffness submatrices of finite elements, as well as generalized coordinate vectors. Sparse matrices are suited for stiffness matrices of very large structures, especially after meshing, since each element is typically only connected to a few neighboring elements. Once sparse matrices are represented, the resolution of canonical linear systems Ax = b, as required in our work, demands specifically algorithms to exploit the matrix sparsity and solve them in typically almost linear time $O(N)$ instead of cubic $O(N^3)$, with N the number of degrees of freedom. Two algorithms have been implemented in the library to solve this linear system: (i) the Cholesky decomposition (LL^T) algorithm for the K_{ff}, converted to a dense matrix, and (ii) Cholesky for the pure sparse matrix case [3]. By default, the dense matrix version is used, since most of the structures analyzed will be of a size small enough for the sparse method to not be computationally advantageous.

2.5 MRPT-opengl Library

MRPT ("Mobile Robot Programming Toolkit") is an open-software project that offers C++ libraries with algorithms and tools for mobile robot programming [12]. Its mrpt-opengl module offers a library for the generation of 3D graphics in a modular way through assembly and composition of basic visual primitives (lines, points, cylinders, etc.), chosen to generate and dynamically update the visualizations of structures.
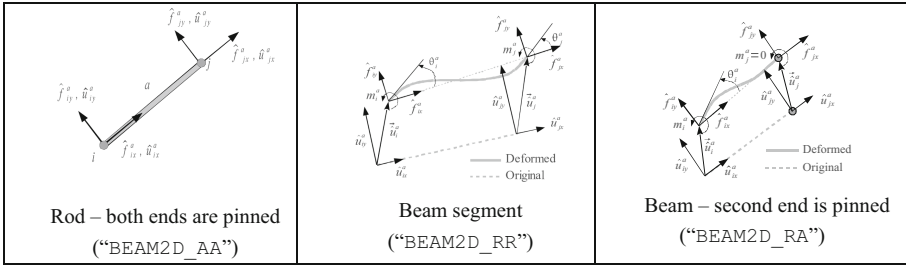
Fig. 1. A few of the available types of finite elements implemented in *libopenbeam*, together with their short names as specified in the structure definition files.

2.6 Emscripten

Emscripten [13] is a project, presented in 2011 and in active development, which provides a modified version of the clang compiler capable of cross-compiling from various languages (including C++) to JavaScript and WebAsm. By compiling MRPT, Eigen3, and OpenBeam all with Emscripten, web applications in Javascript have been developed that make use of all the high-level functions exposed in OpenBeam, such as analyzing a structure definition file, performing static analysis, or generating and updating its graphical representation in an html5 WebGL canvas [14].

3 Results

3.1 The Openbeam C++ Library

The main functionality developed in this work is integrated into a C++ library, which is used by the applications themselves, and which can be used by users interested in creating their own projects.

3.2 Implemented Finite Elements

At present, implemented elements are eminently planar: rods, beams, and springs. Figure 1 illustrates a few of the implemented elements. As can be seen, they are all binary (connecting only two nodes) and each one makes use of a variable number of degrees of freedom at each of its two ends.

3.3 YAML Structure Definition Language

An example in Fig. 2 illustrates how users can describe the structure to analyze by means of our custom structure definition language in YAML [6], with all syntax details available online. Note that, whenever a numerical value is needed, mathematical expressions (algebraic operations, trigonometric functions, etc.) can be used at any point, as well as more complex constructions such as "if… Then… Else" if the user requires it (e.g. to define that a load only exists if a length meets certain criteria), allowing easy parameterization of structures.

```yaml
parameters:
  G: 9.81
  L: 3.0
  H: 4.0
beam_sections:
- name: IPE200
  E: 2.1e11     # Young module
  A: 28.5e-4    # Area
  Iz: 1940e-8   # Second moment of area in z
nodes:
- {id: 0, coords: [0    , 0], label: A}
- {id: 1, coords: [0    , H], label: B}
- {id: 2, coords: [L    , H], label: C}
- {id: 3, coords: [L    , 0], label: D, rot_z: 30.0}
elements:
- {type: BEAM2D_RR, nodes: [0, 1], section: IPE200}
- {type: BEAM2D_RR, nodes: [1, 2], section: IPE200}
- {type: BEAM2D_RR, nodes: [2, 3], section: IPE200}
constraints:
- {node: 0, dof: DXDYRZ}
- {node: 3, dof: DY}
element_loads:
- {element: 1, type: DISTRIB_UNIFORM, q: 1000*G, DX: 0, DY: -1, DZ: 0}
```

(a)
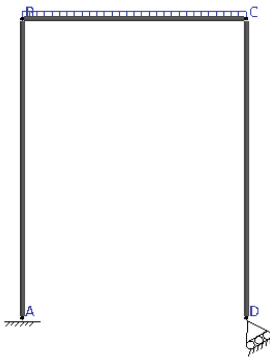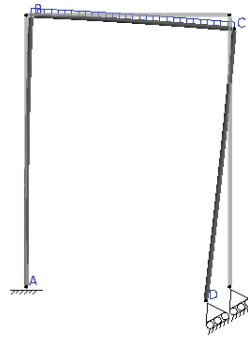
(b)   (c)

Fig. 2. (a) Example of the YAML structure definition language used in OpenBeam. Visual representation of the structure in (b) its original state, and (c) deformed under loads.

3.4 Applications

A command-line off-line program called "ob-solve" has been developed, with more than thirty arguments and flags to: load a structure from a YAML file, show the results of the static analysis to the console or to an HTML file, show the stiffness matrices, generate visualizations of the structure in its original or deformed states, etc. Examples of the results of this program are provided in an online repository[2]. The on-line version of this program is more interactive and is designed to be used by students and professors in the most intuitive way.

---

[2] URL: https://ingmec.ual.es/openbeam/fem/.

4 Conclusions

Several objectives have been achieved with this work: a new open-source library with a high-level API to define mechanical structures and solve static analysis of them. Two ready-to-use tools are also presented: (i) the command line program with potential for both students and professors, and (ii) the web page with the online tool, which makes it, to the best of the authors' knowledge, the first application capable of running on the web and mobile devices that allows arbitrarily complex structures to be defined and calculated, completely free of charge and with open-source code.

References

1. Rubinstein, M.F.: Matrix Computer Analysis of Structures. Prentice Hall (1966)
2. Ghali, A., Neville, A.M., Brown, T.G.: Structural Analysis: A Unified Classical and Matrix Approach, 6th edn. CRC Press (2017)
3. Guennebaud, G., Jacob, B., et al.: Eigen v3, https://eigen.tuxfamily.org/ (2010). Last accessed 1 Feb 2023
4. OpenBeam Homepage: https://open-beam.github.io/openbeam/. Last accessed 20 Mar 2022
5. Blanco-Claraco, J.L., Garrido Jiménez, F.J., López Martínez, J., Jiménez Alonso, J.F., Hernández Díaz, A.M.: Resistencia de materiales: Resumen de teoría y problemas resueltos, vol. 7. Editorial Universidad Almería (2016)
6. Ben-Kiki, O., Evans, C., Ingerson, B.: YAML Ain't Markup Language (YAML) Version 1.2 (2009)
7. Liu, G.R., Quek, S.S.: The Finite Element Method: A Practical Course. Butterworth-Heinemann (2013)
8. Ortiz-Berrocal, L.: Resistencia de materiales. McGraw-Hill (2007)
9. Vázquez, M.: Resistencia de Materiales, 4ª edn. Noela (2008)
10. Blanco-Claraco, J.L., González, A., García-Manrique-Ocaña, J.M.: Análisis estático de estructuras por el método matricial. Servicio de Publicaciones e Intercambio Científico de la Universidad de Málaga, (2012)
11. Smith, R.: Working Draft, Standard for Programming Language C++ N4659. Google Inc, 03–21 (2017)
12. Blanco-Claraco, J.L. et al.: Mobile robot programming toolkit (MRPT) (2022). https://www.mrpt.org. Last accessed 9 Nov 2022
13. Zakai, A.: Emscripten: an LLVM-to-JavaScript compiler. In: Proceedings of the ACM International Conference Companion on Object Oriented Programming Systems Languages and Applications Companion, pp. 301–312 (2011)
14. Parisi, T.: WebGL: Up and Running. O'Reilly Media, Inc. (2012)

Failure Analysis of a Conveyor Belt Rail (Tripper) of Mineral

Carlos Fosca[(✉)]

Pontificia Universidad Católica del Perú, Lima, Peru
cfosca@pucp.edu.pe

Abstract. A failure analysis of a fractured rail corresponding to a railway conveyor belt (Tripper) that operated in service for two years has been carried out. A visual inspection, chemical composition analysis, metallographic analysis, hardness and microhardness measurements were carried out on the failed piece. The rail was made of 0.89% C carbon steel and presented a decarburized area on the running surface, with strong plastic deformation due to the operation and work hardened. The metallurgical root cause is associated with the presence of pro-eutectoid ferrite and non-metallic inclusions that have been severely deformed by rolling stresses, generating a weak continuous region that nucleated rolling contact fatigue cracks (RCF) and accelerated the formation of a longitudinal crack that propagated vertically (vertical split head) as a consequence of other possible material defects.

Keywords: rolling contact fatigue · rail fracture · rail failure analysis

1 Introduction

One of the most common failures in the rails is the fracture due to rolling contact fatigue (Rolling Contact Fatigue), this failure mechanism can have multiple manifestations in the rail as "Gauge Corner Checking", "Head checking", " Pitting", "Spalling", etc. [1]. However, it is also possible that manufacturing defects may occur that cause breaks in service, as is the case with the vertical cracking of the rail head (vertical split head) [2]. Another important factor in fatigue life of a rail is the degree of cold deformation hardening that has experienced the rolling area. As a result, there is a materials anisotropy, that strongly affects the development of rolling contact fatigue (RCF) [3].

The present study corresponds to the fractured rail failure analysis corresponding to a mineral conveyor belt (tripper). Figure 1 shows a piece of the fractured rail next to an unused rail, which were supplied to determine the root cause of the failure. The tripper has four wheels per side, the rails support vertical forces of up to 1027 KN. The amount of cycles per day is 250 on average. After two years of operation, the rail system suffers the fracture at one of its ends.

According to the information provided, the steel of the rail corresponds to a CR104 Steel Head Hardened (HH) and fits the ASTM A759-10 specifications.

Fig. 1. View of the parts of a rail system, supplied for analysis.

2 Results and Analysis

To carry out this fault analysis, the following tests and analysis were carried out:

- Visual and magnetic particles
- Chemical analysis of the rail material
- Hardness tests.
- Metallographic and micro-hardness measurements
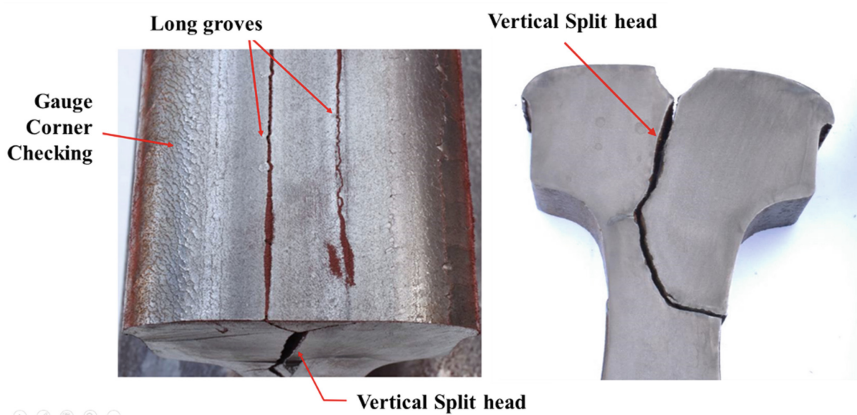
Fig. 2. Long grooves, gauge corner checking and vertical split heads present in the fractured rail.

2.1   Visual Inspection

Two longitudinal cracks (long grooves) were observed on the head of the rail (Fig. 2) that spread into the interior of the material. Subsequently, a vertical crack was developed (vertical split Head). Another important observation is the strong plastic deformation observed in the head of the rail, appreciating a reduction in the height of the same of 3 mm and a widening of the edge of the rail (gauge corner region).

2.2   Chemical Composition Analysis

Samples of the fractured rail and the new rail for their corresponding chemical analysis were extracted. The analysis was performed by optical emission spectrometry according with the ASTM E60-11 standard, the analysis result is shown in Table 1.

Table 1. Chemical composition (% weight) of the failed rail and the new rail

sample	C	Mn	Si	P	S	Ni	Cr	Mo	Cu	V
New Rail	0.80	0.93	0.35	0.014	0.010	0.13	0.19	0.04	0.31	0.00
Cracked rail	0.89	0.68	0.38	0.009	0.009	0.12	0.26	0.03	0.28	0.10
ASTM A759-10	0.67 - 0.84	0.70 – 1.10	0.10 – 0.50	0.04 Max.	0.05 Max.	----	----	----	-----	----

From the chemical analysis results, it can be concluded that the materials of both rail sections comply with the material specifications for crane rails according to the ASTM standard to 759-10. However, the fractured rail presents a slightly higher C content (0.89%C).

2.3   Hardness Measurement

Transversal sections of the supplied rails (new and fractured) were cut. Hardness measurements were carried out using a Equotip® Leeb hardness portable equipment. The new rail presented a hardness in its cross section that ranged between 292–366 HB while the fractured rail had a hardness between 336 and 393 HB. According to ASTM A759-10, high strength rails must have a HB hardness between the range of 321 to 388. According to this, the hardness of the fractured rail conforms better to the specification's standard.

2.4   Metallographic Analysis

A metallographic analysis was carried out in samples extracted from the portion of the new rail and the fractured rail. The metallographic etching was performed using 2% Nital

reagent. The microstructure of the new rail in the surface of the head was Proeutectoid Ferrite (F) and Perlite (P) (Fig. 3.a) while the microstructure of the area immediately under the surface was constituted by equiaxial grains of Perlite (P) (Fig. 3.b). This last microstructure is close correlation with the chemical composition of the steel of the analyzed rail. The microstructure of the head surface is consequence of a decarburization process during the rail manufacturing.
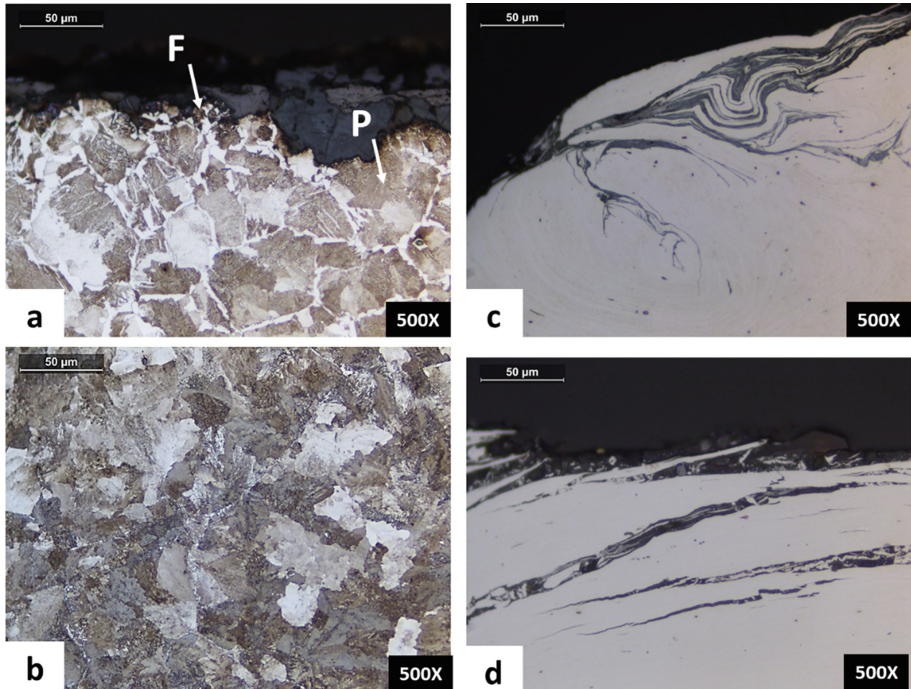
Fig. 3. [a] [b] Micrographs of the original rail (new) showing decarburation zone in the surface [a] (etching: 2% Nital). [c][d] Non etching micrographs of the head zone of failed rail showing non-metallic inclusions strongly deformed and aligned [c] and propagation of micro-cracks following the paths of aligned non-metallic inclusions [d].

The head of the fractured rail presented in the rolling contact area a strong plastic deformation (180–350 microns) that caused the deformation and realignment of non-metallic inclusions (Fig. 3.c). In addition, microcracks that follow the paths of the realigned non-metallic inclusions were observed (Fig. 3.d).

2.5   Micro Hardness Measurement

The strain-hardening layer observed in the head of the fractured rail presented hardness values of up to 573 HV0.5, while the region of the material away from the hardened area it presented hardness between 412–430 HV0.5 (See Fig. 4). Due to the differences in mechanical properties between the pro-eutectoid ferrite (decarburized zones), much

more ductile, and the perlite, the deformation does not occur uniformly at the microstructural level and the pro-eutectoid ferrite is constituted in points of preferential start of fatigue micro-cracks [4–6]. Similarly, ductile non-metallic inclusions such as manganese sulfide can become nucleation points of rolling contact fatigue cracks (RCF) in strongly deformed areas of the rolling surface [7].
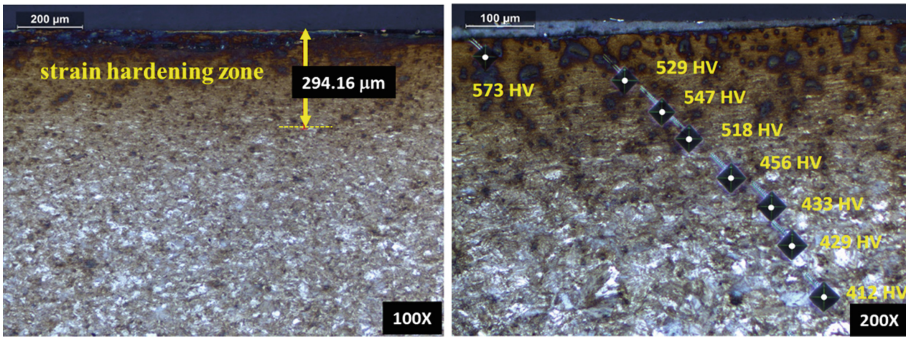
Fig. 4. Micrographs of samples extracted from the head of the fractured rail where the strain-hardening zone and the hardness (HV0.5) values can be seen

These surface cracks are caused by the contact stresses between the crane wheel and the rail. The mechanism that originates them is known as rolling contact fatigue (RCF). These cracks grow preferably in the riel longitudinal direction, but they also spread in the other directions due to the triaxial load system that occurs inside the rail due to the load with the wheel [8]. The trajectory of the crack is determined by the load, the anisotropy of the plastically deformed layer and the weaknesses of the material [3].

The nucleation of these longitudinal surface cracks can have its origin in numerous causes, such as hardening by high localized plastic deformation, presence of non-metallic inclusions aligned (oxides, sulphides) that act as stresses micro-concentrators, surface defects such as laminations, etc.

3   Conclusions

The fractured rail exhibited a combination of defects that acted synergistically in its premature failure (approximately two years). The head rail presented a decarburized surface with the presence of pro-eutectoid ferrite, which coupled with the presence of segregation of realigned non-metallic inclusions, caused a mechanically weak region, compared to the severely strain hardened pearlite.

The cyclic loading originated by the contact between the wheel and the rail, generated rolling contact fatigue damage in different parts of the head of the rail (gauge corner checking) and long grooves more associated with laminations or manufacturing defects, but that was accelerated by cracking in strain hardened layer due to contact fatigue. The confluence of these cracking fronts resulted in the fracture of the component through a vertical crack (vertical Split Head).

References

1. Office of Railroad Safety: Track Inspector Rail Defect Reference Manual. Federal Railroad Administration, USA (2015)
2. NSW: Rail Defects Handbook. Engineering Manual Track, RailCorp Network (2012)
3. Schilke, M.: Degradation of Railway Rails from a Materials Point of View. Chalmers University of Technology, Göteborg, Sweden (2013)
4. Chard, A.: Deformation of Inclusions in Rail Steel Due to Rolling Contact. University of Birmingham, Birmingham (2011)
5. Beynon, J.H., Garnham, J.E., Sawley, K.J.: Rolling contact fatigue of three pearlitic rail steels. Wear **192**, 94–111 (1996)
6. Davis, C.L., Garnham, J.E.: The role of deformed rail microstructure on rolling contact fatigue initiation. Wear **265**, 1363–1372 (2008)
7. Garnham, J.E., Ding, R.-G., Davis, C.L.: Ductile inclusions in rail, subject to compressive rolling–sliding contact. Wear **269**, 733–746 (2010)
8. Németh, A.: Case Studies in Railway Construction: Rolling Contact Fatigue Rail Defects. Széchenyi István University, Győr, Hungary (2017)

Vibration Analysis in Agricultural Vehicles for Fault Detection

Carlos Mafla-Yépez[1(✉)], Cristina Castejon-Sisamon[2], and Higinio Rubio-Alonso[2]

[1] Automotive Engineering Research Group, Faculty of Engineering in Applied Science,
University Técnica del Norte, Ibarra, Ecuador
`cnmafla@utn.edu.ec`

[2] MAQLAB Research Group, Department of Mechanical Engineering, University Carlos III de
Madrid, Madrid, Spain
`{castejon,hrubio}@ing.uc3m.es`

Abstract. Failure analysis of farm tractor's engines and internal combustion engines is done using vibration analysis due to its efficiency and because it is not invasive to the engine operation. In this work, engine failures are studied based on failures of the injectors opening pressure. The vibration data was obtained by a sensor located in the cylinder block close to the compression chamber. The Fast Fourier Transform (FFT) was applied to obtain characteristics in each engine operating status (injector failures). With the statistical analysis, the characteristics are selected for the classification of the engine status and later failures prediction. The results demonstrate the validity of the proposed method.

Keywords: Vibration analysis · agricultural vehicles · fault diagnosis · Internal combustion engines

1 Introduction

Agricultural vehicles have an internal combustion engine, which currently can be monitored in real time using sensors. Engine monitoring can provide large amounts of data containing dynamic, combustion, fluid flow processes and major events of current engine conditions, with this data failure detection can be achieved, thus preventing further damage to the engine, as well as reducing engine performance [1].

Different studies have been carried out on the prediction, evaluation and diagnosis of machine failures using artificial intelligence techniques. Artificial Neural Network (ANN) and a humidity sensor were used for modeling sensor failures applying different temperatures [2]. The Wavelet transform and an ANN classifier to predict failures were used to evaluate bearing operating condition monitoring performance [3]. Several authors used sensors and diagnose motor failures, using the Wavelet packet transform, NN and spectrograms for the autonomous prediction of failures [4, 5]. In the same way there are predictive maintenance techniques based on vibrations to know the state of the engine [6]. Research on engine failure prediction mechanisms to reduce fuel consumption and exhaust emissions is vital and necessary [7].

Vibration in agricultural vehicle engines can be detrimental to their proper functioning, and vibration can affect the life of the engine [8]. Different studies focused on the reduction of maintenance costs, for example, for aircraft engines where they have an expenditure of 10.3% of the budget [9]. Thus, one of the objectives of predictive maintenance is to reduce this expense by using on-board sensors to monitor the health status of machine components. Predictive maintenance aims to identify potential malfunctions in advance, allowing a quick intervention before the actual problem arises. With condition-based maintenance, the aim is to schedule maintenance activities only when a functional fault is detected. Proactive maintenance puts primary emphasis on tracing all failures back to their root cause [10, 11].

To obtain measurements with different states, three levels of failure were simulated in the test bench that are in the injectors by adjusting the opening pressure and that directly affect the combustion and therefore the operation of the rest of the system.

2 Methodology

The data is obtained from a compression-ignition engine with three four-stroke cylinders that has an output of 51.2 HP. Four variables of engine operation at a single speed (idle) are studied. Vibration data is obtained using the ICP® 603C01 piezoelectric accelerometer. The signals are captured and processed using a DAQ NI 9250 data acquisition card with software designed in LabVIEW and they are stored in the computer to be processed. The characteristics obtained from each vibration signal are the number of data obtained per sample is 64,000 with a sampling frequency of 8,000 Hz.

The characteristics obtained from the vibration signal are inputs for the autonomous learning system where the different operating conditions of the motor are grouped. The considered conditions are: normal engine operation (BE) and failure in the opening pressure of the injectors with three levels of failure of opening of injectors 25% (ME25), 50% (ME50) and 75% (ME75). The variables considered have influence on the behavior of the engine, but they do not cause the engine to stop working (serious failure). Therefore, if the engine fails, the classification made in autonomous learning will group the defects according to the conditions entered: BE, ME25, ME50, ME75. Each feature for the different operating variables has 200 samples of 64,000 measurement points of vibration signals, where 80% of the samples are used to train learning and 20% to test and validate each case.

2.1 Decision Tree

It is a scheme that is used to decide and solve problems, to achieve this you must consider criteria and make decisions. Decision trees are a classification technique easy to interpret and use, which generate rules in the form of a tree, where the data set is divided into branches until segments of similar behavior are obtained depending on the target variable, and are used in decision making [12].

Decision trees allow to categorize a series of characteristics and parameters. In condition monitoring, and to guarantee the efficiency of this procedure, different operating conditions must be included, and ranges established for each of them [13].

This study will compare possible engine states mentioned above. The training of the decision tree was done using 5 statistical variables of the vibration signal (Median, Mode, Square Mean, Kurtosis and Asymmetry).

2.2 Obtaining Features

To obtain the characteristics is of vital importance in intelligent classification systems, several investigations have used different methods. This work is framed in the analysis of vibration, in the domain of time (the decision tree uses parameters of the time signal) and additionally a frequency analysis was performed. This methodology has been used by several studies [16]. For frequency analysis, the Fourier transform is traditionally used since it can convert a time domain signal into a frequency domain and thus be able to obtain information on frequencies and amplitude for raw signals.

The vibration data obtained in the time domain were transformed into the frequency domain. We recognized the dominant frequencies in each signal. The amplitude and frequency of each peak becomes the dominant characteristics based on frequency.

2.3 Extracted Characteristics

The extraction of the characteristics tries to filter the data with a high level of similarity [17, 18]. The vibration data obtained and characterized according to their state (BE, ME25, ME50 and ME75) are subjected to statistical calculations to determine the values to be used to perform the training, consequently, the important characteristics that contribute to the classifier to select patterns for prediction will be determined. For the different tests the engine revolutions will be considered according to the operating state (BE-850 RPM, ME25-850 RPM, ME50-900, ME75-1400 RPM). For the classification of failures, an intelligent system is created to predict failures in an engine according to the defined states (BE, ME25, ME50 and ME75).

3 Results

3.1 Feature Analysis

The vibration data obtained will be used in the classification of learning and subsequent failure prediction processes. Figure 1 shows the signal recorded for 0.8 s with an accelerometer, for each of the engine operating states: Good condition (BE) (a), ME25 (b), ME50 (c) and ME75 (d), where a considerable difference is observed compared to the change of engine speed (RPM). When causing a serious failure there are changes in the behavior of the engine and increases the RPM.

The characteristics for the conditions of the study (BE, ME25, ME50, ME75) are described below. Table 2 shows the values, in the frequency domain, extracted from the acquired vibration signal. There are 4 variables from which the characteristics were extracted directly from the sensor, and processed with the Fourier Transform, corresponding to the two amplitude values of the signal max. and their amplitude.

In Fig. 2 a) the area in which the characteristics will be taken is demonstrated to compare and carry out the research, in b) the characterization of the engine in BE status

a) Well working engine vibrations

b) ME25 wrong working engine Vibrations

c) ME50 wrong working engine Vibrations

d) ME75 wrong working engine Vibrations
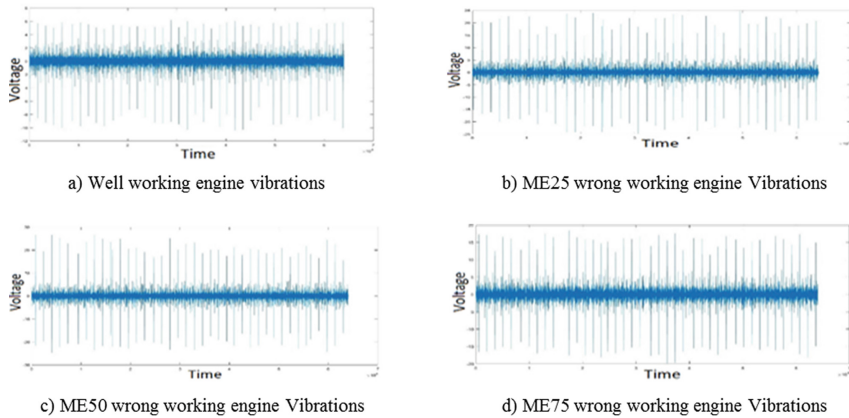
Fig. 1. Raw signals

Table 1. Characterization values

State	Feature 1		Feature 2	
	Frequency (Hz)	Amplitude (V)	Frequency (Hz)	Amplitude (V)
BEE	44	7	58	10
ME25	44	7	58	10
ME50	45	8	61	12
ME75	42	2	55	8

is shown where the main characteristics were selected, which in this study and for all the variables were 2 per sample. Considering (b) we proceed to analyze the other variables. In (c) where the same characteristics can be observed in the ME25 variable, but more pronounced peaks are noted which indicates that a failure may occur in the future, as shown in Table 1, the two characteristics are identical. In (d) presents the ME50 status a difference in the two characteristics is noted where it increases both in frequency and amplitude considering the Fig. 2 (b), having a considerable variation the damage to the engine is identified and in the same way the engine speed varies. The Fig. 2 (e) failure (ME75) a big difference can be noticed with the variable of good condition; this is because it is the strongest fault that can occur, and that the engine can start and work. In this way, characteristics are obtained to achieve adequate training patterns and predict failures of agricultural engines.

Figure 3 presents the scatter plot, which is a method of validation of learning where an efficiency of 95% is obtained and the distribution of the different characteristics obtained based on the variables studied is observed. It is not possible to differentiate or separate the points of the BE and ME25 classes that have similarity with respect to their variance and kurtosis characteristics. However, there is a clear difference of the classes

in the characteristics of ME75, where the engine already has considerable failures in its operation, this failure would be the most severe that can be simulated.

a) Engine in good condition (BE).

b) Engine in poor condition (ME25).

c) Engine in poor condition (ME50).

d) Engine in poor condition (ME75).

e) Area of characteristics to work.
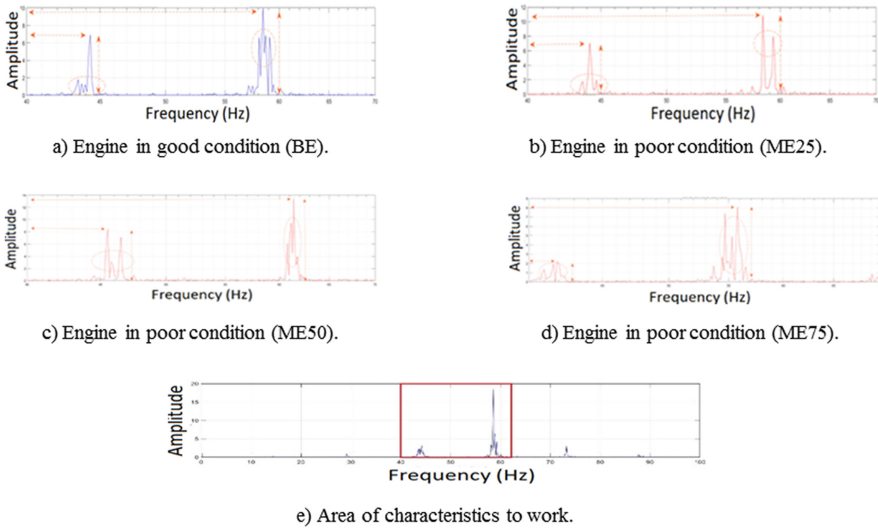
Fig. 2. Vibration characteristics
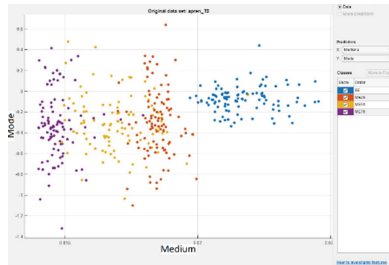
Fig. 3. Scatter plot

4   Conclusion

An analysis of vibration signal characteristics (statistics of the temporal signal and the frequency domain) was carried out for the monitoring of failures in an agricultural vehicle engine. For this research, a methodology was proposed to diagnose engine failures based on three possible defects in the injectors that directly affect combustion. For the experimental part, a sensor located in the cylinder block as close to the combustion chamber was used that acquired the vibration data. The study is designed to distinguish four engine states: good condition (BE), poor condition varying 25%, 50% and 75% injector opening (ME25, ME50 and ME75).

Regarding the analysis of the characteristics of the signals in the frequency domain, we have worked with FFT analysis, on the frequency band delimited between 40 and 65 Hz, since it has been found that the characteristics are good indicators of state change, as shown in Fig. 3, where differences in amplitude values were observed for the case of BE and ME25 states with respect to ME50 and ME75. Regarding the characteristics of the time domain, they have been extracted from the measured vibration signals, and using trees decision it was concluded that, of all the statistical parameters calculated, the Quadratic Mean, Kurtosis and Asymmetry are the most interesting characteristics to monitor when trying to diagnose engine failures.

References

1. Ghazaly, N.M., et al.: Prediction of misfire location for SI engine by unsupervised vibration algorithm. Appl. Acoust. **192**, 108726 (2022)
2. Souhil, K., et al.: ANN modeling of a smart MEMS-based capacitive humidity sensor. Int. J. Control. Autom. Syst. **9**(1), 197–202 (2011). https://doi.org/10.1007/s12555-011-0125-3
3. Kumar, H.S., et al.: ANN based evaluation of performance of wavelet transform for condition monitoring of rolling element bearing. Procedia Eng. **64**, 805–814 (2013)
4. Wu, J.-D., Chuang, C.-Q.: Fault diagnosis of internal combustion engines using visual dot patterns of acoustic and vibration signals. NDT E Int. **38**(8), 605–614 (2005)
5. Yadav, S.K., Kalra, P.K.: Automatic fault diagnosis of internal combustion engine based on spectrogram and artificial neural network. In: Proceedings of the 10th WSEAS International Conference Robotics Control Manufacturing Technology ROCOM'10, pp. 101–107 (2010)
6. Delvecchio, S., Bonfiglio, P., Pompoli, F.: Vibro-acoustic condition monitoring of Internal Combustion Engines: a critical review of existing techniques. Mech. Syst. Signal Process. **99**, 661–683 (2018). https://doi.org/10.1016/j.ymssp.2017.06.033
7. Taghizadeh-Alisaraei, A., Mahdivian, A.: Fault detection of injectors in diesel engines using vibration time-frequency analysis. Appl. Acoustic. **143**, 48–58 (2019)
8. Böyükdipi, Ö., et al.: Experimental investigation and artificial neural networks based prediction of engine vibration of a diesel engine fueled with sunflower biodiesel – NH3 mixtures. Fuel **304**, 121462 (2021)
9. de Pater, I., et al.: Alarm-based predictive maintenance scheduling for aircraft engines with imperfect remaining useful life prognostics. Reliab. Eng. & Syst. Saf. **221**, 108341 (2022)
10. Girdhar, P., Scheffer, C.: Predictive maintenance techniques: Part 1 predictive maintenance basics, Practical machinery vibration analysis & predictive maintance, pp. 1–10 (2004)
11. Giordano, D., et al.: Data-driven strategies for predictive maintenance: Lesson learned from an automotive use case. Comput. Ind. **134**, 103554 (2022)
12. Díaz, B., Meleán, R., Marin, W.: Academic performance of students in higher education: predictions of influential factors from decision trees. Telos **23**, 616–639 (2021)
13. Moshkov, M.: Decision trees for regular factorial languages. Array **15**, 100203 (2022)
14. Harmouche, J., et al.: Improved fault diagnosis of ball bearings based on the global spectrum of vibration signals. IEEE Trans. Energy Convers. **30**(1), 376–383 (2015)
15. Singh, P., Basant, N., Gupta, S.: Support vector machines in water quality management. Anal. Chim. Acta **703**(2), 152–162 (2011). https://doi.org/10.1016/j.aca.2011.07.027
16. Mafla, C., et al.: Predictive maintenance in agricultural tractors. Proposal of methodology oriented to connected maintenance. Ibero-Am. J. Mech. Eng. **26**(1), 63–76 (2022)

Collaborative Project to Improve Teaching of Cams' Kinematic and Dynamic Analysis Using Spreadsheets

Miguel Pleguezuelos[✉] , Miryam B. Sánchez , José I. Pedrero ,
and Miguel Castejón

Universidad Nacional de Educación a Distancia – UNED, Madrid, Spain
{msanchez,mpleguezuelos,jpedrero}@ind.uned.es

Abstract. In this paper, we present a learning experience for the improvement of kinematic and dynamic cam analysis teaching through the development of a collaborative project among subject students, based on the realisation of an application in Excel using its ease of use and matrix calculation capacity. For the examination of various cam types, motion programmes, and kinematic response curves, a large class of families of preconfigured curves is evaluated. Similarly, cam sizing is determined by geometric constraints such as pressure angle and radius of curvature. Students from the UNED School of Industrial Engineering perform all of the tasks described. This experience is part of a series of similar projects aimed at improving the academic performance of students involved in these activities by teaching the theory of machine elements.

Keywords: Collaborative teaching projects · Synthesis and analysis of mechanisms · Spreadsheets

1 Introduction

Distance learning in higher studies is a challenge that requires the use of additional techniques and skills to address similar studies in the face-to-face mode. The use of new communication technologies, adapted computer media and the application of more attractive and effective teaching methods, especially in the teaching of STEM subjects, represent a necessary aid for the achievement of teaching objectives [1].

There are numerous computer programs and platforms for mechanical design and calculation in the field of mechanical engineering, some of which are specifically dedicated to the calculation of cams [2–4]. It is absolutely essential to put it into practice gradually because the correct use of it requires knowledge and understanding of all related theoretical concepts. In this context, this article describes a teaching experience that involved the creation of a group project by the students to improve the teaching of the kinematic and dynamic analysis of cams using the creation of an Excel computer application. This application must facilitate obtaining the most relevant and important results in this kind of system, producing visual and numerical results.

the project's main goals can be summarized as follows:

- User-friendly, intuitive, adaptable, and versatile.
- Easily expandable to other needs or calculation requirements.
- Easily adaptable to other spreadsheets of machine elements.
- Didactic approach: support for students and teachers.
- Follow the calculation scheme and nomenclature of the basic bibliography [5].
- Open access without programming requirements.
- A first Spanish version. Upcoming English versions.

Due to its accessibility, ease of use, and capability to perform matrix calculations, Microsoft Excel spreadsheets [6] were chosen as the base for the software application being created to achieve these goals.

2   Theoretical Basis on the Calculation of Cams

2.1   Introduction, Working Principle, and Applications

A cam-follower system is essentially a four-bar linkage with variable-length links. Because of this fundamental difference, cams are particularly advantageous for producing specific output functions in a flexible manner, as they can produce a wide range of output movements [7]. By causing the output element, or follower, to roll or slide on the atypical profile of the input element, or cam, cams are mechanical components that enable the conversion of rotary motion into oscillating motion. There is some sort of spring used to ensure that the contact between the cam and follower is always maintained.

2.2   Terminology and Classification of Cam Systems

The mechanism under study is that of a cam, which performs a uniform movement, and the follower, which performs a periodic movement. Depending on the movements of these components and according to their geometric characteristics, the types of cam-follower systems are classified: according to the spatial configuration, depending on the output movement of the follower, according to the geometry of the follower, depending on the type of closure of the joint, according to the restrictions and the movement program, etc. The reader is advised to consult the standard literature on cam design [7] for further details on each of these types of cams.

2.3   Fundamental Law of Cam Design and Kinematic Diagrams

The next design challenge is to define the mathematical function with which the follower moves as a function of cam rotation, in accordance with the Fundamental Law of Design of Cams, once the foundations for the operation of cam mechanisms have been established. The above Law is equivalent to matching the value of the boundary functions for displacement, velocity, and acceleration, making the functions of displacement parts have continuity of third degree, and making the jerk function finite by subdividing the cam motion functions into several parts.

2.4 Follower Displacement Math Functions

Simple harmonic movement, cycloidal displacement, modified trapezoidal acceleration, modified sinusoidal acceleration, polynomial 3-4-5, polynomial 4-5-6-7, double harmonic movement, 3-4-5-6 polynomial, critical path motion, and constant velocity motion are among the common mathematical functions used in the design of cams.

2.5 Cam Size

The functions to be used in each section are chosen based on the type of cam and follower. The program's SVAJ functions are then generated, and the design's suitability is checked. It is necessary to provide information on the cam size in order to be able to size the cam profile based on the follower type and the SVAJ diagrams. The eccentricity, the primitive curve, the base circumference, and the main circumference are all defined for this. The pressure angle and the radius of curvature are two crucial cam design elements that are examined from these geometrical elements.

3 Cam Profile Analysis and Design Validation

The steps in the design and validation of a cam are logically ordered: choose the type of cam and follower, create SVAJ diagrams, size the cam and its profile, determine the pressure angle and radius of curvature, and validate the cam design to prevent curve radii that are either negative or larger than the follower radius. The system's dynamic forces, damping ratio, critical damping, and damped and undamped natural frequencies are then calculated using a lumped parameter model to perform a dynamic analysis of the system.

The contact force must then be consistently positive in order to prevent the follower from jumping, and the operating speed must be such as to minimise any potential resonance effects. Finally, the required torque is obtained on the camshaft to be able to drive the cam. The contact efforts made by the cam and follower are examined after the contact force has been determined in order to look for any potential contact surface cracks. In order to achieve this, the Hertz contact theory between parallel cylinders is used, and graphs of the main stresses and Von Mises stresses in the proximity of the contact are obtained.

4 Computer Application Design

The application is being developed with its two primary uses in mind: as a teaching tool and as a professional work tool. In this first version, the application's scope is defined for the following design variants: flat rotational cams, programmes with any sequence of up to eight rising, stopping, or falling segments, roller or flat face followers, and varying sorts of closure of form or force.

The Excel application is organised using a spreadsheet for each of its 14 sections, where the design and operation requirements are examined and the set of results' graphs are created. There are two distinct categories of spreadsheet. For application users, an

external spreadsheet. To avoid accidental editing or change, the internal spreadsheets for the developer are hidden. A user manual is created to make the application easier to use or to clarify any usage questions (Fig. 1).
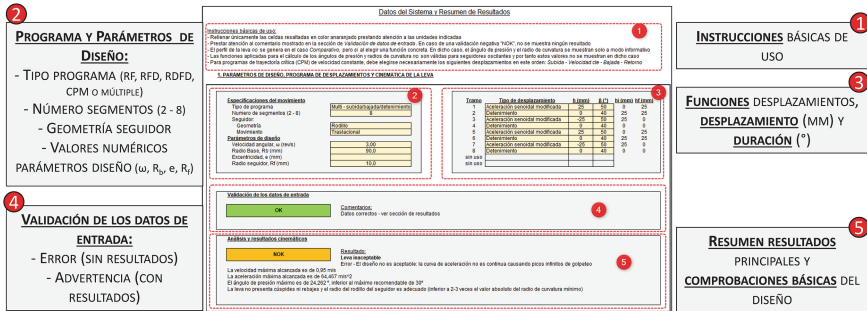
Fig. 1. Kinematic analysis. User interface [8].

4.1   First Part: Kinematic Analysis

The screen is divided into five zones to make it easier to use; numerical data is entered in cells of various colours, and non-numerical data is chosen from drop-down menus:

Zone 1: contains simple operating instructions.
Zone 2: list the type of cam programme and the design that will be examined.
Zone 3: specify the distances and lengths of each segment.
Zone 4: numerous checks produce error or warning messages.
Zone 5: the most significant results are summarised and shown (Fig. 2).

Panel de navegación de la herramienta e indicaciones sobre su contenido

1. Input:	interfaz principal de usuario para entrada de parámetros de diseño y resumen de resultados principales
2. S-V-A-J:	gráficas de desplazamiento, velocidad, aceleración y golpeteo en cada revolución de la leva
3. zoom_S-V-A-J:	mismas gráficas ampliadas en la zona de la primera elevación para mayor detalle
4. φ_p:	gráficas de la evolución del ángulo de presión y del radio de curvatura a lo largo de cada revolución
5. perf_Leva:	gráfica del perfil de la leva junto con circunferencias base y primaria
6. POLAR_perf_φ:	gráfica polar del perfil de la leva con el ángulo de presión superpuesto
7. POLAR_perf_ρ:	gráfica polar del perfil de la leva con el radio de curvatura superpuesto
8. Fuerzas:	fuerza, presión de contacto entre leva y seguidor, y la fuerza de pre-carga
9. Esfuerzos:	tensiones principales (σ, τ, y V.Mises) frente a la distancia de la superficie de contacto adimensionalizada
10. VM_rho:	gráfica del esfuerzo máximo de la tensión de Von Mises representado junto al radio de curvatura de la leva
11. Par_torsión:	gráficas de la fuerza de contacto y el par de torsión del árbol de levas frente al ángulo de giro

Fig. 2. Menu for choosing application results graphically [8].

4.2   Second Part: Dynamic Analysis

The structure and format remain the same as the kinematic analysis part.

Zone 1: introduce the parameters of the concentrated model for the dynamic analysis, as well as the preload deflection.

Zone 2: introduction of material properties and cam width, required to perform contact force calculations.

Zone 3: validate the values needed to continue with the calculations.

Zone 4: displays a summary of the most important results.

Calc. A section hidden in the user's working file that is destined for internal developer use. The Technical Manual explains how it works.

4.3   Spreadsheets of Results

S-V-A-J: SVAJ graphs, with maximum and minimum values for each variable.

Zoom_S-V-A-J: expands the SVAJ graphs, and in the comparative case, five functions are drawn at the same time.

Phi_ρ: pressure angle and radius of curvature over a rotation period.

Perf_leva: the cam's profile, including the base and primary circumferences.

POLAR_perf_φ: cam profile in polar coordinates next to the pressure angle.

POLAR_perf_ρ: cam profile in polar coordinates next to radius of curvature.

Fuerzas: preload force, dynamic force and maximum contact pressure.

Esfuerzos: preload force, dynamic force and maximum contact pressure.

VM_ρ: curvature radius and contact pressure graph.

Par_torsion: torque and the force of contact between the cam and the follower.

Selec. Internal developer section. As a result, it is hidden in the user's work file. The Technical Manual explains how to use it (Fig. 3).
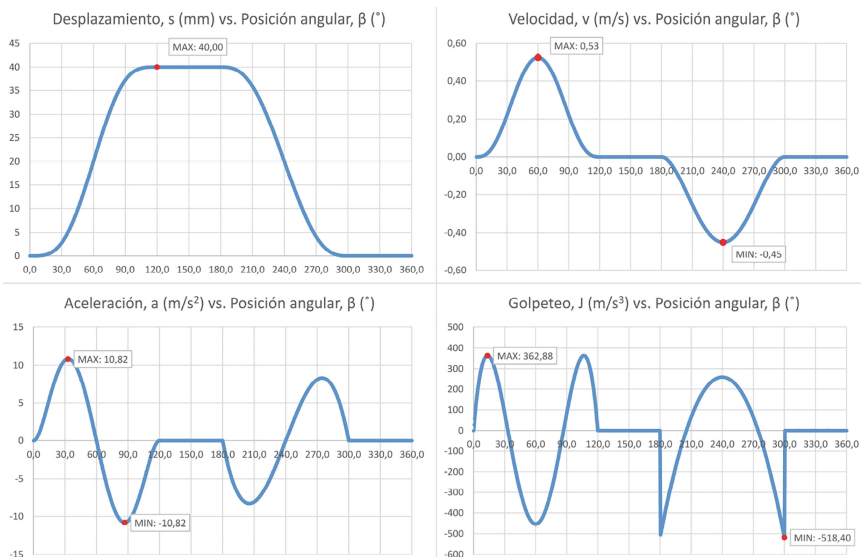
Fig. 3. Results. SVAJ diagrams. [8].

4.4 Technical Manual

The application includes the preparation of a detailed technical manual that explains the operation of the computer application from the developer's perspective. This section is relevant if you want to modify, adapt, or complete the application with a calculation or additional result.

5 Conclusions

As part of a collaborative project carried out by the subject's students, a computer application for the design and calculation of cams was developed, with the following properties: versatile, intuitive, simple, adaptable, and accessible. The goal is to improve the teaching task of the project's developers and student users of the application. It is also a useful tool for teachers in terms of exercise proposal and resolution. Professionals or specialists in cam design can also benefit from the application.

The project is designed to be open to new students' continuous participation in the expansion and improvement of the same, in advanced topics of cams study such as: dynamic study of complete mechanical assemblies, dynamic study of vibrations, study of failure to superficial fatigue, study of wear phenomena, and connection with other axle calculation sheets.

References

1. Artés, M., López, J.: Mechanical engineering at a distance: a review. In: García-Prada, J.C., Castejón, C. (eds.) New Trends in Educational Activity in the Field of Mechanism and Machine Theory, pp. 21–29. Springer International Publishing, Cham (2014). https://doi.org/10.1007/978-3-319-01836-2_3
2. https://saltire.com/analytix/cams.html
3. http://optimusmotus.com/en/cam-gears.html
4. https://psmotion.com/
5. Norton, R.L.: Diseño de Maquinaria, 6a edn. UNED-McGraw Hill, Madrid (2020)
6. Montes, J.M., Ternero, F.: Excel para Ciencia e Ingeniería. 1a ed. Marcombo (2021)
7. Norton, R.L.: Cam Design and Manufacturing Handbook, 2nd edn. Industrial Press (2009)
8. Castejón López, M.: Proyecto Fin de Máster: Aplicación informática para el cálculo de levas. ETSI Industriales. UNED (2022)

Thermo-mechanical Stress Modeling of La(Fe,Co,Si)$_{13}$ Thin Films Deposited on Porous Structures

Francisco Rodríguez-Méndez[1(✉)] , Bruno Chiné[1] ,
and Marcela Meneses-Guzmán[2]

[1] Materials Science and Engineering School, Technological Institute of Costa Rica, Cartago, Costa Rica
frarodriguez@itcr.ac.cr
[2] Industrial Production Engineering School, Technological Institute of Costa Rica, Cartago, Costa Rica

Abstract. The thermo-mechanical behavior of a La(Fe,Co,Si)$_{13}$ thin film deposited on a porous aluminum structure with a uniform geometry has been studied. Computational simulation techniques have been applied to the magnetocaloric material to model the thin film as a material with visco-plastic properties for thermal cycling at room temperature. The values obtained for stress, equivalent strain and cycles necessary for the material failure show a significant improvement in the mechanical stability and fatigue resistance of the metallic porous structure with the La(Fe,Co,Si)$_{13}$ thin film, when compared to a model with the same geometry, but made entirely of La(Fe,Co,Si)$_{13}$. These encouraging results prove the potential that this approach may have in the design and manufacture of magnetocaloric materials for magnetic refrigeration applications.

Keywords: thermo-mechanical stress · magnetocaloric materials · porous structures · computational analysis

1 Introduction

Refrigeration plays a crucial role in a large part of industrial and residential sectors, since the consumption related to thermal management systems is around 30% of the total electricity produced worldwide [1]. Furthermore, current vapor-compression refrigeration systems contribute significantly to global warming due to the release of polluting gases into the atmosphere, such as CO_2 and fluorocarbons commonly used as refrigerants, also demonstrating a poor efficiency in the Carnot cycle (around 10%).

As an environmentally friendly alternative, magnetic refrigeration (MR) has attracted scientific interest as a novel technology with the potential to achieve efficiencies of up to 60% with zero emissions of greenhouse gases [2]. MR is based on the magnetocaloric effect (MCE), which is the response exhibited by a magnetic material when its magnetic moments tend to align parallel to an applied external magnetic field, yielding an increase

in its temperature. The magnetic moments then become randomly oriented when the magnetic field is removed, causing the material to cool down [3].

When developing MR systems, characteristics such as a transition temperature close to room temperature (Curie temperature), first-order magneto-structural transition, zero toxicity, good thermal conductivity, and a high surface area-to-volume ratio [4] must be considered. At the same time, excellent mechanical stability during refrigeration cycles, as well as good ductility and strength, are critical requirements.

Recent investigations [4] have used metal additive manufacturing techniques for the fabrication of MR systems, showing that conforming magnetocaloric materials as uniform porous structures helps maximize heat transfer between the solid refrigerant and the working fluid, while minimizing fluid pressure drop. Also, the possibility of using thin films of magnetocaloric materials deposited on substrates such as metallizations or polymers, has been studied [5]. This configuration can preserve the magnetic and thermal properties of the material, with a non-significant reduction in its MCE.

However, it remains a challenge to ensure a certain degree of ductility and mechanical stability of magnetocaloric materials, as well as fatigue resistance by the normal thermal cycle. As an alternative to improve the mechanical behavior of MR materials, while maintaining its magnetocaloric properties, the objective of this work is to evaluate the thermo-mechanical stress suffered by thin films of a magnetocaloric material when deposited on a porous metallic structure with a uniform geometry, using modeling and computational simulation methods. In particular, $La(Fe,Co,Si)_{13}$ is the alloy of choice as it has a considerable MCE, a manageable Curie temperature in the range of 250 K to 340 K, as well as relatively good mechanical fatigue stability [6].

For the thermo-mechanical stress study, COMSOL Multiphysics software has been used, where the behavior of the magnetocaloric material is modeled as a medium with visco-plastic properties. The fatigue resistance of the material is then calculated using the Morrow model for dissipated energy in defined volumes. Two scenarios were developed: 1) a porous structure made entirely of $La(Fe,Co,Si)_{13}$., and 2) a thin film of $La(Fe,Co,Si)_{13}$ deposited on a porous aluminum structure. Using the numerical results, the performance of the magnetocaloric material in both approaches was compared.

2   Computational Methods

Tensile and compression behaviors of $La(Fe,Co,Si)_{13}$ give a brittle failure with the formation of multiple cracks during the tests and prior to total failure [7, 8]. When analyzing the cracks orientation with respect to the load direction, two failure mechanisms are recognized: 1) fracture due to rupture originated because of transverse tensile stresses parallel to the load, and 2) shear stress fracture created at a 45° angle with respect to the applied force. Both types of fracture are commonly observed in semi- or brittle materials, such as rocks, ceramics, or marble, where they exhibit time-dependent inelastic deformations [9]. Hereby, the mechanical behavior of $La(Fe,Co,Si)_{13}$ can be modeled as a material with visco-plastic properties and crack-induced damage.

Under this approach, the thermo-mechanical stress is solved using the Chaboche model for visco-plastic materials, coupled with the Rankine equivalent deformation model for scalar damage. The magnetization–demagnetization cycle is modeled as a

thermal load in the range of 250 K to 340 K with a cycling frequency of 2 Hz. Finally, fatigue resistance is calculated with the Morrow model for defined volumes.

The geometric pattern of the material consists of a foam-like cellular structure with a matrix of regularly distributed spheres (pores), each one with a diameter of 5 mm and separation distance of 4mm between their centers (Fig. 1(a). The thin film of magnetocaloric material is modeled as a membrane structure with a thickness of 100 nm.
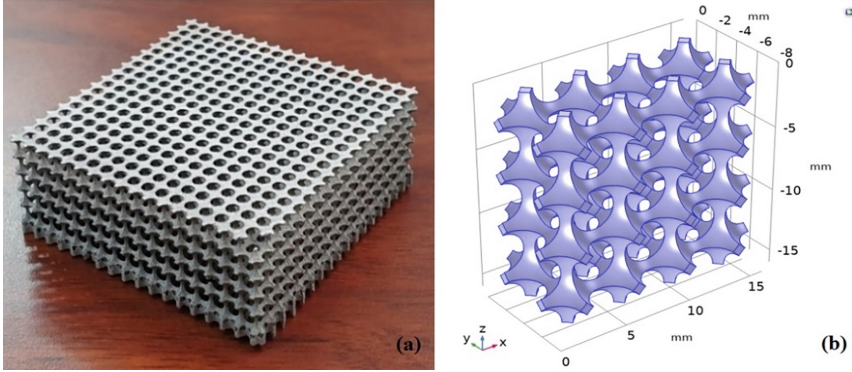
Fig. 1. (a) Porous metallic structure, and **(b)** simplified model for computational analysis.

2.1   Mathematical Model

The visco-plastic strain rate tensor of Chaboche visco-plastic model [10] is given by

$$\dot{\varepsilon}_{vp} = A \left(\frac{F_y}{\sigma_{ref}} \right)^n \boldsymbol{n}^D \tag{1}$$

where A is the coefficient of the visco-plastic change rate (1/s), n is the stress exponent, σ_{ref} is the reference stress level (Pa), and $\boldsymbol{n}^D$ is the tensor coaxial to the stress tensor. The yield function inside the Macaulay brackets in Eq. 1 is defined as

$$F_y = \phi(\sigma) - \sigma_{ys} \tag{2}$$

where the equivalent stress $\phi(\sigma)$ is the von Mises stress. The $\boldsymbol{n}^D$ tensor is calculated by the visco-plastic potential $Q_{vp} = F_y$ when the von Mises equivalent stress is used. G If $\boldsymbol{n}^D{:}\boldsymbol{n}^D = 3/2$, the change rate of the visco-plastic strain is finally determined by

$$\dot{\varepsilon}_{vpc} = \sqrt{\frac{2}{3}\dot{\varepsilon}_{vp} : \dot{\varepsilon}_{vp}} = A \left(\frac{F_y}{\sigma_{ref}} \right)^n \tag{3}$$

On the other hand, the Rankine damage model [11] defines the equivalent strain from the largest undamaged principal stress σ_{p1} as

$$\varepsilon_{eq} = \frac{(\sigma_{p1})}{E} \tag{4}$$

where E is the Young's modulus. In this formulation, Macaulay brackets are used to emphasize the fact that only (positive) tensile stresses can cause damage.

Morrow's expression for fatigue is an exponential relationship given by

$$\Delta W_d = W_f' \left(2N_f \right)^m \tag{5}$$

where ΔW_d is the range of energy density dissipated during one cycle, N_f is the number of cycles until material failure, and W_f' and m are constants of the material.

2.2   Initial and Boundary Conditions

If the thermal load applied is uniform throughout the material, the model geometry can be simplified to the structure shown in Fig. 1(b), with a symmetry condition given to each surface and edge of the model. The mechanical and thermal properties of the magnetocaloric material needed for the analysis are summarized in Table 1 [7, 8].

Table 1. Properties for the La(Fe,Co,Si)$_{13}$ magnetocaloric material.

Parameter	Value	Unit
Young's Modulus	97	GPa
Poisson's ratio	0.3	--
Density	7240	kg/m^3
Thermal expansion coefficient	26.1×10^{-6}	1/K
Tensile strength	620	MPa
Fracture energy	123	kJ/m^3

3   Results and Discussion

For the scenarios analyzed, i.e. the porous structure made entirely of La(Fe,Co,Si)$_{13}$, and the thin film of La(Fe,Co,Si)$_{13}$ deposited on a porous aluminum structure, the resulting Von Misses stress are shown in Figs. 2 and 3 gives the equivalent deformations, while the cycles needed for material failure are depicted in Fig. 4.

Following Fig. 2, stress concentration occurs where the structural link between pores is thinner (less than a 1 mm of bulk material). For scenario 1, von Mises stress at those links exceeds 30 MPa (Fig. 2(a)), but for scenario 2 (Fig. 2(b)), stresses in the thin film of the magnetocaloric material are below the 15 MPa. This behavior is also found in the equivalent deformation results, where the highest change rate in the volume of the La(Fe,Co,Si)$_{13}$ structure for scenario 1 (Fig. 3(a)) occurs at the same spatial points, with a value of 21.19×10^{-4} mm/mm. Instead, the thin film of the same material but for scenario 2 deforms around 48×10^{-6} mm/mm (Fig. 3(b)). The cycles required in scenario 1 for material failure are approximately 5690 (Fig. 4(a)), which falls short if compared

to the fatigue resistance of conventional refrigeration systems (1×10^6 cycles until material failure [7]). For scenario 2, the thin film of La(Fe,Co,Si)$_{13}$ material collapses at approximately 200,000 cycles (Fig. 4(b)), with the thin film being the structure that suffers the rupture, since the aluminum porous structure preserves its integrity practically intact.
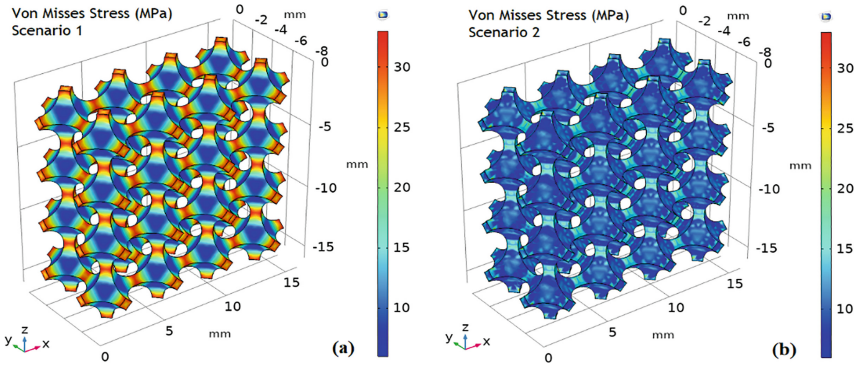
Fig. 2. Von Misses stress for **(a)** first scenario, and **(b)** the second scenario.
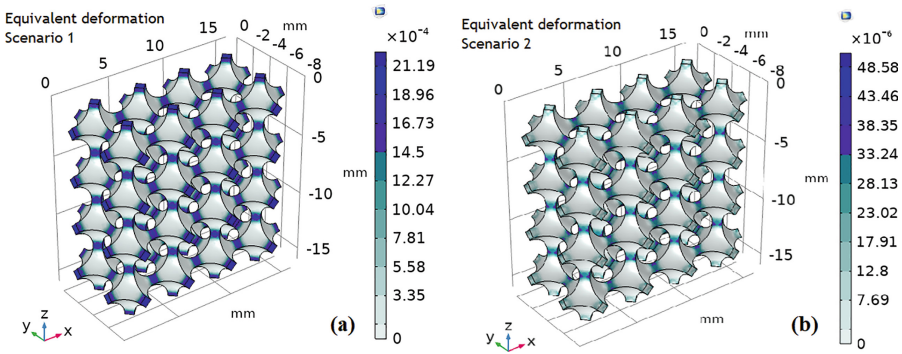
Fig. 3. Equivalent deformation for **(a)** first scenario, and **(b)** the second scenario.

For the results obtained in both scenarios, the significant decrease in the values of stress and deformation of the La(Fe,Co,Si)$_{13}$ thin layer, if compared with the structure of scenario 1, are a consequence of the aluminum core present in the model for scenario 2, as it imposes to a large extent its mechanical behavior over the magnetocaloric material. Also, the similar thermal expansion coefficients of both Al and La(Fe,Co,Si)$_{13}$, assure that the deformations they suffer during magnetic cycling, due to the expansion-contraction phenomenon caused by the temperature change, does not become a source of significant stresses in the magnetocaloric thin film behavior, since the rate at which their volumes change remains relatively close to each other. Finally, these characteristics causes a significant increase in the number of minimum cycles needed for structural failure of the La(Fe,Co,Si)$_{13}$ thin film. Although it is a great improvement, it still does

not reach the performance of conventional refrigeration processes but allowing this app-roach to be considered as a viable alternative when designing and implementing MR systems with enhanced mechanical stability.
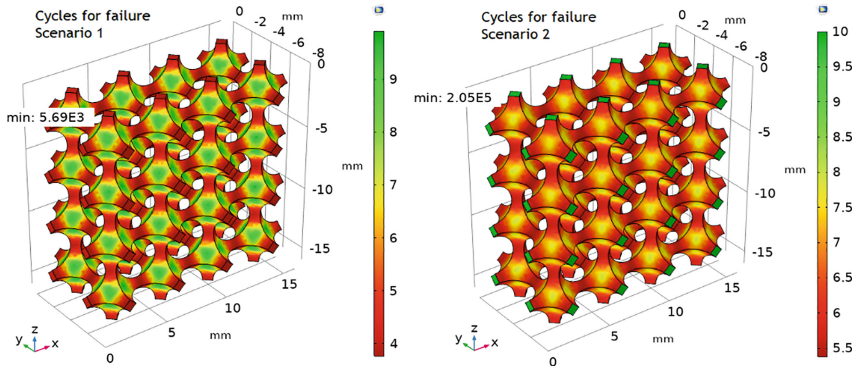
Fig. 4. Cycles needed for material failure for **(a)** the first scenario, and **(b)** the second scenario.

4 Conclusions

Thermo-mechanical and fatigue behaviors of a thin layer of La(Fe,Co,Si)$_{13}$ deposited in a porous aluminum structure were evaluated. The values of stress, equivalent deformation and cycles needed for material failure of the structure were computed for two scenarios: the porous structure made entirely of La(Fe,Co,Si)$_{13}$, and the thin film of La(Fe,Co,Si)$_{13}$ deposited on a porous aluminum structure. The results yielded that the composition in the second scenario have greater mechanical stability and resistance to fatigue if compared to the structure of scenario 1, since its stress and deformation values decrease by a significant amount, while the cycles needed for material failure increase almost 40 times. This outcome shows the potential to create metal-based MR materials with uniform geometries coated with thin layers of magnetocaloric alloys, making this approach a feasible option for the development of enhanced MR systems.

References

1. Silva, D., Ventura, J., Araújo, J.: Caloric devices: a review on numerical modeling and optimization strategies. Int. J. Energy Res. **45**(13), 18498–18539 (2021)
2. Balli, M., Sari, O., Zamni, L.: Implementation of La(Fe, Co)13−xSix materials in magnetic refrigerators: practical aspects. Mater. Sci. Eng. B **177**, 629–634 (2012)
3. Bouchekara, H., Nahas, M.: Magnetic Refrigeration Technology at Room Temperature. de Trends in Electromagnetism – From Fundamentals to Applications. Research Gate (2014)
4. Moore, J., Klemm, D., Lindackers, D.: Selective laser melting of La(Fe Co, Si)13 geometries for magnetic refrigeration. J. Appl. Phys. **114**, 043907 (2013)
5. Krautz, M., Funk, A., Skokov, K.: A new type of La(Fe, Si)₁3-based magnetocaloric composite with amorphous metallic matrix. Scripta Mater. **95**, 50–53 (2015)

6. Lyubina, J., Schäfer, R., Martin, N.: Novel design of La(Fe, Si$)_1$3 alloys towards high magnetic refrigeration performance. Adv. Mater. **22**, 3735–3739 (2010)
7. Rosendahl, B., Kuhn, L., Bahl, C.: Properties of magnetocaloric La(Fe Co, Si$)_1$3 produced by powder metallurgy. J. Magn. Magn. Mater. **322**, 3447–3454 (2010)
8. Glushko, O., Funk, A., Maier-Kiener, V.: Mechanical properties of the magnetocaloric intermetallic LaFe11.2Si1.8 alloy at different length scales. Acta Materialia **165**, 40–50 (2019)
9. Zhou, H., Jia, Y., Shao, J.F.: A unified elastic–plastic and viscoplastic damage model for quasi-brittle rocks. Int. J. Rock Mech. Mining Sci. **45**(8), 1237–1251 (2008)
10. Ambroziak, A., Klosowski, P.: The elasto-viscoplastic Chaboche Model. Task Q. **10**(1), 49–61 (2007)
11. ComsolAB: COMSOL Multiphysics – Structural Mechanics Module, User's Guide (2020)

Isolation and Characterization of Crystalline Cellulose Nanofibers (CNF'S) from Guadua Angustifolia Kunth (GAK)

Jorge Fajardo Seminario[1], Carlos O. Verdugo[1], Cesar A. Paltan[1(✉)], and Robin Zuluaga[2]

[1] Grupo de Investigación en Nuevos Materiales y Proceso de Transformación, Ingeniería Mecánica, Universidad Politécnica Salesiana, Quito, Ecuador
{jfajardo,cpaltan}@ups.edu.ec, cverdugoc@est.ups.edu.ec

[2] Facultad de Ingeniería Agroindustrial, Universidad Pontificia Bolivariana, Antioquia, Colombia
robin.zuluaga@upb.edu.co

Abstract. This work aims to isolate and characterize crystalline cellulose nanofibers from a tropical bamboo named guadua angustifolia. A nanofiber extraction methodology was developed that includes: i) a thermomechanical pretreatment by steam explosion, ii) an acid hydrolysis phase, and iii) a disintegration phase using a supermasscolloid grinder. The nanofibers were evaluated for their morphology (SEM) and (AFM), functional groups (FTIR), thermal degradation (TGA) and crystallinity index (XRD). The diameters of the nanofibers ranged from 20 to 60 nm. FTIR analysis determined an effective removal of functional groups characteristic of non-cellulosic compounds such as lignin and hemicellulose. The nanofibers showed greater thermal stability in relation to the microfibers. The crystallinity index was 75%, evidencing the effectiveness of the methodology to obtain crystalline nanocellulose.

Keywords: Natural fibers · Nanocellulose · Characterization · Guadua

1 Introduction

Thermoplastic matrices have usually been reinforced with synthetic fibers of glass, carbon, aramid, and nylon due to their high mechanical and thermal properties [1, 2]. Additionally, their low density enables the design of lightweight structural components in the automotive, construction and sports equipment industries. But, one of the problems with this type of material is the disposal of the large amount of waste generated. Lately, there is an increase in regulations focused on sustainable production [1, 3], providing an opportunity for the development of renewable resources to replace the economic dependence on non-renewable resources.

For this reason, the use of renewable resources (plant residues) is the focus of attention for the development of more sustainable materials as a responsible production strategy

for the success of a circular economy [4, 5]. These initiatives focus on the development of cellulose nanofibers as an alternative reinforcement for polymeric matrices. Plant species such as sisal, kenaf, abaca, bamboo, flax, coconut, fique, banana, among others, offer advantages of high availability [3, 6], biodegradability [3, 6], high specific properties [2, 6], low cost [3], low abrasion during processing [2, 6], recyclability [2, 6] and lower energy consumption during processing [2]. Guadua angustifolia Kunth (GAK), known as "natural glass fiber", grows in Central and South America. It is one of the largest and most resistant bamboo species in the world. Its mechanical strength is associated with the cellulose content (>50%), strategically located within the culm [7]. When subjected to thermo-mechanical pre-treatment, the nanofibers are ordered as individual entities and offer better reinforcement capabilities in composites [8], as it increases the confinement and toughness of the fiber and slows down crack propagation. The removal of non-cellulosic elements present in the cellulosic matrix of the plant allows obtaining composites with greater mechanical and thermal resistance, low density, and lightness [4]. This article presents a process of isolation of CNFs. The analyses include their morphology by AFM, functional groups by ATR-FTIR, thermal properties by TGA, and crystallinity index by XDR.

2 Materials and Methods

2.1 Materials

The raw material was bamboo culms of the genus "Guadua", species "angustifolia Kunth" (GAK). As a control sample, microfibers obtained mechanically without the use of reagents were isolated, hereinafter referred to as GAKM fiber. This extraction was performed according to the procedure proposed by Ogawa et al. [9]. All reagents used for nanofiber isolation were of analytical grade.

2.2 Isolation of CNF'S

Pretreatment. GAK microfibers were pretreated by a thermomechanical process (steam explosion), hereafter referred to as GAKS fibers. This pretreatment uses steam pressure and temperature to process vegetable raw materials to degrade hemicellulose, soften lignin and decrease the lateral connection strength of the fibers.

Hydrolysis. For the isolation of CNFs, GAKS were dried in an oven at 80 °C for 10 h. Subsequently, they were crushed and sieved according to ASTM E 11–95. For the first treatment of KOH 5 wt.% the ratio is 1:60 (g:mL) at room temperature for 3 h and constant agitation. Then washing with water to neutral pH. The insoluble residue after washing and filtering is carried to the next step. For treatment with 1 wt.% sodium chlorite at pH 5 (with glacial acetic acid) for one hour at 70 °C with constant agitation and a ratio of 1:40 (g:mL). It was then washed with water to neutral pH. For the treatment with KOH 5 wt.% at room temperature for 14 h the ratio was 1:40 (g:mL). Then washed with water until neutral pH. Finally for treatment with 1 wt.% HCl at 80 °C for 2 h, the ratio was 1:40 (g:mL) with constant agitation.

Disintegration. Cellulose free of lignin, hemicellulose, and other cell wall compounds of the GAK biomass were mechanically disintegrated in a Supermasscolloider, Masuko

Sangyo, model: MKCA6-2, with a diameter of 150 mm, entering a cellulose suspension at 2% w/w, until it was reduced to nanometric sizes (diameter 5–60 nm). Finally, 0.1% films were prepared with distilled water and a solution of the CNFs filtered through a vacuum manifold system. The drying process was at 50 °C in an oven for 3 days.

3 Characterization of Microfibers and Nanofibers

3.1 Atomic Force Microscopy (AFM)

The morphology of the CNFs was analyzed by atomic force microscopy. Samples were dissolved in distilled water at concentrations of 0.01% w/w and 0.025% w/w, then sonicated in an Elma Elmasonic P30H type ultrasonic bath at room temp. to disperse the nanofibers. A Bruker BioScope Catalyst microscope mounted on a Leica DMI 4000 B inverted fluorescent confocal laser scanning microscope was used. It was treated by fluorescence microscopy at 495 nm.

3.2 Fourier Transform Infrared Spectroscopy (ATR-FTIR)

The chemical composition and their interactions in the GAKS, GAKM and CNF microfibers were analyzed by ATR-FTIR. An IR Tracer-100 spectrometer provided by Shimadzu, equipped with an ATR single reflection device and a type IIA crystal diamond mounted on tungsten carbide with a resolution of 4 cm-1 in 256 scans.

3.3 Thermogravimetric Analysis (TGA)

Thermal stability of GAKS, GAKM and CNF microfibers was evaluated by TGA using a TG 209 F3 Tarsus equipment with Netzch Proteus® software. Measurements were done on 5–10 mg samples, heated in nitrogen atmosphere (99.5% N) to avoid oxidation. The temp. Profile was from 25 °C to 800 °C with a heating rate of 10 °C min^{-1}.

3.4 X-Ray Diffraction (XDR)

The samples were X-rayed using Panalytical X'Pert Pro MPD equipment with Cu-Ka1 radiation filtered with Ni (k = 1,540 nm) at 45 kV and 40 mA. The data collected in reflection mode at 2H diffraction angle from 5 to 60 in steps of 0.02626.

4 Results and Discussion

4.1 Morphology of CNFs

Downscaling to nanometers is evident in the CNFs, Fig. 1, due to disintegration by the treatments employed.

The treatment exposes the fibers to a rupture of their bonds due to hydrolysis. The homogenization process increases the fibers surface areas as more functional groups are exposed to the surface, creating interactions in the interfacial regions, and ensuring that applied forces are transferred to the CNFs nanoparticles [10].
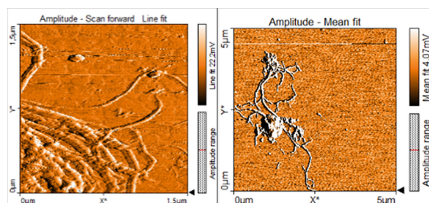
Fig. 1. AFM images of CNFs obtained from GAK biomass.

4.2 Removal of Non-cellulosic Elements (ATR-FTIR)

The corrected and normalized infrared spectra GAKM and CNF are presented in Fig. 2.
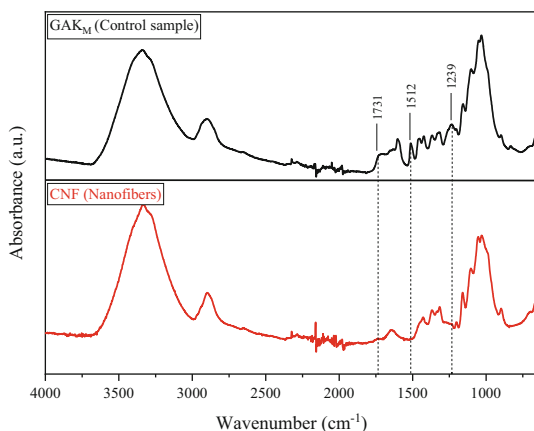
Fig. 2. FTIR spectrum of GAKM and CNFs microfibers.

In the FTIR spectra was observed reduction in the intensity of vibrations corresponding to hemicelluloses and lignins of the pretreated microfibers. The combination of higher stiffness and lower moisture absorption is a characteristic for polymeric matrix reinforcing fibers, indicating the success of thermomechanical pretreatment. The effects will be confirmed by a TGA analysis.

Figure 2 shows FTIR spectra for the CNFs. The first alkaline treatment is not able to change the internal chemical components of the fiber, but it removes certain functional groups present in the plant and even changes the morphology of its surface. Within the spectrum, the peak at 1731 cm^{-1} represents ester bonds of the carboxylic group of the ferulic and p-coumaric acids of hemicellulose, the elimination of this peak after the first treatment is associated with the alkaline treatment with KOH, while the peak at 1512 cm^{-1} is associated with the C = C stretching of the aromatic rings of lignin, the notorious elimination in the spectra from the acid NaCl2 treatment denotes a correct removal of lignin through acid hydrolysis, the peak at 1239 cm^{-1} is attributed to the acyl-oxygen stretching vibration (CO-OR) in hemicellulose and lignin so its elimination represents the successful removal of these two components of the cell wall of the fiber

[11]. Thus, the removal of the lignin functional groups from the nanofibers cell wall is confirmed.

4.3 Thermogravimetric Analysis

Figure 3 shows the thermal degradation of GAKS, GAKM fiber bundles and their derivatives.
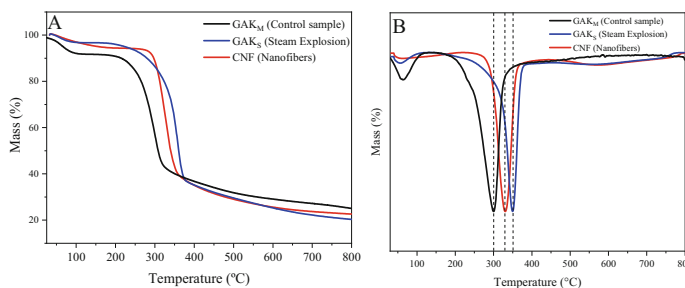
Fig. 3. Thermograms a) TGA and b) DTG of GAKS, GAKM and CNFs microfibers.

The first stage of mass loss occurred in the range of 25 to 120 °C, for the two types of microfibers and corresponds to moisture evaporation (Fig. 2). The lowest mass loss, during this stage, was for GAK$_S$ microfibers. This result confirms that the pretreatment produced more hydrophobic fibers. In the DTG analysis, it was observed that the thermal decomposition of the GAK$_S$ microfibers reached its maximum level of degradation at 336 °C, while the GAK$_M$ microfibers was at 300 °C. This second peak of higher intensity corresponds to the degradation of α-cellulose [12]. A shift of the shoulder associated with the depolymerization of hemicellulose and pectins from 270 °C in GAK$_M$ microfibers towards 295 °C for GAK$_S$ bundles was also observed. This result evidence that the pretreatment removed non-cellulosic components, especially hemicellulose and pectins ratifying the results of the FTIR analysis. After the sequence of treatments, the CNFs showed a thermal degradation peak at 329.9 °C. In Fig. 3, minor evaporative weight loss (about 1.36%) is observed in the fibers subjected to hydrolysis. In the second stage, lignin and hemicellulose decomposition was observed, as predicted by Darus et al. [13]. The ash content of the microfiber was higher than the original biomass, about 21.96%; since an increase in the percentage of cellulose.

4.4 Crystallinity Index (CrI)

The CNFs presented a high crystallinity index in the range between 40–60%. The chemical processes that delignify the sample promote more crystalline regions, in the same way the mechanical milling process increases the crystallinity index in certain regions of the sample because the ICr tends to increase proportionally with the number of pass cycles, due to the forces acting in favor of the amorphous cellulose shortening. The ICr obtained between 75.1% and 76.5% confirms a correct development of the process in favor of the crystallinity of the samples (Fig. 4).
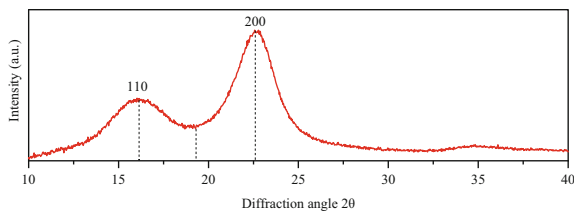
Fig. 4. XRD of BNF from GAK

5   Conclusions

An alteration of the original structure of the fibrous bundle was obtained by the separation and removal of the non-cellulosic components during the extraction process. The ATR-FTIR, TGA analyses confirmed the removal of hemicelluloses and lignins from the pretreated microfibers by steam explosion. These structural changes result in microfibers that combine stiffness, strength and lower moisture absorption, fundamental aspects for a fiber reinforcing polymeric matrices. The isolation method combining pretreatment, acid hydrolysis and disintegration led to obtain crystalline nanocellulose with diameters between 20 and 60 nm from a tropical bamboo species (guadua angustifolia kunth). XRD confirmed the obtaining of nanocelluloses with high crystallinity index between 75–76%. It is demonstrated that it is possible to isolate high quality nanocelluloses to be used as reinforcements in bio composites, which will add value to this plant species abundant in the tropical regions of South America.

References

1. Abdul Khalil, H.P.S., et al.: Bamboo fibre reinforced biocomposites: a review. Mater. Des. **42**, 353–368 (2012)
2. Luna, P., et al.: Guadua angustifolia bamboo fibers as reinforcement of polymeric matrices: an exploratory study. Constr. Build. Mater. **116**, 93–97 (2016)
3. Gurunathan, T., et al.: A review of the recent developments in biocomposites based on natural fibres and their application perspectives. Compos. A Appl. Sci. Manuf. **77**, 1–25 (2015). https://doi.org/10.1016/j.compositesa.2015.06.007
4. Víctor, E.E.: Lignonanofibras de celulosa (lnfc) a partir de residuos agro-industriales no madereros. Obtención, caracterización y aplicaciones. https://dialnet.unirioja.es/servlet/tesis?codigo=236384 (2019)
5. Carpenter, A.W., de Lannoy, C.-F., Wiesner, M.: Cellulose nanomaterials in water treatment technologies. Env. Sci. Tech. **49**, 5277–5287 (2015). https://doi.org/10.1021/es506351r
6. Pickering, K. (ed.): Properties and performance of natural-fibre composites. Elsevier Science, Boca Raton, Fla. : Cambridge, England (2008)
7. Estrada Mejía, M.: Extracción y caracterización mecánica de las fibras de bambú (Guadua angustifolia) para su uso potencial como refuerzo de materiales compuestos. http://168.176.5.108/index.php/acta_agronomica/article/view/195 (2010)
8. Cherian, B.M., et al.: Isolation of nanocellulose from pineapple leaf fibres by steam explosion. Carbohyd. Polym. **81**, 720–725 (2010)
9. Ogawa, K., Hirogaki, T., Aoyama, E., Imamura, H.: Bamboo fiber extraction method using a machining center. JAMDSM **2**, 550–559 (2008). https://doi.org/10.1299/jamdsm.2.550

10. Shao, W., et al.: Preparation of bacterial cellulose/graphene nanosheets composite films with enhanced mechanical performances. Carbohyd. Polym. **138**, 166–171 (2016)
11. Lin, J., Yang, Z., Hu, X., Hong, G., Zhang, S., Song, W.: The effect of alkali treatment on properties of dopamine modification of bamboo fiber/polylactic acid composites. Polymers **10**, 403 (2018). https://doi.org/10.3390/polym10040403
12. Belouadah, Z., Ati, A., Rokbi, M.: Characterization of new natural cellulosic fiber from Lygeum spartum L. Carbohyd. Polym. **134**, 429–437 (2015). https://doi.org/10.1016/j.carbpol.2015.08.024
13. Darus, S.A.A.Z.M., et al.: Physicochemical and thermal properties of lignocellulosic fiber from gigantochloa scortechinii bamboo: effect of steam explosion treatment. Fibers Polym. **21**(10), 2186–2194 (2020). https://doi.org/10.1007/s12221-020-1022-2

Research into Novel Coatings on Composites and Technical Polymers, with Tailored Functionalities for the Transport and Biomedical Industries

Jorge Velasco Manrique[(✉)], Manuel Ignacio González, Carlos Alonso Sastre, Esteban Cañibano Álvarez, and Maria Teresa Fernández Peña

CIDAUT Foundation, Boecillo, Valladolid, Spain
{jorvel,mangon,caralo,estcan,maifer}@cidaut.es

Abstract. This work presents the methodology and results of the research into pre-treatments for thermal spray processes, applied to composites and technical polymers, as preparatory stage for the subsequent coating (ceramic and metallic) deposition via wire arc spray process. The research methodology includes the study of the thermal degradation of substrate materials, as well as the execution and characterization of mechanical (sand blasting), laser (surface texturing) and chemical (acid and base etching) pre-treatments. The quality of the proposed solutions is evaluated through visual inspection of the samples, optical micrography, surface roughness measurements, and mechanical adhesion testing of the coating. Finally, the selection of the most appropriate coating pre-treatment is made, considering technical and scalability criteria.

Keywords: coatings · wire arc spray · composite · technical polymers · pre-treatment

1 Introduction

In the last decades there is a growing trend to make use of high-performance materials, such as composites and technical polymers, in various industry sectors. The main reasons behind this fact can be found in the special properties of these kinds of materials. Apart from having high intrinsic properties, they combine the flexibility in the design of components with the ability to be produced at mass scale with reasonable costs [1].

In the following years the development of materials with even higher performance will be needed, to be used in applications with specific requirements. Thus, the merging into a single hybrid material system of the intrinsic properties of the composites and technical polymers, and the specific properties of the metallic and ceramic coatings, would allow obtaining a tailored material with enhanced properties. In this direction, the COMP_COAT project, whose Consortium is made up of companies located in the Spanish region of Castilla-and-Leon (Cidaut, Aciturri, CTME, Imatec, and MPB), aims

at developing different coating solutions, all of them scalable, through thermal spray processes such as Wire Arc Spray (WAS) (Fig. 1). The main technological challenge to overcome in this project derives from the need to ensure a sufficiently good adhesion between the coating and substrate materials, since their thermal, mechanical, and chemical properties may be noticeably different [2].
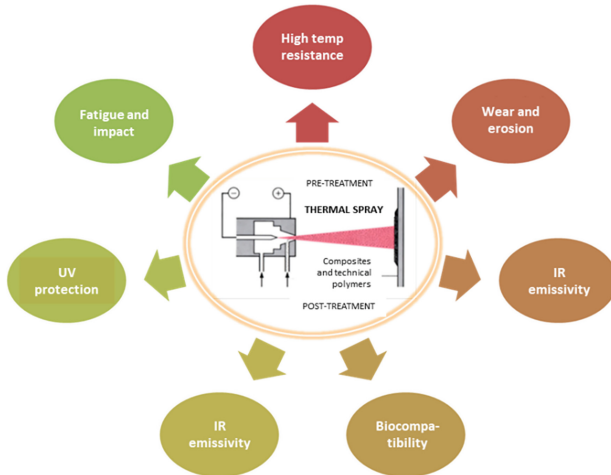
Fig. 1. General overview of the COMP_COAT project

The quality of the substrate-coating adhesion is mainly the result of three stages that are carried out during the thermal spray process: substrate's surface pre-treatment, in which the substrate is prepared (roughness) for the thermal spray; thermal spraying of the specimens; and coating post-treatments, aiming at reducing porosity levels, microstructural modifications, or surface polishing, among others. The work presented in this article is mostly focused on the pre-treatment stage definition and its execution on substrate materials of different nature.

2   Methodology

2.1   Wire Arc Spray Process

Thermal spraying is a surface coating technology that allows obtaining low thickness coatings (0,04–3 mm), starting from a material that is fed in wire or powder format. Especifically, the WAS technology employed by CIDAUT within this project consists of a spray gun feeded with two metallic wires, which serve as electrodes. Initially, they are isolated one from the other, and are fed simultaneously in an automatic manner by the thermal spray equipment, until they meet at a certain point in front of the high pressure gas source. This gas source is the medium that propels the melted metallic particles, which have just been generated by a short circuit when both wires come into contact, towards the subtrate (Fig. 2).
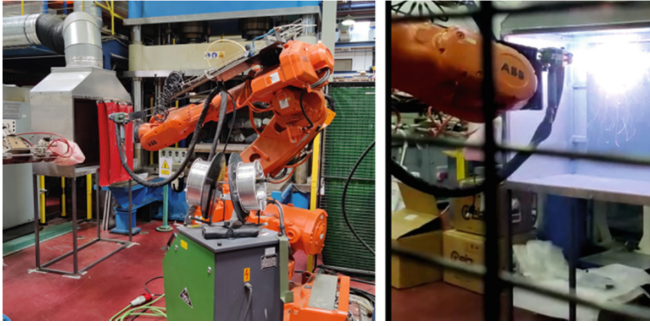
Fig. 2. Robotized WAS facility available at CIDAUT.

2.2 Pre-treatment Selection

The preparation of the substrate for the thermal spraying process is a major aspect to ensure a proper adhesion of the coating particles [3]. The surface preparation processes aims at increasing its roughness, so that the mechanical interlocking between the projected particles and the substrate is favoured. Hence, for the preparation of the composites' and technical polymers'surfaces, several solutions were identified [4], being selected the following ones: chemical pre-treatment (acid and base etching), mechanical pre-treatment (sand blasting), and thermal pre-treatment (laser).

2.3 Pre-treatment Execution

Mechanical Pre-treatment (Sand Blasting): The mechanical pre-treatment consisted of a sand blasting over the material surface to be treated. A parametric study was carried out considering different abrasive materials (composition and particle geometry), gas pressures and exposure times. For this trials, composites of thermoplastic (PPS, PA, PEEK) and thermoset (Epoxy) matrix were used. According to the results found in the literature review, the sand blasting process was stopped and considered acceptable when the surface roughness (Ra) of the substrates reached 20–25 μm.

Laser Pre-treatment: The laser pre-treatment consisted of the application of concentrated energy over a circular shape of 20 mm of diameter, employing a 20 W laser source (nominal power), at different power levels (measured as a percentage of the nominal power) and beam displacement speeds. The pre-treatment was carried out on samples of thermoplastic (PPS, PA) and thermoset (Epoxy) materials, the latter reinforced with two different kinds of fibers, carbon and glass fibers, in order to evaluate the influence of the fiber nature on the energy absorption capabilities of the composite.

Chemical Pre-treatment: The study of the acid/base etching pre-treatment was performed by impregnating the surface of substrate samples (glass fiber and carbon fiber epoxy laminates, and glass fiber reinforced polyamide) with various acid (H_2SO_4, HNO_3) and base (NaOH) compounds, during different exposure times (30 min, 1 h, 2 h, 4 h). The effect of the surface etching in what concerns surface unevenness and

chemical activation was characterized by microscopy and FTIR analysis respectively. In this case, 50×20 mm samples were used.

Mechanical Adhesion Analysis: After the application of the three pre-treatments, the chemical pre-treatment (see Sect. 3.4) was discarded due to the complexity of its proper execution and the low replicability of the results. For the case of sand blasting and laser, the quality of the adhesion was determined by means of adhesion tests following the ASTM C633–2017 standard. To this end, disc specimens with a diameter of one inch were manufactured.

To obtain comparable results, a layer of Sn was sprayed onto all pre-treated samples, using the same WAS process parameters regardless of the particularities of each pre-treatment process. Adhesion tests were considered valid only when failure appeared in the coating-substrate interface.

3   Results

3.1   Mechanical Pre-treatment (Sand Blasting)

The influence of the thermoplastic or thermoset nature of the substrates on the effectiveness of the sand blasting pre-treatment process was analyzed. To this end, surface roughness measurements were carried out at different intermediate stages of a 3 min of total exposure time to sand blasting. The sand blasting pre-treatment is effective when applied to both kinds of substrate materials. Besides, the evolution of the surface roughness is approximately linear with the exposure time to the sand blasting, and therefore easily controllable. The speed at which the substrates are eroded is slightly higher for the case of the thermoplastics.

3.2   Laser Pre-treatment

The surface roughness measurements performed on laser pre-treated samples of different nature led to the following remarks:

– If similar laser parameters are set, the obtained surfaced roughness is higher for the thermoplastic materials, this fact is associated with the existence of weaker links.
– The surface roughness is higher when laser power is increased, or when the laser beam displacement speed is reduced, due to the higher amount of energy provided.
– The reinforcement material does not have influence on the surface roughness.
– At low laser energy levels, the initial roughness state of the sample may hinder the effect of the pre-treatment, if they are already rough enough.

During laser pre-treatment, there is a possibility of irreversibly damaging the substrate, even if the energy put in place is relatively low. As this process is based on the application of localized energy on a tiny region of the samples, the local properties of the material are more relevant here than in other pre-treatments, e.g. sand blasting.

This effect can be seen in Fig. 3, in which microscopy images of the surface of glass fibre-reinforced polyamide samples subjected to laser pre-treatment with different

energy levels are shown. At low energy levels (Fig. 3, left), some composite fibres are exposed. Besides, the path followed by the laser can be appreciated. At medium energy levels (Fig. 3, centre), the number of exposed fibres is higher, and there are also some small regions in which the polyamide is partially melted. Finally, at high energy levels (Fig. 3, right), the polyamide is completely melted, and the fibres are mostly destroyed.
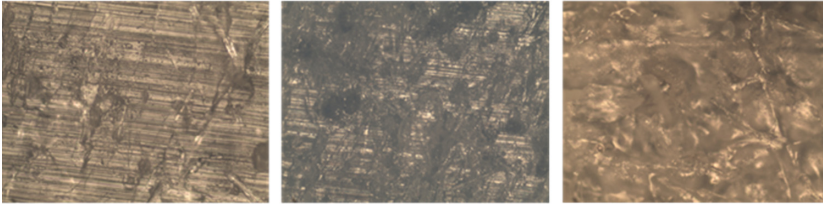
Fig. 3. Effect of the laser energy put in place on the state of the substrate surface.

3.3   Adhesion Test Results

The results of the adhesion tests for a Sn coating are presented in Fig. 4 for a thermoplastic (PPS/Glass fiber), and for a thermoset (Epoxy/Glass fiber) matrix composite.
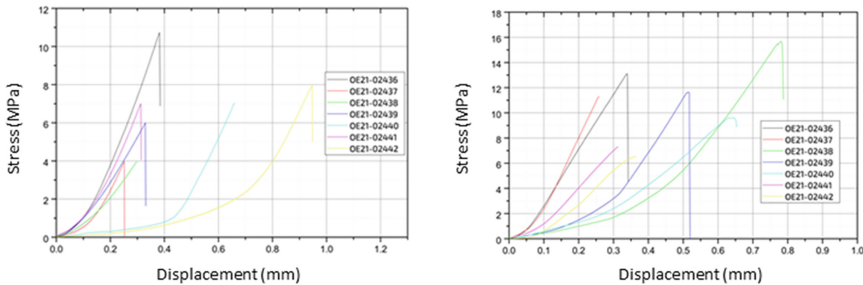
Fig. 4. Adhesion tests results on a thermoplastic (left) and thermoset (right) matrix composite.

It can be concluded that the adhesion is higher for the thermosets, even though there is a strong variability in the results obtained both in terms of stress and maximum displacement measured when failure of the coating-substrate interface occurs. The effect of the pre-treatment (mechanical and laser) on the adhesion strength of a Sn coating was also analysed. PPS was selected as common substrate for all the trials. The results are gathered in Fig. 5. In this case adhesion stress is quite repetitive. In general, a better behaviour of the sand blasted samples was obtained.
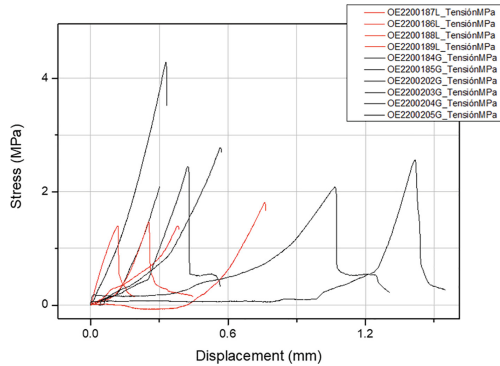
Fig. 5. Results of the adhesion testing of PPS samples subjected to mechanical (in black) and laser (in red) pre-treatment.

4 Conclusions

As a result of the work, the following overall conclusions can be extracted:

- The substrates selected are suitable to be subjected to thermal spray processes.
- Regarding the industrialization of pre-treatment processes of composites and technical polymers, both sand blasting and laser are considered promising solutions. Acid/base etching is discarded, mainly due to the complexity of its execution.
- The degree of adhesion achieved with both pre-treatments, in the preliminary tests employing Sn coating, is deemed acceptable.

References

1. Bobzin, K., Wietheger, W., Knoch, M.A.: Development of thermal spray processes for depositing coatings on thermoplastics. J. Therm. Spray Technol. **30**(1–2), 157–167 (2021)
2. Botana, M., Serrano, F.: Caracterización superficial avanzada de superficies de CFRP previa a la unión adhesive. Tratamiento superficial con peel ply vs láser UV. Materiales Compuestos **4**(2), 97–103 (2020)
3. Yudhanto, A., et al.: Surface preparation strategies in secondary bonded thermoset-based composite materials: A review. Compos. Part A **147**, 106443 (2021)
4. Yang, G., et al.: The influence of surface treatment on the tensile properties of carbon fiber-reinforced epoxy composites-bonded joints. Compos. Part B **160**, 446–456 (2019)

Development of Virtual Tools for the Validation Study of Rigid Catenary Installations

Juan de Dios Sanz Bobi[1](✉) , Álvaro Calvo[2] , Javier Gómez Fernández[1] ,
Miguel Ríos Reyes[3], and Uwe Schoenherr[4]

[1] Universidad Politécnica de Madrid, Madrid, Spain
{juandedios.sanz,javier.gomezf}@upm.es
[2] TÜV Rheinland Ibérica S.A., Barcelona, Spain
alvaro.calvo.hernandez@tuv.com
[3] ADIF-Spanish Railway Infrastructure Manager, Madrid, Spain
mrios@adif.es
[4] SBB Swiss Federal Railways, Bern, Switzerland
uwe.schoenherr@sbb.ch

Abstract. Electrification systems in the railway field have evolved over time, adapting to the new needs that have arisen as technology advanced. The applicable standards seem to leave the systems in which the overhead contact rail is implemented so far in the background, resulting in references to it that are clearly insufficient, even in the most recent revisions of technical requirements. Simulation tools allow a path for the development of studies related to the contact dynamics between pantograph and contact line, focused mainly on improving the exploitation capacities while guaranteeing a correct quality in the process of the current collection. This work contains a procedure for generating a simulation tool. The results are mainly focused on the rigid electrification system and represent a broad knowledge base to introduce a multitude of challenges when it comes to improving the capacity of these railway facilities under operational conditions, to improve the strategies of maintenance and to calculate the life cycle. It can also be verified that the standards applicable to this environment makes possible to clearly identify the fields on which research efforts can be focused, so that a common framework can be established for all the agents involved from the design to the operational phase. This work has been produced under development of UIC-IRS 70,020.

Keywords: Overhead contact rail · Pantograph-OCL interaction · Railway operation

1 Introduction

The main railway subsystems have been involved in continuous evolutions that have allowed the development of increasingly fast, efficient and, above all, safe transport.

Making a special focus on the energy subsystem, the authors of this article have observed that, during the last decades there have been significant advances in the standardization of systems and components. These developments have evolved from what it can be considered guidelines to the application of authentic manuals of good practices, whose level of detail allows the development of the works in an unambiguous way, reducing the subjectivity and the possibility of interpretation of the normative documents.

It is worth asking at this point if the difference between a flexible catenary system and an overhead contact rail system is insurmountable, so that the requirements established for one cannot be directly applicable to the other. The evolution of flexible catenary systems has gone hand in hand with the increase in the maximum operating speed at which trains can circulate. The main aspect that has been modified is the complexity of the assembly of the overhead contact line, supporting cables, Y-Greek hangers, independent compensation systems for the different wires that make up the system have been added, which, for practical purposes, allows the search of a geometrically uniform system achieved by increasing the rigidity of the assembly to the detriment of its elasticity. The range of solutions currently available and widely used should be considered, since otherwise, there are gaps that condition the search for intermediate solutions that allow favoring the operating conditions, maintenance, and the quality of electric current transmission for railway traction.

2   Normative Framework

To establish a simple search and comparison criteria within standards, the word "rigid" and the acronym ROCL for Rigid Overhead Contact Line will be used as key terms as rigid upper contact line or rigid catenary.

EN 50,119:2020 is focused on the installation characteristics of railway current collection systems and recently updated, it can be observed that the word rigid is referenced within the document itself. 15 times, of which only four of them are specific for rigid catenary systems. The ROCL acronym is used only 4 times, linked precisely to the definitions and nuances provided about the catenary system in question.

Given that contact force limits are imposed for the rigid catenary system, it is immediate to introduce the standard EN 50,367:2020, which contains the criteria to achieve technical compatibility between pantographs and overhead contact lines. Then, it focuses on establishing certain parameters and conditions that allow guaranteeing a current transmission between the infrastructure and the rolling stock in a continuous and stable way possible.

Standard EN 50,317:2012 includes the requirements and validation of measurements of the dynamic interaction between pantograph and overhead contact lines, once again completely lacks references to the criteria considered. EN 50,318:2018 standard should therefore be considered, focused on the validation of the dynamic interaction between pantograph and catenary.

3   Simulation Tools Utility

There is a preliminary vision of the electrical and mechanical coupling of the components in particular conditions when simulation tools are used. Credibility finds the correspondence to the standards reference. The simulation process allows to study the quality of the current transmission and to evaluate the continuity of the contact, as well as its aggressiveness with the materials of the contact wire and of the pantograph plates.

For the electrical case, an increase in the contact force leads to an increase in the real contact area between the components of the pantograph and the catenary, so that the resistance to the current at that point is reduced and a minor temperature increase is produced. Reducing the contact force produces the reverse effect, reducing the area of current transmission, increasing the electrical resistance at the point of contact and increasing the temperature.

The extreme case would be for a loss of contact, with the consequent formation of electric arcs at the instants in which both components are very close, but not in contact. The formation of an electric arc is the worst possible situation, since the temperature increase is so high that it can cause loss of material due to its melting. All this, and its application to component wear calculations, is collected according to Archand's formulation (Fig. 1).
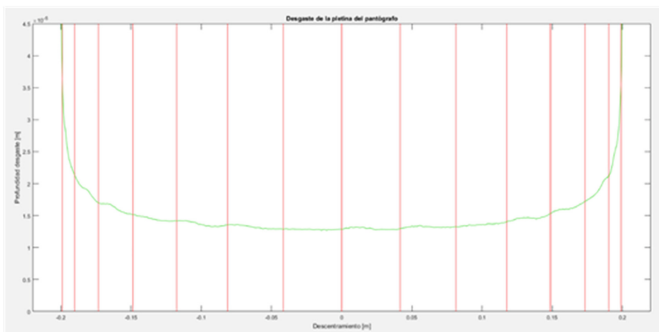
Fig. 1. Wear depth profile of a pantograph plate. Source. Own elaboration

4   Model Development for OCR

This process has been carried out within the framework of the development of the UIC International Railway Solution (IRS) 70,020, which aims to establish a series of recommendations that can guide to the inclusion of rigid catenary systems.

The generated model is based on the use of finite elements [1–3] for the resolution of the rigid catenary structure. Because the main beam of the assembly consist on an element of constant section, the inclusion of the physical characteristics is especially simple within the matrix structure used to solve the problem (Fig. 2).
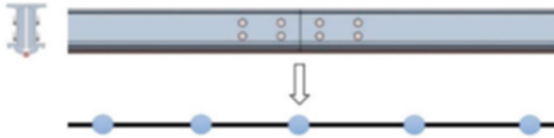
Fig. 2. Simplification of the rigid catenary system through finite elements. Source. Own elaboration

For each element considered, twelve degrees of freedom are taken into account, since, as it is a highly rigid system, the small torsional displacements that occur during the assembly conditions the local behavior of the system.

The simplification of the catenary supports is also considered as an element that only allows vertical displacements of the catenary at the mooring point, so that a node of the beam can be made to match the extreme node of the support and thus close the configuration of the catenary [1, 4, 5]. In the case of the pantograph, the standards themselves include simplified mass models. The use of this type of multibody models has been shown over time to faithfully reproduce the dynamic requirements that are demanded of it, which is why they have been incorporated into the standards. In addition, pantograph manufacturers provide values for this type of reduction with each model they sell.

The integration of both models can be done in a matrix, establishing a relationship of position and mutual force at the point where contact occurs. This point moves in time, so an integration method is needed that can allow the calculation of the temporal evolution of each point or node that composes the structure of the system. With time evolution, we want to refer to the fact that for each point of the system, it is necessary to know, mainly, its position, displacement speed and acceleration, as main variables. In this way, the behavior of the catenary system can be known before the passage of the pantograph, at the exact moment and the behavior of remaining energy dissipation, which sometimes conditions the quality of capture of a second pantograph of the same composition.

For this task, the HHT algorithm (Hilber, Hughes and Taylor) has been used, which is widely applied in the calculations of structural dynamics. One of the main advantages of this method is that the numerical damping can be controlled and adjusted according to the test conditions to adapt it to the reality of the structure. In addition, it allows improving the convergence of the problem, being a robust method of obtaining results in linear and non-linear systems. [6–9]

5   Model Validation

In this work, comparison methods to existing standards for flexible catenary and lab and on-fied tests has been used to validate a simulation for the rigid catenary. The first validation step has been carried out applying the methodology for defining the model and calculating solutions on flexible catenary systems in accordance with the provisions of the EN 50,318 standard. If a spatial position relationship is established to this together with the link with the elements of the environment, the construction of structures is independent of the electrification system.

There is only one exception, and that is the calculation of the length of the hangers. From the installation, they require a variable strength depending on the length of the spans. To address this problem, previous system adaptation periods have been used to calculate the length of the hangers to ensure that the contact wire meets technical and regulatory requirements. Once the simulation method has been tested and its validity verified with respect to the standards, we proceed to the construction of a standard rigid catenary system, considering spans of 10 m distance. Firstly, a series of model characterization tests are carried out for comparison with the real installation to which access is available. These tests are focused on the study of static deformations and the identification of the main natural modes of vibration of the system. For all the tests, a great similarity can be seen with the results obtained, which allows us to assume that the model responds adequately to the previously established verifications (Fig. 3).
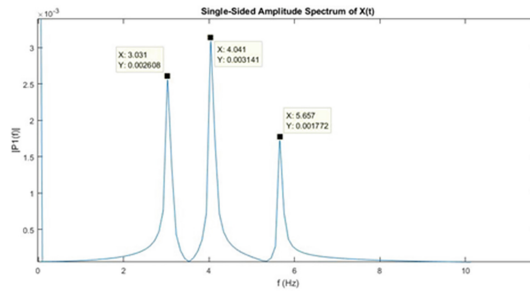
Fig. 3. Detection of the main modes of vibration of the rigid catenary system. Source. Own elaboration

It remains, finally, to evaluate through comparison the dynamic behavior of the set and its ability to emulate the response of the system under operating conditions. To do this, a test scenario identical to the one provided by SBB is programmed in the tool so that, through direct comparison of the statistical values related to the contact force, as stated in the applicable standards, the correctness of the results can be evaluated with the application of the calculation methodology. For the specific case of an installation with spans of ten meters in length, a static force of 85 N and a circulation speed of 110 km/h, we have the following comparative Table 1.

The EN 50,318:2018 standard admits a deviation of the mean force values of $\pm 2{,}5$ N and 20% for the standard deviation value. It can be verified that all the results are framed within the requirements, although the comparison of the elevation of the supports and the displacement of the pantograph head cannot be made since there are no data available, but a result is expected within the required limits given the quality of the result obtained with respect to the forces.

Table 1. Validation of the simulation tool through comparison with real measurements. Source. Own elaboration

Variable	Value Model	Real Value
Measured contact force	80,87 N	80,11 N
Standard deviation	10,34 N	10,99 N
Statistical maximum	111,89 N	113,08 N
Statistial minimum	49,85 N	47,14 N
Real maximum	97,07 N	111,87 N

6   Conclusions

It can be concluded that the use of virtual simulation tools is possible and recommended on electrification systems based on rigid catenary for helping the analysis in the life cycle before and during operation. In particular the work has been achieved to define and to analyze fundamental aspects during IRS 70,020 development.

Even though Rigid Contact Line is a widely extended system and whose use is mainly based on suburban transport systems but the use of this solution in main lines and high speed lines when infrastructure is major favorable for its application (tunnels in main track or urban tunnels), the current standardization standards continue to consider this system as something residual, meaning that the results of the simulations can be framed in ranges of validity.

References

1. Calvo Hernandez, A.: Metodología y desarrollo de herramientas para el estudio de la interacción pantógrafo-catenaria a través de modelos virtuales y su aplicación a sistemas de catenaria rígida. PhD thesis, Mayo (2022). ISBN 978-84-09-39810-2. https://doi.org/10.20868/UPM.thesis.70556
2. Gregori, S., Tur, M., Nadal, E., Aguado, J., Fuenmayor, F., Chinesta, F.: Fast simulation of the pantograph–catenary dynamic interaction. Finite Elem. Anal. Des. **129**, 1–13 (2017). https://doi.org/10.1016/j.finel.2017.01.007
3. Vera, C., Suarez, B., Paulin, J., Rodríguez, P.: Simulation model for the study of overhead rail current collector systems dynamics, focused on the design of a new conductor rail. Veh. Syst. Dyn. **44**(8), 595–614 (2006)
4. Calleja Duro, V., Angel Fernandez Diez, R., Barreiro García, J., Calvo Hernandez, A.: Desarrollo y ensayo de un amortiguador de masas sintonizadas para sistemas de catenaria rigida. DYNA Ingenieria e Industria **92**(1), 680–687 (2017). https://doi.org/10.6036/8498
5. Calvo Hernandez, A., Sanz Bobi, J. d. D.: Compensador de rigidez para sistemas de catenaria rígida. España Patente ES2683778, 14 Enero 2019
6. Suarez, B., Vera, C., Paulin, J.: Optimización de la captación de corriente con catenaria rígida, de Actas del I Congreso Nacional de Innovación Ferroviaria, Calatayud, España (2004)
7. Pombo, J., Ambrosio, J.: Contact model for the pantograph-catenary interaction. J. Syst. Des. Dyn. **1**, 447–457 (2007)

8. Massat, J.P., Laine, J.P., Bobillot, A.: Pantograph–catenary dynamics simulation. Veh. Syst. Dyn. **44**(sup1), 551–559 (2006)
9. Dahlberg, T.: Moving force on an axially loaded beam—with applications to a railway overhead contact wire. Veh. Syst. Dyn. **44**(8), 631–644 (2006)

Assessment of Lower Limb Muscle Activation During Gait Assisted by a Cable-Actuated Exoskeleton

Javier Bermejo-García(✉) ⓘ, Daniel Rodríguez-Jorge ⓘ, Ashwin Jayakumar ⓘ,
Rafael Agujetas Ortiz ⓘ, Francisco Romero-Sánchez ⓘ,
and Francisco Javier Alonso-Sánchez ⓘ

University of Extremadura, Avenida de ElvasS/N, 06006 Badajoz, Spain
`javierbg@unex.es`

Abstract. This study aims to evaluate the modifications that occur in the neuro-muscular system during a walking assistance device through a wearable exoskeleton or exosuit. We propose to study the muscle activations and forces obtained by inverse dynamic analysis at different levels of exosuit actuation and anchor points, with the aim of obtaining an actuation map that will allow us to optimize both the design and the actuation of the exosuit. In addition, metabolic probes were calculated to estimate the influence of the exosuit on energy consumption. The results suggest a reduction in the muscle activations and forces exerted by the hamstring muscles of the actuated leg, especially the semitendinosus muscle and biceps femoris, compared to a non-actuated gait. In contrast, the muscle strength of the other muscles remains unchanged. Our results suggest that the configuration at 70% of femur length shows better results in reducing metabolic cost compared to the other configurations.

Keywords: Exosuit · Muscle-Skeletal Simulations · Assistive Device

1 Introduction

Exoskeletons can be defined as external actuation systems whose purpose is to assist the musculoskeletal system [1]. Although most of these devices focus on user mobility, with complex, bulky, and heavy structures, the trend is for the design of assistive walking devices to become increasingly lighter known as exosuits. These devices are a type of exoskeleton that, using lighter weight actuators, can assist movement, increasing comfort and reducing production costs by eliminating the rigid bars of traditional exoskeletons [1].

Most of these devices are designed primarily to reduce the metabolic cost that the user must perform to carry out an activity, such as walking. The difficulty in the design of these devices depends mainly on the estimation of the assisted joint moment and the way in which the forces are transmitted [2].

To know the impact of the exosuit on the musculoskeletal system, the simulations allow us to calculate muscle activations. In a recent study [3], static optimization was used to calculate muscle activations and the interaction of forces between contact points. Although this is an efficient method of optimization, the absence of correction terms can lead to errors [4]. More recent models propose to relate muscle activations to changes in the model (e.g., position or velocity) so that when considering muscle physiology, the results are more accurate [5, 6]. These simulations are non-invasive tools to quantify the action of the device on the human body [7]. In this sense, the main objective of this work is to evaluate how the use of an exosuit affects the neuromuscular system by studying the muscular forces of the main muscles involved in human gait by varying the anchor point of the device.

2 Materials and Methods

Briefly, we performed a simulation in Opensim [8] to analyze the evolution of muscle activations and the metabolic cost of the cable-driven actuation (Fig. 1).
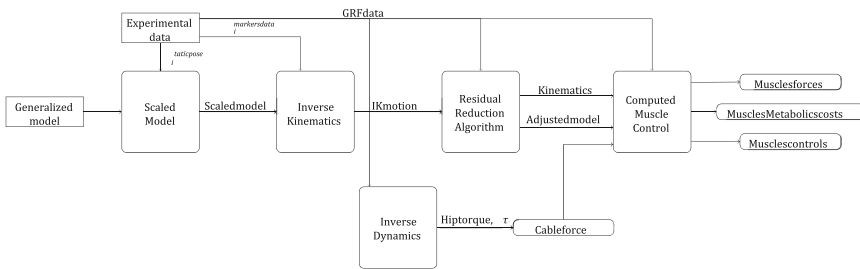
Fig. 1. Scheme of the simulation for the calculation of activations and muscular efforts

2.1 Experimental Data

For the dynamic simulation, we used the data of one participant extracted from a public database by Fukichi et al. [9]. Table 1 shows the data of the subject used for the study.

Table 1. Demographic data of the subject used to run the simulations. Further details in [9, 10]

ID	Sex	Age	Height	Weight	Speed
29	Male	71	1.75	65.35	1.50

Assessment lower limb muscle activation cable-actuated exoskeleton

2.2 Dynamic Simulation

Using the kinematic and kinetic data extracted from the previous database [9], the simulations were generated in OpenSim [8] following the scheme shown in (Fig. 2). The first step is defining a generalized model (12 lower limb bodies, and 2 for the exosuit anchor points, each body is attached by a custom joint [11] giving it 20 degrees of freedom. A total of 18 muscle–tendon actuators [5] were able to generate the forces, and 2 additional actuators (PathActuator class) were implemented for the cable actuation controlled by *ControlLinear Class* [12]). Next, *ScaleTool* adapt the general model to the anthropometric experimental data. The following step is to calculate the joint angles trajectories using the Inverse Kinematic (IK) tool. To reduce the inconsistency between the ground reaction forces (GRF) and the measured moments with the model kinematics, we apply the Residual Reduction Algorithm (RRA) [8, 13]. Then, the muscle activations were estimated through Computed Muscle Control (CMC) [7, 14].

Cable Force PathActuator class were implemented [15]. The cable was attached at 0.32 m from the center of the hip joint. The distal part of the cable has been placed at 30%, 50%, and 70% of the total length of the thigh. The desired hip flexion/extension joint moment is known from the inverse dynamics (ID), and the cable force f is:

$$T_{m \cdot z} = \begin{cases} -r_{AP} \times f|_z & \text{if } \tau_{m,z} > 0 \\ 0, & \text{if } \tau_{m,z} \leq 0 \end{cases} \tag{1}$$

where $\tau_{m.z}$ is the z-component of the joint moment, r_{AP} is the vector of the cable anchored to the thigh. The value 0 means that the cable is in compression.

3 Results

Through the developed simulation framework, the data on muscle activations and metabolic costs are obtained. The results of these are discussed in the following sections.

3.1 Muscle Activations

The muscle activations decrease as the position of the anchor point is further away from the center of the hip joint. As can be seen in Fig. 2, in the hip muscles there is a reduction in muscle activation levels as the exosuit anchor point is positioned further away from the proximal part of the thigh (e.g. vastus lateralis and semitendinosus). This decrease in muscle activations occurs when exosuit begins to act. During the phases prior to exosuit action, muscle activations remain unchanged.

Regarding the muscles of the lower leg (e.g. tibialis anterior and soleus in Fig. 2), the exosuit would not modify the dynamics of the lower leg, and therefore, the kinematics imposed by the subject would not be affected in any way.
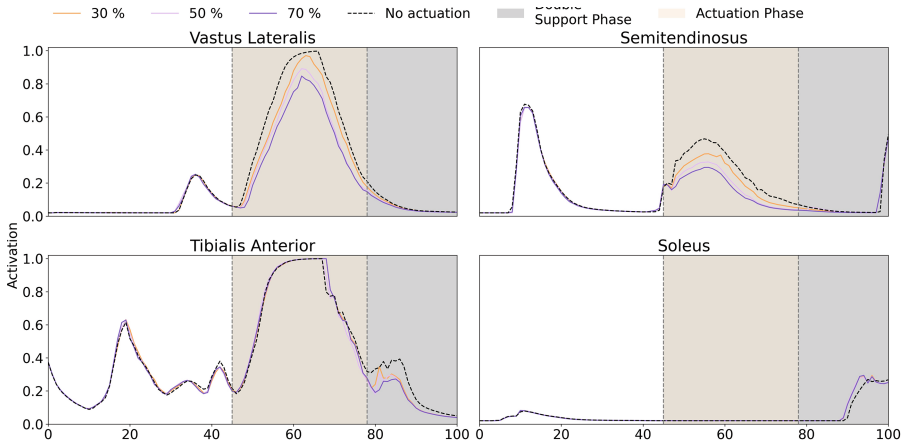
Fig. 2. Muscle activations of the actuating muscles of the model for each of the positions

3.2 Metabolic Cost

As the performance is further away from the proximal hip, a reduction in metabolic cost is seen Fig. 3. It should be noted that, although at the 30% level, there is a reduction in muscle activation, the total metabolic cost is increased compared to the non-actuated gait (1.65%). When the exosuit is placed at mid-thigh, i.e., 50% position, the total metabolic cost is reduced by 6.36% and at 70% position, it is reduced by 10.73% with respect to the metabolic cost of a non-actuated gait.

4 Discussion

In this work, dynamic simulations were generated to obtain the influence of the anchor point, and compare its influence on the muscle activations and metabolic cost. Although this model only includes movement in the sagittal plane, similar results have been obtained with respect to the previous work of Dembia et al. [16]. These authors performed a simulation with a more complex model during an ideal actuator-assisted gait cycle and observed a greater reduction in muscle activation in those muscles that act in more than one degree of freedom (biarticular muscles). In our study, it is shown that muscles such as the semitendinosus muscle show a lower level of activation when compared to the reference simulation in which it is not actuated. For the muscles that are not being actuated, there is no change in the actuation dynamics, therefore, the actuation of the exosuit does not influence those actuators that are not involved in the movement of the hip joint 2. An example of the use of the exosuit for rehabilitation in older adults is the one developed by Jin et al. [17]. In this study, the authors conducted a trial with an older adult walking on a small slope with a cable actuated exosuit, obtaining a significant reduction in metabolic consumption of 7.7%, value similar to our results (Fig. 3). The results of our simulations show that the performance of the exosuit reduces the muscle actuation required by the actuator muscles in the assisted joint, without influencing the dynamics of the others, aiding that would not influence the gait pattern of the subjects.
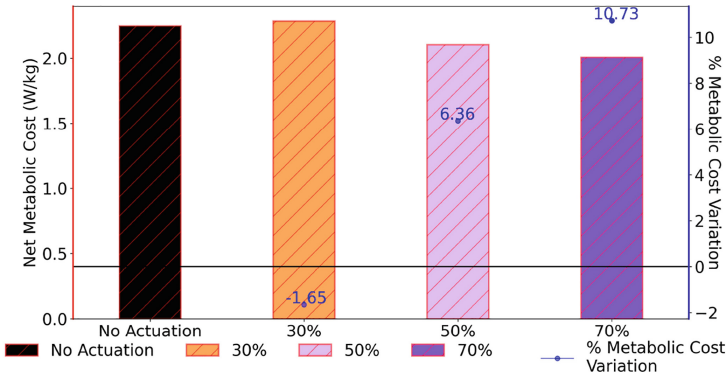
Fig. 3 Average reduction in metabolic cost at different levels of action represented by the red border. In blue, represents the variation in the percentage of metabolic cost

5   Conclusion

A model has been used for the simulation of performance through an exoskeleton (exosuit) in which the activations of 9 muscles are evaluated during a gait cycle. In this work, we propose a study of the influence of the placement of the exosuit performance cable on the person's thigh by studying its influence in various positions.

Our results suggest that as the cable is placed more distal to the hip joint, the activation level exerted by the hip flexor and extensor muscles decreases in the exosuit actuation phase. These simulations serve as a basis for the construction of a wearable exoskeleton to improve the capabilities of the elderly.

References

1. Thalman, C., Artemiadis, P.: A review of soft wearable robots that provide active assistance: Trends, common actuation methods, fabrication, and applications. Wearable Technol. **1**, E3 (2020)
2. Lotti, N., et al.: Adaptive model-based myoelectric control for a soft wearable arm exosuit: a new generation of wearable robot control. IEEE Robot. Automat. Mag. **27**(1), 43–53 (2020)
3. Zhang, L., Liu, Y., Wang, Ruoli, Smith, C., Gutierrez-Farewik, E.M.: Modeling and simulation of a human knee exoskeleton's assistive strategies and interaction. Front. Neurorobot. **15**, 620928 (2021)
4. Cseke, B., Uchida, T.K., Doumit, M.: Simulating ideal assistive strategies to reduce the metabolic cost of walking in the elderly. IEEE Trans. Biomed. Eng. **69**(9), 2797–2805 (2022)
5. Thelen, D.G., Anderson, F.C., Delp, S.L.: Generating dynamicsimulations of movement using computed muscle control. J. Biomech. **36**(3), 321–328 (2003)
6. Lee, L.-F., Umberger, B.R.: Generating optimal control simulationsof musculoskeletal movement using OpenSim and MATLAB. PeerJ **4**, e1638 (2016)
7. Uchida, T.K., Seth, A., Pouya, S., Dembia, C.L., Hicks, J.L., Delp, S.L.: Simulating ideal assistive devices to reduce the metabolic cost of running. PLOS ONE **11**(9), e0163417 (2016)

8. Delp, S.L., et al.: OpenSim: Open-source software to create and analyze dynamic simulations of movement. IEEE Trans. Biomed. Eng. **54**(11), 1940–1950 (2007)

9. Fukuchi, C.A., Fukuchi, R.K., Duarte, M.: A public datasetof overground and treadmill walking kinematics and kinetics in healthy individuals. PeerJ **6**, e4640 (2018)

10. Fukuchi, R.K., Fukuchi, C.A., Duarte, M.: A public datasetof running biomechanics and the effects of running speed on lower extremity kinematics and kinetics. PeerJ **5**, e3298 (2017)

11. Anderson, F.C., Seth, A.: Custom Joint Class Reference. https://simtk.org/api_docs/opensim/api_docs/classOpenSim_1_1CustomJoint.html. Last accessed 4 Aug 2022

12. Anderson, F.C.: Control linear class reference. https://simtk.org/api_docs/opensim/api_docs/classOpenSim_1_1ControlLinear.html. Last accessed 4 Aug 2022

13. Hicks, J.L., Uchida, T.K., Seth, A., Rajagopal, A., Delp, S.L.: Is my model good enough? best practices for verification and validation of musculoskeletal models and simulations of movement. J. Biomech. Eng. **137**(2), 20905 (2015). https://doi.org/10.1115/1.4029304

14. Thelen, D.G., Anderson, F.C.: Using computed muscle control to generate forward dynamic simulations of human walking from experimental data. J. Biomech. **39**(6), 1107–1115 (2006)

15. Seth, A.: PathActuator Class Reference. https://simtk.org/api_docs/opensim/api_docs/classOpenSim_1_1PathActuator.html. Last accessed 4 Aug 2022

16. Dembia, C.L., Silder, A., Uchida, T.K., Hicks, J.L., Delp, S.L.: Simulating ideal assistive devices to reduce the metabolic cost of walking with heavy loads. PLOS ONE **12**(7), e0180320 (2017). https://doi.org/10.1371/journal.pone.0180320

17. Jin, S., Guo, S., Kazunobu, H., Xiong, X., Yamamoto, M.: Influence of a soft robotic suit on metabolic cost in long-distance level and inclined walking. Appl. Bionics Biomech. **2018**, 1–8 (2018)

Development of a Modular Test Bench for Cable-Driven Synergy-Based Exosuit Actuation and Control Strategies

Ashwin Jayakumar[✉] , Daniel Rodríguez Jorge , Javier Bermejo García ,
Rafael Agujetas Ortiz , Francisco Romero Sánchez ,
and Francisco Javier Alonso Sánchez

Universidad de Extremadura, 06006 Badajoz, Extremadura, Spain
{ashwinj,danielrj,javierbg,fromsan,fjas}@unex.es

Abstract. In their survey dated 2019, the UN predicts that the population above the age of 65 will increase from 9%, to 16% by the year 2050 [1]. Ageing results in the eventual loss of muscle mass and strength, joint problems and overall slowing of movements with a greater risk of suffering falls or other such accidents. Gait assist exoskeletons can help promote active ageing in this segment of the population. Since these devices are user specific in terms of the mechanics and control required, the facility to test different parameters becomes indispensable. This work details the design and construction of a modular test bench to implement synergies in an exosuit using motors and cables, and the optimization of the control scheme to better adapt it to specific patients.

Keywords: Exosuit · Modular Test Bench · Synergies

1 Introduction

Wearable exoskeletons, also known as 'exosuits' are relatively recent. One of the first works dealt with lower limb exosuits [2, 3] with textiles for force transmission. These exoskeletons actuate the hip and ankle, using force sensors on the sole of the foot to detect gait phases. Position control based on a predetermined gait was used to drive the motors. These designs allowed a metabolic cost reduction of 6.4% to 19% over several iterations [4]. The XoSoft EU project [5] created an exosuit for people with mobility problems. A prototype beta 1 used an elastic band and clutch in series. Another exosuit design [6] used strain gauges and IMUs to measure the angles and a kinematic model to estimate the gait cycle from these measurements. It used FSRs on the soles of the feet to detect the phase of the gait cycle. Alternatively, there are exosuit designs [7] controlled by PD control with iterative learning (ILC) and able to achieve 15.67% metabolic cost reduction. A recent design [8] features an exosuit that weighs only 1.8 kg. The gait cycle was detected with IMUs as well as measured forces and position by the motor encoders. The trade-off of this weight reduction is a reduction in force transmission (between 50–100 N) compared to other designs, but it still achieved an 11.52% reduction in metabolic cost.

2 Methodology

Weight reduction in such devices is primordial. One such concept used to characterize the largest possible number of movements using the least number of actuators is that of synergies [9, 10]. To characterize these synergies, both the mathematical models and the physical version play important roles in verifying that the system functions as expected. In order to find the optimal actuation scheme, it is necessary to perform several tests, modifying design parameters to see which of them is the most suitable for the needs of this project, to appropriately assist the user's gait. Therefore, this work presents the design and control of a modular test bench that will allow testing different types of actuation systems, control strategies and assistance configurations (ankle only, knee only, hip only or any combination of them) allowing easy assembly and disassembly for rapid prototype development.

2.1 Test Bench Design Theory

The basis for the design of the exosuit based on synergies are the torque curves (Fig. 1) of each leg segment. The torque curves were calculated based on a mathematical model with information from a public database [11], and anthropometric data [12]. The goal is to assist the three segments of the leg with the least number of actuators. Based on the assumption that the exosuit only assists at specific times in the gait cycle, the objective is to assist the subject with the torque necessary to assist a certain percentage of the total joint torque.
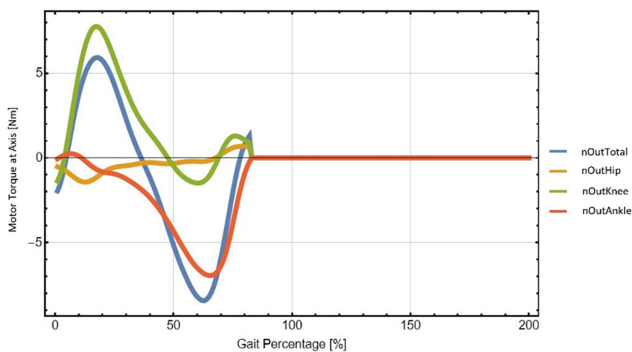
Fig. 1. Joint Torques. Blue: Total. Yellow: Hip. Green: Knee. Red: Ankle.

Observing the graph in Fig. 1 of joint torques, it can be seen that the maximum torque at the hip and ankle is positive at various points of the gait (extension). Due to cable actuation being restricted to extension only, areas where gait assistance is viable are in the negative region (flexion). Moreover, the torque required at the lower leg or knee joint is negative only during a small portion at the end of the gait. Therefore, torque can be supplied to the knee at the end of the cycle to assist gait and achieve a further reduction in metabolic cost. The mathematical model used is detailed in [10]. Thus, it was decided

to actuate the hip and ankle at the same time and the knee at the end of the cycle. Two motors with different pulleys are used for this purpose. One motor has a two-pulley train and the other is a three-pulley train (although only two are used in this trial taking into account the decision taken previously) designed based on subject parameters from the database. The first motor acts according to its own gait curve, generated with the model, controlling the amount of cable extension, winding or unwinding the cable as appropriate to generate the synergy from the tension at the anchor points. The second motor may be activated to restrict the extension, and held still on another run to compare the resulting curves to see the effects of the synergy.

For this purpose, the desired curve of each motor is processed and recorded in the motor controllers. The motors are controlled by a PID controller. To estimate the position values to send to control the motor in angular position, the expression used:

$$P_{desired} = \frac{2^{n_{encoder}} \times G_A \times \omega_{req}}{2\pi \times G_B} \tag{1}$$

where $P_{desired}$ is the position to be sent, $n_{encoder}$ is the number of bits of the motor encoder, G_A and G_B are the reduction coefficients of the motor gearbox, ω_{req} is the desired angular position. A similar equation is used for displacement curves. The resulting cable displacement is calculated from load cell readings, the motor encoders and a linear sensor for accuracy. The tracking error was calculated by comparing the position detected by the encoder versus the desired position. The displacement measured by the motor encoder is calculated knowing the pulses per revolution p_{enc}:

$$d_{cable}^{encoder} = \frac{n_{pulses} \times 2\pi r_{pulley}}{(2)^{p_{enc}}} \tag{2}$$

where n_{pulses} is the number of pulses from the encoder, r_{pulley} is the pulley radius.

In this setup, springs of stiffness k = 1060 N/m were used. Each spring had a maximum displacement of 29.7 mm, so 3 springs were used in series to obtain a total displacement of up to 9 cm. With this range, the scaling factor of the input curves could be as little as half the values needed in the exosuit.

2.2   Construction of the Test Bench and its Modules

Each part was designed and then assembled virtually in CAD to verify compatibility before being assembled on the physical bench. Pulleys and brackets were 3D printed in high-strength PLA 870 filament. The test bench itself is made up of perforated steel plates (R4T6 of 1000 mm × 500 mm) for versatility. The motors used in the test bench are Maxon EC 4-pole (BLDC/brushless) 200 W, with a maximum torque of 95 mNm. In order to increase the torque, two different types of gearboxes were mounted: one 33:1, and the other 79:1, with a resulting torque of 3.13Nm and 7.5 Nm respectively. Both motors have 12/20-bit multiturn absolute encoders for feedback to implement position control of the motors. The motor controllers are the Maxon EPOS4 50/8, to which both the Hall effect sensors of the motors and the absolute encoder are connected. This controller is connected to the PC via USB COM or to the Arduino via RS232, following the object dictionary of the EPOS4. Two types of cables were used as tensile elements

for the tests: one of the cables was a 1.5 mm steel cable consisting of 6 ropes, 7 wires and a load of up to 26 kg with a safety factor of 5:1. The other was a 1.5 mm bicycle brake cable with its corresponding sheath. For the measurement of forces and stresses, Futek S-beam load cells (LSB201) were used, connected to an appropriate amplifier, capable of measuring a maximum load of 445 N. The linear displacement sensor consists of a potentiometer connected to the analog to digital converter (ADC). The travel of the potentiometer is 100 mm, and it has a proportional voltage output. This allows for cable displacement feedback without having to use a very high scale factor, economically and without overcomplicating the design. For the sensor connection interface, a 32-bit Arduino DUE was used. This system was also used to send commands to the motors and to control the clutches.

3   Tests Conducted

3.1   Motor Position Control

The first test consists in assembling the motor with its support, the pulleys or other mechanical parts except the cables. The goal of this experiment is to optimize the operating parameters of the position control system by accounting for the impedance measured in the transmission system to be used.

3.2   Analysis of Synergy Based Actuation Strategies

The next test consists of applying the gait curves obtained by means of synergies to record and evaluate the assistive capacity of the exosuit.
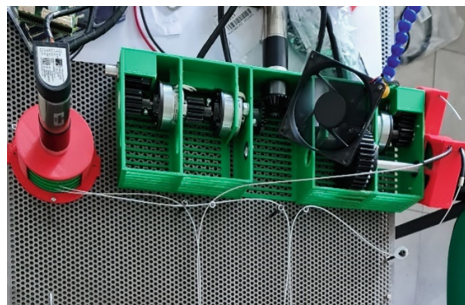
Fig. 2. Dual Motor Synergy Test Setup

This test consists of mounting synergy-based pulley trains designed on the basis of the hip and ankle synergies on each motor and passing the cable between them as in Fig. 2. To record the extension of the cables, load cells are used at the junction points with the corporate segment, using one for each segment to be measured.

4   Results and Discussion

4.1   Adjusting Motor Position Control Parameters

The following graph shows the curve sent to the motor (blue), the position measured through the encoder (red) and the tracking error (green).
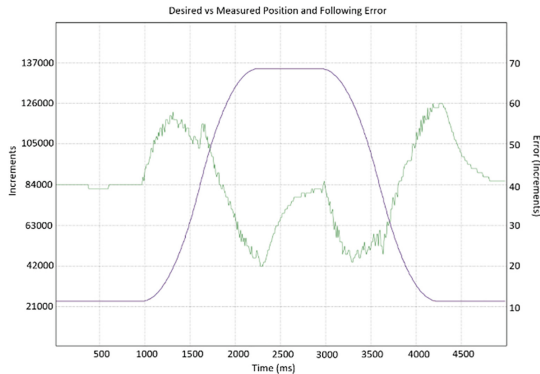
Fig. 3. Tuning the Position Control Algorithm. Blue: Desired Position. Red: Measured Position from Encoder. Green: Error.

As can be seen in Fig. 3, the motor follows the position curve with a high level of accuracy due to the PID controller tuning. After a simple manual optimization, even with a very high acceleration of 4297 RPM/s and a speed of 10000 RPM the maximum position error measured was 60 increments, which corresponds to an angle error at the pulley shaft exit of 0.639°. The results obtained are more than sufficient for present requirements allowing tests to be performed with good accuracy.

4.2   Analysis of Synergy-Based Actuation

As expected, due to the lack of tension on both pulleys at the pulley output due to the current design of the cable feed system, differences in the shape of the tension curves compared to the position curves are observed. Figure 4 shows lack of tension in the ankle cable observable from samples 100 to 170 approximately, where the motor rotates but does not displace the ankle cable correctly. This limitation will be resolved in the future by including a feeder design for the cables to stay properly tensioned.
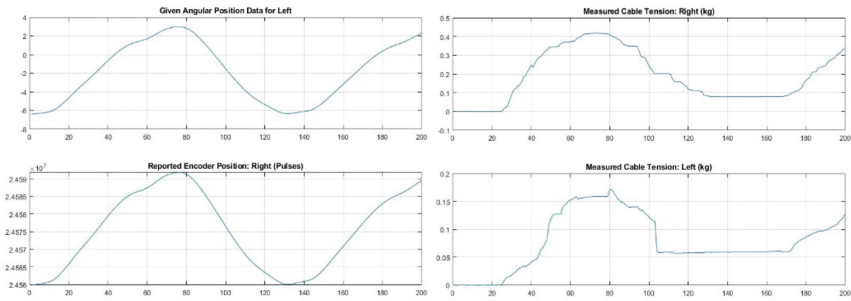
Fig. 4. Synergy Test Results: Two Motors for Two Segments.

5 Conclusions

The bench has been indispensable in the optimization of system parameters for adjusting motor control system parameters, estimating actuation times, deciding the sizes of various system components, etc. to facilitate testing of the actuation systems in exosuits, reducing prototyping and construction costs. A potential improvement is the coupling of a third motor in place of the springs in order to better simulate non-linear dynamics at the output. This motor can be fed with curves that represent some gait pathology such as weak muscles or pathological gait, in order to design, improve and measure how the control system adapts to these irregularities.

References

1. World Health Organization: World Population Ageing 2019 (2019)
2. Asbeck, A.T., Dyer, R.J. Larusson, A.F., Walsh, C.J.: Biologically-inspired soft exosuit. In: IEEE International Conference on Rehabilitation Robotics, no. June, pp. 1–8 (2013)
3. Asbeck, A.T., De Rossi, S.M., Holt, K.G., Walsh, C.J.: A biologically inspired soft exosuit for walking assistance. The Int. J. Robot. Res. **34**(6), 744–762 (2015)
4. Asbeck, A.T., Schmidt, K., Galiana, I., Wagner, D., Walsh, C.J.: Multi-joint soft exosuit for gait assistance. In: Proceedings – IEEE International Conference on Robotics Automation (2015)
5. Di Natali, C., et al.: Design and evaluation of a soft assistive lower limb exoskeleton. Robotica **37**(12), 2014–2034 (2019)
6. Kwon, J., et al.: A soft wearable robotic ankle-foot-orthosis for post-stroke patients. IEEE Robot. Autom. Lett. **4**(3), 2547–2552 (2019)
7. Liu, Y., Chen, C., Lu, J., Liu, Y., Zhang, Y., Wang, Z.: A novel soft exosuit based on biomechanical analysis for assisting lower extremity. pp. 1–6 (2021)
8. Chen, L., Chen, C., Wang, Z., Ye, X., Liu, Y., Wu, X.: A novel lightweight wearable soft exosuit for reducing the metabolic rate and muscle fatigue. Biosensors **11**(7), 215 (2021)
9. Bartenbach, V., Schmidt, K., Naef, M., Wyss, D., Riener, R.: Concept of a soft exosuit for the support of leg function in rehabilitation. In: IEEE International Conference on Rehabilitation Robotics, vol. 2015-Sept, pp. 125–130 (2015). https://doi.org/10.1109/ICORR.2015.7281187
10. Rodríguez Jorge, D., Bermejo García, J., Jayakumar, A., Lorente Moreno, R., Agujetas Ortiz, R., Romero Sánchez, F.: Force and torque characterization in the actuation of a walking-assistance, cable-driven exosuit. Sensors **22**(11), 4309 (2022). https://doi.org/10.3390/s22 114309

11. Fukuchi, C.A., Fukuchi, R.K., Duarte, M.: A public dataset of overground and treadmill walking kinematics and kinetics in healthy individuals. PeerJ **6**, e4640 (2018)
12. Winter, D.A.: Biomechanics and Motor Control of Human Movement. Wiley (2009)

Biomechanical Study of the Addition of the Interferential Screw in the Repair of the Distal Biceps Brachii Tendon

Ana L. Santa-María[1], Marzouk Agharbi[1], Carlos B. Thams[2], and Oscar Martel[1(✉)]

[1] Biomaterials and Biomechanics Research Group, Dpto. de Ingeniería Mecánica, Universidad de Las Palmas de Gran Canaria, Las Palmas de Gran Canaria, Spain
oscar.martel@ulpgc.es
[2] Hospital Perpetuo Socorro, Las Palmas de Gran Canaria, Spain

Abstract. The surgery of the biceps brachii anchors the tendon to the bone, usually using sutures and/or screws. The usual technique is to drill a tunnel in the radius and secure the tendon in it using a small metal piece (button). However, it is also possible to add an interference screw in the bone tunnel to increase the fixation capacity. The objective of this work has been to evaluate the improvement of the repair of the biceps brachii tendon with the use of an interference screw. To this end, reconstructions of the distal tendon were carried out using bones and tendons of animal origin and tested cyclically. The results indicate that adding the screw reduces the displacement and increases the loading capacity significantly. Therefore, the addition of the interference screw is recommended, especially in young and active patients.

Keywords: biceps brachii tendon · interference screw · biomechanical tests

1 Introduction

Distal biceps brachii tendon rupture is not uncommon and most orthopedic surgeons have to deal with this problem at least a few times a year. Clinical units specialized in upper limb surgery treat this injury several times a month. Approximately 90% of all patients are men, between 35- and 50-year-old, with an incidence of 2.5 in 100,000 per year. Usually, it is a sudden eccentric load, rather than a repetitive or heavy load, that causes failure of the anatomic insertion of the tendon. Patients report a sudden pain, often with a pop.

The biceps brachii muscle plays a crucial role in the ability to lift, rotate, and move the upper arm. It is attached to the elbow and shoulder by tendons that, if torn, significantly reduce the strength of the upper arm and its movements can become painful. A distal biceps tendon rupture is the injury that occurs in the elbow joint. Most people who suffer from this injury require surgery to correct it. The objective of the surgery is to re-anchor the tendon to the bone, normally using sutures and/or screws.

The most recommended technique is to perform a bone tunnel in the radius and secure the tendon in with a small metal piece, a button, on the other side of the tunnel [1, 2]. Many biomechanical studies have studied distal biceps brachii tendon repair and there is relative consensus regarding the suitability of the button system [1–11].

However, it is possible not only to use the techniques separately, but to combine them. Specifically, it is also possible to add an interference screw in the bone tunnel when using the button technique, to increase fixation capacity, but this possibility, to the best of our knowledge, has not been biomechanically assessed.

The objective of this work has been to evaluate the biomechanical improvement of the distal biceps brachii tendon repair when introducing an interferential screw in the bone tunnel practiced in the button technique, which we will call the hybrid technique. For this purpose, reconstructions of the distal tendon were carried out using porcine bones and tendons, and cyclical tensile tests were carried out simulating the immediate rehabilitation period after surgery.

2 Methodology

2.1 Materials

Twenty bovine digital extensor tendons and the same number of porcine tibiae were used. Due to the difficulty of obtaining human cadaveric tendons and bones, it has been decided to use animal tissues. Furthermore, this reduces the variability inherent in biological samples, since equal tendon diameters and lengths can be easily selected.

Tendons were removed from bovine legs obtained from a local slaughterhouse and all adjacent tissues were cleaned. A tendon caliper was used to select only the 7 mm diameter tendons. Subsequently, each tendon was wrapped in gauze soaked in saline solution for its conservation, placed in a plastic bag and kept frozen at a temperature of $-20\,°C$ until the tests were carried out.

Porcine tibiae, mimicking the human radius, were obtained from a local butcher shop, and cleaned of surrounding soft tissue. Only tibiae with a diaphyseal diameter of about 20 mm were used. Subsequently, they were preserved under the same conditions as the tendons. Twelve hours prior to the tests, tissues were thawed at room temperature.

Ten distal bicep tendon reconstruction were performed for each of the two techniques tested. In the first group, the reconstruction was performed using only the suture (Fiber-Loop® Nº2) and the button (BicepsButton®, 2.6 × 12 mm), both from Arthrex (FL, USA), and in the second group it was also added the interference screw (7 mm × 10 mm PEEK tenodesis screw) from the same company. The button is made of surgical titanium (Ti6Al4V) and the screw is made of PEEK (polyetheretherketone). We have called the first group the "button technique" and the second group the "hybrid technique".

2.2 Testing Protocol

Each of the 20 reconstructions were tested in a universal testing machine (Microtest EFH/5/FR, Madrid, Spain). A custom made fixation system for the tibia was used to secure its rigid anchorage to the testing machine and to achieve its correct positioning,

placing the bone tunnel in the tensile direction, the worst-case load scenario in clinical practice. The proximal end of the graft was fixed to the machine crosshead by a jaw designed to prevent slippage of the tendon during the test (Fig. 1).
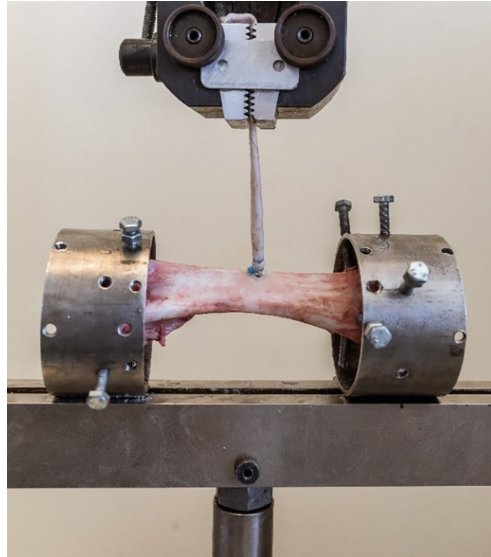
Fig. 1. Tendon attachment reconstruction ready to test

After correct positioning, and before proceeding to the tensile test, an initial preload of 30 N for 2 min was applied. The reconstruction was then subjected to 1,000 load cycles between 10 and 50 N at 0.5 Hz. Once these cycles were completed, it was again preloaded to 55 N for another 2 min, followed by another 1,000 load cycles between 10 and 100 N at 0.5 Hz. Immediately after the second part of the cyclical test, the specimen was subjected to a tensile test until failure at a 20 mm/min rate, simulating the reconstruction failure caused by a traumatic overload.

During all the test, the tendon was kept wet with nebulized saline solution, to avoid dehydration, keeping its mechanical properties throughout the test. At the end of the test, all the specimens were inspected, and the failure mode was recorded, classifying them as: a) tearing of the tendon due to the suture; b) loosening of the knot; and c) rupture of the tendon adjacent to the screw.

2.3 Data Analysis

The force and displacement data were obtained with the sensors and software of the testing machine. The stiffness for each cycle is calculated as the slope of the line that best fits the complete cycle by the method of least squares in the force–displacement graph. The stiffness of the final part of the test (failure) was obtained as the slope of the line of best fit of the final part of the test.

The results of both groups were compared using a Student's t-test for two independent samples (significant difference $p < 0.05$). Previously, a normality analysis was performed with the Shapiro–Wilk test because there were fewer than 30 samples. The results indicated that there was no evidence to reject the normality of the data.

3   Results

Table 1 shows the values obtained in the tests. Mean values of tendon displacement in the hybrid technique were on the order of approximately half those obtained from tests performed with the button technique.

Both repair techniques showed an increase in displacement throughout the test, with significant differences in the value of displacement at the end of the first 1000 cycles (load between 10 and 50 N) and at the end of the second 1000 cycles (load between 10 and 100 N). However, no significant differences were found for the stiffness value at any number of cycles. It is also observed that the repair of the distal biceps brachii tendon using the hybrid technique has significantly higher yield load and ultimate load than the button technique. No significant differences were found regarding the value of stiffness at failure.

Table 1. Results for both tested techniques

	Button	Hybrid	p-value
Displacement at 10th cycle (mm)	0.43 ± 0.20	0.29 ± 0.20	0.148
Displacement at 1000th cycle (mm)	2.53 ± 1.43	1.16 ± 0.35	0.009
Displacement at 1010th cycle (mm)	3.40 ± 1.57	1.86 ± 1.00	0.017
Displacement at 2000th cycle (mm)	5.79 ± 2.27	2.78 ± 1.17	0.013
Stiffness at 10th cycle (N/mm)	86.5 ± 7.5	84.3 ± 14.1	0.667
Stiffness at 1000th cycle (N/mm)	103.1 ± 10.1	102.9 ± 20.1	0.978
Stiffness at 1010th cycle (N/mm)	114.2 ± 11.1	122.2 ± 25.0	0.365
Stiffness at 2000th cycle (N/mm)	120.6 ± 10.8	134.7 ± 29.9	0.191
Yield load (N)	226 ± 94	363 ± 71	0.004
Ultimate load (N)	360 ± 83	486 ± 74	0.003
Stiffness at failure (N/mm)	93.9 ± 39.5	109.6 ± 15.2	0.320

Values given as Mean $\pm$ SD.

All the specimens, except one from the button technique, passed the cyclic load and were subjected to the final tensile test. The failure modes in the button technique were: 5 tearing of the tendon due to the suture, 2 loosening of the knot (the one that did not exceed the cyclic load is included) and 3 combinations of both reasons. There were no deformations of the button or breakage of the suture.

In the hybrid technique, the failure mode in 8 specimens was caused by rupture of the tendon adjacent to the interferential screw, in one specimen the tendon rupture occurred

in the vicinity of the clamp and in the last case the failure was produced by migration of the screw followed by tendon tear.

4 Conclusions

Unrepaired distal biceps tendon rupture causes a 30–50% loss of strength in supination and 30% in flexion. For this reason, surgery is considered the current treatment of first choice in active patients. Recently, much emphasis has been placed on surgical techniques that limit complications and improve tendon-bone fixation strength [3].

In this study, the techniques that are commonly used in the repair of the biceps brachii tendon have been assessed. The ideal technique is the one that guarantees an anatomical reconstruction and sufficient mechanical strength and stiffness for the application of a controlled early mobilization protocol [4].

The repairs carried out were subjected to cyclical tests to simulate the immediate rehabilitation process and to quasi-static tests to simulate failure due to overload. Both the range of loads and the number of cycles used in this study are similar to those used in previous studies [5]. In this study we have focused on three biomechanical parameters to evaluate the clinical success of the reconstruction: the displacement of the tendon in the bone tunnel during cyclic loading, the yield load and the failure mode. Ultimate load and stiffness have also been studied, although we consider them to be of less clinical importance.

The displacement of the tendon in the bone tunnel indicates the laxity with which the repair will remain throughout the rehabilitation. The smaller it is, the better the repair. Actually, it does not consider the effect of biological fixation during the postoperative period, but it clearly indicates the benefits of one repair over another. Data shows that the displacements obtained after the 1000 and subsequent cycles are significantly different between the two techniques, with approximately 50% less displacement when the interferential screw is added.

Although no significant differences have been found regarding stiffness, when both techniques are compared, it is observed that the hybrid technique reaches significantly higher levels of resistance, specifically in terms of the level of yield and ultimate load. The yield load is considered to be the most representative value of the evolution of failure, since if higher tensile loads appear, the damage will be permanent and the displacement will grow very rapidly towards values of laxity that are not admissible in clinical practice.

Regarding the failure mode, in the specimens with the tendon anchored only with the button, the failure mode was tendon tear due to the suture, loosening of the knot, or both. With the hybrid technique, 80% of the failures were due to rupture of the tendon adjacent to the screw. In addition, the only reconstruction that broke before the final tensile test was performed with the button technique. Therefore, it can be inferred that the hybrid technique, limits suture slippage failure and prevents loosening of the knot.

From a clinical point of view, adding the interferential screw to the button system does not significantly increase operating time. Although the use of two implants (button and screw) makes the cost of the procedure more expensive, the good results, the low percentage of complications and the faster return to the activity of daily life, work and/or sports, make it the first therapeutic option in young, active patients with high functional demand.

One limitation of this study is that animal tissues have been used, so the quantitative values resulting from the tests cannot be directly extrapolated to human behavior. However, the results are adequate for the purposes of qualitative comparison between the different techniques.

Finally, the results of this study suggest that, with the hybrid technique, that is, adding the interferential screw, a significantly better repair of the biceps brachii is achieved at its distal insertion. Also, by reducing displacement by approximately half and increasing load capacity, the hybrid technique allows for an early and effective rehabilitation program [12].

References

1. Mazzocca, A.D., et al.: Biomechanical evaluation of 4 techniques of distal biceps Brachii tendon repair. Am. J. Sports Med. **35**(2), 252–258 (2007)
2. Wörner, E., et al.: Higher failure rate of suture anchors in partial distal biceps tendon ruptures in comparison with Endobutton fixation. JSES Int. **5**(4), 821–826 (2021)
3. Spang, J.T., et al.: A biomechanical comparison of Endobutton versus suture anchor repair of distal tendon injuries. J. Shoulder Elbow Surg. **15**(4), 509–514 (2006)
4. Arianjam, A., et al.: Biomechanical comparison of interference screw and cortical button with screw hybrid technique for distal biceps brachii tendon repair. Orthopedics **36**(11), 1371–1377 (2013)
5. Rutka, V., et al.: Distal biceps tendon repair via new knotless Endobutton fixation: a biomechanical study. Shoulder Elbow **13**(3), 321–328 (2021)
6. Greenberg, J.A., et al.: Endobutton-assisted repair of distal biceps tendon ruptures. J. Shoulder Elbow Surg. **12**, 484–490 (2003)
7. Lemos, S.E., et al.: A new technique: in vitro suture anchor fixation has superior yield strength to bone tunnel fixation for distal biceps tendon repair. Am. J. Sports Med. **32**(2), 406–410 (2004)
8. Idler, C.S., et al.: Distal biceps tendon repair: a biomechanical comparison of intact tendon and 2 repair techniques. Am. J. Sports Med. **34**(6), 968–974 (2006)
9. Kettler, M., et al.: Failure strengths in distal biceps tendon repair. Am. J. Sports Med. **35**(9), 1544–1548 (2007)
10. Krushinski, E.M., et al.: Distal biceps tendon rupture: biomechanical analysis of repair strength of the Bio-Tenodesis screw versus suture anchors. J. Shoulder Elbow. Surg. **16**, 218–223 (2007)
11. Chavan, P.R., et al.: Repair of the ruptured distal biceps tendon: a systematic review. Am. J. Sports Med. **36**(8), 1618–1624 (2008)
12. Bisson, L.J., et al.: Is it safe to perform aggressive rehabilitation after distal biceps tendon repair using the modified 2-incision approach? A biomechanical study. Am. J. Sports Med. **35**(12), 2045–2050 (2007)

Analysis of the Dorsolateral Prefrontal Cortex MNI Coordinates

Rosa Pàmies-Vilà[1,3](✉) [ID], Albert Fabregat-Sanjuan[2,3] [ID], Aina Ros-Alsina[1],
Agnès Rigo-Vidal[3] [ID], and Vicenç Pascual-Rubio[3] [ID]

[1] BIOMEC, Mechanical Engineering Deparment, Universitat Politècnica de Catalunya,
Barcelona, Spain
`rosa.pamies@upc.edu`
[2] FUNCMAT, Mechanical Engineering Department, Universitat Rovira i Virgili, Tarragona,
Spain
[3] NeuroÈpia, Clinical Neurophysiology Department, Institut d'Investigació Sanitària Pere
Virgili, Hospital Universitari Sant Joan de Reus, Reus, Spain

Abstract. In recent years, new non-invasive brain stimulation techniques are
appearing which, based on neuromodulation, allow the treatment of pathologies
such as pain or depression. One of the target regions where these techniques are
usually applied is in the dorsolateral prefrontal cortex (DLPFC) and the result of
these procedures depends on the correct and precise location of the point on the
scalp close to this region. According to the literature, the most common methods
that are currently used for the localization of the DLPFC are the Neuroimag-
ing and Neuronaviagtion Systems, the 5cm method, the BeamF3 method and the
international 10–20 System. Montreal Neurological Institute (MNI) space is a 3-
dimensional coordinate system (also known as 'atlas') of the human brain, used
to map the location of brain regions independent of individual differences in the
size and overall shape of the brain. This study reviews the published articles that
attempt to locate DLPFC positions, evaluate the discrepancies and quantify the
differences among different authors.

Keywords: 10/20 · EEG · Neurology · EEG electrode placement · dorsolateral
prefrontal cortex

1 Introduction

The biochemical exchanges between the neurons of our brain take place in the synapses
and produce a small electrical activity detectable by the placement of electrodes on
the scalp using diagnostic neurophysiological recording techniques such as electroen-
cephalography (EEG) or evoked potentials (EP). In addition, in recent years scien-
tific interest in non-invasive brain stimulation techniques has grown, which, through
neuroplasticity, allow the treatment of pathologies such as pain or depression.

The method known as the International 10–20 System was established by Herbert
H. Jasper in 1958 [1]. This method, adopted by the International Federation of Clinical

Neurophysiology, standardises the placement of 21 EEG electrodes on the scalp. Through some percentages of the circumference (either 10% or 20%, hence the name of the method) and distances between four basic anatomical landmarks, the head is divided into proportional positions to offer adequate coverage of all regions of the brain, thus correlating external locations of the skull with the underlying cortical areas. Therefore, this method has the advantage of considering the variability in the size of the patient's skull, since it uses measurements of the head for the placement of the electrodes. The four anatomical landmarks used to perform the percentage position calculations are the Nasion, the Inion, and the left and right preauricular points.

1.1 Dorsolateral Prefrontal Cortex (DLPFC)

One of the brain regions whose location has been mostly studied by researchers is the dorsolateral prefrontal cortex (DLPFC). The DLPFC is an area in the prefrontal cortex of the primate brain, which is not an anatomical structure, but a functional one, located in the middle frontal gyrus of humans, in the lateral part of the 9 and 46 Brodmann areas (BA). The dorsolateral prefrontal cortex (DLPFC), used for both tDCS and rTMS, has been recognized to be critically involved in cognitive control, including cognitive control over emotions, as well as working memory, cognitive flexibility and planning.

The DLPFC is the most commonly used area of stimulation for the treatment of major depressive disorder (MDD) with rTMS [2, 3], and is also typically used for the relief of certain types of pain [4]. Also, in tDCS, DLPFC localization appears to show a positive therapeutic effect in MDD patients. Moreover, it has been shown to improve performance in various cognitive domains such as executive functions, verbal skills, and memory performance with healthy subjects, but also with patients that suffer Parkinson's disease and have suffered a stroke [5].

The Talairach and Montreal Neurological Institute (MNI) spaces are three-dimensional coordinate systems (also known as "atlases") of the human brain, used to map the location of brain regions, regardless of individual differences in the size and general shape of the brain. The first MNI template was the MNI305, generated from the average of 305 brain scans, and the current standard MNI template is the ICBM152 (commonly referred to as MNI152), which is the average of 152 normal MRI scans that have been matched to the MNI305 using a 9-parameter affine transform.

1.2 Localization methods for DLPFC

Likewise, it is important to consider that there is significant variability in the anatomy of the head, which interferes with the location of these brain areas. That is why some localization methods consider the morphological variability of the head to better adapt the localization to each subject. The most common methods currently used to localise the DLPFC are neuroimaging and neuronavigation techniques, the "5 cm" method [7, 8], the intl. 10–20 system and the "Beam F3 method" proposed by [4].

The location of the F3 electrode from the 10–20 system is usually used as a target for the DLPFC [4], so many clinical research applications target this location when applying procedures such as TMS to the DLPFC. As this system uses head measurements, thus accounting for variability in head shape, it seems an accurate way to localise the DLPFC.

However, for clinicians with little experience with the 10–20 system, the numerous measurements and calculations to locate the F3 position can be time consuming and lead to human errors.

This paper offers a review of the location of the DLPFC zone to understand the problems related to the location of brain areas. Therefore, the main objective is to study the existing methods to locate the dorsolateral prefrontal cortex (DLPFC), analysing the discrepancies shown in the literature when it comes to locating this area of the brain.

2   Methodology

Differences on the MNI152 coordinates appears when the DLPFC location is analysed.

We study these differences and compare the location with the position determined by the International System 10–20 for a realistic MNI152 head model (taking the coordinates of [9] as reference). Studies that provide both coordinates (cerebral and scalp) are used to determine the relationship between the two positions. Based on this information, the brain or scalp positions of the woks that only pointed to one of the two locations are extrapolated. With all the information above, the Euclidean distance d between the MNI positions of the different studies and the reference position can be calculated.

The Brainstorm software [13] is used to visualise the points of the DLPFC, both the scalp and brain coordinates, on a real 3D head model adjusted to the MNI152 atlas.

3   Results

3.1   Coordinates in MNI of the DLPFC

Reviewing the literature, it is observed that in each paper the DLPFC is located in different coordinates. This work focuses on 16 articles that provide the coordinates of the left DLPFC in the MNI Coordinate System [6, 11, 12, 14–26]. Some articles that are also included provide the coordinates in the Talairach coordinate system, but later studies converted those coordinates to the MNI System. The coordinates provided by Oostenveld as a F3 is used as a gold standard [9]. The coordinates that located the DLPFC in the brain were plotted on the cerebral cortex of the model provided by Brainstorm, while those that located it on the scalp were plotted on the surface of the head volume.

Each of the brain DLPFC locations can be seen in Fig. 1a. However, [18] (light blue in the Fig. 1 legend) is not visible, as it is in the same place as the pink dot representing the BeamF3 location of [26].

The coordinates of the scalp can be seen in Fig. 1b plotted on the surface of the head. In this case, [17] cannot be seen (in red in the legend to Fig. 1b), since it is in the same location as [11]. The same is true of the [18] and the location of [26] from Beam F3 (in light blue and pink in the Fig. 2b legend), which are not seen on the scalp, as they are in the same location as the F3 Oostenveld location (in black) [22].

In addition to the visualisations, Table 1 shows the differences between these positions and the reference ones [9], both for brain and scalp coordinates, respectively. The mean Euclidean distance from the brain coordinates is 11.50 mm (with a SD of 8.02 mm) and for the scalp coordinates the mean is 13.32 mm (with an SD of 8.72 mm).
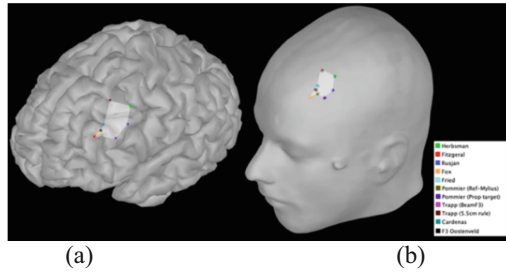
Fig. 1. Coordinates of the literature represented on the Brainstorm segmentation model. a) Cerebral cortex. b) Cranial volume.

Analysing the brain coordinates, it can be seen that the locations that present the most differences are the coordinates provided by [19] and [26], who used the 5 and 5.5 cm methods. These two locations lie further back in the brain than the rest. On the other hand, the works that located the left DLPFC with greater precision to the Oostenveld F3 cerebral location are primarily [15], who uses the International 10–20 System, followed by [18] and [26]. Note that [18] use a T1-weighted anatomical magnetic resonance imaging scan to locate the position, and MNI coordinates provided by [24] are obtained as an average of 81 points (obtained in different 81 heads). Although the mean value in [24] is close to the actual F3, the results show a high variability (possibly influenced on the morphology of the head). Authors specify that the average Euclidean distance from each individual target to the group average centroid was 9.5 ± 6.1 mm. Its SD is close to the one obtained for the 5.5 cm methods (6.6 mm). The results suggest that neither the Beam F3 nor the 5.5 cm rule are valid methods to precisely locate the same location based on the individual patient's head measurements. A recent study [27] has found that Beam F3 introduces an error that is dependent on the head morphology.

Similar results are obtained with the coordinates of the scalp. Again, the locations obtained with the 5 and 5.5 cm methods place the F3 location too posterior in the scalp, while the works that place the DLPFC more similar to Oostenveld F3 are [15], who found the location with the 10–20 IS, followed by [26] (average of 81 heads) and [18] that use images from magnetic resonances.

Table 1. MNI Brain coordinates for DLPFC and Euclidean distance errors with respect to the brain gold standard (dB). MNI Scalp coordinates for DLPFC and Euclidean distance errors with respect to the scalp gold standard (ds)

Study	Brain				Scalp			
	MNIx [mm]	MNIy [mm]	MNIz [mm]	Distance d_B [mm]	MNIx [mm]	MNIy [mm]	MNIz [mm]	Distance d_S [mm]
Cardenas et al., 2022	−42,30	44,46	38,39	2,88	−51,0	51,0	44,0	2,88
Fitzgeral et al., 2009	−41,30	48,90	27,70	9,18	−48,90	55,40	31,70	10,82
Fox et al. 2012	−39,30	46,20	27,50	9,36	−49,30	54,70	32,10	10,26
Fried et al. 2014	−41,50	41,10	33,40	6,32	−51,20	47,90	38,70	6,35
Herbsman et al. 2009	−46,00	23,00	49,00	27,01	−54,10	27,20	54,60	28,99
Pommier et al. 2017 (Ref-Mylius Left)	−40,20	42,30	28,70	9,06	−48,90	48,84	34,31	9,06
Pommier et al. 2017 (Prop target Left)	−45,90	36,40	25,30	15,80	−54,60	42,94	30,91	15,80
Rusjan et al. 2010	−50,00	30,00	36,00	18,61	−58,40	35,10	40,20	19,87
Trapp et al., 2020 (BeamF3)	−40,60	41,70	34,30	5,46	−49,30	48,70	41,00	4,67
Trapp et al., 2020 (5.5 cm rule)	−33,60	30,80	51,10	22,86	−42,00	38,50	60,00	24,47

4 Conclusions

The comparison of the coordinates in the scientific literature allow us to evaluate the existing localization methods and quantify the differences between them. There is a clear discrepancy between the DLPFC coordinates provided in the literature.

It has been observed that the 5 cm method, or its variants such as the 5.5 cm method, point to a DLPFC site more distant from the one considered correct (errors between 24 and 29 mm). In average, the results of the Beam F3 method are close to the actual F3 position. However, the dispersion of the results raises questions about its feasibility to target the same point for different head morphologies.

References

1. Seeck, M., et al.: The standardized EEG electrode array of the IFCN. Clin. Neurophysiol. **128**(10), 2070–2077 (2017). https://doi.org/10.1016/j.clinph.2017.06.254

2. Spronk, D., Arns, M., Fitzgerald, P.: Ch. 10: repetitive transcranial magnetic stimulation in depression: protocols, mechanisms, and new developments. In: Neurofeedback and Neuromodulation Techniques and Applications, pp. 257–291. Elsevier Inc. (2011)

3. Mir-Moghtadaei, A., Siddiqi, S.H., Mir-Moghtadaei, K., et al.: Updated scalp heuristics for localizing the dorsolateral prefrontal cortex based on convergent evidence of lesion and brain stimulation studies in depression. Brain Stimul. **15**(2), 291–295 (2022)

4. Beam, W., Jeffrey, J.B., et al.: An efficient and accurate new method for locating the F3 position for prefrontal TMS applications. Brain Stimul. **2**(1), 50–54 (2009)

5. Keeser, D., et al.: Prefrontal transcranial direct current stimulation changes connectivity of resting-state networks during fMRI. J. Neurosci. **31**(43), 15284–15293 (2011)

6. Pommier, B., et al.: Easy methods to make the neuronavigated targeting of DLPFC accurate and routinely accessible for rTMS. Neurophysiol. Clin. **47**(1), 35–46 (2017)

7. George, M.S., Wassermann, E.M., Williams, W.A., et al.: Daily repetitive transcranial magnetic stimulation (rTMS) improves mood in depression. NeuroReport **6**, 1853–1856 (1995)

8. Pascual-Leone, A., et al.: Rapid-rate transcranial magnetic stimulation of left dorsolateral prefrontal cortex in drug-resistant depression. Lancet **348**, 233–237 (1996)

9. Fox, M., Buckner, R., et al.: Efficacy of transcranial magnetic stimulation targets for depression is related to intrinsic functional connectivity with the subgenual cingulate. Biol. Psychiat. **72**(7), 595–603 (2012)

10. Mir-Moghtadaei, A., Caballero, R., et al.: Concordance between BeamF3 and MRI-neuronavigated target sites for repetitive transcranial magnetic stimulation of the left dorsolateral prefrontal cortex. Brain Stimul. **8**(5), 965–973 (2015)

11. Siddiqi, S., et al.: Brain stimulation and brain lesions converge on common causal circuits in neuropsychiatric disease. Nat. Hum. Behav. **5**(12), 1707–1716 (2021)

12. Oostenveld, O.: High-density EEG electrode placement. Robert Oostenveld's blog. https://robertoostenveld.nl/electrode/ (2006)

13. Tadel, F., et al.: Brainstorm [Computer Software]. https://neuroimage.usc.edu/brainstorm/ (2011)

14. Bradfield, N.I., Reutens, D.C., Chen, J., Wood, A.G.: Stereotaxic localisation of the dorsolateral prefrontal cortex for transcranial magnetic stimulation is superior to the standard reference position. Aust. N Z J. Psychiatry **46**(3), 232–239 (2012)

15. Cardenas, V.A., et al.: Anatomical and fMRI-network comparison of multiple DLPFC targeting strategies for repetitive transcranial magnetic stimulation treatment of depression. Brain Stimul. **15**(1), 63–72 (2022)

16. Cho, S.S., Strafella, A.P.: rTMS of the left dorsolateral prefrontal cortex modulates dopamine release in the ipsilateral anterior cingulate cortex and orbitofrontal cortex. PLoS ONE **4**(8), e6725 (2009)

17. Fitzgerald, P.B., et al.: Exploring the optimal site for the localization of dorsolateral prefrontal cortex in brain stimulation experiments. Brain Stimul. **2**(4), 234–237 (2009)

18. Fried, P.J., Rushmore, R.J., Moss, M.B., et al.: Causal evidence supporting functional dissociation of verbal and spatial working memory in the human dorsolateral prefrontal cortex. Eur. J. Neurosci. **39**(11), 1973–1981 (2014)

19. Herbsman, T., Avery, D., Ramsey, D., et al.: More lateral and anterior prefrontal coil location is associated with better repetitive transcranial magnetic stimulation antidepressant response. Biol. Psychiat. **66**(5), 509–515 (2009)

20. Herwig, U., Padberg, F., Unger, J., Spitzer, M., Schönfeldt-Lecuona, C.: Transcranial magnetic stimulation in therapy studies: examination of the reliability of "standard" coil positioning by neuronavigation. Soc. Biol. Psychiatry **50**(1), 58–61 (2001)
21. Mir-Moghtadaei, A., Caballero, R., et al.: Concordance between BeamF3 and MRI-neuronavigated target sites for repetitive transcranial magnetic stimulation of the left dorsolateral prefrontal cortex. Brain Stimul. **8**(5), 965–973 (2015)
22. Oostenveld, R., Praamstra, P.: The five percent electrode system for high-resolution EEG and ERP measurements. Clin. Neurophysiol. **112**(4), 713–719 (2001)
23. Paus, T., Castro-Alamancos, M., Petrides, M.: Cortico-cortical connectivity of the human mid-dorsolateral frontal cortex and its modulation by repetitive transcranial magnetic stimulation. Eur. J. Neurosci. **14**(8), 1405–1411 (2001)
24. Rajkowska, G., Goldman-Rakic, P.: Cytoarchitectonic definition of pre-frontal areas in the normal human cortex: II. Variability in locations of areas 9 and 46 and relationship to the Talairach coordinate system. Cereb. Cortex **5**(4), 323–337 (1995)
25. Rusjan, P.M., Barr, M.S., et al.: Optimal transcranial magnetic stimulation coil placement for targeting the dorsolateral prefrontal cortex using novel magnetic resonance image-guided neuronavigation. Hum. Brain Mapp. **31**(11), 1643–1652 (2010)
26. Trapp, N.T., Bruss, J., King Johnson, M., et al.: Reliability of targeting methods in TMS for depression: Beam F3 vs. 5.5 cm. Brain Stimulation **13**(3), 578–581 (2020). https://doi.org/10.1016/j.brs.2020.01.010
27. Fabregat, A., et al.: Evaluation of the Beam-F3 method for locating the F3 position from the 10–20 international system. Brain Stimul. **15**(4), 1011–1012 (2022)

Vehicle Engineering

Predictive Methodology to Optimize Knocking Behavior in the Transformation of Engines to Gaseous Fuels

Vicente Bermúdez-Tamarit [iD], Josep Gomez-Soriano [iD], Sebastian Tolvett-Caro[(✉)] [iD], and Raúl Luján

Universitat Politècnica de València, CMT-Motores Térmicos, Camino de Vera s/n, 46022 Valencia, Spain
satolcar@mot.upv.es

Abstract. The growing concern about climate change has prompted national strategies with ambitious greenhouse gas emissions targets. Most of these targets aim at carbon neutrality by 2050. Different approaches propose electromobility as a mitigation measure to replace fossil fuels in vehicle propulsion systems; but, studies show that by 2050 only 31% of vehicles worldwide will be electric. Therefore, to achieve carbon neutrality goals, it will be necessary to develop cost-effective transition technologies that reduce emissions from the remaining fleet. A viable alternative is transforming and optimizing engines for cleaner fuels such as natural gas (NG) or liquified petroleum gas (LPG). This research proposes a predictive methodology to predefine engine conditions related to its compression ratio (CR) to avoid knocking when transforming engines to gaseous fuels.

Keywords: engine conversion · natural gas · liquified petroleum gas · compression ratio · knocking

1 Introduction

Greenhouse gas (GHG) emissions, mainly produced by the combustion of fossil fuels, are responsible for climate change [1]. Within these emissions, internal combustion engines contribute 17% of the total [2, 3]. In response, different cities and countries have agreed to replace internal combustion engines (ICE) with electric powertrains [4]; however, independent analyses [5] project that by 2050, 31% of passenger cars worldwide will be electric, while the rest of the fleet will continue to use traditional fuels. Therefore, to reduce emissions related to fossil fuels, it will be necessary to propose other options for the remaining fleet; some authors suggest alternative fuels, such as natural gas (NG), liquefied petroleum gas (LPG), or hydrogen (H_2) [6, 7]. LPG is one of the leading alternative fuels used in the automotive industry. Its composition is essentially a mixture of propane (C_3H_8) and butane (C_4H_{10}), which varies according to technical requirements defined in standards such as N589 [8]. The main advantage of LPG is that, given its chemical characteristics, it can liquefy at low pressures, allowing it to maintain

an energy density like traditional fuels [9]. However, the massive use of gaseous fuels presents critical challenges in transforming existing engines. One of the main problems is the control of knocking [10–12]. Its occurrence limits the engine's thermal efficiency, restricting the exploitation of its advantages. LPG is sensitive to these effects because its resistance to knock will depend directly on its composition, so the calibration of an engine must consider this parameter. This work proposes a methodology to pre-design the transformation of a combustion engine from the original fuel, allowing it to speed up the process of fuel change and reduce production costs.

2   Methods and Materials

This paper proposes a methodology to understand the effects of a transformation from a base fuel to a new fuel. In this case, the conversion of an engine designed for NG to LPG will be used to apply the methodology. This type of transformation presents challenges; one of the most relevant, considering the properties of both fuels, is determining the admissible compression ratio (CR) for the new fuel. Therefore, the thermochemical effects of changing the fuel are analyzed to determine under what conditions knock combustion will occur.

2.1   Materials

The engine to be converted is a 4L Medium-Duty, a 4-Stroke SI engine with multipoint fuel injection and 12:1 compression ratio, maximum power of 100 kW at 3500 rpm, and maximum torque of 350 Nm at 1500 rpm. The engine was originally designed to run on NG; the objective is to convert the engine to run on automotive LPG, also called AUTOGAS. LPG automotive fuel is composed of propane (C_3H_8) at 38.42% and butane (C_4H_{10}) at 60.37%. Motor Octane Number (MON), in the case of NG (CH_4), is 120, while LPG is 93.63. As LPG is composed of propane and butane, its boiling point varies between -42 ºC and -0.5 ºC, which allows it to liquefy at low pressures.

2.2   Methodology

To carry out the analysis, appropriate engine conditions must be defined to predict under what circumstances the auto-ignition will occur with the new fuel. The study reviewed 12 points of the engine and estimated the pressures to which the cylinder would be subjected according to the fuel. The analysis shows that when the maximum torque is reached, the highest pressures and temperatures appear inside the cylinder for both fuels. It is observed that the pressure for LPG is 5 bars lower than the pressure of NG; however, the antiknock characteristics of LPG are lower than those of NG. In addition, in lower-speed operation, the combustion time is longer, increasing the probability of auto-ignition. Considering the analysis, the engine critical condition was defined at maximum torque and minimum engine speed, i.e., at 350 Nm and 1500 rpm, corresponding to 55 kW of power. Once the critical condition has been determined, it is necessary to estimate the reference pressure and temperature at the bottom dead center (BDC). By establishing the critical condition, it is possible to calculate a compression to determine the mixture

conditions at the top dead center (TDC), i.e., in the worst case and just before combustion occurs.

Equation (1), which corresponds to the effective power, is used to obtain the pressure and temperature at BDC, a reference density(ρ_{ref}) is estimated for the critical condition.

$$N_e = \eta_e \eta_v F_r F_e \rho_{ref} V_T n i LHV \tag{1}$$

The same effective power is used for both fuels to maintain the original engine performance. At the same performance in NG and LPG, the reference density must change, i.e., the inlet conditions of the mixture must be different. Thus, it is possible to determine the conditions at the BDC. Using the ideal gas equation of state, Eq. (2), it is possible to calculate the pressure at BDC for a given temperature and CR; the TDC parameters can be obtained with Eq. (3) if a polytropic compression is assumed.

$$PV = mRT \tag{2}$$

$$PV^n = k \tag{3}$$

Pressure at BDC is obtained considering the reference density and assuming a fixed temperature. A range of 100 ± 20 °C was defined as an appropriate temperature at BDC. Once BDC pressure and temperature conditions are calculated, Eq. (3) is applied to model a polytropic compression[1]. The result corresponds to the conditions at TDC of pressure and temperature according to CR. Once pressure and temperature are calculated for the given conditions, the method performs a predictive study of the combustion process. First, the auto-ignition delay (AID) is calculated, predicting the onset of combustion by detonation. A 0D homogeneous reactor model is used, assuming constant pressure conditions. In addition, laminar flame speed (SL) calculations are performed to estimate the combustion velocity. The CONVERGE v2.4 tool was used for both fuels. The expression ΔKnock, Eq. (4), is proposed to establish the existence of auto-ignition, which is expressed as follows:

$$\Delta Knock = AID_{LPG} - \left(\frac{t_{combustion}}{SL_{LPG}/SL_{BASE}} \right)[ms] \tag{4}$$

Equation (4) compares the LPG's AID with the combustion time ($t_{combustion}$) normalized by the LPG's SL and the base fuel SL ratio, in this case, NG.

3   Results

The combination of both effects (AID and SL) is relevant for the analysis; even though LPG has a higher SL, its AID is lower than NG, so in the same thermodynamic condition, there is likely undesired auto-ignition in the engine. To contextualize this difference, it is necessary to establish a reference corresponding to the combustion time. The reference

---

[1] Polytropic coefficient were determined using a CFD model for NG n = 1.35 and for LPG n = 1.32.

combustion time was estimated according to previous studies. A combustion duration of 40 CAD at a speed of 1500 rpm was defined. The combustion time for the engine under these conditions is 4.44 ms. The proposed hypothesis is that knocking will occur if the AID time is shorter than the combustion time or the combustion time normalized by SL, i.e., if ΔKnock < 0.

3.1 Knocking Zone

To define a zone of knocking appearance, the analysis considers the calculation of a 5 × 5 matrix for each CR (from CR 10:1 to 12:1) by imposing a range of 5 BDC temperatures (80 °C, 90 °C, 100 °C, 110 °C, and 120 °C) and five pressures related to the temperatures. For each matrix, AID and SL are calculated in each cell; then, it is possible to evaluate AID − $t_{combustion}$ and ΔKnock. Finally, the percentage of cells that present knocking conditions (<0) over the total of each CR matrix is established as an indicator, i.e., if 25 out of 25 conditions present negative values, the probability of knocking is 100%. Results of this calculation are shown in Table 1, AID − $t_{combustion}$ situations vary from 0% at CR 10:1 to 96% at CR12:1; in the case of ΔKnock, from CR 10:1 to CR 11:25, the probability is 0%, and CR 12:1, it is 28%.

Table 1. Probability of knocking by CR for LPG

CR	10.00	10.25	10.50	10.75	11.00	11.25	11.50	11.75	12.00
AID − $t_{combustion}$	0%	8%	16%	28%	48%	68%	80%	92%	96%
ΔKnock	0%	0%	0%	0%	0%	0%	8%	20%	28%

In Fig. 1, the upper blue curve corresponds to the percentage of cells, per CR, where AID − $t_{combustion}$ < 0, and the lower blue curve is the percentage of cells where ΔKnock < 0; the area between both curves is defined as the Knocking Zone. It is observed that at CR 12:1, the range of auto-ignition probability is 28% to 96%, while at CR 11:1, the content is 0% to 48%; however, at a compression ratio of 10:1, the knocking probability is 0%.
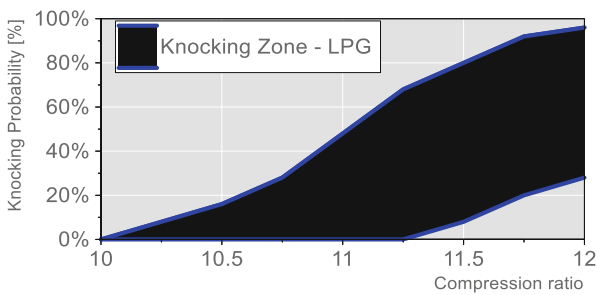
Fig. 1. Knocking Probability (Knocking Zone) for LPG according to compression ratio.

3.2 Experimental Results

Considering the theoretical analysis, it was decided to perform experimental tests on two cylinder heads with different CR, first with a volumetric CR of 11.05:1 and the second with a volumetric CR of 9.86:1. The engine performance was evaluated in an asynchronous dynamometer where the instantaneous brake power and torque were measured. The engine is also instrumented with a pressure sensor inside the cylinder, allowing the analysis of combustion behavior. The conditions of each measurement were at 1500 rpm and maximum torque, which according to the configuration, reached 300 Nm for the 11:1 compression ratio and 280 Nm for the 10:1 compression ratio. Figure 2 shows the in-cylinder pressure for the two proposed arrangements. In the case of CR = 11.05:1, it is observed that there is a dispersion of 25 bar between combustion cycles. In addition, it is possible to observe instability in the signal for a significant number of cycles. However, in the combustion at maximum torque with CR = 9.86:1, it is observed that the dispersion between cycles is 10 bar, with stability in the signal for every measured cycle.
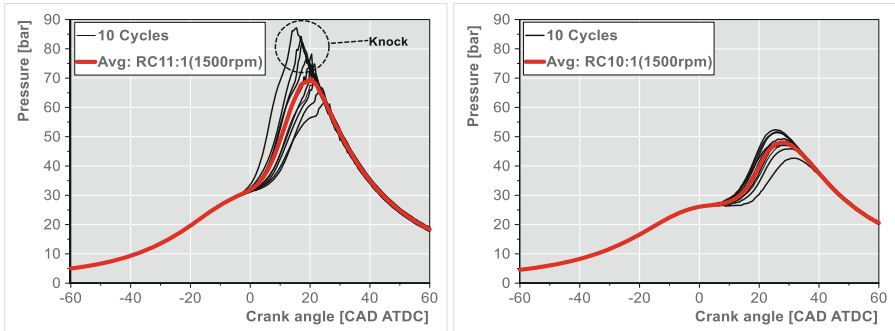
Fig. 2. Average pressure and its dispersion (10 cycles) inside the cylinder for the modified cylinder head with CR = 11.05:1 (left) and CR = 9.86:1 (right), using LPG.

4   Conclusions

This research presents a methodology to promote the transformation of traditional engines to run on zero or low-carbon fuels. This methodology is the first step to defining the conditions where a transformation becomes feasible. The Knocking Zone obtained shows that for LPG, for CR = 12:1, the probability of auto-ignition is between 28% to 96%; for CR = 11:1, the range is 0% to 48%, however, in CR = 10:1, the probability of auto-ignition is 0%. When performing the experimental tests, it was found that with a cylinder head of CR = 11.05:1, at 1500 rpm and maximum torque, there is knocking; however, for a CR = 10:1, this phenomenon does not appear. In the literature, it is defined that CR for engines powered by LPG would be between 10:1 and 11:1 [13, 14], arguing that the optimum point of thermal efficiency would be between CR of 10:1 and 10.5:1. However, other authors analyze that if the auto-ignition level can be controlled,

the maximum efficiencies in LPG would be reached at CR close to 12:1 [15]. Indeed, the calibration process of a converted engine considers an essential number of variables to be adjusted. However, it is relevant to define a priori the feasibility that the base conditions of combustion are favorable. Finally, the methodology allows for predicting the occurrence of knocking in the transformation of an internal combustion engine. The prediction defines a range of circumstances because there are strategies that will enable reducing the occurrence of knocking under certain conditions, such as ignition delay, intake conditions, detection strategies, etc. Despite the uncertainty, the tool allows for designing a pre-conversion strategy based on thermodynamic calculations without having complex combustion analysis models, which is its main functionality.

References

1. Intergovernmental Panel on Climate Change (2014): Climate Change 2014 Mitigation of Climate Change
2. Reitz, R.D., Ogawa, H., Payri, R., et al.: The future of the internal combustion engine. Int. J. Engine Res. **21**, 3–10 (2020). https://doi.org/10.1177/1468087419877990
3. Onorati, A., Payri, R., Vaglieco, B.M., et al.: The role of hydrogen for future internal combustion engines. Int. J. Engine Res. **23**, 529–540 (2022). https://doi.org/10.1177/146808742 21081947
4. Wappelhorst, S.: The end of the road? An overview of combustion engine car phase-out announcements across Europe. Int. Counc. Clean Transp. 1–19 (2020)
5. EIA (2022) Independent Statistics
6. Bae, C., Kim, J.: Alternative fuels for internal combustion engines. Proc. Combust Inst. **36**, 3389–3413 (2017). https://doi.org/10.1016/j.proci.2016.09.009
7. Martins, J., Brito, F.P.: Alternative fuels for internal combustion engines. Energies 13 (2020). https://doi.org/10.3390/en13164086
8. European Standard EN 590:2013 (2013) Automotive fuels - LPG - Requirements and test methods
9. Raslavičius, L., Keršys, A., Mockus, S., et al.: Liquefied petroleum gas (LPG) as a medium-term option in the transition to sustainable fuels and transport. Renew. Sustain. Energy Rev. **32**, 513–525 (2014). https://doi.org/10.1016/j.rser.2014.01.052
10. Morganti, K.J., Foong, T.M., Brear, M.J., et al.: The research and motor octane numbers of Liquefied Petroleum Gas (LPG). Fuel **108**, 797–811 (2013). https://doi.org/10.1016/j.fuel. 2013.01.072
11. Zhen, X., Wang, Y., Xu, S., et al.: The engine knock analysis - an overview. Appl. Energy **92**, 628–636 (2012). https://doi.org/10.1016/j.apenergy.2011.11.079
12. Krieck, M., Günther, M., Pischinger, S., et al.: Effects of LPG fuel formulations on knock and pre-ignition behavior of a DI SI engine. SAE Int. J. Engines **9**, 237–251 (2015). https://doi.org/10.4271/2015-01-1947
13. Ravi, K., Pradeep Bhasker, J., Porpatham, E.: Effect of compression ratio and hydrogen addition on part throttle performance of an LPG fuelled lean burn spark ignition engine. Fuel **205**, 71–79 (2017). https://doi.org/10.1016/j.fuel.2017.05.062
14. Chaichan, M.T., Kadhum, A., Riza, K.S.: Spark ignition engine performance when fueled with NG, LPG, and Gasolin. https://doi.org/10.21276/sjeat.2016.1.3.7
15. Lawankar, S.M.: Influence of compression ratio and ignition timing on the performance of LPG fuelled SI engine. In: SAE Technical Papers. SAE Intl. (2013)

Automatic Sight Distance Estimation
for Overtaking Maneuvers

Felipe Jiménez[(✉)] [ORCID] and Juan Ruiz

INSIA, Universidad Politécnica de Madrid, Madrid, Spain
`felipe.jimenez@upm.es`

Abstract. New assistance systems, as a preliminary step towards automated driving, require a complete knowledge of the environment. To do this, perception sensors are used, but positioning on digital maps is also a valuable tool as a secondary sensor. In this sense, digital maps must contain increasingly greater precision and detail. A variable that is not usually included is the sight distance, which is conditioned by static and dynamic elements. This paper presents a method for its estimation considering the road geometry and other elements that can interfere with driver or sensors vision such as obstacles in the surroundings of the road or a vehicle in front of the ego vehicle (before an overtaking maneuver). The method is applied to data from a real road with the advantage of being able to work in real time so results could be obtained based on the dynamic elements detected by the vehicle's sensors. From the sight distance information, the possibility of carrying out overtaking maneuvers is estimated.

Keywords: sight distance · road geometry · overtaking maneuver

1 Introduction

The new driver assistance systems, as a previous step towards automated driving, require a more complete knowledge of the environment. To do this, perception sensors are used, but also positioning on digital maps is a highly valuable tool that complements the situational awareness information. In this sense, digital maps must contain more and more precision and detail [1].

Although the means used for the construction of digital maps allow the storage of road geometry data [2], the sight distance is not usually obtained directly, but it is of vital importance in some scenarios [3]. Visibility on a road should be understood as the distance up to which an observer can distinguish objects, such as the road itself, other vehicles, signs, obstacles, etc. This visibility is highly influenced by changes in the environment, such as the geography of the terrain, the vegetation, the geometry of the road, the appearance of obstacles that obstruct the line of sight, the weather of the area, the brightness of each hour of the day, etc.

Instruction [4] includes, theoretically, road layout design conditions in terms of braking and overtaking distances, and visibilities. It also raises geometric considerations

about visibility in circular curves and vertical curves. In addition, it indicates that the horizontal and vertical layouts must be coordinated.

In [5], the methods are classified between those that obtain 2D visibility models, both horizontal plane of the road and vertical one, and those that obtain 3D models, combining the methods used in 2D with greater data processing capacity in accordance with technological development. Studies such as [6, 7] stand out methods to estimate the visibility distance based on data previously obtained from the geometry of the road. Another approach is the one presented in [8] in which, based on data included in a Geographic Information System (GIS), visibility zones of a vehicle can be created based on its GPS position.

In this paper, a geometric algorithm is proposed that allows estimation of this sight distance from the map information, which can be updated in real time in the presence of obstacles detected in the movement of the vehicle (detected by on-board sensors) so that the possibility of overtaking can be determined at each point on the road. This flexibility increases its field of application compared to algorithms that only work offline on the road digital map and do not have the capacity to adapt to changing situations of dynamic elements or consider the influence of critical elements for the overtaking maneuver. Thus, it is possible to support the decision-making of driver assistance systems and advanced levels of automated driving.

2   Method

The proposed method is based on the knowledge of the horizontal and vertical road geometry. For decades, there have been methods for measuring this geometry based on driving along the route with an instrumented vehicle [9]. In the case of this paper, this digital map is obtained using a vehicle with a GPS receiver, an inertial system and perception sensors such as cameras and LiDAR [10]. In this way, by merging the first two systems, the inaccuracies and signal losses typical of satellite positioning and the cumulative errors of inertial systems are reduced. On the other hand, the cameras identify the horizontal and vertical signals, and the LiDAR allows obtaining variables such as the dimensions of the transversal section of the road, location of road markings or identification of elements on the sides of the road [11]. In this way, in terms of geometry, the coordinates (x, y, z) of the median line of one of the traffic lanes are obtained and, by knowing the width of the lanes and the total roadway, the reconstruction of the median line of the road, the rest of the lanes and the road edge is possible.

The sight distance calculation is divided in two parts: horizontal and vertical. After carrying out the calculations separately, the sight distance limited by the geometry of the road will be the minimum distance of both, and this must be compared with the distances imposed by other conditions such as the obstacle in front of the ego-vehicle in the overtaking maneuver or the range of onboard perception sensors. The method is presented in a generic way to be adaptable to variable viewpoints, both vertically (height of the driver or position of the sensor on the roof of the vehicle or on the front) and transversally.

In general, in the horizontal projection, the x-y coordinates of the central axis of the road are available. According to Standard 3.1-IC [4], the viewpoint is located at 1.5 m

from the axis of the road, a configurable data. In addition, some adjustable road edges have been used in the distance from the axis, as a corridor, from which it is considered that there is no vision due to obstacles located on the roadsides. These lateral limits are a strong simplification of reality. However, this approach has two advantages: on the one hand, a conservative measure can be obtained by using small values for the width of that corridor; and, on the other, the procedure can be generalized in real time to variable widths based on what is detected by the vehicle's on-board sensors. In this way, vision is limited by the right and left edges of the road, and its range is up to where the center line of the left lane can be seen continuously, which is estimated to be located 1.5 m from the center of the axis as is shown in Fig. 1a.

Regarding the calculation in the vertical projection, according to Standard 3.1-IC [4], the viewpoint is located at a height of 1.1 m from the ground, the same as the minimum height at which a vehicle moving in the opposite direction is detectable, configurable parameters in the calculations. Figure 1b shows the concept for the calculation with which the aim is to find the minimum distance at which a vehicle would stop being seen when the vehicle's vision intersects with the road itself.

The algorithm also considers the visibility restrictions implied by the obstacle that one wishes to overtake, as shown in Fig. 1c. In this case, the closest points of the median line of the lane next to the vehicle that are no longer perceived from the point of view are identified.

Green line: Sight distance.
Red circle: Furthest detected point.
Orange circle: Geometric limitation.
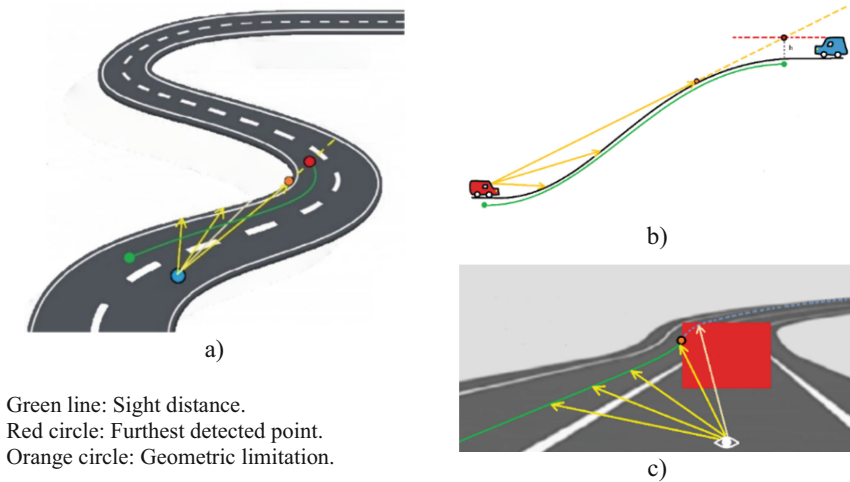
Fig. 1. Diagram of the algorithm to determine the sight distance a) horizontal projection, b) vertical projection, c) facing an obstacle in front of the ego-vehicle

3   Results

The algorithm has been applied on real roads. Specifically, the application to the M-104 road in Madrid (Spain) is shown. It is a single carriageway road, with one lane in each sense, with the particularity of presenting a great diversity of radii of curvature (including

quite small values) and changes in elevation. Figure 2 shows the results of sight distance for each of the profiles calculated by road geometric criteria.
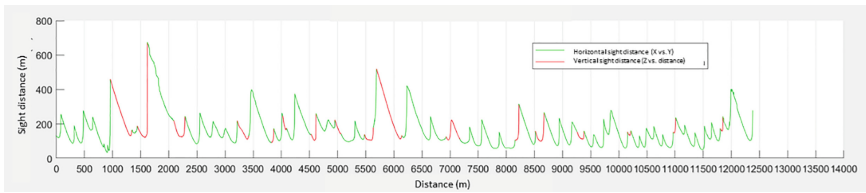
Fig. 2. Sight distance limited by horizontal alignment (green) and vertical alignment (red)

The influence of certain variable parameters on the results is analyzed. Thus, the width of the free section on both sides of the road influences the calculation of the sight distance limited by the horizontal alignment. An almost linear trend is verified between the average visibility distance and the corridor width, so that the most limiting condition is imposed by the horizontal layout versus the vertical one when the corridor narrows (Table 1).

Table 1. Influence of the corridor width

Limiting sight distance factor	Corridor width		
	3 m	5 m	7 m
Horizontal	85,48%	78,77%	74,92%
Vertical	14,52%	21,23%	25,08%

In real-time operation, the corridor width is considered variable over the distance based on the detection of the LiDAR, so obstacles can be characterized on the sides of the road that are detected and positioned on the digital map.

Regarding the height of the vehicle in the opposite direction, the sight distance is highly affected by variations around small values and tends to become more insensitive with variations on large values around 3 m. An analogous situation results from the vertical position of the sensor in the vehicle itself; elevated positions are preferable, although those values have practical implementation limits.

On the other hand, the stretches in which the sight distance is greater than the measurement range of the onboard sensors with assistance systems or partially automated driving are analyzed. Taking an average range of 250 m, on the analyzed road, it is verified that 14% of the total distance would have limited visibility due to the range of the sensor.

Finally, in an overtaking maneuver, the vehicle that is going to be passed represents an obstacle to the field of view of the ego-vehicle. In such a case, both the distance between the two vehicles and the dimensions of the first one are relevant variables. Table 2 shows the results of the influence of the presence of a car that is going to be overtaken that circulates along the median line of the lane. As can be seen, the proximity of the obstacle

greatly influences visibility, especially at short distances. Mainly the biggest influence is at distances less than 50–60 m. Table 3 shows the influence of the size of the obstacle.

Table 2. Influence of the distance between the ego-vehicle and the vehicle to be overtaken.

Distance (m)	50	75	100	Without
Average road sight distance (m)	134,54	149,38	157,16	168,66
Sight distance limited by road geometry	58,34%	71,10%	80,69%	100%
Sight distance limited by obstacle	41,66%	28,90%	19,31%	–

Table 3. Influence of the obstacle size

Size (m)	0,7 × 0,7	1,8 × 1,5	2,5 × 4	Without
Average road sight distance (m)	155,27	134,54	119,50	168,66
Sight distance limited by road geometry	72,35%	58,34%	48,80%	100%
Sight distance limited by obstacle	27,65%	41,66%	51,20%	–

It should be noted that the calculations are made for the entire route, but the method can also be used in specific stretches, or the data can be updated in real time.

4   Conclusions

In this paper, an algorithm has been presented for the automatic and geometric calculation of road sight distance, which can be implemented in real time and integrated with perception systems to modify parameters that influence the calculation.

The study of the influence of various parameters on the results on a single carriageway road reveals the importance of detecting these variables at all times, such as the free cross-sectional corridor that would be easily detected by perception technologies such as LiDAR (for example, due to the presence of obstacles on the sides of the road or an obstacle in front of the vehicle itself that makes it difficult to see the adjacent lane prior to an overtaking maneuver). This flexibility increases its field of application compared to algorithms that only work offline and do not have the capacity to adapt to changing situations. On the other hand, regarding the influence of the height of the obstacle, more or less conservative criteria can be adopted for decision making.

In this way, the algorithm can support decision-making for driver assistance systems or even for advanced levels of automated driving. In this sense, it should be noted that the range of the sensors has a maximum range that, in many cases, limits the sight distance detected by the geometry of the road, which is a relevant limitation and could motivate to resort to other types of technologies such as V2X communications in the framework of connected vehicles and cooperative driving to effectively carry out these overtaking maneuvers [12].

References

1. eSafety Forum. Digital Maps Working Group Final Report. European Commission, Brussels (2005)
2. Jiménez, F., Aparicio, F., Estrada, G.: Measurement uncertainty determination and curve fitting algorithms for development of accurate digital maps for Advanced Driver Assistance Systems. Transp. Res. Part C: Emerg. Technol. **17**(3), 225–239 (2009)
3. Iglesias, L., Castro, M., Pascual, V., De Santos-Berbel, C.: Estimation of sight distance on highways with overhanging elements. In: International Conference on Traffic and Transport Engineering, Belgrade (2016)
4. MOPU. Trazado. Instrucción de carreteras. Norma 3.1-IC. Madrid: Centro de publicaciones del Ministerio de Fomento (2000)
5. Hassan, Y., Easa, S., El Halim, A.: State of the art of three-dimensional highway geometric design. Can. J. Civ. Eng. **25**(3), 500–511 (1998)
6. Khattak, A.J., Shamayleh, H.: Highway safety assessment through geographic information system-based data visualization. J. Comput. Civ. Eng. **19**(4), 407–411 (2005)
7. Castro, M., Anta, A.J., Iglesias, L., Sánchez, J.A.: GIS-based system for sight distance analysis of highways. J. Comput. Civ. Eng. **28**(3), 04014005 (2014)
8. Castro, M., Iglesias, L., Sánchez, J.A., Ambrosio, L.: Sight distance analysis of highways using GIS tools. Transp. Res. Part C-Emerg. Technol. **19**(6), 997–1005 (2011)
9. Castro, M., Iglesias, L., Rodríguez-Solano, R., Sánchez, J.A.: Geometric modelling of highways using global positioning system (GPS) data and spline approximation. Trans. Res. Part C—Emerg. Technol. **14**, 233–243 (2006)
10. Jiménez, F.: Improvements in road geometry measurement using inertial measurement systems in datalog vehicles. Measurement **44**(1), 102–112 (2011)
11. Jiménez, F., Clavijo, M., Castellanos, F., Álvarez, C.: Accurate and detailed transversal road section characteristics extraction using laser scanner. Appl. Sci. **8**(5), 724, pp 1–13, (2018)
12. Talavera, E., Anaya, J.J., Gómez, O., Jiménez, F., Naranjo, J.E.: Performance comparison of Geobroadcast strategies for winding roads. Electronics **7**(3), 15 (2018)

Assessing a Deterministic Model for Autonomous Driving Through Visual Behavior

Sofia Sanchez-Mateo[1]([✉]) , Alfredo Valle-Barrio[1] , Alberto Díaz-Álvarez[2] , and Felipe Jiménez[1]

[1] University Institute for Automotive Research (INSIA), Universidad Politécnica de Madrid, 28031 Madrid, Spain
`sofia.sanchez@upm.es`
[2] Department of Computer Systems, Universidad Politécnica de Madrid, 28031 Madrid, Spain

Abstract. Driving safety has been improved by automated vehicles, particularly in terms of human error-related accidents, which are considered one of the main causes of traffic accidents. However, despite the increase in the number of sensors, full automation still generates conflictive situations where driver intervention is necessary. Many maneuvers are unique and sometimes unrepeatable, due to the multiple factors involved, being the patterns observation for the development of models and their automation complicated. To achieve greater knowledge of the performance during complex maneuvers on interurban roads, this article proposes the development of a deterministic driving model based on real driving data. The intentional phase prior to the maneuver has been studied in detail thanks to information from the driver's visual behavior.

Keywords: eye-tracking · autonomous driving · decision making

1 Introduction

Automated driving systems have improved the vehicle fleet, making the environment safer and reducing the number of accidents [1]. However, the lack of robustness of these systems implies a delay in their progress, given the lack of confidence that they sometimes generate in pedestrians and drivers [2, 3].

In order to achieve a good integration into society and traffic, these systems have been developed based on models which describe how a driver makes decisions facing different events. Driving models are usually divided mainly into two phases, (i) car-following, which determines the acceleration rates of a vehicle based on factors generally related to the preceding vehicle, and (ii) lane-change, which determines how and when a vehicle moves from one lane to another [5].

Regarding the variables used by driving models, several authors focus on the physical parameters evaluation through experimental tests, such as position and velocity, obtained

mainly from Global Positioning Systems (GPS) [6, 7]. On the other hand, the physio-logical parameters acquisition of the driver can enhance the decision rules that compose the algorithms of the decision-making models. One of the most widely used systems, for its lightness and comfort in driving, is the visual tracking. The information acquired by the driver precedes the cognitive processes, being able to anticipate a driver's decisions through his attention. Similarly, eye behavior provides information on the acceptability and distraction of systems, being extensively used in the evaluation of ADAS [8–10].

In this paper, a deterministic driving model focused on highways has been developed, to obtain information about the main parameters involved in decision making, specif-ically in lateral maneuvers. Through visual behavior, glances at the rear-view mirrors, especially the left one, are studied, which are considered an indicator of lane change intention in this study. The data have been collected from real traffic through several instrumented vehicles and a visual tracking system on the main driver.

2 Driving Model

The main objective of this paper is to analyze driver behavior in complex situations such as overtaking on a highway. For this purpose, a driving model for decision making has been developed, considering the actions of car-following, lane change and emergency braking for an interurban environment [11]. The decisions of the model are based mainly on the velocity, distance and time of each vehicle with respect to the ego vehicle, 1, where v_2, t_2, d_2 correspond to vehicle 2 and vi, ti, di, to the vehicles located in the left lane. To ensure that the ego-vehicle chooses the most convenient gap in lane changing, the accelerations and decelerations necessary to enter each of the gaps are calculated. An example of the arrangement of vehicles can be seen in Fig. 1, where vehicle v_i would correspond to v_A, v_{i+1} to v_B and v_{i+2} to v_C.
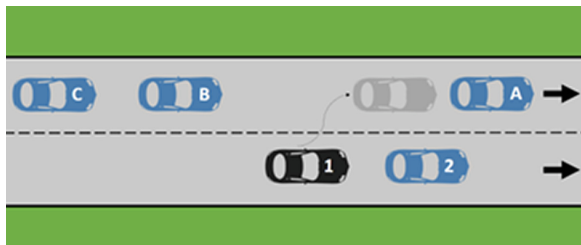
Fig. 1. Definition of the position of the vehicles.

The algorithm operation is based on the distance to the vehicle in front, which determines the switch between car-following and lane-change conditions. At this point, the intention to change lanes is considered, based on the maximum speed of the road, the average speed of the vehicles in the left lane, the speed of vehicle 2 and the minimum braking time. In case of overtaking, the algorithm would count the vehicles placed in the left lane. Depending on the arrangement of these vehicles, the lane change could be made in front of the first, between the first and the second, between the second and

the third, etc. One of the main advantages of this algorithm is that there is no maximum number of participating vehicles, being able to perform infinite iterations until finding a suitable gap to perform the maneuver safely. If no suitable and safe gap is found, it would go back to the beginning of the main loop, waiting for an optimal gap and assuming the car-following action with the change intention.

3 Experiments

A total of 5 vehicles have participated in the evaluation of the driving model, where 1 is the ego vehicle, 2, the front vehicle, and A, B and C are the vehicles located in the left lane of the road.

To feed the model, position and velocity data were collected by means of Global Positioning Systems (GPS) located in each of the participating vehicles. The constant variables of the vehicle and driver have been collected from the literature [12–15], subsequently adding a probabilistic effect in a Gaussian distribution as a function of the impulsivity of each subject [16].

3.1 Participants

A total of 22 driving tests were performed, corresponding to 12 men and 10 women, whose average age was 33.81 years (SD = 6.98). The participants reported a mean of 14.09 years of driving experience (SD = 5.78), being passenger car the most used vehicle (68.18%), followed by motorcycle (22.73%) and SUV type vehicles (9.09%). Most drivers reported driving between 10,000 and 20,000 km per year.

Since the nature of this study is closely linked to driving styles, the features of impatience, aggressiveness and impulsivity have been analyzed by means of a survey [17] with the aim of being able to cover the widest spectrum of different profiles and palliating the effects of the small and homogeneous sample. Each feature was scored out of 10, obtaining an average of 5.64 for impatience (SD = 1.55), 4.07 for aggressiveness (SD = 1.41) and 4.78 for impulsivity (SD = 1.43).

3.2 Instrumentation

The vehicle analyzed, which executes the maneuver, previously called vehicle 1, is a Peugeot 307 with automatic gearbox.

The ocular responses of the drivers have been recorded using an eye tracking system, consisting of two cameras and two infrared sensors in each eye, acquiring mainly the pupil diameter and the fixations.

Five vehicles involved were instrumented with a GPS acquiring real-time data through the M5-Stack device, which is based on the ESP32 SoC (System On a Chip).

3.3 Procedure

An interurban road section of 7.5 km belonging to the M-45 highway in Madrid was used for the experiments. The duration ranged from 35 to 55 min depending on the

traffic and the number of journeys necessary to simulate each case safely. The scenarios are summarized as car-following with and without change intention, and overtaking, classified as: lane change without vehicles (C1), lane change in front of A (C2), lane change behind A (C3), lane change between A and B (C4), lane change between B and C (C5), and lane change behind C (C6).

Prior to the experiments, the participants were instructed to drive as naturally as possible, without further information, in order to avoid suggestion when overtaking. The execution of the maneuvers was randomized, adapting each one to the available traffic. The test design was intrasubject, with each participant performing all the proposed scenarios at least once.

4   Results

The proposed experiments were satisfactorily carried out, despite the variations in traffic. The results obtained in the driving style survey showed that the selected sample was diverse and balanced. The proposed scenarios were repeated between 1 and 4 times by each participant, obtaining an overall mean of 1.77 times, with scenario C2 being the most repeated and C6 the least. In relation to this result, there were 9.81% of unsuccessful maneuvers of the total number, either because of external vehicles in the convoy or because the participant decided not to perform it.

Visual behavior indicated an increase in glances to the left rearview mirror of 13.2504 s on average before crossing the center line of the road during the maneuver (SD = 5.0827), occasionally combined with glances to the inside rearview mirror. The number of glances per second was calculated obtaining an average of 0.4425 and a standard deviation of 0.1835. This data along with the previous one shows that the average number of glances to the rearview mirror is below 6, matching the following frequency graph (see Fig. 2).
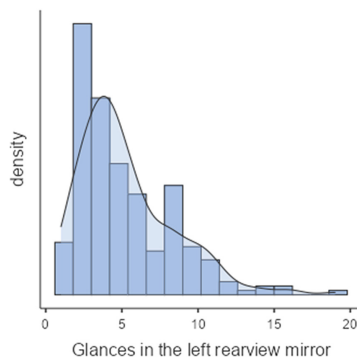
Fig. 2. Frequency of glances to the left rearview mirror in the anticipation period.

There were situations where the minimum number of glances at the mirror was 1 or 2 times, 4.85% and 10.53% with respect to the total. However, in most cases there were higher values, as can be seen in the previous figure (Fig. 2).

5   Conclusions

The characterization of driver behavior based on decision-making models can help in the development of more naturalistic algorithms supporting the integration of autonomous vehicles in mixed traffic. In this study, a deterministic driving model focused on conflicting situations such as overtaking on highways has been developed. The results of real driving overtaking showed that the most repeated condition was the lane change in front of the first vehicle of the convoy in the left lane and the least repeated condition was the lane change behind the last vehicle in the queue. This fact supports the complexity of the last situation, in which all vehicles are involved to perform the maneuver.

Regarding ocular behavior, an increase in glances at the left rear-view mirror prior to overtaking was observed, which is a clear indicator of cognitive preparation for the maneuver. Some drivers also relied on the interior mirror since its width allowed a global knowledge of the scene. The glance sequences ranged according to the environmental complexity and the time exposed, with a glance around every two seconds.

Driver behavior variables contribute to the characterization of the maneuver performance in a driving model, such as lane changing. In-depth knowledge of driver intentions could help the creation of new decision rules in the improvement of driving algorithms for autonomous vehicles.

References

1. Cicchino, J.B.: Effectiveness of forward collision warning and autonomous emergency braking systems in reducing front-to-rear crash rates. Accid. Anal. Prev. **99**(Pt A), 142–152 (2017). https://doi.org/10.1016/j.aap.2016.11.009
2. Terrones Rodríguez, A.L.: Una aproximación general al desarrollo de los coches autónomos. Revista Iberoamericana de Ciencia, Tecnología y Sociedad **16**(47), 153–175 (2021)
3. Ammoun, S., Nashashibi, F.: Real time trajectory prediction for collision risk estimation between vehicles. In: IEEE 5th International Conference on Intelligent Computer and Communication Processing, pp. 417–422 (2009)
4. Alawadhi, M., Almazrouie, J., Kamil, M., Khalil, K.A.: A systematic literature review of the factors influencing the adoption of autonomous driving. Int. J. Syst. Assur. Eng. Manag. **11**(6), 1065–1082 (2020). https://doi.org/10.1007/s13198-020-00961-4

5. Toledo, T.: Driving behaviour: models and challenges. Transp. Rev. **27**(1), 65–84 (2007). https://doi.org/10.1080/01441640600823940

6. Brummelen, V.J., O'Brien, M., Gruyer, D., Najjaran, H.: Autonomous vehicle perception: the technology of today and tomorrow. Transp. Res. Part C: Emerg. Technol. **89**, 384–406 (2018). https://doi.org/10.1016/j.trc.2018.02.012

7. Orlovska, J., Novakazi, F., Lars-Ola, B., Karlsson, M., Wickman, C., Söderberg, R.: Effects of the driving context on the usage of Automated Driver Assistance Systems (ADAS)— Naturalistic Driving Study for ADAS evaluation. Transp. Res. Interdisc. Perspect. **4**(100093) (2020). https://doi.org/10.1016/j.trip.2020.100093

8. Azevedo-Sa, H., Zhao, H., Esterwood, C., Yang, X.J., Tilbury, D.M., Robert, L.P.: How internal and external risks affect the relationships between trust and driver behavior in automated driving systems. Transp. Res. Part C: Emerg. Technol. **123** (2021). https://doi.org/10.1016/j.trc.2021.102973

9. Sánchez-Mateo, S., Pérez-Moreno, E., Jiménez, F.: Driver monitoring for a driver-centered design and assessment of a merging assistance system based on V2V communications. Sensors **20**(19), 5582 (2020). https://doi.org/10.3390/s20195582

10. Sánchez–Mateo, S., Pérez-Moreno, E., Jiménez, F., Naranjo, J.E., Pérez-Flores, C.G., Antoñazas-Teruel, J.: Study of a driver assistance interface for merging situations on highways. In: IEEE International Conference on Vehicular Electronics and Safety (ICVES), pp. 1–5 (2018). https://doi.org/10.1109/ICVES.2018.8519495

11. Zhang, K., Lu, N., Shi, Z.: Motion planning in lane change scenario for autonomous vehicles. In: China Automation Congress (CAC), pp. 7075–7080 (2021). https://doi.org/10.1109/CAC53003.2021.9728035

12. Prestl, W., Sauer, T., Steinle, J., Tschernoster, O.: The BMW active cruise control ACC. SAE Technical Paper 2000-01-0344, SAE World Congress (2000). https://doi.org/10.4271/2000-01-0344

13. Sánchez, F., Seguer, M., Freixa, A., Andreas, P., Sochaski, K., Holze, R.: From adaptive cruise control to active safety systems. SAE Technical Paper 2001-01-3245, SAE World Congress (2001). https://doi.org/10.4271/2001-01-3245

14. Burgett, A., Carter, A., Preziotti, G.: An algorithm for read-end collision avoidance warning systems. In: 17th International Technical Conference on the Enhanced Safety of Vehicles, Amsterdam (2001)

15. Sens, M.J., Cheng, P.H., Wiechel, J.F., Guenther, D.A.: Perception/reaction time values for accident reconstruction. SAE Technical Paper 890732. SAE World Congress (1989). https://doi.org/10.4271/890732

16. McAree, O., Aitken, J.M., Veres, S.M.: Towards artificialsituation awareness by autonomous vehicles. IFAC-PapersOnLine **50**(1), 7038–7043 (2017). https://doi.org/10.1016/j.ifacol.2017.08.1349

17. Pérez-Moreno, E., Hernández-Lloreda, M., Gallego-Largo, T., Castellanos, M.: Impulsive driving: definition and measurement using the i-driving scale (IDS). Spanish J. Psychol. **18**, E93 (2015). https://doi.org/10.1017/sjp.2015.98

Tubular Structure of an Urban Electric Vehicle with High Crashworthiness Performance

Jorge Velasco Manrique(✉), Marta Ingelmo Gómez, Javier Romo García,
José Antonio López Vicente, and Esteban Cañibano Álvarez

CIDAUT Foundation, Boecillo (Valladolid), Spain
{jorvel,maring,javrom,joslop,estcan}@cidaut.es

Abstract. This work summarizes the methodology and results of the design of a light and safe vehicle structure based on high-strength steel, aiming at its introduction in urban environments. The structure is made of a tubular chassis design easily scalable and modular, taking into consideration safety features from the very beginning of the design stage. The structural integrity of the vehicle from a static point of view is validated through torsional and bending stiffness simulations and experiments, as well as fatigue assessment. The crashworthiness is evaluated by applying the procedures set in regulations R137, R95 and R94, with special emphasis on vehicle occupants' protection and on other vulnerable road users, with the objective of achieving a 4-stars EuroNCAP rating.

Keywords: body frame · electric urban vehicle · crashworthiness · occupant protection

1 Introduction

In the last decades, the percentage of people living in urban environments has increased from 65 to 71%, and this trend is expected to continue in the following years [1]. In terms of mobility, this means that traffic congestion and air pollution will intensify. As a result, the EU has emphasized the need to develop lighter and cleaner passenger vehicles, while still providing safety for its occupants, as well as for other road users [2].

The Multi-Moby project, a European initiative within the Horizon 2020 Programme, aims at developing a cost-effective and safe vehicle structure for urban electric vehicles. The structure proposed is based exclusively on high-strength steel tubes, in such a way that it is modular and easily scalable. In practice, this means that the vehicle length, and even the vehicle purpose can be modified just by adapting a few tubular elements, at a much lower cost and time compared to the development of conventional vehicles (Fig. 1).

From a safety point of view, the objective is to design a vehicle structure providing comparable safety performance to that of conventional vehicles of higher dimensions, hence M1 homologation tests are taken as reference for the safety assessment. Besides, the protection of Vulnerable Road Users (VRUs) is considered, therefore the structure designed shall minimize the damage caused to pedestrians in the event of a run over.

Fig. 1. Modular approach: minimum structural changes lead to different vehicle concepts.

2   Methodology

The structural design was optimized via Finite Element analysis. The development process followed several iterative steps until meeting the target key performance indicators concerning the structural stiffness (2.000 N/mm bending stiffness, 3.000 Nm/° torsional stiffness), durability (250.000 km) and crashworthiness (UNECE Regulations). Firstly, the structure was modified until ensuring sufficient stiffness and durability, to enable a proper operation of the vehicle's safety systems, and then the complete vehicle was simulated and physically tested to evaluate its crashworthiness.

2.1   Torsional and Bending Stiffness

The torsional stiffness test serves as reference to assess the robustness of a vehicle structure. From a functional point of view, a minimum torsional stiffness is needed to ensure a correct vehicle behavior, especially in transverse maneuvers such as turns. In this work, the torsional stiffness measurement was carried out without installing the vehicle suspension, to avoid external influences on the results. Tailored tools were manufactured to introduce the torsional loads, concretely by locking the rear axle and allowing only the rotation of the front axle around the longitudinal vehicle direction.
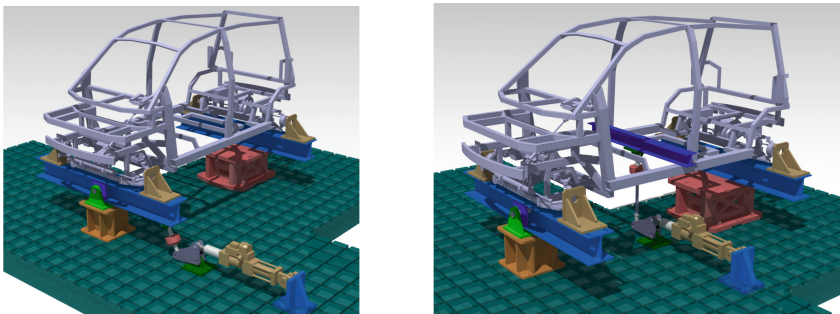
Fig. 2. Torsional (left) and bending (right) test setups.

On the other hand, the bending stiffness test provides information about the robustness of the vehicle structure when subjected to vertical loads due to the weight that is

carried, to acceleration and braking maneuvers, or to the driving over road irregularities. The testing setup also required the manufacturing of specific tools, in this case locking both vehicle axles, with an additional tool for introducing the vertical load in the central part of the structure. Both test setups are depicted in Fig. 2.

2.2 Durability Tests

The durability (fatigue) tests of the structure were carried out taking daily driving maneuvers as starting point for the loads definition. A representative multi-body vehicle model was developed for this purpose and introduced in CarSim software for the estimation of the loads induced to the structure, in the following maneuvers: acceleration, corner braking, driving over a speed bump, and moose test. Additionally, all maneuvers were simulated at different driving speeds, representing different driving profiles. Three aggressiveness levels were defined for the maneuvers: level 1, with longitudinal and transverse accelerations around 0.25 g; level 2, around 0.5 g; and level 3, around 0.75 g. From the simulation results, the cyclic loads were defined for the real tests, in such a way that they induce similar damage to the vehicle structure.

2.3 Crashworthiness Performance

Occupant protection: after analyzing the applicable testing protocols, mainly the UNECE Regulations for the M1 vehicles and the EuroNCAP test procedures, the safety tests according to UNECE Regulations R137 [3], R94 [4], and R95 [5] were selected. Their characteristics are summarized in Table 1. In addition, regarding the biomechanical parameters, a target value for the Occupant Load Criterion (OLC) was set at 40 g.

Table 1. Summary of selected UNECE Regulations for the crashworthiness evaluation

	R137	R94	R95
Crash direction	Frontal	Frontal	Lateral
Overlap	100%	40%	100%
Vehicle speed	50 km/h	56 km/h	0 km/h
Barrier type	Rigid	Deformable	Deformable
Barrier speed	0 km/h	0 km/h	50 km/h

Vulnerable Road Users (VRUs) protection: in what concerns the VRU protection, the study was only performed through simulations. To constraint the great variety of run over events that can happen in real life, the following variables were considered as part of a parametric study: frontal geometry of the vehicle (sharp - aggressive or rounded - smooth edges), bumper stiffness, vehicle speed (20, 30 and 40 km/h), vehicle-dummy relative position (central, left side or right side position) and alert state (preparedness) of the dummy right before the crash (different stiffness of the body muscles).

3 Results

3.1 Torsional and Bending Stiffness

The torsional stiffness was simulated up to 2° of torsion measured in the frontal part of the vehicle, registering a torsional stiffness of 2847 Nm/°. In these conditions, the maximum stresses registered reached 350 MPa, well below the elastic limit of the material, hence ensuring the integrity of the structure. In the physical tests, 1.5° of torsion in the frontal part of the vehicle were reached, registering a torsional stiffness of 3.071 Nm/°, fully aligned with the simulation.

The bending stiffness was simulated introducing a vertical load of 25 kN. In this scenario, a bending stiffness of 2.730 N/mm was measured, and the maximum stresses registered did not surpass 400 MPa, again comfortably below the elastic limit of the material. In what concerns the physical tests, a vertical load of 15 kN was introduced, registering a bending stiffness of 2.330 N/mm, hence validating the simulation results.

3.2 Durability Tests

As in the previous case, the fatigue performance of the structure was studied through simulations and real tests. For the simulation, a vehicle weighing 850 kg (includes batteries and passengers) was considered. The results obtained showed that maximum stresses are kept below 150 MPa in the most loaded areas, what guarantees the durability of the structure. After the simulation, physical tests were conducted. The structure was subjected to a million load cycles, representing the target 250.000 km, distributed as follows: 800.000 cycles under level 1 loads, 190.000 cycles under level 2 loads, and 10.000 cycles under level 3 loads. The structure withstood the test without any visible damage. The structure critical nodes were inspected by liquid penetrants test, to identify small crack that might have appeared during the test, no evidence of damage was found.

3.3 Crashworthiness Performance

Occupant protection: the crashworthiness of the structure was assessed according to the specifications of the aforementioned UNECE Regulations, including for each crash scenario the evaluation of both the structural behavior and the occupant protection.

Frontal impact according to Regulation 137: the structural behavior is highly satisfactory and the simulated performance correlates well with the actual performance of the prototype. The vehicle proves to be safe for its occupants in this load case, and the structural integrity was checked. The OLC value is 38.9g, below the limit values targeted. Likewise, other biomechanical parameters monitored in the dummy are below the threshold values set in the Regulation. Considering that this test configuration is the most severe among the frontal tests covered in the UNECE Regulations, it can be concluded that the structure is suitable to protect the occupants in this kind of crash events. The simulation and physical test results are presented in Fig. 3.

Frontal impact according to Regulation 94: since this load case is slightly less severe than the previous one (deformable barrier and partial overlap), acceptable results were expected. Indeed, the structure maintained its integrity and did not present any potentially
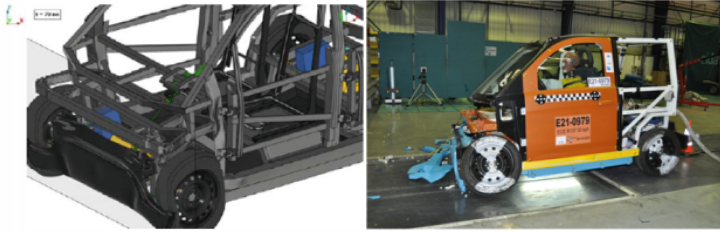
Fig. 3. Vehicle structure after the test according to R137, simulation (left) and real test (right).

dangerous deformation or break in the cabin. Additionally, no relevant intrusions were observed in the occupant surroundings. Figure 4 shows the physical test results.

Fig. 4. Vehicle structure after the test according to R94 (left), and detail of the front-end (right).

Both frontal tests were also employed to assess the battery protection capabilities of the structure, trying to anticipate the potential triggering of thermal runaway phenomenon in the battery that may threaten the safety of the vehicle occupants after a frontal crash. In this direction, acceleration and intrusion levels in the surroundings of the battery pack were measured. In both cases, a relatively smooth behavior (progressive decelerations, no intrusions) was observed, slightly better for the R94 test scenario, mainly due to the lower energy involved in the crash.

Lateral impact according to Regulation 95: the results were also successful, although in this scenario the low weight of the vehicle causes it to be dragged during the crash, what limits deformations, and consequently the energy absorbed by the structure. This test also served to check the outstanding performance of the steel doors. Its stiffness and robustness help control the intrusion of the barrier into the cabin, therefore protecting the occupant. Similarly, the deployment of the side curtain airbag was satisfactory, also contributing to reduce the damage on the occupants. In what concerns the battery integrity, the structure design lets the barrier to slide over the sill, keeping the battery region almost intact. The simulation and physical test results are presented in Fig. 5.

Vulnerable Road Users (VRUs) Protection: The simulation results of the run over scenarios show that the damage induced in the VRU is strongly related with the frontal dimensions of the vehicle. From a certain speed, the short vehicle bonnet forces the dummy head to crash against hard areas of the vehicle, such as the windscreen or the A-pillar, which translates into a severe injury potential. This event is by far the most

Fig. 5. Vehicle structure after the test according to R95, simulation (left) and real test (right).

critical; however, it is observed that at low speeds, if the vehicle has a smooth geometry, the damage induced in the legs and pelvis can be reduced to some extent.

4   Conclusions

Considering the results as a whole, it can be stated that it is feasible to design a safe urban electric vehicle based on a tubular structure made of high-strength steel. The appropriate design of the structure allows obtaining enough stiffness to increase occupant safety, as well as the deformation capability to absorb the energy involved in a crash event. However, it is worth noting that the influence of the vehicle design on the VRUs protection is almost negligible. This result highlights the need for integrating in the vehicle active safety systems specifically targeting VRUs protection.

References

1. Ritchie, H., Roser, M.: Urbanization (2019). https://ourworldindata.org/urbanization
2. European Commission: Roadmap to a Single European Transport Area – Towards a competitive and resource efficient transport system (2011)
3. UNECE: UN Regulation No. 137 - Frontal Impact (Rigid Wall) (2020)
4. UNECE: UN Regulation No. 94 Frontal Impact (Barrier) (2012)
5. UNECE: UN Regulation No. 95 - Rev.2 + Amendements - Lateral collision protection (2019)

On the Use of Carbon Fiber Composites for the Enhancement of the Rollover Resistance of Steel Buses

Daniel Lavayen-Farfán[1,2]([✉]) [ID], José Antonio Butenegro-García[1,2] [ID],
María Jesús López-Boada[2] [ID], Miguel Ángel Martínez-Casanova[2] [ID],
and Jorge Antonio Rodriguez-Hernandez[2] [ID]

[1] Pontificia Universidad Católica del Perú, Universitaria Ave. 1801, 15088 Lima, Perú
`dlavayen@pucp.edu.pe`

[2] Universidad Carlos III de Madrid, de la Universidad Ave. 30, 28911 Leganés, Spain

Abstract. The increasing use of composites in vehicles in recent years is one of the current trends in the automotive industry. In particular, fiber composites are being used as reinforcements for the main structural elements of vehicles, due to their outstanding specific mechanical properties and low weight. When combined with metal parts, fiber composites can significantly enhance the crashworthiness of vehicle structures, by increasing their energy absorption capabilities and resistance to plastic deformations and permanent damage. This work presents CFRP reinforcements as a case study for enhancing the bending collapse behavior and crashworthiness of bus structures. The required calculations are based on a simplified "concept model" that includes the bending collapse behavior of the structural components, based on theoretical models calibrated with experimental results. The results demonstrate that the use of CFRP reinforcements improves the rollover crashworthiness of a bus structure, and need not be applied to the entire structure, but only to the critical parts where bending collapse is most likely to occur in a rollover accident.

Keywords: Carbon fiber composites · vehicle structures · bending collapse · concept modelling

1 Introduction

Design of lightweight structures often considers the full load capacity of a material instead of the yield strength [1]. This implies working in the plastic range of a material, which can be advantageous in applications with energy absorption and dissipation requirements. For instance, automobiles require that their structures absorb the kinetic energy of an impact accident, so it does not reach the passengers. On the other hand, weight reduction is required to reduce material and manufacturing costs, as well as fuel consumption. This means that the crashworthiness design needs be done with weight and manufacturing in mind.

Additionally, rollover of buses is an extremely dangerous scenario. Although rare, circa 3% of all accidents, they are known to be particularly lethal [2]. For this reason, several efforts have been devoted to avoiding and preventing rollovers [3, 4], as well as to mitigate the potentially deadly effects, mainly by improving the bending collapse behavior of the steel tubes used [5–11]. Regulations and design rules have also been implemented internationally, with the UN/ECE R66 [7] being the most used. This regulation requires the characterization of the bending collapse of the tubes that form the structure.

In this study, previously developed localized reinforcements and collapse theories implemented in [12, 13] are employed and introduced into a "concept model" representative of a bus structure in a rollover test. It is noteworthy that although this is not the first-time concept models have been used to analyze structures in plastic regimes, it is one of the first times for multimaterial systems: steel structures reinforced with composite materials.

2   Methodology

2.1   Bending Collapse Experimental Setup

In order to characterize the bending collapse, three-point bending experiments are performed on a universal testing machine, following the schemes shown in Fig. 1.
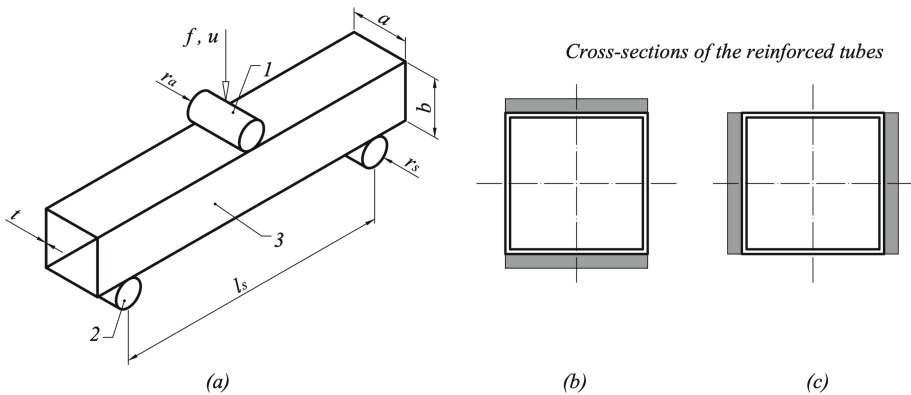
Fig. 1. (a) Three-point bending test scheme aimed to produce failure in the middle of the test specimen. (1) force applicator, (2) fixed support cylinders, (3) test specimen. (b) Cross-section of tube with reinforced flanges or UD reinforcements. (c) Cross-section of tube with reinforced webs or LR reinforcements.

The test specimens are based on tubes of S275 steel. The reinforcements are made from carbon fiber reinforced polymer (CFRP), based on bidirectional carbon fiber weave and epoxy resin as polymer. Hand layup is used to prepare CFRP plates, which are then cut to the size of the steel tubes. Both materials are then joined with an epoxy-based structural adhesive Sikapower 1277.

Once specimens are ready, three sets of bending experiments are performed:

1. Specimens without reinforcements (steel tubes). The results of this set are used as a baseline to evaluate the influence of the reinforcements.
2. Specimens with Up-Down reinforcements (UD), shown in Fig. 1(b), cover the flanges of the tube.
3. Specimens with lateral or Left-Right reinforcements (LR), shown in Fig. 1(c), cover the webs of the tube.

2.2   Concept Modeling of the Structure

The results of the bending tests are used to calibrate the theoretical models developed by the authors [12, 13]. The output of these tests is moment – angle $(M - \theta)$ curves, as shown in Fig. 2. Note that during these tests, the influence of the reinforcements is readily apparent.
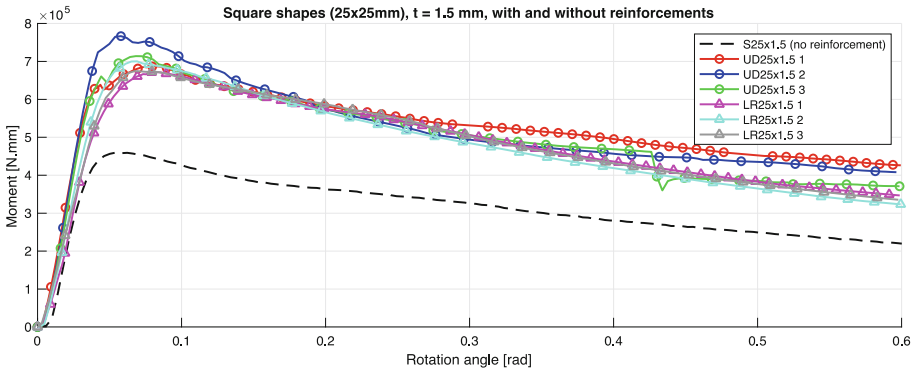
Fig. 2. Example of experimental M – θ curves for a tube of 25 mm and thickness of 1.5 mm. S25x1.5 represents a tube without reinforcements. Results based on [12].

The structure itself is modeled as beam line elements (see Fig. 3), and the zones prone to bending collapse are modeled as non-linear springs with the $M - \theta$ curves as their constitutive law; as this method provides accurate results [14–16].

Additionally, to simulate a rollover event, quasi-static loads are applied through a rigid inclined plane, which represents the ground. The calculation is carried out until contact between the residual space and the structure is detected. The residual space is modeled as a rigid surface fixed to the ground. In this calculation, the measured or observed quantities are the force (F) and displacement (u) of the rigid inclined surface (see Fig. 3). Therefore, the absorbed energy (E_{abs}) by the structure can be calculated as

the area under the curve F-u as shown in Eq. 1:

$$E_{abs} = \int_{0}^{u_{max}} F.du \tag{1}$$

To obtain a complete vision of the influence of the reinforcement and tube sizes on the crashworthiness, ten different dimensions for the structural loop of the concept model are tested. These dimensions are defined using Latin Hypercube sampling and allow to have a complete vision of the influence of every parameter. Furthermore, similarly to the bending tests, three sets of simulations are performed:

1. Rollover of the concept model of a steel structure.
2. Rollover of the concept model of a steel structure with UD reinforcements.
3. Rollover of the concept model of a steel structure with LR reinforcements.
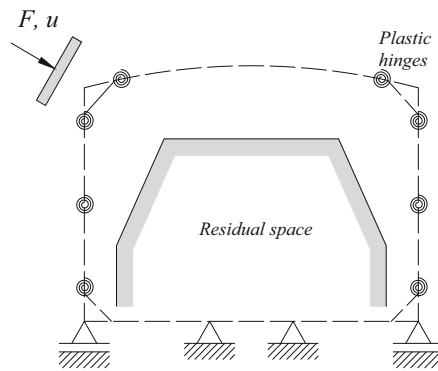
Fig. 3. Concept model of the bus structure. The springs are defined with a non-linear curve obtained from the bending collapse theoretical models.

3   Results

Three-point bending tests reveal important details about the failure modes, some exemplified in Fig. 4. As expected, steel shapes concentrate the plastic deformations in the "bulges". Reinforced shapes also show damaged composites due to delamination in the zones near the "bulge", with the rest of the composite seemingly showing no damage. Since damage is only restricted to the collapse zone (see Fig. 4), then the reinforcements only need to be applied in the critical zones, and thus significant savings in CFRP manufacturing can be achieved when applied to a large structure.

Furthermore, the bus structure simulations show that most of the tested sizes benefit from the composite reinforcements, regardless of the variant, as shown in Table 1. Additionally, the UD reinforcements can provide in general a better enhancement in crashworthiness than the LR reinforcements, which can be explained by the larger increase in the moment of inertia of the cross section. On the other hand, by comparing shapes of

<center>a)   b)</center>
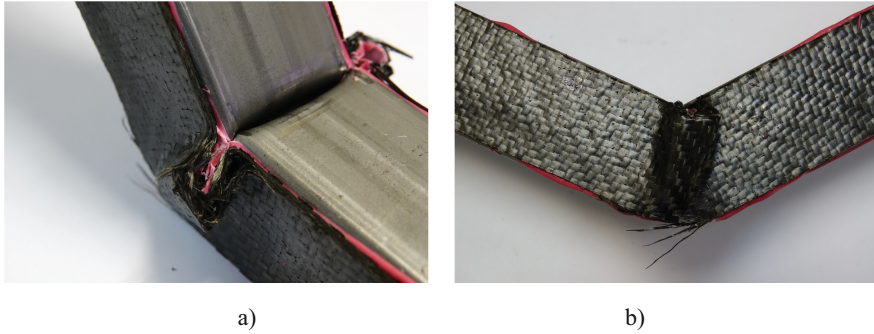
Fig. 4. Plastic deformation produced by bending collapse on a tube with LR reinforcements. Failure and delamination of the composite is restricted to the collapse zone. The CFRP does not suffer dam-age outside the collapse zone.

similar thickness, it can be inferred that the addition of any type of localized reinforcement can have a similar effect than increasing the thickness of the steel base shape. By increasing the thickness of a shape, the whole structure grows in weight, since shapes are produced with a constant thickness. However, if the CFRP reinforcements are applied only to the critical zone, the crashworthiness is enhanced without a significant increment in weight.

Table 1. Results of the rollover calculations of structures with base tubes of different sizes and different reinforcements. The percentages are taken using the steel structure as reference.

ID	Height b [mm]	Width a [mm]	Thickness t [mm]	UD reinforc		LR reinforc	
				Fmax %	Eabs %	Fmax %	Eabs %
1	62.5	32.5	2.6	+18.9	+2.8	+18.7	+2.4
2	52.5	72.5	1.6	+60.5	+64.5	+27.2	+34.0
3	32.5	77.5	3.9	+8.7	+0.0	+8.5	−0.4
4	77.5	57.5	3.8	+18.7	+1.7	+18.7	+1.2
5	57.5	62.5	3.1	+36.6	+16.6	+28.9	+14.6
6	37.5	37.5	3.4	+6.5	−2.7	+6.3	−3.4
7	47.5	42.5	2.9	+19.4	+6.1	+19.2	+5.6
8	42.5	52.5	2.1	+39.1	+24.0	+29.5	+20.9
9	67.5	47.5	2.4	+38.9	+21.0	+28.4	+18.0
10	72.5	67.5	1.9	+45.5	+55.2	+27.5	+32.3

4   Conclusions

This study explores the impact of adding composite material reinforcements, specifically CFRP, on the rollover resistance of a bus. The results show that partial local reinforcements, located in the areas prone to bending collapse, have a positive effect on the structure's rollover resistance (up to 64% increase) and increase the absorbed energy (up to 60% increase) in the event of an accident, without significant weight penalties (up to 15% increase). The use of recycled composite materials is also a possibility, which extends the composite's lifespan and makes it an environmentally friendly alternative [17, 18]. However, covering an entire metal structure with composite material can be costly, so incorporating composite materials only in areas that are prone to localized failure is a more cost-effective solution. This method is not only applicable to new designs but also existing structures that need repair or reinforcement to comply with current and newer regulations and standards.

References

1. Friedrich, H.E. (ed.): Leichtbau in der Fahrzeugtechnik. A, Springer, Wiesbaden (2017). https://doi.org/10.1007/978-3-658-12295-9
2. Peruvian National Police Yearbook. https://web.policia.gob.pe/anuario_estadistico/anuario_policial.html. Accessed 01 Feb 2023
3. Chu, D., Li, Z., Wang, J., Wu, C., Hu, Z.: Rollover speed prediction on curves for heavy vehicles using mobile smartphone. Measurements **130**, 404–411 (2018)
4. Gauchía, A., Olmeda, E., Aparicio, F., Díaz, V.: Bus mathematical model of acceleration threshold limit estimation in lateral rollover test. Veh. Syst. Dyn. **49**(10), 1695–1707 (2011)
5. Ha, N.S., Lu, S.: Thin-walled corrugated structures: a review of crashworthiness designs and energy absorption characteristics. Thin-Walled Struct. **157**, 106995 (2020)
6. Bai, J., Meng, G., Zuo, W.: Rollover crashworthiness analysis and optimization of bus frame for conceptual design. J. Mech. Sci. Technol. **33**(7), 3363–3373 (2019). https://doi.org/10.1007/s12206-019-0631-4
7. UN/ECE 66, Regulation No 66 of the Economic Commission for Europe of the United Nations (EN/ECE) - Uniform technical prescriptions concerning the approval of large passenger vehicles with regard to the strength of their superstructure (2007)
8. Huang, Z., Zhang, X., Yang, C.: Experimental and numerical studies on the bending collapse of multi-cell aluminium/CFRP hybrid tubes. Compos. B Eng. **181**, 107527 (2020)
9. Baroutaji, A., Sajjia, M., Olabi, A.G.: On the crashworthiness performance of thin-walled energy absorbers: recent advances and future developments. Thin-Walled Struct. **118**, 137–163 (2017)
10. Hussein, R.D., Ruan, D., Lu, G., Thomson, R.: An energy dissipating mechanism for crushing square aluminium/CFRP tubes. Compos. Struct. **183**(1), 643–653 (2018)
11. Kim, S.Y., et al.: Energy absorption characteristics of aluminium/CFRP hybrid beam under impact loading. Int. J. Crashworthiness **22**(2), 190–201 (2017)
12. Lavayen-Farfan, D., Butenegro-Garcia, J.A., Boada, M.J.L., Martinez-Casanova, M.A., Rodriguez-Hernandez, J.A.: Theoretical and experimental study of the bending collapse of partially reinforced CFRP–Steel square tubes. Thin-Walled Struct. **177**, 109457 (2022)
13. Lavayen-Farfan, D., Boada, M.J.L., Rodriguez-Hernandez, J.A.: Bending collapse analysis for thin and medium-thin-walled square and rectangular hollow shapes. Thin-Walled Struct. **165**, 107934 (2021)

14. Park, S. J., Yoo, W.S.: Rollover analysis for the body section structure of a large bus using beam and non-linear spring elements. Proc. Inst. Mech. Eng. Part D J. Automob. Eng. **222**(6), 955–962 (2008)
15. Bai, J., Meng, G., Wu, H., Zuo, W.: Bending collapse of dual rectangle thin-walled tubes for conceptual design. Thin-Walled Struct. **135**, 185–195 (2019)
16. Stigliano, G., Mundo, D., Donders, S., Tamarozzi, T.: Advanced Vehicle Body Concept Modeling Approach Using Reduced Models of Beams and Joints. In: SMA 2010 - International Conference on Modal Analysis Noise Vibration Engineering. 20–22 Sept. 2010, Leuven, Belgium, pp. 4179–4190 (2010)
17. Butenegro-Garcia, J.A., Bahrami, M., Abenojar, J., Martinez-Casanova, M.A.: Recent progress in carbon fiber reinforced polymers recycling: a review of recycling methods and reuse of carbon fibers. Materials **14**(21), 6401 (2021)
18. Butenegro-García, J.A., Bahrami, M., Swolfs, Y., Ivens, J., Abenojar, J., Martinez-Casanova, M.A.: Novel thermoplastic composites strengthened with carbon fiber-reinforced epoxy composite waste rods: Development and characterization. Polymers **19**(14), 1–19 (2022)

Numerical-Experimental Analysis of the Sealing Efficiency Utilizing Stresses Produced to an Engine Gasket Manufactured by CRS of ¼ Hardness with a Nitrile Coating on Both Sides

Félix Omar Soto-Barrón[(⊠)], Martín García-Pérez, Guillermo Urriolagoitia-Sosa, Beatriz Romero-Ángeles, Antonio Hernández-Cerón, Diego Sabas-Gonzalez, José Luis Reyes-Reyes, Martín Guzmán-Baeza, and Belén Alejandra Contreras-Mendoza

Grupo de Biomecánica, Instituto Politécnico Nacional, SEPI ESIME Zacatenco, Mexico City, Mexico

{fosotob,maguzmanb}@ipn.mx

Abstract. The evaluation of a cold assembled engine gasket provides data to analyze if a new design complies with requirements. The main cause of damage is the working temperature. High temperatures are due to refrigerant leakage. In addition to sealing the cylinder, the head gasket seals water and oil passages between the head and the block, preventing engine failure. Different gaskets will fail at different temperature ranges and this is relevant for the structural analysis of the engine. The durability of the gasket and its ability to seal the engine in all condition makes the design a challenge. The non-uniform thermal expansion of the motor makes difficult to design a uniform bead height in the gasket. This makes necessary to include a temperature map in all 3D analyses. This work shows the thermal analysis of an engine head gasket with prestressing of the assembly bolts, the results guarantee an efficient sealing and optimal operation.

Keywords: Sealing · gasket · numerical · evaluation · contact · stresses

1 Introduction

The main cause of head gasket failure is extreme engine temperature. High engine temperatures are often caused by a refrigerant leak. Different gaskets will fail at different stages and temperatures. Temperature changes are relevant when a metal has a high thermal expansion rate [1]. Analytical calculations are difficult and experimental evaluation are expensive. Nowadays, numerical analyses are a reasonable solution. Figure 1 shows the temperature distributions predicted by FEA [2]. It shows a highest temperature of 280 ºC, located by the flame cover of the cylinder head. The max. Temperature experienced by the gasket is approximately 200 ºC. These resulting temperatures, in the form of nodal temperatures, form the important heat load for structural analysis of the

engine assembly. Therefore, in all 3D analysis, we must include a temperature map and simulate the various operating conditions of the engine [2]. Temperatures vary a lot in a very small space. The fuel mixture when ignited can reach between 700 ℃ to 900 ℃. The hottest point of the engine is the exhaust manifold, just beyond the cylinder head cooling, where it can reach 500 ℃ to 700 ℃.
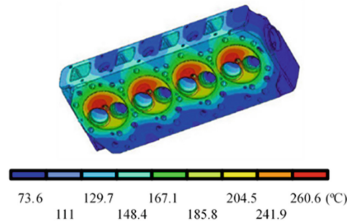
Fig. 1. Temperature distribution on engine cover.

This work investigates engine gasket sealing efficiency and cylinder head stress behavior under load conditions, using contact theory and thermal stress analysis. The thermal simulation analysis will provide some important thermal parameters, namely the heat transfer coefficients and the corresponding bulk temperatures. A finite element analysis (FEA) thermal simulation with those heat transfer coefficients and global temperatures will provide the temperature distribution of the engine assembly [2].

2   Methodology for Performing Thermal Analysis

Thermal analysis is an analytical technique most used in the field of materials science. Where changes in material properties are examined concerning the component at service temperature. The numerical thermal analysis procedure can be divided into four steps: containing defining elements, material properties, discretization, and results [3]. It requires to consider the structural evaluation of the component to conduct the thermal evaluation. The type of analysis is known as coupled. Discretization is relevant to simulate composite materials with coatings (Fig. 2).

Bottom layer
Two layers of *NBR* 0.0254 mm (0.001") and at the middle a *CRS* ¼ hard 0.2032 mm (0.008")

Top layer
Two layers of *NBR* 0.0254 mm (0.001") and at the middle a *CRS* ¼ hard 0.2032 (0.008")

Fig. 2. MLS Gasket Composite Material

Regarding the definition of material data, it is necessary to evaluate them carefully, since one of the objectives of the analysis is to verify the existence of regions where there are losses of stiffness, caused by the phenomenon of plasticity. The effect of temperature

can be significant, because the material can suffer a great loss of stiffness and consequent reduction in the ability to follow the movements of the flange. This is the result of stored energy being lost with temperature stress relaxation (Tables 1 and 2).

Table 1. Materials stress-strain data.

No.	NBR75		CRS ¼ hard	
	Strain (mm $\times 10^{-1}$)	Stress (MPa)	Plastic strain (in $\times 10^{-1}$)	Stress (psi)
1	0.001171	0.034477	0	50555
2	0.003122	0.070269	0.0004	60198
3	0.013077	0.29914	0.0043	95189
4	0.022055	0.49617	0.0093	99215

Table 2. Basic elastic properties for the gasket components

Gasket layer	Material	Thickness (mm)	Young´s modulus
Top	NBR75	0.0254	5.8 MPa
Middle	CRS ¼ Hard	0.2032	190 GPa
Bottom	NBR75	0.0254	5.8 MPa

The engine head gaskets modeling is complex due to the nonlinear response of the materials. Material responses can lead to significant errors in the results [8]. This paper provides an overview of the construction and assembly process to create a head gasket model, describes the nonlinear nature of the materials used and presents the results.

Engine sealing components must be designed to provide adequate tightness to avoid leakage [9]. But they must not induce stresses on engine components that could impair engine performance and/or function. Engine sealing components must also be designed to operate for many millions of cycles without failure. The thermal problem can be classified as steady-state or transient, linear or nonlinear. Transient analysis is characterized by the evolution of the solution over time and, in addition to the exchange of energy with the environment, involves thermal energy storage. Steady-state analysis refers to the state-point solution to fixed-boundary condition problems [9]. Nonlinearities go into both stationary and transient solutions across several areas. The most common nonlinearity is associated with temperature-dependent material properties (Figs. 3 and 4).

With the generation of the gasket model, a preliminary thermal analysis is carried out to estimate the heat flow and identify the critical zones. With these data, a nonlinear static analysis is executed to evaluate the distribution of loads. The boundary conditions applied to the motor head gasket sealing system include the displacement limit condition, the contact limit condition and the load limit condition [5]. For the contact boundary condition, it is assumed that the contact surfaces between the cylinder head, the bolts and the gasket are not completely flat. The cylinder head gasket suffers an elasto-plastic
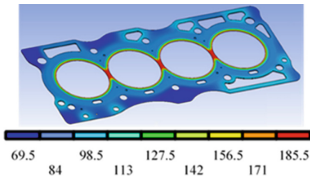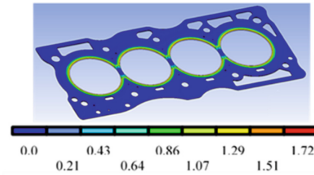
Fig. 3. Temperature distribution.

Fig. 4. Total heat flux.

deformation process until the full contact force is supported. The size of the region of the plastically deformed gasket is directly proportional to the contact pressure and inversely proportional to the hardness of the material [5]. To avoid insufficient gasket sealing, bolts are pre-stressed into the range of 28–80 kN [10]. The initial effects that occur into the gasket depends directly on the tightening of the screws to close the motor, which is responsible to achieve the perfect seal of the system. A force of 80 kN was applied for the screws tightening in the monoblock assembly. The total force exercised in the engine and gasket system is 800 kN. The behavior of the combustion process depends on maximum pressure, temperature, gasket and monoblock materials (bolts, force, location, etc.) and sealing. The model presents difficulties for the analysis convergence process. The analysis is restricted to the number of significant digits, which directly interferes with the analysis result, once the cutoff errors accumulate, they create difficulties in reaching equilibrium and solving the problem. Complexity is due to non-linearities [11, 12] and care must be taken with discretization.

To execute the thermal analysis of the gasket, the maximum temperature is be 200 °C in the area of cylinders (Fig. 5a). In the part of the water and oil passages, a temperature of 90 °C is taken (Fig. 5b). Figure 6 and Fig. 7 show the result of the distribution of temperatures acting on the gasket. The highest point of heat is the cylinder area, as the water and oil passages influence the temperature, they should maintain the gasket at a controlled temperature, so it does not suffer deterioration due to temperature changes.
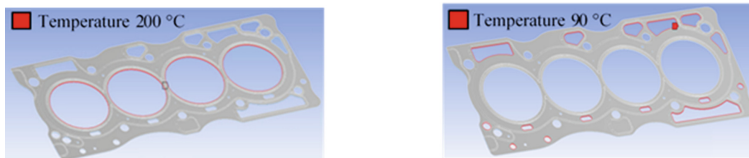
Fig. 5. a. Introduction of temperature. **b.** Introduction of temperature for water and oil passages

3   Solution and Results of Static Analysis with Thermal Loads

The objective of the global model is to observe the general performance of the component identified by the distribution of loads and stresses, temperatures, and contact pressures. Therefore, it is possible to identify the critical areas from the point of view of sealing.

For this case, the temperature characteristics are imported into the static analysis (Fig. 8 and 9). In other words, the ones with the smallest applied load to provide the seal, as well as the areas subjected to the most rigorous conditions where the phenomenon of plasticity can be witnessed (deeply undesirable). Subsequently, the creation of a detailed model can be carried out based on this information.

Inherent in the uncertain contact problem, which determines the existence of a variable charge vector. Another detail concerns the geometry approach. The use of contact elements determines the choice of linear elements, to avoid errors related to the application of load in the intermediate nodes of the element edges. Since the elements have an isoparametric formulation, the geometry is defined by linear interpolation functions. As an unavoidable consequence, there are sharp corners joining elements, in the definition of curvilinear surfaces.
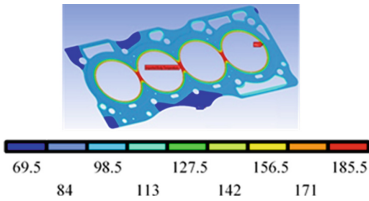
Fig. 6. Upper gasket temperatures
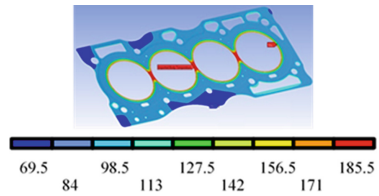
Fig. 7. Lower gasket temperatures
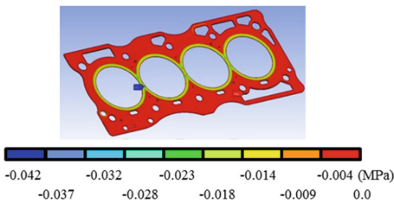
Fig. 8. Maximum principal stress in cylinder zone, refrigerant and lubrication passages in lower and upper seal
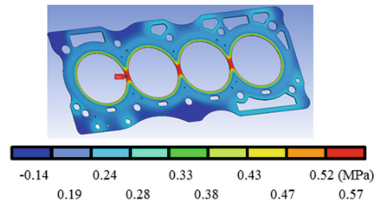
Fig. 9. von Mises stress at lower and upper gasket

4 Conclusions

The results consider the effect of temperature, acting load and contact. This kind of numerical evaluation shows the importance on the engine head gasket sealing reliability and proves its importance and efficiency on the finding results. Also, has the advantage in time saving and cost reduction. Concluding that heat dissipation flows from the highest to the lowest temperature zones. The results show the maximum main stresses to which the engine gasket is subjected, already with the action of temperature. They also show an increase in the area of water and oil passages. This is due to the actions of the thermal loads in the actuation of the system, improving the sealing of the joint. Results illustrate the importance of the local distribution of the ribbed means. Also, a continuous sealing

area is formed where all stresses are similar around the coolant holes and the lubrication holes that according to the material specifications meets the initial requirements of the customer. While von Mises stresses shows that a ductile material begins to yield at a location when the stress is equal to the elastic limit, it would indicate if the material could fail in this zone. When a head gasket is installed between the cylinder head and the engine block, tightening the head bolts slightly compresses the gasket, allowing the soft material in the gasket to conform to minor surface irregularities of the platform and the block. This allows the gasket to seal cold, so refrigerant doesn't leak out until the engine is started. There is a decrease in height in ribbed areas and near the combustion chamber. As well as, in areas of the passage of water and oil. This indicates that due to the pressure of the screws when mounting them to the engine, they generate a reaction force that creates the seal through the ribs. The gasket assembled with the two layers shows that the displacements suffered are minimal and do not affect the function of the engine gasket. According to the results obtained this kind of gasket would present no problem for operation, since the stress limits of the materials used are not exceeded. Meanwhile, the contact forces are the most basic and important index on the sealing reliability of the engine head gasket. The general distribution of stresses in the contacts in the system were estimated. The full stresses of the ribs in the cylinder bores are greater than half the stresses of the beads in the cooling bores and oil bores. It is also observed that in the cylinder area there is a stress of approximately 50 MPa, enough to meet the factory requirement on sealing pressure. The pressures in the cylinder area must be more than 20 MPa according to the customer's requirements. By producing a proper sealing, the engine efficiency and performance could be increase.

References

1. Vijaya-Baskar, L.: Thermal analysis of cylinder head gasket using Ansys. Imperial J. Interdisc. Res. **2**(12), 772–779 (2016)
2. Shanmugam, M., Setty, S.: Simulation-driven design and development of MLS gasket assembly. In: SAE 2018 WCX World Congress Experience, pp. 1–7 (2018)
3. Arjun, V., et al.: Thermal analysis of an engine gasket at different operating temperatures. Int. J. Mag. Eng. Tech. Manage Res. **2**(12), 2029–2037 (2015)
4. Alkidas, A.C.: The effects of head gaskets geometry on engine-out HC emissions from S.I. engines. J. Fuels Lubr. **108**(4), 1833–1845 (1999)
5. Bond, S., Youngman, J., Turland, D.: A new coating for multi-layer steel exhaust gaskets. In: SAE 2004 World Congress & Exhibition, pp. 1–9 (2004)
6. Czernik, D.E.: Gasketing the internal combustion engine. In: 1980 Automotive Engineering Congress and Exposition, pp. 1–16 (1980)
7. Urriolagoitia-Sosa, G.: Analysis of prior strain history effect on mechanical properties and residual stresses in beams. Ph. D. thesis, Oxford Brookes University (2005)

8. Raub, J.: Structural analysis of diesel engine cylinder head gasket joins. In: SAE Technical Paper 921725, International Off-Highway & Powerplant Congress & Exposition, pp. 1–8 (1992)
9. Popielas, F., Chen, C., Obermaier, S.: CAE approach for multi-layer-steel cylinder head gaskets. In: SAE 2000 World Congress Detroit, pp. 1–15 (2000)
10. Harlan, C., Novaria, P., Robinson, M.: Process and performance modelling of gasket components. J. Engines **102**(3), 139–146 (1993)
11. Hebert, C., Webster, W.: Cylinder head gasket simulation in finite element analysis. In: International Congress& Exposition, pp. 1–8 (1998)
12. Srikanth, M., Balakrishnan, M.: Cylinder head gasket analysis to improve its thermal characteristics using advanced fem tool. Int. J. Mach. Constr. Eng. **2**(1), 1–17 (2015)

Low-Cost Model for the Estimation of Pollutant Emissions Based on GPS and Machine Learning

Néstor Rivera-Campoverde[1,2]([✉]) [ID], José Muñoz Sanz[1] [ID],
and Blanca Arenas-Ramirez[3] [ID]

[1] Machine-Engineering Division, ETSII, Universidad Politécnica de Madrid, José Gutierrez Abascal 2, 28006 Madrid, Spain
n.riverac@alumnos.upm.es, joseluis.munozs@upm.es
[2] Grupo de Investigación en Ingeniería del Transporte, Universidad Politécnica Salesiana, Calle Vieja 1230 and Elia Liut, 010105 Cuenca, Ecuador
[3] Instituto Universitario de Investigación del Automóvil Francisco Aparicio Izquierdo, UPM, Universidad Politécnica de Madrid, José Gutierrez Abascal 2, 28006 Madrid, Spain
blanca.arenas@upm.es

Abstract. This paper presents a novel method for estimating pollutants emitted by vehicles powered by internal combustion engines in real driving, without the need for extensive measurement campaigns or the use of instrumentation in the vehicle for long periods of time; for which it is based on the positioning and speed signals generated by the GPS (Global Positioning System) and the machine learning application. To obtain the training data and validation of the model, two road tests are carried out using the Euro 6 directives for the estimation of pollutants through RDE (Real Driving Emissions), in which a portable emission measurement system is used, and a recorder that stores data from OBD (On Board Diagnostics) and GPS. Based on the data obtained in the first route, the vehicle's performance is determined and, through automatic learning, the model that estimates polluting emissions is generated, which is validated with the data from the second route. When comparing the results generated by the model against those measured in the RDE, relative errors (%) of 0.0976, -0.2187, 0.2249 and -0.1379 are obtained in the emission factors of CO_2, CO, HC and NOx respectively. Finally, the model is fed with data obtained in 1218 km of random driving, obtaining similar results to models based on OBD and closer to the real driving conditions generated by models such as the IVE (International Vehicle Emissions).

Keywords: low cost model · pollutant estimation · machine learning · GPS-based emissions

1 Introduction

Vehicles powered by internal combustion engines are one of the main causes of pollution in urban areas [1], and they are the subject of study in order to determine the amount of pollutants they emit [2, 3]. Current regulations stipulate that pollutant emissions must

be measured during real driving [4], since these are substantially higher than those obtained in laboratory tests [5], because they consider factors such as traffic, route selection and the type of driving conditions that directly influence consumption and the emissions generated [6]. Ortenzi and Castermans et al. determine that parameters such as excessive acceleration and deceleration, wrong selected gear and high engine and vehicle speed, increase the emission of pollutants [7, 8], but to determine their real influence, extensive campaigns are needed. Measurement with widely instrumented vehicles [9]. [10] determines that polluting emissions depend on factors specific to the vehicle such as the model, weight, type of fuel, technological level and route, and operational factors such as speed, acceleration, gear selection, road gradient and ambient temperature, so all emission models must consider these factors.

This article presents a novel method to estimate polluting emissions using vehicle driving variables such as speed and gradient as input data, obtained by GPS through the application of techniques such as Kmeans, classification trees and neural networks. In order to create a model for estimating pollutant emissions, a Real Driving Emissions (RDE) test was carried out on a route in which emissions data as well as OBD and GPS data were obtained, with these data an ANN (Artificial Neural Network) that was validated with the data obtained in a second RDE test, confirming the validity of the emissions estimator. This estimator was applied to a data set of 1.218 km of actual driving. The results obtained were compared with those obtained in the IVE model and OBD test, showing similar results.

2 Materials and Methods

2.1 Proposed Methodology

Polluting emissions must be measured in real driving conditions [4], with this, different factors such as driving style, type of fuel, geographical location and environmental conditions in which the vehicle circulates are considered within the results [11], which are currently not considered in the models used by the Mobility Company of the city of Cuenca (EMOV-EP). For the estimation of pollutants based on GPS data and machine learning, the following steps are proposed: a) Collection of GPS data and pollutant emissions in real driving conditions on two routes based on [4], b) Train the model based on machine learning with the data from route 1, c) Validation of the model obtained with the data from Route 2, d) Application of the model generated to the data set of 1218.9 km and e) Processing and presentation of results.

2.2 Data Collection in Real Driving Conditions

For data collection, the vehicle used is a 2018 model Kia Sportage, according to [12] it is the best-selling vehicle in Ecuador in the SUV segment. It has a 2.0L DOHC engine, 6-speed manual transmission and at the time of the experimentation it had 18.720 km of travel and all the maintenance operations recommended by the manufacturer. The portable emission measurement system (PEMS) used is the Brain Bee AGS-688 gas analyzer that works using the non-dispersive infrared absorption method (NDIR) for

the measurement of CO_2 [%], CO [%] and HC [ppm] and electrochemical cell for the measurement of O_2 [%] and NO_X [ppm]. The equipment is powered by a battery independent from the test vehicle as established in [4]. Fuel consumption is measured using the AIC Fuel Flow Master 5004. The GPS used is the one incorporated into the Freematics ONE+ data logger, which stores latitude (Lat), longitude (Long), height (Alt) and speed (V_{GPSo}) data of the vehicle on an SD card in CSV format. In addition to the GPS data, the equipment stores driving data from OBD such as engine speed (RPM), intake manifold pressure (MAP), and vehicle speed (V_{OBD}).

2.3   Test Routes

Two routes, in the city of Cuenca-Ecuador, were selected for data collection. They have urban, rural and highway segments: the Historic Center, the Panamericana Norte motorway and the Cuenca Azogues motorway respectively. Following the provisions of [4] to determine the emissions in real driving conditions (RDE). Both tests were done under the same conditions, without the presence of rain or strong winds, at an average ambient temperature of 14 °C, with a hot engine and a total mass of m = 1719.5 kg, corresponding to the vehicle with full fuel tank, the instrumentation and two passengers.

2.4   Estimation of Pollutants

The emissions generated in real driving conditions on the 2 established routes are measured by the gas analyzer in volumetric concentration, and it is necessary to convert them to mass concentration using the procedure described in [4]. Emission factors $F_{j,k}$ of each pollutant (g/km) in section k of the RDE is determined, where $m_{j,k}$ is the mass of the contaminant j and s is the distance traveled in section k of the RDE, k assumes the values of *u, r, a* for the urban, rural and motorway sections respectively. The results obtained in route 1 are shown in Table 1.

Table 1. Emission Factors

F[g/km]	Urban	Rural	Motorway
CO_2	82.574	79.410	45.598
CO	2.8442	6.6942	6.6363
HC	0.0314	0.0427	0.0736
NO_X	0.6597	0.8088	0.6821

As shown in [13] the most influential variables in the generation of polluting emissions are CO2: [G, RPM, TPS, MAP], CO: [TPS, MAP, V_{OBD}, RPM], HC: [TPS, MAP, V_{OBD}, G] and NOX: [MAP, RPM, GEAR, V_{OBD}], respectively. These predictors are obtained directly through OBD, so they cannot be used to train the GPS-based model. The gear used by the driver cannot be determined directly by V_{GPS} since, the selected gears do not depend on the driving speed. For this purpose, relationships should be

sought between the data provided by the GPS and the performance of the engine. Vehicle speed is related to engine speed by the gear ratios of each of the vehicle's 6 gears. In order to obtain a label for training a classification tree that estimates the gear used by the driver, the data obtained in route 1 is used, to which the Kmeans algorithm is applied, specifically to the vector: $R_i = \frac{VSS_i}{RPM_i}$. Which generates a label for each of the 7 groups obtained from their centroids, the groups generated correspond to each of the 6 gears of the vehicle and to the neutral position. The R_{TG} value is obtained by estimating the median of R_i for each gear. For the analysis vehicle, the 5th gear $(G = 5)$ is direct, so the transmission ratio $R_5 = 1$, from this the transmission ratio of the differential crown group R_C is determined by $R_C = \frac{3.6\pi R_N}{30R_5}$, where $R_N = 0.3607$ m which corresponds to the value of the effective radius of the tire. The rotating mass factor is determined and the efficiency of each gear is determined by (1) and (2) respectively.

$$\gamma_G = 1.04 + 0.0025R_G{}^2 \tag{1}$$

$$\eta_G = \frac{0.8R_G}{R_G - \frac{0.1}{G_{max}}} \tag{2}$$

The torque values obtained in the dynamometric bench at different throttle openings with which Eq. (3) determines the acceleration value of the vehicle, where T is the torque delivered by the engine as a function of the gear chosen by the driver. The tractive force of the vehicle F_T is related to the longitudinal acceleration a_x, the braking force, the rolling and aerodynamic resistance, and the resistance to slopes, see Eq. 3.

$$m\frac{T\eta_G R_G}{m\gamma_G R_N} = F_T - mg\left(f + f_0 V_{GPS\,i}{}^{2.5}\right) + \frac{1}{2}\rho C_X A_f V_{GPS\,i}{}^2 - mg\left(f + f_0 V_{GPS\,i}{}^{2.5}\right) \tag{3}$$

The rolling and aerodynamic resistance are obtained by (3), in which the coefficients of static and dynamic adhesion are $f = 0.015$ and $f_0 = 0.01$ respectively, the density of air $\rho = 0.89$, drag coefficient $C_X = 0.33$, and the frontal area of the vehicle $A_f = 3.015\,\mathrm{m}^2$. The tractive force of the vehicle is expressed in (3), and can be determined with the data coming from the GPS. The braking force is applied when F_T is null, that is to say, the accelerator and the brake cannot be activated at the same time. Traction force depends on engine performance, which involves throttle opening, intake manifold pressure, and the gear selected by the driver, thus obtaining a predictor element that, like longitudinal acceleration and gear label selected are used to train a classification tree that determines the gear used by the driver. The vector taken in route 1 for training is $I_{ni} = [F_{Ti}, a_{xi}, V_{GPSi}]$. The classification tree obtained has 7, the highest rate of hits occurs in neutral (99.5%), 1st (89.3%), 2nd (82.5%) and 3rd gears (83.6%), while in 4th (61.5%), 5th (45.3%) and 6th (71.9%). The efficiency of the given model decreases, because the performance of the vehicle under these conditions is very similar. The values obtained can be seen in Fig. 2, which when compared with the data obtained by OBD show significant differences in gear changes. During the gear change, the driver does not apply the accelerator, so the engine speed drops to the idle value of 663 RPM determined by the mode of the dead time in route 1, as shown in Fig. 1.

With the data obtained from Ii and the label of each march, 4 neural networks are trained to estimate pollutant emissions. Each network has 3 neurons in the input layer, 10 in the hidden layer, and one at the output. The R2 determination indices obtained are 0.935, 0.923, 0.914 and 0.943 for CO2, CO, HC and NOx emissions respectively. The data obtained in 1218 km of random route in the urban, rural and highway areas of the city of Cuenca are applied in the generated model. In Fig. 2 it can be seen that the 1st, 2nd and 3rd gears are used at low average speeds, on short journeys that occur mostly in urban areas and very rarely in rural areas and highways, and that at higher speeds CO2, CO and NOX emissions decrease.
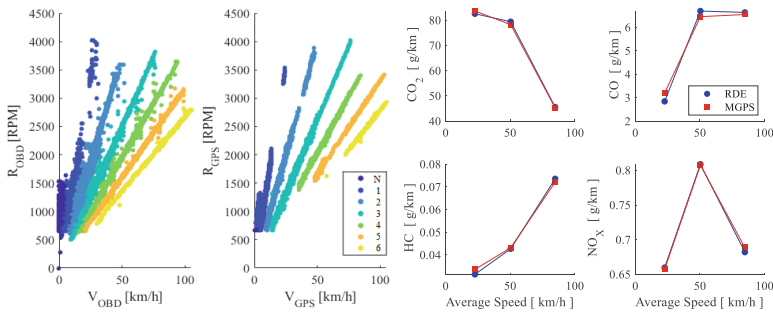
Fig. 1. Model Results

Fig. 2. Emission Factors

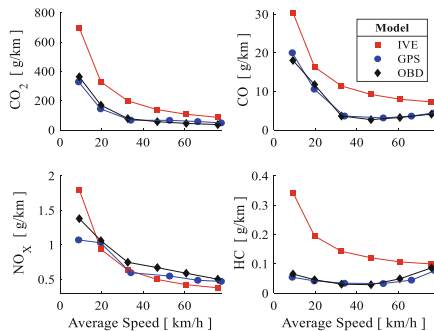The error obtained in calculating the average driving speed in each gear is due to the model that determines the gear selected by the driver. The average emission factors for each model are shown in Table 2, the values estimated by IVE are higher than the other models analyzed, the main difference is the CO2 emission factor that is strongly influenced by the low speeds of circulation in urban zone.

Table 2. Emission Factors

F[g/km]	IVE	RDE	MGPS
CO_2	208.97	70.23	110.93
CO	11.83	5.33	6.95
NO_X	0.661	0.7199	0.69
HC	0.1477	0.0485	0.041

3 Conclusions

This work proposes a method for the estimation of pollutant emissions based on data from GPS applying Machine Learning. For it, initially a highly effective classifier was obtained for the evaluation of the gear selected by the driver, based on the Obtaining labels through Kmeans and the subsequent training of a classifying tree, the errors generated occur in the small moments that the transition between gears lasts. The calculation of pollutant emissions was given from the determination of the importance of the predictors in the data obtained in two routes of the RDE test, to later train 4 ANNs that obtained high R2 determination indices that validate the applied method. The model obtained is more robust to different traffic conditions and presents better results in circulation at low average speeds than the IVE and RDE models, so it is recommended to be used for calculating emission factors and estimating emission inventories vehicular.

References

1. UN. The World's Cities in 2016, vol. 8, United Nation. New York (2013)
2. Wang, S., Li, Z., Tan, J., Guo, W., Li, L.: A method for estimating carbon dioxide emissions based on low frequency GPS trajectories. In: Proceedings - 2017 Chinese Automation Congress, CAC 2017, vol. 2017-Janua, pp. 1960–1964 (2017)
3. Kan, Z., Tang, L., Kwan, M.P., Zhang, X.: Estimating vehicle fuel consumption and emissions using GPS big data. Int. J. Environ. Res. Public Health **15**(4), 1–23 (2018)
4. REGLAMENTO (UE) 2016/427. Diario Oficial de la Unión Europea, vol. 82, pp. 1–98 (2016)
5. Kurtyka, K., Pielecha, J.: The evaluation of exhaust emission in RDE tests including dynamic driving conditions. Transp. Res. Procedia **40**, 338–345 (2019)
6. Fontaras, G., Zacharof, N.G., Ciuffo, B.: Fuel consumption and CO_2 emissions from passenger cars in Europe – Laboratory versus real-world emissions (2017)
7. Ortenzi, F., Costagliola, M.A.: A new method to calculate instantaneous vehicle emissions using OBD data. SAE Technical Papers (2010)
8. Castermans, J., Brusselmans, A., Jean-Pandazis, C.: Cooperative Mobility Systems and Services for Energy Efficiency (2010). https://cordis.europa.eu/project/id/247908/es
9. Hajmohammadi, H., Marra, G., Heydecker, B.: Data-driven models for microscopic vehicle emissions. Transp. Res. D Transp. Environ. **76**(October), 138–154 (2019)
10. Boulter, P.G., Barlow, T.J., et al.: Emission factors 2009: Report 1 – a review of methods for determining hot exhaust emission factors for road vehicles. PPR353, p. 116 (2009)
11. Samaras, C., Tsokolis, D., Toffolo, S., Magra, G., Ntziachristos, L., Samaras, Z.: Enhancing average speed emission models to account for congestion impacts in traffic network link-based simulations. Transp. Res. D Transp. Environ. **75**, 197–210 (2019)

12. Asoc. de Empresas Automotrices de Ecuador. Automotive in figures. AEADE. Quito (2018)
13. Rivera-Campoverde, N.D., Muñoz-Sanz, J.L., Arenas-Ramirez, B.D.V.: Estimation of pollutant emissions in real driving conditions based on data from OBD and machine learning. Sensors **21**(19), 6344 (2021)

Energy and Thermal Engineering

Development of a Reactor Network Model to Predict Pollutant Emissions from Aviation Gas Turbines

Jose M. Garcia-Oliver[1]([envelope]) [ID], Jaime Gimeno García[1] [ID], Borja Martínez Corzo[1], Javier Navarro Laboulais[1], and Penélope Leyland[2] [ID]

[1] Universitat Politècnica de Valencia, Valencia, Spain
jgarciao@mot.upv.es
[2] Advanced Engineering Design Solutions (AEDS), Lausanne, Switzerland

Abstract. The present work focuses on the prediction of pollutant emissions in gas turbine engines by means of a reactor network considering chemical kinetics. The network was developed based on the CFM56 -7B27/B1F aviation engine, calibrated with the pollutant emission data (EINOx, EICO and EIHC) provided by ICAO at maximum power and compared to other operating conditions. A study of local species formation in every reactor was carried out to analyze the differences and similarities between the model and experimental data.

Keywords: Chemical kinetics · reactor network · pollutant emissions · gas turbine · combustion

1 Introduction

Accurate predictions of combustion and pollutant emissions are necessary to improve new engine gas turbine designs or to make prospective analysis of how a particular engine parameter may engine performance. Pollutants are strongly coupled to chemical kinetic effects, and therefore demand a high number of species and reactions to be quantified, which may result in too high computational efforts for typical Computational Fluid Dynamics (CFD) calculations. Reactor networks offer an optimum approach with a good accuracy in terms of pollutant predictions but at a much lower computational demand [1–5]. The present paper reports a modelling effort aimed at the development of a reactor network with Cantera [6], an open-source software tool, to enable predictions of the engine emissions indexes. This introduction is followed by a methodology section, where the main ideas around the network construction are described. After that, the main results for two engine operating conditions are presented and main conclusions are derived.

2   Methodology

The modelling workflow starts from the aeroengine geometrical and thermodynamic data, from which a zero- and one-dimensional (0D/1D) network is built. For every reactor, inlet temperature, pressure and composition must be defined, as well as the reactor volume for 0D reactors, or reaction area and length for 1D reactors. Both types are considered as ideal gas, constant pressure systems, with 0D being modelled as Perfectly Stirred Reactors (PSR) and 1D modelled as Plug Flow Reactors (PFR). Evolution of species is quantified by means of the corresponding balance equations, which include chemical kinetic terms. In the present case, Luche [7] chemical mechanism has been used to model the reaction rates, and the surrogate fuel is a mixture of decane, propyl-bencene and cyclo-hexane.

PSR and PFR reactors are the modules upon which the reactor network is built to emulate the combustion chamber of the aeroengine. Figure 1 shows a schematic of an annular combustion chamber of a conventional gas turbine engine, upon which the corresponding zones, which will be later considered as reactors, are superimposed. The center part of the chamber volume, which will be referred to as the chamber core, is mainly divided into three parts, namely Primary Zone (PZ), Intermediate Zone (IZ) and Dilution Zone (DZ), with corresponding rich, lean and very lean equivalence ratio ϕ values. To improve the description of the combustion phenomena, two additional zones are defined. The first one, still at the core, is the Flame Front (FF), with a similar cross-section to that of PZ and a close-to-stoichiometric equivalence ratio. The second one is the Wall Zone, with an important length and small cross-section, which is located around the core and mainly transports air. The latter zone is divided into two parts (WZ and WZ2) to better model the interaction between wall and core flows.
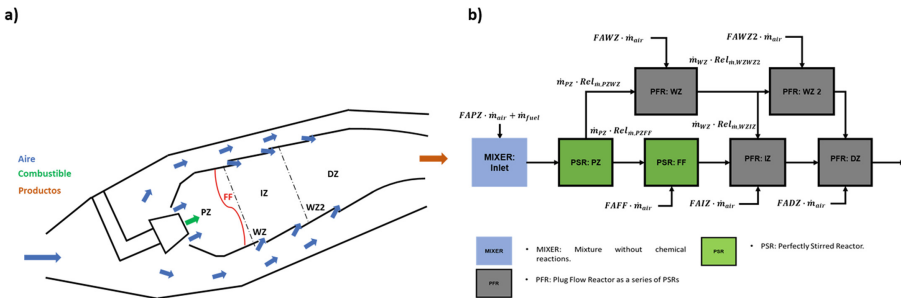
Fig. 1. Combustion chamber schematic for a generic aviation engine (a) and reactor network schematic for CFM56 7B27/B1F aeroengine (b).

Figure 1 shows the layout of the developed reactor network. Reactors where equivalence ratio is lean have been modelled as PFR, to better capture CO evolution. Zones where equivalence ratio is rich and stoichiometric, where NOx are formed due to the high temperatures, are modelled by means of PSR reactors. The air addition into the burner, which occurs by means of the side orifices, is emulated in the reactor network by means of air flow additions to every reactor, which control the corresponding equivalence ratio value.

The model has been developed for the CFM56 7B27/B1F engine similarly to [8]. The present study focuses on engine operating conditions from the ICAO database [9], for which corresponding combustion chamber inlet conditions are summarized in Table 1. Fuel temperature has been assumed to be constant and equal to 400 K, while PZ is fed with a stream resulting from the adiabatic mixing of both fresh air and fuel. Geometrical data of each reactor has been summarized in Table 2, where the area of the core and wall reactors are shown to correspond to 80 and 20% of the total area, respectively. Lengths and areas for every zone are derived from the burner geometry except for the length of FF, which has been considered as a calibration parameter.

Table 1. CFM56 7B27/B1F engine operating conditions.

Operating parameter	Take-off	Climb	Approach	Iddle
$\dot{m}_{air}[kg/s]$	44.52	39.1	20.87	12.12
$\dot{m}_{fuel}[kg/s]$	1.28	1.04	0.349	0.119
$P[MPa]$	2.9	2.48	1.13	0.559
$T[K]$	800	764	613	505
$\phi_{glob}[-]$	0.42	0.39	0.245	0.144

Table 2. Reactor Network geometrical data.

	PZ	FF	IZ	WZ	WZ2	DZ
L [m]	0.05137	See Table 3	0.0597	0.0597	0.0648	0.0648
A [m^2]	0.1816	0.1816	0.2160	0.0580	0.0580	0.2880

Table 3. Reactor Network calibration results.

$F_{A,PZ}$	$F_{A,FF}$	$F_{A,IZ}$	$F_{A,WZ}$	$F_{A,DZ}$	$F_{A,WZ2}$	$REL_{\dot{m},PZFF}$	$REL_{\dot{m},PZIZ}$	$L_{FF}[m]$
0.20	0.21	0.29	0.01	0.29	0.00	0.99	0.80	0.00173

3 Results

The developed network is calibrated by optimizing some of the model parameters so that emission indices match the corresponding ICAO LTO test values at take-off conditions. These parameters are the fraction of air flowing into each of the reactor zones $F_{A,i}$, the relative flow split $REL_{\dot{m},PZFF}$ at the exit of PZ between the core and wall, and the relative flow split $REL_{\dot{m},WZIZ}$ at the exit of WZ1 between DZ and WZ2, and the length of the flamefront zone L_{FF}. Optimized results are reported in Table 3.

A local analysis of the reactor state is shown in Fig. 2 for two operating conditions, namely take-off and idle, where pollutant predictions are most and least accurate, respectively. Agreement for climb and approach (not shown for the sake of brevity) are similar to take-off. For both cases plot lines mimic the two paths followed by the flow along the combustion chamber, i.e. the CORE path including the main flow reactors PZ, FZ, IZ and DZ, and the WALL path including PZ, WZ, WZ2 and DZ. Results in Fig. 2 show that for take-off condition the equivalence ratio distribution is in agreement with the initial definition of the reactors, i.e. PZ corresponds to a rich equivalence ratio followed by a close-to-stoichiometric equivalence ratio at the FF, where the main reaction zone is located, and further downstream lean values for the remaining reactors are found. Corresponding reactor temperatures show that peak values are reached for stoichiometric conditions, i.e. at FF. For idle conditions, the larger air quantity reduces the global equivalence ratio, as well as those of the local reactors, even for PZ and FF. This behaviour brings down temperatures and has a major influence on pollutant formation, as will be discussed below. On the other hand, residence time values are lower for idle than for take-off conditions, due to the lower mass flow through the burner. Maximum residence times are found for WZ, due to the very small mass flow compared to the reactor size (only 1% of the total mass flow follows the wall path according to the calibration results in Table 3).

The previous combustion description has a direct influence on pollutant formation along the reactor network, which is analysed in Fig. 3 for both take-off and idle in terms of mass fraction of unburnt hydrocarbons (UHC), carbon monoxide (CO) and nitrogen oxides (NOx). DZ values are compared to the experimental values from ICAO [9]. Model predictions are in good agreement for take-off, as well as for climb and approach (not reported), while discrepancies are quite evident at idle. Results show that, for take-off condition, both UHC and CO appear in the first two reactors PZ, FF, with rich-stoichoimetric equivalence ratio values, and then disappear (note the very low numerical values) because oxidation is completed due to the high enough combustion temperatures and long enough residence times. As for the wall path, both species drop abruptly at WZ due to the combination of a lean equivalence ratio and long residence time, which makes it possible to reach an essentially zero value, preventing from the formation of these species at WZ2. Note that for take-off condition, with the engine at maximum power, numerical values agree with the reported experimental ones, i.e. essentially zero UHC,CO emissions. As for NOx, Fig. 3 shows that they are mainly formed at FF, with local equivalence ratio closest to stoichiometric values and peak reactor temperatures. This result highlights the governing role of the thermal mechanism in NOx pollutant production. Further downstream along the core path, NOx drops due to the addition of fresh air, which has both a dilution and cooling effect. The concurrent contribution of low equivalence ratio and combustion temperatures justifies the null contribution of wall reactors to NOx formation. Model predictions are pretty accurate in all three pollutant species.

For the idle operating condition UHC and CO have a similar evolution to that of take-off, with higher values at the PZ and FF that a later drop along the core path towards the final DZ value. Wall path also produces virtually no UHC and very low

CO amounts. Prediction of both pollutants at DZ is higher for idle than for the take-off condition, in agreement with ICAO cycles, but experimental values at idle are not accurately reproduced by the model. At idle, all the reactors are operated under lean conditions, which results in lower UHC and CO formation, but also lower combustion temperatures occur. This prevents from a complete oxidation, especially when compared to take-off. Therefore, resulting values for both UHC and CO at the last reactor are higher than for take-off condition, where the balance between formation and oxidation is governed by the second process due to the high temperatures. Finally, NOx production at idle shows a very different behaviour compared to take-off. Production occurs at PZ, which corresponds to the closest to stoichiometric reactor and peak temperatures. Reduction process, however, freezes due to the lower combustion temperatures, and burner outlet values are slightly higher if compared to experiments.

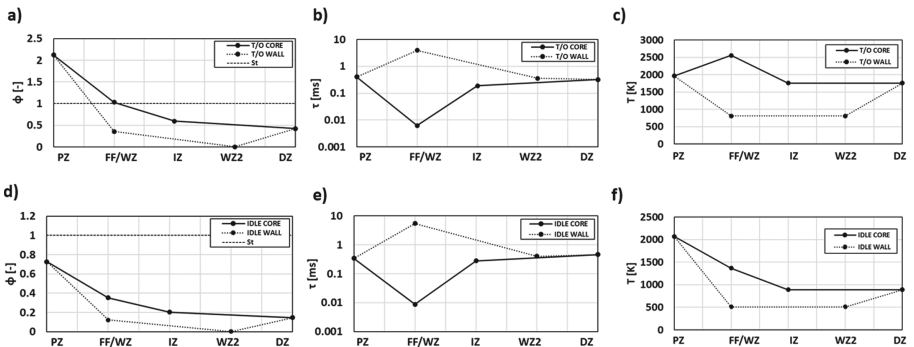
Fig. 2. Local equivalence ratio, residence time and temperature for each of the reactors at two operating conditions, take-off (a, b, c) and idle (d, e, f).
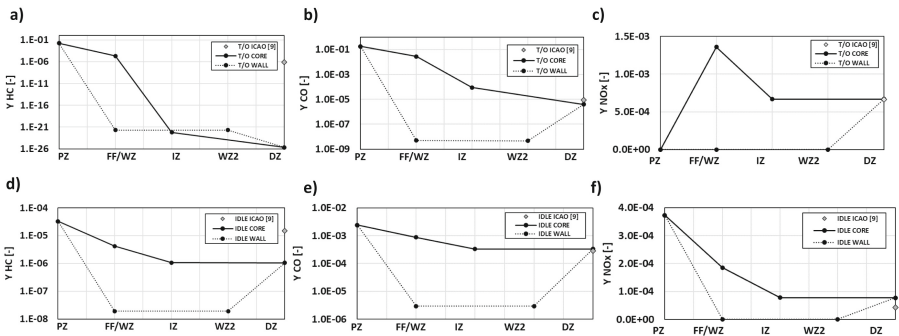

Fig. 3. Pollutant mass fraction (UHC, CO and NOx) for each of the reactors at two operating conditions, take-off (a, b, c) and idle (d, e, f). Experimental values from ICAO LTO cycle are shown on top of the DZ modelling results.

4 Conclusions

A reactor network model has been developed for a gas turbine engine to predict pollutant emissions with chemical kinetic approach. The model creates a number of zones with different equivalence ratios corresponding to the burner primary zone, flamefront, intermediate, dilution and wall zones. It has been calibrated for the CFM56 7B27/B1F engine. Predictions of mission indices match experiments from ICAO LTO cycle for UHC, CO and NOx, over the whole power range. Divergences are evident only for idle conditions, where the model underpredicts both UHC and CO, while NOx is overpredicted. This behaviour hints at an excess of energy conversion to final products by the model, which does not occur in the actual engine operation, most probably due to the highly simplified approach. Discrepancies could also be due to the chemistry simplification or even the surrogate fuel formulation, which may be limiting for conditions where combustion rate diminishes due to the lower temperatures. Still, the model can be used to assess the engine operation with good accuracy and a reduced computational cost.

References

1. Allaire, D.L.: A Physics-Based Model for Aircraft Gas Turbine Combustors. Massachusetts Institute of Technology MIT (2006)
2. Ramachandran, N.: Prediction of emissions for lean-premixed gas turbine combustors. Carleton University (Canada) (2009)
3. Rosati, B.: Prediction of emissions from combustion systems using 0D and 1D reaction flow models. Chemical reactor network modelling. Delft University of Technology (2010)
4. Celis, C.: Evaluation of environmentally friendly aircraft propulsion systems. Cranfield University CU (2010)
5. Pervier, H.: Emissions modelling for engine cycle and aircraft trajectory optimization. Cranfield University (2013)
6. Goodwin, D.G., et al.: Cantera: an object-oriented software toolkit for chemical kinetics, thermodynamics, and transport processes. https://cantera.org. Accessed 07 Feb 2023
7. Luche, J.: Obtention de modèles cinétiques réduits de combustion. Application à un mécanisme du kérosène, Universite d'Orleans (2003)
8. Saboohi, Z., Ommi, F., Fakhrtabatabaei, A.: Development of an augmented conceptual design tool for aircraft gas turbine combustors. Int. J. Multiphys. **10**, 1 (2016)
9. European Union Aviation Safety Agency, EASA. https://www.easa.europa.eu/domains/environment/icao-aircraft-engine-emissions-databank. Accessed 30 June 2022

Electricity and Hydrogen Generation from Food and Vegetable Wastes – Technical and Economic Analysis

Raul Pereira Micena[1(✉)], Paulo Sérgio Duque de Brito[2], Celso Eduardo Tuna[1], and José Luz Silveira[1,3]

[1] Laboratory of Optimization of Energy Systems (LOSE), Institute of Bioenergy Research (IPBEN-UNESP), UNESP - São Paulo State University, Araçatuba, Brazil
{raul.micena,celso.tuna,jose.luz}@unesp.br

[2] VALORIZA-Research Center for Endogenous Resource Valorisation, Polytechnic Institute of Portalegre, 7300-555 Portalegre, Portugal

[3] Waste Revaluation Center, Federal University of ABC (UFABC), Santo André, Brazil

Abstract. The city of Guaratinguetá, Brazil, produces 104 tons of MSW daily, 45.3% of which is its organic fraction, and the rest is divided between recyclable material and waste without use. This study proposes the calculation of the biogas production potential from the anaerobic digestion of the Organic Fraction of Municipal Solid Waste (OFMSW). This fraction is mainly composed of food residues, such as fruits and vegetables, as well as paper and cardboard, among others, being a compound able to be processed in a biodigester. A production potential of 3,1 Nm^3 of biogas per day, or 3,6 kg/day, was calculated. An electricity generation potential of 6.3 MWh/day was calculated. Considering the use of all this electrical potential in a water electrolysis process, a production potential of 107 kg/day of electrolytic hydrogen was calculated. An economic analysis of electricity generation is carried out, resulting in a cost of electricity between 34.7 and 41.2 USD/MWh, depending on the interest rate applied. The payback of the investment in electricity generation was calculated between 3 and 4 years, considering the local electricity tariff of 74 USD/MWh.

Keywords: municipal solid waste · food wastes · biogas · power generation · hydrogen

1 Introduction

In 2018 in Brazil, about 40% of MSW collected in 2018 was disposed of inappropriately in open air dumpsites, with 53% of municipalities disposing of their MSW in open air dumpsites or controlled landfills, while 46.1% disposed of it in sanitary landfills [1].

Anaerobic Digestion (AD) of organic material in dedicated anaerobic reactors results in the production of biogas, with a high concentration of methane, which can be used as a fuel in the generation of electricity, mechanical work or heat. Thus, this process is

an attractive way to treat organic waste, since it allows the energy use of its biomass contained and therefore a renewable energy resource.

The present work analyzes the possibility of using all the organic waste contained in the MSW generated in the city of Guaratinguetá, Brazil, aiming at the production of biogas through anaerobic digestion. In this city 104 tons of MSW are produced daily.

According to data from the Brazilian Association of Public Cleaning Companies and Special Waste (ABRELPE) [2], 45.3% of the MSW mass in Brazil is composed of organic material, 28.6% of recyclable materials (paper, metals, glass, wood, plastics) and 26.1% of others (cloths, rags, rubbers and other materials).

Assuming that the complete sorting of MSW generated in Guaratinguetá is done, the organic material is separated from the others by mechanical processing, and is then called Organic Fraction of Municipal Solid Waste (OFMSW). Household food scraps, leftovers from pruning and open fairs, and horticultural discards are the main components of OFMSW. For this specific type of waste, the results of the physical-chemical characterization performed by [3] with samples of MSW composed of 35% fruit, 35% other vegetables, 20% cardboard and 10% plastic are used.

The potentials for biogas production from the anaerobic digestion of OFMSW, as well as for electricity generation through the combustion of this gas in generator sets with Brayton cycle Gas Turbines (GT) will be calculated using the Eqs and relationships given. The potential for hydrogen production is then calculated with the full use of this electricity in an electrolysis process.

2 Methodology

2.1 Technical Analysis

Biogas Production. Considering the composition given by ABRELPE [2], 45.3% are apt to compose a digestible material, here called OFMSW. It is assumed that all this material will be processed for the typical conditions of anaerobic digestion in reactors developed specifically for this purpose. The potential biogas production can be calculated, as shown below, with Equations adapted from [4]. Equation 1 gives the amount of available OFMSW after sorting and treatment of MSW:

$$OFMSW_T = MSW_T - MSW_{LF} - MSW_{rec} \tag{1}$$

where MSW_T is the total colected MSW (t/day), MSW_{LF} is the total part of MSW sent to the landfill (t/day) and MSW_{rec} is the total MSW sent to recycling (t/day). Equation 2 gives the amount of OFMSW available after MSW sorting and treatment:

$$OFMSW_{SV} = OFMSW_T \times \eta_{VS} \tag{2}$$

where $OFMSW_{SV}$ is the total (t/day) Volatile Solids (VS) contained in the organic fraction of the waste and η_{MV} is percentage of volatile matter (% VS / VT). The biogas generation potential is given by Eq. [3]:

$$m_{Bio} = OFMSW_{SV} \times \eta_{Bio} \tag{3}$$

where m_{Bio} (kg/dia) is the daily biogas produced, η_{Bio} (kg$_{biogas}$/tSV) is the conversion ratio of SV into biogas. The biogas is assumed to have a volumetric composition of 65% CH_4 and 35% CO_2, as verified by [5].

Electricity Generation. Figure 1 shows the components of the plant to generate electric power and biohydrogen from the biogas produced in the biodigester with the AD of OFMSW. The desulfurization of biogas is performed in the component indicated with the letter "L", following to the combustion chamber (CC) of the gas turbine, with mechanical shaft power P_{TG} (kW). The generator converts this mechanical power into daily E_{el} generation (MWh).
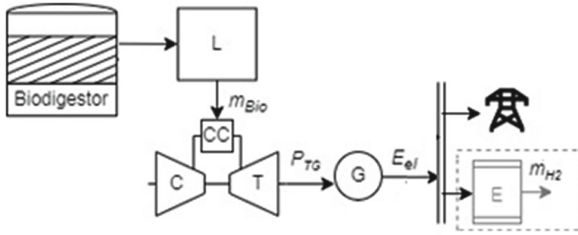
Fig. 1. Electricity generation and hydrogen production plant (elaborated by the author).

Adapting equations from [6], the energy generation is calculated with Eqs. 4 to 6:

$$E_{el} = P_{el} * t_{op} \tag{4}$$

$$P_{el} = \eta_{ge} * P_{GT} \tag{5}$$

$$P_{TG} = \eta_{T,GT} * m'_{Bio} * LHV_{Bio} \tag{6}$$

where P_{TG} is the mechanical shaft power of TG [kW], LHV_{Bio} Lower Heating Value of biogas [kJ/kg], m_{Bio} the mass flow of biogas [kg/s], $\eta_{T,TG}$ the thermal efficiency of GT [%] and η_{ge} conversion efficiency into electric power of the power generator [%].

Hydrogen Production. The case study for electrolytic hydrogen production considers the electrolyzer connected to the generator output bus, consuming the electrical energy generated by the plant. Figure 2 shows the electrolyzer (E), in which electric energy E_{el} (MWh) is consumed, originating quantities of hydrogen (m_{H2}) and oxygen (m_{O2}) from an input mass of water (m_{H2O}). The electrolysis reaction is described as a stoichiometric equation $(H_2O \rightarrow H_2 + \frac{1}{2}O_2)$. Considering an efficiency of 57%, the hydrogen potential can be calculated with Eq. 7 [7]:

$$\eta_{ele} = \frac{\dot{m}_{H_2}.LHV_{H_2}}{P_{el,eletr}} \tag{7}$$

where m_{H2} is the massic flow of hydrogen from the electrolyzer (kg/s), LHV_{H2} is the hydrogen Lower Heating Value (120 MJ/kg) and $P_{el,eletr}$ is the electric power of the electrolyzer (MW).

2.2   Economic Analysis for Bioelectricity Generation

Using the methodology proposed by Silveira, Tuna and Lamas and Lamas [8] the cost of electric power generated by a generating plant is calculated with Eq. 8:

$$C_{el} = \left(\left(I_{pl} \times f \right) / \left(365 \times t_{Op} \times P_{el} \right) \right) + CO\&M \tag{8}$$

where I_{pl} is the total investment [US$], f is the annuity factor [1/year], t_{Op} is the daily operating time [h/day], P_{el} is the electric power [kW], and $C_{O\&M}$ is the operating cost [US$/kWh], assumed as 3% of the investment. The annuity factor is the value of a cash flow that produces profit in a given period, the annuity factor is given by Eqs. [7] and [8]:

$$f = \left(q^k \times (q-1) \right) / \left(q^k - 1 \right) \tag{9}$$

$$q = 1 + r/100 \tag{10}$$

where f is the annuity factor [1/year], k is the number of years [years], and r is the annual rate of interest [%].

3   Results and Discussion

3.1   Technical Analysis

With Eq. [1] a quantity of 47.3 ton/day of OFMSW was calculated. Considering a η_{SV} of 18%, an amount of 8.51 t/day of volatile matter is obtained, which can be converted into biogas. With Eq. [3], taking a conversion rate of 367 m^3/t$_{VS}$, a potential of 3,125 Nm^3/day of biogas is calculated.

Through Eq. [6], considering a thermodynamic efficiency of the gas turbine of 33% ($\eta_{T,TG}$) and efficiency of the generator (η_{ge}) of 95% [9], a flow of 0.0556 kg/s of biogas over an operation time (t_{Op}) of 18 h/day, and with the LHV of biogas calculated as 20.2 MJ/kg, a power (P_{TG}) of 352 kW is obtained. With Eqs. [5] and [6], using a 95% efficiency of the generator, a total of 6.34 MWh of daily electric generation potential is obtained.

By the Eq. [8] it is possible to calculate the daily mass of hydrogen produced by electrolysis, considering that all the electricity generated was destined to this process. Considering the electrolyzer's efficiency of 57% [10], was calculated a daily production of 107 kg of hydrogen through the electrolysis of water with electricity generated.

3.2   Economic Analysis of Electricity Production

The costs of the generated electricity were calculated varying amortization periods up to 20 years. An investment cost of 720 USD/kW was used for the TG and 375 USD/ton/day the investment in the biodigester, in relation to its daily processing capacity. The O&M cost of the TG corresponds to 75 USD/kW/year while for the anaerobic reactor this cost is 38 USD/ton/day capacity. Figure 2 shows the electricity costs as a function of the
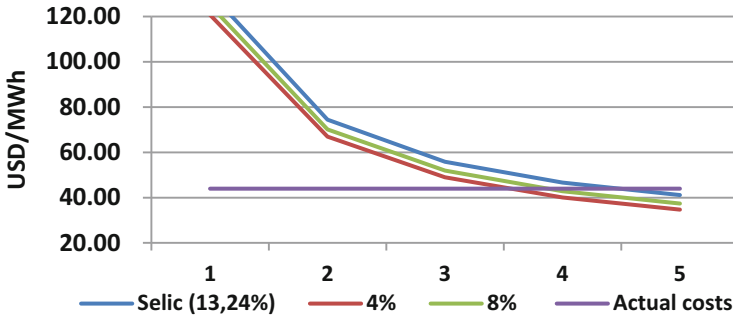
Fig. 2. Electricity costs (USD/MWh) and amortization periods

amortization time, using rates of 4% and 8% per year, and the basic interest rate of the Brazilian economy [11], of 13.24% .

Thus, for 5 years, a cost of 34.68 USD/MWh was reached for an interest rate of 4%, 37.41 USD/MWh for an interest rate of 8% and 41.16 USD/MWh for the SELIC rate of 13.25% y.. Compared to the current local Electric Tariff (ET) of 43.98 USD/MWh [12], the paybacks for the 3 scenarios are between the 4th and 5th year.

4   Conclusions

Considering the daily generation of MSW in the city, it was calculated a potential production of 3,1 Nm^3/day of biogas from the AD of the OFMSW, equivalent to 3,6 ton/day of biogas with a LHV of 20.2 MJ/kg. Considering the burning of this gas in a gas turbine it is possible to generate 6.34 MWh/day, which means a generation of 60.96 kWh per ton of collected MSW.

A total of 107 kg/day of hydrogen can be produced with this electrical potential. In this way, it was possible to estimate the potential for electricity generation from the AD of the OFMSW of a medium-sized municipality, which is of public interest, both in the energy sphere, since it is possible to generate this energy close to the consumer center, and also environmentally, since methane is no longer emitted into the atmosphere.

The cost of generating this electricity was calculated as being between 34.7 and 41.26 USD/MWh. If compared to the local Electricity Tariff, the payback of the investment in electricity generation will occur between the 4th and 5th year.

This is, therefore, a case where the issue of MSW can be addressed not only as a sanitation or public health problem but, on the other hand, as a profitable opportunity to generate renewable electricity, as well as the possibility of enabling the production of an emerging energy vector with broad applications, such as hydrogen.

References

1. Ministério do Meio Ambiente, "PLANO NACIONALDE RESÍDUOS SÓLIDOS (2022). https://sinir.gov.br/. Accessed 20 July 2022
2. ABRELPE, "PANORAMA DOS RESIDUOS SÓLIDOS NO BRASIL 2020" (2020)
3. Peces, M., Astals, S., Mata-Alvarez, J.: Assessing total and volatile solids in municipal solid waste samples. Environ. Technol. **35**(21–24), 3041–3046 (2014). https://doi.org/10.1080/095 93330.2014.929182
4. Valente Santos, M.A.: Avaliação do potencial de produção de Biohidrogénio na ETVO da Valorsul, Universidade Nova de Lisboa, Lisboa (2020)
5. Xavier, B.H.: Aspectos termodinâmicos, ecológicos e econômicos de sistemas de cogeração com motores de combustão interna operando com gás natural, biogás e gás de síntese, Guaratinguetá (2016)
6. Paulino, R.F.S., Essiptchouk, A.M., Costa, L.P.C., Silveira, J.L.: Thermodynamic analysis of biomedical waste plasma gasification. Energy **244**, 122600 (2022). https://doi.org/10.1016/J. ENERGY.2021.122600
7. Hosseini, M., Dincer, I., Rosen, M.A.: Hybrid solar-fuel cell combined heat and power systems for residential applications: energy and exergy analyses. J. Power Sources **221**, 372–380 (2013). https://doi.org/10.1016/j.jpowsour.2012.08.047
8. Silveira, J.L., Tuna, C.E., De Queiroz Lamas, W.: The need of subsidy for the implementation of photovoltaic solar energy as supporting of decentralized electrical power generation in Brazil (2013). https://doi.org/10.1016/j.rser.2012.11.054
9. Aparecida, Y., et al.: Performance Study of a Microturbine System for Cogeneration Application Using Biogas from Manipueira Gas Enthalpy at T 2 (kJ/kg) h 6 Enthalpy of saturated steam at the heat recovery outlet temperature (kJ/kg) h 7 Enthalpy of saturated liquid at 90 °C (kJ/kg) h 8 Compressor inlet temperature (°C). https://doi.org/10.1007/s12155-019-10071-0
10. Micena, R.P., Llerena-Pizarro, O.R., de Souza, T.M., Silveira, J.L.: Solar-powered hydrogen refueling stations: a techno-economic analysis. Int. J. Hydrog Energy (2019). https://doi.org/ 10.1016/j.ijhydene.2019.11.092
11. Taxa Selic. https://www.bcb.gov.br/controleinflacao/taxaselic. Accessed 20 July 2022
12. Tarifas - clientes atendidos em Baixa Tensão (Grupo B). https://www.edp.com.br/distribuicao-sp/saiba-mais/informativos/tabela-de-fornecimento-baixa-tensao. Accessed 22 July 2022

Experimental Study of Two-Phase Thermosyphons with a Constant Length-To-Inner Diameter Ratio for Geothermal Applications

Matías Salinas-Moreno, Nelson Melo-Arce, Luis H. R. Cisterna, Alexis Fuentealba, Camilo Flores Condori, Alexis Gabriel Fuentealba Orrego, and Luis Rodriguez Cisterna[✉]

University of Tarapacá, 1000000 Arica, CL, Chile
`lrodriguez@academicos.uta.cl`

Abstract. In this work, the validity of the length-to-inner diameter ratio (L/D) as a scaling tool in extra-long two-phase thermosyphons for geothermal applications has been experimentally studied. Two thermosyphons with different dimensions were studied, maintaining the L/D equal to 110. The results obtained show that the thermosyphon of smaller size and larger inner diameter operated at higher vapor temperatures (up to 20 °C) and lower thermal resistances (up to 50%), showing that the L/D ratio is not sufficient to scale thermosyphons without losing fundamental information on the operation of these devices. A characteristic length, given by D^2/L, has been proposed, which allows reducing by 30% the differences between the thermal resistance of both thermosyphons.

Keywords: Two-phase thermosyphon · length-to-inner diameter ratio · geothermic · Hot Dry Rock

1 Introduction

Geothermal energy is an energy resource which has its reserves in the depths of the earth, where heat is extracted and used to generate electricity in various applications [1]. The existing systems for its extraction are divided into two types: Conventional geothermal system (Hydrothermal) and enhanced geothermal system also known as Hot Dry Rock (HDR) [2]. The latter can be implemented in regions with lower geothermal potential than the conventional system and not necessarily near thermal water sources [2]. Three types of technologies can be used in HDR systems, Engineered Geothermal System (EGS), Downhole Heat Exchanger (DHE) and Super-Long Geothermal Heat Pipe (SLGHP) [3], this last one using heat pipe technology.

Heat pipes, or two-phase thermosyphons, are highly efficient heat transfer devices that operate in a closed cycle of evaporation and condensation [3], making them ideal for use in the geothermal industry. However, the main challenges are related to the difficulty

and risk of working with thermosyphons up to 100 m without first corroborating with laboratory-scale studies that reliably represent the main physical phenomena associated with thermosiphon length. Several authors ([4–9]) mention the existence of an L/D (length-to-inner diameter) ratio as a key factor in the design of these large devices.

Lin et al. [4] carried out an experimental study of extra-long two-phase thermosyphons for geothermal applications. These authors concluded that one of the most problematic operational constraints in these devices is the flooding limit for L/D ratios greater than 1200. Seo et al. [5] and [6] developed a correlation to determine the flooding limit from the L/D ratio in extra-long heat pipes. They also suggest the development of further empirical studies to relate the flooding limit to the thermal performance of these devices. Cen et al. [7] studied the performance of a two-phase thermosyphon with an L/D ratio of about 1700. The experimental results obtained by the authors indicate that thermosyphons with extremely large L/D ratios can operate with similar performance to conventional thermosyphons.

Chen et al. [8] made a study on two-phase thermosyphons with high L/D ratio (>5000), where different multiphase flow regimes and their relationship with the device performance were observed. Based on the results, these authors showed that the Geyser Boiling regime is most likely in high L/D ratio thermosyphons.

The research presented above mention the L/D ratio as an alternative to analyze the performance and operational limits of super long two-phase thermosyphons. However, there is no research in literature presenting a study keeping the L/D ratio constant as a scaling alternative for this type of devices. In this context, the objective of this work is to experimentally study two thermosiphons with constant L/D ratio equal to 110, to compare the thermal performance of these devices and verify if it is possible to scale thermosiphons using only the geometric L/D ratio, aiming geothermal applications.

2 Experimental Setup

Two copper two-phase thermosyphons (Fig. 1 a) were fabricated with different internal diameters and lengths, keeping the L/D ratio constant at 110 [9]. The working fluid used was deionized water with a filling factor of 100%, i.e., with a fluid volume equal to the evaporator volume. Thermosyphon 1 has an internal diameter of D1 = 13.9 mm was manufactured with a total length of L1 = 1532 mm and a ratio between the dimensions of its sections, evaporator (le), adiabatic section (la) and condenser (lc) of le:la:lc = 1:3:1 [9]. Thermosyphon 2 was manufactured with an internal diameter of D2 = 10.8 mm, an overall length of L2 = 1191 mm and a ratio of le:la:lc = 1:1.13:1. The differences between the section sizes of the thermosyphons (evaporator, adiabatic and condenser) were chosen in order to keep the heat transfer areas equal in both devices.

Figure 1 b, shows the experimental bench used in this work, consisting of: two-phase thermosyphon (1); heat supply system formed by a wire electrical resistance (2) of 28 Ω and 24.5 Ω for Thermosyphons 1 and 2 respectively, connected to a power supply (3) of the ISO-TECH brand, model IPS303DD; data acquisition system (4) of the Agilent brand, model 34970a; a cooling system consisting of a copper coil heat exchanger (5) with an external diameter of 6 mm, a total effective length of 500 mm and a pitch of 35 and 28 mm for Thermosyphons 1 and 2 respectively; a hydraulic bench (6) pumping

water to the heat exchanger, instrumented by a rotameter (7) with a measuring range of 4 to 18 g/s and a maximum error of ± 0.2 g/s.
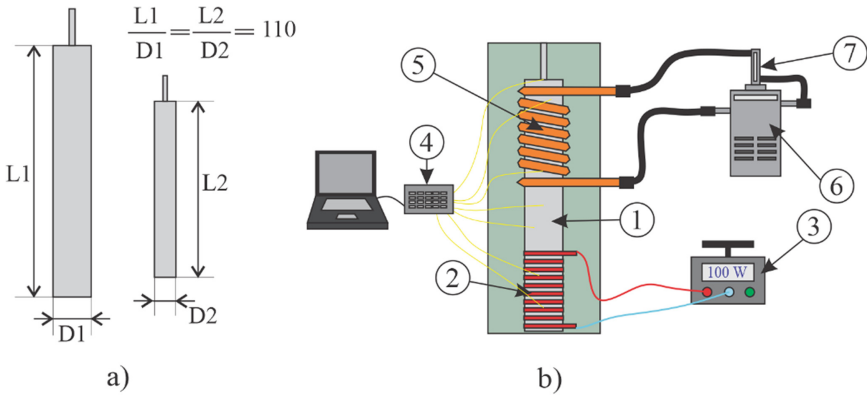

Fig. 1. a) Geometrical relationship of two-phase thermosyphons b) Simplified scheme of the experimental bench

The thermosyphons were instrumented with 8 K type thermocouples, with a maximum error of $\pm c$, distributed as follows 3 in the evaporator, 2 in the adiabatic section and 3 in the condenser. In addition, two K-type thermocouples were connected at the inlet and outlet of the heat exchanger to monitor the temperature of the refrigerant throughout the operation of the unit. Finally, the thermosyphons were thermally insulated with glass wool with a thermal conductivity of 0.04 W/m^{2}K.

Seven heat transfer rates were studied, applied in the following order: 25, 50, 75, 60, 40, 20 and 10 W. In each case, steady state was reached when the variation in the average temperature of each section after 10 min was less than 0.5 °C. It is important to note that the heat transfer rate was measured experimentally from Joule's law, i.e., the product of the current and the voltage supplied by the power source.

3   Results

Figure 2a and 2b show the behaviors of the average temperatures of the evaporator, adiabatic section and condenser as a function of time for each of the heat transfer rates applied to the thermosyphons. It can be observed that both thermosyphons show large temperature oscillations when the heat transfer rate was lower than 25 W. These oscillations can be attributed to the Geyser Boiling phenomenon, which is characterized by symmetrical oscillations of the evaporator and condenser temperatures [10], i.e., when the evaporator temperature increases abruptly, the temperatures of the adiabatic zone and the condenser decrease abruptly and instantaneously. Similarly, when the evaporator temperature decreases abruptly, the temperatures of the other sections increase instantaneously, demonstrating the release cycle and the formation of vapor bubbles during the Geyser Boiling regime [11].
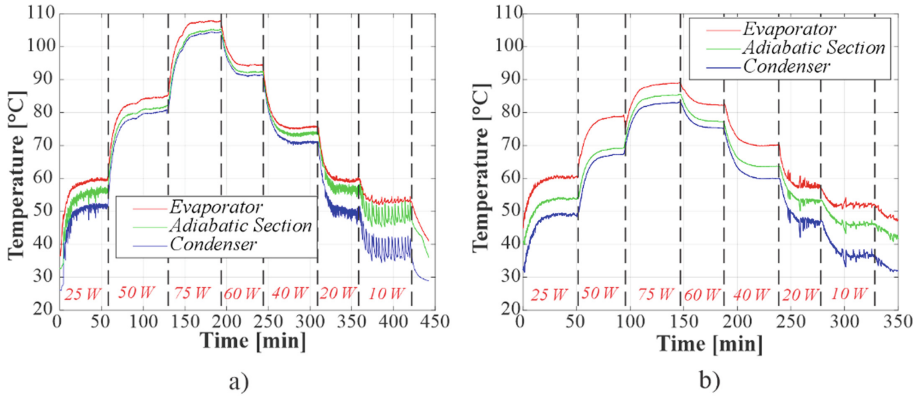
Fig. 2. Behavior of the temperatures of thermosyphon as a function of time a) Thermosyphon 1. b) Thermosyphon 2

Furthermore, it is observed that Thermosyphon 2 (Fig. 2b), regardless of the analyzed heat transfer rate, always reached steady state at significantly lower temperatures than those recorded for Thermosyphon 1 (Fig. 2a), which could lead to a wrong interpretation regarding the performance of the devices, i.e., interpreting that thermosiphon 2 operated with a better performance than thermosiphon 1. For example, there is a difference of approximately 3 °C for the heat transfer rate of 10 W and approximately 20 °C for the heat transfer rate of 75 W.

Figure 3a shows the performance of the two-phase thermosyphons based on the comparison of thermal resistances as a function of heat transfer rate. The thermal resistance was defined as the quotient of the temperature difference between the evaporator and condenser and the heat transfer rate. It was observed that for heat transfer rates less than 20 W, the resistances of Thermosyphon 1 were 6% lower than Thermosyphon 2. For heat transfer rates greater than 20 W, Thermosyphon 1 showed 50% lower thermal resistances than Thermosyphon 2, suggesting that Thermosyphon 1 has better thermal performance according to this criterion, differing to what was analyzed in Fig. 2. However, it is shown that the constant L/D ratio is not sufficient to reach the two-phase thermosyphon scale.

Figure 3b shows a graph between the thermal resistances of the two thermosyphons as a function of the heat transfer rate per unit length characteristic of the two-phase thermosyphon, which was defined as the quotient of the square of the inner diameter and the length of the device, in order to present a new option of scaling extra-long two-phase thermosyphons.

The results obtained from Fig. 3b show that the difference between the thermal resistances of the two thermosyphons was always less than 30%, which is significantly less than that obtained from Fig. 3a, but still large enough to conclude that only the use of this characteristic length is sufficient for scaling extra-long two-phase thermosyphons. These discrepancies may be related to the observed differences in the vapor temperatures of the two thermosyphons (Fig. 2), which cause significant changes in the thermophysical properties of the working fluid, mainly in density and viscosity, the properties associated with the interaction between the condensed liquid and vapor [12].
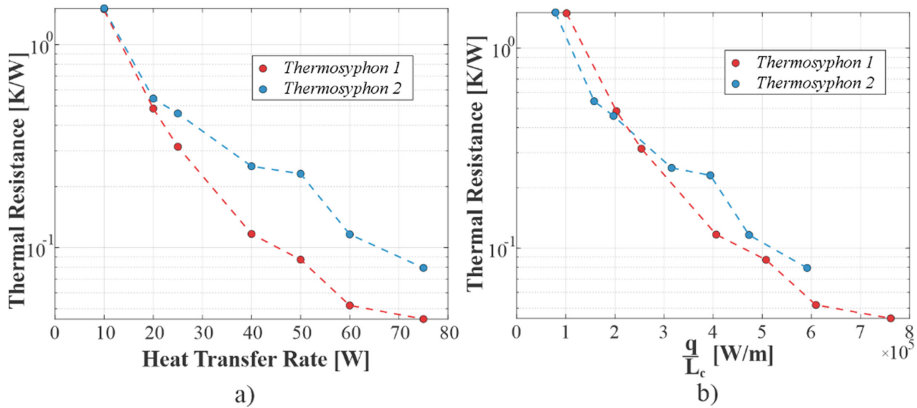
Fig. 3. Thermosyphon thermal resistance. a) as a function of heat transfer rate. b) as a function of heat transfer rate per unit length characteristic.

4 Conclusions

Two thermosyphons of different dimensions were studied, keeping the L/D ratio constant, equal to 110. It was found that Thermosyphon 1 operated at vapor temperatures up to 20 °C higher than Thermosyphon 2 and thermal resistances up to 50% lower than Thermosyphon 2. The above mentioned shows that the geometrical L/D ratio is not sufficient for the design of extra-long two-phase thermosyphons. A characteristic length has been proposed to reduce the differences between the thermal resistances of both thermosyphons, achieving differences of less than 30%. However, further experiments with two-phase thermosyphons of different dimensions and constant characteristic length are suggested. Furthermore, it is suggested that the scaling analysis of extra-long two-phase thermosyphons should include thermophysical properties of the working fluid such as density and viscosity.

References

1. Gupta, H.K., Roy, S.: Geothermal Energy: An Alternative Resource for the 21st Century (1.a ed.). Elsevier Science (2006)
2. Aghahosseini, A., Breyer, C.: From hot rock to useful energy: a global estimate of enhanced geothermal systems potential. Appl. Energy **279**, 115769 (2020)
3. Huang, W., et al.: Heat extraction from hot dry rock by super-long gravity heat pipe: a field test. Energy **247**, 123492 (2022). https://doi.org/10.1016/j.energy.2022.123492
4. Lin, T., Quan, X., Cheng, P.: Experimental investigation of superlong two-phase closed thermosyphons for geothermal utilization. Int. J. Therm. Sci. **171**, 107199 (2022). https://doi.org/10.1016/j.ijthermalsci.2021.107199
5. Seo, J., Bang, I.C., Lee, J.Y.: Length effect on entrainment limit of large-L/D vertical heat pipe. Int. J. Heat Mass Transf. **97**, 751–759 (2016)
6. Seo, J., Lee, J.Y.: Length effect on entrainment limitation of vertical wickless heat pipe. Int. J. Heat Mass Transf. **101**, 373–378 (2016)

7. Cen, J., Li, F., Li, T., Huang, W., Chen, J., Jiang, F.: Experimental study of the heat-transfer performance of an extra-long gravity-assisted heat pipe aiming at geothermal heat exploitation. Sustainability **13**(22), 12481 (2021). https://doi.org/10.3390/su132212481

8. Chen, J., Cen, J., Huang, W., Jiang, F.: Multiphase flow and heat transfer characteristics of an extra-long gravity-assisted heat pipe: an experimental study. Int. J. Heat Mass Transf. **164**, 120564 (2021). https://doi.org/10.1016/j.ijheatmasstransfer.2020.120564

9. Wang, X., Yao, H., Li, J., Wang, Y., Zhu, Y.: Experimental and numerical investigation on heat transfer characteristics of ammonia thermosyphons at shallow geo-thermal temperature. Int. J. Heat Mass Transf. **136**, 1147–1159 (2019). [12]

10. Pabón, N.Y.L., Mera, J.P.F., Vieira, G.S.C., Mantelli, M.B.H.: Visualization and experimental analysis of Geyser boiling phenomena in two-phase thermosyphons. Int. J. Heat Mass Transf. **141**, 876–890 (2019). https://doi.org/10.1016/j.ijheatmasstransfer.2019.06.052

11. Cisterna, L.H., Milanez, F.H., Mantelli, M.B.: Prediction of geyser boiling limit for high temperature two-phase thermosyphons. Int. J. Heat Mass Transf. **165**, 120656 (2021). https://doi.org/10.1016/j.ijheatmasstransfer.2020.120656

12. Mantelli, M.B.H.: Thermosyphons and Heat Pipes: Theory and Applications (2021 ed.). Springer, Cham (2021). https://doi.org/10.1007/978-3-030-62773-7

Design of a Condensing Heat Recovery Integrated with an Electrostatic Precipitator for Wood Heaters

Oscar Farías[✉] [iD], Pablo Cornejo [iD], Cristian Cuevas [iD], Jorge Jimenez [iD], Meylí Valín, Claudio Garcés, and Sebastian Gallardo

University of Concepción, Concepción, Chile
`ofarias@udec.cl`

Abstract. High emission of particulate matter from fixed sources of biomass combustion and the effects on the health of the population have driven the implementation of public policies for changes in the energy matrix and a technological replacement in Chile. Due to this, a prototype of a condensing heat exchanger is developed integrating an electrostatic precipitator, seeking to enhance the positive effects of these technologies in a single and relatively compact device. The state of the art shows similar developments, but with high levels of complexity in construction, as a shell and tube heat exchanger, that is why the concept of a thermocannon was optimized to condense the moisture present in the fumes and reduce smoke emissions through an electric field. It is expected that using an electrostatic precipitator, up to 90% of particulate matter emissions will be captured, and thermal efficiencies of an additional 9%. For its design, heat transfer and thermodynamics models were used and validated through CFD modeling.

Keywords: Domestic hot water · Condensing heat exchanger · Electrostatic precipitator · Biomass

1 Introduction

In Chile, biomass is the second primary energy source after oil corresponding to 23% of the total energy matrix of the country [1]. However, it is responsible for air quality problems in the main populated areas of the country contributing to 81.5% of the particulate matter (PM) emissions [2], mainly from residential wood combustion.

More than half of the Chilean population is currently exposed to concentrations of fine particulate matter or $PM_{2.5}$ (particulate matter with aerodynamic diameter $\leq 2.5\,\mu m$) above the annual limit being one of the highest levels among OECD countries [3]. Air pollution is the most important environmental problem in Chile [4], since it has negative effects on human health from exposure to particulate matter are associated with cardiovascular and pulmonary mortality and morbidity events.

Proposed improvements for wood heater included catalyst filters with PM reduction efficiency near 60% [5] or living filters that reach efficiencies of 95% [6]. Some

manufacturers incorporate post-combustion chambers with secondary air injection that reduce PM emissions and other pollutants by up to 90% [7]. In addition, electrostatic precipitators are available to adapt to the chimney, with PM reduction efficiency up to 90% [8] or installed in the combustion chamber with 44% reduction efficiency [9].

To improve the thermal efficiency of wood heaters, water heating thermos (thermocannon or thermosyphon) add-on are available with capacities from 70 to 110 L. A second combustion chamber also favors energy efficiency by providing additional convective heat to the radiation emitted by a conventional stove, saving up to 50% in fuel [7]. Proposed solutions for wood heaters consisting of compact shell and tube condensing heat exchangers [10–12] may increase thermal efficiency up to 33% and can incorporate a MP reduction device.
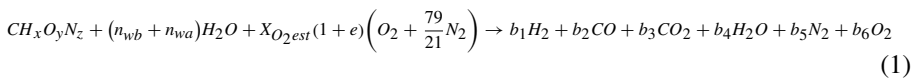
This study optimizes the thermocannon concept by improving heat transfer and integrating an electrostatic precipitator to reduce PM emissions. It is expected that, as in [12], a synergy between both devices would reduce PM emissions by 85% and increase thermal efficiency by 20%.

2   Methodology

A thermodynamic model was developed for the numerical simulation of a modified thermocannon prototype. The first step considers the combustion and heat transfer processes in the heater. The second step includes the heat exchange between the gases and the water in the thermocannon, and the capture of PM and the condensation of the fumes. The last step comprises a 3D simulation, through the finite volume method using the Ansys Fluent CFD tools to evaluate aspects related to the fluid dynamics of heat transfer from the combustion gases to help through the design of an optimized solution, which will be further implemented and validated in an experimental environment.

2.1   Combustion

The biomass combustion step was modeled from the chemical reaction Eq. (1) to characterize the products present in the combustion fumes. In the reactants, the fuel of composition CHxOyNz was considered, including humidity (n_{wb}), combustion air (n_{wa}), excess of air (e) and the stoichiometric oxygen fraction ($XO_{2\ est}$).

$$CH_xO_yN_z + (n_{wb} + n_{wa})H_2O + X_{O2est}(1 + e)\left(O_2 + \frac{79}{21}N_2\right) \rightarrow b_1H_2 + b_2CO + b_3CO_2 + b_4H_2O + b_5N_2 + b_6O_2$$

$$(1)$$

Once the composition of the combustion products (b_i) is known, the temperature of the fumes (T_h) entering the heat exchanger is obtained using Eq. (2) to determine the yield (η_{fumes}) by the indirect method or smoke losses (Q_{fumes}) and by incomplete combustion of carbon monoxide (Q_{CO}) based on its lower heating value (LHV_{CO}), where Q_{comb} represents the energy contributed by the fuel based on its lower heating value (LHV_{comb}). The enthalpy of the gases exiting the heater was the same at the entrance of the heat exchanger with a reference temperature (T_r) of 25 °C. The above

is resolved iteratively by setting a thermal performance for the heater, considering 80% [13].

$$\eta_{fumes} = 1 - \frac{Q_{fumes} + Q_{CO}}{Q_{comb}} \tag{2}$$

$$Q_{fumes} = \sum_{i=1}^{6} b_i[h_i(T_h) - h_i(T_r)] \tag{3}$$

$$Q_{comb} = LHV_{comb} \cdot n_{comb} \tag{4}$$

$$Q_{CO} = LHV_{CO} \cdot b_2 \tag{5}$$

Then, considering a perfect gas mixture, it is possible to calculate the dewpoint temperature (T_{dewp}) by determining the partial pressure of water in the gas flow.

2.2   Heat Exchanger Design

The design was based on a concentric tube attached to the exhaust of a wood stove in which water is heated through a two-stage heat exchanger (Fig. 1) to increase the residence time and turbulence of the fumes. In the second stage, an electrode was integrated based on a commercial 15 kV device. Preliminary dimensions were height 1.35 m, effective length 1.30 m and width 0.46 m (18″ largest diameter). Figure 1 shows improvements added to the original model including a divider plate moved towards the first stage and added turbulence generators to increase the residence time of the fumes.

Heat transfer was calculated using correlations included in the Engineering Equation Solver software, described in [14]. The calculation of the global heat transfer coefficient was simplified since the film thickness in case of condensation does not influence more than 3%, as well as the wall thickness [15]. With the preliminary dimensioning and characterized fume flows, the prototype was modeled in CFD for the initial design.
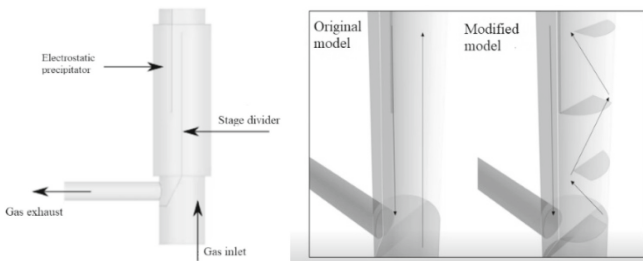

Fig. 1. Original design and improvement proposal.

The behavior of the flow of gases in the heat exchanger used the Cold Flow scope excluding the chemical interactions between the particles and considering only the physical interactions between them and the surrounding geometry [16]. The k-ω SST turbulence model [17, 18] was selected with mesh amounts up to 3.7 million cells.

3   Results

Input parameters for the simulation of the wood combustion and heat exchanger model are shown in Table 1.

Table 1. Input variables for computational study in CFD using the Cold Flow scope.

Variable	Water	Gases	
		Stage 1	Stage 2
Inlet temperature [C]	14.9	183.0	138.6
Outlet temperature [C]	18.6	138.6	107.0
Dew point [C]		51.29	
Flow [kg/s]	0.04167	0.00745	
Convective coefficient [W/m²-K]	114.7	2.767	2.598
Reynolds number	71	1664	1808
Density [kg/m³]	1000	0.850	
Combustion gas composition	CO [%]	0.160	
	CO_2 [%]	10.780	
	N_2 [%]	68.610	
	O_2 [%]	7.287	
	H_2O [%]	13.160	

Figure 2 shows the behavior of the gas flow through the representation of the current lines. It is appreciated that the turbulence generators increase the speed of the flow and the intensity of turbulence by 18% in the first stage.
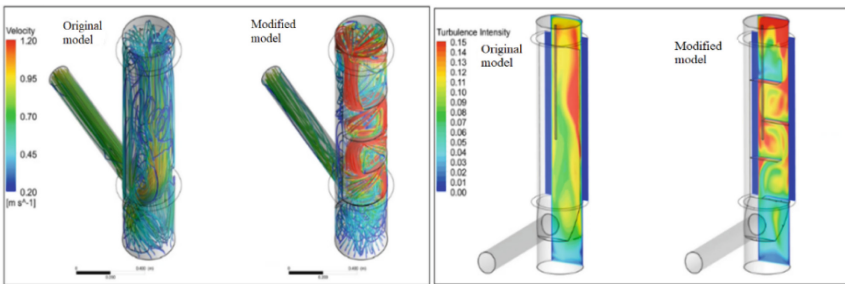

Fig. 2. Streamlines for the models (left) and turbulence intensity section plane, stage 1 (right)

Figure 3 shows the temperature profiles in a section plane of the first stage of the heat exchanger evidencing the improvement in the optimized design. 1.

The new model allows a 15 °C reduction in the temperature of the gases exiting the exchanger (from 82 to 67 °C). The dewpoint temperature was approximately 60 °C and the pressure drop was 12 Pa. The latter occurs due to the low outlet temperature and throttling by the modification in stage Based on the results, it was considered necessary to add a fan at the chimney outlet to push the fumes during the ignition phase.

Concerning the installation of the electrode that delivers the electric charge to the particles in the fumes, the results suggested adequate conditions for its operation with phase velocities of 0.6 m/s [19, 20] and temperature below 90 °C [21, 22]. Regarding energy recovery efficiency, the temperature of the combustion gases was reduced from 183 °C to 67 °C, equivalent to 0.96 [kW] transferred to the water. In theoretical terms and pending the experimental validation of the CFD model, the heat exchanger may increase the overall efficiency by 9.9%.
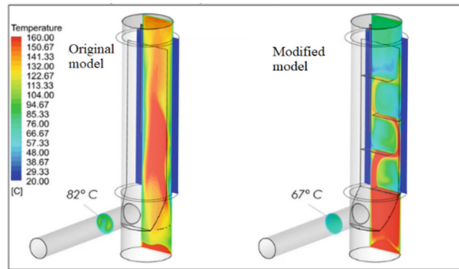

Fig. 3. Temperature profile, section plane (stage 1)

4 Conclusions

A two-stage thermocannon design was proposed for heat recovery and PM emission reduction for wood stoves and heaters. The presence of condensate is still not significant due to the lower heat exchange in the second stage, which is restricted to incorporate modifications due to the presence of an electrostatic precipitator that requires a free cross section of at least 5″ in diameter. Recent literature indicates that the integration of both devices allows to enhance its overall performance, which is expected to be validated in a laboratory environment. Although the alternatives proposed in the literature have higher thermal efficiencies, they are solutions of high cost and complexity. Therefore, the proposed design is adequate for current needs in Chile.

One matter to be resolved during the design process corresponds to the maintenance of the heat exchanger, since the electrostatic precipitator will deposit particulate material on the walls of the device, transforming the surface into a conductive material over time, with possible short-term problems. Due to the complexity of the design, especially stage 1, a configuration that allows easy access to both stages for proper wall and electrode maintenance is in the iteration process, without compromising the efficiency and performance of the device.

References

1. Comisión Nacional de Energía Chile: Anuario Estadístico de Energía 2020 (2020)
2. Ministerio del Medio Ambiente: Tercer Informe del Estado del Medio Ambiente (2020)
3. OECD: Environmental Performance Reviews, Chile 2016. OECD (2016). https://doi.org/10.1787/9789264252615-en
4. Bergamini, K., Irarrázabal, R., Monckeberg, J., and Pérez, C.: Principales problemas ambientales en Chile: desafíos y propuestas, Temas de la agenda pública (2017)
5. Purexhaust Cero Emision: Retrocatt Filtro para calefactores a leña. https://www.purexhaust.com/productos-y-servicios/retrocatt/. Accessed 13 Apr 2021
6. Filtro Vivo: Sistema de descontaminación Filtrovivo Industrial y Habitacional. www.filtrovivo.cl. Accessed 13 Apr (2021)
7. Ecoturbo: Quemador convectivo de gases. https://www.ecoturbo.cl. Accessed 02 Feb 2022
8. Filtro – MPzero. https://www.mpzero.cl/filtrompzero. Accessed 13 Apr 2021
9. Suhonen, H., Laitinen, A., Kortelainen, M., et al.: Novel fine particle reduction method for wood stoves based on high-temperature electric collection of naturally charged soot particles. J. Clean. Prod. **312**, 127831 (2021)
10. Gröhn, A., Suonmaa, V., Auvinen, A., Lehtinen, K., Jokiniemi, J.: Reduction of fine particle emissions from wood combustion with optimized condensing heat exchangers. Environ. Sci. Technol. **43**(16), 6269–6274 (2009)
11. de Best, C., van Kemenade, H., Brunner, T., Obernbergert, I.: Particulate emission reduction in small-scale biomass combustion plants by a condensing heat exchanger. Energy Fuels **22**(1), 587–597 (2008)
12. Grigonytė-Lopez Rodriguez, J., et al.: A novel electrical charging condensing heat exchanger for efficient particle emission reduction in small wood boilers. Renew. Energy **145**, 521–529 (2020)
13. Farías O.: Informe técnico final: Prototipo de cocina a leña multifuncional basado en tecnología de gasificación (INNOVA BIOBIO 15.239-EM.CIE.) (2017)
14. Nellis, G., Klein, S.: Heat Transfer, 1st edn. Cambridge University Press, Cambridge (2009)
15. Jeong, K., Kessen, M., Bilirgen, H., Levy, E.: Analytical modeling of water condensation in condensing heat exchanger. Int. J. Heat Mass Transfer **53**(11), 2361–2368 (2010)
16. Azad, A., Halder, P., Nanthagopal, K., Ashok, B.: Investigation of diesel engine in cylinder flow phenomena using CFD cold flow simulation. In: Advanced Biofuels: Applications, Technologies and Environmental Sustainability, pp. 329–336 (2019)
17. Rumsey, C.: Turbulence Modeling Resource - The Menter Shear Stress Transport Turbulence Model (2021). https://turbmodels.larc.nasa.gov/sst.html. Accessed 03 Aug 2022
18. ANSYS Inc.: ANSYS Fluent Theory Guide, 14th edn. ANSYS Inc., Canonsburg (2011)
19. Teng, C., Fan, X., Li, J.: Effect of charged water drop atomization on particle removal performance in plate type wet electrostatic precipitator. J. Electrostat. **104**, 103426 (2020)
20. de Oliveira, A., Guerra, V.: Influence of particle concentration and residence time on the efficiency of nanoparticulate collection by electrostatic precipitation. J. Electrostat **96**, 1–9 (2018)

21. Noda, N., Makino, H.: Influence of operating temperature on performance of electrostatic precipitator for pulverized coal combustion boiler. Adv. Powder Technol. **21**(4), 495–499 (2010)
22. Wang, G., et al.: Jiang, J: Characteristics of particulate matter from four coal–fired power plants with low–low temperature electrostatic precipitator in China. Sci. Total Environ. **662**, 455–461 (2019)

Effect of the Sierpinski Carpet on the Convective Flow on a Squared Fin Under Natural Convection

Aram Torres-Bárcenas, Roberto Alejandro Vargas-Domínguez,
Carlos Arturo Debernardi-Aguirre, Francisco Javier Solorio-Ordaz,
and Rafael Chávez- Martínez[✉]

Thermofluids Department, Faculty of Engineering, Universidad Nacional Autónoma de México,
04510 Mexico City, Mexico
`rafael.chavez@ingenieria.unam.edu`

Abstract. The present experimental work is aimed to study the convective flow generated on the surface of four squared copper fins of 10 cm per side and 0.314 cm thickness. Three of them were manufactured according to the first three iterations of the Sierpinski carpet fractal. The experiments were carried out for different input power at the base of the fins, 4.7 W, 9.0 W, and 13.7 W. Particle image velocimetry was used to measure the velocity fields and the Schlieren technique to visualize the thermal boundary layer. Results showed that higher the input power, higher the velocity of the hydrodynamic boundary layer. In addition, the thermal and the hydrodynamic boundary layers increased in thickness. On the other hand, the heat exchange area diminishes for the higher iterations of the fractal, resulting in lower velocities of the hydrodynamic boundary layer and smaller temperature gradients on the thermal boundary layer. Furthermore, the manufactured perforations disturb the convective flow.

Keywords: Fractal Fin · Sierpinski Carpet · Convective Flow

1 Introduction

Heat exchangers are widely used in multiple industrial processes [1]. For this reason, the objective to increase the heat transferred while reducing the pressure drop and minimizing the size of the thermal conversion systems has turned into a relevant milestone due to its practical purposes. Different approaches have been studied to improve the convection heat transfer of a fin and diminishing at the same time its mass such as geometric modifications [2], material reduction [3], and topological modifications [4–6], among others. Because of the last premise, a tendency (research area) is to manufacture windows (holes, openings) according to pre-fractal patterns, like the Sierpinski carpet. Numerical and experimental work has been carried out studying the total heat transfer, efficacy, and efficiency; results are promising, reporting an increase in the energy dissipated per unit mass.

The present work is aimed to study the convective flow on the surface of four squared-copper fins oriented vertically with gravity. Perforations were manufactured according to the first four iterations of the Sierpinski carpet, starting from iteration 0. Particle image velocimetry was used to study the velocity fields and the Schlieren technique to visualize the thermal boundary layer. As far as it is known, these kinds of studies have not been performed previously for this type of fins. The perforations are believed to perturb the convective flow, improving the heat transfer in the regions close to them.

2   Experimental Methods

The experimental setup shown in Fig. 1 was installed in an experimental area of 4.3 m length, 3.1 m width, and 3 m height. Components of the particle image velocimetry and the schlieren system were also installed in this space, all but laser. During experimentation, the ambient temperature in the room was 22.7 °C ± 0.4 °C.

Four copper plates were used to manufacture the fractal fins, each 10.5 cm in height, 10 cm in width, and 0.17 cm in thickness. No modifications were made to the first one, which is considered the baseline. The other three were manufactured according to the first three iterations of the Sierpinski carpet fractal. These were named IT0 to IT3, as shown in Fig. 1. The fins were inserted 0.5 cm in a heating base to minimize temperature gradients, conformed by a trapezoidal copper bar of 10 mm and 3.15 mm bases, 10 mm in altitude, and 10 cm in length. The thermal resistance was minimized by applying thermal grease. All elements were painted matte black to have uniform emissivity; laboratory tests showed $\varepsilon = 0.97$. The coordinate system was fixed at the lower-left corner of the fins, which are oriented parallel to gravity. The temperature of the fins was incremented using an electrical heater of 2.8 Ω, adhered to the bottom of the heating base; it was insulated using acrylic of 0.5 cm in thickness. Electrical energy was supplied by an adjustable DC power supply (GW GPS-1850D). Details about construction of the experimental model and setup can be consulted in [7].

Six type T thermocouples (Omega TT-T-30-SLE) were instrumented. Three were used to monitor the temperature of the heating base, inserted in holes of 0.5 cm in depth and 0.25 cm in diameter manufactured at locations of $Y/L = -0.03$ and $Z/L = -0.25$, -0.5, and -0.75. Two were used to compute de heat loss through the heating base insulation, adhered on the surfaces of the acrylic. One was used to monitor the ambient temperature of the confined space; it was installed 1.5 m from the ground level and 0.5 m far from the experimental model. The thermocouples were connected to a National Instruments data acquisition system integrated by a thermocouple module (PXIe$-$453) and chassis (PXIe$-$1073). Readings of the thermocouples were monitored and recorded in real-time using a program based on the LabVIEW software.

The convective flow around the four fins was experimentally studied using particle image velocimetry (PIV) and schlieren visualization. The PIV system was integrated by a Kiralux CMOS camera (CS135MUN) using a Navitar lens (MVL12WA) and a Spectra-Physics continuous laser (177-G0323) with a maximum output power of 400 mW. A Powell lens with 110° fan angle was used to generate the light sheet. A Dantec Dynamics fog generator (10D90P) was used to seed the particles of 5 µm diameter on average. The Stokes number is smaller than 0.1, so the particles have good tracing accuracy.
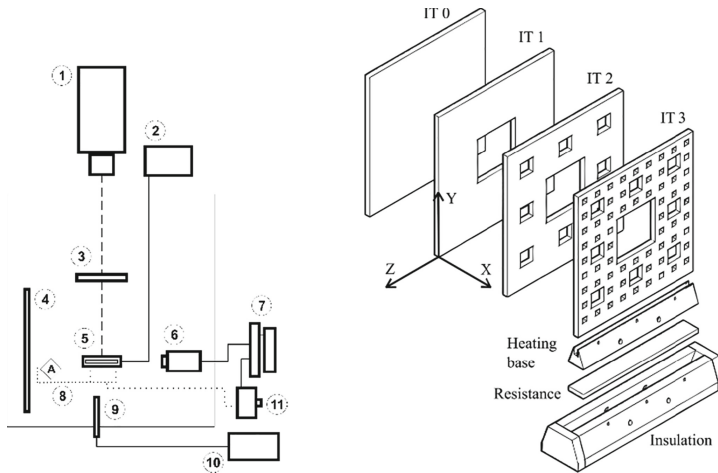
Fig. 1. Fins and heating base.

The Z-type Schlieren system consisted of two parabolic mirrors of 121 cm of focal length and 15.24 cm diameter each, an adjustable light source (Dolan-Jenner DC-950), an aspheric lens of 5 cm diameter an 0.5 normal aperture, a variable slit, two flat mirrors, a razor blade as knife-edge, and a concave lens of 5 cm diameter to project the images on a squared ground glass diffuser of 15 cm per side. Images were recorded with the Kiralux CMOS camera. The components were installed so that the collimated beams were parallel to the fins. The knife-edge was positioned at the focal plane of the second mirror in vertical position; it can be moved along the direction of the bigger temperature gradients, i.e., X-axis. To minimize optical aberrations the off-axis angle was 3°.

Runs were carried out for power inputs of 4.7 W, 9.0 W and 13.7 W at the base of the fins after losses. The experimental space was closed 24 h before experimentation to minimize external perturbations. The activities started introducing the seeding particles to the area and turning-on the power supply. At least two hours were necessary to fins reach steady conditions. One hundred photographs were taken for PIV analysis and 10 for schlieren visualization.

For each case, PIV measurements were taken in positions parallel to the XY-plane at $Z/L = -0.166$, -0.375 and -0.5. The open-source PIVlab software was used to compute the velocity fields [8]. Cross-correlation in two steps was used to analyze the images; interrogation areas of 64×64 pixels and 32×32 pixels were used in the first and second steps, respectively. The one hundred velocity fields were averaged to obtain a resultant velocity field. A velocity uncertainty of 4.4×10^{-3} m/s was estimated. For schlieren visualization, the knife-edge was adjusted to block 40% of the light spot to improve the contrast of the images and the edge detection of the thermal boundary layer. The technique averages the temperature fluctuations on the surface of the fin along the path light, i.e., the Z-axis.
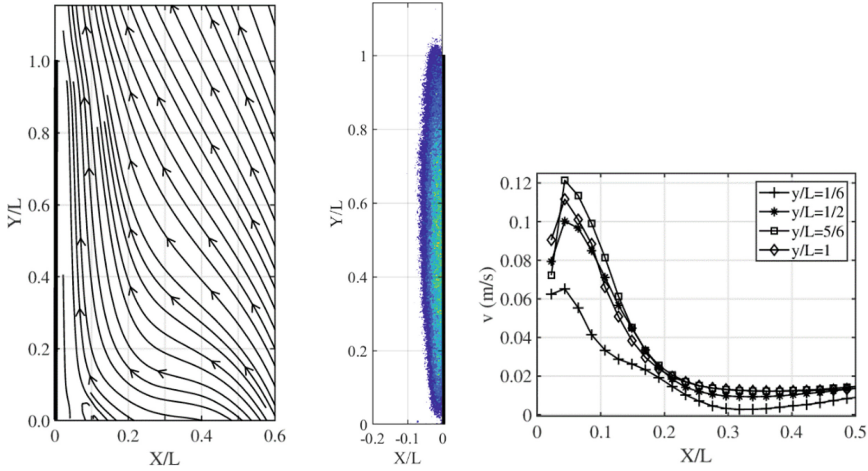
Fig. 2. Experimental results for IT0 and 4.7 W, measurement plane Z/L = −0.5. Left: streamlines, Center: Schlieren visualization. Right: velocity profiles of *v*.

3 Results

In Fig. 2 the results of IT0 are presented for 4.7 W at Z/L = −0.5. An upward flow parallel to the fin can be observed on the streamline plot. It skirts the experimental model from the heating base to the trailing edge of the fin, where the flow bends left to occupy the zone behind the fin. Additionally, a secondary flow is induced by drag far from the fin. The velocity profiles of the *v* component depict that the thickness of the hydrodynamic boundary layer reaches X/L = 0.2. For all profiles, the velocity peak is reached at X/L = 0.043. As the flow travels on the surface of the fin, its velocity increases to 0.12 m/s at Y/L = 5/6. On the other side, the velocity of the secondary flow is 1.3×10^{-2} m/s. With respect to the thermal boundary layer, it has a maximum thickness of 9 mm and covers the whole surface of the fin. The bigger temperature gradients are presented on the surface of the fin from Y/L = 0.2 to Y/L = 0.8. The black lines in plots represent the area occupied by the fin. In the contour plots, bigger temperature gradients are colored in yellow tones and the smaller ones in blue.

In Fig. 3 are presented the velocity profiles of *v* for the three supplied powers, for middle plane Z/L = 0.5, at Y/L = 1/2. Increasing this parameter, the velocity of the hydrodynamical boundary layer increases as can be seen in *v* the velocity profiles for 4.7 W and 9.0 W. But for 13.7 W only the secondary flow is affected, reaching 5.7 $\times 10^{-2}$ m/s. Additionally, the base temperature was incremented for all fins, as seen in Table 1. On the other hand, for all fins the thickness of the thermal boundary layer increases as higher the supplied power, and its extension has the same behavior. For example, the thickness of IT0 and 13.7 W was 10 mm, and it extended far from Y/L = 1.2, i.e., is out of the visualization area of the schlieren system.

Referring to the effect of the Sierpinski fractal iteration, the higher the iteration, the fewer the heat transfer area of the fins. Consequently, for the same power the temperature of the base of the fins increases, as shown in Table 1. The decrease in the area diminishes
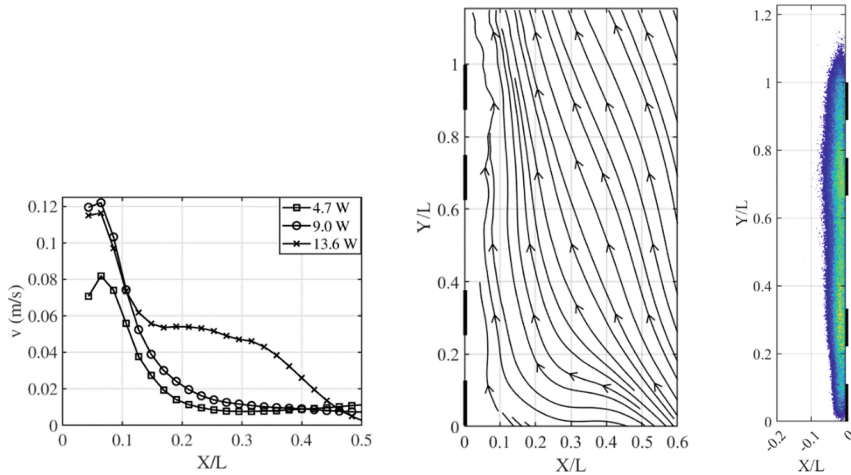
Fig. 3. Effect of the supplied power and the fractal iteration. Left: velocity profiles of v, at Y/L = 1/2. Center and Right: Streamlines and schlieren visualization, for IT2 and 9.0 W.

the buoyancy forces, so the velocity in the hydrodynamic boundary layer decreases too. Furthermore, the thermal boundary layer shrinks in thickness and extension; for example, IT0 and IT2 in Figs. 2 and 3 have the same thickness, although the power in IT2 is bigger. The perforations manufactured to the fins affect the convective flow, generating a rippled flow as shown by the streamlines in Fig. 3.

Table 1. Temperature of the base of the fins.

	Temperature, °C			
	IT0	IT1	IT2	IT3
4.7 W	41.3	42.2	42.0	42.5
9.0 W	56.0	57.7	58.2	59.1
13.6	68.2	71.9	72.8	74.0

4 Conclusions

In the current work, the velocity fields and the temperature gradients on the surface of four pre-fractal fins were measured and visualized. Each fin was analyzed for three different power supplies on the heating base, obtaining the following conclusions:

- For larger supplied power, the faster the speed of the hydrodynamic boundary layer. At the same time, the thickness of the thermal and hydrodynamic boundary layer increases.

- Due to drag effects, a secondary flow is generated far from the fin, and for a higher power, the interaction between this flow and the hydrodynamical boundary layer was more evident.
- The perforations affect the thermal and hydrodynamical boundary layer, and its effect can be identified as a waving movement of the flow.
- The higher the fractal iteration, the lower the heat transfer area of the fins; consequently, the temperature of its base incremented.

References

1. Theodore, L.: Heat Transfer Applications for the Practicing Engineer, 1st edn. John Wiley & Sons Inc., Hoboken (2011)
2. Ghandouri, I., Maakoul, A., Saadeddine, S., Meziane, M.: Design and numerical investigations of natural convection heat transfer of a new rippling fin shape. Appl. Thermal Eng. **178**, 115670 (2020)
3. Huang, C., Liu, Y., Ay, H.: The design of optimum perforation diameters for pin fin array for heat transfer enhancement. Int. J. Heat Mass Transfer **84**, 752–765 (2015)
4. Calamas, D., Dannelley, D., Keten, G., Hines, P.: Thermal performance of Sierpinski carpet fractal fins in a natural convection environment. Heat Transfer Thermal Eng. **8**(B), 1–7 (2015)
5. Calamas, D., Dannelley, D., Keten, G.: Experimental effectiveness of Sierpinski carpet fractal fins in a natural convection environment. J. Heat Transfer **139**(9), 1–12 (2017)
6. Ebrahimi, K., Ebrahimi, S., Ebrahimi, K.: Fractal pattern effects on natural convection heat transfer and flow characteristics. In: 19th IEEE ITHERM Conference, pp. 357–365. IEEE Xplore, Orlando (2020)
7. Debernardi, C., Martínez, L., Godínez, F., Solorio, F.J., Chávez, R.: Transferencia de calor en aletas de geometría pre-fractal: Experimentos y simulaciones numéricas. In: Memorias del XXVII Congreso Internacional Anual de la SOMIM, pp. 232–241, Publicaciones SOMIM, México (2021)
8. Thielicke, W., Sonntag, R.: Particle image velocimetry for MATLAB: accuracy and enhanced algorithms in PIVlab. J. Open Res. Softw. **9**(12), 1–14 (2021)

Initial Considerations for a P2P Trading Model for Electricity Generated from Photovoltaic Solar Energy Based on Blockchain Technology

Sarkkinen Veikka[1], Alex Alcântara Renó[2], Ali Khosravi[3], and Juan J. Garcia Pabon[2(✉)]

[1] Department of Mechanical Engineering, School of Engineering, Aalto University, Espoo, Finland

[2] Programa de Pós-graduação em Engenharia Mecânica, Universidade Federal de Itajubá, Itajubá, Brazil
`jjgp@unifei.edu.br`

[3] Department of Mechanical and Electrical Engineering, SDU Mechateronics (CIM), University of Southern, Sønderborg, Denmark

Abstract. The article proposed a list and discussion of the aspects that should be considered before implementing Blockchain technology in the renewable energy trade. In the proposed model, electricity is generated by solar energy and uses consumption and production data, among other things, to price electricity in a double auction, in which sellers present their prices and buyers send their bids at the same time. The use of Blockchain technology allows real-time monitoring of consumption and production, and real-time trading where third parties are not needed. It also has the potential to maximize profits from the perspective of prossumidor and minimize electricity losses. Considering Finland, it is already possible to realize that customer segments are delimited in subgroups within cities and requires the involvement of the electricity company, awareness at the state level and inversion in pilot projects.

Keywords: Blockchain · energy market · distributed energy · photovoltaic energy

1 Introduction

Microgenerators with renewable energy and their microgrids are presented as an option to overcome this challenge of electrification of the energy system. In order to integrate the new prosumers of renewable energy into the conventional electricity grid, it is necessary to evolve to a new stage, called smart grids. According to Ref. [1], a smart grid is defined as an electrical system that uses information, two-way communication technologies, cybernetics and intelligent software applications at various layers of the power system, from electricity generation and storage to the endpoints of consumption. These transformations are bringing new ways of seeing the energy market.

Peer-to-peer (P2P) electricity trading allows prosumers and consumers to trade electricity with each other to balance supply and demand. For example, when a user installs photovoltaic solar panels (becoming known as a prosumer), and they have an excess of electricity, they can exchange it for other consumers in exchange for a financial benefit. These new energy market transactions need to be secure, transparent and efficient.

Blockchain technology means building consensus in negotiations directly between the actors (without additional intermediaries) giving transparency and trust to the system, and it is not just for the purchase and sale of energy. It is also possible to apply Blockchain technology to the mapping of values and rights (transparency of origin and ownership), among others. Smart contracts, for example, allow the cooperation and performance accounting of autonomous systems, and mean traceability and irreversibility in the generation of renewable energy [2].

This article aims to discuss the initial phase to develop a business model for a P2P electricity trading system, taking as a case study in Finland based on the business model of Ref [3]. Thus, the objective of the work is to identify and list the necessary challenges so that Block-chain technology can be used to commercialize photovoltaic energy credits between consumer, pro-consumer and energy company.

2 Methodology

Initially, the type of Blockchain technology with the most promising results in P2P electricity trading was identified based on existing research, and then they were compared with each other and applied in this business model. The business model was built based on Ref. [3] which is divided into nine sections which are: Key Activities, Partners, Resources, Value Propositions, Customer Relationship, Cost Structure and Revenue Streams. Each section was then evaluated with a focus on previous research and results from pilot projects.

2.1 Key Activities

Key activity factors such as the use of Blockchain and photovoltaic solar energy production are the main topics to be considered.

Use of Blockchain. For a local energy market, a Blockchain allows the use of smart contracts and data sharing. With a Block-chain, every transaction can be seen from the ledger, and everything is transparent. This helps bring more confidence to the system from the user's point of view [9, 10].

Blockchain can be of two types: public or private. A private Blockchain allows the use of a system in which the verification of any transaction takes place by a private operator, and does not keep the system open to everyone, as is the case with a public Blockchain. Since the purpose of Blockchain, in this context, is to serve users in a certain geographic area and ensure security and transparency, a private Blockchain is a more suitable option [4].

In a P2P electricity trading system, transparency is crucial for the consumer to see how much electricity is available to buy and for a prosumer to see the demand. A smart

meter makes it possible to visualize data in real time. In the case of the Brooklyn Micro-grid, consumption and generation data are transferred from the participants' Transactive Grid smart meters to their Blockchain accounts [5].

Production of Photovoltaic Energy. Finland's climate and geographical location were considered in the challenges. Although Finland is located in the North and solar radiation is relatively low compared to countries in the South, achieving a surplus in a residential household with solar photovoltaics is possible even during certain hours of October with sufficient installed capacity of photovoltaic panels.

2.2   Partners

The main activities, the use of Blockchain and energy trading include the strong involvement of prosumers and consumers, which makes them the main participants. Prosumers handle renewable energy generation and consumers play an important role in creating demand. The third partner is the network company. The supply drops to zero at certain hours, for example, during those hours when solar radiation is very low [6]. This leads to the situation where both consumers and prosumers must buy their electricity from an external source, which in this case is the electric company.

2.3   Resources

Key Resources are the tools and materials needed to implement the main activities of the business model. For this procedure, everything from electrical energy production to distribution must be considered, in addition to researching the most optimal technology. To go into detail, the necessary resources are the hardware such as smart meters, the software, the distribution network and the system participants [7].

2.4   Cost Structure

As the model aims to offer greener electricity at a lower price. Costs such as initial investment, transaction costs on Blockchain and electricity transmission costs must be considered.

Cost of Photovoltaic Generation System. In the simulation of the LAMP project in Germany by [5] 25% of the participants were prosumers and the photovoltaic panels were all 5kWp, as a result it was noted that the P2P system did not lower the electricity price as much as expected. In order to lower the price of electricity further, and to have a more successful P2P power project, the local production of photovoltaic energy must be higher.

Blockchain Transaction Costs. Since the most important activity of the P2P power system is trading, most of the costs come from it. The entire system runs on Blockchain, which consumes energy, portrayed as "gas" for Ethereum, which forms a significant

portion of the costs. For comparison, PayPal transactions are twice as expensive compared to Ethereum transactions [8]. Gas consumption depends on the number of market participants, the trading mechanism and the trading interval.

Ref. [4] simulated gas consumption for an Ethereum within a local energy market with different trading structures and number of participants. Whether trading is live or next day influences gas usage and therefore costs. Next day trading is more gas efficient due to the lesser amount of information required compared to live trading. In real-time trading, trading ranges are an important factor driving gas usage. 15-min trading intervals are suggested to reduce trading costs compared to using a 5-min trading interval.

Electricity Grid and Distribution Costs. One factor in the costs that a traditional centralized system faces is the cost that the loss of electricity with long transmission lines causes. With a decentralized system, these costs are reduced, as electricity is generally transported within the local system and the negotiation algorithm favors shorter transmission lines [11]. The simplest way to take care of transmission costs would be to include them in smart contracts so that transmission is paid immediately with the transaction payment.

2.5 Revenue Streams

This model's revenue streams were identified by comparing Blockchain algorithms to each other and recognizing algorithms for trading and managing load and generation that result in higher profits and less wasted electricity. In the search for the most optimal trading mechanism, factors such as gas consumption, trading intervals and electricity cost were evaluated. The trading mechanism was then chosen based on the evaluation. The need for a Blockchain algorithm for load and generation management was recognized by identifying the challenges of high demand and supply peaks in a P2P electricity system. The structure of the dual auction framework. In addition to being fully automated and having a market-clearing price that connects supply and demand, it is also cost-effective, which is naturally important for consumers. A double auction mechanism is also secure, and the level of decentralization is the highest.

2.6 Value Propositions

The process of finding value propositions focused heavily on developing a Business Model that meets the future requirements of CO_2 emissions in energy production. An added value that the P2P system offers is the price reduction. The electricity price of the P2P system is lower than the retail price of the main network [12]. One value that is added to prosumers is the profit from trading energy for peers. Since profits stay in the community instead of going to a centralized system, community approval is higher. The P2P system adds sustainability beyond just creating financial value to its users.

2.7 Customers

Previous pilot projects of P2P power grids were carefully examined to identify the required customer segments. The results of these projects also helped to identify the

Relationship with the Customer that this model creates. Prosumers can then be divided into different segments by form of residential construction. Apartment buildings can become prosumers by installing photovoltaic panels on their roofs. In this way, the initial investment can be divided by the number of apartments. Detached houses are one of the main customer segments of the P2P system. They can be prosumer simply by installing photovoltaic panels on their roofs and easily generate surplus electricity even without having an installed capacity of 19.1kWp, as shown by [6].

3 Conclusions

This research aimed to develop a business model for a P2P electricity trading model in Finland. As there is no prior research for this area covering P2P electricity trading in Finland, this research article brought together existing research on electricity trading using Blockchain technology.

Challenges of decentralized energy systems and the need for more renewable energy were identified, and the demand for a business model for a decentralized energy system was recognized. Based on promising results with Blockchain technology and distributed energy systems, it was noted that a business model for P2P electricity trading is required.

Blockchain algorithms are crucial to the functioning of this system. Systems aim to be fully automated where algorithms are important. They are needed to calculate the price, to execute trades and to control generation and load. It was also found that using a Block-chain algorithm to control generation and manage load is suggested. Due to climate variation and peaks in electricity consumption, such an algorithm is necessary. Load and generation management has been found to increase both prosumer and consumer profits by reducing wasted energy.

References

1. Gharavi, H., Ghafurian, R., (eds.): Smart Grid: The Electric Energy System of the Future, vol. 99, pp. 917–921. IEEE, Piscataway (2011)
2. Foti, M., Vavalis, M.: Blockchain based uniform price double auctions for energy markets. Appl. Energy **254**, 11, Article 113604 (2019). https://doi.org/10.1016/j.apenergy.2019.113604
3. Osterwalder, A., Yves, P.: Business model generation: a handbook for visionaries, game changers, and challengers, vol. 1. Wiley, Hoboken (2010)
4. Blom, F., Farahmand, H.: On the scalability of blockchain-supported local energy markets (2018)
5. Mengelkamp, E., Gärttner, J., Rock, K., Kessler, S., Orsini, L., Weinhardt, C.: Designing microgrid energy markets a case study: the brooklyn microgrid. Appl. Energy **210**, 870–880 (2018). https://doi.org/10.1016/j.apenergy.2017.06.054

6. Simola, A., Kosonen, A., Ahonen, T., Ahola, J., Korhonen, M., Hannula, T.: Optimal dimensioning of a solar PV plant with measured electrical load curves in Finland. Sol. Energy **170**, 113–123 (2018). https://doi.org/10.1016/j.solener.2018.05.058

7. Kabi, O.R., Franqueira, V.N.L.: Blockchain-based distributed marketplace. In: Abramowicz, W., Paschke, A. (eds.) BIS 2018. LNBIP, vol. 339, pp. 197–210. Springer, Cham (2019). https://doi.org/10.1007/978-3-030-04849-5_17

8. Albrecht, S., Reichert, S., Schmid, J., Strüker, J., Neumann, D., Fridgen, G.:. Dynamics of blockchain implementation – a case study from the energy sector. In: Proceedings of the 51st Hawaii International Conference on System Sciences, pp. 3527–3536 (2019). http://hdl.handle.net/10125/50334

9. Thukral, M.K.: Emergence of blockchain-technology application in peer to peer electrical energy trading: a review. Clean Energy **5**, 104–123 (2021). https://doi.org/10.1093/ce/zkaa033

10. Yu, Y., Guo, Y., Min, W., Zeng, F.: Trusted transactions in micro-grid based on blockchain. Energies **12**(10), 16 (2019). https://doi.org/10.3390/en12101952

11. Tsao, Y.-C., Thanh, V.-V., Wu, Q.: Sustainable microgrid design considering blockchain technology for real time price-based demand response programs. Electr. Power Energy Syst. **125**, 14, Article 106418 (2021). https://doi.org/10.1016/j.ijepes.2020.106418

12. Christidis, K., Sikeridis, D., Wang, Y., Devetsikiotis, M.: A framework for designing and evaluating realistic blockchain-based local energy markets. Appl. Energy **281**, 17, Article 115963 (2021). https://doi.org/10.1016/j.apenergy.2020.115963

Competitive Strategies for Renewable Energies: Brazilian Market

Cynthia Siqueira Corrêa and Diego Mauricio Yepes Maya[✉] [iD]

Federal University of Itajubá, Itajubà, MG 37500-903, Brazil
{cynthia.sc,diegoyepes}@unifei.edu.br

Abstract. Renewable energy sources are sustainable alternatives for the electrical and energy development of countries. This paper analyzes the different mechanisms applicable to the Brazilian scenario. Brazil has several fronts and has direct policy instruments, such as subsidies and tax incentives, and indirect mechanisms. We analyze the need to expand existing mechanisms, implement new strategies, and improve the dissemination of existing programs to increase public awareness and pursue of a more efficient renewable energy transition. The participation of renewable sources, such as solar and wind, are gaining more and more space in the energy market in Brazil and much of this is due to incentives, such as tax and tariff rebates and long-term contracts. In 2021, the expansion of the Brazilian electric matrix was almost 1 GW (957.03 MW), according to the National Agency of Electrical Energy (ANEEL). Of this total power, 80% comes from renewable plants, from wind, hydro and solar sources.

Keywords: Barriers · Renewable Sources · Strategies · Alternatives

1 Introduction

The power sector currently attracts more investment than oil and gas combined investment needed as the generation mix changes and obsolete infrastructure is upgraded [1]. Three-quarters of global greenhouse gas emissions result from burning fossil fuels for energy. Fossil fuels are responsible for a large amount of local air pollution, causing health problems that lead to at least 5 million premature deaths each year. To reduce CO_2 emissions and air pollution, the world needs to rapidly shift to low-carbon energy sources. The structure of the Brazilian energy matrix defines Brazil as a world leader in electricity generation from renewable sources [2]. The main source of electricity generation in Brazil is still hydraulic power, making up more than 70% of the country's generation capacity, even though the country has great potential for exploring other renewable energy sources, such as wind, solar, and biomass [3]. With a new approach to the energy resources used, factors such as sustainability, environmental pollution and energy security have become frequent agendas, especially in emerging countries. The search for an offer of electric energy capable of meeting the growing demand, the decrease in the dependence on the use of fossil fuels like oil, natural gas, and coal is making countries like Germany, Sweden, Spain, Australia, China and Brazil, invest in renewable energy sources, e.g.: such as wind, solar, and biomass energy.

2   Methodology

Brazil has a great potential in renewable sources such as wind and solar energy. According to the Reference Center for Solar and Wind Energy - CRESESB/CEPEL, Brazil has a potential of 143 GW of wind energy that can be harnessed, besides having regions in the national territory compared to the best irradiation regions in the world of solar rays for photovoltaic energy generation. Since this reality, existing mechanisms were reviewed, to study the promotion of new incentive strategies for the expansion of the renewable electricity matrix in Brazil, some global strategies were also studied. A description of the main incentives follows. **Applied Discounts TUSD/TUST**: The law No. 9,427 was created, establishing that the enterprises framed in § 1 of its article 26 could, by determination of the National Agency of Electrical Energy (Aneel), receive the minimum 50% discount to be applied to the Tariffs for Use of the Transmission Systems (TUST) and Distribution Systems (TUSD), affecting the production and consumption of the energy sold [4]. The TUST and the TUSD are paid by the free, regulated and special consumers and by the electricity generators that need to use the transmission and distribution networks, i.e., they are tariffs paid for providing a service. Consumers pay TUST and TUSD to receive the energy purchased, while generators, for send the energy produced [5]. **PROINFA:** Created in 2002, after the rationing, the Alternative Sources Incentive Program (Proinfa) came into operation in 2004 with the aim of increasing the participation of alternative sources in the National Interconnected System. The calculation of the quotas is based on the Annual Plan of Proinfa (PAP) prepared by Eletrobras and forwarded to ANEEL. The cost of the program, whose energy is contracted by Eletrobras, is paid by all final consumers (free and captive) of the SIN, except those classified as low income. **LAW Nº 10.438, OF APRIL 26:** 2002, Art. 1, establishes that the costs, including those of an operational, tax and administrative nature, related to the acquisition of electric power (kWh) and the contracting of generation or power capacity (kW) by the Comercializadora Brasileira de Energia Emergencial - CBEE will be apportioned among all classes of end consumers served by the SIN, proportionally to the individual consumption verified, by means of specific additional tariffs, according to regulations to be established by the Agência Nacional de Energia Elétrica - Aneel. [6]. According to Convention **101/97- CONFAZ:** Convention 101 of the National Council of Fiscal Policy (CONFAZ) grants exemption from the Tax on Circulation of Goods and Services (ICMS) in operations involving various equipment and components for the use of solar and wind energy, among which are aerogenerators and photovoltaic generators, inverters, and other system components [7]. **ICMS Agreement no. 16/2015 – CONFAZ**: Convention No. 16 of the National Council of Finance Policy (CONFAZ) concerns the collection of ICMS on energy injected into the grid in order to grant exemption in internal operations related to the circulation of electric energy, subject to billing under the Electric Energy Compensation System dealt with in Normative Resolution No. 482, of 2012, of the National Agency of Electric Energy - ANEEL. Thus, the energy injected into the grid is compensated in the same amount in the consumer unit. However, as the consumption tariff is composed of two factors: the TE (Energy Tariff) and the TUSD, some states apply the ICMS exemption only on the energy portion, leaving a small portion of taxes to be paid [8]. **Distributed Power Generation Development Program (ProGD)**: The ProGD is a program of the Ministry of Mines and Energy created to

stimulate the generation of renewable energy by consumers themselves, especially solar photovoltaic energy. To this end, it foresees the movement of R$ 100 billion in investments in the area until 2030 and establishes more competitive reference values for the remuneration of the consumer who delivers energy to the distribution network through the generated surplus [8]. **PRONAF:** The National Program for the Strengthening of Family Agriculture (Pronaf) is one of the main government incentives for small farmers to finance photovoltaic systems up to R$ 300,000. Interest rates vary between 2.5% and 5.5% per year and the farmer starts to pay back after 36 months of acquiring the credit [8]. **BNDES:** The National Bank for Economic and Social Development (BNDES) offers a line that provides financing for up to 80% of the cost of the work with an interest rate of approximately 5% per year, helping to implement large photovoltaic energy projects [8]. Other types of incentives for solar generation involve the possibility of financing micro and mini solar/photovoltaic distributed generation systems since different banking institutions offer lines with attractive interest rates [9, 10]. **Investment Funds:** BNDES, ANEEL and the financial development institution Finep have jointly created a fund (INOVA ENERGIA) to finance grants and loans for projects related to smart grid and ultra-high voltage transmission, solar and wind technology, and vehicle energy efficiency (INTL. RENEWABLE ENERGY AGENCY, 015). The INOVA ENERGIA 2013 program, with up to R$5 billion in funding, provides subsidies of up to 90% of project costs for R&D projects related to smart grids, renewable energy, hybrid vehicles, and energy efficiency in transportation [11]. **REC Brazil:** The Renewable Energy Certification Program is a joint initiative of the Brazilian Clean Energy Generation Association (Abragel) and the Brazilian Wind Energy Association (ABEEólica), with support from the Chamber of Electric Energy Commercialization (CCEE) and the Brazilian Association of Energy Commercializers (ABRACEEL), and aims to foster the market of energy generated from renewable sources and with high performance in terms of sustainability. The program consists of two interrelated certifications, which bring benefits to energy generators and voluntary consumers of Renewable Energy [12, 13]. **REIDI:** The Special Regime of Incentives for Infrastructure Development (REIDI) is a program created by Law 11.488/2007 and regulated by Decree 6.144/2007 as a tax incentive to enable the realization of projects for the implementation of infrastructure works in the sectors of transport, ports, energy, sanitation and irrigation [14]. The adhesion to REIDI suspends the requirement of Contributions to the PIS/PASEP and COFINS, in acquisitions, leases and imports of goods and services, linked to the approved infrastructure project, carried out within five years from the date of qualification of the legal entity, owner of the project [15].

3   International Mechanisms that can be Incorporated in Brazil: Germany and Sweden

Governments in different countries have been striving to develop regulations and policies aimed at the stimulation of energy generation from renewable sources, as well as efficiency strategies and technological innovations. It is important to develop sustainable energy policies and provide relevant and appropriate policy recommendations for end users [16]. The strategies act in different areas to promote the intensification of the use

of renewable sources, acting on the development of new technologies and strategies by encouraging R&D, promoting facilities and monetary. In the German case, the mainly solar-focused initiatives have had significant effects. Firstly, they induced several new, often small, companies to enter and expand the sector, and also, the large number of cities with local feed-in laws and a proliferation of green pricing schemes led to a broad public interest in increasing the diffusion rate [17]. German renewable energy policy also showed impressive results in the 1990s. Between 1990 and 2002, 13,000 MW in new capacity came on stream. The costs of wind and solar energy decreased by about 30% and 60% between 1990 and 2000 [18].

In the case of Sweden, financial incentives used in conjunction with mandatory regulations, such as Net metering and Portfolio Standard, seem to have been the most effective. Public benefit funds (supported by surcharges on electricity users) have also played a role in stimulating RE technologies and promoting green electricity products. In conjunction with green energy education programs, these instruments can be critical to the long-term development of the renewable energy industry [18].

Table 1. Consolidated comparison of strategies and mechanisms used in Brazil and in the world

Incentive Methodology	BRAZIL	Germany	Sweden	Spain	USA	Argentina	Chile	Uruguay	China	Australia
Feed-in Tariff	[21, 23]	[17, 18, 20, 21]		[19–21]	[21]	[21, 23]		[21]	[21, 24]	[21]
Feed-in Award		[21]		[20, 21]						
Renewable Energy Target		[18]			[21]		[21]			[21]
Green Energy Certificates	[13]		[18, 21]	[21]	[21, 22]				[21]	[21]
Standard of Port. /Obl. to Quota			[18, 21]		[21, 22]	[23]			[21]	[21]
Carbon Policies			[21]						[21]	[21]
Grant	[21, 23]	[17, 18, 21]	[18, 21]	[18, 21]	[18, 21, 22]	[21]		[21]	[21]	[21]
R&D		[17]	[18]		[18]				[23]	
Tax Exemption/Tax Incentive	[21, 23]	[18, 21]	[18, 21]	[18, 21]	[18, 21]		[23]	[21, 23]	[21, 23]	
Net-metering	[21, 23]			[21]	[21]	[23]	[23]	[21, 23]		
Auctions	[23]					[23, 24]	[23, 24]	[23, 24]		
Funds	[11]	[24]								
Bidding	[21]	[21]		[21]		[21]	[21]	[21]	[21]	[21]
Financing/Reduced Interest	[10]	[18]		[18]						
Disclosure Policies		[22]								

4 Comparative Results

Renewable sources, such as solar and wind, are gaining more and more space in Brazil's energy market, and much of this is due to incentives, such as tax and tariff discounts and long-term contracts. In 2021, the expansion of the Brazilian electricity matrix was

almost 1 GW (957.03 MW). Table 1. Presents a compilation of the main references that present the mechanisms currently applied in developed countries.

5 Conclusions

In the last 20 years, many countries have started to create policies to encourage generation from more sustainable energy sources, creating mechanisms that make the generation, transmission, and consumption of these sources feasible through tax incentives, discounts, and subsidies, among others. Brazil has a lot of potential to expand the participation of renewable sources and already has several strands of incentives in place, only 5 of the 15 mechanisms mentioned in Table 1 are not yet used. However, this does not mean that the current incentives are de-signed in the most efficient way, since the growth of renewable sources in Brazil is, so far, at a slow pace. Some policies are also going out of force, such as the TUSD and TUST. Another mechanism that risks being cancelled is the current exemption from wire usage charges for distributed generation systems, through PL 5829/19. Due to rising costs and public budget constraints, many of the incentive schemes are being phased out in other countries, as well as in Brazil, following a path contrary to the evolution of the energy context towards retrogression. In order to improve the internal policy of incentives for renewable sources, Brazil can expand the projects already in place by increasing fiscal incentives, ex-tending and adding tax exemption on products and technologies related to generation by RES, greater investment in R & D in order to develop national technology and make installations cheaper and also study the implementation of mature mechanisms in other countries, as the sale of carbon credits.

References

1. IEA. IEA. https://www.iea.org/fuels-and-technologies
2. da Costa Gehm, S., Canha, L.N.: Potencial para gerenciamento energético municipal a partir do biogás oriundo de aterros sanitários e da queima de resíduos sólidos urbanos. XXV Sem. Nacional de Produção e Transmissão de Energia Elétrica (2019)
3. Morais, L.C.: Unesp Faculdade De Engenharia Programa De Pós-Graduação Em Engenharia Elétrica Estudo Sobre O Panorama Da Energia Elétrica No Brasil E Tendências Futuras, pp. 1–136 (2015). https://repositorio.unesp.br/bitstream/handle/11449/132645/000852309.pdf?sequence=1&isAllowed=y
4. Montalvão, E., Silva, R.M.D.: Descontos na TUST e na TUSD para Fontes Incentivadas: uma avaliação, p. 57 (2015)
5. Borges, G., Salles, M.B.: A Política de Descontos para as Energias Renováveis no Brasil. 14 ago (2020)

6. Dutra, L., Schwinden, N.B.C., Andrade, S.F.: Future scenarios and trends in energy generation in brazil: supply and demand and mitigation forecasts. J. Cleaner Prod. **103**, 197–210 (2015)
7. BRASIL. CONVÊNIO ICMS 101/97. Brasil (1997). https://www.confaz.fazenda.gov.br/legislacao/convenios/1997/CV101_97
8. BRASIL. CONVÊNIO ICMS 16, DE 22 DE ABRIL DE 2015. Brasil (2015). https://www.confaz.fazenda.gov.br/legislacao/convenios/2015/CV016_15
9. ENGIE. Incentivos governamentais impulsionam a energia fotovoltaica (2021). https://blog-solucoes.engie.com.br/energia-solar/incentivos-governamentais-energia-solar/
10. Maltchik, V.F.S., Silveira, P.A.C.V.D.: Incentivos Fiscais À Energia Fotovoltaica : Um Estudo Comparado Entre Brasil e Alemanha (2020). https://www.pucrs.br/direito/wp-content/uploads/sites/11/2020/04/victoria_maltchik.pdf
11. International renewable energy agency. Renew. Energy Policy Brief Brazil. 1–12 (2015)
12. ABRAGEL. Certificado de Energia Renovável. https://www.abragel.org.br/energia-renovavel/. Accessed 2 Nov 2021
13. INSTITUTO TOTUM. REC Brasil. https://www.institutototum.com.br/index.php/selo/56-certificacao-e-selo-de-energiarenovavel. Accessed 2 Nov 2021
14. BRASIL. REIDI. https://www.gov.br/mdr/pt-br/assuntos/mobilidade-eservicos-urbanos/reidi. Accessed 10 Nov 2021b
15. MME. Energia renovável chega a quase 50% da matriz energética brasileira. Disp. em: <https://www.gov.br/pt-br/noticias/energia-minerais-e-combustiveis/2021/08/energiarenovavel-chega-a-quase-50-da-matriz-eletrica-brasileira-1>
16. Lu, Y., et al.: A critical review of sustainable energy policies for the promotion of renewable energy sources. Sustainability (Switzerland) **12**(12), 1–30 (2020)
17. Jacobsson, S., Lauber, V.: The politics and policy of energy system transformation—explaining the German diffusion of renewable energy technology. Energy Policy **34**(3), 256–276 (2006)
18. Gan, L., Eskeland, G.S., Kolshus, H.H.: Green electricity market development: lessons from Europe and the US. Energy Policy **35**(1), 144–155 (2007)
19. WWF. Além de grandes hidrelétricas (2012)
20. Nicolini, M., Tavoni, M.: Are renewable energy subsidies effective? Evidence from Europe. Renew. Sustain. Energy Rev. **74**, 412–423 (2017)
21. Çiçek, A., et al.: Comprehensive survey on support policies and optimal market participation of renewable energy. Electric Power Syst. Res. **201**, 107522 (2021)
22. Delmas, M.A., Montes-Sancho, M.J.: U.S. state policies for renewable energy: context and effectiveness. Energy Policy **39**(5), 2273–2288 (2011)
23. Washburn, C., Pablo-Romero, M.: Measures to promote renewable energies for electricity generation in Latin American countries. Energy Policy **128**, 212–222 (2019)
24. Zhao, Z.Y., Chen, Y.L., Chang, R.D.: How to stimulate renewable energy power generation effectively? – China's incentive approaches and lessons. Renew. Energy **92**, 147–156 (2016)

A Comparative Study of the Recent A&F Model with Conventional Thermoeconomic Methodologies in the Waste Treatment in a Regenerative Gas Turbine Cogeneration System

Rodrigo Guedes dos Santos[1,2(✉)] , Atilio Barbosa Lourenço[2] ,
Pedro Rosseto de Faria[2,3] , Igor Chaves Belisario[1] , Marcelo Aiolfi Barone[2] ,
and José Joaquim C. S. Santos[2]

[1] Federal Institute of Espírito Santo (IFES), Vitória, Brazil
`rodrigo.guedes@ifes.edu.br`
[2] Federal University of Espírito Santo Federal (UFES), Vitória, Brazil
[3] Federal Institute of Espírito Santo (IFES), Cariacica, Brazil

Abstract. Thermoeconomics is a science that reconciles thermodynamic and economic concepts. It can be divided into three fields of action: cost allocation, diagnosis and optimization. Most thermoeconomicists agree that exergy is the most appropriate thermodynamic magnitude to associate with cost. In some applications, exergy disaggregation is required. Literature shows several thermoeconomic methodologies. Despite the wide use and their respective fields of action, all models have limitations in the dissipative equipment isolation and waste treatment or an increase in complexity in thermoeconomic modeling. In order to fill part of this scientific gap in thermoeconomics, a recent methodology, the A&F Model, is proposed. This new approach disaggregates physical exergy into just two terms, namely Helmholtz energy and flow work. This work presents for the first time the use of this new approach, through a cost allocation, in a cogeneration system with regenerative gas turbine, and compares it with conventional thermoeconomic methodologies.

Keywords: Thermoeconomic Modeling · Waste Cost Allocation · Physical Exergy Disaggregation

1 Introduction

Thermoeconomics is a science that combines thermodynamic and economic concepts and can be divided into three fields of application: cost allocation, diagnosis, and optimization. The way the productive structure is defined (input and output) is a key point in thermoeconomic modeling [1], and one of the best thermodynamic magnitudes to associate with the cost is the exergy [2]. Depending on the type of analysis, different levels of accuracy of the results are required, which means that each thermoeconomic analysis requires a specific level of disaggregation of the components and flows [3].

According to [1], the deeper and more detailed the disaggregation, the clearer the interpretation of the costs obtained and the greater the possibility of applications in theoretical and practical problems. By disaggregating the physical exergy, it is possible to obtain better accuracy of the results in the thermoeconomics [4]. Nevertheless, there is a consequent increase in the complexity of thermoeconomic modeling [5]. In this paper, five thermoeconomic models are studied: E, E^T & E^M [6], H&S [7], UFS [8] and the recent A&F Model [9]. The plant chosen for the analysis allows the approach of a very latent theme in thermoeconomics which is the waste cost allocation.

In order to fill a part of the scientific gap in waste treatment in thermoeconomics, a recent methodology, the A&F Model, has been proposed. This new approach disaggregates the physical exergy into only two terms, namely Helmholtz energy and flow work. This work has chosen the plant used in the CGAM Problem [10] exactly to be able to exemplify how this new methodology treats the residues of a thermal system.

This study presents the use of this new approach, through a cost allocation, in a regenerative gas turbine cogeneration system and compare it with conventional thermoeconomic methodologies highlighting the waste treatment used by each one. The results show that in terms of complexity, the A&F Model is close to the E^T&E^M and H&S Models and specifically in relation to the UFS Model, it shows a reduction in the number of flows, junction-bifurcations, and cost equations, thus highlighting a lower complexity. It also shows that for the A&F Model, the environment acts as a consistent device in the thermoeconomic analyses of cogeneration systems, allowing the proper internalization of the waste of the thermal system.

2   Thermoeconomic Modeling

The thermoeconomic model is accomplished by using Eq. (1) and (2). The resolution of the cost equation set, Eq. (1), is the monetary unit costs of all internal flow and final product. In Eq. (1), Z represents the external hourly cost of the subsystem due to the capital, operation, and maintenance costs of each subsystem (in \$/h); E_F is consumption (kW) and c_F is the monetary unit cost, both from the external fuel exergy. The unknown variables c_{out} and c_{in} are the monetary unit cost of the internal flows at the outlet and at the inlet of each subsystem (in \$/kWh), respectively; and Y_{out} and Y_{in} mean the generic thermodynamic magnitude (power (W), heat exergy (Q), total exergy (E), and physical exergy terms) of the internal flows at inlet and outlet of each subsystem. The solution results in the monetary unit costs of each internal flow and each final product.

$$\sum(c_{out} \cdot Y_{out}) - \sum(c_{in} \cdot Y_{in}) = c_F \cdot E_F + Z \qquad (1)$$

$$\sum(k_{out} \cdot Y_{out}) - \sum(k_{in} \cdot Y_{in}) = k_F \cdot E_F \qquad (2)$$

In Eq. (2), the unknown k_{out} and k_{in} are the exergetic unit costs of the internal flows (output/input) of each subsystem; and the hourly cost of the subsystem, due to the capital cost, operation, and maintenance, must be zero (Z = 0). Since there is no information about the resource, k_F is assumed to be 1.00 kW/kW [3]. The exergetic unit cost of a flow is the amount of external exergy unit required to obtain one unit of this flow, meaning that the exergetic unit cost of a flow is a measure of the thermodynamic efficiency of the production process when producing this flow [3].

3 Physical Structure

Figure 1 represents the cogeneration system with a regenerative gas turbine of the CGAM Problem [10]. The system is composed of: air compressor (AC), regenerator (R), combustion chamber (CC), gas turbine (GT), and recovery boiler (RB). The operating parameters are the same as for the CGAM Problem [10].
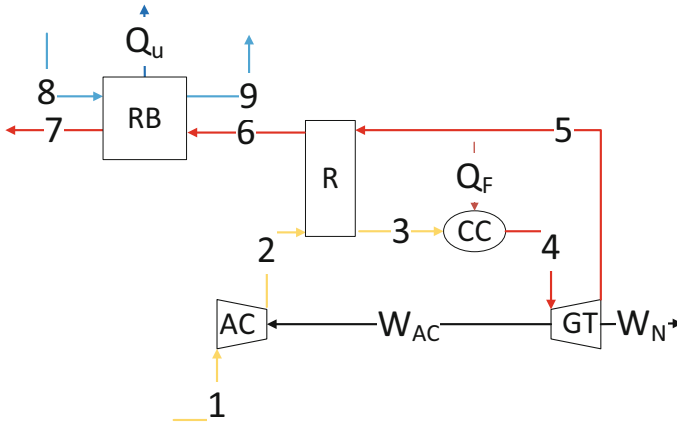

Fig. 1. Cogeneration system with regenerative gas turbine.

4 Thermoeconomic Methodologies

In this work, four conventional methodologies and the recent approach A&F Model are applied. The exergy and monetary unit costs are calculated for all of them.

4.1 A&F Model

The A&F Model [9] is a recent thermoeconomic approach, it was developed with the premise of reducing the complexity and computational efforts compared to other methodologies that are capable of isolating (defining input and output) dissipative equipment, such as a valve. This model also uses the physical exergy disaggregation and the definition of its terms are Helmholtz energy E^A and flow work E^F. They can be estimated, specifically by Eq. (3) and (4), which together with chemical exergy are used to define the productive flows for this model. It is important to highlight that the Helmholtz energy term can be mathematically interpreted as a combination of the internal energy (E^U) and the entropic (E^S) terms. However, it is worth mentioning that this combination is not simply and purely a mathematical algebraic, it presents a consistent thermodynamic concept, characterized by the Helmholtz energy. Figure 2 illustrates the productive diagram for the cogeneration system using the A&F Model. Regarding waste cost treatment, this

methodology uses the environmental device (E) in its modeling. It is worth mentioning that the internalization of waste costs is initially through Helmholtz energy term ($E^A_{1:7}$).

$$\dot{E}^A = \dot{E}^U + \dot{E}^S = \dot{m}.C_v.(T - T_0) - \dot{m}.T_0.C_p.ln\frac{T}{T_0} + \dot{m}.R.T_0.ln\frac{p}{p_0} \tag{3}$$
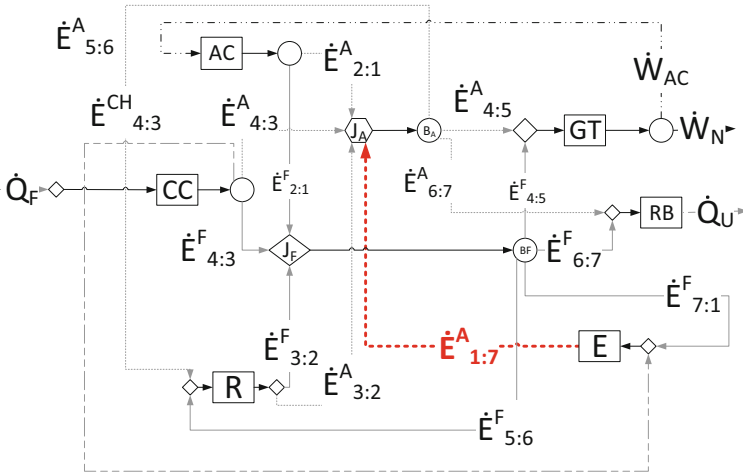
$$\dot{E}^F = \dot{m}.R.(T - T_0) \tag{4}$$

Fig. 2. The A&F Model represented in a productive diagram for the cogeneration system.

4.2 Conventional Methodologies

The conventional methodologies studied in this work are E, $E^T \& E^M$, H&S, and UFS Models. Figure 3 illustrates the productive diagrams for these methodologies, besides highlighting the internalization of waste cost.

5 Results

Figure 4 presents the monetary and exergy unit costs for the five thermoeconomic models applied to the regenerative gas turbine cogeneration system. It can be observed that the results present a linear trend, which implies coherent results from a thermoeconomic point of view. Specifically, in relation to the A&F Model, it is noted that their respective results present a high degree of similarity with the E Model. This is an interesting result since for thermal systems, where dissipative equipment is not present, the E Model is widely used and accepted from the scientific point of view.

Averaging between the extremes arrives at a value of 29.58 and 36.05 ($/MWh) for the monetary unit cost of power and heat, respectively. Analogously, an average value of 1.86 and 2.23 (kW/kW) are reached for the exergy unit cost of power and heat. These values are close to those obtained by the A&F Model, respectively 28.51 and 38.57 ($/MWh) and 1.81 and 2.36 (kW/kW).

E Model

E^T&E^M Model

H&S Model

UFS Model
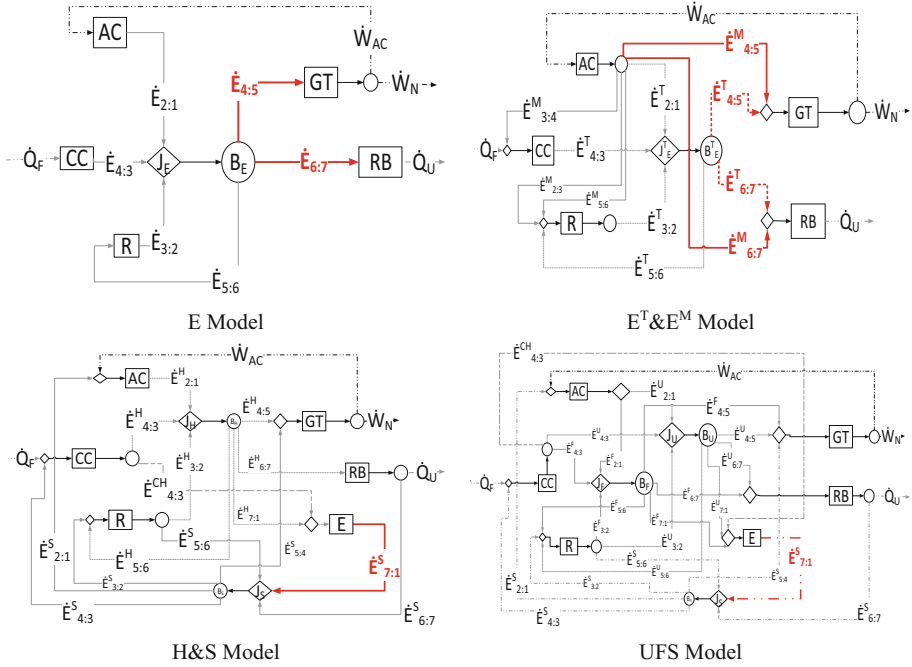
Fig. 3. The conventional methodologies represented in their respective productive diagrams.
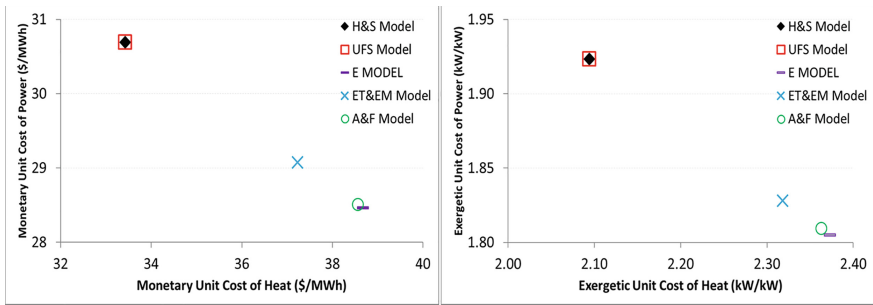
Fig. 4. Monetary and exergetic unit cost obtained by the thermoeconomic methodologies.

6 Conclusions

This work presented the use of a recent approach for exergy disaggregation in a regenerative gas turbine cogeneration system, called the A&F Model, which is a consistent alternative for total disaggregation of the system in thermoeconomic modeling, especially when there are dissipative components and waste in the system under analysis. Nonetheless, it is worth noting that in this work, the focus was directed on waste treatment. The two physical exergy terms in this model have a thermodynamic meaning: Helmholtz energy and flow work. Regarding waste treatment, the A&F Model uses the

environmental device, through its respective product. Its internalization initializes with the Helmontz energy term. The cost results showed a small variation from an average cost value, for both unit costs, which leads to an interpretation of improved precision of the results rather than a large difference between the methodologies regarding waste treatment for this plant. Finally, besides having applied the A&F Model to the regenerative gas turbine cogeneration system and compared its results with conventional methodologies, this work presented this recent approach to disaggregate physical exergy as a coherent and consistent alternative to solve a difficult problem in thermoeconomics related to the waste treatment of thermal systems, besides presenting a lower complexity in thermoeconomic modeling, since the disaggregation of physical exergy is performed in two terms only.

References

1. Lozano, M.A.; Valero, A. Thermoeconomic Analysis of Gas Turbine Cogeneration Systems. ASME, NEW YORK, NY,(USA). 1993, 30, 311–320
2. Valero, A.: Exergy Accounting: Capabilities and Drawbacks. Energy **31**, 164–180 (2006). https://doi.org/10.1016/j.energy.2004.04.054
3. Valero, A.; Serra, L.; Uche, J. Fundamentals of Exergy Cost Accounting and Thermoeconomics. Part I: Theory. *J Energy Resour Technol* **2006**, *128*, 1–8, doi:https://doi.org/10.1115/1.2134732
4. Lazzaretto, A., Tsatsaronis, G.: SPECO: A Systematic and General Methodology for Calculating Efficiencies and Costs in Thermal Systems. Energy **31**, 1257–1289 (2006). https://doi.org/10.1016/j.energy.2005.03.011
5. Arena, A.P., Borchiellini, R.: Application of Different Productive Structures for Thermoeconomic Diagnosis of a Combined Cycle Power Plant. Intl. J. of Thermal Sciences **38**, 601–612 (1999). https://doi.org/10.1016/S0035-3159(99)80040-3
6. Frangopoulos, C.A.: Application of the Thermoeconomic Functional Approach to the CGAM Problem. Energy **19**, 323–342 (1994). https://doi.org/10.1016/0360-5442(94)90114-7
7. Santos, J.J.C.S., et al.: On the Negentropy Application in Thermoeconomics: A Fictitious or an Exergy Component Flow? Intl. J. of Thermodynamics **12**, 163–176 (2009)
8. Lourenço, A.B., Santos, J.J.C.S.; Donatelli, J.L.M. Thermoeconomic modeling of a simple heat pump cycle: an alternative approach for valve isolation. In: Mitrović, D., Laković, M. (eds.) Proceedings of the 15th Symposium on Thermal Science and Engineering Serbia; Sokobanja, Serbia. SimTerm 2011, pp. 453–446 (2011)
9. dos Santos, R.G., Lourenço, A.B., de Faria, P.R., Barone, M.A., Santos, J.J.C.S.: A new exergy disaggregation approach for complexity reduction and dissipative equipment isolation in thermoeconomics. Entropy **24**, 1672 (2022). https://doi.org/10.3390/e24111672
10. Valero, A., et al.: CGAM problem: definition and conventional solution. Energy **19**, 279–286 (1994). https://doi.org/10.1016/0360-5442(94)90112-0

Exergetic Analysis of a Double Flash Geothermal Plant Integrated with a Central Solar Receiver

Orlando Anaya-Reyes, David A. Rodriguez-Alejandro$^{(\boxtimes)}$![ORCID],
Alejandro Zaleta-Aguilar ![ORCID], and Sergio Cano-Andrade ![ORCID]

Department of Mechanical Engineering, Universidad de Guanajuato, 36885 Salamanca, GTO,
Mexico
`o.anaya.reyes@ugto.mx`

Abstract. A double-flash geothermal Rankine cycle integrated with a central solar receiver is proposed. The solar field is analyzed by optimizing the radiation flux in the receiver, reaching values of 555.40 kW/m^2 for a 44.32 m tower, with a receiver of 3.90 m high by 4.99 m in diameter, and a total of 417 heliostats. The cycle is analyzed by optimizing its power delivered, based on the separation pressures of both flash chambers, reaching a power of 25734 kW when the pressures are 8.668 and 2.768 bar, respectively. Results show that this type of systems are a good alternative to reduce the dependence on fossil fuels.

Keywords: Solar energy · Geothermal energy · Exergy · Optimization

1 Introduction

To reduce dependence on fossil fuels, the International Energy Agency (IEA) tries to reduce its consumption from 81.1% registered during 2016 to 68.1% for the year 2030 [1]. Geothermal and solar energy has high potential as a substitute for fossil fuels due to its low carbon emissions and sustainability. In 2014, Zhou [2] investigated a hybrid geothermal-solar plant of parabolic troughs integrated with an organic Rankine cycle (ORC), showing how the output power increases between 22 and 78% depending on the size of the solar field. Astolfi *et al.* [3], combined an ORC geothermal plant with a concentrating solar plant, obtained a reduction of 54 to 60% in the cost of energy. Mir *et al.* [4] developed an evaluation model for geothermal-solar systems, achieving a reduction in the consumption of the geothermal resource of approximately 10%. Lentz *et al.* [5], modeled two strategies for the combination of a flash geothermal system with parabolic collectors in Mexico, increasing the quality of the steam by 10%. This paper evaluates the integration of a double flash plant with a central solar receiver, using specialized software to determine the appropriate size and the optical performance of the solar field for environmental conditions of Baja California, Mexico.

2 System Description

The system consists of a double flash geothermal Rankine cycle based on the config-
uration proposed by Cardemil *et al.* [6] integrated with a central solar receiver. The
geothermal fluid passes through a flash process, where the saturated vapor is separated
from the saturated liquid. The liquid is heated using a heat exchanger to produce an addi-
tional percentage of saturated vapor that is again separated and mixed with the vapor
coming from the first flash chamber, which is superheated in another heat exchanger
before expanding in a high-pressure turbine. The remaining liquid is conducted to a
second flashing process. Through an additional heat exchanger, the resulting saturated
steam is superheated and mixed with the steam that comes out of the high-pressure tur-
bine to enter a low-pressure turbine Finally, the steam is condensed and cooled before
returning to the production well (Fig. 1).

Fig. 1. System layout.

The main operating parameters to model the Rankine cycle and the solar field are
shown in Table 1, selecting the Valley of Mexicali, Baja California, Mexico as a case
study. The mathematical model considers:

- Components operate under steady state conditions.
- The pressure drops are negligible in the heat exchangers.
- Changes in kinetic and potential energy are negligible.
- The geothermal fluid has the same thermodynamic properties as water.

Table 1. System parameters

Parameter	
Direct normal irradiation (DNI)	940 W/m^2
Heliostat size	12 × 12 m
Heat transfer fluid (HTF)	60% NaNO$_3$ - 40% KNO$_3$
Heat exchanger effectiveness (ε)	70%
Dry steam isentropic efficiency	85%
Extraction enthalpy	1520 kJ/kg
Condensing temperature	50 °C

3   Mathematical Model and Optimization

The thermodynamic and exergetic model of the geothermal Rankine cycle are developed using Engineering Equation Solver (EES®) by applying mass, energy and exergy balances respectively, as:

$$\sum_i \dot{m}_i - \sum_o \dot{m}_o = 0 \tag{1}$$

$$\dot{Q} - \dot{W} + \sum_i \dot{m}_i(h_i) - \sum_o \dot{m}_o(h_o) = 0 \tag{2}$$

$$\sum_j \dot{E}_{q,j} - \sum_k \dot{E}_{w,k} \sum_i \dot{m}_i(e_i) - \sum_o \dot{m}_o(e_o) - \dot{E}_d = 0 \tag{3}$$

The cycle was optimized by the genetic algorithm of EES®, establishing as objective function the net power of the plant with limits defined in Table 2, and subject to restrictions established by the balances of mass, energy, and exergy.

$$Max\left[\dot{W}_{net}\left(\overrightarrow{x}\right)\right] \tag{4}$$

$$\dot{W}_{net} = \dot{W}_{TAP} + \dot{W}_{TBP} \tag{5}$$

$$\overrightarrow{x} = \left(P_{sep1}, P_{sep2}\right) \tag{6}$$

The solar field was optimized by the COBYLA algorithm of Solar Power Tower Integrated Layout and Optimization Tool (SolarPILOT®). The objective function is:

$$Z(\overrightarrow{x}) = \frac{C_{tot}(\overrightarrow{x})}{E_{an}(\overrightarrow{x})}\left(1 + \left(1 - min\left[\frac{\dot{q}_{cs}(\overrightarrow{x})}{\dot{q}_{cs,dis}(\overrightarrow{x})}\right]\right)P\right) \tag{7}$$

where $\overrightarrow{x}$ is the set of variables, C_{tot} is the total cost of the plant, E_{an} is the expected annual energy production of the field, $\dot{q}_{cs}$ is the real thermal power of the field, $\dot{q}_{cs,dis}$ is the thermal power of the field and P is a penalty constant.

Table 2. Operating ranges of the design variables.

Parameter	Inferior limit	Superior limit
First separation pressure	5 bar	15 bar
Second separation pressure	1.5 bar	4.5 bar

4 Results

In order to compare the performance of the plant working individually and integrated with the solar receiver, the net power of the plant is maximized based on the separation pressures. The results are shown in Table 3.

Table 3. Rankine Cycle Optimum Values.

Parameter	Individual Rankine cycle	Hybrid Rankine cycle
First separation pressure	8.28 bar	8.66 bar
Second separation pressure	1.80 bar	2.76 bar
Output power	20807 kW	25734 kW
Thermal efficiency	14.57%	14.97%
Exergetic efficiency	45.81%	41.21%

Figure 2 shows the effect of both separation pressures on the output power, which reaches values of 25734 kW. Since the ranges in the separation pressure of both chambers are different, one of these two will be the one that influences the maximization of the output power; i.e., once the separation pressure in the first chamber is defined, the second separation pressure does not show a significant variation in the output power.

Figure 3a shows a comparison between the thermal efficiency and the exergetic efficiency when the plant is working individually and when it is integrated with the solar receiver. It is observed that the thermal efficiency shows similar values for both cases; while the exergetic efficiency is lower when the hybrid system is considered. Figure 3b shows a comparison of the exergy destructions that occur in the main components of each system, with the solar field showing the highest exergy destruction ratio followed by the condenser and the first flashing process. The components with a lower destruction rate are the low-pressure turbines and the second flashing process. In the case of the individual cycle, it does not present the destruction of the field or of the exchangers as they do not have these devices.
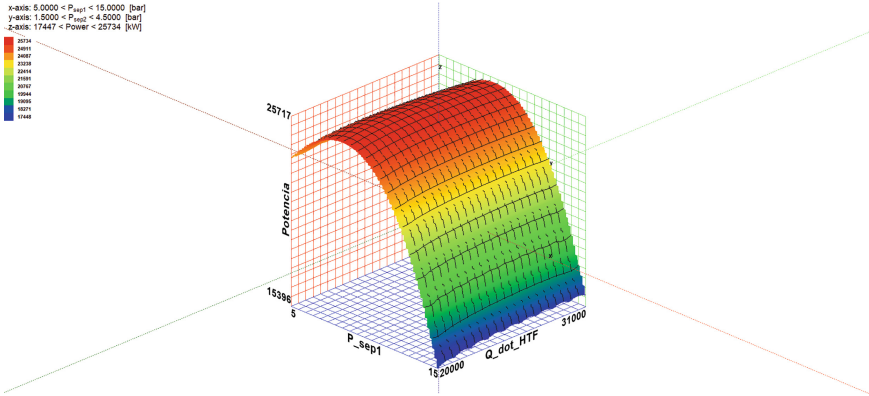
Fig. 2. Exergetic efficiency as a function of separation pressures.
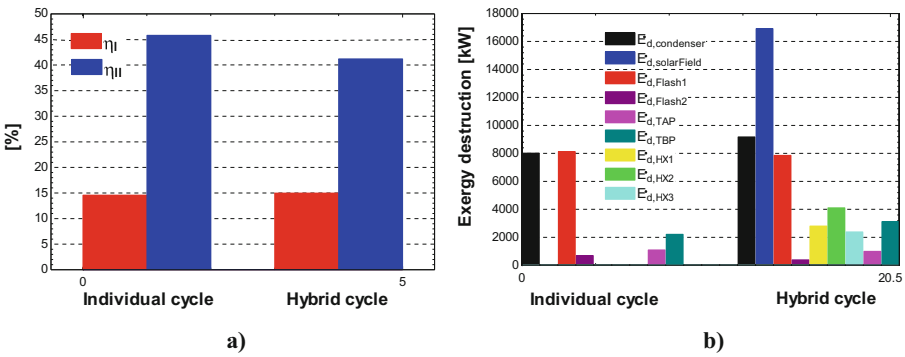
Fig. 3. Comparison between a) Thermal and exergetic efficiencies. b) Exergy destruction rates.

The results of the optical optimization are shown in Table 4. It is observed that a flux of 555.40 kW/m^2 is reached for a tower 44.32 m high, with a receiver 3.90 m high by 4.99 m in diameter and a total of 417 heliostats. With these values, the configuration of the resulting solar field is shown in Fig. 4a, where its annual optical efficiency is observed, reaching an average value of 60.02%, with a maximum value of 87% and a minimum value of 40.1%. One of the most important results in the design of these fields is the flow profile or solar "spot", which is shown in Fig. 4b, and represents the flow distribution that each one of the heliostats projects onto the surface of the receiver, preferring that it be as uniform as possible to concentrate the energy more efficiently.

Table 4. Solar field Optimum Values.

Parameter	
Heliostats	417
Tower height	44.3 m
Receiver height	3.9 m
Receiver diameter	4.9 m
Optical efficiency	60.02%
Receiver incident flux	555.4 kW/m^2

a)   b)
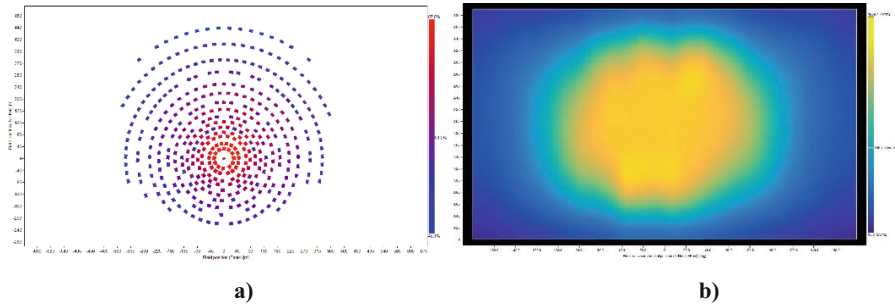
Fig. 4. a) Optimum solar field geometry. b) Receiver flux profile

5   Conclusions

In this work, the integration of a double flash geothermal Rankine cycle with a central tower solar field was analyzed in order to compare their performance individually and together. The results show that assisting the geothermal system with solar energy to superheat the inlet steam in the turbines can considerably increase power production. Despite the fluctuation of the solar resource, the present work does not contemplate a thermal storage system due to the large additional costs involved, since in this case, the solar resource is used only as an auxiliary to improve performance, but its variation is not significant as the geothermal deposit is the main source of energy. These types of combinations are a viable alternative in the Mexican energy market, due to its high solar incidence, as well as its location in the "*Pacific ring of fire*", an area with great geothermal activity.

References

1. Colgan, J.D.: The international energy agency. Challenges for the 21st Century. GPPi Energy Policy Paper, vol. 6 (2009)
2. Zhou, C., Doroodchi, E., Moghtaderi, B.: An in-depth assessment of hybrid solar–geothermal power generation. Energy Convers. Manage. **74**, 88–101 (2013)

3. Astolfi, M., Xodo, L., Romano, M.C., Macchi, E.: Technical and economical analysis of a solar–geothermal hybrid plant based on an organic Rankine cycle. Geothermics **40**(1), 58–68 (2011)
4. Mir, I., Escobar, R., Vergara, J., Bertrand, J.: Performance analysis of a hybrid solar-geothermal power plant in northern Chile. In: World Renewable Energy Congress-Sweden; 8–13 May; 2011; Linköping; Sweden. No. 57, pp. 1281–1288. Linköping University Electronic Press (2011)
5. Lentz, Á., Almanza, R.: Solar–geothermal hybrid system. Appl. Therm. Eng. **26**(14–15), 1537–1544 (2006)
6. Cardemil, J.M., Cortés, F., Díaz, A., Escobar, R.: Thermodynamic evaluation of solar-geothermal hybrid power plants in northern Chile. Energy Convers. Manage. **123**, 348–361 (2016)

Cavitation Analysis in Kaplan Turbines at the Yacyretá Hydropower Plant

Liz Esquivel Maldonado[1], Vivian González Benitez[1], Fernando Arenas Aguilera[1], Elías Espínola Fleitas[1], Jovan Toews Doerksen[1], Patrik Kehler Ratzlaff[1], Ferdinand Meixner Suárez[1], Herminia Duarte Cabañas[2], Marcelo Subeldía Duré[3], and Jorge Kurita Nagasawa[1(✉)]

[1] Department of Mechanical and Electromechanical Engineering, Faculty of Engineering, Universidad Nacional de Asunción, San Lorenzo 2160, Paraguay
jkurita@fiuna.edu.py
[2] Graduate School, Universidad Nacional de Itapúa, Encarnación 6000, Paraguay
[3] Yacyretá Hydropower Plant, Ayolas 4830, Paraguay

Abstract. The cavitation effect occurred during the operation of hydraulic machinery is a widely known and thoroughly studied phenomenon. This research work presents a case study of cavitation analysis that was conducted on the Kaplan turbines at the Yacyretá hydropower plant. This effect was observed during scheduled maintenance routines of the power generating units. These turbines belonged to the Entidad Nacional Yacyretá (EBY) [1]. The cavitation phenomenon could cause significant damage to blades and other turbine components under certain operating conditions [2].

Keywords: Kaplan Turbine · Cavitation · CFD Analysis · EBY

1 Introduction

Paraguay is one of the most remarkable countries in the South American continent when it comes to clean and renewable energy generation. Paraguayan hydropower plants satisfy the entirety of the local energy demand, as well as a significant percentage of the energy demand in two of its neighboring countries: Argentina and Brazil. It is for this reason that hydropower plants play an essential role in the socio economical development of Paraguay.

The Yacyretá Hydropower Plant, also known as Entidad Binacional Yacyreta (EBY) in Spanish, is located on the Paraná River, this is, the border between Paraguay and Argentina. This plant counts with 20 generating units equipped with vertical axis Kaplan turbines, and it has an average gross electricity yearly generation of 20.000 GWh.

Kaplan turbines are highly efficient axial flow turbines, and its ideal application is in projects with a large flow volume and a small net head.

The main advantage of Kaplan turbines, when compared to other types of turbines, is the possibility to automatically adjusting blade attack angles, during machine operation, to adjust to the optimal efficiency angle, in function to the energy demand.

Cavitation has been a subject of study for decades, its effect brings erosion and chemical corrosion on the blade surfaces and other components. This in turn decreases efficiency and generates noise with intense vibrations [3]. These are few of the other consequences cavitation effects may arise. Therefore, in order to obtain optimal efficiency and reduce maintenance cost;, in practice, turbines are allowed to operate under controlled cavitation conditions, in which the damage caused to the blades can be easily repaired during scheduled maintenance operations, keeping generating units operating as continuous as possible.

Since the turbines of this case study are not exempt from the cavitation phenomenon, different manufacturer guaranteed "safe operation" points. In this work, these points were analyzed through the use of Computational Fluid Dynamics.

2   Materials and Methods

2.1   Model and Mesh Configuration

The CAD software used to design the Kaplan turbine was Solid Edge. This model was provided by the technical department team at the Yacyretá Hydropower Plant to the Mechanical Engineering Department of the Faculty of Engineering at Universidad Nacional de Asunción.

The analysis was performed by first establishing an internal flow of water in the computational domain, which includes the turbine pre-distributor and the top region of the draft tube, as shown in Fig. 1.
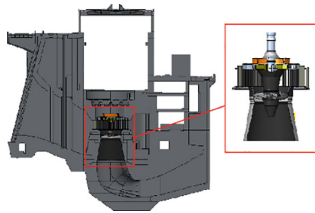
Fig. 1. Control volume adopted for the internal flow analysis. Its position in the CAD model is outlined in red.

An academic version of the flow simulation software SolidWorks was employed to conduct this part of the analysis. The main reason this software was chosen for the analysis was the simplicity it offers when it comes to setting up boundary conditions. This is useful given that technicians and engineers from the plant have expressed their interest in testing different operating points themselves in the future once the model is validated.

The mesh configuration was set up as a combination of two different mesh types: a level 5 global mesh for the entire computational domain, along with a level 3 local mesh located on the top and bottom blade surfaces.

This configuration was applied in order to obtain sufficient finite volume elements in critical regions, like the turbine blades and rotor. This is critical to obtain a reliable and accurate results.

2.2   Simulation Parameters and Considerations

In order to perform as much realistic simulation as possible, real turbine operating conditions were adopted. The applied conditions were the following:

a) The working fluid employed for the simulation was water at a temperature of 30 °C.
b) The operating points chosen for the analysis are located within the region delimited by the enclosed polygon shown in the Prototype Collinear Hill Diagram provided by the turbine manufacturer. This region is also known as the continuous or warranted operation region. The diagram parameters are detailed in Fig. 2 but are presented in dimensionless form for copyright reasons.
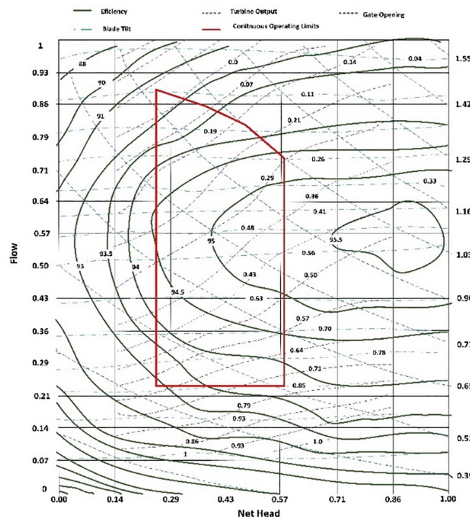
Fig. 2. Prototype Collinear Hill Diagram provided by the turbine manufacturer with dimensionless parameters

c) The inlet condition is the absolute pressure of a point located on the midplane between the pre-distributor and the turbine (Level 52 msnm), and the outlet condition is the operating volume flow of the turbine.

d) The selected turbine operating points are detailed in Table 1. The pressure and head values were obtained during on-site measurements by plant personnel, and the volume flow values were obtained from the Prototype Collinear Hill Diagram from Fig. 2.

2.3   Equations Used

In this section we will detail the analytical process used to obtain the boundary conditions for each operating point, i.e., pressures and volume flows.

   Moreso, a cavitation analysis using Thoma's cavitation coefficient is included.

Table 1. Selected turbine operating points

Operating Point	Generated Power P_G [MW]	Net Head H (mca)	Flow Volume $Q = \left(\frac{m^3}{s}\right)$	Pre-distributor Pressure p_2[Pa]
1	75	23,27	350	404.734,39
2	120	23,04	620	404.244,07
3	128	23,01	678	404.018,53
4	135	22,99	740	403.851,82
5	145	22,987	770	403.655,69
6	155	21,90	786	403.420,42

2.3.1 Determination of the Turbine Operating Point and the Pre-distributor Pressure

For the calculation of pressure p_2 at the computational domain inlet, Bernoulli's Eq. (1) [3] was employed between points 1 and 2. Point 1 is located on the reservoir level of the dam and point 2 is located on the pre-distributor midplane inside the semi-spiral chamber.

$$\frac{p_1}{\rho g} + z_1 + \frac{V_1^2}{2g} - H_{r1-2} = \frac{p_2}{\rho g} + z_2 + \frac{V_2^2}{2g} \tag{1}$$

The density and water saturation pressure employed are, respectively, 995,65 [kg/m^3] and 4.246,7 [Pa]. The acceleration of gravity at this location is of 9,7912 [m/s^2].

2.3.2 Thoma's Cavitation Coefficient

As a way to verify the accuracy of the results obtained from the CFD simulations at the analyzed operating points, cavitation coefficients or Thoma coefficient σ were calculated. The formula is detailed in Eq. (2) [4].

$$\sigma = \frac{\frac{(p_{atm}-p_s)}{\rho g} - H_s}{H} \tag{2}$$

For the studied turbines, the suction height is the height difference between the centerline of the impeller, located at level 48,00 msnm, and the restitution head.

The results obtained from Eq. (2) are then compared to the sigma value of the plant σ_{plant} of the original project, equal to 0,68.

The criteria adopted for the analysis is the following: if the resulting Thoma coefficient for a specific operating point is lower than the project value σ_{plant}, this would hint the presence of cavitation in the turbine.

The cavitation coefficients for each operating point are detailed in Table 2.

Table 2. Cavitation coefficient at operating points

Operating Point	Net Head H	Restitution Head N_{REST} [msnm]	Suction Height H_s	Thoma's Coefficient σ
1	23,27	59,75	−11,75	0,870
2	23,04	59,75	−11,75	0,944
3	23,01	59,757	−11,757	0,956
4	22,99	59,749	−11,749	0,965
5	22,97	59,742	−11,742	0,979
6	22,90	59,75	−11,75	0,995

3   Results

In Fig. 3, CFD simulation results for Table 1 operating points can be observed. All images show pressure distribution on the blades on the low-pressure side of the turbine.
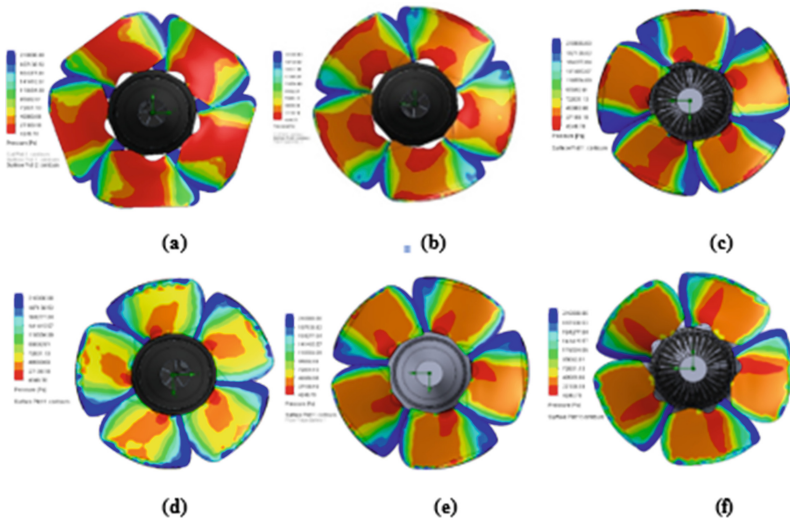
Fig. 3. Pressure distribution in blades on the low-pressure side of the turbine (a) 75 MW – Point 1, (b) 120 MW – Point 2, (c) 128 MW – Point 3, (d) 135 MW – Point 4, (e) 145 MW – Point 5 and (f) 155 MW – Point 6.

All results obtained from the simulations suggest the absence of cavitation for the points inside the safe operating zone warranted by the turbine manufacturer.

These results coincide with the estimated cavitation coefficients calculated previously.

4 Conclusions

Through this research work the CFD results, using CAD model provided by EBY, was validated. This model, along with the computational software Solidworks Flow Simulation, showed reliable results on the study of cavitation phenomena in these turbines. This proved to be a very useful tool for the future analysis of a wider range of turbine operating points, especially by the power plant operators.

Furthermore, the analytical results and the results obtained through the use of CFD simulations demonstrated that, effectively, the analyzed operating points correspond to the safe operating points warranted by the manufacturer.

References

1. Website - Entidad Binacional Yacyretá (2022). https://www.eby.gov.py/
2. Moll, F., Manuele, D., Coussirat Núñez, M.G., Guardo Zabaleta, A.D.J., Fontanals García, A.: Caracterización del tipo de cavitación mediante dinámica computacional de fluidos para posteriores aplicaciones al estudio experimental del daño por cavitación. In Mecánica computacional, vol. 6, pp. 435–450 (2011)
3. Hewitt, P.G.: Bernoulli's principle. Sci. Teach. **71**(7), 51 (2004)
4. Mataix, C.: Mecánica de fluidos y máquinas hidráulicas. No. 620.106 M38 2012. Jharkhand, India: Harla (1982)

Three-Stage Combustion Modeling of a Binary Mixture-Fueled CI CRDI Engine

Luis Tipanluisa[1,2](✉) ⓘD, José López-Martínez[1] ⓘD, Jesús Casanova[1] ⓘD, and Natalia Fonseca[1] ⓘD

[1] INSIA, Universidad Politécnica de Madrid, 28031 Madrid, Spain
luis.tipanluisa@espoch.edu.ec

[2] Faculty of Mechanical, Esc. Sup. Politécnica de Chimborazo, 060155 Riobamba, Ecuador

Abstract. The global trend towards stricter vehicle emission standards requires more knowledge about the use of renewable fuels to design strategies to reduce the use of non-renewable fossil fuels and the environmental impacts of road transport vehicles equipped with Diesel engines. In this study, a simple phenomenological model with three combined Wiebe functions is used to describe the main injection heat release rate of an unmodified heavy-duty diesel engine fueled with binary blends of n-butanol (up to 20% by volume) with diesel fuel. Conventional diesel was used as the reference fuel to compare combustion characteristics with the binary blends (DBu5, DBu10 and DBu20). The results show that the apparent heat release rate (*AHRR*) calculated from the model is in good agreement (RMSE ≤ 3.80 J/°CA) with the experimental values. The maximum *AHRR* values (J/°CA) for the fuel blends DBu5, DBu10, DBu20 and the reference diesel were 220.7, 219.1, 211.8 and 217.7 respectively.

Keywords: Diesel/n-butanol blends · Single-zone combustion · Wiebe function

1 Introduction

The growing problems of environmental pollution and global warming have been a concern for governments and other social institutions for the past decades. Emissions from the transportation sector are estimated to be one of the main sources of air pollution affecting human health and the environment [1, 2]. In addition, the global trend to adopt stricter vehicle emission standards [3, 4] makes it necessary to consider the possibility of using alternative environmentally friendly fuels to replace fossil diesel [5].

The use of simple combustion models, such as the Wiebe function [6], to analyze or predict the combustion process can accelerate knowledge and help optimize engine performance with alternative fuels. The diesel combustion phenomenon is usually divided into three phases, namely, premixed combustion, diffusion combustion, and late combustion phase [7]. Each of these phases has a different combustion rate, so no single Wiebe function can be applied for the characterization of the entire combustion process [6]. Serrano et al. [8] simulated the premixed, diffusion, and late combustion phases of

a turbocharged diesel engine by combining three Wiebe functions. Xu et al. [9] used the triple Wiebe function (to represent the premixed, main, and late combustion phases) and found that the triple Wiebe function was more accurate and preferable in terms of predicting the evolution of the mass fraction burned. A similar observation was made by Awad et al. [10] who experimentally studied the three combustion phases of a diesel engine fueled with diesel and biodiesel.

This study models the experimental data of an unmodified four-cylinder Diesel engine consuming diesel/n-butanol blends using a single zone combustion model along with the modified triple Wiebe equation.

2   Materials and Methods

2.1   Experimental Setup

The experimental setup consists of an engine (Table 1), dynamometer control unit, fuel metering unit, eddy current dynamometer, in-cylinder pressure recording unit and data acquisition system.

Table 1. Engine specifications.

Items	Value
Engine Type	Common rail turbo charged with intercooler
Number of cylinders	4 in-line
Displacement (cm^3)	4462
Bore (mm)	107
Stroke (mm)	124
Compression ratio	17.3:1
Rated Power	135 kW/2300 rpm
Rated torque	700 Nm/1200–1600 rpm
After-treatment system	SCR

In-cylinder pressure data acquisition was performed using a combustion analysis system (KiBox) consisting of an AVL GH14D cylinder pressure transducer, a charge amplifier, and a crankshaft angle adapter. Data were collected in KiBox for 100 consecutive cycles with a crankshaft angle resolution of 0.1°CA. The engine was preconditioned for 10 min following the procedure established in regulation 49 [11]. Then, it was run for the prescribed time in mode 11 of the World Harmonized Stationary Cycle at the speed of 1260 rpm and 50% load. All fuels were tested three times to ensure that the results were sufficiently repeatable.

Table 2. Physical and chemical properties of analyzed fuels.

Property	Methods	Diesel	Butanol	DBu5	DBu10	DBu20
Density (kg/m^3)	ASTM D 4052	844.1	813.4	841.4	840.8	838.9
Kinematic viscosity at 40 ºC (mm^2/s)	ASTM D 445	2.856		2.825	2.637	2.520
Cetane number	ASTM D613	51.7		50.3	49.1	46
Flash point (ºC)	ASTM D93	62.5		40.5	39	37.5
Low Heating Value (MJ/kg)	UNE 51123	43.828	35.744	43.488	43.029	42.135
C (wt.%)[a]		86.48	61.68	84.95	84.26	81.92
H (wt.%)[a]		12.83	12.33	12.57	12.73	12.57
N (wt.%)[a]		0.03	0.03	0.04	0.04	0.04
O (wt.%)[a]		0.66	25.96	2.44	2.97	5.47

[a]Obtained from elemental analysis

2.2 Fuels

Four fuels were tested. Pure diesel (called Diesel) as reference, and three binary blends: DBu5/10/20; with 5%, 10% and 20% n-butanol added to neat diesel (Table 2).

2.3 Wiebe Function for Combustion Model

The Wiebe function represents the evolution of the fuel burned fraction during combustion phenomena [7, 10, 12]. The triple Wiebe function used in this study is Eq. (1).

$$X_b(\theta) = \sum_{i+1}^{3} \frac{1 + sign(\theta - \theta_i)}{2} \beta_i \left\{ 1 - exp\left[-a_i \left(\frac{\theta - \theta_i}{\Delta \theta_i} \right)^{m_i + 1} \right] \right\} \quad (1)$$

where for $\theta > \theta_i$; $sign(\theta - \theta_i) = 1$, else. $sign(\theta - \theta_i) = -1$; $\theta\_i =$ crank angle at which ith phase of combustion starts; $\Delta\theta_i =$ combustion duration of ith phase of combustion; $a_i =$ efficiency factor for the ith phase of combustion; $m_i =$ form factor for the ith phase of combustion; $\beta_i =$ total burn fraction for the ith phase of combustion.

The model approximation *AHRR* compared with experimentally calculated *AHRR*. Equation (2) was used to predict the gross apparent heat release rate (Q_{ch}) [7, 12].

$$\frac{dQ_{ch}}{d\theta_{model}} = \frac{dX_b(\theta)}{d\theta} m_f \cdot LHV_{fuel} \cdot \eta_{comb} \quad (2)$$

where X_b (θ) is the burn fraction at a particular crank angle (θ) predicted using triple Wiebe function, m_f is the fuel consumption per cycle (g), LHV_{fuel} is the lower heating value of fuel (J/g), η_{comb} is the combustion efficiency [7].

The modeled heat release rate data were used to predict in-cylinder pressure using Eq. 3 [12] derived from the analysis of the first law of thermodynamics.

$$p_{i+i} = p_i + \frac{\frac{\Delta Q_n}{\Delta \theta} - \left(\frac{\gamma}{\gamma - 1}\right) p_i \frac{\Delta V}{\Delta \theta}}{\left(\frac{1}{\gamma - 1}\right) V} \Delta \theta \tag{3}$$

V is the in-cylinder volume, γ is the specific heat ratio, p is the in-cylinder pressure.

3 Results and Discussion

Figure 1 shows the comparison between experimental and simulated in-cylinder pressure values for diesel fuel. The combustion model was validated using the fitted Wiebe function to estimate the heat release rate, this rate was used to predict the in-cylinder pressure during the combustion process. The accuracy of each format of the triple Wiebe function was evaluated using the root-mean-square error ($RMSE$) to compare the predicted heat release rate and in-cylinder pressure to the experimental data. The RMSE values determined are ≤ 1.2 bar for all fuels. The max. in-cylinder pressure values (bar) for fuel DBu5/10/20 and diesel were 110.2, 111.0, 112.2 and 111.1 respectively. The max.in-cylinder temperatures (°C) were 2265, 2256, 2256 and 2262.
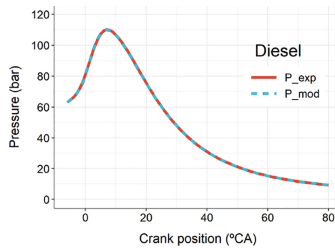
Fig. 1. Experimental vs. model pressure for reference diesel fuel.

The parameters of the Wiebe triple function obtained by curve fitting of the experimental data on the combustion fraction are given in Table 3. The form factor values in the first stage (m_1) of combustion are significantly larger than those in the second stage (m_2) for diesel and binary blends. This is because the initial combustion is slower during the start of combustion, while the initial combustion is faster during the second stage of combustion, which is obvious from the nature of premixed combustion in the IC engine [10]. Moreover, the Wiebe triple function predicted the mass fraction burned (X_b) with good accuracy ($R^2 = 0.99$).

Figure 2 and 3 show the X_b and $AHHR$ profiles for all fuels, respectively. The $AHRR$ calculated with the model is in good agreement with the experimental $AHRR$ ($RMSE \leq 3.80$ J/°CA). The low n-butanol contents in the binary mixture do not show considerable variations in the combustion process. It is important to note that the DBu20 blend leads to a slower initial combustion (Table 3) due to the lower CN of n-butanol.

Table 3. Triple Wiebe function parameters.

Fuel	Start of each burn stage			Burn fraction			Combustion duration			Form factors			Efficiency factors			R^2
	θ_1	θ_2	θ_3	β_1	β_2	β_3	$\Delta\theta_1$	$\Delta\theta_2$	$\Delta\theta_3$	m_1	m_2	m_3	a_1	a_2	a_3	(%)
Diesel	−8.1	−0.53	12.38	0.45	0.51	0.04	14.9	43.4	67.1	1.56	0.13	1.77	4.23	4.50	2.63	99.9
Bu5D	−8.1	−0.48	12.47	0.45	0.52	0.03	14.8	43.7	67.3	1.53	0.10	2.05	4.27	4.46	2.61	99.9
Bu10D	−8.1	−0.43	10.01	0.49	0.48	0.03	14.6	42.7	68.4	1.62	0.17	1.72	4.36	4.59	2.48	99.9
Bu20D	−8.1	−0.42	13.80	0.49	0.49	0.02	14.7	43.6	67.2	1.57	0.13	2.16	4.33	4.47	2.62	99.9

The maximum AHRR value for diesel was 217.7 J/ºCA, which decreased to 211.8 J/ºCA when adding n-butanol (DBu20 fuel blend) due to the lower calorific value of the n-butanol blended fuel [13]. The maximum AHRR values of DBu5 (220.7 J/ºCA) and DBu10 (219.1 J/ºCA) are slightly increased without considerable variations, due to the proper atomization and air/fuel mixing of oxygenated fuels with n-butanol [14].

The combustion starts earlier and has a shorter ignition delay (6.1°CA) for diesel compared to DBu20 (7.1°CA). The addition of n-butanol increases the ignition delay from 6.1°CA to 7.1°CA. This is expected because n-butanol has a lower cetane number than diesel [15]. With the use of DBu5 and DBu10 blends the effect on ignition delay is less evident, with values of 6.1°CA and 6.7°CA, respectively.
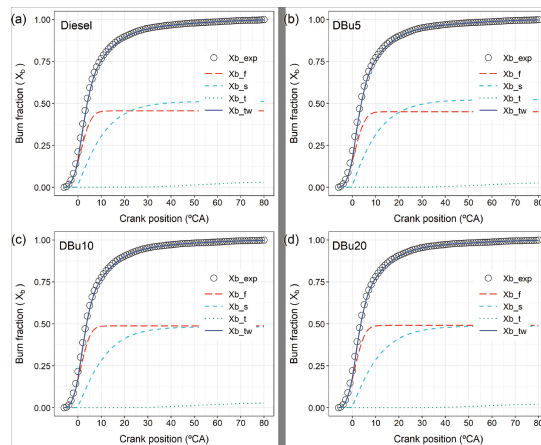
Fig. 2. Experimental vs. model Burn faction (X_b) [Xb_exp – experimental burn fraction, Xb_tw – burn fraction fitted applying triple Wiebe function, Xb_f – burn fraction of first phase, Xb_s – burn fraction of second phase, Xb_t – burn fraction of third phase] for all fuels.
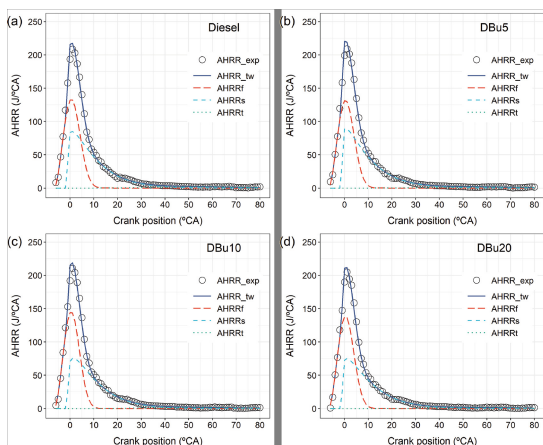
Fig. 3. Experimental vs. model Apparent heat release rate (*AHRR*) [*AHRR_exp* – experimental *AHRR*, *AHRR_tw* – AHRR calculated applying triple Wiebe function model] for all fuels.

4   Conclusions

The zero-combustion model using Wiebe's triple combustion fraction predicted the AHRR data with good accuracy for all fuels. The results show that the DBu5 and DBu10 blends did not alter the peak in-cylinder pressure and peak apparent heat release rate (AHRR) values, while slightly decreasing the peak in-cylinder temperature, with no significant changes in ignition delay and combustion duration. The DBu20 blend has no relevant variations in peak in-cylinder pressure and temperature, slightly reduced peak AHRR, also increased ignition delay and reduced combustion duration. The results may be beneficial to promote the use of n-butanol as an alternative renewable fuel in diesel engines to comply with emission control regulations.

References

1. Jeyaseelan, T., et al.: A comprehensive review on the current trends, challenges and future prospects for sustainable mobility. Renew. Sustain. Energy Rev. **157**, 112073 (2022)
2. EIA. International Energy Outlook 2021 - U.S. Energy Information Administration (EIA) 2021. https://www.eia.gov/outlooks/ieo/. Accessed 9 Oct 2022
3. Mendoza-Villafuerte, P., et al.: NOx, NH3, N2O and PN real driving emissions from a Euro VI heavy-duty vehicle. Impact of regulatory on-road test conditions on emissions. Sci. Total Environ. **609**, 546–55 (2017)
4. Verger, T., et al.: Biomass-based fuel blends as an alternative for the future heavy-duty transport: a review. Renew. Sustain. Energy Rev. **161**, 112391 (2022)

5. Directive (EU) 2018/2001 of the European Parliament and of the Council of 11/12/2018 on the promotion of the use of energy from renewable sources. Off. J. Eur. Union **328**, 82–209 (2018). http://data.europa.eu/eli/dir/2018/2001/oj. Accessed 26 Sept 2022
6. Ghojel, J.I.: Review of the development and applications of the Wiebe function: a tribute to the contribution of Ivan Wiebe to engine research. Int. J. Eng. Res. **11**, 297–312 (2010)
7. Thakkar, K., et al.: Combustion investigation of ternary blend mixture of biodiesel/n-butanol/diesel: CI engine performance and emission control. Renew. Sustain. Energy Rev. **137**, 110468 (2020)
8. Serrano, J.R., et al.: Methodology for characterisation and simulation of turbocharged diesel engines combustion during transient operation. Part 2: Phenomenological Combustion Simulation. Appl. Therm. Eng. **29**, 150–158 (2009)
9. Xu, S., et al.: A phenomenological combustion analysis of a dual-fuel natural-gas diesel engine. Proc. Inst. Mech. Eng. Part D J. Automob. Eng. **231**, 66–83 (2017)
10. Awad, S., et al.: Single zone combustion modeling of biodiesel from wastes in diesel engine. Fuel **106**, 558–568 (2013)
11. Regulation No 49 UN/ECE—Uniform provisions concerning the measures to be taken against the emission of gaseous and particulate pollutants from compression-ignition engines and positive igniti. Off. J. Eur. Union **171**, 1–390 (2013)
12. Liu, J., Dumitrescu, C.E.: Single and double Wiebe function combustion model for a heavy-duty diesel engine retrofitted to natural-gas spark-ignition. Appl. Energy **248**, 95–103 (2019)
13. Huang, H., et al.: Influence of n-butanol-diesel-PODE3-4 fuels coupled pilot injection strategy on combustion and emission characteristics of diesel engine. Fuel **236**, 313–324 (2019)
14. Emiroğlu, A.O., Şen, M.: Combustion, performance and emission characteristics of various alcohol blends in a single cylinder diesel engine. Fuel **212**, 34–40 (2018)
15. Yusri, I.M., et al.: Evaluation of engine combustion and exhaust emissions characteristics using diesel/butanol blended fuel. Appl. Therm. Eng. **156**, 209–219 (2019)

Novel Methodology for Optimization Energy of Heat Treatment Furnaces

Pablo Restrepo-Barrientos[1]([✉]), Juan C. Maya[2], and María E. Muñoz Amariles[3]

[1] GTS, Facultad de Minas, Universidad Nacional de Colombia Sede Medellín, Medellín, Colombia
prestrepob@unal.edu.co

[2] TAYEA, Facultad de Minas, Universidad Nacional de Colombia Sede Medellín, Medellín, Colombia
jcmaya@unal.edu.co

[3] Departamento de Ingeniería Mecánica, Universidad Nacional de Colombia – Sede Medellín, Medellín, Colombia
memunozam@unal.edu.co

Abstract. In this work, a new optimization methodology for heat treatment furnaces based on the variation of the geometric distribution of the heating elements is developed. For this, it is implemented a heat transfer model for simulating the homogenization periods during the treatment, which leads to the appearance of an objective function that allows simultaneously optimizing thermal homogeneity and heat transfer to the piece. In this way, it is possible to avoid the use of multi-objective optimization schemes that require the use of arbitrary criteria for the determination of an absolute optimum. Finally, the proposed methodology is applied to a radiant tube heat treatment furnace, with which it is possible to reduce fuel consumption by around 10% .

Keywords: Simulation · Optimization · Heat Transfer

1 Introduction

The interest in controlled atmosphere heat treatment processes is to increase energy efficiency as much as possible. At first, it would seem that bringing the heating elements closer to the part being treated would increase irradiation and thus energy efficiency. However, the proximity of the heating elements to the treated part causes temperature gradients, which is detrimental to thermal homogeneity and increases the total process time. On the other hand, moving the heating elements away from the part improves thermal homogeneity, but requires an increase in supplied power to achieve a given heating rate. Therefore, it is necessary to find a strategy that can simultaneously satisfy the requirements of adequate thermal homogeneity and irradiation in this type of process [1]. In this sense, this work presents a simulation-based methodology to determine the optimal configuration of the heating elements in controlled atmosphere heat treatment furnaces. This methodology only applies to treatments controlled by radiation and with

thermal homogeneity requirements, such as stress relief, annealing, tempering, or normalizing in inert atmospheres. Furthermore, to facilitate the understanding of the reader, the methodology is explained with a practical example: stress relief treatment of a real Francis runner for hydraulic generation in a vault-type furnace heated with radiant tubes.

2   Methodology

To implement the methodology proposed in this document, it is necessary to develop a mathematical model for the heat transfer processes that take place inside the furnace. Additionally, since the optimization process requires multiple simulations of the heat treatment, it is necessary to strike a balance between the detail of the thermal model and the computational time required to solve it. As mentioned above, stress relief treatment for a Francis runner will be studied. This process consists of three fundamental stages: heating, holding, and cooling. During the heating period, the heating elements radiate heat to the part so that the part increases its temperature at a specified rate until the so-called holding temperature is reached. At this point, the holding period is given in which the piece maintains its constant temperature for a given time. Finally, the heating elements are turned off so that the cooling stage can take place, in which the piece reduces its temperature to a safe value to be removed from the furnace.
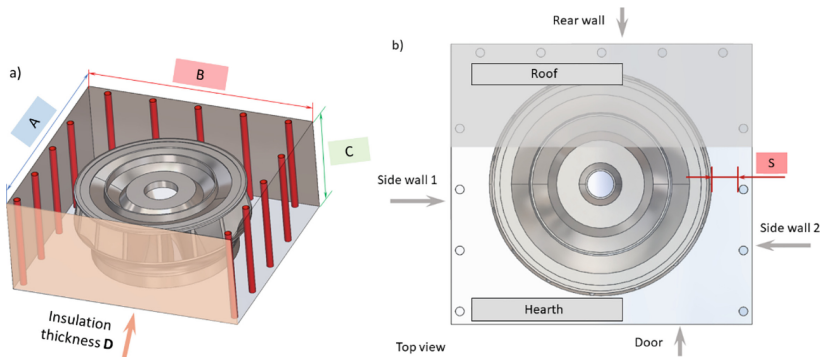
Fig. 1. Diagram of the EPM vault-type controlled atmosphere heat treatment furnace. a) isometric and b) top view.

Figure 1 shows a schematic of the controlled atmosphere treatment furnace that includes the walls, a door, a roof, a floor, and 13 cylindrical radiant tubes. For these elements, the energy balances must be solved, making simplifications that obey the reality of the specific treatment process, and it is also necessary to consider the criterion of thermal homogeneity. In this sense, the control systems of this type of furnace are based on a set of thermocouples located at key points of the piece, between which there must be a controlled temperature difference. Thus, if said temperature difference is below a value ΔT_{max}, the part is heated; however, if this value is exceeded, a homogenization period begins in which the average temperature remains constant until the temperature difference between the gradient measurement points reaches a value ΔT_{min}. Therefore,

a strategy proposed in this work consists of dividing the piece into surfaces whose temperatures must be controlled. For the specific case of the Francis runner in this study, a subdivision is made into 6 surfaces as shown in Fig. 2.
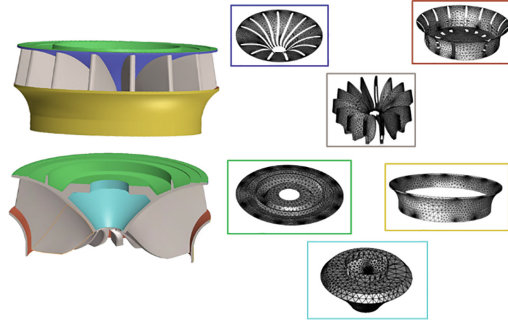
Fig. 2. Sectional view of the Francis runner and surfaces of interest.

The energy balance equation for each of the twelve surfaces inside the runner is given by the following equation

$$\rho_i dr A_i C_{pi} \frac{dT_i}{dt} = F_{t,i} \dot{Q}_{tubos} + A_i * \sum_{j=1}^{12} F_{ij} * (J_j - J_i) - hA_i(T_i - T_{Ar}) - \sum_{k=7}^{12} \frac{(T_i - T_k)}{R_{ik}} \tag{1}$$

where ρ_i is the density, A_i is the surface area, C_{pi} is the heat capacity, T_i is the temperature, F_{ij} is the view factor, J is the radiosity, h is the convective heat transfer coefficient inside the furnace, $\dot{Q}_{tubos}$ is the net power radiated by the tubes, $F_{t,i}$ is the view factor from the radiant tubes to the surface i, R_{ik} is the thermal resistance to conduction between two surfaces i and k of the piece. The model also considers the one-dimensional conduction equation inside the furnace walls, roof, door and floor, and the heat transfer by radiation between the surfaces of walls, roof, door and floor in a similar way to Eq. (1). Additionally, to emulate the control system of the thermal homogeneity of the furnace, the following function will be used by sections

$$\dot{W} = \begin{cases} \sum_{i=1}^{N_r} F_i \dot{Q}_{tubos} + \dot{Q}_{pérdidas} & si \quad T_{max} - T_{min} \le \Delta T_{max} \\ \dot{Q}_{pérdidas} & si \quad \Delta T_{max} \ge T_{max} - T_{min} \ge \Delta T_{min} \end{cases} \tag{2}$$

This expression establishes that when the temperature difference between two surfaces does not exceed an established maximum value, the energy supplied is equal to that required to raise the impeller temperature at the rate established by the treatment and additionally compensate energy losses to the surroundings. On the other hand, when the maximum temperature difference allowed between two surfaces is exceeded, the so-called homogenization period takes place and the radiant tubes deliver only the energy necessary to compensate the thermal losses with the environment, that is, to maintain the average temperature constant. Finally, when a temperature difference between the two surfaces ΔT_{min} is reached, the heating of the part continues. Thus, it is established that

the maximum temperature difference between any surface of the impeller and surfaces 1, 2, and 3 must not exceed 5 °C. On the other hand, the maximum temperature difference between any surface of the impeller and surfaces 4, 5, and 6 must not exceed 10 °C. It is worth mentioning that there are two different values of $\Delta Tmax$ due to the requirements of the specific heat treatment studied in this work since depending on the zone of the Francis runner there are different levels of risk of failure.

3 Predictions of the Heat Transfer Model

The numerical model was solved to simulate the heating of the piece during a heat treatment cycle with an average rate of 23 °C/h until the piece reaches an average temperature of 620 °C. Subsequently, a holding period of 12 h is carried out. Finally, the radiant tubes are turned off so that the piece cools down by exchanging heat with the environment. The simulations carried out were compared with the predictions of a steady-state model built with commercial finite-volume software and maximum deviations of 5% were found, with computational times up to 1000 times less for the model proposed here, which proves that it achieves to capture the physics of the treatment process. The parameters used during simulations are reported elsewhere [2].
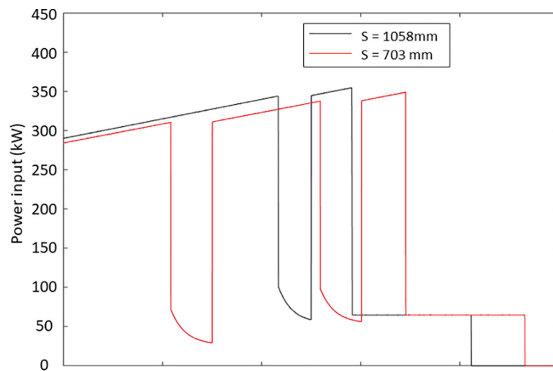
Fig. 3. Predictions of power supply for different configurations.

Figure 3 shows the predicted power profiles for dimensions S of 1058 mm and 703 mm. In these curves, it can be seen that there are some abrupt drops in power, which correspond to the periods of homogenization. However, without taking these periods into account, the supplied power increases with time because the energy losses with the surroundings increase with the increase in temperature. An interesting behavior that we can observe in this figure is that for the configuration with the best irradiation (S = 703 mm), the power supply is always below that of the configuration with S = 1058 mm for the same instant of the process (except, clearly, the periods of homogenization). This is because a better irradiation to the piece implies a lower energy requirement to obtain a given heating rate. However, the configuration with better irradiation requires that the total process time be greater because more periods of homogenization are necessary.

Consequently, the best irradiation of the part implies longer process times and lower power supplies, which implies that there is a geometric configuration that simultaneously allows optimal process times and power supplies. Now, if we analyze the total energy consumed in the treatment, we have that this can be calculated from the following expression

$$E = \int_0^{t_{final}} \dot{W} \, dt \qquad (3)$$

Based on Eq. (3), it is clear that the thermal energy consumed in the process is no more than the area under the power curve shown in Fig. 3. In this way, we see that the better irradiation associated with the proximity of the radiant tubes to the piece implies a lower "height" of the polygon formed by the Power vs. time curve; however, it also implies a "horizontal elongation" of this polygon. In this sense, it is concluded that there must be a configuration that allows obtaining a minimum area under the curve, i.e., an optimal value of energy consumption. In other words, the objective function is given by the minimization of the total energy consumed:

$$FO = Min \ E \qquad (4)$$

The great advantage of using Eq. (4) as an objective function is that it is capable of simultaneously taking into account the effects of irradiation and thermal gradients in the part, which avoids the need to use two objective functions for these two variables. Additionally, it is essential to mention that the appearance of said optimal value is mainly due to the ability of the proposed mathematical model to reproduce the homogenization times, which are the ones that generate the so-called "horizontal elongation" of the Power vs. time curve. Finally, to obtain an optimal configuration of the heating elements inside the furnace, the final step of the methodology consists in varying the location of the radiant tubes inside the furnace until a minimum value of energy consumption is obtained.

4   Results

To determine the optimal configuration of the heating elements, the dimensions A, B, C, and S (see Fig. 1a) of the furnace were varied. The first dimension that was analyzed was the separation S and, as seen in Fig. 4, a minimum consumption value appears for S = 950 mm. This same analysis can be carried out for the variation of any other level inside the furnace. Thus, after taking 1560 view factor data by using commercial software of finite volumes for different locations of the radiant tubes inside the furnace, it was found that the optimal elevations of the furnace are as follows: A = 6403 mm; B = 6900 mm; C = 2880 mm and S = 950 mm.
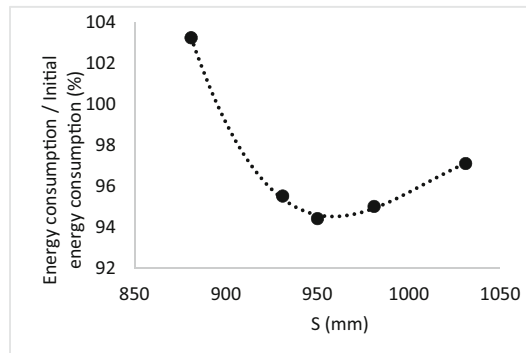
Fig. 4. Effect of dimension S on energy consumption.

5   Conclusions

A new method was created to improve the design of controlled atmosphere heat treatment furnaces. It uses a heat transfer model to emulate the temperature gradients in the piece, resulting in minimum energy consumption without additional optimization criteria. The proposed model was found to have deviations of only 5% compared to a commercial finite volume model, and its computation time is 1000 times faster, making it more practical for optimization processes. The method was applied to optimize a vault-type furnace for a Francis turbine runner, resulting in minimum energy consumption during treatment.

References

1. Mei, C., Zhou, J., Peng, X., Zhou, N., Zhou, P.: Simulation and Optimization of Furnaces and Kilns for Nonferrous Metallurgical Engineering, pp. 1–340. Springer, Heidelberg (2010). https://doi.org/10.1007/978-3-642-00248-9
2. Restrepo-Barrientos, P., Maya, J.C., Muñoz Amariles, M.E.: Novel mathematical model for heat treatment furnaces: application to furnaces for surface treatment of critical components of hydroelectric and gas plants. In: 11th International Conference on Engineering & Natural Sciences, ISPEC, pp. 387–395 (2021)

Modeling and Simulation of Heat Transfer in a Cold Wall Vacuum Furnace Considering Geometric Optimization of Heating Elements

Pablo Restrepo-Barrientos[1(✉)], Juan C. Maya[2], and María E. Muñoz Amariles[3]

[1] GTS, Facultad de Minas, Universidad Nacional de Colombia Sede Medellín, Medellín, Colombia
`prestrepob@unal.edu.co`

[2] TAYEA, Facultad de Minas, Universidad Nacional de Colombia Sede Medellín, Medellín, Colombia
`jcmaya@unal.edu.co`

[3] Departamento de Ingeniería Mecánica, Universidad Nacional de Colombia – Sede Medellín, Medellín, Colombia
`memunozam@unal.edu.co`

Abstract. This work proposes the thermal sizing of a furnace, starting from a review of the state of the art of furnaces with similar characteristics and thus defining the general concept. Then, a transient state analytical model is developed that allows to know the necessary power for the heating elements, the temperature profile on the walls of the furnace, the amount of insulation needed to protect internal components, and other related specifications. Due to the parameterization of the model, it is possible to perform sensitivity analyses to verify the behavior of the system with the variations of thermophysical properties of interest.

Keywords: Heat treatment furnace · modelling · heat transfer

1 Introduction

The Colombian energy matrix is mainly based on the generation in hydroelectric and thermal power plants, for which large volume and weight turbines and parts are required. Empresas Públicas de Medellín provides electricity in Antioquia through 25 hydroelectric plants, 1 thermal power plant, and 1 wind power plant. The need for thermal treatment furnaces to repair key elements in these plants leads to a project to design a controlled argon atmosphere thermal treatment furnace with an operating temperature of 1200 °C, pressures from 1×10^{-4} torr to 1.2 bar, and temperature control of ± 10 °C. A typical furnace design is used for reference. This work proposes the thermal sizing of the furnace through a review of similar furnaces and the development of an analytical model to determine the power of heating elements, wall temperature profile, insulation needs, and other specifications [1, 3]. The model also allows for sensitivity analyses to evaluate system behavior with changes in thermophysical properties.

2 Loading Scenario

In this furnace, it is of special interest to treat and repair parts of the thermal power plants in Antioquia-Colombia. Therefore, the main load scenario of the system corresponds to the first stage nozzle presented in Fig. 1, this piece operates in La Sierra thermal power plant in the department of Antioquia in Colombia where up to 460 MW of power is produced.

Fig. 1. First stage nozzle (thermal power plant).

This piece is made of a nickel-based alloy (Inconel 625), has a diameter of 2650 mm and a mass of 2500 kg. The treatment must be done by following heating and cooling rates of 100 °C/h and a temperature during the holding of 1200 °C while also maintaining control in critical areas of the piece of ± 10 °C to prevent breakages in the joint areas.

3 Thermal Modelling

3.1 Hot Chamber Radiation

Most thermal treatments in the furnace occur under vacuum conditions, where heat transfer from heating elements to the load occurs mainly by radiation. A common approach in analytical models is to treat the elements as black bodies and use the Stefan-Boltzmann law for calculation, which is quick but not accurate enough. A radiation heat transfer model is implemented in the hot chamber, considering view factors that represent real thermal radiation distribution. To calculate view factors, a simplified CAD model is entered into finite element software and calculated during the configuration phase.
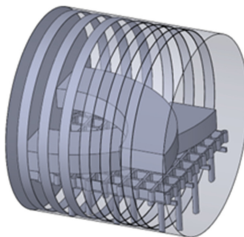
Fig. 2. Simplified CAD for radiation view factors calculation.

Figure 2 shows the simplified CAD model used, which utilizes symmetry and includes key elements and the main load scenario to reduce computational cost.

Finally, the average view factors on the surfaces of interest are obtained as shown in Fig. 3. This graph only reflects the values obtained for the load, however, the view factors corresponding to all the components that will be subjected to radiation within the furnace such as the loading fixture, the covers, the cylindrical wall, and others are obtained.
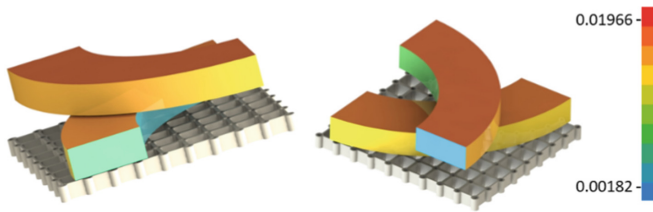
Fig. 3. Average radiation view factors in load.

3.2 Heat Transfer Across the Furnace

As previously mentioned, it is necessary to know the thermal behavior of the insulation shell and thus make decisions regarding the components of the system [5]. To do this, a heat transfer model by conduction through the cylindrical surface and the cover of the furnace is proposed. A scheme that shows the layers to be modeled is presented in Fig. 4.
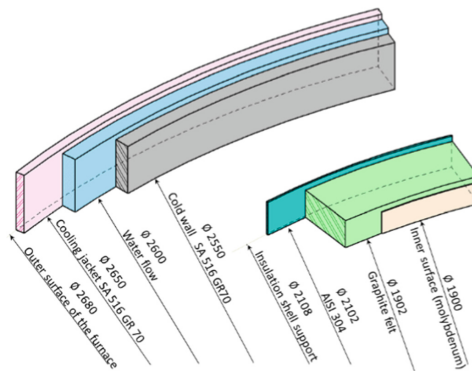
Fig. 4. Schematic of the furnace layers.

The analytical model has two key limitations. First, the heating element power is a variable parameter that can be adjusted to meet the system's heating requirements. Second, the cooling section on the furnace's outer layer must maintain temperatures within acceptable limits to ensure the system's tightness, protect control elements and

avoid the use of special refractory materials. The equations for the system's energy balance and radiosity consider average temperatures for internal surfaces and the load, with a material mesh for the insulation shell. The equations for the load's energy balance and the general equation for the system radiosity are presented [2, 4].

$$mC_p \frac{dT}{dt} = QF_{ri} + A_i \sum_{j=1}^{n} \left(F_{ij}[J_j - J_i] \right) \tag{1}$$

$$J_i = \sigma \epsilon_i T_i^4 + \sum_{j=1}^{n} F_{ij} J_j (1 - \epsilon_i) \tag{2}$$

where m is the mass of the load, Cp is the heat capacity of the piece, QF_{ri} is the product of the power and the view factor from the heating elements to surface i, A is the area according to the surface, and $F_{ij}[J_j - J_i]$ is the product of the view factor from one surface to another and the difference of radiosity (which represents the heat emitted and reflected), σ is the Stefan-Boltzmann constant and ϵ_i the emissivity of each surface.

4 Results

Initially, a steady-state analysis is carried out with the model already proposed and restricting the temperature of the load to 1200 °C which corresponds to the holding stage, with this it is possible to determine the temperature profile that the furnace will have and the power that corresponds to 146 kW, this value refers to the power necessary to supply the system losses in the stationary or holding stage. The behavior mentioned can be appreciated in Fig. 5.

It can be seen in Fig. 5 that the stabilization of the system with the holding power (steady state) is achieved in a time of around 25–30 h, this makes the heating rates established in the furnace specifications not met. To achieve the required rates, a transient state analysis is carried out with the variation of the system power.
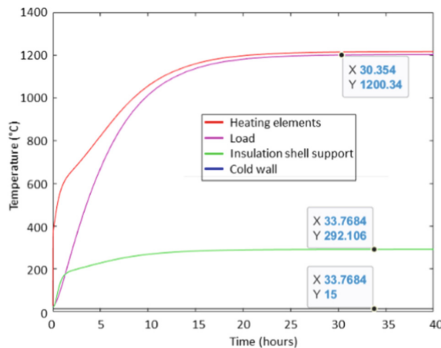
Fig. 5. Steady state temperature profile.

To meet the heating and cooling time requirements, an iterative analysis is performed using the power parameter. Figure 6 shows the three stages of thermal treatment (heating,

holding, and cooling) for key elements in the furnace, such as the heating elements, load, insulation support (stainless steel support), and outer wall. The main advantage of the model is its ability to evaluate the furnace's thermal behavior over an extended period (80 h) without extensive computing and simulation. The model provides average temperatures, but not detailed profiles. After consolidating the model, the optimum configuration (180 mm separation, 890 mm internal radius) is selected based on energy efficiency.
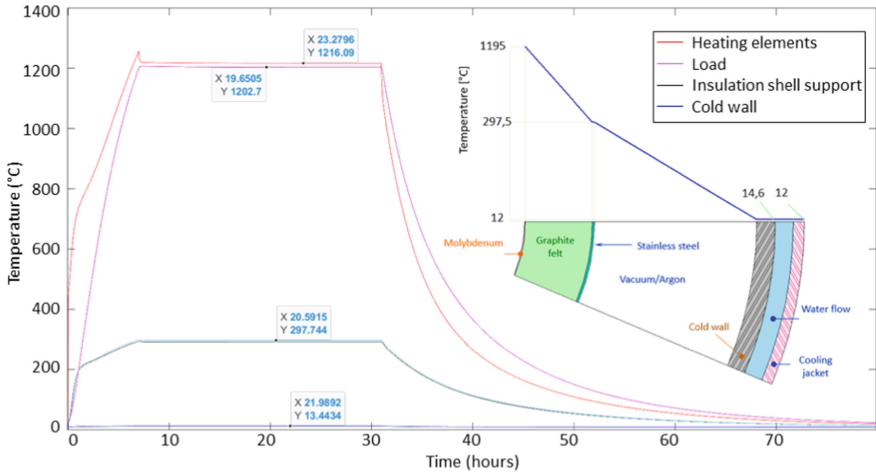
Fig. 6. Transient state temperature profile.

Figure 7 shows the temperature profile of a simulation carried out on conventional finite elements software with the same properties. The outer surface of the insulation shell is 400 °C, higher than the analytical model's result of 292 °C, due to the specific geometries like the load columns that increase heat transfer in the outer zone. Figure 7 shows the average temperatures on the outer surface of the furnace with the same water parameters. The blue values mostly match the analytical model. The argon inlet pipe causes a hot zone where the water does not circulate well, but the proposed model still offers good results for average temperatures, mass, energy balances, etc.
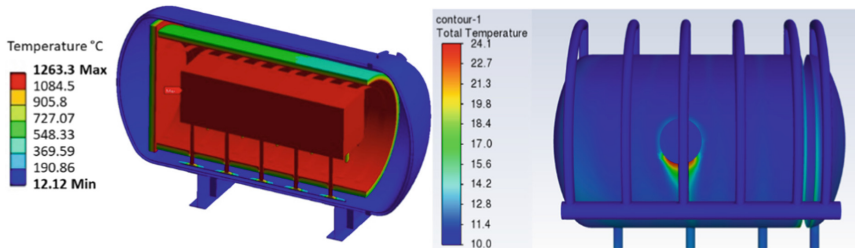
Fig. 7. Validation by a conventional finite elements software.

5 Conclusions

The study develops a model for predicting the thermal behavior of a cold-wall vacuum furnace, which has reliable results and faster computation for transient simulation. The model enables fast parameter changes for easier system design. Although it does not evaluate specific geometry, the results are consistent with reality and validated with conventional software, making it useful in design.

References

1. Reim, K.: U.S. Patent Office Issues Solar Manufacturing 20 Bar Furnace Patent 9,187,799 - Solar Manufacturing. Solar Manufacturing. https://solarmfg.com/u-s-patent-office-issues-solar-manufacturing-20-bar-furnace-patent-9187799/. Accessed 23 July 2022
2. Abaqus Theory Guide (6.14). Wufengyun.com. http://wufengyun.com:888/books/stm/default.htm?startat=ch02s11ath47.html. Accessed 23 July 2022
3. Wilkinson, J.: Hot Zones - Choosing the Right Hot Zone for Your Application. AZoM.com. https://www.azom.com/article.aspx?ArticleID=13305. Accessed 23 July 2022
4. Incropera, F.P., DeWitt, D.P., Bergman, T.L., Lavine, A.S.: Incropera's principles of heat and mass transfer, p. 1000. Wiley (2017). https://www.wiley.com/en-ie/Incropera%27s+Principles+of+Heat+and+Mass+Transfer%2C+8th+Edition%2C+Global+Edition-p-9781119382911. Accessed 13 July 2022
5. Macchion, O., Zahrai, S., Bouwman, J.: Heat transfer from typical loads within gas quenching furnace. J. Mater. Process. Technol. **172**(3), 356–362 (2006). https://doi.org/10.1016/j.jmatprotec.2005.10.017. Accessed 23 July 2022

Dynamic Performance Analysis of a Direct Expansion Solar Heat Pump Water Heater for Different Evaporator/Condenser Area Ratios

Luis E. Parada-Guzmán[✉], Santiago Valencia-Cañola, Cesar A. Isaza-Roldán, David A. Duarte-Hernández, Carolina Mira-Hernández, and Carlos A. Bustamante

Facultad de Ingeniería Mecánica, Grupo de Energía y Termodinámica, Universidad Pontificia Bolivariana, Medellín 050031, Colombia

`luis.parada@upb.edu.co`

Abstract. To mitigate the deleterious effects of climate change, sustainable energy technologies need to be developed and widely adopted. This study analyzes the effect of the evaporator/condenser area ratio on performance for a direct expansion solar heat pump water heater system operating in Medellín, Colombia. For the analysis, a dynamic simulation of the system is carried out via a numerical approximation using Python with the Coolprop library. Results shows that the evaporator area is more relevant than condenser area for the system performance. Also, an increase in evaporator area results in a better system efficiency. An area ratio between evaporator and condenser above 10 deteriorates the system performance.

Keywords: Solar Energy · Water Heater · Heat Pump · Condenser Area · Evaporator Area

1 Introduction

Global warming is a phenomenon caused by the accumulation of greenhouse gases, such as CO, CO_2 and O_2; which sufficiently increases the temperature of the Earth to cause an imbalance in ecosystems. The generation of greenhouse gases is mostly a consequence of human activities as power generation, cooling and heating and transport [1]. In Colombia, 7% of residential energy consumption is destined to water heating [2]. Therefore, harnessing clean energy sources for the operation of heating systems with improved efficiency could contribute to the reduction of greenhouse gas emissions. Currently one of the most efficient systems to produce thermal energy is a Direct Expansion Solar Heat Pump Water Heater (DX - SHPWH) which has a huge potential to increase the efficiency of heat pump systems thanks to the utilization of solar thermal energy in the evaporator [3]. In a DX-SHPWH system, a solar collector acts as the evaporator, absorbing the incident solar radiation and increasing the thermal energy of the refrigerant, which heats water in an accumulation tank as it condenses. The study carried out by

Valencia et al. [4] reflect the benefits of the DX - SHPWH systems in reducing energy consumption and environmental impact. In this study, results of a dynamic numerical model indicate that a COP above 3.5 can be obtained using renewable energy sources, exceeding the performance of traditional systems.

The study of the relationships between geometric parameters in this type of systems is relevant to improve the performance as Ma et al. [5] reports. In this article, by means a numerical model, the area ratio between the evaporator and the condenser of a DX-SHPWH is analyzed in order to determine the effects on the systems performance in terms of the COP.

2   System Description

A DX - SHPWH is a type of water heater in which water is stored in a tank and heated using mainly solar thermal energy and thermal energy from the environment by means of a heat pump. The system has four main elements: a compressor, a helical condenser submerged in a water storage tank, a solar collector that acts as an evaporator and an expansion device. A refrigerant circulates cyclically absorbing and transferring heat into the system as it changes phase. The evaporation process occurs directly inside the solar collector, hence, is a direct expansion system.

As shown Fig. 1, at point 1, the refrigerant in vapor phase enters the compressor, where its temperature and pressure are increased to enter point 2 as superheated vapor. Then the refrigerant enters the condenser and changes to liquid phase while transferring heat to the water [6]. From point 3, the liquid flows through the expansion valve to reach point 4 with a lower pressure and temperature. Finally, the refrigerant enters the evaporator, where it absorbs thermal energy from the solar radiation and the surrounding air.
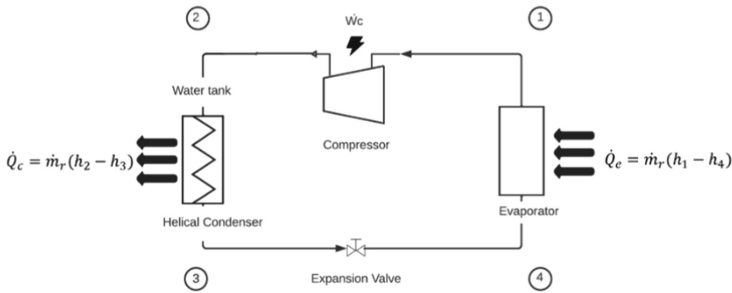
Fig. 1. Thermodynamic cycle of DX - SHPWH scheme.

Equation (1) states and energy balance for the cooling system.

$$\dot{Q}_e + \dot{W}_c - \dot{Q}_c = 0 \tag{1}$$

The steady-state system COP is the relation between the useful heat transfer from the condenser and the power consumption, as expressed in Eq. 2.

$$COP_{HP} = \frac{\dot{Q}_c}{\dot{W}_c} \tag{2}$$

Heat transfer rates in the evaporator and condenser $\dot{Q}_e\,\dot{Q}_c$ are indicated in Fig. 1, where $\dot{m}_r$ is the refrigerant mass flowrate and h is the refrigerant enthalpy in each point of the cycle, The compressor power $\dot{W}_c$ is calculated according a characteristic polynomial equation for the compressor selected in this work, Tecumseh Masterflux SIERRA02-0434Y3 in terms of compressor speed (n),condensation temperature (Tc) and evaporation temperature (Te). The equation is presented in the manufacturer's data sheet [7] and is solved as reported in ref. [4].

3 Mathematical Model

To estimate the different thermodynamic and heat transfer processes that occur within the system, a pseudostationary mathematical model is used that guarantees energy conservation for the components of the cooling cycle assuming steady state, and updates the temperature of the water in the tank considering a time dependent energy balance. The model was developed with the following assumptions: i) the compressor operates at constant speed, ii) negligible pressure drops in the heat exchangers, iii) constant pressure in the water tank and iv) uniform temperature in the water tank.

3.1 Mathematical Model of Collector/Evaporator

In the present study, the evaporator is designed to take advantage of solar radiation (αI_T) and convective heat transfer from the environment ($U_{LC}(T_e - T_\infty)$). The energy absorbed by the evaporator is estimated by Eq. (3)

$$\dot{Q}_e = F'A_e[\alpha I_T - U_{LC}(T_e - T_\infty)] \tag{3}$$

The efficiency factor F′ can be evaluated using the Hottel Whilliar Bliss model proposed in [8] and shown in Eq. (4), Where F is the fin efficiency, D is the outer diameter of the tube, and W is the pitch of the tube, Cb is bond conductance. F can be calculated from traditional model for fins.

$$F' = \frac{1}{U_L}\left\{ W\left[\frac{1}{U_L((W-D)F+D)} + \frac{1}{C_b} \right] \right\}^{-1} \tag{4}$$

3.2 Mathematical Model of Helicoidal Condenser and Water Tank

To simulate the water temperature (T_w) evolution during heating, the transient energy balance given by Eq. (5) is numerically solved. m_w, C_{pw}, U_{Lt}, A_t, T_∞ are, respectively,

water mass in the tank, water specific heat, overall heat loss coefficient for the tank, tank superficial area and ambient temperature.

$$C_{pw}\frac{dT_w}{dt}m_w = \dot{Q}_c - U_{Lt}A_t(T_w - T_\infty) \tag{5}$$

The heat transferred by the helical condenser $\dot{Q}_c$ is estimated using the logarithmic mean temperature difference ΔT_{lm} as described in Eq. (6):

$$\dot{Q}_c = U_C A_C \Delta T_{lm} \tag{6}$$

The global heat transfer coefficient of the condenser, U_C, is calculated assuming that the conduction resistance through the walls of the condenser pipe is negligible, as indicated in Eq. (7)

$$U_c = \left(\frac{A_{c,o}}{h_{c,r}A_{c,i}} + \frac{1}{h_w}\right)^{-1} \tag{7}$$

The inside ($h_{c,r}$) and outside (h_w) convection coefficients are calculated via empirical correlations for internal forced condensation and natural external flow in circular pipes. $A_{c,o}$ and $A_{c,i}$ are the condenser internal and external areas, respectively.

4   Numerical Algorithm

Computational implementation is carried out in Python language, according to the numerical scheme presented in [4]. In this work, the algorithm is modified by neglecting the variable speed in the compressor to avoid possible noise in the geometrical analysis.

After varying the area ratio (AR), between the solar collector/evaporator area and the condenser area for different geometrical configurations, results are obtained and analyzed. The numerical algorithm runs f until the water in the tank reaches the target temperature of 60 °C.

5   Results and Discussions

The numerical model is used to predict the performance of a proposed DX-SHPWH basic design with the characteristics listed in Table 1. The DX-SHPWH operates under local average weather conditions, using the typical meteorological year (TMY) of Medellín [9]. The initial AR is 15.9 where the evaporator area is 1,4 m^2 and the condenser area is 0.087 m^2. Starting from the initial areas, a series of variations above and below are made, in equal percentages, for both the evaporator and condenser areas. The variations are made every 20% of the previous value, until obtaining 5 values above and 5 below the initial areas, and the resulting combinations are simulated. Finally, COP for each AR is obtained, and the results are compared.

Figure 2 shows the influence of AR on the system average COP. Each line represents a specific value of the evaporator area while the condenser area is varied. When the AR increases above 10, a gradual decrease of the COP is observed. The large imbalance

Table 1. DX-SHPWH basic design for study case.

Parameter	Value (SI)
Compressor reference	Tecumseh Masterflux SIERRA02-0434Y3
Type of refrigerant	R1234YF
External diameter of the condense tube	0.009525 m
Internal diameter of the condenser tube	0.008005 m
Tank volume	0.11 m^3
Target temperature	60 °C

between the heat transfer areas increases the superheating at the compressor inlet and causes poor heat transfer at the condenser, which is compensated with a higher condensing pressure. Hence, the power consumption also increases. It can also be observed that the COP is very sensitive to changes in the evaporator area, obtaining higher COP values when the evaporator is larger, because more energy can be absorbed from the environment, which improves the efficiency of the system.
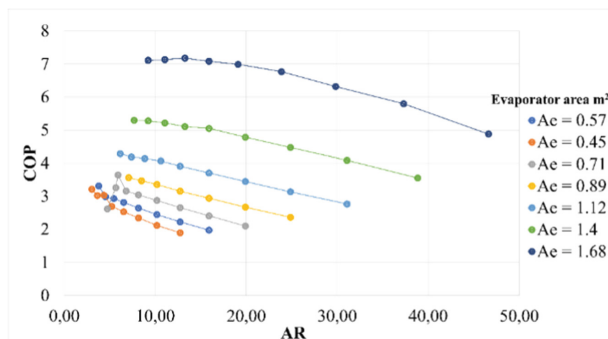
Fig. 2. Impact of AR on system COP for different evaporator areas. Own source.

Figure 3 shows in detail the influence of the condenser area on the average COP of the system. Initially there is a favorable trend in the COP when the condenser area is increased. However, a stabilization point is reached where the COP approaches a constant value with increasing condenser area. This shows that the condenser area has a smaller impact on system performance in comparison to the evaporator area. A configuration with large evaporator area and AR below 10 is advisable for good system performance.
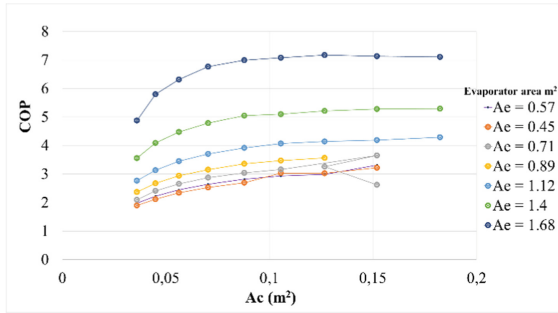
Fig. 3. Impact of condenser area on system COP for different evaporator areas. Own source

6 Conclusions

The proposed study demonstrates the importance of geometric parameters on the performance of. An increase of the area of the solar collector or evaporator tends to improve the performance because the system can more readily absorb heat from the environment. However, under a constant collector area, increasing evaporator/condenser area ratio beyond10 causes a gradual decrease of the COP, because the condensing pressure needs to be increased to compensate for the restricted heat transfer in the condenser. In addition, it is observed that the COP tends to a constant value as the condenser area is increased. Hence, after a threshold value for the condenser area the system is mainly sensitivity to changes in the evaporator area. A system with large evaporator area and an evaporator/condenser area ratio below 10 is recommended for good performance.

References

1. EEA. La energía y el cambio climático (2017)
2. Enersinc. Energy Demand Situation in Colombia (2017)
3. Chua, K.J., Chou, S.K., Yang, W.M.: Advances in heat pump systems: a review. Appl. Energy **87**(12), 3611–3624 (2010)
4. Valencia-Cañola, S., Bustamante, C.A., Mira-Hernández, C., Isaza-Roldán, C.A.: Thermo-economical performance analysis of a direct-expansion solar heat-pump water heater driven by a photovoltaic array and the electrical grid in Medellín Colombia. Appl. Therm. Eng. **222**(119930) (2023)
5. Ma, K., Wang, Z., Lia, X., Wub, P., Li, S.: Structural optimization of collector/evaporator of direct-expansion solar/air-assisted heat pump. Alex. Eng. J. **60**(1), 387–392 (2021)

6. Charter, W.W.S., de Forest, L., Dixon, C.W.S., Taylor, L.E.: Design and performance of some solar booster heat pumps. In: ANZ Solar Energy Conference (1980)
7. MasterFlux (2021). https://www.masterflux.com/products/sierra/?pid=22
8. Hawlader, M.N.A., Chou, S.K., Ullah, M.Z.: The performance of a solar assisted heat pump water heating system. Appl. Therm. Eng. **21**, 1049–1065 (2001)
9. EPW. Repository of free climate data for building performance simulation (2014). https://climate.onebuilding.org/

Application of New Conformal Cooling Systems for Sustainable Injection Molds

Abelardo Torres-Alba[1,2], Jorge Manuel Mercado-Colmenero[1,2] ,
José Antonio Amate-Teva[1,2], and Cristina Martín-Doñate[1,2(✉)]

[1] Department of Engineering Graphics, Design and Projects, Campus Las Lagunillas s/n. A3 Building, 23071 Jaén, Spain
cdonate@ujaen.es

[2] INGDISIG Jaén Research Group, Campus Las Lagunillas s/n. A3 Building, 23071 Jaén, Spain

Abstract. The cooling phase in the cycle time of the injection molding process is currently the phase with the greatest influence on energy expenditure and sustainability. Traditional designs are not capable of perform an adequate thermal exchange between the coolant and the mold cavity, especially in parts with complex geometries and deep cores. For this reason, the conformal cooling channels provide greater flexibility to the design, achieving efficient heat exchange between the surface and internal layers of the plastic part. The present research describes the application of a new conformal cooling system to optimize the cooling phase of a complex plastic part with great depth where the use of traditional cooling is inefficient. The results of the presented research greatly improve the uniformity of temperatures on the surface of the plastic part, reducing the cycle time by more than 37%. These results are perfectly aligned with the objective of improving the sustainability and efficiency of the manufacturing process.

Keywords: Conformal Cooling · Injection Molding · Sustainability · Industrial Design

1 Introduction

The plastic injection molding process is currently one of the most widespread plastic transformation processes worldwide due to its high productivity and its ability to manufacture complex textured parts, with different colors, etc. [1]. The injection molding process basically consists of injecting a plastic polymer at high temperature and pressure inside the mold cavity [5]. Next, the molten plastic is cooled to a temperature range capable of guaranteeing the expulsion of the part without deforming it [2]. To achieve this cycle in the shortest possible time, a coolant is passed through a network of channels located in both cavities of the mold, with the aim of improving the heat transfer process and accelerating solidification of the melt polymer [3]. This manufacturing process is cyclical and any type of optimization produces a significant impact on productivity and from an environmental perspective, reducing energy expenditure throughout the injection cycle [4–6].

Cooling phase is an essential process in the molding cycle, which requires the design and detailed analysis of the cooling channels location responsible for perform the heat exchange process between the melt plastic and the cavity surface. During the design of any mold, it is essential to analyze the thermal function due to the large amount of heat received from the plastic material. This heat must be partially extracted and in a minimum time in order to reduce the temperature of the piece below the expulsion temperature [7, 8]. Currently, most of the mold designs include cooling systems conceived with traditional methods, based on the CNC machining of the channels. This fact limits the shape of the channel section, and the drawing of non-rounded corners in the layout of the circuits [9, 10]. These restrictions largely condition the mold cooling system, directly affecting the cooling time and the quality of the molded product. A non-uniform or asymmetric cooling directly impacts not only the profitability of the process but also the quality of the part, causing deformations mainly due to differential contractions, defects in the surface finish, residual stresses, etc. [11].

In order to minimize or avoid these problems, it is possible to use technologies such as additive manufacturing. This manufacturing technology applied to molding allows the design and manufacture of channels adapted to the geometry of the part, maintaining a constant distance between the contour of the cavity and channels. This fact influences the design of both channels and layouts, obtaining optimal results both at the process level and at the level of the finished product. Finally, these circuits require the use of additive manufacturing technologies such as SLM or SLS, characterized by their efficiency and versatility, being much more respectful of the environment than traditional technologies. The geometry, size, and location of conformal cooling channels have a great influence on process variables, such as the performance of the thermal exchange system and, therefore, the total cycle time used.

The article presents the results of the application of a new conformal channel design apply to a large and deep geometry that is difficult to cool properly. The numerical results obtained show that the methodology used for the conformal design of the cooling channels greatly optimizes the manufacturing process of the studied part.

2 Materials and Methods

In this section, the geometrical, functional, and manufacturing characteristics associated with the plastic part under study are described. Technological details regarding the selection of the plastic material for the injection molding manufacturing process and the boundary conditions of the manufacturing process itself are also specified. Figure 1 shows the geometrical characteristics of the plastic part under study. The part has been designed as an interior element of the "Volkswagen Golf MK7" vehicle with a double purpose, aesthetically matching the interior of the cabin and functional as a housing close to the driver and passenger location.

The dimensions of the study piece are 150 mm wide, 256 mm long, highlighting its great depth of 91.5 mm. The thickness is variable, being between 3.0 and 5.0 mm. The material selected to inject the part is ABS from the manufacturer SABIC with the trade name "Cycolac FR23". To cool the plastic part using traditional methods, a 10 mm diameter channel grid has been defined in both areas of the cavities. The
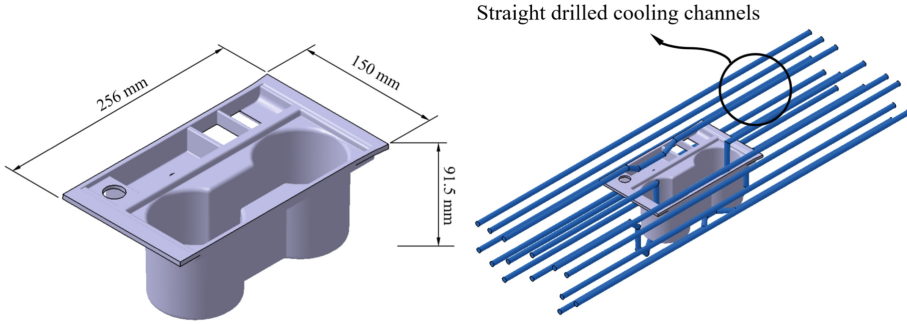
Fig. 1. Geometry of the plastic part under study and traditional cooling system design

separation distance between the part and cooling channels complies with traditional design requirements, which is 20 mm, as well as with structural safety distances between the injection mold elements (see Fig. 1). The interior area of the part is cooled by means of a circuit system close to its surface, trying to reproduce its shape.

In order to improve the cooling phase of the plastic part, a uniform geometric distribution of the conformal type cooling elements has been designed (see Fig. 2), which allows them to surround the plastic part and improve the heat exchange, making it more uniform and efficient. In this way, a network of cooling channels of the conformal type of 10 mm in diameter has been proposed, ensuring that their location covers the free spaces between the elements of the injection mold. The location of the channels complies with the industrial safety distance, which is 10 mm, with respect to the rest of the elements.
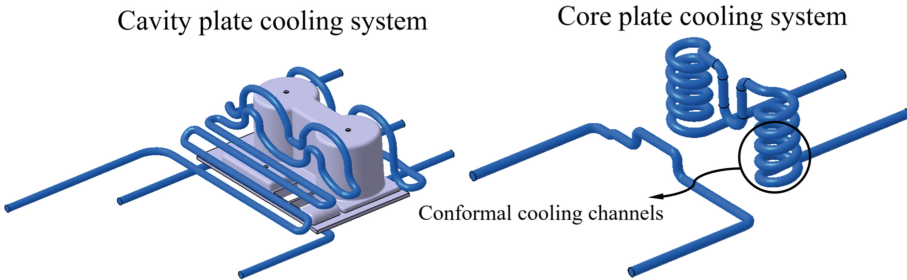
Fig. 2. Conformal cooling system design

3   Thermal Modeling of Numerical Simulations

After generating the 3D CAD modeling of the different cooling systems proposed, (see Fig. 1 and Fig. 2) and, based on the results obtained, the thermal behavior and final quality obtained for the present case study are analyzed. In this way, the cooling phase of the analyzed plastic part and, consequently, the total injection cycle has been analyzed based on the performance of the process and the quality of the final product. The commercial

software used to perform such numerical analyzes (CAE) is Moldex3D (version R21, CoreTech System Co., Ltd., Zhubei City, Taiwan). Next, according to the methodology to define the boundary conditions established by the numerical software, the thermal modeling of the system begins with the discretization of the geometry using finite elements. In particular, the different meshes have been generated using second-order tetrahedral elements, together with second-order prismatic elements of the boundary layer type, along the surface of the geometries, improving the interface between the melt plastic flow and the surface of the cavity. Furthermore, the element size used for the defined meshes is 0.5 mm.

Every 3D computational domain defined in numerical simulations must have an associated material definition. The thermoplastic material considered for the part is Cycolac FR23, the base material for the injection mold is P-20 steel (1.2709 alloy steel) and the coolant defined is water. Finally, to complete the definition of boundary conditions required for the simulations, the set of technological injection parameters used during its modeling is detailed. Table 1 shows the magnitudes of the rheological, thermal and technological variables defined to configure the numerical simulations.

Table 1. Rheological and thermal variables defined to set-up the numerical simulation.

Description	Units	Study case Cycolac FR 23 (ABS)
Filling, Packing and Cooling Time	s	2.5 – 5.0 – 20.4
Melt, Mold, Ejection and Coolant Temperature	°C	270.0 – 60.0 – 85.0 – 49.0
Coolant Flow Rate	cm^3/s	130.0
Maximum Injection and Packing Pressure	MPa	43.5 – 40.9

4 Results

After solving the simulation through the Moldex 3D solver module, the results are analyzed in order to:

– Analyze in detail the thermal behavior of the system through the results obtained during the cooling phase. Finite element modeling of the plastic part and cooling channels allows the simulation of the heat exchange between the part and the injection mold. Factors such as the temperature of the coolant, pressure drop of the cooling systems or the part temperature throughout the cooling phase, allow the optimization of the parameters within the process, as well as determining the optimal cooling system.
– Analyze the deformations of the plastic part, contemplating determinant factors in these such as internal residual stresses accumulated during injection and during the cooling phase. The deformations obtained from simulation can be quantified according to determining factors such as cooling design, part design and fiber arrangement

in case of use of loaded injection material. This analysis makes it possible to predict the final deformation of the part and the cause of this deformation.

Thus, based on the results obtained, the present research work compares the thermal performance of the traditional cooling system and the new proposal conformal cooling system. Both designs have been analyzed, obtaining the conditions that determine the final quality of the plastic part under study, as well as the performance of the cooling system. Table 2 shows the numerical results obtained for the technological parameters: time to reach the ejection temperature, mold temperature difference, total warpage and thermally induced Von Misses residual stress.

Table 2. Numerical Results.

Description	Units	Traditional cooling design	Conformal cooling design	Improvements
Time to reach ejection temperature	s	66.433	41.500	37.5%
Average mold temperature difference	℃	11.47	7.34	36.0%
Total Warpage	mm	1.064	1.10	3.5%
Thermal residual stress	MPa	16.995	12.849	24.4%

5   Conclusions

From the numerical results obtained in the thermal and rheological simulations analyzed, it is shown that the conformal design methodology applied to the cooling channels optimizes the manufacturing process of the part under study. In particular, the conformal cooling design reduces the cycle time 24.933 s compared to traditional cooling system design. Similarly, the temperature gradients analyzed at the plastic part surface indicate greater homogeneity achieved with the conformal cooling design and a 7.34 ℃ reduction on the mold temperature difference between the conformal and traditional cooling design. This means an optimization of 37.5% and 36.0% in both parameters respectively. In this way, the final quality of the plastic part under study is improved by achieving a more uniform temperature map, after the cooling phase, throughout the entire part and reducing surface and mechanical defects derived from thermally induced residual stresses and deformations. In particular, the total deformation is reduced by a magnitude of 0.02 mm. Whereas, the thermally induced Von Misses residual stress is reduced by a magnitude of 4.146 MPa. This supposes an optimization of 3.5% and 24.4% respectively for both parameters.

The development of additive manufacturing technology in recent years has made it possible to optimize the process and improve its requirements. Currently, metallic materials have thermal and structural properties similar to the metallic materials used

for the manufacture of plastic injection molds. Finally, it is justified that the use of 3D additive manufacturing techniques, applied to the manufacturing process through injection molds, improves the productivity and economy of the process. Since it reduces its cycle time, it optimizes the cooling phase of complex surfaces and improves the final quality of plastic parts, allowing compliance with the strict functional requirements and geometric and dimensional tolerances established for this industrial sector.

References

1. Kuo, C.C., You, Z.Y.: Enhancing the Structural Strength for Injection Molding Tooling With Conformal Cooling Channels Using ANSYS Software (2021). https://doi.org/10.21203/rs.3.rs-399879/v1

2. Singh, D., Joshi, K., Patil, B.: Comparative economic analysis of injection-moulded component with conventional and conformal cooling channels. J. Inst. Eng. (India): Ser. C **103**, 307–317 (2021). https://doi.org/10.1007/s40032-021-00778-5

3. Torres-Alba, A., Mercado-Colmenero, J.M., Caballero-Garcia, J.D.D., Martin-Doñate, C.: Application of new triple hook-shaped conformal cooling channels for cores and sliders in injection molding to reduce residual stress and warping in complex plastic optical parts. Polymers **13**(17), 2944 (2021)

4. Doñate, C.M., Paramio, M.R.: New methodology for demoldability analysis based on volume discretization algorithms. Comput. Aided Des. **45**(2), 229–240 (2013)

5. Mercado-Colmenero, J.M., Torres-Alba, A., Catalan-Requena, J., Martin-Doñate, C.: A new conformal cooling system for plastic collimators based on the use of complex geometries and optimization of temperature profiles. Polymers **13**(16), 2744 (2021)

6. Martin-Doñate, C., Shaikheleid, S., Torres-Alba, A., Mercado-Colmenero, J.M.: A new smart web platform for plastic injection molds in industry 4.0 environments. In: Roucoules, L., Paredes, M., Eynard, B., Morer Camo, P., Rizzi, C. (eds.) JCM 2020. LNME, pp. 309–315. Springer, Cham (2021). https://doi.org/10.1007/978-3-030-70566-4_49

7. Kuo, C.C., Xu, J.Y., Zhu, Y.J., Lee, C.H.: Effects of different mold materials and coolant media on the cooling performance of epoxy-based injection molds. Polymers **14**(2), 280 (2022)

8. Kanbur, B.B., et al.: Metal additive manufacturing of plastic injection molds with conformal cooling channels. Polymers **14**(3), 424 (2022)

9. Huang, W.T., Tasi, Z.Y., Ho, W.H., Chou, J.H.: Integrating Taguchi method and gray relational analysis for auto locks by using multiobjective design in computer-aided engineering. Polymers **14**(3), 644 (2022)

10. Kuo, C.-C., Chen, W.-H., Lin, Y.-X., Gao, Q., Gian, S.-J., Xiao, C.-X.: Effects of different fillers on the silicone rubber mold with conformal cooling channels. Int. J. Adv. Manuf. Technol. **108**(5–6), 1509–1525 (2020). https://doi.org/10.1007/s00170-020-05508-2

11. Torres-Alba, A., Mercado-Colmenero, J.M., Caballero-Garcia, J.D.D., Martin-Doñate, C.: A hybrid cooling model based on the use of newly designed fluted conformal cooling channels and fastcool inserts for green molds. Polymers **13**(18), 3115 (2021)

Manufacturing Engineering

Planetary Dragging Cutting Edge Treatment and Edge Rounding Prediction on Carbide Tools

Cristian Pérez-Salinas[1]([✉]) [iD], L. N. López de Lacalle[2,3] [iD],
Pablo Fernández-Lucio[3] [iD], and Octavio Pereira-Neto[2] [iD]

[1] Universidad Técnica de Ambato UTA, Av. los Chasquis and Rio Payamino Street, Ambato,
Ecuador
cf.perez@uta.edu.ec

[2] Aeronautics Advanced Manufacturing Centre (CFAA), 48170 Zamudio, Spain

[3] University of the Basque Country UPV-EHU, 48013 Bilbao, Spain

Abstract. This paper describes the use of the "Dragging" (*DF*) cutting edge preparation process with 2 grit sizes and three mixing ratios. Both the immersion depth of the tool in the abrasive medium and the dragging duration time were manipulated. A Repeatability and Reproducibility (*R&R*) analysis and edge radius (*ER*) prediction were carried out using Machine Learning by Artificial Neural Network (*ANN*). The results achieved were that the influencing factors on the ER in order of importance were drag depth, drag time, mixing percentage and grain size respectively. Furthermore, the reproduction accuracy of the *ER* is reliable in comparison with traditional processes such as brushing and blasting and the prediction accuracy of the *ER* of preparation with *ANN* was 94% showing the effectiveness of the algorithm. Finally, it is demonstrated that *DF* has reliable feasibility in the application of cutting-edge preparation on carbide tools.

Keywords: Polishing · Dragging cutting edge · Carbide tools · *ANN* Prediction

1 Introduction

The performance of cutting tools is directly related to the macro and micro geometry of the tool, cutting materials and coating systems. Recent studies show that the micro geometry of the tool has a very important influence on the cutting process [1, 2]. Furthermore, extending the lifetime of the cutting edge is possible with a specific shape of the cutting edge [3–6]. In this sense, achieving an effective geometry is the main concern of researchers and the manufacturing industry.

There are several cutting-edge preparation processes that have evolved with the emergence of new technologies, each of which has its advantages and limitations [2]. One process that has become relevant and very useful in recent years is the "Dragging" or "Drag Finishing" abrasive preparation process [7, 8]. Its low cost and versatility to work with the grinding of complex geometries are advantages that make it relevant and useful [9]. However, in the specialized literature there is little information on the working

methodology, its limitations, its precision, and its influential parameters in obtaining the cutting microgeometry. Consequently, the need to find the process parameters to find the sharpest cutting-edge sharpness is vital.

Measurement and test results are always subject to a certain uncertainty. Traditionally, accuracy, linearity and stability were characteristics considered in the evaluation of measurement systems. However, it is now recognized that important properties such as repeatability and reproducibility *R&R* need to be included in the measurement system as an indicator of a reliable process [10, 11]. In this sense, their usefulness is relevant for *DF* process evaluation [11, 12].

Due to the rise of Industry 4.0, the inclusion of Machine Learning for process monitoring is a field of high importance and demand in the industry. Artificial neural networks are a type of artificial intelligence that allow the prediction of variables. Authors such as [13, 14] used the artificial neural network model to study and predict tool wear from machine working parameters and observed the effectiveness of the algorithms. Therefore, seeing similarity in the investigated object of study, the neural network could predict the evolution of cutting-edge preparation.

This work describes the use of the *DF* cutting edge preparation process and all its characteristics to allow a better understanding of the process, to verify its accuracy, reproducibility, limitations, and influential parameters applied to carbide tools with the abrasive material Alumina (Al2O3) and Silicon Carbide (SiC) in two grain sizes.

2   Methodology

The An OTEC-DF drag finishing machine was used with abrasive grains of Silicon Carbide (SiC) and Alumina (Al2O3) in two different sizes 24 and 46 according to the sieve aperture given by ASTM D E 11-70 (Fig. 1a and 1b). The tool tested (Fig. 2), was a triangular insert for turning operation without K10-Co7% Tungsten Carbide K10-Co7% coating. The experiment consisted of varying three drag depth (*ID*) levels, three abrasive mixing ratios (*RM*) with two grit sizes (*GZ*) and drag duration times (*DT*) to achieve expected edge radii ranges (Fig. 1). The variants are shown in Table 1. Subsequently, the *ER* was measured using a TMAlicona InfiniteFocusG5 edge profile measuring device with a 10X lens as well as the surface roughness with a 20X lens.

The *R&R* analysis was performed by measuring 24 randomly chosen parts with 3 technicians with 3 repetitions each giving a total of 72 measurements each. Finally, the prediction of the edge radius artificial neural network *ANN*. The experimental data set used for the training stage was divided by cross-validation into 80% for training and 20% for validation. It was developed with a feed-forward and backpropagation neural scheme on the total experimental data.
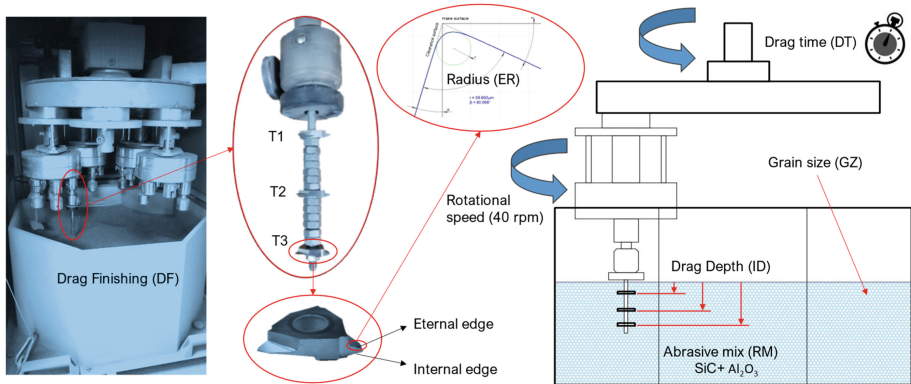
Fig. 1. Experimental scheme and description of parameters.

Table 1. Variation of factors in experimental design

Factors	I	II	III
Abrasive type	SiC	Al_2O_3	–
Grit size [μm] Grit size [μm]	390 (A)	390+750 (AB)	750 (B)
Percentage by weight of SiC [%]	50	66	75
Dragging time [min]	10/10	15/15	20/20
Dragging depth [mm]	10	60	120

3 Results

Figure 2 shows the effect of each dragging parameter on the cutting-edge radius. All parameters show equal incidence on the internal edge *Ri* as on the external edge *Re*. All parameters are increasing except for the abrasive mixture percentage *RM*, where the effect is intermittent. The combined effect of grit size *GZ* and drag depth *ID* causes an increase in radius (Fig. 3). This is because face contact (drag force) increases due to the higher pressure that the cutting edge is subjected to when it is under more abrasive (Fig. 1). Therefore, the rapidity and severity of the cutting-edge rounding process is directly related to *DT*, *GZ* and *ID*.
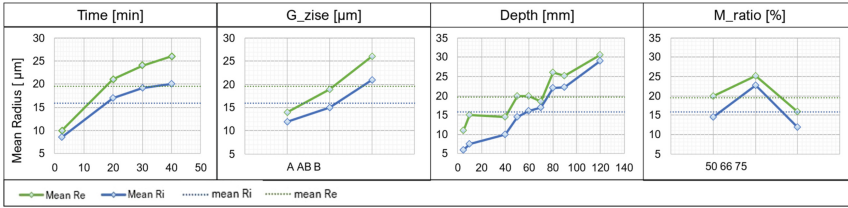
Fig. 2. Effect of parameters on the cutting-edge radius ER
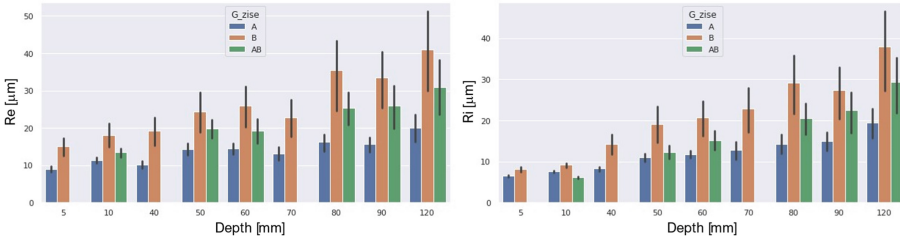
Fig. 3. Combined effect of grain size and drag depth on ER cutting edge radius, a) Re and b) Ri.

The roughness *Ra* achieved on the surface of the cutting-edge radius is uniform. But the *Rz* differs in its values between the outer and inner cutting edges (Fig. 4). *Rz* is more sensitive to the detection of machined surface imperfections. Therefore, it is used for the control and monitoring of surface irregularities [15, 16]. It was found that the higher inclusion of alumina in the mixture makes the abrasive mixture more aggressive (*RM* = 50%). However, the *Rz* values obtained by Drag Finishing in this study are lower or equal to those obtained in tool manufacturing by grinding operation [15, 16].
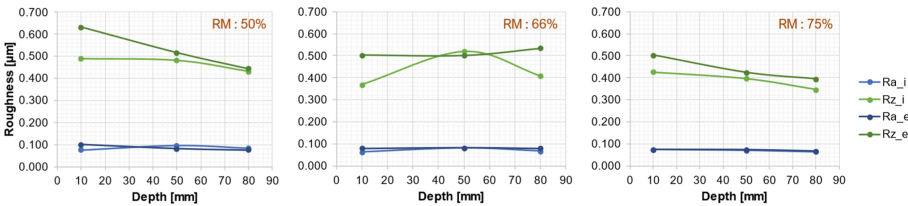
Fig. 4. Surface roughness performance as a function of drag depth (IR) and abrasive mixture ratio (MR)..

Table 2 indicates the sources of variation of the *R&R* analysis of the measurement system in obtaining the cutting-edge radius. The result of the analysis shows that the variation of the measurement system is equal to 19.35% of the process variation. Moreover, the contribution of repeatability is higher than reproducibility, which indicates that the system is in the marginal zone. Consequently, the acceptance is possible if the limitations of the process, the importance of the application and the cost are known [17, 18].

Table 2. Contribution of variables in R&R analysis.

Source	Standard deviation (σ)	Study deviation ($6 \times \sigma$)	% Study deviation
Gage R&R total	1,9977	11,986	19,35
Repetibility	1,5844	9,5067	15,35
Reproducibility	1,2167	7,2999	11,78
Technical	0,2385	1,4311	2,31
Technical*Ref	1,193	7,1582	11,55
Part to part	10,1303	60,7816	98,11
Total variation	**10,3254**	**61,9522**	**100**
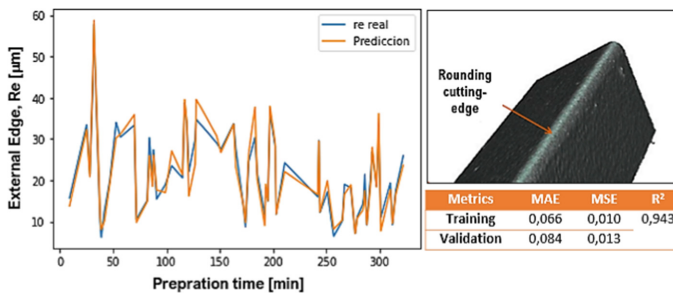
Fig. 5. ANN prediction results of cut-edge radius growth (ER).

In reference to the neural network prediction, for the algorithm validation, only 363 epochs were needed to find the best training. Meaning that the errors were no longer reduced but stabilized. A coefficient of determination R^2 of 0.943 with a standard deviation of 0.0104 was obtained. Therefore, the prediction was continued (Fig. 5). Finally, the average prediction error was 8.81% compared to the actual edge rounding values.

4   Conclusions

The parameters involved in obtaining a cutting-edge radius were, in order of importance: immersion depth, drag time, abrasive mixture percentage and abrasive size.

The difference found between *Re* and *Ri* indicates that the location and orientation of the cutting edge when dragging in the abrasive directly influences the result. In addition, grain mixing rate and grain size influence the surface roughness.

The dragging process allows a reduction of the roughness in terms of *Ra* and *Rz* (average: $Ra = 0.12\ \mu m$, $Rz = 0.5\ \mu m$), and the edge radius reproduction is acceptable compared to traditional processes such as brushing and blasting.

The prediction accuracy of the preparation radius with *ANN* was 94%, which proves the efficiency of the algorithm.

References

1. Bergmann, B., Grove, T.: Basic principles for the design of cutting edge roundings. CIRP Ann. **67**, 73–78 (2018). https://doi.org/10.1016/J.CIRP.2018.04.019
2. Zhuang, K., Fu, C., Weng, J., Hu, C.: Cutting edge microgeometries in metal cutting: a review. Int. J. Adv. Manuf. Technol. **116**(7–8), 2045–2092 (2021). https://doi.org/10.1007/s00170-021-07558-6
3. Cortés, C.: Cutting Edge Preparation of Precision Cutting Tools by Applying Micro-abrasive Jet Machining and Brushing. Kassel University Press GmbH (2009)
4. Bouzakis, K.D., et al.: Effect of cutting edge preparation of coated tools on their performance in milling various materials. CIRP J. Manuf. Sci. Technol. **7**, 264–273 (2014). https://doi.org/10.1016/J.CIRPJ.2014.05.003
5. Karpuschewski, B., et al.: Magneto-abrasive machining for the mechanical preparation of high-speed steel twist drills. CIRP Ann. **58**, 295–298 (2009). https://doi.org/10.1016/J.CIRP.2009.03.046
6. Magalhães, F.C., et al.: Experimental and numerical analysis of hard turning with multi-chamfered cutting edges. J. Manuf. Process. **49**, 126–134 (2020). https://doi.org/10.1016/J.JMAPRO.2019.11.025
7. Priarone, P.C., et al.: Effects of cutting angle, edge preparation, and nano-structured coating on milling performance of a gamma titanium aluminide. J. Mater. Process. Technol. **212**, 2619–2628 (2012). https://doi.org/10.1016/J.JMATPROTEC.2012.07.021
8. Pérez-Salinas, C.F., et al.: Estimation of drag finishing abrasive effect for cutting edge preparation in broaching tool. Materials **15**, 5135 (2022). https://doi.org/10.3390/MA15155135
9. Denkena, B., Biermann, D.: Cutting edge geometries. CIRP Ann. **63**, 631–653 (2014). https://doi.org/10.1016/J.CIRP.2014.05.009
10. Zanobini, A., et al.: Repeatability and Reproducibility techniques for the analysis of measurement systems. Measurement **86**, 125–132 (2016). https://doi.org/10.1016/J.MEASUREMENT.2016.02.041
11. Maria Mendes Araújo, L., et al.: New indicators for measurement error detection in GR&R studies. Measurement **140**, 557–564 (2019). https://doi.org/10.1016/J.MEASUREMENT.2019.03.059
12. Shirodkar, A., Rane, S.: Evaluation of coordinate measuring machine using gage repeatability & reproducibility. Int. J. Syst. Assur. Eng. Manag. **12**, 84–90 (2021). https://doi.org/10.1007/S13198-020-01050-2/TABLES/9
13. Ghosh, N., et al.: Estimation of tool wear during CNC milling using neural network-based sensor fusion. Mech. Syst. Signal Process. **21**, 466–479 (2007). https://doi.org/10.1016/J.YMSSP.2005.10.010
14. Panda, S.S., Chakraborty, D., Pal, S.K.: Flank wear prediction in drilling using back propagation neural network and radial basis function network. Appl. Soft. Comput. **8**, 858–871 (2008). https://doi.org/10.1016/J.ASOC.2007.07.003

15. Núñez, D., et al.: Spray lubrication in turning processes, effects on productivity and quality. Dyna (Spain) **94**, 561–567 (2019). https://doi.org/10.6036/8843
16. Cruz, D.C., et al.: Assessment of the surface integrity of ground cemented tungsten carbide cutting inserts and its influence on tool wear in turning of ferritic nodular cast iron. CIRP J. Manuf. Sci. Technol. **37**, 613–622 (2022). https://doi.org/10.1016/J.CIRPJ.2022.03.014
17. Marques, A.M., et al.: Multivariate GR&R through factor analysis. Measurement **151**, 107107 (2020). https://doi.org/10.1016/J.MEASUREMENT.2019.107107
18. Pereira, R.B.D., et al.: Combining Scott-Knott and GR&R methods to identify special causes of variation. Measurement **82**, 135–144 (2016). https://doi.org/10.1016/J.MEASUREMENT.2015.12.033

Determination of Tool Wear in Peripheral Milling Operations Based on Acoustic Emission Signals

Ricardo Alzugaray-Franz[1,2(✉)], Eduardo Diez-Cifuentes[1], Erardo Leal-Muñoz[1], Mónica Villaverde-San José[2], and Antonio Vizán-Idoipe[2]

[1] Departamento de Ingeniería Mecánica, Universidad de La Frontera, Temuco, Chile
ricardo.alzugaray@ufrontera.cl

[2] Departamento de Ingeniería Mecánica, Universidad Politécnica de Madrid, Madrid, Spain

Abstract. In this work, an indirect approach based on acoustic emission signals is presented to predict progressive tool wear in peripheral milling operations. Measurements of flank wear and cutting forces are considered in order to assess the performance of the method. The acoustic emission is found to be sensitive to changes of tool condition and the evolution of the wear land. The latter provides experimental evidence to support the current knowledge on tool wear estimation towards the definition of tool-life criteria based on indirect process variables.

Keywords: flank wear · acoustic emission · cutting forces · peripheral milling

1 Introduction

Tool wear is a detrimental progressive phenomenon with negative impacts on productivity, efficiency, and safety of machining operations. Although tool wear mechanisms are diverse, flank wear is commonly used in milling processes. It is a consequence of the sliding contact between the flank face of the cutting edge and the newly machined surface of the workpiece. Flank wear can be estimated directly from geometric parameters of the wear land [1] or by means of indirect methods based on physical magnitudes that carry information of the development of the process [2, 3]. From the latter, the acoustic emission has been widely used for characterization of machining operations [4–7]. It has the advantage of being a non-intrusive method which does not require major modifications in the work area of the machine tool. Moreover, it can be recorded without interrupting the machining process and its frequency range is less influenced by machine vibrations or any surrounding sources. Regarding tool wear monitoring, the acoustic emission has been object of intensive research efforts [8–12], however the evidence is not conclusive and the methods developed are far from being implemented in practice.

In this contribution, an indirect method based on the acoustic emission signal is presented to estimate the progressive tool wear in peripheral milling operations. The measurement of flank wear and the cutting forces are considered in order to establish comparisons and to perform analysis of sensitivity to changes in tool condition.

2 Methodology

Due to causality between cutting speed and tool wear, a one-factor and two-level experiment is proposed as shown in Table 1. To improve the accuracy of the observations, four replicates were set up for each treatment. This gives a total of 8 experimental trials, which were randomized to minimize the occurrence of systematic errors.

The experiments were performed in a Deckel Maho DMC 1035 V Eco machine center under constant cutting conditions. They consist of a series of consecutive passes of peripheral milling on a prismatic AISI 4340 workpiece with a cutting length of 90 mm. Each treatment starts with a fresh tool, and it ends when a predetermined level of tool wear has been reached. A two-flute helical endmill is selected, however one of the cutting edges is removed to avoid runout, allowing to determine the progression of tool wear with a constant chip load.

Table 1. Experimental cutting conditions. Cutting tool: HSS helical endmill, 9 mm diameter, with 2 teeth and 30° helix angle. Nomenclature: cutting velocity V_c, spindle speed N, cutting length of each pass L_c, axial cutting depth a_p, radial cutting depth a_e and feed per tooth f_z.

Treatment No (Replicate)	V_c[m/min] (N [min^{-1}])	L_c[mm]	a_p[mm]	a_e[mm]	f_z[mm/tooth]
1 (4)	33.93 (1200)	90	8	0.2	0.1
2 (4)	84.82 (3000)				

Visual inspections of the tool have been conducted after each cutting pass and a complete map of the cutting edge is captured by a digital microscope Dinolite AM4815ZTL. The acoustic emission is measured by a Kistler 8152C0050500 piezoelectric transducer coupled to a Kistler 5125C unit which provides an analog output within a frequency range of 50 and 400 kHz. The AE sensor is rigidly mounted to a fixing plate that holds the workpiece, providing a direct transmission path to the excitation source. The three components of the cutting forces are measured with a dynamometric platform Kistler 9257BA connected to a Kistler 5233A1 control unit which delivers analog outputs in a frequency range between 200 and 2000 Hz. The data acquisition system is based on a NI PXI platform equipped with a NI PXI-6132 card to record the acoustic emission signal with a sampling frequency of 2 MHz, and a NI PXI-4472B card dedicated to the cutting forces at a sampling frequency of 20 kHz.

The flank wear (VB) is determined from image processing and by following the recommendations of ISO 8688–2 [1]. The instantaneous mean and maximum values of the flank width, thereafter referred as VB_{mean} and VB_{max}, are selected as characteristic values that represent the uniform and localized growth behavior of the wear land profile, respectively. On the other hand, the response of the acoustic emission and cutting forces to changes in tool condition is evaluated in terms of the peak amplitude of each cutting cycle, giving a measure of the prominence of the signals. A moving window is used as a data reduction method which allows to get the mean value and standard deviation of all instantaneous values within the zone where the tool is fully engaged.

3 Results

3.1 Flank Wear VB

Figure 1(a) shows the progression of flank wear. If the tool life criterion is set to 300 μm, one finds that tool life for the first treatment is 900 s, while for the second treatment it reduces to 400 s. The latter confirms the relationship between tool wear and cutting speed. Moreover, by examining the differences between the curves of VB_{max} and VB_{mean}, it can be noticed that the cutting speed might also affect the shape of the wear land profile. As for the first treatment, both curves are found to be very close to each other, whereas in the second treatment, these two curves change at a different rate which is a clear indication of localized growth. This feature is also observed from the microscope images depicted in Fig. 1(b) and Fig. 1(c).
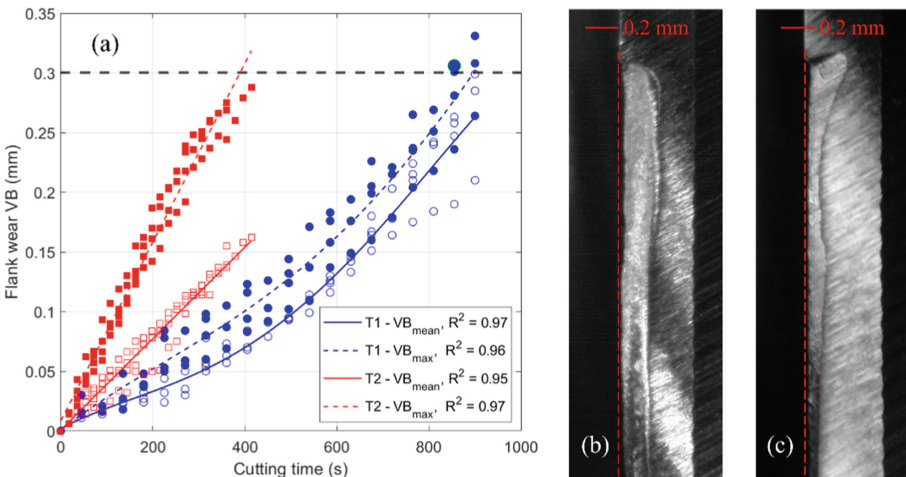
Fig. 1. (a) Evolution of progressive flank wear over cutting time. (b) Uniform wear land profile for Treatment No. 1 at $t_c = 900$ s. (c) Non-uniform wear land profile with localized growth for Treatment No. 2 at $t_c = 400s$.

3.2 Analysis of Indirect Variables

Figure 2 shows the evolution of the mean peak value of the acoustic emission and the cutting force F_{xy}. A potential model for these two magnitudes has been adjusted to describe the trend of data points. In both cases, the amplitude of the mean peak value increases as a function of cutting time. This confirms that these variables can be considered as valid descriptors of the process and they can be readily applied in tool condition monitoring.

On the other hand, if one compares the rate of change of the indirect variables and the flank wear curves shown in Fig. 1(a), it can be noticed that the acoustic emission is
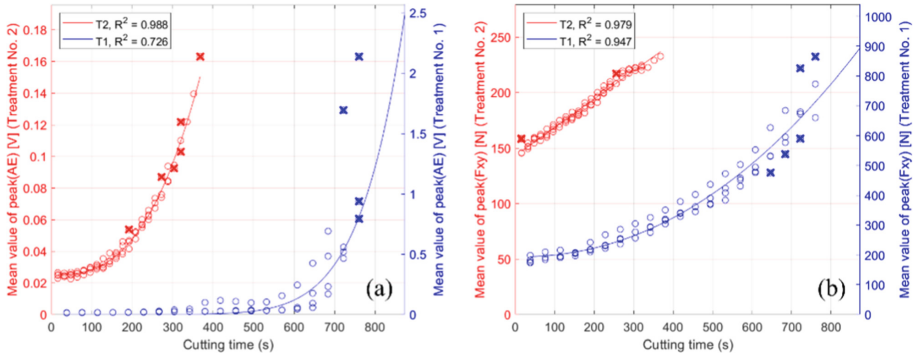
Fig. 2. Evolution of mean peak value. (a) Acoustic emission and (b) cutting force F_{xy}. Data points are marked with circles and outliers are highlighted with crosses.
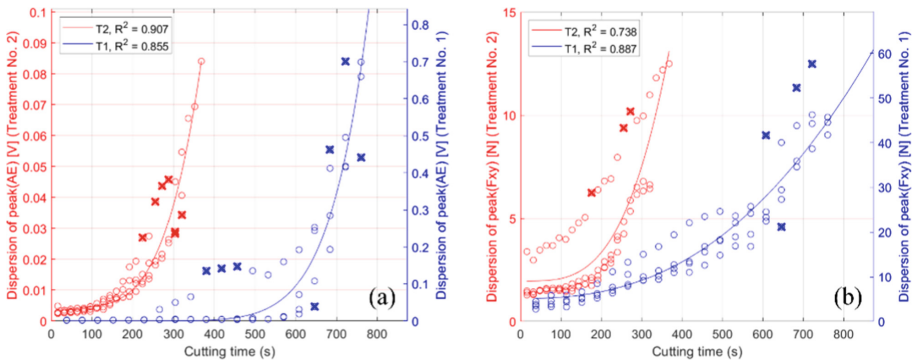
Fig. 3. Evolution of the dispersion of peak value. (a) Acoustic emission and (b) cutting force F_{xy}. Data points are marked with circles and outliers are highlighted with crosses.

not only more sensitive to flank wear than the cutting forces, but also it has the ability to distinguish whether the wear land profile follows a uniform behavior or not.

Analogously, Fig. 3 shows the standard deviation of the mean peak value of the magnitudes of interest. A potential model also has been adjusted to the experimental data. At first glance, the evolution of the dispersion of the acoustic emission and the cutting forces looks similar to the previous results, however, in this case the cutting forces reveal better agreement with the behavior of the flank wear curves. Physically, this means that a tool in good condition exhibits uniform cutting cycles, while in a degradation state it begins to differ from the average value given by normal operation. Therefore, the standard deviation of the mean peak value can be considered as a complementary indicator of flank wear.

Although the mean and standard deviation of the peak value constitute suitable indicators of tool wear progression, the definition of a tool life criteria based on process variables still requires establishing a threshold value. In this regard, the waveform analysis of the instantaneous peak value allows to incorporate additional information to strengthen the decision process. Figure 4 shows a waterfall plot of the instantaneous

peak value of the acoustic emission signal as a function of the stationary cutting time and the cutting pass number for Treatment No. 2. For instance, by tracking the waveform amplitude changes between cutting passes, one can observe that the cutting tool starts to wear out at a more accelerated rate from pass 11, which is equivalent to approximately 50% of the lifetime given by the flank wear criterion of VB = 300 μm. This might appear as a qualitative analysis, but it opens the possibility to apply statistical methods to extract quantitative values representative of the tool life.
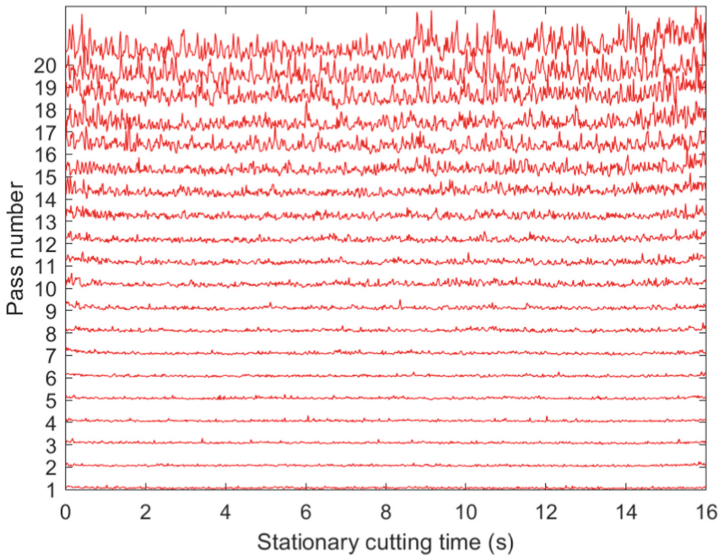
Fig. 4. Evolution of instantaneous peak value of the acoustic emission for Treatment No. 2.

4 Conclusions

This work presents an indirect method to estimate tool wear in peripheral milling operations under stationary cutting conditions based on the acoustic emission and the cutting forces. Comparisons with direct flank wear measurements confirm that cutting speed has a strong influence in tool life and in the shape development of the wear land profile along the cutting edge. Experimental evidence suggests that feature extraction can be used to estimate flank wear and also to define a tool life criterion based on indirect variables of the process.

References

1. International Standardization Organization (ISO): ISO 8688, Tool life testing in milling — Part 2: End milling (1989)
2. Wong, S.Y., Chuah, J.H., Yap, H.J.: Technical data-driven tool condition monitoring challenges for CNC milling: a review. Int. J. Adv. Manuf. Technol. **107**(11–12), 4837–4857 (2020). https://doi.org/10.1007/s00170-020-05303-z
3. Li, X., Liu, X., Yue, C., et al.: Systematic review on tool breakage monitoring techniques in machining operations. Int. J. Mach. Tools Manuf. **176**, 103882 (2022). https://doi.org/10.1016/j.ijmachtools.2022.103882
4. Blum, T., Inasaki, I.: A study on acoustic emission from the orthogonal cutting process. J. Eng. Ind. **112**, 203–211 (1990). https://doi.org/10.1115/1.2899576
5. Byrne, G., Dornfeld, D., Inasaki, I., et al.: Tool condition monitoring (TCM) — the status of research and industrial application. CIRP Ann. **44**, 541–567 (1995). https://doi.org/10.1016/S0007-8506(07)60503-4
6. Teti, R., Jemielniak, K., O'Donnell, G., Dornfeld, D.: Advanced monitoring of machining operations. CIRP Ann. **59**, 717–739 (2010). https://doi.org/10.1016/j.cirp.2010.05.010
7. Kishawy, H.A., Hegab, H., Umer, U., Mohany, A.: Application of acoustic emissions in machining processes: analysis and critical review. Int. J. Adv. Manuf. Technol. **98**(5–8), 1391–1407 (2018). https://doi.org/10.1007/s00170-018-2341-y
8. Diei, E.N., Dornfeld, D.A.: Acoustic emission sensing of tool wear in face milling. J. Eng. Ind. **109**, 234–240 (1987). https://doi.org/10.1115/1.3187124
9. Dornfeld, D.: Application of acoustic emission techniques in manufacturing. NDT E Int. **25**, 259–269 (1992). https://doi.org/10.1016/0963-8695(92)90636-U
10. Diniz, A.E., Liu, J.J., Dornfeld, D.A.: Correlating tool life, tool wear and surface roughness by monitoring acoustic emission in finish turning. Wear **152**, 395–407 (1992). https://doi.org/10.1016/0043-1648(92)90135-U
11. Kakade, S., Vijayaraghavan, L., Krishnamurthy, R.: In-process tool wear and chip-form monitoring in face milling operation using acoustic emission. J. Mater. Process. Technol. **44**, 207–214 (1994). https://doi.org/10.1016/0924-0136(94)90433-2
12. Hase, A., Wada, M., Koga, T., Mishina, H.: The relationship between acoustic emission signals and cutting phenomena in turning process. Int. J. Adv. Manuf. Technol. **70**(5–8), 947–955 (2013). https://doi.org/10.1007/s00170-013-5335-9

An Intelligent Machine Learning Based Method for Tool Wear Estimation in the Vertical Broaching Process

Ibon Holgado[1(✉)] , Cristian Pérez-Salinas[2,3] , Naiara Ortega[1,3] ,
L. N. López de Lacalle[1,3] , and Ander del Olmo[1,3]

[1] Aeronautics Advanced Manufacturing Centre (CFAA), 48170 Zamudio, Spain
ibon.holgado@ehu.eus

[2] Facultad de Ing. Civil y Mecánica, Universidad Técnica de Ambato, Ambato 180103, Ecuador

[3] Faculty of Engineering of Bilbao, UPV/EHU, Plaza Ingeniero Torres Quevedo 1, 48013 Bilbao, Spain

Abstract. This work describes a machine vision system workflow to automatically estimate the broaching tool wear. The proposed system offers the possibility to evaluate the evolution of wear under different machining conditions and to decide when a tool should be replaced, guaranteeing the quality of the machined part and avoiding catastrophic tool breakage. In addition, the paper discusses the advantages of the proposed method over the traditional and widely used ISO 3685:1993 based methods, which are highly influenced by the operator. The proposed method uses a novel wear area segmentation technique based on *Machine Learning* artificial intelligence, generating highly reproducible values, saving technicians labor-intensive tasks, and obtaining values with high accuracy. The results show a strong relationship between the values obtained by the proposed automatic method and the experimental ones, with errors below 0.17% and 2.88% corresponding to the *MSE* and *MAE* respectively.

Keywords: Machine Learning · image processing · wear · broaching process

1 Introduction

The new idea of Industry 4.0 aims to implement all technological advances in various fields to boost production capabilities, streamline production processes, and make it easier for operators to do their tasks. One of the existing technologies that represents great advantages in the automation of production processes is artificial vision based on artificial intelligence [1].

To achieve the highest quality material cutting during the machining process, tool integrity is essential [2]. Therefore, new manufacturing models require intelligent machining to cope with dynamics, process variations and complexity. In this field, studies related to machining tool wear are necessary to achieve high quality parts. Various recent studies have attempted to monitor the machining process by considering different

information such as torque [3], vibration signals [1], acoustic signals [4] and process images [2] to estimate tool wear. However, some studies [1, 2] point out that there is still a lot of work to be done as estimating tool wear is a challenging task, frequently subjective and even more complex when the tool dimensions are in the order of micrometers, as is the case of broaching process. Broaching is a machining process used in the manufacture of complex shapes, both internal and external, required by many industrial sectors such as aeronautics, automotive and marine [3]. A common application of the broaching process is the manufacture of the aero-engine turbine discs fir trees, where both the level of surface and dimensional integrity and the cost of manufacture are critical. Therefore, the interest and requirement for reliable control of tool integrity is of great importance in the broaching process [2, 5, 6].

Direct measurement of flank wear in accordance with ISO 3685:1993 is a frequently used technique for evaluating the broaching tool wear [5]. Nevertheless, this method is laborious and subjective, as it depends on the experience of the operator performing the measurements. However, Machine Learning *ML* is the basis of many recent advances in artificial intelligence that have been developed in terms of improving evaluations of cutting tool wear. Machine learning is a subfield of artificial intelligence that allows machines to learn, improve and perform a specific task using process data. Thus, the main disadvantages of manual wear measurements can be overcome by *ML* techniques, which generate highly reproducible values, save technicians labor-intensive tasks and can obtain values with high accuracy. *ML* algorithms can be divided into three categories depending on the learning system and the type of input data (supervised learning, unsupervised learning, reinforcement learning). These algorithms attempt to perform two main tasks: clustering, in which data is separated into specific classes, and regression, looking for a trend within the data. The various methods used to achieve the different objectives will determine the type of algorithm used, for example Support Vector Machines *SVM*, Random Forest *RF*, k-nearest neighbors, etc. [1].

In this work, a machine vision system workflow to automatically estimate the broaching tool wear is proposed. The proposed method is established on in-process images of the tool and is based on the classification of pixels corresponding to the tool wear class. This classification is performed by supervised learning using one of the best performing algorithms in the field of digital image processing, Random Forest *RF* [1]. In the framework of this study, additional tests are carried out comparing the traditional measurement results using ISO 3685:1993 with the prediction results obtained by the *RF* algorithm.

2 Methodology

This section describes the broaching tests carried out, as well as the wear assessment by the traditional and the proposed ML-based machine vision method.

2.1 Broaching Test

Figure 1 shows the set-up of the method. The machined part was an Inconel 718 turbine disc of Ø500 mm diameter and a thickness of 34 mm. The experimental set-up was carried out on an EKIN vertical broaching machine working, Fmax = 70kN with an

uncoated 18-tooth Tungsten Carbide (Co10%) tool of grade S10. The images of the tool were obtained in process every 5 broaching cycles with a telecentric lens camera, LED light source, and integrated commercial imaging software. The resolution of all images was 1280x1024 and recorded with (.jpg) extension.
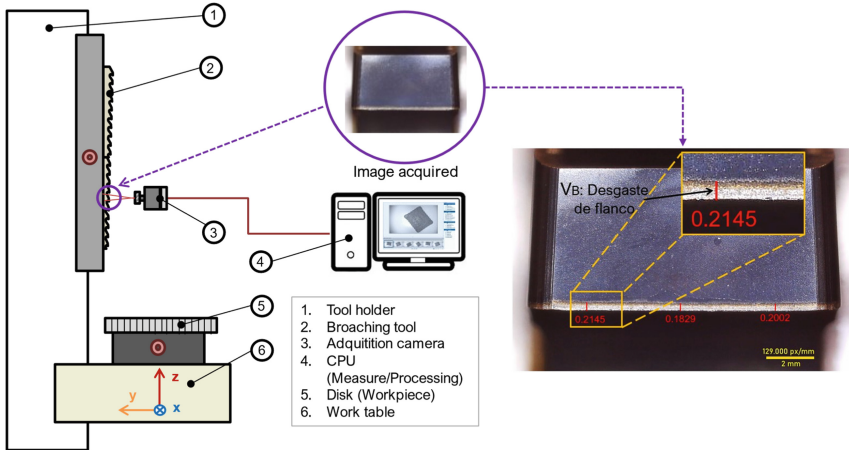

Fig. 1. Data acquisitions system architecture, a) parts and b) Measurement of flank wear under the traditional process.

2.2 Flank Wear Measurement by ISO 3685 Method

Firstly, once all the images of each flank were captured at different slots, the flank wear was measured in the traditional way according to the ISO 3685:1993 ISO8688-1 and 2 standards [6, 7]. Based on several studies [3, 5, 8], when machining with flat-faced tools, flank wear (*VB*) or crater wear (*KT*) are considered as main tool wear measurement parameters. Therefore, the procedure described in ISO 3685 (Fig. 1b) is applicable to the broaching process for the measurement of wear on its cutting tool.

2.3 Flank Wear Prediction by Machine Vision

The process of predicting flank wear by machine vision is shown in Fig. 2. First, after preliminary tests using a calibrated standard, the angle of image acquisition that was most representative of the actual magnitude of flank wear was determined. Then, a software tool was developed to delimit the Region of Interest (ROI), in which the tool wear occurs, thus avoiding undesiring effects that may lead to errors in prediction. This automated approach, which is based on morphological procedures, was successful with all of the test images (Fig. 2a). As the broaching tool comprises cutting-edge, 18 images were obtained in each slot. The labelling was performed on 5% of the pixels for only three out of the eighteen images in each pass. The pixels where classified into 5 classes (for a multi-class classification), including wear, background, tool, drill, and chip. Thereafter,

the attributes of the model were obtained. In this study, more than 150 digital filters were assigned as attributes (Fig. 2a). After the attributes were obtained, the RF classification algorithm implemented in the Scikit-learn python library, version 1.0.2 was used for multi-classification [9]. The number of trees used in each prediction was 100. Finally, once the RF classifier was trained, the model can be used to predict tool wear in new images.
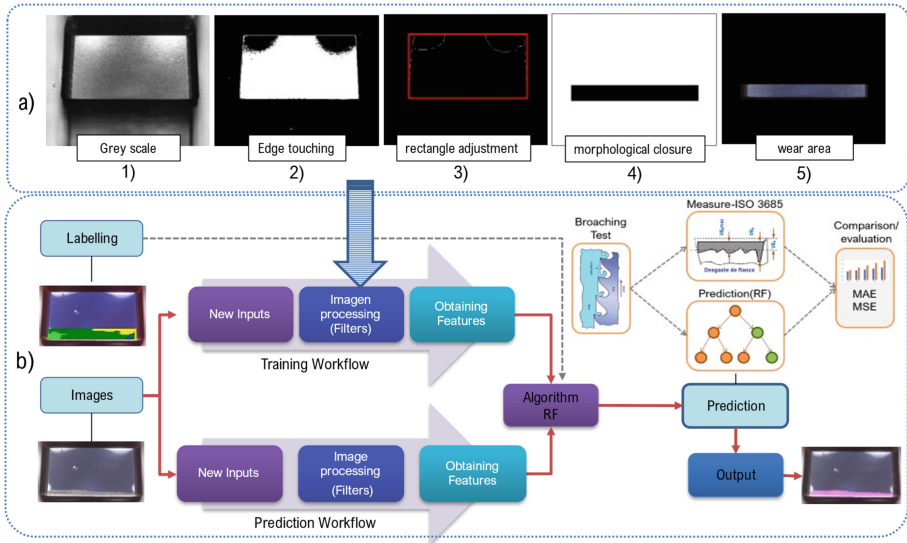
Fig. 2. ML- based Image processing technique for estimating tool wear

2.4 Predictive Performance

Through the comparison of a set of experimental data with the prediction results, it is possible to estimate the performances of various types of AI algorithms, such as shallow neural networks (*SNN*), deep neural networks (*DNN*), and Random-Forest (*RF*) algorithms. Mean Absolute Error (*MAE*) and Mean Squared Error (*MSE*) are two commonly used comparative metrics. Thus, in the present work, both *MAE* and *MSE* metrics were used to evaluate the accuracy of the proposed model. Equations (1) and (2) indicate the determination of the above metrics:

$$MAE = \frac{1}{n}\sum_{i=1}^{n}\left|\left(y_{exp} - \hat{y}_{pred}\right)\right| \tag{1}$$

$$MSE = \frac{1}{n}\sum_{i=1}^{n}\left(y_{exp} - \hat{y}_{pred}\right)^2 \tag{2}$$

where, y_{exp} represents the experimental values obtained by the traditional method based on ISO 3685:1993 and y_{pred} the values predicted by the model.

3   Results

Figure 3 shows the results of flank wear measurements using the traditional method (Fig. 3a) and the proposed (Fig. 3b). Progressive wear is observed as the number of machined grooves increases. The result is consistent with the nature of the process, as each edge is theoretically designed to cut through more and more matter. However, adhesion may occur at the cutting edge, increasing the cutting cross-section and thus leading to increased flank wear (case of the cutting-edge number 9).
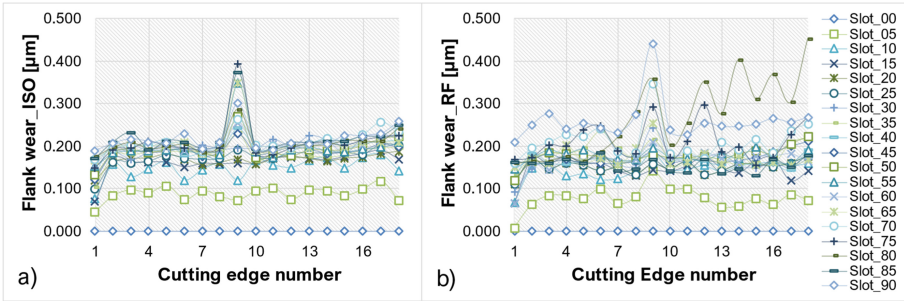
Fig. 3. Evolution of slot wear measurement by a) ISO method, b) Machine Learning.

By comparing both methods prediction results, an *MSE* of 0.17% and *MSA* of 2.88% were achieved (Fig. 4a). Although noise was present in certain sets of acquired images, the algorithm was able to classify the flank wear accurately (results in line with the ones obtained by the traditional method (Fig. 4b), in much less time and in an automatic way. In addition, it is observed that the flank wear and the wear area obtained by the *RF* algorithm have a direct relationship which is reflected in the trend of wear progress. Consequently, these two metrics are considered useful for assessing wear growth.
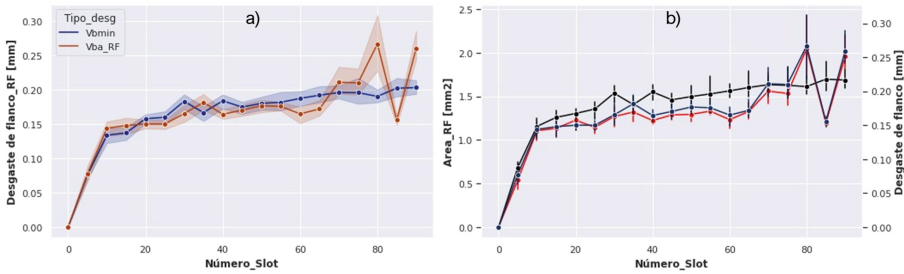
Fig. 4. Wear metrics obtained from the applied methods.

4 Conclusions

In this paper, flank wear on tool edges in broaching operation was evaluated using two methods: a traditional method under ISO 3685:1993 and by means of a Random Forest (*RF*) machine learning algorithm. The performance of the algorithm was evaluated on images acquired in process. The performance was determined using the *MSE* and *MSA* indicators, resulting in 0.17% and 2.88% respectively. It is therefore concluded that the Random Forest algorithm has potential utility for assessing flank wear development.

It is known that labelling improves the accuracy and indicators of the model. This study concludes that with the labelling of 3 mages of the 18 that confirm the broaching tool, a high density of labelling (5% of the pixels of the image), and with 4 different classes is sufficient to obtain repeatable and reliable results of tool wear.

Although not demonstrated in this study, the proposed *ML*-based method could be transferred to industrial environments and implemented in collaborative robots, increasing the level of automation and monitoring of tool wear in production processes.

In the future, a comparison of the performance of the Random Forest algorithm with other *ML*-based image processing algorithms will be carried out. Learning will also be extended to other weathering phenomena, such as cratering.

References

1. Kim, D.-H., et al.: Smart machining process using machine learning: a review and perspective on machining industry. Int. J. Precis. Eng. Manuf.-Green Technol. **5**(4), 555–568 (2018). https://doi.org/10.1007/s40684-018-0057-y
2. Fernández-Robles, L., Sánchez-González, L., Díez-González, J., Castejón-Limas, M., Pérez, H.: Use of image processing to monitor tool wear in micro milling. Neurocomputing **452**, 333–340 (2021). https://doi.org/10.1016/J.NEUCOM.2019.12.146
3. del Olmo, A., et al.: Tool wear monitoring of high-speed broaching process with carbide tools to reduce production errors. Mech. Syst. Signal Process. **172**, 109003 (2022). https://doi.org/10.1016/J.YMSSP.2022.109003
4. Elangovan, M., Devasenapati, S.B., Sakthivel, N.R., Ramachandran, K.I.: Evaluation of expert system for condition monitoring of a single point cutting tool using principal component analysis and decision tree algorithm. Expert Syst. Appl. **38**, 4450–4459 (2011). https://doi.org/10.1016/J.ESWA.2010.09.116
5. ISO - ISO 3685:1993 - Tool-life testing with single-point turning tools. https://www.iso.org/standard/9151.html. Accessed 01 June 2022
6. ISO - ISO 8688–1:1989 - Tool life testing in milling — Part 1: Face milling. https://www.iso.org/standard/16091.html. Accessed 14 July 2022

7. ISO - ISO 8688–2:1989 - Tool life testing in milling — Part 2: End milling. https://www.iso.org/standard/16092.html. Accessed 14 July 2022
8. Tool Life Testing with Single - Point Turning Tools – ASME. https://www.asme.org/codes-standards/find-codes-standards/b94-55m-tool-life-testing-single-point-turning-tools/1985/drm-enabled-pdf. Accessed 01 June 2022
9. Scikit-learn: Machine Learning in Python. https://jmlr.csail.mit.edu/papers/v12/pedregosa11a.html. Accessed 14 July 2022

Influence of Material Properties in Milling Forces of AISI 316L Obtained by L-PBF

Nicolás Díaz-Plaza De Los Reyes[1] , Ricardo Alzugaray-Franz[1],
Erardo Leal-Muñoz[1] , Iván La Fé-Perdomo[2] , Jorge Ramos-Grez[2] ,
and Eduardo Diez-Cifuentes[1(✉)]

[1] Department of Mechanical Engineering, Universidad de La Frontera, Temuco, Chile
eduardo.diez@ufrontera.cl
[2] Department of Mechanical and Metallurgical Engineering, Pontificia Universidad Católica de
Chile, Santiago, Chile
jramos@ing.puc.cl

Abstract. Technologies associated with additive manufacturing enabled the realization of several new products, providing high flexibility to the processes and high material usage efficiency. Furthermore, additively manufactured metals exhibit differences in surface topography and mechanical properties, primarily due to changes in the printing strategies and production parameters. Nowadays, postprocessing techniques are necessary to produce a quality printed metal product, due to the high initial surface roughness that every additive specimen presents. In this study, milling tests of additively manufactured AISI 316L workpieces obtained under different conditions were performed to investigate the influence of printing volumetric energy density, material density, and material ultimate tensile strength on cutting forces. The analysis revealed an association between cutting forces amplitude and the analyzed material properties. Also, similar machinability between the printed and the hot rolled metal was found when the density of the material was similar.

Keywords: LPBF · AISI 316L · milling forces

1 Introduction

Stainless Steel 316L has been in the additive manufacturing industry for a long time, being the laser powder bed fusion (L-PBF), the most common method applied to printing the material. Even so, many phenomena are yet to be investigated, especially in subjects associated with postprocessing. In additive manufactured components, material properties will notably change due to different factors, mainly, the printing parameters and printing strategy will strongly influence the final mechanical properties and surface roughness of the printed specimen. Therefore, there does not exist perfect printing parameter combination for all the situations [1, 2]. In [3] was concluded that it can be obtained L-PBF 316L pieces of nearly the same density that the material obtained by

conventional methods, but with higher deformations and UTS. Although mechanical properties of the additive material can be acceptable, in [4] pointed out that the surface roughness of the additive 316L is extremely poor and non-acceptable, always making necessary a postprocessing technique.

Milling of additive metals is still a field in exploration. Usually, in milling of additive metals, axial depth of cut varies between 0.1 to 0.2 mm, and finishing machining parameters are used to improve surface roughness [5]. Due to the L-PBF process nature, the printed specimen machinability will depend on the building orientation and laser scan strategy, requiring special planification for its machining [6]. The present investigation objective is to determine how the volumetric energy density and the material properties, density, and ultimate tensile strength, affect the milling forces of AISI 316L specimens, obtained by the additive process of L-PBF.

2 Methodology

2.1 Materials

The workpieces consist of a set of eight prismatic samples of AISI 316L 20x10x6 mm, manufactured through the L-PBF process using a General Electric Concept Laser MLAB 200R machine. Laser scanning strategy (LSS) used a 67° interlayer rotation MEANDER pattern (Fig. 1). All the samples were obtained through a wire EDM cut from bigger workpieces. Different mechanical properties, density and UTS, were obtained for the samples through variations in the volumetric energy density. UTS was measured in a INSTRON 4206 machine following ASTM E8/E8M-21 standard. Samples properties are listed in Table 1, including the properties of a conventional 316L hot rolled sample for further machinability comparisons. For the milling experiments, 5 mm diameter, two flute IPFE2050–05 Korloy mills were used.

Table 1. AISI 316L Samples properties.

Sample	Volumetric energy density (J/mm^3)	Density (g/cm^3)	UTS (MPa)
1	166.67	7.64	616.82
2	148.15	7.60	620.39
3	100.00	7.55	578.34
4	83.33	7.49	569.08
5	95.24	7.47	543.16
6	72.92	7.41	556.29
7	66.67	7.19	470.20
8	64.81	7.17	474.25
Hot rolled	–	7.85	485

2.2   Experimental Procedure

In order to measure milling forces of the 316L samples, slot milling experiments were performed in all the samples. Milling experiments were realized on a DMG DMC 1035V Eco machining center equipped with a KISTLER 9257BA dynamometer to measure cutting forces. Cutting-edge monitoring was performed with a microscope camera Dinolite AM4815ZTL and an acoustic emission sensor KISTLER 8152C. Force and acoustic emission signals were sampled at 25 kHz with a NI4472B data acquisition device. The data acquisition task was programmed in LabVIEW.
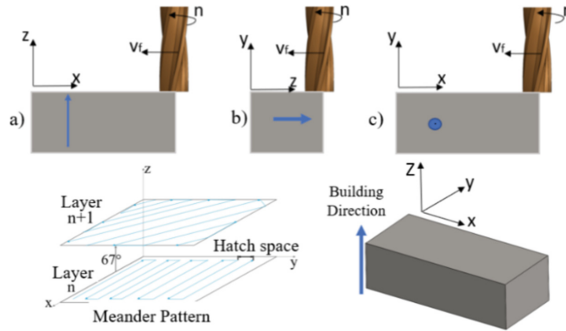
Fig. 1. Workpiece-tool orientations a) orientation 1, b) orientation 2, c) orientation 3.

Preliminary machining tests were performed to determine the best cutting parameters. For the milling of the samples, three different workpiece-tool orientations were established (Fig. 1). Before the machining test, the first layer was removed to ensure a flat workpiece surface parallel to the dynamometric platform surface. Two slots were machined in all the samples for each orientation, widening the slots 0.2 mm each wall to ensure that the second slot force measuring was not affected by the previous pass. For each test, F_x and F_y force signals were measured and F_{xy} signal was calculated as the F_x and F_y signals module. To avoid the effect of tool runout, the global value F_{xy} RMS was calculated for each tool revolution and averaged to analyze the forces independently of the tool runout. The signal considered 100 stationary cutting cycles, i.e., the entry and exit of the tool were removed for computing the cycle F_{xy} RMS. The routine includes the calculation of the standard deviation of the averaged value.

3   Results

The preliminary machining tests revealed that thermal effects significantly affect the tool life when milling AISI 316L. Figure 2 shows a microscopic view of the tooltip and the acoustic emission pattern measured during one of the milling tests. The tests did not show a correlation between tool wear, material properties and acoustic emission. But the cutting tool showed a short life, where material adhesion and chipping were the primary sources of tool wear. The cutting speed was increased, and the feed rate was decreased to facilitate heat dissipation and reduce chip load. After preliminary tests, definitive tests
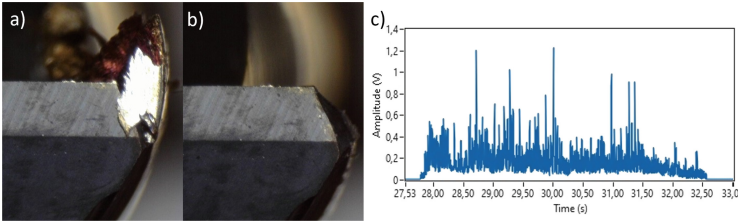
Fig. 2. Cutting tool in one of the preliminary tests a) showing adhesion of workpiece material to cutting edge, b) wear of the tooltip and c) acoustic emission pattern.

were executed with the finishing cutting conditions: cutting speed 55 m/min, feed per tooth 0.02 mm, and axial depth of cut of 0.5 mm.

3.1 Milling Forces

Figure 3a to 3c shows the F_{xy} RMS value for different material densities, UTS and volumetric energy densities in the first workpiece-tool orientation, which exhibited the larger force amplitudes. Figure 3d gathers the forces for the three different workpiece-tool orientations. Error bars depict the standard deviation of all experiments. Some outliers (not shown) that affected the curve fit were detected and removed using the Mahalanobis distance method. Outliers are supposed to exist due to tool wear or variations of axial depth of cut. For the hot rolled AISI 316L specimen, a F_{xy} RMS value of 37.25 N was calculated for the 100 cycles.
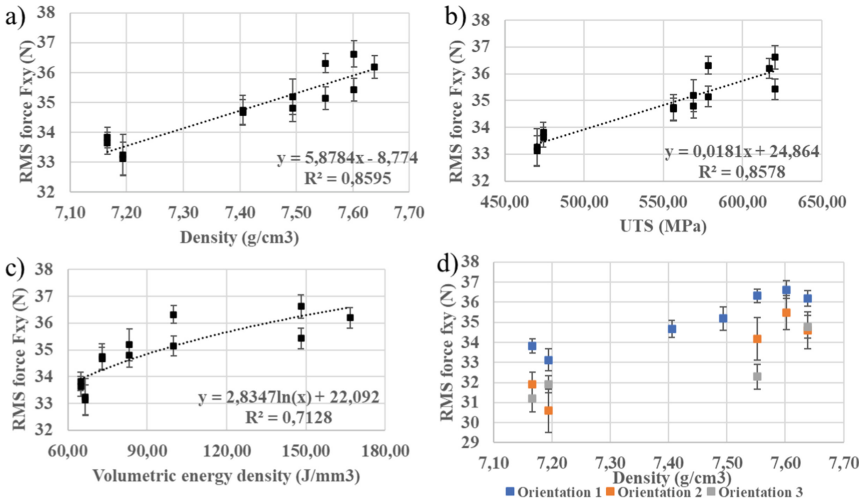
Fig. 3. Variation on RMS Fxy force value due to a) density b) UTS c) Volumetric energy density d) workpiece-tool orientation.

3.2   Material Machinability Based on Milling Forces

Based on the prior results, Fig. 4a shows the comparison of milling forces between hot rolled AISI 316L and the first sample of the L-PBF specimens (with highest density). Figure 4b shows the comparison of the milling forces between the hot rolled AISI 316L specimen and sample 8 of the L-PBF specimens (with the lowest density).
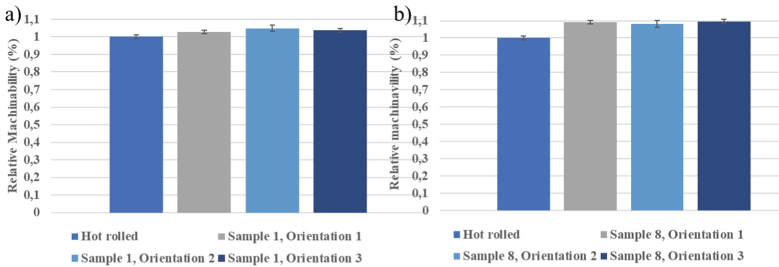
Fig. 4. Relative machinability based on milling forces in the first orientation for a) sample 1 of high-density b) sample 8 of low density, and hot rolled material.

4   Discussion

The additive 316L samples used in this study had changes in density and UTS of 6% and 24%, respectively. Those variations in the material properties were obtained due to changes of almost 60% in volumetric energy density used in the printing process. All these changes resulted in variations of almost 10% in the RMS Fxy value of the milling forces with a linear increase for the material properties, and a logarithmic growth for the volumetric energy density. The results represent a novelty in the study of additive metal machining.

For additive 316L samples and based on the results of Fig. 3d, the laser scanning strategy used for the samples showed that milling with the tool parallel to the building direction will produce slightly larger forces than produced in directions 2 and 3, where the tool axis is perpendicular to the building direction. These results are comparable to the ones presented by Fei et al. [6] for the Nickel Inconel 625 obtained through DMLS, concluding that milling parallel or perpendicular to the building direction will produce different results, and the LSS will affect the milling forces.

Figure 4 shows the machinability based on milling forces. The results indicate that machining of the printed material is similar to the machining of the hot rolled one, this when the density of the materials is similar. Lower milling forces are obtained when milling a low-density specimen; therefore, better machinability in terms of milling forces is obtained. It is important to notice that volumetric energy density and material density are correlated, meaning that an increase in the volumetric energy density will produce higher densities on the printed material. Hence, lesser energy density consumption during the printing process will produce lower milling forces.

5   Conclusions

This experimental work analyzed the influence of the density and UTS of L-PBF printed workpieces on milling forces. Results are compared to milling forces of hot-rolled AISI 316L. Results obtained in this study showed that there is no considerable difference when machining hot rolled 316L in comparison with L-PBF 316L as long as properties such density and UTS are similar, especially density.

Forces in milling of additive samples of 316L manufactured with L-PBF, increases with the increment of the density and UTS material properties. The volumetric energy density used to print the samples directly influences the mentioned properties, therefore milling forces also increase with higher values of volumetric energy densities. A 9% increase in the milling forces was observed for 6% changes in material density.

The Fxy RMS force analysis revealed that milling with the tool parallel to the building direction will produce up to 4% higher cutting forces than milling with the tool perpendicular to the building direction.

Machinability of additive 316L based on milling forces, is slightly better than the machining of the hot rolled material, when the densities are similar. Results showed that lower densities of the printed metal are associated with lower milling forces.

References

1. Shrinivas Mahale, R., et al.: Processes and applications of metal additive manufacturing. Mater. Today Proc. **54**, 228–233 (2022). https://doi.org/10.1016/j.matpr.2021.08.298
2. Górski, F., Kuczko, W., Wichniarek, R.: Influence of process parameters on dimensional accuracy of parts manufactured using fused deposition modelling technology. Adv. Sci. Technol. – Res. J. **7**(19), 27–35 (2013). https://doi.org/10.5604/20804075.1062340
3. Liverani, E., Toschi, S., Ceschini, L., Fortunato, A.: Effect of selective laser melting (SLM) process parameters on microstructure and mechanical properties of 316L austenitic stainless steel. J. Mater. Process. Technol. **249**, 255–263 (2017). https://doi.org/10.1016/j.jmatprotec.2017.05.042
4. Kaynak, Y., Kitay, O.: The effect of post-processing operations on surface characteristics of 316L stainless steel produced by selective laser melting. Addit. Manuf. **26,** 84–93 (2019). https://doi.org/10.1016/j.addma.2018.12.021
5. Pérez-Ruiz, J.D., de Lacalle, L.N.L., Urbikain, G., Pereira, O., Martínez, S., Bris, J.: On the relationship between cutting forces and anisotropy features in the milling of LPBF Inconel 718 for near net shape parts. Int. J. Mach. Tools Manuf. **170**, 103801 (2021). https://doi.org/10.1016/j.ijmachtools.2021.103801
6. Fei, J., Liu, G., Patel, K., Özel, T.: Effects of machining parameters on finishing additively manufactured nickel-based alloy Inconel 625. J. Manuf. Mater. Process. **4**(2) (2020). https://doi.org/10.3390/jmmp4020032

CT-Based FEM: Assessment of the Influence of Porosity on the Mechanical Behavior and Failure of AM Components

Alejandro Pascual[1,2(✉)], Soraya Plaza[2], Naiara Ortega[2], Sara Sendino[1], and Silvia Martínez[1]

[1] Aeronautics Advanced Manufacturing Center, CFAA (UPV/EHU), Bizkaia Technology Park, Building 202, 48170 Zamudio, Spain
alejandro.pascual@ehu.eus

[2] Faculty of Engineering of Bilbao, UPV/EHU, Plaza Torres Quevedo 1, 48013 Bilbao, Spain

Abstract. This work aims to present a digital-twin for prediction of the mechanical behavior and failure of additive manufacturing components, considering the characteristics of heterogeneities, mainly porosities, which appear during the manufacturing process. Therefore, the proposed methodology is based on the development of a CT-based FEM model, as well as the study of different porosity features by CT analysis and FEM modelling. Their influence on predictions is also evaluated. To this end, tensile test specimens were manufactured by means of L-PBF, according to ASTM E8/E8M. Afterwards, the analysis and digitalization of each specimen were carried out using CT, followed by FEM modelling of each one. Finally, the results obtained by the analysis were correlated with experimental tensile tests. Taking advantage of the virtual model proposed, virtual cases and hypothesis were also analyzed. Hence, the promising future of the proposed methodology is highlighted.

Keywords: CT · FEM · Additive Manufacturing · Porosity

1 Introduction

Currently, lightweight and safety components are sought-after by most of technological industries, from transport industry to healthcare applications. In this context, additive manufacturing (AM) emerges as the most suitable manufacturing process. This is due to the fact that AM techniques, like laser powder bed fusion (L-PBF), enable the construction of complex designs generated by the most advanced techniques such as topology optimization. Nonetheless, L-PBF is subjected to the appearance of defects, mainly porosity, which compromise the performance of the component. These defects result in discontinuities, which yield stress concentrations that promote the failure of the component driven by void growth and coalescence [1]. Thus, the characterization of these defects, regarding features like shape, orientation or spacing, in addition to the typical ones such as distribution, percentage and size, is essential to estimate the mechanical behavior of the component.

To this end, the combination of X-ray Computed Tomography (CT) [2] with Finite Element Method (FEM) is considered as a promising strategy. Thus, the main aim of this work is to develop a FEM model based on CT digitalization for the assessment of porosity influence on the mechanical behavior and failure of the component.

2 Methodology

According to the previous statement, the presented methodology focuses on the construction of a CT-based FEM model as a digital-twin of the samples. Additionally, virtual case studies are also modeled to analyze different load cases.

2.1 Experimental Procedure

Specimens Design. Four tensile test specimens made of Inconel 718 were designed for the study, according to the standard ASTM E8/E8M. To analyze the influence of different porosity features, one specimen (Specimen 1) was defined without voids while the other ones (Specimen 2, 3 and 4) were designed with induced artificial porosity. Only the shapes of defined voids were modified, preserving the volume of voids, location and distribution, as shown in Fig. 1. Aspect ratio (β), defined by Eq. (1), is selected as an indicator of the voids shape.

$$\beta = \frac{\max(a, b)}{c} \tag{1}$$
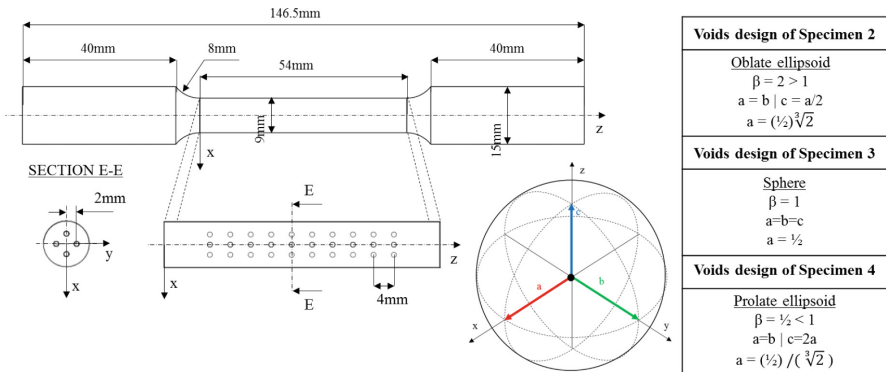
Fig. 1. Test specimen dimensions according to ASTM E8/E8M. Schematic representation of void distribution and shape types.

Manufacturing Process. These specimens were manufactured by L-PBF, using Renishaw AM400 manufacturing system (Renishaw, Wotton-under-Edge, UK). The layer

thickness was set at 60 μm and the laser paths were modified 67 degrees between layers. Samples were placed vertically, according to the building direction of the system. Finally, these specimens were blasted with white corundum WSK 80.

CT Inspection Procedure. For scanning purpose, an X-ray system model X-Cube Compact (Baker Hughes, Houston, TX, USA) was used. The scanning conditions by CT are summarized in Table 1.

Table 1. Scanning conditions by CT.

Focal spot size [mm]	Hardware filters	Voltage [kV]	Current [mA]	Exposure time [ms]	Projections	Magnification
0.4	1mm Cu + 0.5mm Sn	195	2.2	100	750	2.231

Experimental Tensile Test. Finally, the experimental tensile tests were carried out using the Instron 8801 system (Instron, Norwood, MA, USA). Considering ASTM E8/E8M standards, the speed of the tests was established at 0.05 s^{-1}.

2.2   Digital Twin

Defect Detection and Characterization by CT. The data of the scanned specimens by CT were processed by using the specific software VGStudio MAX 3.4 (Volume Graphics, Heidelberg, Germany). For porosity detection, VGEasyPore algorithm was utilized. Finally, the following void features are defined for characterization: 1) Volume, 2) Projected area (XY), 3) Aspect ratio (β), which is defined by Eq. (1), 4) Gap, which is computed as the minimum distance between surfaces of the circumscribed spheres of the nearest detected voids, and 5) Minimum edge distance, referred to the minimum distance between the surface of each void and the determined surface of the sample.

Modelling by FEM Technique. The FEM model has been built in ABAQUS 6.14 software. As stated above, the geometry of the model was defined by the CT digitalization. Owing to the complexity of the geometry, an unstructured mesh was selected. In this case, second order tetrahedral elements (C3D10M) were used to maximize the accuracy of the model. On the other hand, material properties were defined according to the experimental results of the Specimen 1. The Poisson's ratio and material density were established at 0.29 and 8.2 g·cm^{-3}, respectively. Fracture behavior was defined following the ductile damage theory developed in the frame of continuum damage mechanics [3]. This phenomenological model focuses on void nucleation, growth and coalescence. According to this method, damage depends on stress parameters such as triaxiality, which demonstrate the influence of the stress state. Finally, the boundary conditions were defined according to the experimental test.

3 Results and Discussion

3.1 CT Porosity Analysis

The results of defect detection for each as-built and fractured sample are presented in Fig. 2. The comparison between test specimens before and after the tensile test reveals interesting information about the detection of new defects and the growth of those detected prior to the test. In addition, Fig. 2 reveals that both the volume growth and the reduction of the aspect ratio (β) increase with the initial aspect ratio.
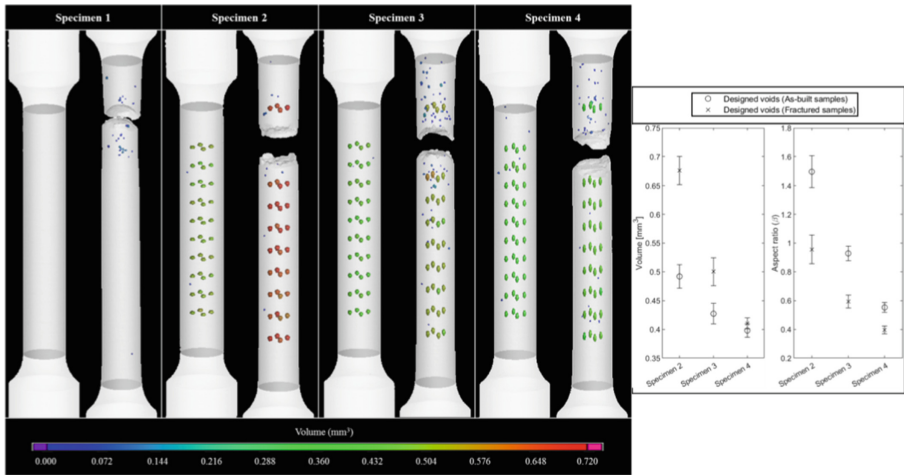

Fig. 2. CT porosity analysis of each specimen. As-built and fractured samples are displayed. Void growth analysis of designed voids is also included.

Apart from designed porosity, this study is conditioned by the appearance of non-intended defects in the as-built samples. The results of each porosity feature defined per detected void are presented in Fig. 3. As shown, fracture levels are strongly dependent on the presence and characteristics of non-defined voids. Specimens 2 and 3 demonstrate that the fracture takes place at levels where defined voids are close to non-defined voids with worse results. Finally, although Specimen 4 is subjected to the presence of 7 non-defined voids, three of them are located around the same level of defined voids, where the final failure takes place.
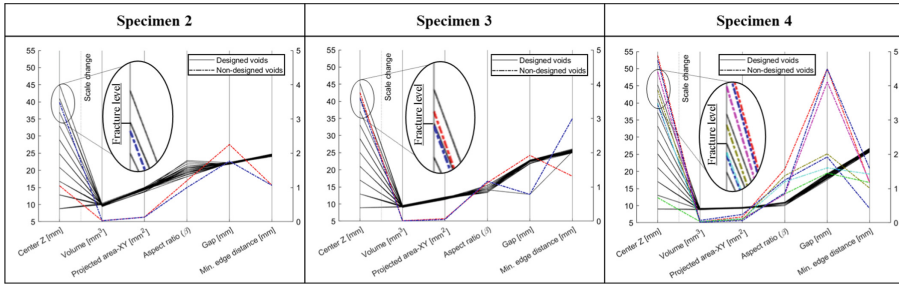
Fig. 3. Analysis of the porosity features by CT of each as-built sample.

3.2 Experimental Tensile Test

The results of the experimental tensile test of each specimen are presented in Fig. 4. Necking region and final fracture exhibit the major differences between samples. Hence, ultimate tensile strength and elongation at fracture are considered as the most representative indicators of the porosity influence on the mechanical behavior.
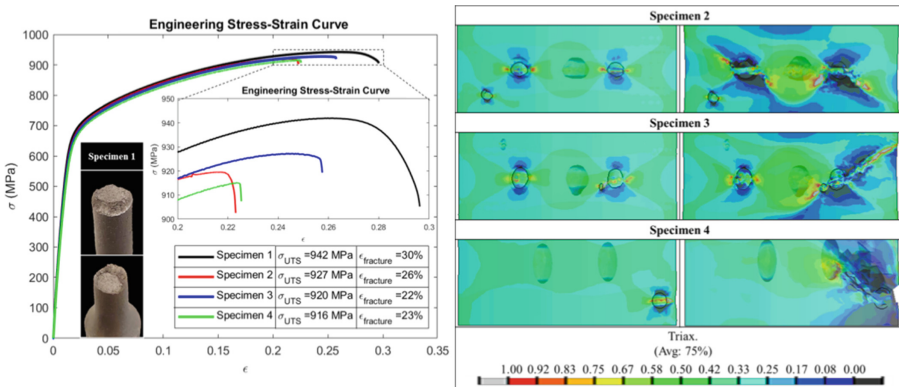
Fig. 4. Stress-strain curves of test specimens. Ultimate tensile strength and elongation at break results. Additionally, FEM results of each specimen according to stress triaxiality, detailing failure onset and propagation.

3.3 Digital Twin

Virtual Tensile Tests. FEM results of each specimen according to stress triaxiality are presented in Fig. 4, showing the detail of failure onset and propagation. As a result, it is proven that the high stresses produced by porosity defects lead to the final fracture of the component. Finally, the results obtained by the virtual tensile tests are summarized in Table 2, which reveal a high accuracy with errors lower than 2.5% for the ultimate tensile strength and 4% for the elongation at break.

Table 2. Ultimate tensile strength and elongation at fracture obtained by virtual tensile testing.

Specimen	1	2	3	4
σ_{UTS} (MPa)	951.6	921.0	936.5	927.1
$\varepsilon_{fractura}$ (%)	29.7	22.9	25.9	23.4

Virtual Case Studies. In order to analyze the influence of void size and shape on the stress field, different case studies were defined according to Fig. 5. For comparison, the solutions were computed in the elastic region. The results show that increasing the aspect ratio produces a higher stress concentration, while increasing the size shows an enlargement of the area of influence of the stress concentration.
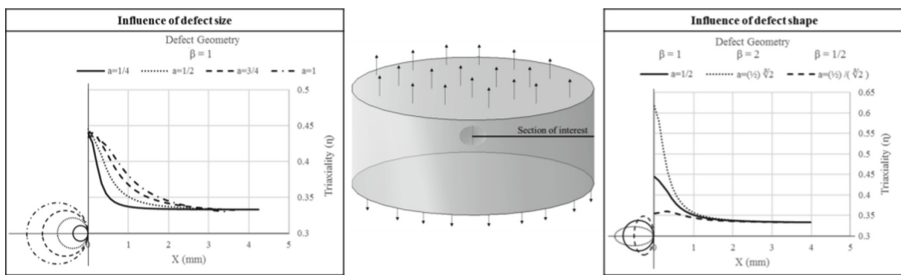
Fig. 5. Analysis of the influence of void size and shape on the stress field. Representation of the stress triaxiality (η) in the section of interest.

4 Conclusions

The increase in volume, shape (increasing aspect ratio (β)) and projected area in a plane normal to the loading direction, as well as the reduction of the gap between voids or distance to the edge of the component, promote stress concentration and, thus, enhance an increase of stress triaxiality (η), thereby leading to final failure.

Regarding the defect evolution during the tensile test, the effect of volume growth and reduction of the aspect ratio (β) intensifies as the initial aspect ratio (β) increases.

Finally, the proposed CT-based FEM provides well-established results to predict ultimate tensile strength and elongation at fracture. Maximum errors of 2.5% and 4% were reached, respectively.

References

1. Al-Maharma, A.Y., Patil, S.P., Markert, B.: Effects of porosity on the mechanical properties of additively manufactured components: a critical review. Mater. Res. Express **7**(12) (2020)
2. du Plessis, A., Yadroitsava, I., Yadroitsev, I.: Effects of defects on mechanical properties in metal additive manufacturing: a review focusing on X-ray tomography insights. Mater. Des. **187**, 108385 (2020)
3. Hooputra, H., Gese, H., Dell, H., Werner, H.: A Comprehensive failure model for crashworthiness simulation of aluminium extrusions. Int. J. Crashworthiness **9**(5), 449–464 (2004)

Influence of Ball Burnishing on the Improvement of Surface Quality and Mechanical Performance of Parts Obtained by FFF

Héctor García de la Torre , Ariadna Chueca de Bruijn ,
Giovanni Gómez-Gras$^{(\boxtimes)}$, and Marco A. Pérez

Group of Applied Mechanics and Advanced Manufacturing, IQS School of Engineering,
Universitat Ramon Llull, Via Augusta 390, 08017 Barcelona, Spain
`{hectorgarciat,giovanni.gomez}@iqs.url.edu`

Abstract. Additive manufacturing parts often need post-treatment due to inherent shortcomings, such as poor surface quality or mechanical performance. Ball burnishing, a plastic deformation technique, can reduce these drawbacks. In this research, a specific tool was designed, and statistical models were used to determine optimal process parameters. Flexural and fatigue tests were conducted to assess the effects of ball burnishing on surface and dimensional quality, hardness, and mechanical behavior. The study shows that ball burnishing can benefit cast filament parts made of three materials and provides generalizations for its application. This research represents a novel contribution to using ball burnishing and highlights its advantages.

Keywords: Ball Burnishing · Additive Manufacturing · Fused Filament Fabrication · Surface Roughness · Mechanical performance · Fatigue Life

1 Introduction

The demand for prototypes has been overgrowing due to industries' desire to bring products to market as quickly as their competitors. Additive Manufacturing (AM) technologies, such as Fused Filament Fabrication (FFF), have made this possible by enabling the production of components previously considered unachievable or too expensive to produce [1]. Despite the extensive potential applications of AM, it must still meet the quality and durability standards necessary for a wide range of industrial uses [2]. Surface roughness is a crucial factor affecting the products' overall quality, including their functionality, assembly tolerances, and fatigue resistance.

The surface roughness arises from the elliptical shape of the filament layers deposited in a step-by-step manner, resulting in the "staircase effect" [3]. As a result, it is essential to undertake post-processing procedures to enhance the part's characteristics and guarantee its optimal performance [4]. The Ball Burnishing (BB) process is a technique classified under Severe Plastic Deformation (SPD). It consists of an indenter's action on the part's surface, which reduces irregularities and improves the surface finish. In addition, BB

tools can be coupled to conventional manufacturing machines, thus reducing operating costs. In metallic materials, BB parameters that influence roughness and hardness were identified, including ball diameter, applied force, feed rate, number of passes and use of lubricants [5, 6]. These studies demonstrate improved surface friction coefficient, wear rate and surface hardness [7].

However, the advantages of BB on polymeric parts obtained by FFF still need to be defined. To the authors' knowledge, only one investigation addresses the influence of BB on FFF parts using a conventional BB tool and PEI as base material. It reveals improvements in fatigue life, reduction of surface roughness and improvement in impact energy absorption [8]. This work aims to validate the BB process's effectiveness in improving FFF-polymeric components' surface quality and mechanical performance. Tough PLA, PC, and PC-ISO were tested using a state-of-the-art tool, analyzing surface and dimensional qualities, flexural strength, and fatigue life. Results were obtained using statistical, surface, dimensional, and microscopy image examination to determine the effects of BB parameters. The study contributes to a better understanding of the BB process's potential to enhance FFF polymeric components.

2   Materials and Methods

Plates of 150 mm in length and 110×4 mm^2 cross-section were designed to determine the range of magnitudes that enhanced surface roughness. In addition, three-point bending, and flexural fatigue specimens were fabricated. All samples have a linear infill of $\pm 45°$, solid infill and a single outer contour. All samples were obtained in XY and XZ building orientations.

Table 1. Experimental factors and their levels.

Variable	Levels		
Applied Force [N]	100	200	300
Number of tool passes	1	3	5

BB was performed with a specific tool designed and manufactured for this research, mounted on a CNC milling machine. The spherical indenter is 10 mm diameter chrome-hardened steel with two spherical bearing races of the same material. The plates were fixed in an epoxy resin block, while the standardized specimens were set inside a silicone mold to guarantee their correct position without hindering the expansion of the material. Based on results obtained before this research, the evaluation of two statistically significant BB process parameters was determined: the applied force and the number of tool passes. Previous works have reported the lateral path width and the tool feed rate with minor relevance. Consequently, the values have been set to 0.32 mm and 1000 mm/min, respectively.

A full factorial design of 3^2 was conducted to determine the influence of the chosen BB parameters. The aim is to identify the factor levels that yield the best results in terms

of surface quality. Table 1 summarizes the distribution of factors and levels in the design of experiments. A roughness tester measured the impact on R_a and R_z roughness profiles before and after being subjected to a BB. Dimensional analysis was performed according to the corresponding standard [9] to determine cross-section dimension variations from the BB process. Finally, BB's influence on the samples' hardness was evaluated using a Shore D durometer following the ISO 868:2003 [10].

The mechanical behavior of each material was assessed by standardized three-point bending and flexural fatigue tests. Three-point bending tests were conducted on specimens with a cross-section of 4×10 mm^2 and a length of 127 mm following procedure A of ASTM D790 [11]. Fatigue tests were performed on a dynamic testing machine with a three-point bending fixture following the ASTM D7774 [12]. Frequency and support spacing were set at 5 Hz and 64 mm, respectively. Specimens were tested using loads equivalent to 20%, 40%, 60%, and 80% of the maximum flexural strength of each material and manufacturing configuration.
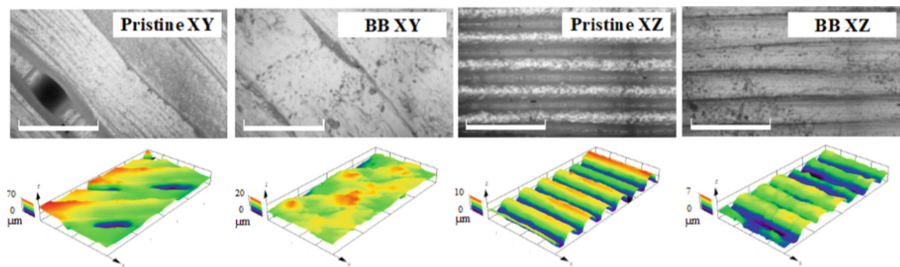
Fig. 1. Optical microscope images (surface and 3D texture) of pristine and ball burnished XY and XZ samples using the optimum process parameters. The white scale mark is 300 μm.

Table 2. Optimal ball burnishing parameters resulting from the design of experiments.

Material	Orientation	Applied Force [N]	Number of tool passes
Tough PLA	XY	200	3
	XZ	200	3
PC	XY	300	3
	XZ	300	3
PC-ISO	XY	300	3
	XZ	300	5

3   Results and Discussion

3.1   Ball Burnishing Influence on Surface Roughness

R_a and R_z values were determined for each set of experiments and processed to extract each variable's contributions and calculated p-values. Results were considered statistically significant as the p-value is lower than 0.05. The results are reflected in the microscopy images in Fig. 1 and Table 2, where the optimum process parameters are reported, with a better surface quality obtained in the PC-ISO XY samples with a variation of R_a and R_z of 93% and 90%, respectively.

3.2   Dimensional Quality and Surface Hardness Assessment

Figure 2a and 2b present the width and height dimensions of the pristine and burnished specimens. The dimensional deviation does not exceed 6.0% and 2.5% for XY and XZ, respectively. This is because the width was increased, and the height was reduced by the applied force, indicating densification. Still, dimensions close to the digital model can be guaranteed, with a maximum difference of 1.25%. The dimensional variation can be explained by the BB and printing error associated with the FFF technology.

Hardness tests on pristine and burnished specimens were conducted, and the results are shown in Fig. 2c. The highest surface hardness was found in specimens printed in the XZ orientation due to the contour stiffness compared to filler layers. Surface hardness was improved in all configurations and materials for BB specimens, with an improvement of up to 10%. This phenomenon is due to the reduction of the cross-section, which increases the density of the samples and strengthens the layer bonds.
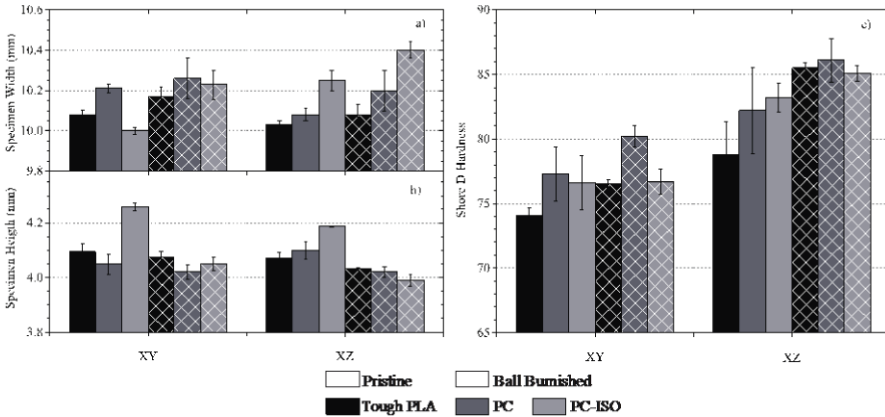
Fig. 2. a) and b) Width and height values of the specimens. The process was performed on both sides using the optimum parameters. (c) Shore D hardness of the specimens.

3.3 Mechanical Performance

The BB specimens show a higher flexural modulus, while the flexural strength remains unchanged. Results show differences in stiffness, maximum stress, and material failure based on the specimens' internal structure and manufacturing orientation, highlighting the anisotropy of the FFF. The results are presented in Fig. 3.

The increased flexural modulus of BB specimens is due to the stiffening and plasticization of the outer layers. The burnishing process introduces compressive stresses, bringing the polymer chains closer and consequently increasing binary contacts and hardness [13]. This explains the improvement in flexural properties of the BB specimens compared to the pristine ones. However, there is no variation in the flexural strength of the samples. Burnishing reduces the flexural strength of XZ specimens due to the filament orientation in the outer layer, while it enhances the intra-layer bonding of the top layer in XY specimens, leaving them unaffected.
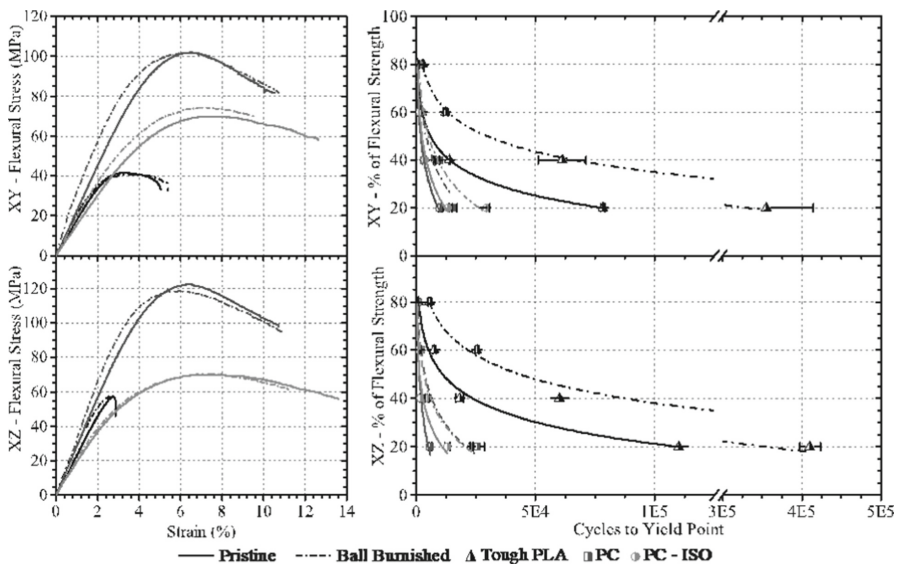
Fig. 3. To the left, representative stress-strain curves obtained from flexural tests. To the right, S-N R-1 curves resulting from the 3-point bending fatigue tests.

The results presented for three-point bending dynamic tests correspond to the number of cycles in which the displacement exceeded 10%, i.e., the elastic limit, since none of the specimens fractured before that point. Due to the differences observed in the flexural strength of the pristine and burnished specimens during the flexural tests, the criterion for the reference stress value in the specimens was the worst case. Therefore, all samples were tested with the same oscillation stress, and a two-way comparison of the results could be obtained. Improvements between 100 and 500% are observed. Based on the results, the occurrence of compressive residual stresses in the outer layers of the burnished specimens, together with the subsequent densification and surface hardening,

reduces the occurrence and propagation of cracks and, therefore, is responsible for the improvement to the dynamic response of the specimens.

4 Conclusions

The developed tool proved to work successfully on FFF parts, as demonstrated by its performance. The results established that this post-process is effective for a wide range of thermoplastics used in FFF. The influence of force and the number of tool passes on the surface quality of the samples was evaluated, and the best parameters were determined for each material. Overall, the improvement in R_a and R_z for the three materials is about 80% and 77%, respectively, and the dimensional variation does not exceed the standard deviation of the fabrication process. In addition, the densification of the outer layers improved the surface hardness of the parts by about 10%.

Regarding the mechanical performance, the results show a discrete improvement in flexural modulus while maintaining the same flexural strength, attributed to plasticization, and thinning of the outer layer. However, static test results require more variability to yield conclusive statements. Regarding fatigue behavior, the three materials substantially improved the number of cycles, resulting in a two-fold increase compared to the pristine specimens. In addition, the compaction of the layers hinders the appearance and propagation of cracks, increasing dynamic performance.

References

1. Forés-Garriga, A., et al.: Role of infill parameters on the mechanical performance and weight reduction of PEI Ultem processed by FFF. Mater. Design **193** (2020)
2. Piyush, et al.: 3D printing of food materials: A state of art review and future applications. Mater. Today: Proc. **33**, 1463–1467 (2019)
3. Eswaran, P., et al.: Investigations on acute angle parts fabricated fusion deposition modelling parts volumetric shrinkage and surface roughness. Mater. Today: Proc. **45**, 930–935 (2021)
4. de Bruijn, A.C., et al.: A comparative analysis of chemical, thermal, and mechanical post-process of fused filament fabricated polyetherimide parts for surface quality enhancement. Materials (2021)
5. Swirad, S., Wdowik, R.: Determining the effect of ball burnishing parameters on surface roughness using the Taguchi method. Procedia Manuf. **34** (2019)
6. Shiou, F.J., Chen, C.H.: Freeform surface finish of plastic injection mold by using ball-burnishing process. J. Mater. Process. Technol. **140**(1–3), 248–254 (2003)
7. Low, K.O., Wong, K.J.: Influence of ball burnishing on surface quality and tribological characteristics of polymers under dry sliding conditions. Tribol. Int. **44**(2), 144–153 (2011)
8. de Bruijn, A.C.,et. al.: On the effect upon the surface finish and mechanical performance of ball burnishing process on fused filament fabricated parts. Addit. Manuf. **46** (2021)
9. ISO - ISO 4288:1996, Geometrical Product Specifications (GPS) - Surface texture: Profile method - Rules and procedures for the assessment of surface texture, International Organization for Standardization, Geneva, Switzerland (1996)
10. UNE-EN ISO 868:2003 Plastics and ebonite. Determination of indentation hardness by means of a durometer (Shore hardness). International Organization for Standardization, Geneva, Switzerland (2003)

11. ASTM D790-17, Standard Test Methods for flexural properties of unreinforced and reinforced plastics and electrical insulating materials, ASTM International, West Conshohocken, PA (2017)
12. ASTM D7774-17, Standard Test Method for flexural fatigue properties of plastics, ASTM International, West Conshohocken PA (2017)
13. Bartczak, Z., Galeski, A., Argon, A.S., Cohen, R.E.: On the plastic deformation of the amorphous component in semicrystalline polymers. Polymer **37**(11), 2113–2123 (1996)

Development and Processing of Inconel 718 Tools for Friction Stir Welding Additively Manufactured by Laser Metal Deposition

Marta Alvarez-Leal[1]([✉]) [iD], Oscar Rodriguez-Alabanda[2] [iD], Pablo E. Romero[2] [iD], Esther Molero[2] [iD], and Julia Ureña[1] [iD]

[1] Group of Materials and New Manufacturing Processes, Technology Centre of Metal-Mechanical and Transport (CETEMET), 23700 Linares, Spain
m.alvarez@cetemet.es

[2] Mechanical Department, University of Córdoba, 14071 Córdoba, Spain

Abstract. This work investigates the feasibility of processing the nickel superalloy INCONEL 718 using Laser Metal Deposition (LMD) additive manufacturing technology (with filament) for the processing of Friction Stir Welding (FSW) tools. The FSW tools must have a specific design and characteristics adapted to the material to be welded, so new fast, dynamic and cheaper manufacturing techniques are required. Different heat treatments were performed to achieve optimum properties of the manufactured IN718 compared to forged and cast IN718. The densification analysis showed a material free of major defects and high densification. In addition, excellent mechanical behavior was obtained, with a maximum strength (UTS) of 1256 MPa, which is an improvement over conventional IN718 and could validate the use of LMD technology for FSW tooling.

Keywords: Laser Metal Deposition (LMD) · Inconel 718 superalloy · Friction Stir Welding (FSW) · mechanical properties

1 Introduction

In Laser Metal Deposition (LMD) a laser source is used to create an energy beam focused to melt the metal which is deposited through a nozzle. The deposited material could be powder or filament and it is deposited layer by layer only in the needed areas to achieve the final geometry of the part. Through LMD technology, medium or large preforms and final parts may be manufactured, mainly depending on the real printing volume of the printing equipment employed [1]. Compared to traditional repair technologies such as TIG or WAAM welding processes, LMD allows the material deposition with the following benefits: (i) low heat transference which means less distortion and reduced thermal stresses on the substrate; (ii) higher material deposition rate compared to other AM technologies, e.g. powder bed fusion [2].

The interest in the Inconel 718 (IN718) superalloy is highly increasing in additive manufacturing (AM) due to the wide use of this kind of alloy in the aerospace sector

or the field of repair components. The IN718 material is well known for applications where high temperatures, excellent mechanical properties, and corrosion resistance are required [3]. However, the presence of niobium as an alloying element in this alloy tends to segregate, which strongly influences the precipitation of hardening phases. Some research studies have employed different strategies to control and minimize the niobium-enriched eutectoids in both welding and AM processes [4].

Friction Stir Welding (FSW) is a solid-state joining process [5, 6]. It uses a non-consumable tool to join two facing workpieces without melting the workpiece material. FSW is carried out by a rotating cylindrical tool composed of a pin and a shoulder. The tool is inserted and moved forward between the two work pieces to join. The generated frictional heat together with that obtained by the mechanical mixing process turns the stirred materials to soften without melting.

Due to its high energy efficiency, environment friendly and versatility, the joining FSW process is considered one of the most innovative developments for metal joining within the last decades [7]. Although the FSW tool is defined as a non-consumable tool, it can be considered when very high-resistance materials or difficult-to-weld materials are joining. In this case, different FSW tools are needed since they are changed when are damaged or worn. These FSW tools are also replaced when the rest of the softened materials remained adhered to the tool. Using damaged FSW tools creates a non-reproducible join or low-quality welding [8]. The cost of these commercially available FSW tools is around 1000 €/unit for Inconel superalloys which can limit their use.

As an alternative, in this work, the advanced metal AM LMD technology is used for the processing of tools for an innovative joining process through FSW technology. The material selected to be processed by LMD was the nickel-based IN718 superalloy due to its excellent mechanical properties. The IN718 superalloy is found in powder and wire material, thus a wide range of technologies can be employed to process this alloy.

This research results in relevant benefits for the industry using process-energy saving, material reduction, and higher affordable FSW tools together with a faster method of production. A high value is added to this research study through the possibility of customization of these FSW tools by the employ of the LMD technology.

2 Experimental Procedure

2.1 Design and Manufacturing of the FSW Tools

IN718 tools for the robotic FSW process have been manufactured. The selection and design study of the tools was performed using CATIA V5. A holistic approach to the tool design specifically adapted to the thickness of the material to be welded and to the FSW head was conducted. The commercial FSW spindle employed was a CYSTIR model from CYTEC. The FSW head was placed in a KUKA robot.

The used LMD system was an M450 device with a multi-laser metal deposition printhead (Meltio). The used process parameters were: Laser speed 450 (mm/min), layer height 1.2 (mm), laser power 900 (W), hatching distance 1 (mm), current 2 (A) and gas flow 10 (L/min). These optimized parameters were defined in a previous work.

The Nippon Gases (NIPPON M-218) Inconel 718 superalloy wire material was used. Its chemical composition (in wt. %) was: C (0.05), Mn (0.2), Si (0.2), Cr (19), Mo (3),

Fe (20), Ti (0.9), Al (0.5), Nb+Ta (5.2), Ni (balance). The FSW tool was designed for its manufacturing by the M450 LMD technology. A machining post-process was needed to achieve its final geometry (Fig. 1). Before the machining process, the tools were separated from the build plate and thermally treated.
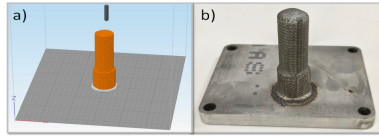

Fig. 1. a) 3D-model of the FSW tool, and b) IN718 FSW tool manufactured by LMD.

2.2 Heat Treatments

To find the optimum heat treatment for the material, four blocks of dimensions 120 mm × 25 mm × 50 mm were manufactured in the IN718 material. The heat treatments performed consisted of TT1-initial heat treatment for stress relief and TT2-additional heat treatment for ageing. Of the four blocks manufactured by LMD, two of them underwent TT1 and the other two underwent TT1+TT2. Details are shown in Table 1.

Table 1. Heat treatment conditions of the IN718 specimens manufactured by LMD.

Heat treatments for the material IN718 processed by LMD-wire		
	Procedure	Time (h)
PHASE 1 (TT1)	Heat to 980 ℃	1
	Hold at 980 ℃	1
	Cooling with argon up to 100 ℃	–
PHASE 2 (TT2)	Heating from 100 ℃ to 720 ℃	2
	Hold at 720 ℃	8
	Cool to 620 ℃	1h 50 min
	Hold at 620℃	8
	Cooling with argon to room temperature	–

2.3 Characterization of the Manufactured Material

The material was characterized by optical microscopy (OM) to obtain the level of densification/porosity and the quality of the manufactured tool. A statistical study of defects and densification value was determined. Image analysis was carried out using ImageJ software and the mean value represented corresponds to the analysis of four images

for each manufacturing plane. IN718 tensile samples were machined from the original blocks for mechanical characterization in the different heat treatment states. The mechanical anisotropy between the XY plane (direction parallel to the material deposition) and XZ plane (direction parallel to the manufacturing direction) was considered, therefore tensile specimens were obtained in the two different directions for complete characterization. Cylindrical specimens of 5 mm diameter × 32 mm length were tested in an INSTRON universal tester at room temperature (ISO 6892-1:2020B).

3 Results and Discussion

Figure 2 shows the optical microscopy (OM) images of the IN718 material fabricated by LMD with TT1+TT2 heat treatment in both planes XY and XZ. In general, high densification has been obtained in the analysed samples, however small defects associated with the AM process itself have been found. Small circular pores could be distinguished, which are usually associated with gas bubbles trapped during the process. Irregular defects were also observed, which may be evidence of certain points with a lack of fusion in some regions. However, the overall densification is above 99%. The values obtained are 99.30% ± 0.28 for the XY plane and 99.03% ± 0.24 for the XZ plane.
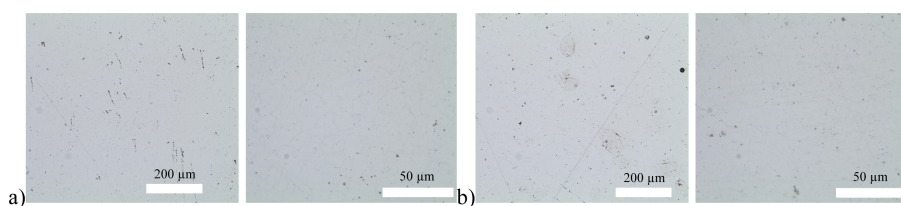
Fig. 2. OM images of the IN718 material processed by LMD after stress relief heat treatment-ageing. Densification of the material obtained in a) XY and b) Z.

Table 2 shows the results of the mechanical properties of the material manufactured by LMD. It shows the average values obtained in the different tensile tests performed. The IN718 material manufactured by LMD was submitted to different heat treatments (TT1-stress relieved and TT1+TT2-stress relieved + ageing) for the XY and XZ manufacturing planes. Table 2 also shows the reference values for forged and cast IN718.

In both planes, XY and XZ, good mechanical properties: tensile strength (UTS), yield strength (yield) and elongation; were observed for the LMD manufactured material.

Comparing the results of the mechanical tests between the different heat treatments, it has been observed that the combination of TT1+TT2 significantly improves the UTS and yield compared to TT1 performed individually. This behaviour has also been found by other authors [9]. The values compared were those obtained for the same plane, XY or XZ. The UTS values indicate an increase of 23.6% and 30.6% for the XY and XZ planes, respectively, for the IN718 with TT1+TT2 compared to TT1.

In the XY plane, a yield increase from 631 MPa to 980 MPa was identified. After the combination of TT1+TT2, the strength increased up to 55.3%. The elongation, however, is slightly higher for the material with the TT1 treatment compared to TT1+TT2.

Table 2. Tensile mechanical properties of the IN718 material manufactured by LMD with different heat treatments and their comparison with the standards.

Manufacture Method	Mechanical tests		
	Tensile strength – UTS-(MPa)	Yield strength – Yield-(MPa)	Elongation (%)
Forging (AMS 5662)*	1241	1034	10
Casting (AMS 5383)*	802	758	5
LMD + Stress relieved TT1 (XY)	1016 (± 28)	660 (± 10)	18 (± 6)
LMD + Stress relieved TT1 (XZ)	925 (± 86)	631 (± 2)	15 (± 2)
LMD + Stress relieved + Aging TT1+TT2 (XY)	**1256** (± 11)	1025 (± 7)	11 (± 1)
LMD + Stress relieved + Aging TT1+TT2 (XZ)	1208 (± 49)	980 (± 2)	10 (± 5)

Values of 18% and 15% were obtained in the TT1 treatment, for the TT1+TT2 treatment which showed elongations of between 11% and 10%, in XY and XZ planes, respectively. One possible reason could be the extra hardening process induced with heat treatment TT1+TT2 for TT1. In metals, it is known that an increase in the strength (UTS and yield), directly related to microstructure, causes a decrease in ductility. Because of the deformation mechanisms operating during deformation, which dependent on grain size, solutes and distance between precipitates. This behaviour was already noted in the Selective Laser Melting (SLM) for the same alloy (IN718) [10].

TT1 stress relieving provides reasonable UTS properties with exceptional ductility values for this material as well as a lower yield value compared to the reference values. The TT1+TT2 treatment increased the strength from 20% to 50% with excellent UTS and yield properties, maintaining a similar ductility to the forging values. Elongation was higher than 10% in all the conditions. This means that the LMD process for IN718 retains or improves the reference values, as also was found in similar studies [9, 11].

Regarding XY and XZ building directions, UTS and yield values were higher in the XY plane. For the optimized heat treatment (TT1+TT2), the average strength of UTS and yield was about 4% higher in the XY plane compared to the XZ plane. The ductility was very similar between the two build directions, indicating that the anisotropy did not have a relevant impact on this LMD-processed material. This anisotropy in mechanical properties between the different XY and XZ build planes relates to the AM process, due to the layer by layer deposition, thermal and microstructural gradients are created. This is fundamental for the optimization of the processing by AM [12].

In general, the IN718 alloy manufactured by LMD presented mechanical properties equal to or better than the standard forging values and far superior to those of the as-cast

alloy, especially for the LMD-manufactured and TT1+TT2 heat-treated material. The ductility was equal or improved depending on the case. With these results, the LMD AM technology with wire material has been validated for this application.
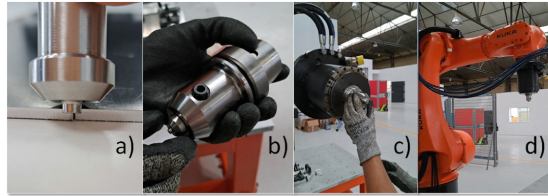

Fig. 3. Robotic FSW lab at Cetemet. a) The machined IN718 tool, b) the tool inserted in the holder, c) the tool holder with the spindle and d) the Robot positioned for FW.

The LMD-manufactured and machined IN718 tool was installed in the tool holder to be used in the robotic FSW application. The spindle, tool holder and tool were installed on the heavy-duty robot located at the facilities of Cetemet in Spain (Fig. 3).

4   Conclusions

The nickel-based IN178 superalloy was successfully additively manufactured by Laser Metal Deposition (LMD) technology for Robotic Friction Stir Welding (RFSW).

The LMD process parameters allowed good overall material properties. The densification of the processed material was above 99%. It was 99.30% $\pm$ 0.28 and 99.03% $\pm$ 0.24 for the XY and XZ build planes, respectively. The mechanical properties of the manufactured and heat-treated material were even higher than the standard IN718 forged alloy. An average maximum strength (UTS) of 1256 MPa was achieved in the XY plane. The ductility values were the same or slightly higher compared to the standard values of IN718. The TT1+TT2 (stress relieving-ageing) heat treatment for IN178 highly improved the mechanical behavior. The yield strength increased up to 55.3%.

The use of the LMD processing has allowed: a) cost reduction of the FSW tool, b) decrease of the whole manufacturing time, including processing and machining, c) reduction of the lead time from weeks/months to hours/days, d) the dynamic tool customization to fit specific welding needs by only re-designing and 3D printing.

References

1. Pratheesh Kumar, S., et al.: A review on properties of Inconel 625 and Inconel 718 fabricated using direct energy deposition. Mater. Today Proc. **46**, 7892–7906 (2021)
2. Paskual, A., Alvarez, P., Suarez, A.: Study on arc welding processes for high deposition rate additive manufacturing. Procedia CIRP **68**(April), 358–362 (2018)
3. Hosseini, E., Popovich, V.A.: A review of mechanical properties of additively manufactured inconel 718. Addit. Manuf. **30**(8) (2019). https://doi.org/10.1016/j.addma.2019.100877
4. Sreekanth, S., et al.: Effect of direct energy deposition process parameters on single-track deposits of alloy 718. Metals (Basel) **10**(1), 96 (2020)

5. Thomas, W.M., Dolby, R.E.: Friction stir welding developments. In: Proceedings of the Sixth International Trends in Welding Research, pp. 203–211 (2003)
6. Mishra, R.S., Ma, Z.Y.: Friction stir welding and processing. Mater. Sci. Eng. R **50**, 1–78 (2005)
7. Deivanai, S., Wattal, R., Rani, S., Verna, S.L.: Green Technology friction stir welding of al-uminium alloy 1100. Int. Rev. Appl. Eng. Res. **4**(2), 93–98 (2014)
8. Bist, A., et al.: A review of tool wear prediction during friction stir welding of aluminium matrix composite. Trans. Nonferrous Met. Soc. China **26**(8), 2003–2018 (2016)
9. Ramiro, P., et al.: Effect of heat treatment on the microstructure and hardness of Ni-based alloy 718 in a variable thickness geometry deposited by powder fed directed energy deposition. Metals (Basel) **12**(6), 952 (2022). https://doi.org/10.3390/met12060952
10. Zhang, D., et al.: Effect of standard heat treatment on the microstructure and mechanical properties of selective laser melting manufactured Inconel 718 superalloy. Mater. Sci. Eng. A **644**, 32–40 (2015). https://doi.org/10.1016/j.msea.2015.06.021
11. Schneider, J.: Comparison of microstructural response to heat treatment of Inconel 718 prepared by three different metal additive manufacturing processes. JOM **72**(3), 1085–1091 (2020). https://doi.org/10.1007/s11837-020-04021-x
12. Mitchell, A., et al.: Additive manufacturing—a review of 4D printing and future applications. Addit. Manuf. **24**, 606–626 (2018)

Effects of Temperature and Vacuum Pressure on the Mechanical and Surface Enhancement of FFF Parts

Giovanni Gómez-Gras [iD], Ariadna Chueca de Bruijn[iD], Manuel D. Abad [iD],
Albert Forés-Garriga [iD], and Marco A. Pérez$^{(\boxtimes)}$ [iD]

Group of Applied Mechanics and Advanced Manufacturing, IQS School of Engineering,
Universitat Ramon Llull, Via Augusta 390, 08017 Barcelona, Spain
marcoantonio.perez@iqs.url.edu

Abstract. This study deals with a novel post-process for polymeric components obtained by FFF based on the combination of annealing at controlled temperatures and isostatic vacuum pressing. The experimental development based on the Response Surface Methodology (RSM) allowed us to define an optimal combination of process parameters. The experimental results confirm the enhancement for different printing orientations showing a significantly improved intralayer and interlayer adhesion and demonstrating the capability of the proposed method to reduce the anisotropy of the treated parts, which can be extrapolated to other FFF polymers.

Keywords: Additive manufacturing · Fused filament fabrication · Thermal annealing · Mechanical performance

1 Introduction

Fused Filament Fabrication (FFF) is an Additive Manufacturing (AM) technology that still presents certain limitations limiting its industry consolidation. Two examples are the mechanical performance, which is affected by the anisotropy derived from the technology and the poor surface quality, influenced by interlayer and interfilament bonding [1]. However, post-treatments can address these drawbacks [2, 3], such as thermal annealing [4–6] or other post-processes capable of decreasing the characteristic surface roughness and improving part performance [7, 8].

This research aims to provide experimental evidence on the benefits of thermal post-processing of FFF polymers, aimed at improving the bond strength between filaments, thus reducing the mechanical anisotropy through a densification process while introducing an improvement in the surface quality of the components.

In this work, the high-performance polyetherimide PEI Ultem 9085 is used. Ultem 9085 is an advanced polymer used in the aerospace and automotive industries due to its outstanding strength-to-weight ratio and FST (flame retardant, low smoke, and toxicity). This research provides a new high-temperature thermal annealing approach, carried out in a pressurised environment, to treat Ultem PEI parts obtained by AM.

2 Methodology

The present study is an iterative process to improve printed parts' mechanical properties and anisotropy. First, specimens were fabricated in the XY and XZ direction and heat treated with and without vacuum, according to an initial experimental Doehlert matrix. Then, dimensional changes and mechanical properties were evaluated, and the pressurised environment was fixed for the second iteration until an optimum point was obtained. Finally, the results of both orientations are compared to evaluate the reduction of anisotropy and the improvement in mechanical performance.

ASTM D790 bending specimens (4 × 10 × 127 mm) were fabricated on a Fortus 400mc industrial printer using Ultem 9085. The printing parameters were a layer width of 0.254 mm, solid infill arranged at ±45° with a single contour, and a printing temperatures chamber of 195 °C and material extrusion of 380 °C. Samples were printed in the XY and the XZ orientation (worst-case condition). Post-treatment was carried out in a thermal chamber TH2700. To study the combined effect of heat treatment with vacuum pressure, some specimens were introduced into a polyamide vacuum bag with a valve connected to a 0.1 MPa vacuum device. The thermal process was done in three stages: initial heating (at a constant rate of 5 °C-min^{-1}), maintenance at the target temperature (according to DoE times) and cooling (gradual in the chamber itself). The mechanical testing was done on a Zwick Roell Z030 universal testing machine with a three-point bending test setup according to ASTM D790.

The Response Surface Methodology (RSM) was chosen to determine the significance of the results. Specifically, the Doehlert Design (DD) matrix was used to minimise the number of experiments, detect the lack of fit of the model and create sequential designs. For the factors (pressure and temperature) optimisation, the coded matrix (see Table 1) was used, obtaining seven equispaced experiences in the experimental domain in the form of a regular hexagon with a central point (Fig. 1). The process temperature was chosen as variable x_1 (175 to 201 °C), and the time the specimen was kept at that temperature as x_2 (0.5 to 3.4 h). The second DD variables were x_1 (191 to 205 °C) and x_2 (3 to 6 h). The experimental matrix was obtained by converting the values of the coded variables into uncoded values using Eq. 1:

$$V_{real} = \frac{L_{upp} + L_{low}}{2} + \frac{L_{upp} + L_{low}}{2} \cdot V_{codif} \qquad (1)$$

The presence of a pressurized environment was considered a categorical factor (not contemplated in the Doehlert matrices), so the matrix experiments were performed in duplicate: under atmospheric pressure and in a pressurized environment. Three response factors related to the flexural mechanical behaviour were selected to investigate the adequacy of the process and carry out the optimization: E_{flex}, σ_{max} and $\varepsilon(\sigma_{max})$. The statistical analysis of the results was carried out with Minitab software.

Table 1. Coded Doehlert matrix for two factors.

ID	1	2	3	4	5	6	7
x_1	−1	−0.5	0.5	1	0.5	−0.5	0
x_2	0	0.866	0.866	0	−0.866	−0.866	0
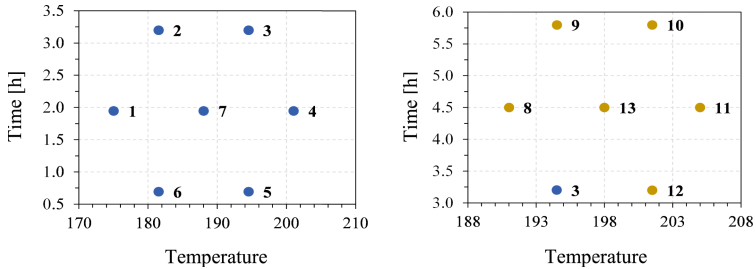
Fig. 1. Graphical representation of the first (left) and second (right) Doehlert design.

3   Results and Discussion

Table 2 shows the average results obtained in the three-point bending tests after heat treatment of the ZX specimens, according to the first Doehlert design. Apparent differences were observed between the flexural modulus of the specimens treated in a pressurised environment (ID 1–7) to those treated under atmospheric pressure (ID 1*–7*). It should also be noted that the specimens with improved strength (3–5, 7, 4* and 5*) are also more ductile, i.e., indicating a decrease in possible printing defects. Statistical analysis established that the optimum process conditions were 201 °C and 3.2 h under a pressurised environment. These values are at one extreme of the experimental domain, indicating that moving it towards the optimum point is necessary while keeping a pressurised environment in the new iteration.

Table 2. Results matrix first Doehlert. The asterisk refers to tests under atmospheric pressure.

ID	E_{flex} [MPa]	σ_{max} [MPa]	$\varepsilon(\sigma_{max})$ [%]	ID	E_{flex} [MPa]	σ_{max} [MPa]	$\varepsilon(\sigma_{max})$ [%]
1	1927 ± 112	63 ± 1	3.3 ± 0.1	1*	1936 ± 2	62 ± 2	3.3 ± 0.1
2	2153 ± 47	69 ± 4	3.6 ± 0.2	2*	1924 ± 35	65 ± 1	3.5 ± 0.1
3	2250 ± 35	98 ± 4	4.6 ± 0.4	3*	1885 ± 24	68 ± 2	3.8 ± 0.0
4	2306 ± 48	108 ± 1	5.6 ± 0.1	4*	1889 ± 136	86 ± 2	5.3 ± 0.4
5	2310 ± 148	85 ± 4	4.0 ± 0.3	5*	1908 ± 54	78 ± 4	4.8 ± 0.6
6	1872 ± 124	67 ± 3	3.5 ± 0.1	6*	1919 ± 32	64 ± 2	3.5 ± 0.0
7	1980 ± 45	78 ± 0	3.9 ± 0.1	7*	1979 ± 36	69 ± 0	3.8 ± 0.0

Figure 2 shows the results of dimensional changes caused by heat treatment of ZX and XY specimens in percentage variation. The diagram of the specimens qualitatively indicates the increase or decrease in dimension according to the direction of the arrows. The differences between the XY specimens treated at atmospheric pressure are generally more significant than those of the ZX specimens. This conclusion agrees with that postulated by Zhang et al. [9]. By allowing thermal relaxation, residual stresses on faces perpendicular to the printing direction are relieved, thus increasing the dimension. Post-treatments performed in a pressurized environment show not only that the dimensional changes are minor but also that there is a compaction of the specimen as the decrease in the height dimension is not compensated by an increase in the rest of the dimensions.
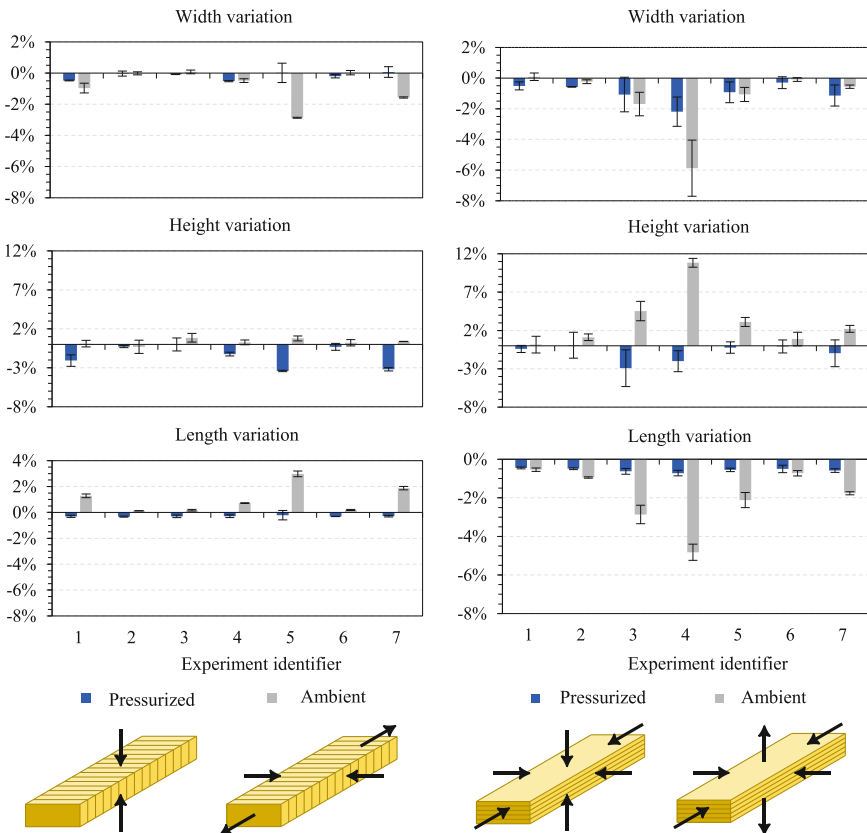
Fig. 2. Percentage dimensional changes of ZX (left) and XY (right) specimens after heat treatment.

The second experimental domain is shown in Fig. 1 (right). Table 3 collects the mean values of the bending test results, showing an apparent increase in all mechanical properties compared to the results of the first experimental matrix. However, differences between the values are minor, indicating a stabilization in the improvements produced by post-processing. Particularly relevant is the increase in the strain at maximum stress, attributed to increased cohesion between the layers.

Statistical processing of the results established that a vacuum pressure post-treatment at 201 °C for 4.4 h could provide optimum mechanical properties. This point's mechanical property prediction intervals were calculated, and the corresponding confirmatory experiments were carried out. The values of E_{flex}, σ_{max} and $\varepsilon(\sigma_{max})$ obtained with a 95% prediction interval were 2359 ± 204 MPa, 117 ± 9 MPa, and $7.2 \pm 1\%$, respectively. Looking at those intervals, it can be seen that, except for experimental points 3, 8, and 9, all other points of the second iteration have resulted in optimal. Thus, rather than a single optimum point, an optimum zone comprised of heat and vacuum pressure treatments ranging from 198 °C for 3.2 h to 204 °C for 5.8 h has been reached.

Table 3. Results matrix of the second Doehlert design.

ID	E_{flex} [MPa]	σ_{max} [MPa]	$\varepsilon(\sigma_{max})$ [%]
3	2250 ± 35	98 ± 4	4.6 ± 0.4
8	2278 ± 20	93 ± 7	4.3 ± 0.4
9	2300 ± 25	108 ± 0	5.6 ± 0.0
10	2267 ± 69	117 ± 1	7.4 ± 0.0
11	2240 ± 120	118 ± 1	7.7 ± 0.3
12	2444 ± 95	116 ± 3	7.0 ± 0.6
13	2361 ± 18	114 ± 2	6.7 ± 0.2

Finally, Table 4 collects the results of ZX and XY specimens treated under the optimum conditions. The improvements for the XY specimens are less pronounced, as expected. The most notable improvements are found at bending stress (75% increase in ZX specimens) and maximum strain (83% increase in ZX specimens). Figure 3 (left) depicts the differences between the stress-strain curves of both cases. Comparing ZX and XY orientations, the differences are reduced to 1% and 23%, respectively, indicating the suitability of the treatment. The 3D profile in Fig. 3 (right) also shows a much flatter surface after treatment. This is due to the combined effect of temperature and vacuum pressure, which shifts the softened material from the peaks to the valleys (filament bonding). On average, ZX samples have decreased their R_a and R_z by 90%, while XY samples have decreased their R_a and R_z by 50%. The dimensional changes suffered by the specimens treated with the optimum conditions were not more significant than a 4% decrease in height, the changes in the other two dimensions being negligible.

Table 4. Results of untreated and treated samples under the optimum process conditions.

Sample	E_{flex} [MPa]	σ_{max} [MPa]	ε (σ_{max}) [%]	R_a [µm]	R_z [µm]
ZX untreated	1909 ± 70	64 ± 5	3.5 ± 0.3	17.27 ± 0.26	71.06 ± 1.53
ZX treated	2310 ± 49	112 ± 2	6.3 ± 0.5	1.18 ± 0.25	6.30 ± 1.24
Differences ZX	$+21\%$	$+75\%$	$+83\%$	-93%	-91%
XY untreated	1923 ± 90	85 ± 3	7.6 ± 0.3	16.07 ± 1.39	75.37 ± 4.77
XY treated	2104 ± 21	113 ± 0	7.8 ± 0.0	6.77 ± 0.99	45.20 ± 5.09
Differences XY	$+9\%$	$+34\%$	$+3\%$	-59%	-40%
Initial anisotropy	1%	33%	120%		
Final anisotropy	9%	1%	23%		

4 Conclusions

This research demonstrates the feasibility of post-processing Ultem 9085 parts fabricated by FFF to improve their mechanical performance and the quality of inter-layer and intralayer bonds. The main conclusions can be summarized as follows:

- Dimensions of faces perpendicular to the fabrication direction tend to increase when heat is treated under atmos. Pressure. When using isostatic pressure, these changes are minimized, and specimens are compacted, i.e., densified.
- The response surface methodology has proven to be suitable for evaluating the change in properties of the treated specimens and finding an optimum zone.
- Experimental results confirm that the optimum point (201 °C for 4.4 h with pressure) is within the prediction range of the statistical method.
- The treatment has strengthened the intra- and interlayer bonds.
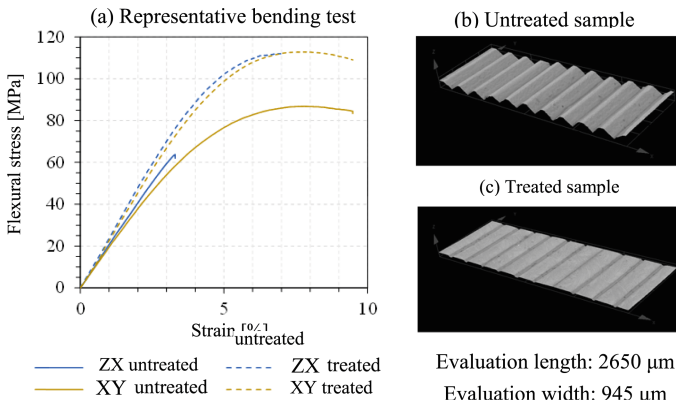
Fig. 3. Comparison of the results of the optimum point with respect to the pristine case in terms of mechanical performance (stress-strain curves) and surface quality (profiles).

- The specimens fabricated in both directions using the optimal process parameters show a significant reduction of mechanical anisotropy, which is one of the main challenges for the industrial consolidation of this technology.

References

1. Morales, N.G., et al.: The effect of interlayer cooling on the mechanical properties of components printed via fused deposition. Addit. Manuf. **24**, 243–248 (2018)
2. Chohan, J.S., Singh, R.: Pre and post processing techniques to improve surface characteristics of FDM parts: a state of art review and future applications (2017)
3. Shelton, T.E., et al.: Effects of thermal process parameters on mechanical interlayer strength for additively manufactured Ultem 9085. Polym. Test. **81**, 106255 (2020)
4. Sreejith, P., et al.: A thermodynamic framework for AM using amorphous polymers capable of predicting residual stress, warpage and shrinkage. Int. J. Eng. Sci. **159**, 103412 (2021)
5. Wach, R.A., et al.: Enhancement of mechanical properties of FDM-PLA parts via thermal annealing. Macromol. Mater. Eng. **303**, 1800169 (2018)
6. Padovano, E., et al.: Mechanical and thermal behavior of ultem 9085 fabricated by fused-deposition modeling. Appl. Sci. **10**, 3170 (2020)
7. Chueca de Bruijn, A., et al.: Optimization of a thermal annealing and isostatic pressing process for mechanical and surface enhancement. J. Manuf. Process. **85**, 1096–1115 (2023)
8. Chueca de Bruijn, A., et al.: A comparative analysis of chemical, thermal, and mechanical post-process of FFF PEI parts for surface quality enhancement. Mater. **2021**, 14 (2021)
9. Zhang, Y., Moon, S.K.: The effect of annealing on additive manufactured ULTEM 9085 mechanical properties. Materials **14**, 2907 (2021)

An Integrated Methodology for the Optimization of Process Parameters in Micromanufacturing: A Micromilling Case Study

David Serje Martínez[1(✉)] , Eduardo Diez Cifuentes[2] ,
Michael Miranda Giraldo[3] , and Jovanny Pacheco Bolívar[3]

[1] Universidad Simón Bolívar, Barranquilla, Colombia
`david.serje@unisimon.edu.co`
[2] Universidad de la Frontera, Temuco, Chile
[3] Universidad del Norte, Barranquilla, Colombia

Abstract. Micromachining combines a series of material removal processes that give flexibility and efficiency while manufacturing microcomponents in a wide range of materials, and geometries. On the micro-scale, some challenges must be addressed due to size effects, vibrations, tool rigidity, and others. Therefore, often process parameters tend to be very conservative and may not achieve the expected performance level. This study proposes an integral methodology for optimal parameter selection, being applied in the Titanium micromilling. The results show that it is possible to optimize the process parameters with a hybrid strategy with efficient use of time and resources.

Keywords: Micromanufacturing · Microcutting · Methodology · Optimization · Micromilling

1 Introduction

Miniaturization capability has been considered as a significant indicator of technical development in the modern world. This allows achieving size reductions in mechanical and electronic components which is a critical task to consolidate a set of functional characteristics in microdevices [1]. Multiple benefits are associated with this reduction in size, such as low energy and material consumption, low weight, compact size and an excellent cost-performance ratio; which are highly demanded in the medical, transportation and communications sectors, among others [2, 3].

Micromachining processes emerge as a response, consolidating as a set of key technologies capable of reaching the specifications required by these microcomponents. Micromachining processes stand out within micromanufacturing technologies because through the removal of material they allow multiple advantages over other processes in terms of work materials, precision and complexity of the geometries that can be produced [3, 4].

Material removal processes on the micro scale increase existing problems on the macro scale such as elastic/plastic deformations, fracture at high strain rates and high temperature gradients. Additionally, others are added such as the effect of size, influence of the microstructure, influence of the dynamics that become more relevant on this scale. There are modeling techniques to analyze these processes based on theoretical approaches by analytical [5] or numerical [6], mechanistic or semi-empirical [7], empirical-experimental [8] methods. However, there are still challenges for the prediction of micromachining performance such as tool life, surface integrity, chip formation, which provide vital information for use in the industry [9].

In accordance with the above, the present work presents a new methodological approach towards finding a set of optimal of process parameters for micromachining. For this purpose, modeling techniques are integrated, numerical (finite element) and experimental (experimental design) methods that allow a cost-effective addressing of optimal operating parameters selection. The developed methodology was applied in different micro-milling processes, proving to be effective as a support tool for the process optimization task.

2   An Integrated Methodology

In micromachining processes, multiple aspects are compromised, such as cutting forces, burr formation, surface finish, material removal rates, and tool wear among others, which are affected by the selection of parameters and process conditions such as cutting speeds, feed, depth of cut, tools, coolants among others.

The parameters optimization is a multi-objective task that must be adapted to the resources and times available in each scenario. It is a complex process that often requires intuition, creativity, critical reasoning, added to the implementation of existing information (documents, previous experiences, empirical knowledge). Figure 1 illustrates the steps of the proposed methodology:

1. The starting point is to define the process variables and responses to be considered in compliance with current needs and available resources. Cutting speeds, feeds, depths and tools are usually some of the variables considered in micromachining processes and removal rates, surface finish as some of the responses or performance indicators of the process that is being measured. This is a critical step where objectives and constraints are clearly defined.
2. Establish a knowledge base with appropriate information about the selected parameters and their effects on process responses. The foregoing may include previous empirical or analytical knowledge about the process from previous experiences (of researchers, manufacturers, machinists, etc.) to contribute to the design space of the parameters to be explored. Material properties such as density, elastic modulus, constitutive and fracture models with their respective parameters, as well as thermal properties, among others, may be required and even require additional tests for an adequate measurement of them under desired/expected conditions.
3. Develop and evaluate numerical models with their respective formulation (by finite elements, smoothed particle hydrodynamics, molecular dynamics, or others) according to the resources, skills and required factors. Some fundamental parameters such
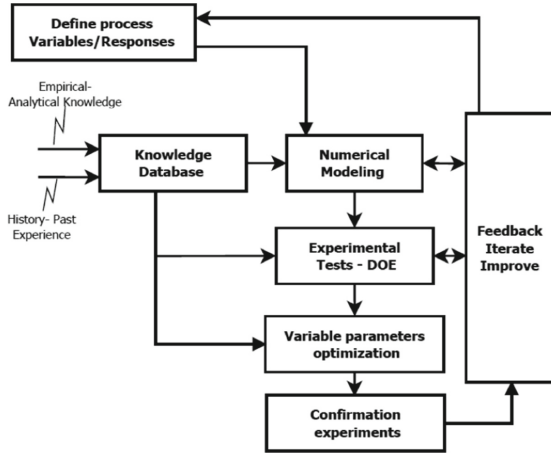
Fig. 1. Proposed methodology flowchart.

as forces, stresses, deformations, strain rates, temperatures, and chip formation can be explored in this phase. Simulations include only computational cost (as they do not imply infrastructure or costly equipment) allowing us to evaluate under different working conditions to focus the successive steps according to the results obtained.

4. Perform experimental tests with recommended ranges defined in previous stages (steps 1 to 3) by applying systematic design of experiment techniques according to the requirements that can allow deriving valid conclusions from a statistical approach. For example, fractional experimental designs or Taguchi orthogonal designs may permit low-cost screening and rapid assessment of process responses. Other types of design such as central composite designs, D-optimum or Box-Behnken can also be used for process optimization, allowing the creation of a response surface, but also limiting the required time and resources. Through experimentation, industry-relevant parameters such as tool life, surface finish, and burrs of the machined component can be measured in this step as required.

5. Apply optimization strategies (Taguchi, fuzzy logic, neural networks, or others) to obtain a set of optimal parameters that achieve the expected performance.

6. Apply confirmatory tests to verify the quality of the experimental results and the consistency with the predictions of the numerical and experimental models.

7. Adjustments to the method can arise in any of the previous stages, so it is vital to provide feedback to each phase towards improvement, for example suggesting modifications to the process variables, and adjusting their limits or design space, among others.

2.1 Defining Objectives and Constraints

In micromachining, it is very common to use more conservative process parameters due to the inherence of other insignificant effects on the macro scale and the relative fragility of microtools. The market often demands high removal rates as an indicator of productivity while keeping operating costs low. For this reason, the main objectives

of micromachining processes can be classified into two large categories such as those based on quality or related to economic criteria.

- Costs: Machining time and production costs are the main representatives of this category.
- Quality: In this group different factors are associated that significantly affect the quality of the machined components. Some of them are tool wear, tool life, component precision, surface finish, among others.

2.2   Process Modeling and Simulation

Predictive models resulting from simulations can be integrated into process planning to improve productivity and the quality of the final product. A hybrid strategy is highly recommended to develop a model from multiple inputs (like material parameters, process cutting conditions, machine tool, and interface characteristics) and process different output variables that may be fundamental (such as forces, stresses and strains which are significant for the scientific approach) or relevant to industry and product manufacturing (like tool life, surface roughness, and burrs). A numerical/empirical approach is recommended, in such a way that the capacities of each modeling scheme are improved, allowing the validation of the results and a cost-effective methodology.

Some numerical techniques that have been applied to simulate the response of the micromachining process (shown in Fig. 2) are Finite Elements [10], Smoothed Particle Hydrodynamics [11], Molecular Dynamics [12], and Multi-Scale [10]. Some of them have been successfully used to analyze cutting forces, stress-strains, temperature distributions, chip and burr formation, and residual stresses.
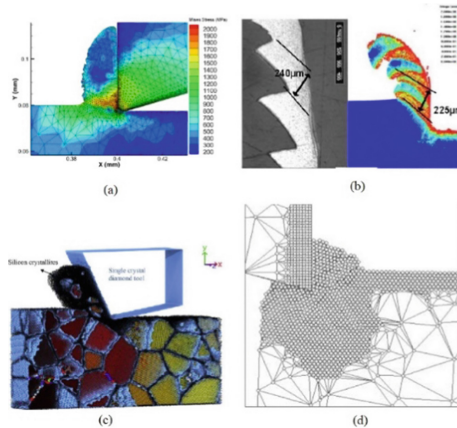
Fig. 2. Simulations for microcutting processes. Source: (a) [13], (b) [11], (c) [12], (d) [14].

3   Case Study

This case study is focused on increasing the performance of the commercially pure Titanium (ASTM B265 GR2) micro-milling process by optimizing basic process parameters to reduce cutting forces, tool wear, and burr formation while preserving a moderate material removal rate (productivity). A series of simulations, coupled with a Taguchi orthogonal array set of experimental runs, allowed the investigation of multiple parameters (shown in Fig. 3, and Table 1). Further details can be found in [15].

Table 1. Experimentation tests and results.

No	Spindle Speed (kRPM)	Feed (μm/tooth)	Depth of cut (μm)	Cutting Force (N)	Tool Wear (%)	Burr Area ($\mu m)^2$	MRR (mm^3/min)	Grey Rel. Grade
1	12	1.4	200	0.777	23%	122,660	7	0.810
2	12	2	400	1.468	106%	262,568	19	0.581
3	12	2.6	600	3.855	19%	635,106	37	0.725
4	15	1.4	400	5.124	90%	152,742	17	0.519
5	15	2	600	4.241	22%	1,100,259	36	0.642
6	15	2.6	200	1.659	37%	176,915	16	0.683
7	18	1.4	600	3.417	38%	572,029	30	0.587
8	18	2	200	2.251	61%	119,025	14	0.627
9	18	2.6	400	3.62	22%	194,975	37	0.811
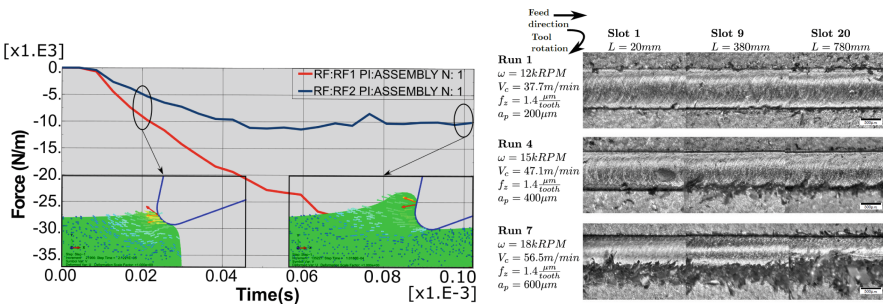
Fig. 3. Finite Element cutting simulation and machined slots burrs.

4   Conclusions

In the present study, a new methodological approach is proposed for the optimization of process parameters in micromachining. This approach integrates modeling techniques, particularly numerical and experimental methods supported by statistical analysis, which allows to effectively address the selection of optimal operating parameters

reducing the use of time and resources for its application compared to traditional methods. This methodology can also be extrapolated to other subtractive or additive processes, materials, and responses.

References

1. Hashmi, S.: Comprehensive Materials Processing, Elsevier Science (2014)
2. Qin, Y.: Micromanufacturing Engineering and Technology. Elsevier Science (2015)
3. Serje, D., Pacheco, J., Diez, E.: Micromilling research: current trends and future prospects. Int. J. Adv. Manuf. Technol. **111**, 1889–1916 (2020)
4. Jain, V.K., Sidpara, A., Balasubramaniam, R., Lodha, G.S., Dhamgaye, V.P., Shukla, R.: Micromanufacturing: a review—Part I. Proc. Inst. Mech. Eng. Part B: J. Eng. Manuf. **228**, 973–994 (2014)
5. Budak, E., Ozlu, E., Bakioglu, H., Barzegar, Z.: Thermo-mechanical modeling of the third deformation zone in machining for prediction of cutting forces. CIRP Ann. Manuf. Technol. **65**, 121–124 (2016)
6. Sahoo, P., Patra, K.: Mechanistic modeling of cutting forces in micro-end-milling considering tool run out, minimum chip thickness and tooth overlapping effects. Mach. Sci. Technol. (2018)
7. Davoudinejad, A., Tosello, G., Parenti, P., Annoni, M.: 3D finite element simulation of micro end-milling by considering the effect of tool run-out. Micromachines **8** (2017)
8. Miranda, M., Serje, D., Pacheco, J., Bris, J.: Tool edge radius wear and material removal rate performance charts for titanium micro-milling. Int. J. Precis. Eng. Manuf. **19**, 79–84 (2018)
9. Arrazola, P.J., Özel, T., Umbrello, D., Davies, M., Jawahir, I.S.: Recent advances in modelling of metal machining processes. CIRP Ann. Manuf. Technol. **62**, 695–718 (2013)
10. Cheng, K., Huo, D.: Micro-Cutting: Fundamentals and Applications. Wiley (2013)
11. Limido, J., Espinosa, C., Salaun, M., Mabru, C., Chieragatti, R., Lacome, J.L.: Metal cutting modelling SPH approach. Int. J. Mach. Mach. Mater. **9**, 177–196 (2011)
12. Goel, S., Luo, X., Agrawal, A., Reuben, R.L.: Diamond machining of silicon: a review of advances in molecular dynamics simulation. Int. J. Mach. Tools Manuf **88**, 131–164 (2015)
13. Zhou, L., Peng, F., Yan, R., Dong, Q., Yang, C.: Prediction and experimental validation of micro end-milling forces with finite element method. In: Liu, H., Kubota, N., Zhu, X., Dillmann, R., Zhou, D. (eds.) ICIRA 2015. LNCS, vol. 9245, pp. 664–675. Springer, Cham (2015). https://doi.org/10.1007/978-3-319-22876-1_58
14. Sun, X., Chen, S., Cheng, K., Huo, D., Chu, W.: Multiscale simulation on nanometric cutting of single crystal copper. Proc. Inst. Mech. Eng. Part B: J. Eng. Manuf. **220**, 1217–1222 (2006)
15. Serje Martínez, D.A.: A micro-milling cutting force and chip formation modeling approach for optimal process parameters selection. Universidad del Norte (2018)

Optical Evaluation of Surface Roughness in Wood Parts Processed by Robotic Sanding

Fabián Iglesias[1] , Alfredo Aguilera[2], Arturo Padilla[1] , Matías Madaf[1], and Eduardo Diez[1(✉)]

[1] Department of Mechanical Engineering, Universidad de La Frontera, 4811230 Temuco, Chile
f.iglesias01@ufromail.cl, eduardo.diez@ufrontera.cl
[2] Instituto de Bosques y Sociedad, Universidad Austral de Chile, 5110566 Valdivia, Chile

Abstract. Surface roughness is an essential property in the manufacturing industry to assess the quality of its products after finishing operations. However, the evaluation of surface quality in wood products usually depends on the subjective inspection of the operators, which implies a high variability in the final quality of the pieces. This study proposes a new method to estimate roughness parameters by applying algorithms on images of wood parts processed by robotic sanding. For this purpose, this article presents a hybrid approach based on features using the co-occurrence matrix applied to greyscale images processed with five edge detection algorithms. For the evaluation of the performance of this method, the researchers correlated five features for each edge detection algorithm with standard surface roughness parameters, obtaining high correlations. The results of this study constitute a first step in implementing the proposed method in inspection systems for optical roughness measurement of wood products in automated industrial environments.

Keywords: Robotic Sanding · Wood · Surface Roughness · Machine Vision

1 Introduction

Multiple studies are underway to automate the sanding operation using industrial robots [1]. Advances in this area require further knowledge and modelling of the robotic sanding process, considering the operating conditions and material properties. According to Gurau [2], the results of surface roughness evaluation on processed wood vary depending on many factors, such as: wood species, cut direction, structural elements of the wood, moisture content, operating conditions and measuring instrument.

Wood has a strong anisotropy, making the process's influence on the piece's roughness challenging to investigate. However, Medium Density Fibreboards (MDF) are more homogeneous materials, with no distinction in the fibre directions [3]. This characteristic makes it an appropriate material to investigate the influence of the operating conditions on the surface quality, reducing the variability in the results.

Gurau & Irle [4] reviewed surface roughness evaluation methods, indicating that wood products have no standardised procedure for calculating the amplitude parameters.

A less explored field is non-conventional techniques for estimating wood roughness based on two-dimensional images.

Techniques based on two-dimensional images make possible fast, low-cost results, and allow easy integration into inspection lines or intelligent manufacturing devices. Ghodrati et al. [5] proposed a roughness evaluation method for plastic parts using edge detection algorithms in images, showing a high correlation between the features extracted from the images and the standardised roughness parameters, but it also presented variations at different resolutions. Gadelmawla [6] used features extracted from the grey-level co-occurrence matrix to estimate the surface roughness of turned parts. However, this technique is highly dependent on the illumination conditions.

Based on the background, there still needs to be a consensus on applying machine vision algorithms to evaluate surface roughness. There is also a gap in the literature on applying this algorithm in wood and its derivatives. To reduce this gap, we propose to evaluate the application of image-based algorithms to estimate surface roughness parameters in wood parts processed by robotic sanding.

2 Methodology

We proposed a method based on features using the grey-level co-occurrence matrix, applied to images processed with edge detection algorithms to reduce illumination effects. Then we evaluate Pearson's r between the features and the roughness parameters.

2.1 Experimental Trials

The robotic sanding station consists of a servomotor-driven sander integrated with a structure mounted on the flange of a UR10e collaborative robot. The sanding station processed 15 MDF specimens ($180 \times 110 \times 15$ [mm^3]) with the same operating conditions, except for sanding grit size, with levels P80, P120 and P240. The three types of circular sandpaper were 3M™ Cubitron™ II Hookit™ 127 [mm] diameter, with perforations for particle suction. The general conditions of the experimental trials were:

- a normal force of 20 [N], controlled by the collaborative robot;
- a rotational speed of 2000 [rpm] on the servomotor; and,
- a feed rate of 0.02 [m/s], defined through a linear movement of the robot.

The total number of specimens was subdivided into three groups of five: the first group was processed with sandpaper P80, the second with P120 and the third was processed with two passes, one P120 and one finer pass P240, considering the need for incremental sanding when using finer grits.

2.2 Roughness Measurement

We used a Mitutoyo SJ-310 contact roughness profilometer to measure surface roughness (three measurements at the centre of each specimen in the feed direction) to calculate roughness parameters (R_a, R_{sm}, R_{sk}, R_z, and R_p) according to ISO 21920-2 [7].

The mechanical profile was processed in MATLAB (version R2021b). First, we applied a Gaussian S-filter to remove the *small lateral scale components* (short wavelength), with nesting index $N_{is} = 0.008$[mm]. Then, we used the F-operation, consisting of the adjustment and subtraction of a sixth-order polynomial, to remove the profile shape [8]. Finally, we applied a Gaussian L-filter, which removes the *large lateral scale components* (long wavelength) with nesting index $N_{ic} = 2.5$[mm].

The uncertainty was estimated by pooling the three measurements of the five processed specimens with the same grit number, calculating 95% confidence intervals using a Student's t-distribution.

2.3 Image Acquisition and Processing

Image acquisition was executed in a darkroom with side LED illumination, with a SONY STL-A58 camera with DT 3.5–5.6/18–55 SAM II lens, focal length 30 mm, aperture F14, exposure time 10 s, ISO 100, parallel to the specimen surface at 400 mm. After capture, images were cropped in the central area of the MDF specimen with a size of 78 × 676 px, equivalent to approx. 4.5×39 mm^2. The processing included three steps:

- **Step 1. Edge detection.** Edge detection algorithms typically consider three stages: a filtering stage to remove noise; an enhancement stage to facilitate edge detection based on intensity changes; and a detection stage with a thresholding criterion to discern between points that are edges and those that are not. This work will only apply the enhancement stage because using a filter or threshold could reduce the relevant information describing the quality of the surface. We used five enhancement algorithms, three based on the first derivative of the image intensity (*Roberts*, *Sobel*, and *Prewitt*) and two on the second derivative (*Laplacian* and *Laplacian of Gaussian*). The derivatives are approximated by differences using convolution masks [9].
- **Step 2. Co-occurrence Matrix.** The grey-level co-occurrence matrix (GLCM) [10] is widely used to analyse texture in images, it is a second-order statistical technique that estimates the probability of spatial relationship between two pixels. The co-occurrence matrix is added with its transposed, resulting in a symmetric matrix, which is then normalised. It considers a co-occurrence matrix with a maximum of 8 levels and a displacement vector of $d = (1, 0)$, perpendicular to the sanding marks.
- **Step 3. GLCM Features.** The features are obtained according to the definitions of [10]. The five features are: *Uniformity of energy* (U), *Contrast* (C), *Homogeneity* (H), *Correlation* (*Autocorrelation* in this paper) (A) and *Entropy* (S).

3 Results

3.1 Surface Roughness

In the results, Fig. 1 shows three roughness profiles obtained with the contact roughness profilometer for each sandpaper grit and the amplitude distribution of each profile. It is possible to appreciate the reduction of profile heights as the grit size increases and the amplitude distribution that reduces its dispersion. Figure 2 shows the roughness parameter mean for each group of specimens sanded with different grit sizes. All roughness

parameters show a decrease for finer grit sizes. Parameters R_a, R_z and R_p, which describe the roughness profile height, present a reduction of the confidence intervals as finer grit is applied. This does not occur with R_{sm}, and neiher with the skewness R_{sk} increases its confidence intervals with finer grits.
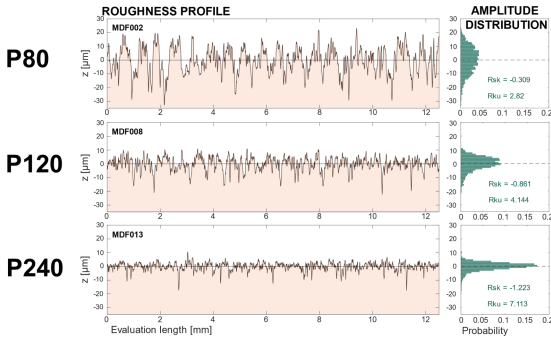

Fig. 1. Roughness profiles and amplitude distribution on sanded specimens with different grit sizes.
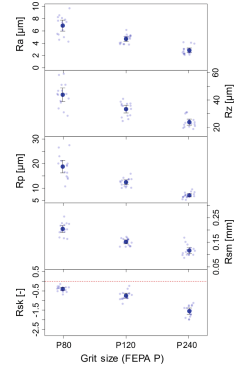
Fig. 2. Roughness parameter means.

3.2   Image Processing

We applied five edge detection algorithms to each image according to the methodology. Figure 4 shows the result after processing one image corresponding to a piece sanded with the coarser grit sandpaper (P80). As the image section corresponds to the central area of the wooden specimen, streaks resulting from the tangential speed of sanding pad rotation can be distinguished perpendicular to the operation's feed. Figure 3 shows feature means extracted from the GLCM matrix with different edge detection algorithms for each grit size.
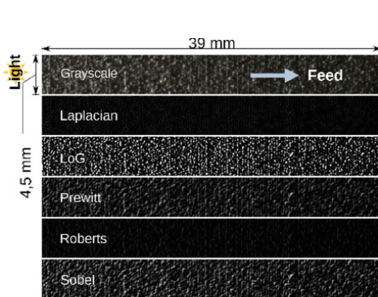
Fig. 3. Result of image processing with edge detection algorithms.
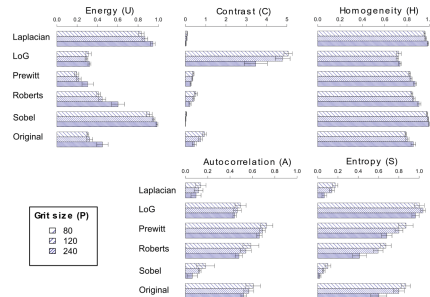
Fig. 4. Means of features for different edge detection algorithms and grit size.

In the case of the images resulting from the application of *Roberts* and the *Laplacian* algorithms, it is possible to distinguish a lower light intensity. We obtain a higher contrast in images enhanced with *Laplacian of Gaussian* algorithm.

Figure 4 shows an overlap in confidence intervals between P80 and P120 sandpaper trials where the means do not show a relevant variation in both sandpaper grit size levels. However, this does not occur with P240 sandpaper trials, in which the mean value is distinguishable from the mean values of the other two groups.

3.3   Correlations

The Pearson's *r* between the features obtained from images processed with edge detection algorithms and the roughness parameters are presented in Table 1. These results show high correlation levels using edge detection algorithms combined with GLCM features.

Table 1. Correlations between features extracted from the images and roughness parameters.

	Laplacian					LoG					Original				
	A	C	H	S	U	A	C	H	S	U	A	C	H	S	U
Ra	0.82	0.91	-0.90	0.91	-0.90	0.89	0.74	0.04	0.13	0.10	0.95	0.90	-0.85	0.94	-0.78
Rz	0.84	0.91	-0.90	0.91	-0.90	0.90	0.73	0.05	0.12	0.10	0.95	0.89	-0.84	0.94	-0.77
Rp	0.74	0.93	-0.92	0.92	-0.92	0.87	0.76	0.02	0.13	0.08	0.92	0.93	-0.87	0.95	-0.80
Rsk	0.43	0.92	-0.92	0.92	-0.92	0.55	0.92	-0.45	0.54	-0.37	0.65	0.95	**-0.96**	0.90	-0.90
Rsm	0.80	0.90	-0.90	0.91	-0.90	0.83	0.78	-0.06	0.22	0.00	0.90	0.90	-0.86	0.93	-0.78
	Prewitt					Roberts					Sobel				
	A	C	H	S	U	A	C	H	S	U	A	C	H	S	U
Ra	0.96	0.93	-0.86	0.91	-0.84	0.91	0.96	-0.96	0.96	**-0.96**	0.94	0.91	-0.82	0.89	-0.79
Rz	**0.97**	0.92	-0.84	0.90	-0.83	0.90	0.94	-0.94	0.95	-0.95	0.95	0.91	-0.81	0.88	-0.79
Rp	0.93	0.95	-0.87	0.91	-0.84	0.92	0.97	-0.97	**-0.98**	0.91	0.93	-0.83	0.89	-0.80
Rsk	0.69	0.93	-0.95	0.93	-0.93	0.81	0.88	-0.88	0.88	-0.87	0.64	0.93	-0.94	0.93	-0.92
Rsm	0.92	0.93	-0.88	0.91	-0.86	0.87	**0.95**	-0.95	**0.95**	-0.95	0.90	0.92	-0.84	0.90	-0.83

When analysing the results, the highest correlations occur using the *Roberts* edge detection algorithm, while the best-evaluated feature corresponds to *Contrast*. When calculating the mean of the correlations in absolute value for each edge detection algorithm, *Roberts's* algorithm has the highest result with a mean correlation of 0.93. For the features extracted from the GLCM matrix, the highest average correlation occurs in *Contrast* with 0.90. Equally, the *Roberts* algorithm and the *Contrast* feature have the highest absolute correlations above 0.90.

Although the high correlations suggest that the method proposed in this work is suitable for assessing the roughness of sanded MDF parts, further tests with images at different resolutions and illumination modes are needed. In addition, the methodology needs to be repeated in other areas of the specimen surface to assess whether the behaviour is the same. Another relevant aspect necessary to evaluate are the configurations of the GLCM hyperparameters, such as the displacement vector and the number of levels.

4 Conclusion

This work studied a new surface roughness evaluation method employing images of the surface of sanded MDF specimens. We obtain high correlations with the standardised roughness parameters, suggesting that the *Roberts* algorithm and the *Contrast* feature are suitable for evaluating the surface quality of sanded wooden parts.

Before establishing models to obtain roughness parameters based on the proposed methodology, it is necessary to optimise the vision system and evaluate the algorithms' sensitivity with different resolutions and illumination conditions. However, based on the current results, we realised that this methodology based on the capture and processing of two-dimensional images has the potential to improve performance and quality control in the wood sanding industry.

References

1. Wen, Y., Pagilla, P.R.: A novel 3D path following control framework for robots performing surface finishing tasks. Mechatronics **76**(December 2020), 102540 (2021)
2. Gurau, L.: Testing the processing-induced roughness of sanded wood surfaces separated from wood anatomical structure. Forests **13**(2) (2022)
3. Csanády, E., Magoss, E.: Mechanics of Wood Machining. Springer, Cham (2013). https://doi.org/10.1007/978-3-030-51481-5
4. Gurau, L., Irle, M.: Surface roughness evaluation methods for wood products: a review. Curr. For. Rep. **3**(2), 119–131 (2017). https://doi.org/10.1007/s40725-017-0053-4
5. Ghodrati, S., Mohseni, M., Gorji Kandi, S.: Application of image edge detection methods for precise estimation of the standard surface roughness parameters: polypropylene/ethylene-propylene-diene-monomer blend as a case study. Meas. J. Int. Meas. Confed. **138**, 80–90 (2019)
6. Gadelmawla, E.S.: Estimation of surface roughness for turning operations using image texture features. Proc. Inst. Mech. Eng. Part B J. Eng. Manuf. **225**(8), 1281–1292 (2011)
7. ISO 21920-2:2021(en): Geometrical product specifications (GPS)—Surface texture: Profile—Part 2: Terms, definitions and surface texture parameters (2021). https://www.iso.org/standard/72226.html
8. Piratelli-Filho, A., Sternadt, G.H., Arencibia, R.V.: Removing deep valleys in roughness measurement of soft and natural materials with mathematical filtering. Cienc. Eng. Sci. Eng. J. **21**(2), 29–34 (2012)
9. Ramesh, J., Kasturi, R., Schunck, B.: Machine Vision. McGraw-Hill, Inc. (1995)
10. Haralick, R.M., Shapiro, L.G.: Computer and Robot Vision, 1st edn. Addison-Wesley Publishing Company (1992)

Development of Powder Bed Laser 3D Printing in Polar Coordinates and Its Comparison with Conventional Cartesian Laser 3D Printing

Jorge Andrés Ramos-Grez[1,2(✉)] ⓘ, Maximiliano López Norambuena[1],
Ignacio Jeria Pérez[1], Domingo Gallardo Saavedra[1], and Matías González Aguilera[1]

[1] Department of Mechanical and Metallurgical Engineering, Pontificia Universidad Católica de Chile, Av. Vicuña Mackenna 4860, Macul, Santiago, Chile
jramos@uc.cl

[2] Centro de Investigación en Nanotecnología y Materiales Avanzados CIEN-UC, Pontificia Universidad Católica de Chile, Santiago, Chile

Abstract. Powder bed laser 3D printing performed using polar coordinates, called Spiral Growth Manufacturing (SGM), allows manufacturing axisymmetric revolution parts in less time compared to conventional cartesian laser printing or Selective Laser Melting (SLM). In this work, a device to perform SGM operating under polar coordinates is presented. The study considered the manufacture of rings by 3D laser printing, both polar (SGM) and cartesian (SLM), from AISI 316L steel powder. These were compared dimensionally and with regards to density and build rate efficiency of the process. The rings have a nominal outer diameter of up to 75 mm and inner one of 45 mm. Results indicate that geometric dimensional precision, specific and nominal density of the polar rings are very close to those obtained through cartesian process. Build rate efficiency of rings by polar printing is on average 5% higher than for cartesian obtained rings.

Keywords: Spiral Growth Manufacturing · Steel AISI 316L · Build rate Efficiency

1 Introduction

3D printing using a laser and a bed of metal powder is an established technology in the additive manufacturing market. [1] Its current operation is based on three-dimensional movements within a cartesian coordinate system (i.e., x-y-z). This makes it possible to manufacture complex objects by stacking layers of metallic powder, which are applied discreetly and sequentially by a roller generally in the vertical direction. A high-power focused laser beam is actuated in the x and y directions over each layer by means of galvanometric mirrors. The powder layer is thus selectively melted giving the process its known name and acronym, Selective Laser Melting (SLM). Alternatively, since 2005 [2], researchers have worked the idea of dispensing the powder in a rotary or polar coordinate manner, thus giving way to a continuous powder layer process. At the University of

Liverpool, Egan [3] proposed a new printing technique from a continuous layer in the form of a spiral. He coined it Spiral Growth Manufacturing or simply SGM. This method is based on SLM, except that, the part is continuously being printed, due to the rotation of the powder bed. Later, Zañartu and Ramos [4] designed and built a similar device that worked under spiral binder-jetting printing. On the occasion, they made rings based on ceramic powders (e.g., calcium sulphate). Following the same line of research, Vera [5], redesigned the previous device and created a prototype 3D printer for the consolidation of molten powder by laser under a controlled atmosphere; here again, the working axes were in cylindrical coordinates and not cartesian. Achieving rings made from a Cu-Ni-Sn alloy with layer thicknesses between 400 to 600 µm at an angular speed of one revolution per minute. Thus, verifying the technical feasibility of the method, but not yet its effectiveness at the level of functional manufactured parts. More recently in 2020, Carter et al. [6] began investigating SGM technology in the manufacture of large aviation engine parts.

According to [7], who carried out the superficial melting treatment of 316L steel metal rings, thermal fields differ between a cartesian and a polar process, because the trajectory of the laser beam on the surface of the powder layer is distinct under each processing scheme; affecting thermal gradients and cooling rates locally. This is expected to have a favorable impact on the control of residual stresses by avoiding, for example, post-recovery or annealing heat treatments commonly used today in parts printed using lasers in cartesian printing processes.

In this work, preliminary measurement results of dimensional characteristics of parts printed using both polar and cartesian techniques and the specific and nominal density using the Archimedean method are presented. Based on the results, it was possible to estimate and compare the build rate efficiency (i.e., mass rate efficiency [8, 9]) between both processes and correlate the values with the volumetric energy density used.

1.1 Build Rate Efficiency

Build rate efficiency, or mass rate efficiency, is defined by Eq. (1) [8, 9] as the quotient between the real mass rate and the theoretical mass rate. The first is obtained from the experimental printing process by weighing the part and recording the effective printing time (subtracting dead times, e.g., time to spread the powder as in the SLM process). The second corresponds to the maximum amount of mass possible the system can melt per unit of time considering adiabatic conditions from a given heat source of power P, applied to the surface of the powder, and its thermophysical properties.

$$\eta_b = \frac{\dot{m}_{real}}{\dot{m}_{theoretical}} = \frac{\Delta m/\Delta t}{P/(Cp\Delta T_f + \Delta h_f)} = \eta_m \qquad (1)$$

1.2 Volumetric Energy Density

On the other hand, the volumetric energy density for a cartesian printing system is given by Eq. (2) [1] and is calculated as the ratio between the power of the heat source P and

the product of the scanning speed (v), layer thickness (e) and the spacing between laser pass lines, i.e. hatch spacing (ϕ).

$$E_{d-SLM} = \frac{P}{v \cdot e \cdot \phi} \qquad (2)$$

For a polar system, on the contrary, it is necessary to include the average traverse speed of the heat front, which is a function of the *rpm* times the average length of the heat line (for a ring, it corresponds to one quarter the difference between the outer diameter d_o and inner diameter d_i, both squared). The expression is given by Eq. (3) [10].

$$E_{d-SGM} = \frac{4P}{\frac{\pi}{60} \cdot rpm \cdot e \cdot \left(d_o^2 - d_i^2\right)} \qquad (3)$$

Finally, the input variables of the SGM and SLM processes are adjusted so that they generate comparable results, this to study the effect on the dimensions, specific - nominal density and build rate efficiency between both printing methods.

2 Methods

The input parameters of the polar (SGM) printing process are illustrated in Fig. 1 (a) and correspond to: laser power (P in watts), laser scan speed (v in mm/s), layer thickness (e in mm), and powder bed angular speed (*rpm* in rev/min); for a certain height (h), outer (d_o) and inner (d_i) diameters of the ring. These parameters allow the fabrication of metal rings such that they can be compared according to the values of the output variables: obtained dimensions, specific - nominal density, and build rate efficiency.

2.1 Laser Scanning Patterns

Figure 1(b) illustrates the differences between the laser beam scanning patterns of a cartesian and a polar process. The cartesian scan pattern is dependent on the scan angle with respect to the geometry of the cross section of the part, with the possibility of very long and very short linear heat segments. In the case of the polar process, the heat segments are shorter, symmetrical, and constant in length in the case of rings. This has an effect regarding the accumulation of heat at any point on the surface, since the longer the heat line is, the waiting time between consecutive passes of the heat source is greater and therefore there is more time for the heat to dissipate towards cold zones. Increasing the rate of cooling and thus generating residual stresses of greater magnitude [11].
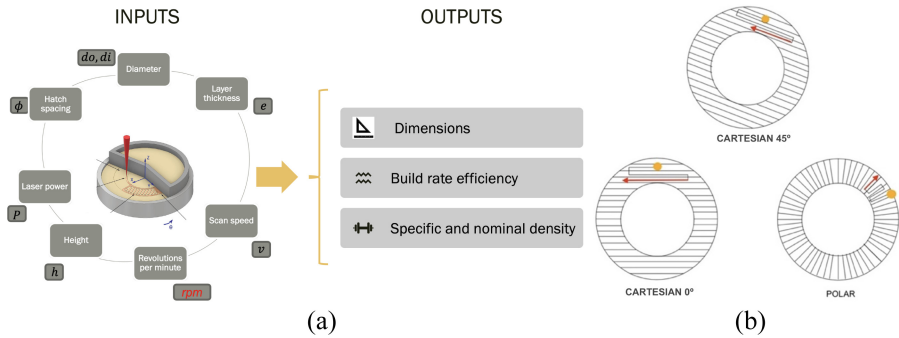
Fig. 1. (a) I/O parameter set of SGM process. (b) Schematic difference of laser scan patterns.

2.2   Polar and Cartesian Laser Printing Systems

The two laser-powder-bed 3D printing systems used are described below and preliminary results from the rings printed in 316L steel are presented as follows.

SGM Printing System (Polar).   Figure 2(a) shows the integration of the polar SGM system consisting of a 300W (1064 nm) IPG fiber laser, a SINTEC x-y scanner, vacuum chamber, power and electro-mechanical control system. The possible layer thicknesses obtained ranged from 140 to 400 microns. The nominal laser power varied between 170 and 240 W, obtaining volumetric energy densities from 6 to 32 J/mm^3. Figure 2(b) shows one of the rings printed. The ring is fused to a build platform of the same steel. The ring has a nominal inner diameter of 45 mm and an outer diameter of 75 mm, it was manufactured at 1 rpm with a laser power of 216 W, focused at 75 µm, a layer thickness of 200 µm and a laser scanning speed of 990 mm/s.

Fig. 2. (a) SGM printing system. (b) SGM printed 316L ring.

SLM Printing System (Cartesian).   A commercial SLM-type 3D printing system, GE Additive MLab 200R, which operates under a cartesian coordinate scheme was used. It has a 200 W (1064 nm) IPG fiber laser, a Super Scan x-y scanning head with speeds of up to 7 m/s, a print throughput volume of 10 cm x 10 cm x 10 cm, with a minimum layer

thickness of 15 µm and laser focal spot of 75 µm. Table 1 presents the parameters used in the manufacture of the rings by the polar (SGM) and cartesian (SLM) method.

3   Results

Geometric dimensions, mass, and printing time results allowed the calculation of the specific and nominal density, mass rates and build rate efficiency of the printed rings under both processes. These are presented and summarized in Tables 1 and 2.

3.1   Geometry Dimensions, Specific and Nominal Density

From the results presented in Tables 1 and 2, the achieved specific and nominal density of the rings are very close in magnitude under both processes. In relation to the width of the rings, the cartesian process tends to slightly overestimate the nominal value, while the polar process underestimates it in certain cases.

Table 1. Process parameters and results under cartesian (SLM) printing of 316L rings.

Specimen	Specific Density (kg/m³)	Nominal Density (%)	Height h (mm)	Width (do - di) / 2 (mm)	Real Mass (g)	Printing Time (min)	Real Mass Rate (gr/s)	Thoeretical Mass Rate (g/s)	Build Rate Efficiency (%)	Laser Power (W)	Layer Thickness (mm)	Hatch Spacing (mm)	Energy Density (J/mm³)
1	7920	99,2	8,95	15,40	148,1	107,3	0,023	0,164	14,0	140	0,050	0,080	35,0
2	7928	99,3	7,80	15,18	152,2	92,6	0,027	0,164	16,5	140	0,050	0,080	35,0
4	7530	94,3	9,65	15,03	187,7	222,4	0,014	0,164	8,5	140	0,030	0,066	70,7
5	7900	98,9	4,14	15,15	71,0	24,3	0,049	0,234	20,9	200	0,100	0,080	25,0
9	7800	97,7	4,39	14,70	91,1	171	0,009	0,164	5,5	160	0,040	0,075	83,3

Table 2. Process parameters and results under polar (SGM) printing of 316L rings.

Specimen	Specific Density (kg/m³)	Nominal Density (%)	Height h (mm)	Width (do - di) / 2 (mm)	Real Mass (g)	Printing Time (min)	Real Mass Rate (gr/s)	Thoeretical Mass Rate (g/s)	Build Rate Efficiency (%)	Laser Power (W)	Layer Thickness (mm)	RPM	Energy Density (J/mm³)
3	7830	98,0	6,77	15,06	97,6	29	0,056	0,199	28,1	170	0,233	1,0	15,5
6	7830	98,0	3,62	15,25	45,9	17	0,045	0,281	16,0	240	0,241	1,0	21,1
8	7710	96,5	2,89	14,81	34,8	10	0,058	0,222	26,1	190	0,241	1,0	18,3
10	7690	96,3	4,13	10,13	25,9	14	0,031	0,253	12,3	216	0,140	2,0	29,5
11	7340	91,9	9,94	15,03	128,7	49	0,044	0,253	17,4	216	0,200	2,0	12,5
12	7450	93,4	1,59	10,00	11,3	6	0,031	0,253	12,3	216	0,170	1,5	32,4
13	7360	92,1	1,34	9,80	8,7	4	0,036	0,253	14,2	216	0,170	2,0	24,3
15	5260	65,8	2,75	14,85	26,2	10	0,044	0,233	18,9	209	0,400	2,0	6,0

3.2   Build Rate Efficiency vs Volumetric Energy Density

Figure 3 shows the plot of the build rate efficiency versus the volumetric energy density for the polar and cartesian parts built. It is observed for SGM parts to achieve a higher build rate efficiency at energy densities lower than those used in SLM. The average build rate efficiency of the SGM parts (18.2%) is 5% higher than the SLM process (13.1%). Dead times between layer applications makes the latter less process efficient.

Global trend shows that higher energy density renders lower build rate efficiency, since a higher laser power is used, resulting in higher theoretical mass rate, which reduces the build rate efficiency; a result previously observed by Ramos-Grez et al. (2022) [10].
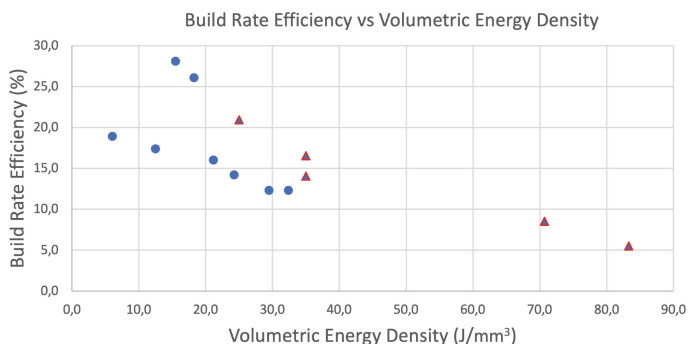
Fig. 3. Build rate efficiency vs energy density: polar (●) and cartesian (▲) process.

4 Conclusions

The results presented here indicate that the geometric dimensional precision and the specific - nominal density of rings manufactured using the polar (SGM) process is very close in magnitude to those obtained by the cartesian (SLM) process.

On the other hand, build rate efficiency is on average 5% higher for the polar (SGM) process than for the cartesian (SLM). However, a decreasing trend with volumetric energy density is observed in both processes.

The comparison of the distribution of residual stresses between both processes is the next step to study; anticipating that the SGM process should concentrate more heat, since the delay time of the heat front at each point is shorter. This would in turn increase the temperature locally, reducing thermal gradients and producing an in-situ recovery heat treatment, allowing to relieve residual stresses in the polar printed object.

References

1. Gibson, I., Rosen, D., Stucker, B.: Additive Manufacturing Technologies, 3rd edn. Springer, London (2010)
2. Hauser, C., Sutcliffe, C., Egan, M., Fox, P.: Spiral growth manufacturing (SGM) - a continuous additive manufacturing technology for processing metal powder by selective laser melting. In: SFF Symposium, Austin, Texas (2005)
3. Egan, M.J.: Spiral growth manufacture: a continuous additive manufacturing technology for powder processing. Thesis, University of Liverpool, Liverpool (2007)
4. Zañartu-Apara, G., Ramos-Grez, J.: Characterization of the mechanical properties of samples fabricated by an experimental SGM device. Rapid Prototyping J. **16**(5), 356–364 (2010)
5. Vera, J.: Influencia de parámetros de operación en Sistema de impresión 3D basado en el crecimiento en espiral de objetos sólidos. Thesis, Pontificia Universidad Católica de Chile, Santiago (2018)

6. Carter, W.T., et al.: A large format DMLM system using a continuously rotating powder bed. Addit. Manuf. **31** (2020)
7. González, M., Ramos-Grez, J., Jeria, I., Guerra, C., Solís, R., Carvajal, L.: Effects of laser surface modification on stainless steel 316L thin annular discs under radial and cartesian scans. J. Opt. Laser Technol. (2022)
8. Gutowski, T., et al.: Note on the rate and energy efficiency limits for additive manufacturing. J. Ind. Ecol. **21**(S1), 569–579 (2018)
9. La Fe-Perdomo, I., Ramos-Grez, J.: An insight into adiabatic efficiency hybrid modeling in laser powder bed fusion of 316L stainless steel. J. Opt. Laser Technol. (2023)
10. Ramos-Grez, J.A., Vera, J., Walczak M.: Spiral growth selective laser melting of axisymmetric objects from Cu-Ni-Sn alloy powder: a mass rate efficiency study. Int. J. Adv. Manuf. Technol. (2022, Submitted)
11. Jain, P.K., Pandey, P.M., Rao, P.V.M.: Effect of delay time on part strength in selective laser sintering. Int. J. Adv. Manuf. Technol. **43**, 117–126 (2009)

Determination of the Influence on the Dimensional Characteristics of the Parts Manufactured in 3D Printers of Temperature, Printing Speed and Layer Height During Manufacturing

Alberto Mínguez-Martínez, Fernando Ramos-González, Gonzalo Quirós-Torres, and Jesús de Vicente y Oliva$^{(\boxtimes)}$

Laboratorio de Metrología y Metrotecnia, Escuela Técnica Superior de Ingenieros Industriales, Universidad Politécnica de Madrid, Madrid, Spain
a.minguezm@upm.es, jvo@industriales.upm.es

Abstract. Additive manufacturing technologies, among which is 3D printing, is one of the fundamental pillars of Industry 4.0, since it allows to obtain prototypes and manufactured parts in a fast, versatile, and economical way. The result of the 3D printing process is affected by the effects that the different parameters of the process have on materials such as PLA, which is the most widely used. In this article, the effect of layer height, speed and printing temperature on parts manufactured with 3D printing will be studied, making a dimensional study with a profile projector. It has been determined that, among the three parameters, the extrusion temperature has the greatest effect.

Keywords: 3D printing · additive manufacturing · dimensional metrology

1 Introduction

The Fourth Industrial Revolution, also known as Industry 4.0, is changing the way businesses operate and therefore the environments in which they are forced to compete, as stated in [1]. The term "Industry 4.0" was introduced in 2011 at the Hannover Fair and immediately became the focus of attention of both the German government and other European countries [2]. Industry 4.0 is interpreted as the application of cyber-physical systems to industrial production chains, extending far beyond the limits of the Internet of Things, which is typically where many or s approaches to the phenomenon begin and end [1, 2]. The main economic potential of Industry 4.0 is its ability to accelerate corporate decision-making and adaptation processes. This applies both to processes to drive efficiency in engineering, manufacturing, services, and sales and marketing, as well as to the focus of entire business units or business model changes [2].

AM is a manufacturing technology that basically consists of the manipulation of a material on a micrometric scale, so that it melts and can be deposited gradually and very

precisely, generating layer by layer a solid with the desired geometry [2–4]. This technology, in general, and 3D printing, in particular, allows manufacturers to obtain prototypes and proof-of-concept designs, which simplifies and streamlines the process of designing and manufacturing new products [2, 5]. The main advantage of this type of technology is that any geometry that may be needed, however complex, can be reproduced without the need for tools or complex manufacturing processes [3]. Therefore, the main characteristics that distinguish the process of manufacturing solids by addition of layers of material from any other industrial manufacturing process, and that give it enormous competitive advantages, are the following: geometric complexity and customization of the design process.

As has been explained, AM allows the design of different components with fewer restrictions than with traditional manufacturing processes and provides a much higher production capacity, which allows great improvements in production time and flexibility and cost reduction. However, although it represents a major change and advance, traditional manufacturing methods cannot be replaced due to the disadvantages of AM technologies [4]: size restrictions, production time, cost, regulation problems, limited mechanical strength, difficulty of controlling precision in manufacturing and surface quality of the parts.

In this work, the influence of different 3D printing parameters to obtain the best results from the dimensional point of view is studied. As set forth in [6], the mechanical properties of parts manufactured using 3D printing are affected by the printing parameters. This study will study the effect on dimensional stability of the following process parameters: printing temperature, filament extrusion speed and layer height.

2 Materials and Methods

2.1 Design of the Standard Part

The design has the following characteristics (see Fig. 1):

- A square base of 20 mm side. The size of the design is designed to minimize errors that may occur in the scales of the 3D printer
- Grooves of 3 mm wide that will serve as a stroke to have reference of the measurements.
- Protrusions to be able to tie the piece when measuring.

The design is based on a stage micrometer, which is one of the most widely used reference standards in the calibration of optical amplification measuring instruments [7]. With these measuring instruments, it is necessary to always make the same flushing and, therefore, the width of the stroke must be considered.

2.2 3D Printing Process

For the process of layering and tracing the print path of the parts, the Ultimaker Cura 4.12.1 software was used. The parts will be manufactured on an Anycubic i3 Mega 3D printer using the thermoplastic polymer polylactic acid (PLA) as a filament.
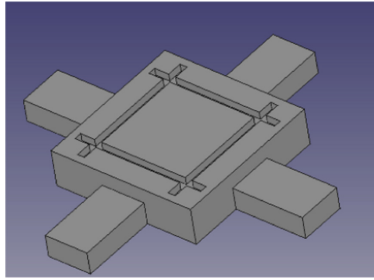
Fig. 1. Design of the material standard.

In this work, the dimensional variation obtained by varying the printing temperature, extrusion speed and layer height throughout its range will be studied. The effect of each parameter will be evaluated using five study points. To determine the printing parameters of each study point to evaluate how each parameter affects, two of the parameters are set at a reference value and the parameter to be studied is varied. The printing parameters of the different samples are shown in Table 1:

Table 1. Printing parameters.

#	Temperature (ºC)	Printing speed (mm/s)	Layer height (mm)	Printing time (min)
1	180	50	0.15	24
2	190	50	0.15	24
3	200	50	0.15	24
4	210	50	0.15	24
5	220	50	0.15	24
6	200	50	0.04	92
7	200	50	0.10	37
8	200	50	0.20	18
9	200	50	0.32	12
10	200	20	0.15	55
11	200	35	0.15	33
12	200	65	0.15	20
13	200	80	0.15	18

2.3 Measuring Process

A calibrated profile projector of horizontal axis profiles of the brand NIKON, model H14B and with serial number 10129 that allows the illumination of the samples both diascopically (by transmitted light) and episcopically (by reflected light) The measurement fields of the projector are CX $= 200$ mm, CZ $= 100$ mm y α $= 360°$ and its resolutions are EX $=$ EZ $= 0.001$ mm taken digitally and Eα $= 1'$ taken analogically. For this experiment a 100X amplification will be used.

For the measurement of parts in general with profile projectors, the typical uncertainty calculated with Eq. (1) must be considered (L is expressed in meters):

$$u = (1.25 + 1.25 \cdot L) \mu m \tag{1}$$

The distance between the midlines of the grooves that are in a vertical position will be determined. The measurements will be taken with 90°, 180° and 270° turns. Measurements will be taken at five different heights according to the measurement scheme in Fig. 2:
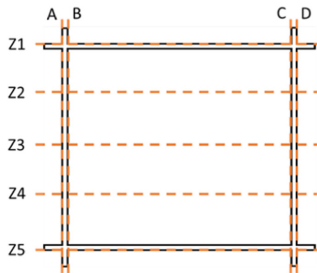
Fig. 2. Measuring strategy.

The nominal distances of the grooves are collected in Table 2:

Table 2. Nominal distances of the grooves.

Distance	Value (mm)
A – B	1
A – C	13
A – D	14
Z1 – Z2	4
Z1 – Z3	6.5
Z1 – Z4	9
Z1 – Z5	14

The estimation of the uncertainty, will be accomplished considering:

- Nominal distance between grooves (x): 13 mm.

- Typical uncertainty (u(x)) of the measurement with the profile projector, calculated with Eq. (1): 0,018 mm.
- For the calculation of expanded uncertainties (U(x)) a coverage factor k = 2 is used, which is the one that ensures a probability of coverage of approximately 95%.

The uncertainties of the measures shall be calculated according to Eq. (2):

$$U(x) = k \cdot \sqrt{\frac{s^2(x)}{5} + u_{PROY}^2 + \frac{e^2}{12}} \tag{2}$$

where $s(x)$ is the standard deviation of the measurements, u_{PROY} is the uncertainty provided by the profile projector and e is the scale division of the profile projector.

3   Results

The results of the different tests are summarized in Fig. 3.
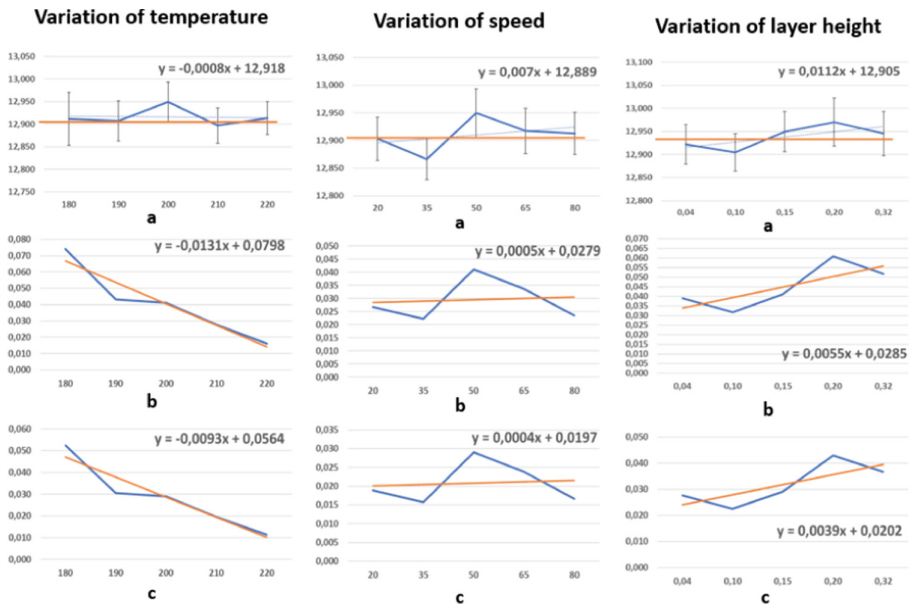
Fig. 3. Results of the different tests.

4   Conclusions

From the data obtained during the present study it can be seen that:

- The parameter that has the greatest influence seems to be the extrusion temperature.

- There is a difference in the errors the printer makes between the X and Y axis.
- The 3D printer needs corrections in both the X axis and the Y axis, being more necessary in the latter.

As for the study of the parameters, it seems that the printing speed and layer height do not have clear effects. However:

- At high temperatures, lower standard deviation is obtained. In this case, the standard deviation would measure the reproducibility of the printer, that is, the ability to produce parts with the same dimensions (whatever they are, close or not to the prescribed nominals). With low temperatures, there can be variations of up to $4*s = 0.2$ mm between two manufactured parts one after the other and that for a dimension of 13 mm. However, for high temperatures the above effect seems to be reduced to $4*s = 0.044$ mm.
- At high temperatures, there are fewer differences between the X and Y dimensions of the part: it goes from about 0.08 mm to only 0.02 mm. The error is divided by four.

Therefore, only temperature seems to affect. And the results are better the higher the temperature:

- Smaller differences between the dimensions of the part in X and Y.
- Better reproducibility (the manufactured parts have dimensions closer to each other).

References

1. Cottelleer, M., Sniderman, B.: Deloitte Insights - Forces of change: Industry 4.0, online document. https://bit.ly/2ZKPgtE. Accessed 09 July 2022
2. Ghobakhloo, M.: The future of manufacturing industry: a strategic roadmap toward Industry 4.0. J. Manuf. Technol. Manag. **29**(6), 910–936 (2018)
3. Zahera, M.: La fabricación aditiva, tecnología avanzada para el diseño y desarrollo de productos. In: XVI Project Engineering International Congress, Valencia (2012)
4. Attaran, M.: The rise of 3-D printing: the advantages of additive manufacturing over traditional manufacturing. Bus. Horiz. **60**, 677–688 (2017)
5. Subramaniam, S., et al.: 3D printing: overview of PLA progress. In: AIP Conference Proceedings, vol. 2059, no. 020015 (2019)
6. Fernandes, J., Deus, A., Reis, L., Vaz, M., Leite, M.: Study of the influence of 3D printing parameters on the mechanical properties of PLA. In: 3rd International Conference on Progress in Additive Manufacturing (Pro-AM 2018), Singapore (2018)
7. Centro Español de Metrología (CEM), Procedimiento DI-001 para la Calibración de Proyectores de Perfiles, Madrid: Publicaciones del Ministerio de Industria y Energía y del Ministerio de Fomento **2**(5), 99–110 (2016). uthor, F.: Article title. Journal

Determination of Calibration Corrections and Study of the Reproducibility of a 3D Printer

Alberto Mínguez-Martínez, Gonzalo Quirós-Torres, Fernando Ramos-González,
and Jesús de Vicente y Oliva[✉]

Laboratorio de Metrología y Metrotecnia, Escuela Técnica Superior de Ingenieros Industriales,
Universidad Politécnica de Madrid, Madrid, Spain
a.minguezm@upm.es, jvo@industriales.upm.es

Abstract. Additive manufacturing technologies, among which is 3D printing, is one of the fundamental pillars of industry 4.0, since it allows to obtain prototypes and manufactured parts in a fast, versatile and economical way. To ensure the quality of production, it is necessary that all parts obtained through any manufacturing process meet the specifications of the design. However, it is not enough for a certain part to meet the dimensional design specifications, but most parts manufactured on the same machine must do so. This paper proposes two pattern models to study the reproducibility and for the correction of the scales that must be applied to a commercial 3D printer to obtain printed parts by fused filament deposition (FDM).

Keywords: measurement · reproducibility · 3D printing

1 Introduction

In the environment of industry 4.0, additive manufacturing (AM) represents one of the most important technological trends since it allows obtaining small batches of products with a high degree of customization [1]. AM technologies bring these two characteristics together and have the potential to be at the center of the industry's development for years to come. In fact, they are currently already implanted in very important industries, such as automotive, naval, military, electronics or medical [2–4]. Additive manufacturing is a manufacturing technology that represents a breakthrough since it allows the construction of parts with geometries that are difficult or impossible to achieve through traditional processes [5]. To do this, the different AM technologies divide the digital 3D models into layers and the piece is obtained by adding, layer by layer, of material [6, 7].

The main goal of this article is to propose a procedure to determine the corrections that must be applied in an AM machine to obtain parts accurately. In this case we will study the particular case of 3D printing, since it is one of the most accessible technologies on the market. To do this, in this document we will carry out a metrological study on samples manufactured by 3D printing and we will perform the measurement with a profile projector.

2   Materials and Methods

2.1   Material Measures

In literature, material measures with simple geometry (usually parallelepipeds) have been proposed, from which the distance between the outer faces was measured. Based on the concept of manufacturing custom measurement standards set out in [8], Two different models are proposed, one to study the reproducibility of the 3D printer and another for the correction of its scales. They are based on a stage micrometer, which is a measuring instrument widely used in the field of dimensional metrology for the calibration of optical measuring instruments (such as microscopes or profile projectors). This geometry allows to have more measurement points, which allows to lower the measurement uncertainty.

In this case, it was proposed that the material standards be calibrated with a profile projector with reflected light, to simplify the calibration process. Therefore, the characteristics of the measuring instrument have been taken into account in the design of the measurement standards. To perform the measurements correctly, the maximum possible contrast is required at the measuring points. This is usually achieved with corners at 90º, without roundings or chamfers. The lower the angle of the chamfer, the lower the contrast and therefore the quality of the measurement will worsen due to the inability of the operator to distinguish the edges of the structures well.

Design for the Study of the Reproducibility of the 3D Printer
This design has a parallelepiped base 100 × 100 mm and height 15 mm. The pitch, i.e. the nominal distance between grooves, is 12.5 mm wide forming a grid (see Fig. 1 left). The cross-section of the grooves could be also observed in Fig. 1 (right).
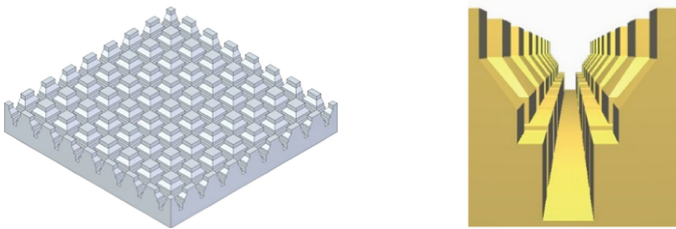
Fig. 1. Reproducibility material standard (left) and its cross-section (right).

The reproducibility study shall consist of determining the average step and standard deviation on 10 samples manufactured under the same conditions.

Design for the Correction of the Scales of the 3D Printer
This design consists of a cube 100 mm side and with a grid on each side (see Fig. 2). It has eight vertical and horizontal V-shaped grooves (with a 60º angle). The nominal pitch between the grooves is 10 mm.
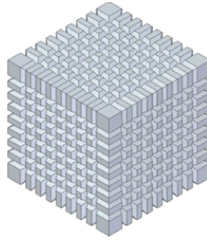
Fig. 2. Scale correction material standard

2.2   Manufacturing of the Parts

The parts will be manufactured on an ANYCUBIC i3 MEGA 3D printer. As for the printing conditions, it must be taken into account that the printing parameters significantly affect the dimensional quality of the manufactured parts. In this case, the material used as filament is PLA, Considering the parameters proposed in literature [9, 10], the samples will be printed at 200°C, with a printing speed of 30 mm/s and producing layers 0.2 mm high.

2.3   Measurement of the Samples

A calibrated profile projector of horizontal axis profiles of the brand NIKON, model H14B and with serial number 10129 that allows the illumination of the samples both diascopically (by transmitted light) and episcopically (by reflected light) The measurement fields of the projector are CX = 200 mm, CZ = 100 mm y α = 360° and its resolutions are EX = EZ = 0.001 mm taken digitally and Eα = 1′ taken analogically. For this experiment a 100X amplification will be used.

For the measurement of parts in general with profile projectors, the typical uncertainty calculated with Eq. (1) must be considered (L is expressed in meters):

$$u = (1.25 + 1.25 \cdot L)\mu m \tag{1}$$

Measuring Strategy
The measurement will be carried out in a one-dimensional way, that is, only measurements will be taken on the X axis of the profile projector. The distance between the midlines of the grooves that are in an upright position will be determined. Measures will be taken according to the schemes in Fig. 3.

Once the distances with the profile projector have been determined, the part is measured with 90°, 180° and 270° turns.

Measuring Strategy
Below is a correction model for the scales of the 3D printer, based on [11]

$$\begin{bmatrix} x \\ y \\ z \end{bmatrix} = \begin{bmatrix} C_x & \theta_{xy} & \theta_{xz} \\ \theta_{xy} & C_y & \theta_{yz} \\ \theta_{xz} & \theta_{yz} & C_z \end{bmatrix} \cdot \begin{bmatrix} p \\ q \\ r \end{bmatrix} \tag{2}$$
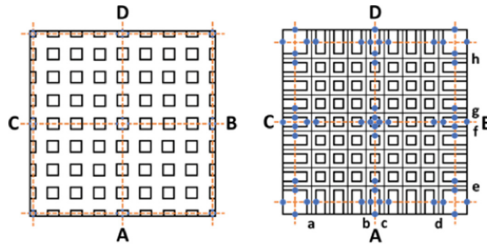
Fig. 3. Measuring strategy.

where (x, y, z) are the corrected measures, (p, q, r) are the raw data obtained from the measurement process, the factors C_x, C_y y C_z are those that correct the deviations of the measurements in each axis with respect to the nominal value and the factors θ_{xy}, θ_{xz} y θ_{yz} are those that correct the perpendicularity deviations between the axes.

3   Results

3.1   Study of Reproducibility

Table 1 shows the results of this experiment.

Table 1. Process axis results of reproducibility patterns.

Measurement	Value	Units
Average step in X-axis	**12.518**	mm
Standard deviation in X-axis	**0.014**	mm
Difference from nominal	**−0.018**	mm
Average step in Y-axis	**12.475**	mm
Standard deviation in Y-axis	**0.018**	mm
Difference from nominal	**0.025**	mm
Average step	**12.497**	mm
Standard deviation	**0.027**	mm
Difference from nominal	**0.003**	mm
Average percentage errors in X-axis	**0.098%**	
Average percentage errors in Y-axis	**0.114%**	
Global average percentage errors	**0.111%**	

3.2   Study of 3D Printing Process Scales Correction

Figure 4 shows the error maps corresponding to each face. The vectors represent the direction in which errors are made on each axis of each face.
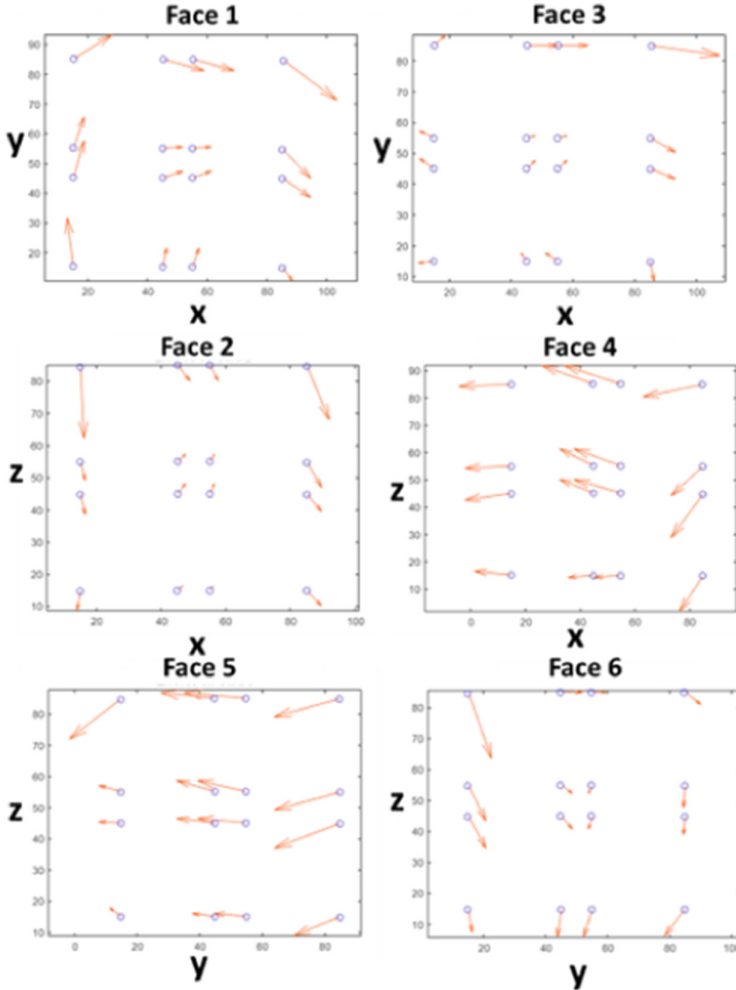
Fig. 4.   Error maps of each face of the correction material standard.

3.3   Study of Corrections to the Printing Process

Through a least squares adjustment, the corrections to be applied on each face are determined. It is important to note that each face allows us to estimate the corrections corresponding to two axes of the machine and that, for each pair of axes, we have two

estimates of each correction factor. Therefore, the correction factor is the average of the two estimates. The correction matrix is:

$$\begin{bmatrix} C_x & \theta_{xy} & \theta_{xz} \\ \theta_{xy} & C_y & \theta_{yz} \\ \theta_{xz} & \theta_{yz} & C_z \end{bmatrix} = \begin{bmatrix} 1,9 & -0,1 & -0,8 \\ -0,1 & -2,2 & 0 \\ -0,8 & 0 & -0,7 \end{bmatrix} \cdot 10^{-3} \tag{3}$$

The uncertainties associated with each correction factor are those shown in Table 2:

Table 2. Uncertainties associated with correction factors.

Correction factor	Value
C_x	**0.0025**
C_y	**0.0034**
C_z	**0.0042**
$\theta_{xy} = \theta_{yx}$	**0.0031**
$\theta_{xz} = \theta_{zx}$	**0.0040**
$\theta_{yz} = \theta_{zy}$	**0.0065**

4   Conclusions

In this work it is proposed to manufacture two designs of material standards to study the reproducibility and calibrate the axes of a 3D printer. These material stantards have been measured with a profile projector with low uncertainties. This procedure can be adapted for other additive manufacturing machines and measuring instruments.

References

1. Ghobakhloo, M.: The future of manufacturing industry: a strategic roadmap toward Industry 4.0. J. Manuf. Technol. Manag. **29**(6), 910–936 (2018)
2. Vafadar, A., et al.: Advances in metal AM: a review of common processes, industrial applications, and current challenges. Appl. Sci. **11**, 1213 (2021)
3. Sarvankar, S., Yewale, A.: AM in automobile industry. Int. J. Res. Aeronaut. Mech. Eng. **7**(4), 01–10 (2019)
4. Strickland, J.: Applications of AM in the marine industry. In: 13th Int. Symposium on Practical Design of Ships and other floating structures, Copenhagen (2016)
5. Vora, H., Sanyal, S.: A comprehensive review: metrology in AM and 3D printing technology. Prog. Addit. Manuf. **5**, 319–353 (2020)
6. Zahera, M.: La fabricación aditiva, tecnología avanzada para el diseño y desarrollo de productos. In: XVI Project Engineering International Congress, Valencia (2012)
7. Attaran, M.: The rise of 3-D printing: the advantages of additive manufacturing over traditional manufacturing. Bus. Horiz. **60**, 677–688 (2017)

8. Mínguez Martínez, A., et al.: Design of industrial standards for the calibration of optical microscopes. Materials **14**(1), 29 (2021)
9. García Plaza, E., et al.: Analysis of PLA geometric properties processed by FFF AM: effects of the process parameters and plate-extruder precision motion. Polymers **11**, 1581 (2019)
10. Luis-Pérez, C., et al.: Modeling of the influence of Input AM parameters on dim. Error and form errors in PLA parts printed with FFF tech. Polymers **13**, 4152 (2021)
11. Mínguez Martínez, A., de Vicente y Oliva, J.: Industrial Calibration Procedure for Confocal Microscopes. Materials **12**, 4137 (2019)

5-Axis Machining Center OMM Uncertainty Estimation

Guillermo González[1]([✉]) [iD], Brayan Eduwars Medina[1] [iD], Naiara Ortega[2] [iD],
Soraya Plaza[2] [iD], and Gaizka Gómez[1] [iD]

[1] Aeronautics Advanced Manufacturing Centre (CFAA), 48170 Zamudio, Spain
guillermo.gonzalezm@ehu.com
[2] University of the Basque Country UPV-EHU, 48013 Bilbao, Spain

Abstract. Nowadays, on-machine tool measurement (OMM) and coordinate measuring machine measurement (CMM) are the most common inspection methods. Although the ex-situ CMM measurements usually offers higher accuracy and reliability, OMM can inspect the workpiece without removing it from the machine tool. Therefore, it is possible to perform both *in-process* and *post-process* measurements, avoiding possible unclamping errors. However, due to the non-constant conditions in which machine tools usually operate, it is difficult to guarantee the traceability of measurements over time. For example, thermal fluctuations become a potential source of uncertainty.

This paper presents a methodology for ensuring the traceability of OMM on shop floor conditions. For this purpose, several features of a prismatic workpiece are measured on a five-axis machining center. The measurement results and its corresponding uncertainty budget are presented. For the uncertainty estimation the substitution method based on ISO 15530-3:2011 standard is used. In order to identify the impact of the different error sources on the results, a breakdown of the relative weights of the factors that may have an influence on the uncertainties is also given,

Keywords: On-machine measurement (OMM) · traceability · uncertainty

1 Introduction

The incorporation of measurement procedures into the production line has become essential under the Industry 4.0 framework. It is typical to have at least one measuring probe built into the machine tool (MT) in order to carry out quality controls where the machining process is place (*in-situ*). In addition to usual *post-process* quality controls, since the workpiece does not need to be unclamped, *in-process* measurements can be carried out. Unlike *ex-situ* CMM measurements, which are only carried out at the final stage of the manufacturing process, with OMM the entire machining phase may be monitored and controlled. Thanks to these *in-process* measurements, enable quicker error detection for latter correction in following machining operations. In industries like aerospace, where

high value-added, high-precision customized components are required, this is a particularly appealing solution for lowering the amount of rejected components. Therefore, the main OMM advantages are [1]:

1. MT geometry monitoring: By quantifying the geometrical errors caused by machine deformation over time, the machine can be self-calibrated [2].
2. Workpiece alignment on MT: When the coordinate system changes between machining processes, accurate part alignment is extremely important for non-defect manufacture. The coordinate system can be more precisely reconstructed by using an appropriate measurement approach.
3. Machining process: The flexibility to use the same alignment and clamping system on both the production and measurement processes is the major advantage of integrating metrology systems into MT. This has proven to be more effective than simply performing a post-process quality control, where the range of actuation is more limited.
4. Workpiece quality control: Workpiece quality control: Making sure the part's key dimensions are within tolerance before it is taken out of the machine decreases the probability that it will be deemed unsuitable during a subsequent ex-situ quality control. If the specified tolerances are not met, corrective measures can be taken while the workpiece is still clamped.

However, as the machining and measuring operations are performed on the same equipment, both operations are affected by the same geometric errors. As a result, identifying and correcting these problems becomes challenging [3]. Schmitt et al. [4] suggest two solutions to get over this restriction: volumetric calibration of the MT or integrating an external metrology system to regulate the tool tip location over time. Furthermore, the uncontrolled environment in which OMM operates (thermal fluctuations, presence of coolant oils, etc.) represent a potential source of uncertainty. This uncertainty assesses the reliability of the measurement and determines the quality of the results. Therefore, decreasing the measurement uncertainty is a challenging task.

Three uncertainty estimation methods have been developed based on GUM ISO Guide 98-3:2008. The ISO 15530-3 stabilizes the traceability chain using a calibrated reference artifact and is based on the substitution approach. ISO 15530-4, on the other hand, calculates the uncertainty through an iterative simulation-based process. Finally, VDI guideline 2617-11 estimates the influence of each error source on each measurement independently.

In this study, the substitution method is used to assess the uncertainty of numerous properties of a prismatic part under OMM conditions (ISO 15530:3 standard). A CMM was used to calibrate them in order to have their reference value [5].

2 Methodology

2.1 Measurement Strategy

The targeted component is a prismatic workpiece made of 7075 aluminum (100 mm × 100 mm × 50 mm). The intersection of planes A and B (X-axis), the intersection of planes B and C (Z-axis), and the intersection of planes A, B, and C (origin "P") were used to establish the coordinate system (CS) (see Fig. 1).
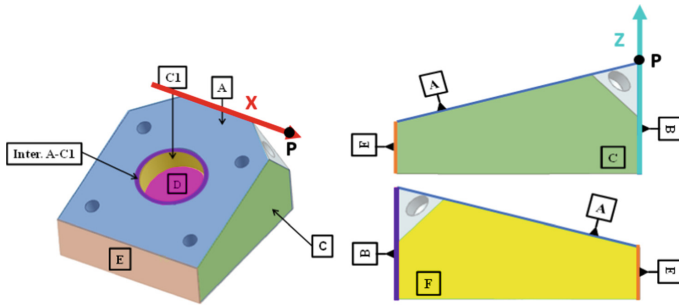
Fig. 1. CS and measured geometrical elements.

Using these geometric elements, five dimensional tolerances (references 101–105) seven form errors (references 201–207), five orientation tolerances (references 301–305) and three position tolerances (references 401–403) were analyzed (see Table 1).

Table 1. Description of the evaluated features.

Ref	Description	Nominal	Ref	Description	Nominal
101	Ø C1	40 mm	206	F Flatness	0 mm
102	A-D distance	15 mm	207	C1 Cilindricity	0 mm
103	B-E distance	100 mm	301	Parallelism of D to A	0 mm
104	C-F distance	100 mm	302	Parallelism of E to B	0 mm
105	A-B angle	100 mm	303	Parallelism of F to C	0 mm
201	A Flatness	0 mm	304	Perpendicularity of C1 to A	0 mm
202	B Flatness	0 mm	305	Perpendicularity of C to B	0 mm
203	C Flatness	0 mm	401	Position intersec. A-C1 (X)	0 mm
204	D Flatness	0 mm	402	Position intersec. A-C1 (Y)	0 mm
205	E Flatness	0 mm	403	Position intersec. A-C1 (Z)	0 mm

2.2 Uncertainty Estimation

The OMM was performed ten times on an Ibarmia THR16 Multiprocess five-axis machining center using a 100 mm long and 6.048 mm touch probe (1m repeatability). Using a coverage factor of k = 2, the expanded uncertainty (U_{MP}) was estimated (Eq. 1).

$$U_{MP} = k \cdot \sqrt{u_{cal}^2 + u_p^2 + u_b^2} \tag{1}$$

The calibration of reference values (u_{cal}), process repeatability (u_p), and systematic error correction (u_b) contribute to the estimation of the measuring process uncertainty.

Bias (b), which is the difference between the calibrated and measured values, can influence the uncertainty in two ways. If it remains constant over the measurements, it can be categorized as a systematic error and corrected using Eq. 2, where $\bar{y}_{cal}$ is the average of the calibrated measurement; $\bar{y}$ is the average of the OMM; y_{MP} is the uncorrected OMM value and Y_{MP} is the corrected value.

$$b = \bar{y}_{cal} - \bar{y}; \quad Y_{MP} = y_{MP} - b \pm U_{MP} \tag{2}$$

If not, bias must be taken into account as an extra source of uncertainty. In this study, the first option was chosen since bias did not change over the repetitions. Thus, the component u_b is only influenced by the workpiece's temperature T, the material's uncertainty in its thermal expansion coefficient ($u_\alpha = 4.702 \cdot 10^{-6}$ mm/°C) and the measurement length L (Eq. 3):

$$u_b = (T - 20\,°C) \cdot u_\alpha \cdot L \tag{3}$$

The repeatability of the process, assessed as the standard deviation of the measurements contributes to u_p, where $\bar{y}$ is the mean value of the feature, y_i is the measured value for repetition i and n is the number of repetitions (Eq. 4).

$$\bar{y} = \frac{1}{n} \cdot \sum_{i=1}^{n} y_i ; \quad u_p = \sqrt{\frac{1}{n-1} \cdot \sum_{i=1}^{n} (y_i - \bar{y})^2} \tag{4}$$

The part was measured using a 55 mm long, 5 mm stylus and a Mitutoyo Crysta Apex S9106 3+2 axis CMM (positional repeatability of 0.4 m at 100 mm). Equations 5 and 6 give the characteristics of the CMM, where MPE stands for the maximum permissible error, A is equal to 1.7 µm, B is equal to 0.003 µm/mm, L is the measurement length, MPE_p is the maximum probing error (1.7 µm) and σ_i is the standard deviation of the calibration error for each stylus configuration.

$$MPE = A + B \cdot L \; \mu m \; (L : mm) \tag{5}$$

$$MPE_{pcorr} = MPE_p + Max(\sigma_i) \; \mu m \tag{6}$$

This component u_{cal} was estimated according to the ISO 15530:2 standard, with u_{geo} indicating the reproducibility of the measurement process u_E the calibration uncertainty of the CMM, and u_{rep} its repeatability (Eq. 7) [5].

$$u_{cal} = \sqrt{u_{geo}^2 + u_E^2 + u_{rep}^2} \tag{7}$$

The u_{geo} component is related to the geometric inaccuracies of the CMM. The part was measured using four different probe configurations to evaluate them independently (Eq. 8). In this equation, n_2 is the number of probe configurations, $^j\bar{y}$ is the mean value in orientation j and $\bar{y}$ is the mean value across all configurations:

$$u_{geo} = \sqrt{\frac{1}{n_2} \times \frac{1}{n_2 - 1} \times \sum_{j=1}^{n_2} \left(^j\bar{y} - \bar{y}\right)^2} \tag{8}$$

According to the type of the assessed feature (Table 1), u_E was estimated using one of the following equations [6] (Table 2):

Finally, Eq. 4 was used to estimate u_{rep}, replacing the OMM results with those got in CMM. 20 repetitions were made in this instance (5 per probe configuration).

Table 2. Estimation of u_E according to the type of feature.

Equation	Type of feature	Equation	Type of feature
$u_E = \dfrac{MPE}{\sqrt{3}}$	Dimensional tolerances	$u_E = 0$	Angles
$u_E = \dfrac{MPE_{pcorr}}{\sqrt{3}}$	Form errors	$u_E = \dfrac{2*MPE}{\sqrt{6}}$	Paralelism
$u_E = \dfrac{2*A}{\sqrt{3}}$	Perpendicularity	$u_E = \dfrac{A}{\sqrt{3}}$	Position error

3 Results

For quality control, reliable measurements are crucial, but as OMM is vulnerable to numerous variable sources of error, this is difficult to guarantee. To ensure OMM traceability, this study conducts an experimental test in accordance with ISO 15530-3:2011 standard identifying the main error sources that influence the uncertainty (Fig. 2).

101	39.884±0.004mm	201	10±2.8µm	206	12±7.1µm	304	5±4.2µm
102	15.092±0.004mm	202	12±7.6µm	207	11±3.7µm	305	10±6.6µm
103	99.736±0.011mm	203	12±7µm	301	9±3.1µm	401	-517±6.6µm
104	99.367±0.009mm	204	5±2.4µm	302	11±1.8µm	402	344±11.6µm
105	75.920±0.003°	205	4±2.4µm	303	15±5.7µm	403	343±7.1µm
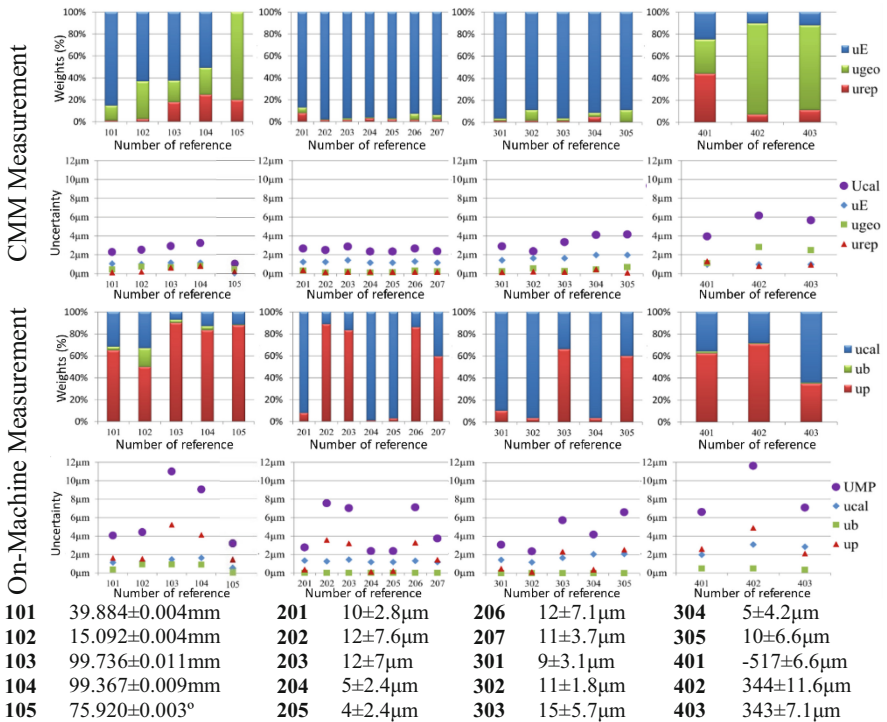
Fig. 2. OMM and CMM measurement results.

The findings indicate that the workpiece calibration uncertainty u_{cal} is primarily caused by the CMM calibration component u_E. With the exception of the angular tolerance ($u_E = 0°$ by definition) and the position tolerances, where reproducibility is more crucial, its weight exceeds 50% in the majority of circumstances. This, in turn, increases the subsequent value of U_{MP}.

In contrast, for OMM, repetition becomes the main source of uncertainty. The repeatability of the measuring process decreases increasing weight of u_p by as much as 90%, when rotary table interpolation is required, as for measuring C or F planes.

It is important to note that the u_b component remained less than 1 μm in every case that was examined. Due to the small size of the prismatic part and as the test's temperature (18.37 °C) remains so close to the reference temperature of 20 °C, its impact was nearly nonexistent. However, the contribution of this component to the uncertainty would be more substantial for larger components or if the temperature changes rise.

4   Conclusions

An overview of the relative contributions of each measurement uncertainty source to OMM is given in this paper. The main cause of uncertainty turned out to be the lack of repeatability brought on by the unpredictable climatic conditions and the presence of coolant oils, particularly when the machine's rotating axes were interpolated. In addition, the use of a different calibration device is suggested for future investigations in order to decrease the weight of u_E in the overall measurement uncertainty.

References

1. Mutilba, U., Gomez-Acedo, E., Kortaberria, G., Olarra, A., Yagüe-Fabra, J.A.: Traceability of on-machine tool measurement: a review. Sensors **17**(7), 1605 (2017)
2. Ding, D., Zhao, Z., Li, Y., Fu, Y.: Calibration and capability assessment of on machine measurement by integrating a laser displacement sensor. Int. J. Adv. Manuf. Technol. **113**(7), 2301–2313 (2021)
3. Wang, S., Cheung, C., Kong, L.: A fiducial-aided reconfigurable artefact for the estimation of volumetric errors of multi-axis ultra-precision machine tools. Appl. Sci. **12**(4), 1824 (2022)
4. Schmitt, R., Petere, M.: Traceable measurements on machine tools-Thermal influences on machine tool structure and measurement uncertainty. Procedia CIRP **33**, 576–580 (2015)
5. Sładek, J.A.: Coordinate Metrology. Accuracy of systems and measurements (2016)
6. Cheng, Y., et al.: Evaluation and optimization of task-oriented measurement uncertainty for coordinate measuring machines based on geometrical product specifications. Appl. Sci. **9**(1), 6 (2018)

Micro Cutting Tool Tip Tracking
with a Piezoelectric Matrix

Marcelo Fajardo-Pruna[1]([✉]) [ID], Luis López-Estrada[2] [ID], Christian Tutivén[1] [ID],
Santos Gualoto-Cóndor[2], and Antonio Vizán[2]

[1] Escuela Superior Politécnica del Litoral, ESPOL, Guayaquil, Ecuador
`mrfajard@espol.edu.ec`
[2] Universidad Politécnica de Madrid, Madrid, Spain

Abstract. In search of an alternative to micro-milling, a new micromachining technology based on the principles of single-edge cutting has been successfully developed. To have full control of the cutting process, an artificial vision system has been developed, which is able to locate the tip of the cutting tool and thus calculate the forces that develop along the programmed cutting path. As a complementary measuring system, a piezoelectric matrix sensor has been developed that through the composition of the forces in each of the axes of the cutting micro machine can locate the tip of the tool. Preliminary tests yield results that agree with the artificial vision system, the use of this matrix force sensor is a competent complement to the artificial vision system when it does not have the right conditions for its operation.

Keywords: Single edge cutting · micro machining · micro machining strategies · micro cutting tool

1 Introduction

Micromachining with a single edge tool has proven to be a competent alternative to micro-milling, due to having a tool with simpler geometry and a robust control system capable of correcting the tool path as the cut is made. The success of this technology is based on the development of a hybrid machine with six degrees of freedom, which consists of a combination of parallel mechanisms, the rotation of the tool in its own axis and a traditional coordinate stage (3PRS-XY-C) [1].

One key element for trajectory control is an artificial vision system, which can locate the position of the tool tip during the cutting process. The data obtained is the basis for the calculations sent to the CNC for the correction of the cutting path [2].

The stability and accuracy of the cutting tip position data are critical to the success of single edge micromachining, having a concurrent sensor system is a guarantee of a successful cutting process, with this idea a new sensor is proposed, which by recording the cutting forces is capable of locating the cutting tip.

Shear forces are a source of information that describe the nature of the process, however, recording them is not a simple task due to their order of magnitude, the wrong choice of these sensors would acquire unwanted data, which can be confused with electronic noise, vibrations [3] or even temperature variations [4].

2   Methodology

A hybrid machine tool and a single-edged cutting process have been developed as an efficient alternative to the more widespread micro-manufacturing processes such as micro-milling, micro-turning or micro-grinding [1].

In recent years, the measurement of forces and momentums has been widely used to evaluate processes in manufacturing industries [6]. The data is used to guarantee quality during manufacturing processes [7], or to generate adaptive process control in milling, grinding and turning.

Typically these 6 DOF measurements are achieved using commercially available sensors mounted near the center point of the tool. These forces and momentums can also be obtained from drive currents, but these measurements have limited accuracy due to non-linear and stochastic influences from mechanics that interfere between the force application and measurement [8].

In the hybrid machine tool 3PRS + XY + C there are 6 DOF. The 3PRS parallel mechanism has 3 DOF, one actuation in each of its prismatic pairs **Z1**, **Z2** and **Z3**. The tool head has 1 DOF, which is the rotation about the relative axis $z3$ of the cutting tool. Finally, the XY stage has 2 DOF, one in each general X and Y axis of the fixed frame on the machine tool (Fig. 1A).

This configuration allows a wide range of orientations and positions of the cutting tool which enables it to generate various cutting paths with different characteristics, such as straight lines, curves in different orientations, circles, etc.

During the single edge micro cutting process, the position of the tool tip is a key factor in the resulting work piece, for this reason an artificial vision system is used to acquire the real position of the tip of the tool, which influences the measurements of forces and momentums [9]. These measurements are used to generate an adaptive process control that compensates for tool path errors, this minimizes geometric errors in features generated on the workpiece [2].
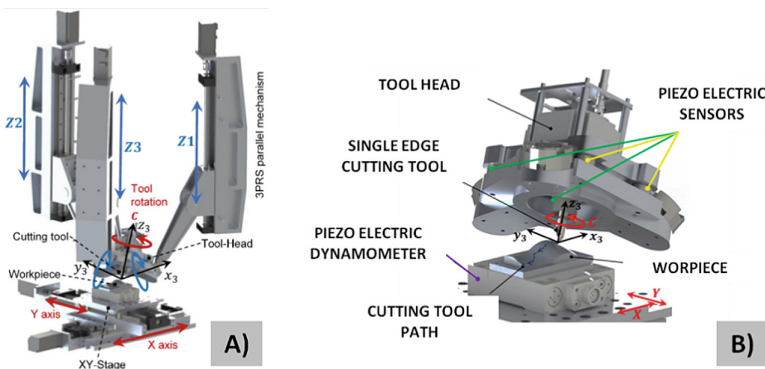
Fig. 1. A) 3PRS-XY-C machine tool. B) Schematic representation of the configuration of the tool head in the 3PRS-XY-C machine

Since it is not common for machine tools to have integrated force sensors, a measurement system must be mounted on the machine tool, which is capable of measuring

in 6-DOF. To achieve a complete reading of these cutting forces a matrix of sensors is developed, 4 KISTLER tri-axial piezoelectric sensors are integrated into the 3PRS-XY-C machine in the tool head, which are complemented by a KISTLER 9265C1 dynamometer where the work piece is placed. (Fig. 1B).

2.1   Measurement Process

To produce work piece surfaces with various features, different paths for the cutting tool are planned and executed on the hybrid machine. In order to define the cutting paths and the positions of the tool tip, it is necessary to use three reference systems, a general frame, which is also known as the machine frame (fixed), a reference frame of the work piece and a reference frame of the cutting tool (Fig. 2A). The surface quality of the work piece was characterized using a surface roughness tester and an optical microscope.
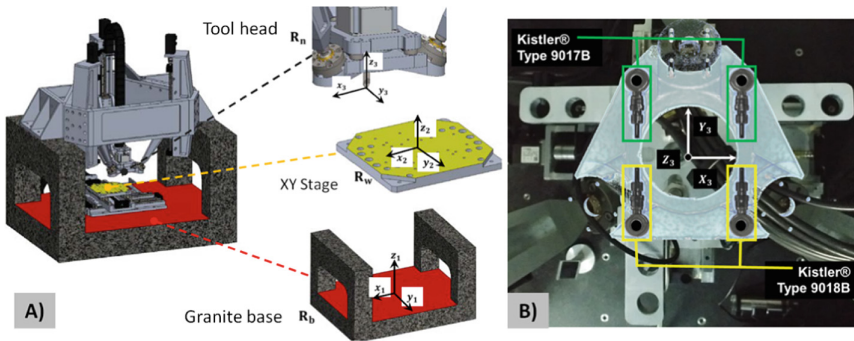
Fig. 2. A) Reference systems of the machine tool. B) Arrangement of piezoelectric sensors in the tool head.

The position of the sensors in the tool head is fundamental for the composition of the cutting forces, using a matrix arrangement of 4 sensors it is possible to acquire the 6 main reactions, 3 forces and 3 torques that occur during the cutting process (Fig. 2B). These force and torque measurements allow us to know if there has been a deviation from the forces expected in the process due to tool wear, change in the geometry of the tip and other phenomena that alter the cutting section and the point of application of the cutting force.

The artificial vision system consists of a pair of cameras placed perpendicular to each other, which are also aligned to the XZ and YZ plane respectively. The planes in which the cameras are placed are coplanar to those of the tool tip coordinate system ($\mathbf{R_{ct}}$), which by means of the machine kinematics is related to the coordinate systems of the tool stage coordinates. X-Y ($\mathbf{R_w}$), and that of the granite base ($\mathbf{R_b}$), which is the basis for the calculation of the tool path and its position throughout the machining time. The behavior of the X-Y stage mechanism is accomplished by a direct drive on each axis, while the serial parallel mechanism requires a combination of the drive of the Z axes and two rotations, the rotation of the **C** axis along the trajectory is necessary to compensate
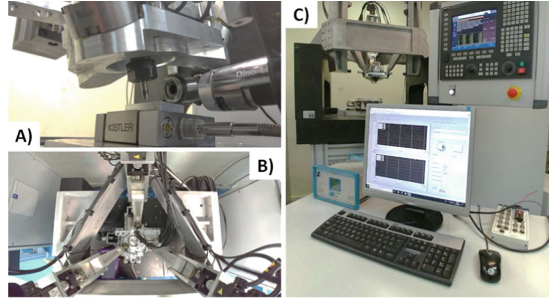
Fig. 3. 3PRS-XY-C with all sensor systems implemented. A) Head of the tool with the artificial vision system. B) Top view of the 3PRS system with the piezoelectric sensors in the head. C) System of acquisition and analysis of cutting forces.

the parasitic movements that exist by the nature of the parallel series mechanism, the disposition of the elements of the vision system are shown in Fig. 3.

In order to define the real position of the cutting edge, it is necessary to measure the deviation that the tool has in relation to the coordinate system (R_{ct}), the necessary values for the correction of the position of tool tip are Δx, Δy and $\Delta \theta$ which correspond to the deviation in x_3, y_3 and the angular position around z_3 respectively.

2.2 Tool Path Correction with the Obtained Data.

Taking the offset of the tip with respect to the axes x_3, y_3, (Δx, Δy) and an initial position of the C axis ($\Delta \theta$) that are represented in (1), the necessary calculations are made for the correction of the position of the tool (4) and (5) to keep the cutting edge tangent to the path P.

These displacements correspond to the movements of a circle whose radius is the delta (r_Δ)) which is obtained from (3), obtained with a real position of the cutting edge defined by Φ and where γ is the angular sum of the parasitic movements of the serial-parallel mechanism in conjunction with the action of axis C (2).

$$\Delta \theta = \operatorname{atan}\left(\frac{\Delta_x}{\Delta_y}\right) \tag{1}$$

$$\phi = \frac{\pi}{2} + \Delta \theta + \gamma \tag{2}$$

$$r_\Delta = \sqrt{\Delta_x^2 + \Delta_y^2} \tag{3}$$

With the calculations obtained from the previous equations, a rotation matrix is applied to them to relate them to the granite coordinate system (R_b), which is the general coordinate system (6).

$$\delta_{xr} = r_\Delta \cos \phi \tag{4}$$

$$\delta_{yr} = r_\Delta \sin \phi \tag{5}$$

$$\begin{bmatrix} \delta_x \\ \delta_y \\ \delta_z \end{bmatrix}_{\mathbf{R_b}} = \mathbf{R} \begin{bmatrix} \delta_{xr} \\ \delta_{yr} \\ 0 \end{bmatrix}_{\mathbf{R_{ct}}} \tag{6}$$

As a last step, the displacements corresponding to the axes are calculated, which will be used as an input in the ISO code of the cutting path, the data is obtained from (7), (8) and (9).

$$X_p = X + \delta_x \tag{7}$$

$$Y_p = Y + \delta_y \tag{8}$$

$$Zi_p = Z_i + \delta_z \tag{9}$$

3 Results

To verify the behavior of the model, in the hybrid machine tool linear micro cuts are machined with a tool with $\chi_r = 60°$ at different inclinations, the machine tool follows a straight trajectory along a 7075 Aluminum specimen- T6 staggered at 25, 20, 15, 10 and 5°. In each ramp, cuts are made from 50×50 μm down to 5×5 μm, which recreates a wide range of machining conditions, thus is warranted as an adequate test of the proposed cutting model. In the results obtained, the magnitude of the force varies according to the size of the cutting area, being the areas with the greatest dimension those with the greatest cutting force, an additional effect on the forces is not observed, so the cutting conditions are have been able to maintain regardless of the inclination at which it is machined, the results of the experiment are shown in Fig. 4. This allows us to indicate that the corrections made with the artificial vision system allow maintaining homogeneous cutting conditions during the manufacturing process.
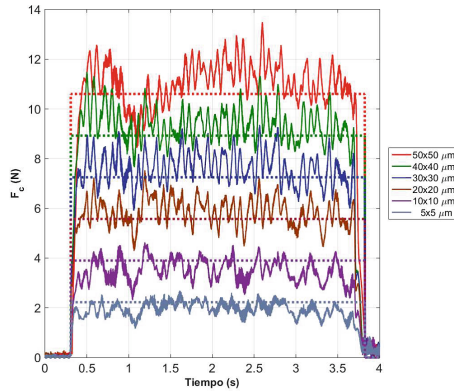
Fig. 4. Force graph of the cutting process, measured vs. predicted.

4   Conclusions

The results obtained show uniform behaviours when the cutting conditions are maintained, then, if the cutting conditions are not disturbed by sudden changes in section, wear of cutting tools or other phenomena that may affect the cutting forces; the quality of the generated surface is adequate. The developed vision system is a non-invasive technique for locating the tool tip which is crucial for achieving precise and controlled machining of desired geometries, when used in tandem with the matrix of force sensor is a very powerful technique of concurrent measurement that is capable of ensuring that the quality of the process will be maintained.

References

1. Fajardo-Pruna, M., López-Estrada, L., Pérez, H., Diez, E., Vizán, A.: Analysis of a single-edge micro cutting process in a hybrid parallel-serial machine tool. Int J Mech Sci. **151**, 222–235 (2019)
2. López-Estrada, L., Fajardo-Pruna, M., Sánchez-González, L., Pérez, H., Fernández-Robles, L., Vizán, A.: Design and implementation of a stereo vision system on an innovative 6DOF single-edge machining device for tool tip localization and path correction. Sensors **18**(9), 3132 (2018)
3. Lee, W.B., Cheung, C.F., To, S.: Materials induced vibration in ultra-precision machining. J. Mater. Process. Technol. **89–90**, 318–325 (1999)
4. Chen, G., Ren, C., Zhang, P., Cui, K., Li, Y.: Measurement and finite element simulation of micro-cutting temperatures of tool tip and workpiece. Int. J. Mach. Tools Manuf. **75**, 16–26 (2013)
5. López Estrada, L.A.: Modelado y análisis del proceso de micromecanizado realizado con herramientas de filo único. Universidad Politécnica de Madrid (2019)
6. Axinte, D.A., Gindy, N., Fox, K., Unanue, I.: Process monitoring to assist the workpiece surface quality in machining. Int. J. Mach. Tools Manuf. **44**(10), 1091–1108 (2004)
7. Brecher, C., Eckel, H.-M., Motschke, T., Fey, M., Epple, A.: Estimation of the virtual workpiece quality by the use of a spindle-integrated process force measurement. CIRP Ann. (2019)

8. Friedrich, C., Kauschinger, B., Ihlenfeldt, S.: Decentralized structure-integrated spatial force measurement in machine tools. Mechatronics **40**, 17–27 (2016)
9. López-Estrada, L., Fajardo-Pruna, M., Sánchez-González, L., Pérez, H., Vizán, A.: Design and implementation of a vision system on an innovative single point micro-machining device for tool tip localization. In: Pérez García, H., Alfonso-Cendón, J., Sánchez González, L., Quintián, H., Corchado, E. (eds.) SOCO/CISIS/ICEUTE -2017. AISC, vol. 649, pp. 219–228. Springer, Cham (2018). https://doi.org/10.1007/978-3-319-67180-2_21

Automation and Artificial Intelligence

Analysis of the Behaviour of Vertical Articulated Robots in Machining Operations

Eugenio Ferreras-Higuero[1]([✉]) [ID], Eduardo Díez-Cifuentes[2] [ID],
Erardo Leal-Muñoz[2] [ID], Miguel Clavijo-Jiménez[1] [ID], and Antonio Vizán-Idoipe[1] [ID]

[1] Universidad Politécnica de Madrid, Dpto. Ingeniería Mecánica, 28008 Madrid, Spain
`ferreraseu@gmail.com`
[2] Universidad de La Frontera, Dpto. Ingeniería Mecánica, 4811230 Temuco, Chile

Abstract. The aim of this work is to improve the productivity of manufacturing cells by reallocating tasks between the machine tools and the robot. The true working capacity of the robot is established considering the process forces and taking into account the specified precision of the product to be manufactured by accurately modelling its behaviour. This modelling has been carried out using the multi-body method and considering a variable stiffness in the robot joints. The behaviour of the robot at different points in the work area is determined, determining where the best results are produced. This results in the possible reallocation of tasks, the positioning point and the orientation of the workpiece in the working area.

The simulated or measured cutting force is fed into the model, modified according to variations in the machining parameters. These variations occur due to deviations of the robot during the machining path. A function is defined where the influence on the value of the force is recorded. This input information can be modified based on feedback from the estimated behaviour of the robot. The results of the modelling of the robot and its interaction with the cutting forces show the influence of the type of robot and the work area in which it is working, allowing the process to be characterised.

Keywords: position · robot · multibody system · machining · milling

1 Introduction

The range of possibilities and expectations for robot applications in machining and pre-machining tasks is reflected in the large collection of reviews and papers in the specialized literature [1–3]. The major challenges facing machining with robots versus machining with machine tools remain today [4] the characterization of robot stiffness and robot configuration [5], path planning and dynamics, vibration during machining [6] and robot deformation and compensation [7].

One way to confirm whether a robot is capable of performing a machining operation, minimizing the use of expensive tests, is through an efficient model that simulates its

dynamic behaviour. For this reason, a robot model has been developed using the multi-body method with mixed natural coordinates (MBSmc). As a result of this application, a trajectory and its deviation as a function of the process forces can be simulated.

2   Methodology

For the modelling of the robot, the MBSmc method has been selected [8]. The MBSmc formulation allows to apply driving forces, torques and to evaluate positioning errors in each of the links. This results in relating the angular response of the link motion to its corresponding drive.

In this application of the MBSmc method, the joints are considered as flexible solids. The scheme of the proposed model is shown in Fig. 1.
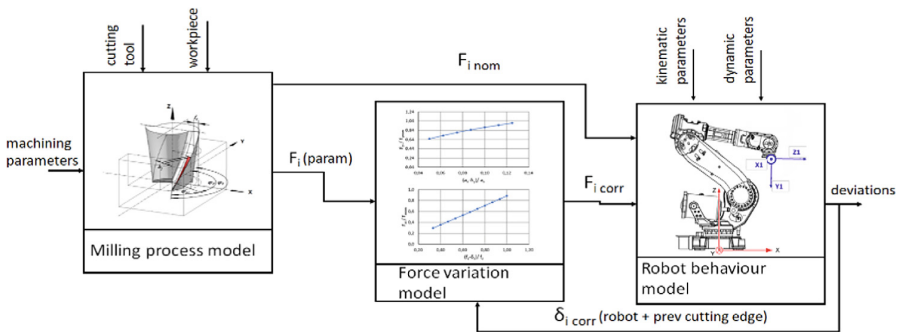
Fig. 1.   Model for the robot milling system.

Since the main deformations are located at the joints (compared to the stiffness of the links), the direction of the forces and torques that will play out during the execution of the applied machining have a relevant influence, as well as the configuration of the robot.

3   Robot Model

The model presented is a simulation model of the robot's behaviour that takes into account the forces of the milling process. For this purpose, it interacts with the process based on the estimation of how the evolution of the forces evolves with the robot's deviations and, therefore, with the modification of the machining parameters.

In this way, the deviation of the robot path δ_{robot} is defined as the difference between the nominal movement of the TCP and its real position (Eq. (1)).

This variation is caused by deviations in the positioning of the robot and by deviations caused by deformations of the robot as a consequence of the forces and torques generated during the process being performed. The calculation of the estimation of this deviation

can be done by simulating the behaviour of the robot, determining the deviation as the difference between the nominal and simulated trajectories or positions.

$$\delta_{robot} = q^{TCP} - q^{TCP}_{real} \tag{1}$$

The position q for all points and vectors of the robot (see Fig. 2) is modelled using the MBSmc method. The robot motion is obtained with a trajectory generated by a discrete set for each programmed robot position through master positions. All robot positions must fulfil the function of the non-linear constraint equations for each instant t (Eq. (2)).

By first performing the function of Eq. (2) in the inverse dynamics and then using the results of the inverse dynamics in the direct dynamics, the coordinates of the robot's TCP displacement are calculated for each trajectory configuration.

$$\Phi(q_{sim}, t) = 0 \tag{2}$$
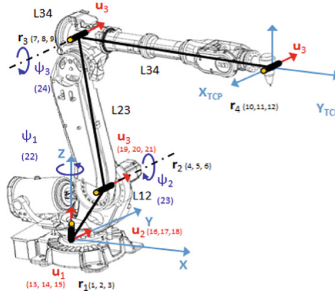
Fig. 2. Multibody model of the robot with mixed natural coordinates.

In the formulation of the simulated rotation angles Ψ_{sim} (Eq. (3)), the dependence of the theoretical rotation angles Ψ and the term φ [8] is proposed. The torques τ that each motor produces at its joint are related to its angular stiffness k (Eq. (4)). The negative sign explains the direction of the torques from machining, which are the opposite of the motor torques.

$$\psi_{sim} = \psi + \Delta\psi_{Kpos} + \varphi \tag{3}$$

$$\varphi = -\frac{\tau}{k} \tag{4}$$

In order to know which are the torques τ_i that the motors produce in each joint as a consequence of the process forces that are playing, it is necessary to solve the inverse dynamic problem, using the virtual method power (Eq. (5)).

$$\tau = R^T InR\ddot{\psi} - R^T InSc - R^T Q - \tau_{mach} \tag{5}$$

Operating with the direct dynamic model, the corrected angular accelerations of the joints are obtained. By applying ODE-type integration methods, the angles and their corrections due to the gain at each position of the trajectory are calculated (Eq. (6)).

$$\left\{ \ddot{\psi}^T + \Delta\ddot{\psi}^T_{Kpos}, \dot{\psi}^T + \Delta\dot{\psi}^T_{Kpos} \right\}_t \overset{ode113}{\rightarrow} \left\{ \dot{\psi}^T + \Delta\dot{\psi}^T_{Kpos}, \psi^T + \Delta\psi^T_{Kpos} \right\}_{t+\Delta t} \tag{6}$$

With the simulated angles Ψ_{sim}, the natural coordinates for all the points of the robot at each instant t of the trajectory are generated using the cubic spline method.

4   Interaction Between the Robot and the Process

Once the robot has been modelled, the process forces are introduced. In this way, the process is modelled taking into account the influence of the process forces and the influence of the robot's deformations on them.

The deviation of the robot in the direction of motion affects the instantaneous cutting edge feed rate and thus the average chip thickness. Robot deflections in the transverse direction will affect the cutting width, the engagement angle and the chip thickness. The robot deviation in the perpendicular direction to the robot base modifies the axial depth of cut.

The fact that the cutting forces are modified means that the reaction of the robot will be different. Therefore, it must be known to what extent the values of the machining forces will be modified, for which a complete model of the process has been chosen as described in [9] for peripheral end milling operations.

The cutting force in the tangential direction is expressed according to Eq. (7). Analogously, the forces in the radial and axial directions can be obtained.

$$F_c(\varphi_j) = k_{c0} \cdot a_p \cdot \left[\frac{1}{\varphi_j - (\varphi_j - \varphi_{pr})} f_z \big(\cos(\varphi_j - \varphi_{pr}) - \cos\varphi_j \big) \right]^{1-m_c} \tag{7}$$

The corrections applied to each of the force components are a function of position.

The calculation of the feed rate fz_i at each point on the path takes into account the nominal feed rate fz, the deformation of the robot in the feed direction at that point and what the previous edge at that point did not cut, according to Eq. (8).

$$fz_i = fz + \delta_{roboti} + \delta_{prev\ cutting\ edge\ i} \tag{8}$$

With respect to the cutting width a_{ei}, also for each position of the path, an analogous expression is used (Eq. (9)) where the cutting width a_e is affected by the effect of the transverse deformation of the robot at that point.

$$a_{ei} = a_{ei} + \delta_{robot\ i} \tag{9}$$

In both cases, the calculation of the robot deformation at each position takes into account the stiffness of the joints and is simulated by means of the direct dynamics along the entire path with the torques obtained from the inverse dynamics when the process forces are introduced.

Once the corrections have been made and fz_i and a_{ei} have been obtained, the corrected forces for each point are obtained (Eq. (10)).

$$Q_{sim\,forces} = Q_{nom\,forces} \cdot \frac{fz_i}{fz} \cdot \frac{ae_i}{ae} \tag{10}$$

The designed algorithm calculates, individually for each point, the inverse and direct dynamics with the corrected forces. This process is repeated for each point until the result converges and the deviation of the robot can be obtained (Eq. (1)). The procedure is applied to each position in the trajectory.

5 Results

The modelled (see Fig. 3) and measured (see Fig. 4) milling forces applied at the TCP are shown, together with their correction by the model, in the transverse direction of the feed. The effect of the forces on the motion is shown in Fig. 5. As a consequence of the deformations of the robot and what the previous cutting edge has not cut, the process forces decrease. This deviation varies as the cutting edge rotates.
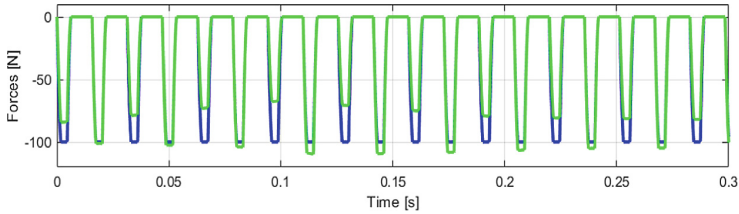
Fig. 3. Modelled (blue) and corrected (green) transverse forces at the TCP.
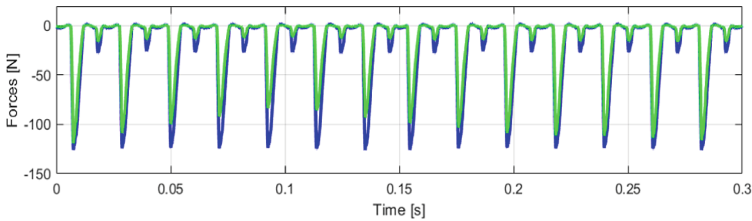
Fig. 4. Measured (blue) and corrected (green) transverse forces at the TCP with runout.
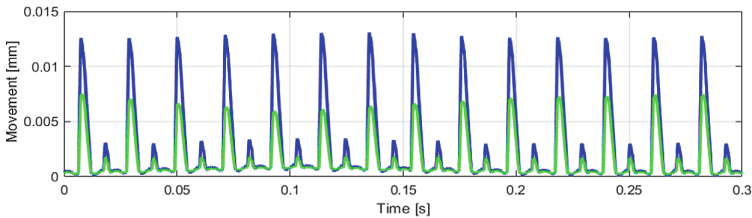
Fig. 5. Movement for the TCP due to measured forces (blue) and their corrections (green) with runout.

6 Conclusions

From the results obtained it is concluded that:

- The model allows knowing the deviations of the TCP when interacting with the machining forces.

- The behaviour of the robot reflects the evolution of the variable forces in milling operations.
- The corrections are calculated from the configuration of the robot and the machining at each position of the cutting edge, taking into account the situation of the previous cutting edge in the same position.
- The established procedure makes it possible to predict the deviations of the robot, depending on its mechanical characteristics.

References

1. Ji, W., Wang, L.: Industrial robotic machining: a review. Int. J. Adv. Manuf. Technol. **103**(1–4), 1239–1255 (2019). https://doi.org/10.1007/s00170-019-03403-z
2. Tao, B., Zhao, X., Ding, H.: Mobile-robotic machining for large complex components: a review study. Sci. China Technol. Sci. **62**(8), 1388–1400 (2019). https://doi.org/10.1007/s11431-019-9510-1
3. Verl, A., Valente, A., Melkote, S., Brecher, C., Ozturk, E., Tunc, L.T.: Robots in machining. CIRP Ann. **68**(2), 799–822 (2019)
4. Zhu, Z., et al.: High precision and efficiency robotic milling of complex parts: ahallenges, approaches and trends. Chinese J. Aeronaut. **35**(2), 22–46 (2022)
5. Liao, Z.Y., Li, J.R., Xie, H.L., Wang, Q.H., Zhou, X.F.: Region-based toolpath generation for robotic milling of freeform surfaces with stiffness optimization. Robot. Comput. Integr. Manuf. **64**, 101953 (2020)
6. Cui, G., Li, B., Tian, W., Liao, W., Zhao, W.: Dynamic modeling and vibration prediction of an industrial robot in manufacturing. Appl. Math. Model. **105**, 114–136 (2022)
7. Nguyen, V.L., Kuo, C.-H., Lin, P.T.: Compliance error compensation of a robot end-effector with joint stiffness uncertainties for milling: an analytical model. Mech. Mach. Theory **170**, 104717 (2022)
8. Ferreras-Higuero, E., Leal-Muñoz, E., García de Jalón, J., Chacón, E., Vizán, A.: Robot-process precision modelling for the improvement of productivity in flexible manufacturing cells. Robot. Comput. Integr. Manuf. **65**, 101966 (2020)
9. Diez, E., Perez, H., Guzman, M., Vizan, A.: An improved methodology for the experimental evaluation of tool runout in peripheral milling. Int. J. Adv. Manuf. Technol. **65**(1–4), 283–293 (2013)

AI Training for Application to Industrial Robotics: Trajectory Generation for Neural Network Tuning

Mikel Merino[1]([✉]), Javier Ibarrola[1], Jokin Aginaga[1,2], and Mikel Hualde[1]

[1] Departamento de Ingeniería, Universidad Pública de Navarra, Pamplona, Spain
mikel.merino@unavarra.es
[2] Institute of Smart Cities (ISC), Universidad Pública de Navarra, Pamplona, Spain

Abstract. In the present work robot trajectories are generated and kinematically simulated. Different data (joint coordinates, end effector position and orientation, images, etc.) are obtained in order to train a neural network suited for applications in robotics. The neural network has the goal of automatically generating trajectories based on a set of images and coordinates. For this purpose, trajectories are designed in two separate sections which are conveniently connected using Bezier curves, ensuring continuity up to accelerations. In addition, among the possible trajectories that can be carried out due to the different configurations of the robot, the most suitable ones have been selected avoiding collisions and singularities. The designed algorithm can be used in multiple applications by adapting its different parameters.

Keywords: Industrial robotics · Trajectory planning · Artificial Intelligence

1 Introduction

In recent years, the rapid advance of industrial robotics has made it possible to automate a multitude of operations. However, automation is more complicated for certain operations that present some degree of randomness. The development of neural networks (NN) in the field of artificial intelligence (AI) is making it possible to automate this type of task. Specifically, in the project in which this work is included, a NN will be used to generate trajectories from images. The algorithm will be able to identify the object to be picked up and command the trajectory. This work will focus on generating the data sets in the form of images and time series necessary to adjust the parameters of the NN in the initial training phase.

2 Trajectory Generation

In robotics, a trajectory is the desired motion of a manipulator from an initial point to an end point, described by the position and orientation of the robot's end effector. The generation of trajectories seeks to find the functions that describe the position, velocity

and acceleration as a function of time of the joints, knowing the desired initial and final position and orientation for the end effector. In this work a series of trajectories will be generated using the UR10e robot. It is a serial manipulator with 6 degrees of freedom whose kinematics have been described using the Denavit-Hartenberg parameters [1–3]. The robot has the task of gripping a cable whose position will determine the final position of the end effector.

Trajectories can be defined either in the operation space or in the joint space. Both are related by means of direct and inverse kinematics. The direct kinematics has only one solution, while the inverse kinematics has 8 solutions for the UR10e robot. In this work, both the operation space and the cartesian space will be used, since the trajectory has been divided into two distinct sections. The first section is called *approach* and the robot moves from its initial pose (P1) to an intermediate pose (P2) close to the final pose (P3). In this stage, the aim is that the robot travels the distance in the shortest possible time, and it is based on the joint space. An intermediate pose is reached and the necessary orientation for the subsequent manipulation of the object is achieved. The second section is called *slow*, moving the robot from P2 to P3. In this section the manipulator moves to P3 with reduced speed and without changing the orientation of the end effector. This section has been defined in the operating space.

2.1 Trajectory Point Calculation

To generate the trajectory given the initial and final pose of the robot, the first step is calculating the intermediate pose where the two sections of the trajectory meet. This pose has the same orientation as the final pose and x,y,z cartesian coordinates that are calculated with the desired distance (in modulus) between the cartesian coordinates that define P2 and P3. Then, using inverse kinematics [4, 5], the joint coordinates of the initial, intermediate and final poses are obtained. The same configuration of the robot has been used for the three calculations so that it uses the same configuration during the whole trajectory. After this process, the joint coordinates of the robot (vector $\boldsymbol{q}$) and the cartesian coordinates of the end effector (vector $\boldsymbol{x}$) have been obtained for poses P1, P2 and P3.

2.2 Trajectory Design Using Bézier Curves

In this work polynomial Bézier curves have been used to design the two sections that will compose the complete trajectory of the robot. For the first section of the trajectory, a total of 6 Bézier curves have been defined since there are 6 joint coordinates. To guarantee continuity up to accelerations, the control points of the vector of control points $\boldsymbol{c} = [c_1, c_2, c_3, c_4, c_5, c_6]^T$ have been defined in such a way that they fulfill certain requirements. In order that the joint velocities ($\dot{\boldsymbol{q}}$) and accelerations ($\ddot{\boldsymbol{q}}$) are zero at the initial instant, it has been imposed that the first three control points have the value of the joint coordinates at P1, so that $c_{1i} = c_{2i} = c_{3i} = \theta_{i,P1}$ where i refers to the i-th joint coordinate. To ensure continuity in positions at P2, it must be satisfied that $c_{6i} = \theta_{i,P2}$, i.e., the last control point must be equal to the joint coordinates of P2. To ensure continuity in velocities and accelerations at P2, the values of c_{5i} and c_{4i} are calculated in such a way that the desired velocities and accelerations are equal to the ones

from the Bézier curves. In the second section, since the orientation of the end effector is constant, only 3 Bézier curves are necessary. An analogous procedure to the first section has been followed and the results have been transferred to the joint. Hence, the complete trajectory is univocally described Fig. 1.
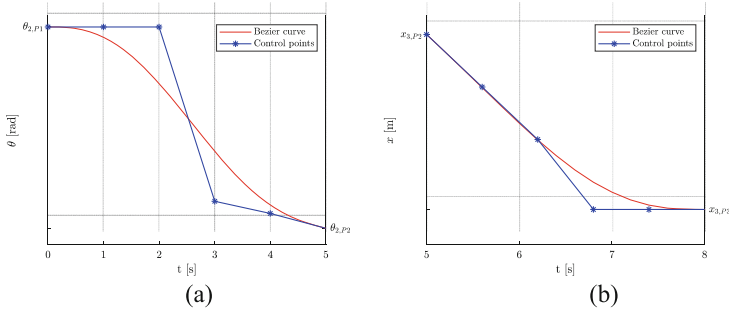
Fig. 1. (a) Joint coordinate θ_2 evolution in first trajectory section. (b) Cartesian coordinate x_3 evolution in second trajectory section.

3   Trajectory Selection

Under the assumptions of Sect. 2, a total of 8 trajectories have been generated for given initial and final poses, so that each trajectory corresponds to each of the robot configurations. These 8 trajectories represent 8 possible solutions for the robot to move from the same initial pose to the same final pose.

In order to eliminate trajectories in which there is some type of collision (self-collision or with an object in the environment), a collision detection algorithm has been designed. The robot has been modeled using rectangular parallelepipeds in order to simplify and speed up the algorithm, as shown in Fig. 2.
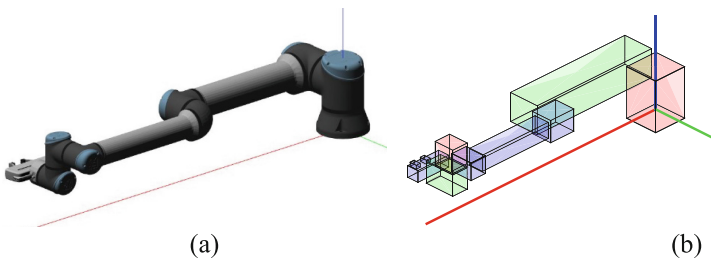
Fig. 2. (a) Original solid modelled robot in Gazebo. (b) Collision solid modelled robot.

On the other hand, the trajectories in which the robot passes close to a singularity [6, 7] have been eliminated by establishing a threshold value of the condition number

of the Jacobian matrix. When this threshold is exceeded trajectory is rejected. Figure 3 shows an example of trajectory rejection due to collision and singularity.

Finally, three criteria have been defined in order to select among the trajectories not rejected: minimization of the maximum joint velocity, minimization of the distance covered by the end effector and minimization of the maximum value of the condition number. The final trajectory selection algorithm is described in Fig. 4.

(a)   (b)
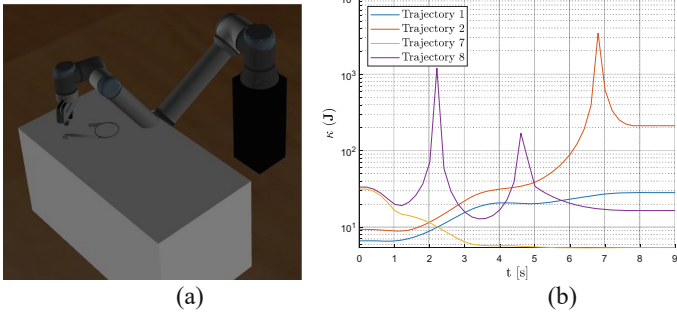
Fig. 3. Trajectory rejection criteria application. (a) Collision based example. (b) Singularity based example (trajectories 2 and 8 rejected).
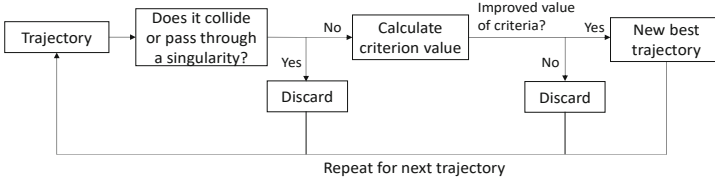
Fig. 4. Trajectory selection algorithm diagram.

4 Generation of Data Based on the Optimal Trajectory

In order to feed the neural network, a single trajectory is not enough, being necessary a large number of trajectories in which some of their parameters are varied. In order to generate this set of trajectories, the following parameters of the cable to be taken by the robot have been randomly varied: position, radius, opening angle, torsion angle of the terminals and length of the cable. Thus, the final pose to be reached by the robot can be varied and a large number of random trajectories can be created. The generated data sets are composed of a series of images and text files with time series (position, joint velocity and acceleration, position and orientation of the end effector, etc.) organized as shown in Fig. 5.

The images of the manipulator carrying out the trajectory at different time instants is the part that provides the most information to the AI since after the training with these images it will be able to generate trajectories autonomously. These images have been

obtained using the free robotics simulation software Gazebo, where a virtual environment as close as possible to the real one has been created. Thus, at each discrete instant of the trajectory, the position of the robot has been varied and the necessary images have been taken.
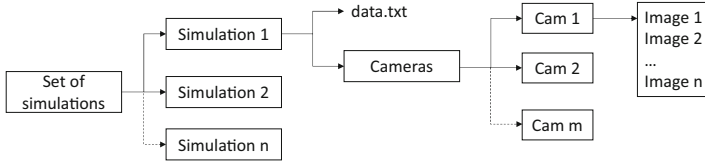
Fig. 5. Organization of a data-set.

On the other hand, the time series data is stored in a text file containing the header in the first row with all the names of the variables to be stored: time, joint coordinates, velocities and accelerations, and position and orientation of the end effector in cartesian coordinates. The remaining rows represent the value of each of these variables at a given time instant.

5 Results

In this Section the results obtained after generating several datasets that can be used to feed the AI will be analyzed. First, a single trajectory will be analyzed as an example and then some general results of the data sets obtained will be discussed.
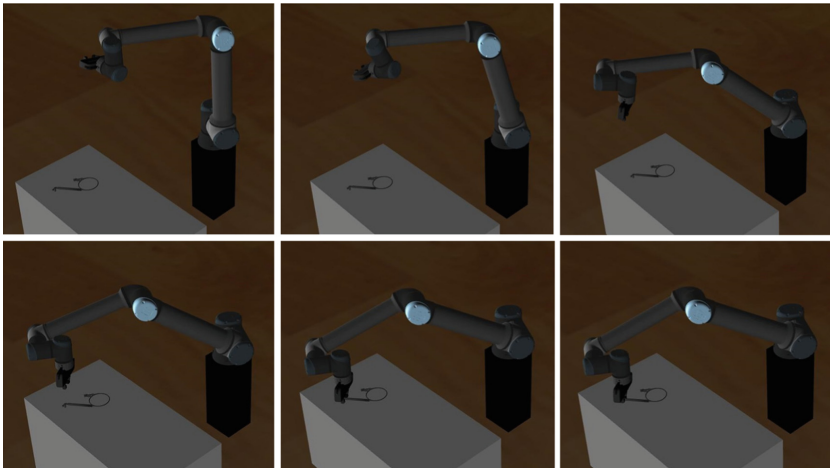
Fig. 6. Example trajectory evolution.

In this example, 4 of the 8 trajectories have been discarded (trajectories 3–6) due to collisions with the table on which the cable is located. These configurations are called

"elbow down" configurations. Configurations 2 and 8 have also been discarded since they exceed the threshold established for the condition number of the jacobian matrix. Among the remaining valid trajectories number 1 has been chosen based on the criterion of minimizing the maximum number of condition. Images of different instants of the selected trajectory can be seen in Fig. 6.

Regarding the results of the complete data set composed of 1000 trajectories, it has been found that trajectories 1 and 7 are the most used with usage percentages of 42.84% and 26.35% respectively. Configurations 3 to 6 have not been used in any occasion because they always collide with the table as they are "elbow down". Trajectories 2 and 8 have a very low percentage of use of 3.2% and 0.46%, the rest (27.15%) are erroneous trajectories where all the trajectories have been rejected due to collisions and/or singularities.

6   Conclusions

This work presents a methodology to create robotic trajectories and select between them in order to obtain a data-set to train a neural network. The advantages of generating trajectories in a kinematic way in terms of simplicity of trajectory generation and ideality of the trajectories have been tested. An algorithm has been created to avoid collisions and also singularities and their neighborhood. The generated trajectories have been used to export a series of data (images and time series) that will be used for the first training phase of the neural network. In addition, the algorithm has been designed parametrically so that it could be used for other similar applications.

References

1. Denavit, J., Hartenberg, R.S.: A kinematic notation for lower-pair mechanisms based on matrices. J. Appl. Mech. **22**, 215–221 (1965)
2. Siciliano, B., et al.: Robotics: Modelling. Planning and Control. Springer, London (2010)
3. Angeles, J.: Fundamentals of Robotic Mechanical Systems. Springer, New York (2007). https://doi.org/10.1007/978-0-387-22458-9_4
4. Zaplana, I., Claret J.A., Basanez, L.: Análisis cinemático de robots manipuladores redundantes: Aplicación a los Robots Kuka LWR 4+y ABB Yumi. In: Revista Iberoamericana de Automática e informática Ind. **15**, 192–202 (2018)
5. Qiang, L., et al., W.: Research on kinematic modeling and analysis methods of UR robot. In: 2018 IEE 4th Information and mechatronics Engineering Conference, pp. 159–164 (2018)
6. Craig, J.J.: Introduction to Robotics: Mechanics and Control. Pearson Education, New Jersey (2005)
7. Tsai, L.-W.: Robot Analysis. Wiley, New York (1999)

Analysis of Navigation Algorithms for a Fleet of Mobile Robots by Means of Digital Twins

Alberto Martínez-Gutiérrez[✉] ⓘ, Javier Díez-González ⓘ, Paula Verde ⓘ, Rubén Ferrero-Guillén ⓘ, and Hilde Perez ⓘ

Intelligent Systems for Manufacturing, University of León, León, Spain
{amartg,jdieg,pverg,rferrg,hperg}@unileon.es

Abstract. Industrial maintenance is undergoing a process of digitalization and automation through the use of Industry 4.0 technologies. An example is the employment of digital twins which allow virtualizing assets such as a fleet of Autonomous Mobile Robots (AMR) . In this paper, we analyze two local navigation algorithms for AMRs navigation in a digitized environment: Dynamic Window Approximation (DWA) and Time Elastic Band (TEB) . For this purpose, a digital twin is implemented in the ROS ecosystem. In this environment, a combined mission of a fleet of three AMRs is simulated where they navigate together in order to compare the behavior of the algorithms in dynamic industrial environments. As a result, the trajectories of each AMR that are key for production cost planning are analyzed. Finally, we introduce in this work a web server to interact with the developed digital twin facilitating its use.

Keywords: Industry 4.0 · Autonomous robots · Digital twins · Simulation

1 Introduction

The manufacturing industry is undergoing a digital transformation process where different technologies are converging towards flexible, individualized, and efficient production. For this purpose, the digitization of assets in industrial processes is essential in the creation of a collaborative environment to generate greater added value. Under this paradigm, the concept of Industry 4.0 is born where the integration of heterogeneous technologies is a requirement to achieve more efficient production [1]. In this sense, Cyber-Physical System (CPS) are key to merge the physical level with the digital level enabling the interconnection of the entire value chain [2]. The Industrial Internet of Things (IIoT) concept is being developed where policies and methods for data and information transmission are used to enable a collaborative manufacturing.

Within this context of digitization and connectivity, industrial handling is an asset where coordination of other manufacturing processes is needed in order to be efficient. To achieve efficient transportation, data generation of the different processes through SCF is necessary to obtain information for decision making. In this sense, decision making can be executed by an expert system because the necessary information is digitized.

However, for full automation of internal transportation, autonomous vehicles capable of safely navigating the manufacturing plant are required. These vehicles are referred to as Autonomous Mobile Robots (AMR) in the scientific literature. AMRs are equipped with different sensors that allow them to recognize the environment as well as some on-board intelligence to navigate safely.

However, the adaptation of AMRs to industrial environments is unknown due to the heterogeneity of machine distributions as well as the dynamic location of personnel. Nevertheless, the evaluation of AMR behavior is essential for cost forecasting and production planning. In this context, Digital Twins (DT) enable the virtualization of an environment as well as the modeling of AMRs. By using DT, it is possible to analyze trajectories, times and even battery consumption, which are key to planning and optimizing the production activity.

In this context, there is a study [3] which analyzes the behavior of a single AMR in a DT compared to a real robot. In this study, two scenarios with static obstacles are recreated, reaching a high level of similarity; however, this work does not analyze the behavior with several AMR simultaneously. Moreover, the navigation of an AMR fleet presents several peculiarities in the field of navigation, planning or simulation. For this reason, this work studies the navigation behavior of an AMR fleet making use of a DT which is a novelty in the literature to the authors' knowledge.

In this work, in addition to the creation of the DT with several AMRs, we intend to evaluate the behavior of two different local navigation algorithms. The objective of this study is to establish which one offers lower transport times once its parameters have been configured and adapted to avoid collisions between them. Furthermore, to make the evaluation comparable, it is performed in the same industrial simulation environment with identical case studies supposing the same requirements for AMRs navigation.

2   Case Study

AMRs are a fundamental asset for internal transportation in the industrial plant [4]. To perform this demonstrator and study with a fleet of AMRs, an industrial plant for the manufacturing of parts will be recreated virtually. For this purpose, the parts need to be moved from one machine to another to be stored in a warehouse.

With this case, the objective is to analyze the trajectories and times associated with the autonomous transport of these vehicles. However, in order to analyze the behavior of the navigation algorithms with moving obstacles, a scenario of small dimensions has been recreated to maximize the encounters with the AMRs.

2.1   Description of the AMR Used in This Paper

The autonomous industrial vehicle used is a non-holonomic mobility robot [5]. In this case, the robot has two independent driving wheels providing two Degrees Of Freedom (DOF) as opposed to the 3 DOF of the holonomic robots (i.e., two for position and one for orientation).

As for its kinematics, it is based on a differential traction movement by means of two conventional fixed wheels. However, at its ends, it has off-center steerable wheels for load distribution and stability, which are not driven.

The driving wheels are located on the sides of the geometric center of the robot, allowing it to rotate on itself without the need to move. In this way, a high mobility in confined spaces is achieved, which is considered in the navigation algorithms.

In addition, this autonomous vehicle under study is marketed by the company Mobile Industrial Robots (MIR) and is widely used in industry. Specifically, the model is the MIR100, which is capable of carrying 100 kg of payload with a maximum speed of 1.5 m/s.

2.2 Mission Definition

To evaluate both algorithms, the environment and objectives must be the same to be comparable. For this purpose, a mission has been established for each of the AMRs. In this way the environment and circumstances are identical, in order to attain comparable results for both algorithms.

For this case study, all AMRs are sent missions at the same time, moving to two different targets. The mission constraints stipulate that two vehicles cannot be parked on the same machine. The missions defined for each AMR are shown in Table 1.

Table 1. Definition of missions for the evaluation of navigation algorithms.

AMR missions			
Position	AMR-1	AMR-2	AMR-3
Initial	Saw	Milling	Lathe
Intermediate	Lathe	Warehouse	Saw
Final	Milling	Saw	Warehouse

Once the missions and the case study have been established, we proceed to the resolution of the problem.

3 Methodology

For the comparative analysis of the navigation algorithms, the ROS ecosystem has been used, where the interconnection between a set of libraries and tools has been established. The navigation stack is summarized in the *move_base_node* where it receives the positioning information according to the theoretical framework [6].

To integrate multiple robots, the authors have decided to create prefixes in order to load the same features and parameters without cloning the code. In this way with a single XML file, we can reproduce the AMRs in the same simulation environment.

The virtualized dynamic simulation environment is realized with gazebo where AMRs are spawned for navigation. The environment has been designed and exported in Spatial Data Files (SDF) for interpretation in the ROS ecosystem [7]. The manufacturing plant is quadrangular in shape with a size of 16 m on a side.

After the creation of the environment, the AMR poses have been defined at the points of interest defined in the mission.

4   Results and Discussion

This section shows the sailing times of each AMR, as well as the trajectories for comparison purposes.

4.1   Trajectories

The AMR trajectories is an indication of how the navigation algorithms work. In this case, the actual AMR trajectories are shown as a result. To reach the resulting trajectory, the local planning algorithms also rely on the global trajectory, as well as its nearest environment. The authors have employed the *rviz* tool to obtain the resulting trajectories as well as the mapped environment.

First, the trajectories with the DWA local planning algorithm will be shown. For the sake of clarity Fig. 1 shows only the resulting trajectory, ignoring the global trajectories of each AMR.
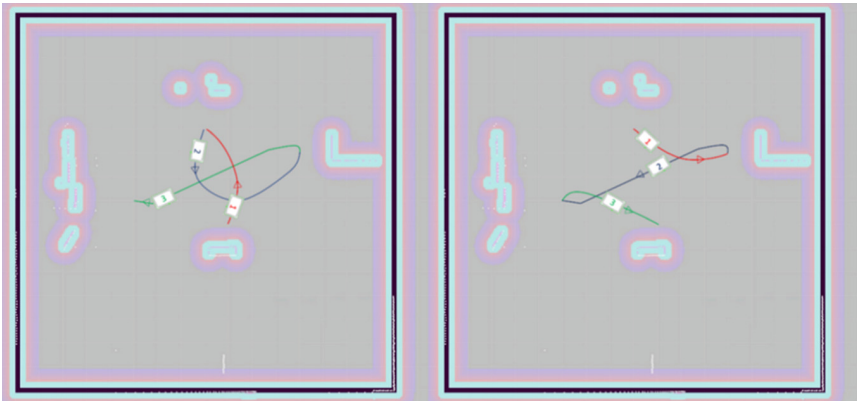
Fig. 1. AMR trajectories in the digital twin with the DWA local planning algorithm.

According to Fig. 1, each AMR is differentiated with a number. Furthermore, the mission has been divided into two maps as a consequence of the two trajectories. In the same way as in the DWA algorithm, the trajectories of the local planning algorithm TEB are presented in Fig. 2.

In addition, the maps in Figs. 1 and 2, which have been generated by *rviz*, show the cost map and its value by means of a color gradient in shades of blue. However, the dynamic obstacles caused by the AMRs have not been represented for clarity.

4.2   Navigation Times

In addition to the trajectories, the time taken to navigate the AGVs has been measured with the DWA and TEB algorithms, the results of which can be seen in Table 2.
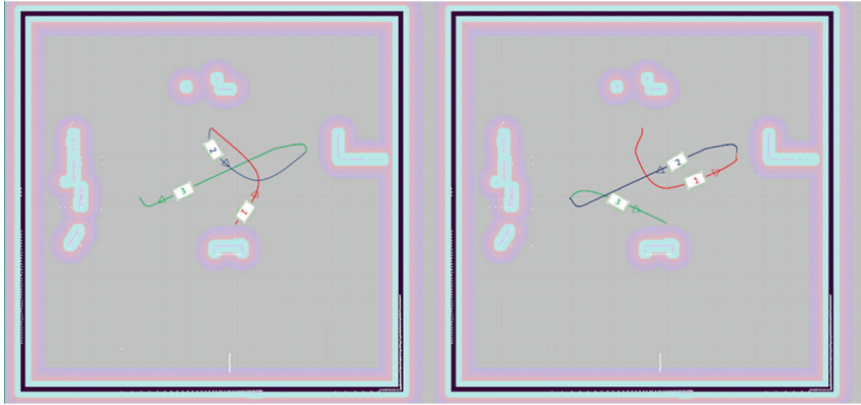
Fig. 2. AMR trajectories in the digital twin with the TEB local planning algorithm.

Table 2. Comparison of navigation times between the DWA and TEB algorithms.

Navigation times [s]		
Mission	DWA	TEB
Initial-intermediate	31.23	28.12
Intermediate-final	30.25	25.24
Total	61.48	53.36

4.3   Discussion

The TEB algorithm, being based on the temporal optimization of trajectories, seeks more optimal times compared to the DWA algorithm. Therefore, the results are consistent with the mathematical principles on which these two algorithms are based.

5   Conclusions

DTs are key for the virtualization of the environment and the generation of information for intelligent decision-making. In this sense, two navigation algorithms have been analyzed: DWA and TEB. For this purpose, an industrial environment has been virtualized with three AMRs in order to acquire the trajectories and navigation times for the same mission. Consequently, the ROS ecosystem has been used to evaluate the algorithms. According to the results obtained, the TEB algorithm offers reduced operation times than the DWA for dynamic obstacles. Therefore, it can be concluded that TEB is still better when dealing with moving obstacles. Also, the trajectories with TEB are more suitable for the objective function, although the fulfillment of the constraints is not guaranteed. In addition, a web interface has been developed to allow interaction between users and the DT within the ROS ecosystem, facilitating its use. Therefore, the initial objectives of this work have been successfully completed by analyzing and extracting

interesting conclusions on local navigation algorithms for AMRs fleet navigation using an interactive digital twin.

References

1. Lasi, H., Kemper, H-G., Feld Dipl-IT, Hoffmann Dipl-HM.: Industry 4.0. Negocios e información (2014).https://doi.org/10.1007/s12599-014-0334-4
2. Zhang, Y., Zhu, Z., Lv, J.: CPS-based smart control model for shopfloor material handling. IEEE Trans Industr Inform **14**, 1764–1775 (2018). https://doi.org/10.1109/TII.2017.2759319
3. Martínez-Gutiérrez, A., Díez-González, J., Ferrero-Guillén, R., et al.: Digital twin for automatic transportation in industry 4.0. Sensors **21**, 3344 (2021). https://doi.org/10.3390/s21103344
4. Kosacka-Olejnik, M., Kostrzewski, M., Marczewska, M., et al.: How digital twin concept supports internal transport systems - literature review. Energies **14**, 4919 (2021). https://doi.org/10.3390/EN14164919
5. Udengaard, M., Iagnemma, K.: Kinematic analysis and control of an omnidirectional mobile robot in rough terrain. In: IEEE International Conference on Intelligent Robots and Systems, pp. 795–800 (2007).https://doi.org/10.1109/IROS.2007.4398996
6. Cybulski, B., Wegierska, A., Granosik, G.: Accuracy comparison of navigation local planners on ROS-based mobile robot. In: 12th International Workshop on Robot Motion and Control, RoMoCo 2019 - Workshop Proceedings, pp.104–111 (2019). https://doi.org/10.1109/ROMOCO.2019.8787346
7. Martínez, A., Díez, J., Verde, P., et al.: Digital twin for the integration of the automatic transport and manufacturing processes. In: IOP Conference Series Material Science and Engineering, vol. 1193, p. 012107 (2021).https://doi.org/10.1088/1757-899X/1193/1/012107

Towards Digitalizing Rolling Stock Maintenance

Alejandro Bustos[1]([✉]) [iD], Higinio Rubio[2] [iD], Cristina Castejon[2] [iD],
Enrique Soriano-Heras[2] [iD], and Juan Carlos Garcia-Prada[1] [iD]

[1] Universidad Nacional de Educación a Distancia, c/Juan del Rosal 12, 28040 Madrid, Spain
albustos@ind.uned.es
[2] Universidad Carlos III de Madrid, Av. De la Universidad 30, 28911 Leganes, Spain

Abstract. The advent of Industry 4.0 has revolutionised the way in which all aspects of a product or service are approached, and the railway sector is moving toward the adoption of this new paradigm. Maintenance in railways is traditionally based on a preventive approach that replaces parts at regular intervals or when a failure occurs. However, the 4.0 revolution implies the use of new strategies based on condition monitoring and predictive maintenance for moving towards Maintenance 4.0. In this work, the creation of a digital twin that helps in the adoption of new technologies is established. The proposed digital twin covers the trailer bogie of a high-speed train and is composed of three models: a 3D geometrical model, a finite element model and a multi-body model. These three models provide the initial information about the dynamic performance of the bogie that should be completed with feedback from the actual bogie operating in the real world.

Keywords: Industry 4.0 · Digital Twin · Maintenance 4.0

1 Introduction

The fourth industrial revolution, called Industry 4.0, is based on the digitalization of processes thanks to the "Internet of Things", so every component of the processes is connected to the Internet and can send and receive information. This revolution is changing not only the ways in which products are designed but also the internal organization of companies and the relationship between them and society [1]. Connecting thousand or millions of devices and processing huge amounts of information requires technologies such as Big Data, Artificial Intelligence, data fusion, etc. In addition, other technologies such as additive manufacturing and Digital Twin are also used in Industry 4.0. The application of these new technologies to traditional predictive maintenance leads to Maintenance 4.0.

The implementation of Maintenance 4.0 in railways is slow and, up to day, focused mainly on the infrastructure. Kaewunruen et al. [2] proposed the use of Building Information Modeling (BIM) to create a Digital Twin embedded in the life cycle of railway infrastructure. It is applied to Taipei Metro to enhance its performance in operation and

maintenance. Fuzzy logic is proposed by Karakose [3] for the predictive maintenance of rails, overhead lines and pantographs. The monitoring of track condition through signals collected from multiple trains is proposed by Lederman [4].

The most advanced implementation of Maintenance 4.0 in rolling stock is, probably, the work developed by the company East Japan Railway in the last years [5]. The strategy followed for implementing this paradigm is based on four pillars: condition-based monitoring, asset management, database integration and work supported by artificial intelligence. East Japan Railways is currently operating the series E235 commuter rolling stock, which is able to monitor not only its own systems but also infrastructure systems such as the track and the overhead line.

According to Grieves and Vickers [6], *"the Digital Twin is a set of virtual information constructs that fully describes a potential or actual physical manufactured product from the micro atomic level to the macro geometrical level. At its optimum, any information that could be obtained from inspecting a physical manufactured product can be obtained from its Digital Twin"*. Although this technology is widely used in product design, life cycle management or logistics, its application to the railway industry is limited and mainly focused on infrastructure or traffic management [7].

This work presents an application case for applying Maintenance 4.0 to a high-speed train designed and built before the advent of the paradigm through the development of a Digital Twin.

2 Digital Twin

The high-speed train studied in this work is composed of two motor cars with two bogies each and 8 articulated cars that rest on 9 trailer bogies. The train opened the first high-speed line in Spain and has been travelling through Spain and the south of France up to 300 km/h since then. We will focus on the trailer bogie of the eighth car which is the nearest to the second motor car. One wheelset of this bogie is equipped with uniaxial accelerometers in the three space directions to measure vibrations.

The bogie's digital twin presented in this work is developed from technical data to characterise it and develop improvements if needed. The digital twin is composed of three models: a 3D CAD model, a FEM model and a multibody model.

The CAD 3D model is made using the PTC CREO Parametric software. This detailed model (see Fig. 1) includes the bogie frame, two wheelsets, four axle boxes, the brake system, the primary and secondary suspensions, and the car-bogie joints. There are three accelerometers placed in the real bogie for signal acquisition and processing purposes that are also modelled.

The FEM model is developed using ANSYS software from the 3D CAD model. The geometry of key elements such as the bogie frame (see Fig. 2) is imported into ANSYS in order to perform modal analyses and obtain their natural frequencies.

The multibody model is developed with the help of Universal Mechanism software, which includes specific tools for the dynamic simulation of rail vehicles. The multibody model is assembled taking into account the data from the 3D CAD model, paying special attention to the inertial properties of the bodies and the physical relationship between them. Thanks to this multibody model, it is possible to better understand the behaviour

of the real bogie under different traffic operating conditions. This model is shown in Fig. 3.

The accelerometers are placed on the axle box, so the performance of the roller bearings is easily accessible. In case a fault in the roller bearings occurs, it should be visible in the spectra. These frequencies are calculated by using the equations proposed by Palmgren [8].
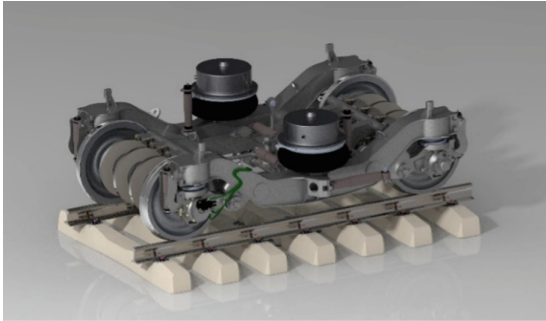
Fig. 1. Bogie 3D CAD model developed in CREO Parametric.
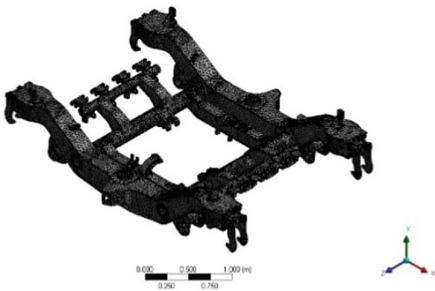
Fig. 2. FEM model of the bogie frame in ANSYS.
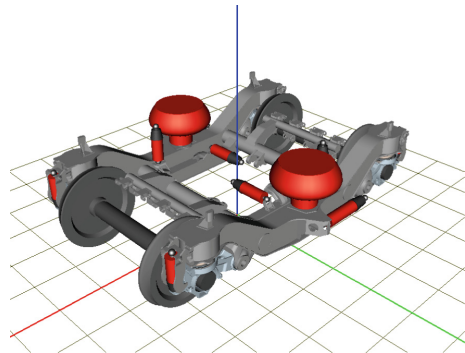
Fig. 3. Multibody model of the bogie in Universal Mechanism.

3   Results

Due to the limited space available, only a selection of the characteristic frequencies of the bogie is listed in Table 1. Roller bearing fault and sleeper pass frequencies are computed from theory. Natural modes of the bogie frame, wheelset and axle box are computed by FEM. It should be noted the proximity between the BSF (Ball Spin Frequency) and the sleeper pass frequency, which can lead to mixing up both phenomena and inferring false roller bearing failures.

Irregularities on the track and the wheels can be simulated in the multibody model, trying to represent the actual conditions of the train. For this, harmonic irregularities

Table 1. Selection of characteristic frequencies calculated theoretically and using FEM.

Phenomenon	Frequency	Phenomenon	Frequency
BPFI	372.60 Hz	Wheelset 2nd & 3rd mode	76.79 Hz
BPFO	303.03 Hz	Bogie frame 1st mode	30.43 Hz
BSF	139.06 Hz	Bogie frame 2nd mode	54.40 Hz
FTF	13.19 Hz	Axle box 1st mode	219.67 Hz
Sleeper Pass	138.9 Hz	Axle box 2nd mode	326.94 Hz

are introduced both in the two wheels of the front axle of the bogie and on the track. In the wheels, these defects have an amplitude of 0.01 mm and a total of 100 waves along the wheel perimeter. In the track, very short wave defects (wavelength of 0.04 m and amplitude of 0.05 mm) are combined with random irregularities generated according to the indications of the European Rail Research Institute (ERRI) [9].

Random irregularities are created from Eqs. (1) to (3), which define the frequency spectra for the track horizontal irregularities, half the sum of the vertical irregularities and half the difference of the vertical irregularities, respectively. The values of the parameters used are listed in Table 2.

$$\Phi(\Omega) = \frac{a_h \cdot \Omega_c^2}{\left(\Omega^2 + \Omega_R^2\right) \cdot (\Omega^2 + \Omega_c^2)}, \Omega > 0 \tag{1}$$

$$\Phi(\Omega) = \frac{a_v \cdot \Omega_c^2}{\left(\Omega^2 + \Omega_R^2\right) \cdot (\Omega^2 + \Omega_c^2)}, \Omega > 0 \tag{2}$$

$$\Phi(\Omega) = \frac{1}{b_A^2} \cdot \frac{\Omega^2}{\Omega^2 + \Omega_s^2} \cdot \frac{a_v \cdot \Omega_c^2}{\left(\Omega^2 + \Omega_R^2\right) \cdot (\Omega^2 + \Omega_c^2)}, \Omega > 0 \tag{3}$$

Table 2. Values for generating frequency spectra according to [9].

Parameter	Value
a_h	$0.6125 \cdot 10^{-6}$ cm^2·rad/m
a_v	$1.08 \cdot 10^{-6}$ cm^2·rad/m
Ω_c	0.8246 rad/m
Ω_R	0.0206 rad/m
Ω_s	0.4380 rad/m
b_A	0.75 rad/m

Once the parameters of the irregularities have been established, a simulation of the bogie is carried out under a load of 15 t/axle at a speed of 300 km/h. The accelerations

computed by Universal Mechanism in the left end of the front wheelset, in the vertical direction, are recorded. This measurement point is chosen because it corresponds to the location of the accelerometers on the actual train.

In order to compare the simulated and the measured signals, the simulation step is set in a way that the simulated and measured signals have the same sampling frequency. Figure 4 shows the comparison, in frequency terms, of the simulated signal and the actual acceleration measured in the train also at 300 km/h.

Comparing both spectra, it can be seen that the frequency components of the simulated signal have much less noise than those of the real signal. This affects the amplitudes of the main components of the simulated spectrum, which are considerably larger than the ones of the real spectrum. These differences can be minimized by adjusting the model accordingly and always keeping in mind its limitations.

The qualitative analysis of the spectra in Fig. 4 is much more interesting because, if attention is paid to the active zones of the spectra, it can be observed that these zones coincide. In both cases, three active zones are distinguished: 0 Hz–200 Hz, 800 Hz–1,100 Hz and 1,900 Hz–2,200 Hz. By selecting one type of defect in the multibody model, it is possible to study which areas of the spectrum are stimulated by each type of defect and, extrapolating to actual signals, qualitatively determine the possible physical origin of the spectrum components. In this way, it is possible to advance in the detection of the condition of the state of the mechanical system. Specifically, the frequency regions higher than 800 Hz are activated when the very short wave defect into the track is introduced.
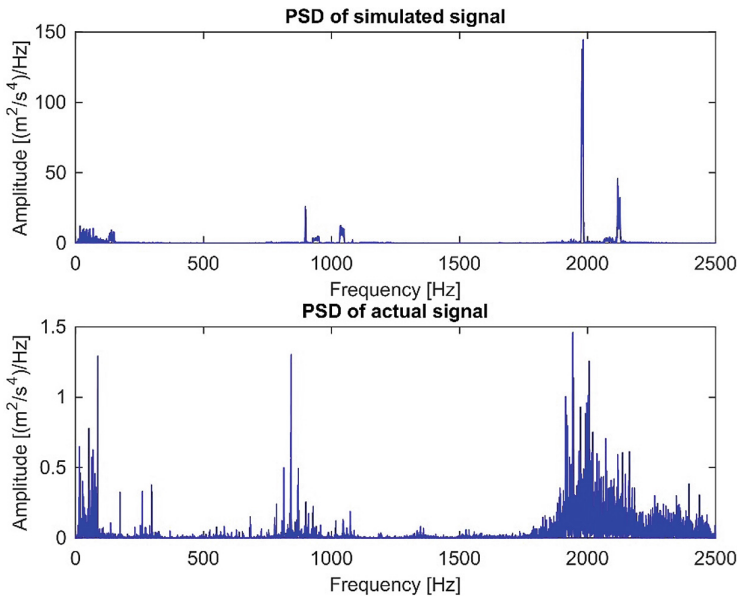
Fig. 4. Comparison of power spectra of the simulated and real signals.

4 Conclusions

This work presents an application case for applying Maintenance 4.0 to a high-speed train designed and built before the advent of the paradigm through the development of a Digital Twin.

The Digital Twin of the high-speed train bogie has been developed, which consists of three interrelated models: a 3D CAD model developed in CREO Parametric, a finite element model in ANSYS and a multi-body model in Universal. Mechanism. From these models, it is possible to determine the characteristic frequencies of the actual system and identify them in the frequency spectrum of the measured vibratory signals. In addition, they allow studying different operating situations of the real train.

Feedback from the measured data helps to improve the tunning of the multibody model and, therefore, to build up a Digital Twin which can be used within Maintenance 4.0 to identify the probable causes of the frequency components that appear on the spectra and establish the condition of the high-speed bogie. Significant frequency components have been identified that correspond to phenomena such as defects in the track, or the harmonic coupling of the shaft rotation frequency with certain natural frequencies.

References

1. Lasi, H., Fettke, P., Kemper, H.-G., Feld, T., Hoffmann, M.: Industry 4.0. Bus. Inf. Syst. Eng. **6**(4), 239–242 (2014). https://doi.org/10.1007/s12599-014-0334-4
2. Kaewunruen, S., Sresakoolchai, J., Lin, Y.: Digital twins for managing railway maintenance and resilience. Open Res. Europe **1**, 91 (2021). https://doi.org/10.12688/openreseurope.138 06.2
3. Karakose, M., Yaman, O.: Complex fuzzy system based predictive maintenance approach in railways. IEEE Trans. Ind. Inf. **16**, 6023–6032 (2020). https://doi.org/10.1109/TII.2020.297 3231
4. Lederman, G., Chen, S., Garrett, J.H., et al.: A data fusion approach for track monitoring from multiple in-service trains. Mech. Syst. Signal Process. **95**, 363–379 (2017). https://doi.org/10. 1016/j.ymssp.2017.03.023
5. Takikawa, M.: Innovation in railway maintenance utilizing information and communication technology (smart maintenance initiative). Jpn. Railw. Transp. Rev. **14** (2016)
6. Grieves, M., Vickers, J.: Digital twin: mitigating unpredictable, undesirable emergent behavior in complex systems. In: Kahlen, F.-J., Flumerfelt, S., Alves, A. (eds.) Transdisciplinary Perspectives on Complex Systems, pp. 85–113. Springer, Cham (2017). https://doi.org/10.1007/ 978-3-319-38756-7_4

7. In-depth focus: digital twins. Glob. Railw. Rev. **27**, 19 (2021)
8. Palmgren, A.: Ball and Roller Bearing Engineering, 3rd edn. SKF Industries Inc., Philadelphia (1959)
9. ERRI B176/DT 290: B176/3 Benchmark Problem, Results and Assessment. European Rail Research Institute (1993)

Automatic Identification of Kinematic Diagrams with Computer Vision

Gabriel Fontenla-Carrera[1(✉)] [iD], Ángel Manuel Fernández Vilán[2] [iD], and Pablo Izquierdo Belmonte[2] [iD]

[1] CINTECX, University of Vigo, CIMA Group, 36310 Vigo, Spain
`gabriel.fontenla@uvigo.es`
[2] Area of Mechanical Engineering, School of Industrial Engineering, University of Vigo, 36310 Vigo, Spain

Abstract. In this work, a computer vision algorithm for the detection and recognition of 2D kinematic diagrams, both from paper schemes and digital files, was developed. Furthermore, it runs even with hand-made diagrams, which can be correctly identified. The algorithm is mainly based on the use of the free computer vision library OpenCV, being able to identify each element of the kinematic diagram, its connection with the other elements and store its pixels, which will allow in future research the implementation of motion in the sketches themselves. Allowed elements are revolute, prismatic, fixed, cylindrical and rigid joints and rigid bars. The main applications of this work are focused on the teaching world, communication of ideas in a quickly and graphical way and for fast and preliminary designs of new mechanisms as people can draw the diagram in a Tablet or paper and simulate it in real time, avoiding the necessity to learn how to operate a specialized simulation software and the time it takes to prepare the virtual model and obtain its results.

Keywords: computer vision · OpenCV · kinematic diagrams · mechanisms · object recognition

1 Introduction

The design of mechanisms is a problem of great interest in the fields of mechanics and robotics. For this reason, kinematic diagrams or schemes are essential to represent these designs. In addition, hand-made drawings present advantages in terms of efficiency, visualization and communication of new ideas in mechanical design or education [1–3]. Nevertheless, analyzing the kinematics on the diagrams *per se* can be complicated and using a specialized software for simulation requires time to familiarize with it, create virtual models and calculate solutions [1, 3]. Consequently, it would be really interesting that virtual design and simulation tools could interact with those freehand drawings in order to optimize the process of solving kinematics and dynamics [1].

On the other hand, computer vision is increasingly present in society. Computer vision techniques allow the detection of different types of shapes and patterns automatically, with multiple technological and industrial applications in fields as diverse as military, automotive, agriculture, medicine, security and surveillance, etc. [4].

The aim of this work is to couple kinematic diagram drawings, both on digital board and on paper, with virtual design and simulation tools. Therefore, it is proposed an algorithm that, using tools from the open-source library OpenCV, recognizes kinematic diagrams from digital files (JPG or PNG) and extracts the necessary data to implement in simulations.

Currently, the state of the art for these applications is scarce. In [2] and [3], authors propose and test the recognition of kinematic diagrams composed by revolute joints and rigid bars using computer vision methods and a multi-objective optimization algorithm, specifically the NSGA-II. On the other hand, in [1] and [5], different freehand engineering symbols and diagrams are recognized applying convolutional neuronal networks (CNN). The algorithm presented in this paper, however, stands out for its simplicity. It is based on finding rectangles, circumferences and segments to subsequently associate these shapes with the elements that constitute kinematic diagrams, distinguishing between rigid bars and guides (straight lines), rigid joints (convergence of at least two rigid bars), fixed joints (three close short lines), revolute joints (circumferences), prismatic joints (rectangles) and cylindrical joints (rectangles with a circumference inside) (see Fig. 1). To achieve this, mathematical morphology operations and other basic computer vision and post-processing techniques are used.
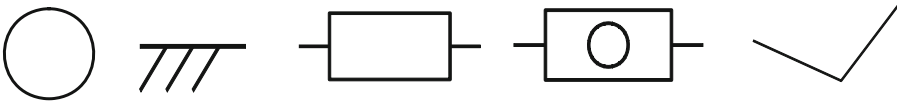
Fig. 1. Allowed symbology. From left to right: revolute, fixed, prismatic, cylindrical and rigid joints.

Among this symbology, important elements are not contemplated in this first research. For the specific case of a revolute joint with a fixed joint, as an alternative, the formulation showed in Fig. 2 is proposed.
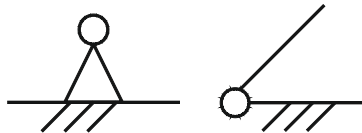
Fig. 2. Symbology of a revolute joint attached to a fixed joint (left). Alternative proposed (right).

Lastly, the pixels of each element of the diagram are stored separately, being not only capable of generating a virtual diagram which represents the original one for the calculation of kinematics, but also the kinematics could be solved on the drawing itself, being able to create animations with it.

2   Methodology

In this section the proposed method will be explained. Figure 3 shows a flowchart of the operation of the algorithm.
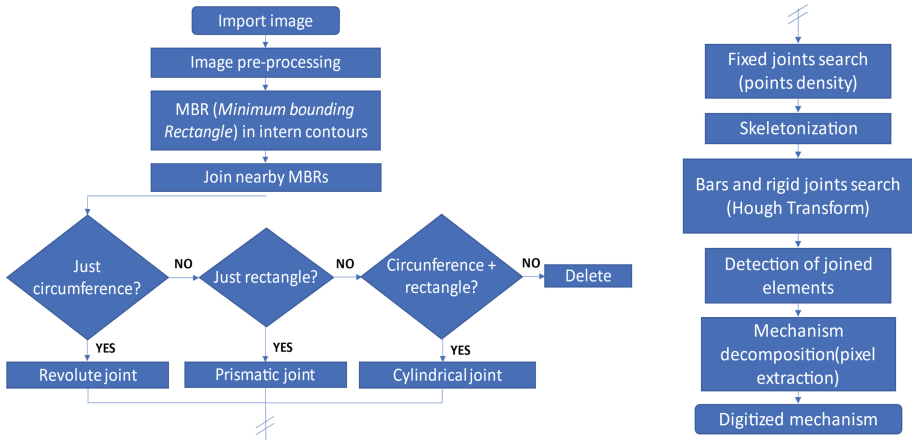
Fig. 3. Algorithm flowchart.

The first step is to import a RGB image with the kinematic diagram and convert it into a binary one. Then, some basic image filters and morphological operators to clean the noise and enhance certain properties can be applied [6]. Moreover, a size filter for symbols will be calculated considering the stroke width and the image dimensions.

After that brief pre-processing, the algorithm itself can start its process. Firstly, closed contours, which will correspond to circumferences and rectangles, are located by Minimum Bounding Rectangle (MBR) techniques, which can inscribe figures using the minimum possible area. This is a common strategy to store approximations of objects that can fulfill certain characteristics that will be analyzed in future steps [7]. For this reason, to ensure all figures are closed, the most common practice will be, at least, to introduce an initial dilation. In addition, outer contours could encompass several symbols, therefore only inner contours will be analyzed. Inner contours may be broken for different causes, as, for example, if a prismatic or cylindrical joint is drawn on a rigid bar (guide) and this guide breaks the joint in two parts. To solve this drawback, nearby MBRs are unified.

Then, a first classification is applied. A MBR can enclose a circumference (revolute joint), a rectangle (prismatic joint) or both shapes at the same time (cylindrical joint).

Before beginning the fixed joints recognition, all the symbols found in the previous step will be erased in order to simplify the image and avoid false positives. Fixed joints will be detected from the drawing by analyzing the density of stroke pixels as, after deleting the other figures, the higher density of points will belong to them.

At this point, only straight lines remain without identifying. They can represent rigid bars, guides or rigid joints. Since the 60s, the main form of detecting lines is the Hough Transform (HT) and its later more sophisticated variants [6, 8]. In this work it was

used the Progressive Probabilistic Hough Transform (PPHT), which is implemented in OpenCV [9], being more effective and less time-consuming than the traditional Hough Transform [10]. Due to the fact that line strokes are more than one pixel width and they are not completely straight as they can be hand-made, if the PPHT was applied, the result would have duplicate and broken lines [11, 12]. A skeletonization will remove the repeated information [6] before executing the PPHT and for avoiding broken lines, considering the initial and final points of the obtained lines, if slopes are similar, they will be joined together forming a single long line, but if slopes are different, a rigid joint will be identified [11, 12]. Once lines are detected, connections between elements can be established analyzing the position of the ends of the lines. Finally, guides will be recognized when a rigid bar has the same slope than a prismatic or cylindrical joint and intersection points are found between them.

Once all the elements are recognized, pixel extraction is easy: element by element, they are isolated in a ROI (region of interest) in which all the stroke pixels will belong to that figure, hence the only necessary operation will be storing the position of those pixels with respect to the global image.

2.1 Stroke Dilations: Structuring Element Size

Stroke dilations are essential for the correct functioning of the algorithm. Until four dilations are applied, being the only mandatory parameters to adjust. The first one is applied before finding the MBRs in order to close possible openings in figures, as it was explained above. The last three are intended to improve the capability of detection for circumferences, rectangles and fixed joints, respectively, since hand-made drawings can present some imperfections that must be removed.

In order to obtain the stroke dilations, rectangle structuring elements formed by square matrices are applied. The higher the value of the size of these matrices is, the wider the dilation of the stroke will be.

3   Results

The results are acquired after a series of tests carried out on a set of drawings made both in digital whiteboard and paper. These drawings were generated by different researchers, using different colors and strokes. Below a series of examples and their corresponding results are shown (Fig. 4) together with a table with the structuring element sizes used in each case (Table 1).

It is remarkable to say that although there are infinite positive integers to establish the structuring element size, it was not necessary to apply any number up to 9. Likewise, even though the values of the tables are highly variables, knowing the algorithm execution order, the calibration process is very intuitive. Firstly, if the original image figures are completely closed, then the first dilation will be small. Then, if the detection of the circumferences fails, a higher value of the circumference dilation will be needed. Subsequently, the same process must be followed for the detection of rectangles and fixed joints.
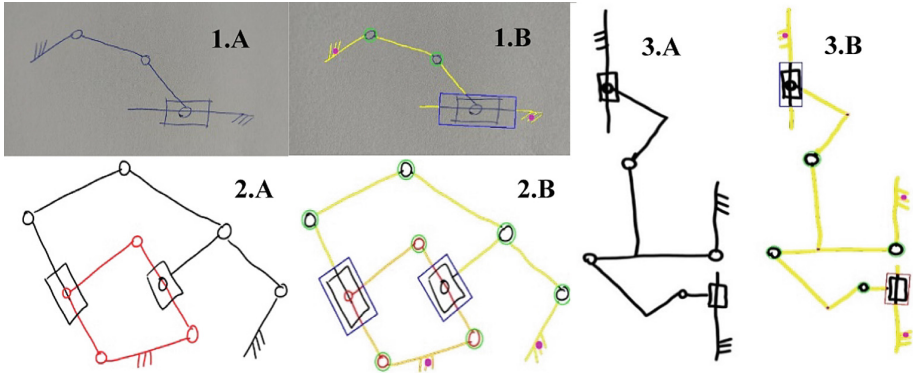
Fig. 4. Examples of hand-made kinematic diagrams (A) and their identification (B).

Table 1. Structuring element sizes used for diagram detection in Fig. 4

Stroke dilations	Structuring element size ($n \times n$)		
	1	2	3
Initial (MBR detection)	7×7	3×3	1×1
Circumference detection	7×7	7×7	3×3
Rectangle detection	9×9	5×5	3×3
Fixed joint detection	5×5	5×5	1×1

3.1 Algorithm Limitations

Due to the simplicity and novelty of the algorithm, there are some limitations that future research will try to solve.

- The use of mechanical symbols not contemplated in this article is not allowed. The algorithm could collapse or show wrong results.
- Cross bars without contact cannot be used. In this case, the algorithm will correctly detect all the elements of the mechanism. However, it will fail establishing the connections between the elements, interpreting cross bars as if they had a rigid joint between them.
- Images with more than 1,5 million of pixels should be avoided. Some errors were found during experiments if pictures were too big. This is because the size filter applied in symbols based on the image dimensions and the stroke width was not intended for this type of images.

4   Conclusions

It was shown how the recognition of freehand kinematic diagrams, both from digital devices and paper drawings, is possible even in real time. The proposed algorithm is fast, simple and could be run on any electronic device, such as a tablet or computer.

Future research will seek to improve the robustness and reliability of the algorithm, while incorporating new, more complex symbology. Finally, although in this article only kinematic schemes previously drawn were considered, in parallel work an algorithm which allows the identification of each element as it is drawn on a digital whiteboard is being developed. This will allow the correct identification of more difficult geometries and kinematic diagrams, being the final idea to merge both algorithms into a single one and, therefore, creating a software with much more potential.

References

1. Eicholtz, M., Kara, L.B.: Intermodal image-based recognition of planar kinematic mechanisms. J. Vis. Lang. Comput. **27**, 38–48 (2015). https://doi.org/10.1016/j.jvlc.2014.10.024
2. Fu, L., Kara, L.B.: Recognizing network-like hand-drawn sketches: a convolutional neural network approach. In: Proceedings of the ASME 2009 International Design Engineering Technical Conferences and Computers and Information in Engineering Conference, vol. 5, pp. 671–681. ASME, San Diego (2009). https://doi.org/10.1115/DETC2009-87402
3. Eicholtz, M., Kara, L.B., Lohn, J.: Recognizing planar kinematic mechanisms from a single image using evolutionary computation. In: Proceedings of the 2014 Annual Conference on Genetic and Evolutionary Computation (GECCO 2014), New York, pp. 1103–1110 (2014). https://doi.org/10.1145/2576768.2598354
4. Batchelor, B.G.: Machine Vision Handbook, 1st edn. Springer, London (2012). ISBN 978-1-84996-168-4
5. Fu, L., Kara, L.B.: From engineering diagrams to engineering models: visual recognition and applications. J. Comput.-Aided Design **43**, 278–292 (2011). https://doi.org/10.1016/j.cad.2010.12.011
6. Davies, E.R.: Computer and Machine Vision, 4th edn. Elsevier (2012). ISBN: 978-0-12-386908-1
7. Papadias, D., Theodoridis, Y., Sellis, T., Egenhofer, M.J.: Topological relations in the world of minimum bounding rectangles: a study with R-trees. In: Proceedings of the 1995 ACM SIGMOD international conference on Management of data, pp. 92–103 (1995). https://doi.org/10.1145/223784.223798
8. Kälviäinen, H., Hirvonen, P., Xu, L., Oja, E.: Probabilistic and non-probabilistic Hough transforms: overview and comparisons. J. Image Vision Comput. **13**, 239–252 (1995). https://doi.org/10.1016/0262-8856(95)99713-B
9. Hough Line Transform, OpenCV. https://docs.opencv.org/4.x/d6/d10/tutorial_py_houghlines.html
10. Matas, J., Galambos, C., Kittler, J.: Robust detection of lines using the progressive probabilistic Hough transform. J. Comput. Vision Image Underst. **78**, 119–137 (2000). https://doi.org/10.1006/cviu.1999.0831
11. Samarasekara, N.: Sports analysis using video tracking. Moratuwa (2015). https://doi.org/10.13140/RG.2.2.34195.78883
12. Lowe, D.G.: Three-dimensional object recognition from single two-dimensional images. J. Artif. Intell. **31**, 355–395 (1987). https://doi.org/10.1016/0004-3702(87)90070-1

Using Artificial Intelligence to Predict Lubricated Friction in Microtextured Mechanical Contacts

Francisco Franco-Martínez[(✉)], Jorge Juan García Moltó, Javier Echávarri Otero, Enrique Chacón Tanarro, and Andrés Díaz-Lantada

Machine Engineering Research Group, Department of Mechanical Engineering, Universidad Politécnica de Madrid, Madrid, Spain
`francisco.franco@upm.es`

Abstract. It has been shown that surface microtexturing is useful for improving lubrication. It offers strong reductions in the friction coefficient under operation conditions which compromise the maintenance of full film lubrication. To study the influence of texturing in the reduction of the friction coefficient, an Artificial Intelligence algorithm will be used. Its performance will be optimized. Afterwards, the algorithm will be applied to a new set of textured surfaces with the objective of finding the optimal one, that is, the one capable of reducing friction under different operating conditions. The selection of the optimal texturing will be based on the Weighted Mean Value of the friction coefficient (WMPT), a metric that was specifically created for this purpose.

Keywords: Tribology · Artificial Intelligence · Microtextured surfaces

1 Introduction

Controlled surface microtexturing is an interesting option to reduce friction, since it can improve lubrication conditions, especially when the operation of the system compromises the maintenance of full film lubrication [1, 2]. Therefore, the main effect takes place in the transition from full film lubrication to mixed lubrication conditions, as is the case of machine elements that operate with high load and/or low speed, such as bearings, gears, etc. There are numerous references that experimentally quantify the effect of dimple-based microtexturing on lubricated friction, through the analysis of several types of patterns, geometries, texturing densities, and manufacturing methods [1, 3–5]. Regarding the mechanisms that reduce friction, the literature describes the capability of texturing to form lubricant microreservoirs [6], which allow the surfaces to be separated through the formation of local hydrodynamic wedges [2, 7]. Although there are study sources, attempts to model the operation of textured surfaces are relatively scarce, except for those presented in references [8, 9] and some others. The complexity of the interactions between textured surfaces makes it difficult to model their performance. To address this problem, the use of Artificial Intelligence (AI) algorithms can be of great

benefit since they ease the handling of all the experimental information available. These algorithms can be applied to predict the friction between textured surfaces and to opti-mize their performance, without the need to model the complex phy-sical phenomena that take place in the contact. In fact, AI has been used successfully in many tribological applications as is gathered in references [10, 11]. Echávarri Otero et al. have investigated the use of neural networks to predict the lubricated friction coefficient in textured point contacts using the Matlab Deep Learning Toolbox [1].

The present article analyses the use and optimization of an Artificial Intelligence (AI) algorithm for predicting the friction coefficient (CoF) in lubricated contacts with different microtexturing patterns. Then, it will be used to find the textured surface that reduces the friction coefficient to a greater extend under a range of operating conditions.

2 Methodology

2.1 Obtaining the Initial Data

For this study, a series of friction tests carried out on the Mini-Traction Machine (MTM) are used as data set. 21 microtextured copper test samples with different geometric patterns are used, in contact with a ¾" diameter (19 mm) steel ball, resulting in a point contact. The lubricant is a PAO-6 base oil. The test conditions are:

- Slide-to-Roll ratio, SRR (%): it is the quotient between the sliding speed and the average speed: 5, 10, 20 50, 75 and 100%.
- Average speed (mm/s): value range from 100 to 3500 mm/s.
- Normal contact load (N): 5 and 20 N.
- Lubricant bath temperature (ºC): 40 and 80 ºC.
- The geometric characteristics of the microtextured patterns are as follows:
- Shape: The data set includes specimens with circular, elliptical and radial microtex-turing pattern, as well as untextured samples. This variable is categorical and allows differentiating between each type of microtexture.
- Dimension 1 (μm): radius for circular textures or minor axis length in the sliding direction for elliptical samples or groove width for radial pattern. Values between 0–350 μm.
- Dimension 2 (μm): radius for circular textures or major axis length in the sliding direction for elliptical samples or groove width for radial pattern. Values between 0–11000 μm.
- Texturing density (%): surface area that has been textured relative to the total area. Values between 0–25%.
- Depth (μm): depth of the pattern. Values between 0–185 μm.
- Roughness (μm): Average surface roughness of the test sample before texturing. Specimens with 0.007 and 0.1 μm of Ra roughness have been used.
- Regarding the tests with these microtextured samples, 9 pairs of average speed-friction coefficient values are obtained, for each Stribeck curve. The curves for each sample correspond to a typical performance of the Stribeck curves in reference [1].

2.2 Artificial Intelligence Algorithm, Data Preprocessing, Training and Evaluation

In order to have a larger data set, the first goal has been to carry out a data augmentation. To this end, the UnivariateSpline function available in the Scipy python library has been used. A total of 160 pairs of values of friction coefficient and average speed are obtained.

Machine learning algorithms present optimized performance when the values are in an identical and small range, the second stage in data preprocessing is the scaling of each variable in the range of values from -1 to 1. To achieve this, the MinMaxScaler function available in the SciKitLearn library is used [12, 13]. Then, the data set formed by 40320 data is divided into two sets using a pseudorandom function by defining a value called "seed":

- Training data set: is formed by 90% of the data set.
- Validation set: is formed by the remaining 10% of the data set. From these data, the prediction of the network can be evaluated through different evaluation metrics. After this, the algorithms hyperparameters are modified to optimize its performance.

The case study is a supervised learning approach since the values of the output variable, the friction coefficient, to be predicted are already known. The input variables are these shown in Sect. 2.1.

The algorithm has been trained following an iterative method, in order to optimize their operation from the evaluation of their performance according to mathematical metrics used on the training and validation data set. The metric used to evaluate the algorithm is the mean squared error quality metric (MSE).

The algorithm selected for this study is a Sequential Neural Network, which is a model made up of artificial neurons connected to each other and grouped in the form of layers. The Back Propagation algorithm is selected for carrying out the learning process.

2.3 Optimal Microtexturing Prediction.

Once the best algorithm for predicting the CoF has been chosen, we proceed to predict this coefficient with new microtexturing patterns which are different from those that form the training and validation set. Selecting the microtextured surface that achieves the lowest friction for the two studied loads and six Slide-to-Roll ratios can be an overly complex task. For this reason, it is decided to apply the calculation of a weighted mean value of the friction coefficient per test (WMPT), as a method of comparison and selection. In the calculation of WMPT, "test" alludes to a Stribeck curve. This weighted mean value is chosen to give more significance to the lowest average speeds (from 100 to 1000 mm/s), since the microtextures are expected to improve the behavior at these speeds, in which the test conditions are more severe and mixed lubrication is achieved.

The WMPT value is calculated for each test, considering the 9 predicted friction coefficient values f_i for the following average speeds: 100, 250, 500, 1000, 1500, 2000, 2500, 3000 and 3500 mm/s in a weighted way, according to Eq. (1). The values $c1$ and $c2$ have been stablished as 0.15 and 0.08 respectively. Each test sample is tested at 2 loads and 6 different SRR for each load, a total of 12 tests are obtained and the WMPT metric is calculated on each of them. As a control test, an untextured sample is tested

and the WMPT metric is calculated again for each of the tests, which is called WMPTc. Then the WMPT of each test is compared with the value of the control test (WMPTc). With this result, a counting procedure is followed using Eq. 2:

$$WMPT = c_1 \sum_1^4 f_i + c_2 \sum_5^9 f_i \qquad (1)$$

$$x = \begin{cases} 1, \, if \, (WMPT - WMPTc > 0) \\ 0, \, if \, (WMPT - WMPTc < 0) \end{cases} \qquad (2)$$

Finally, the sum of the x values of each test sample is performed, thus obtaining a criterion that allows deciding which type of microtextured surfaces reduce friction on average for the combinations of load and SRR.

3   Results

Sequential neural network is a deep learning algorithm, a Machine learning subset which is typically used to solve highly complex problems. The neuronal algorithm is built with the so-called Dense layer of Keras programming library [12, 13]. It has been trained with different network configurations, using different amounts of neurons and hidden layers. The optimal parameters and the obtained MSE are shown in Table 1.

Table 1. Optimal parameters and mean squared error results for the Sequential Neural Network algorithm.

Neurons	Hidden Layers	Optimizer	Learning Rate	Loss Function	MSE validation
64	1	RMSprop	0.001	MSE	1.44e−04

The MSE is very low, revealing an accurate prediction of the friction coefficient on the validation data. Furthermore, the MSE value for the training and validation data sets becomes very similar in last training epochs. Thus, it is concluded that no overfitting is presented. A minimum value of 1.44e−04 can be found in epoch 491.

Once the Neural Network has been chosen as the appropriate algorithm, by using it and applying the method described in Sect. 2.3 it is made the prediction and selection of the optimal microtextured surface. To achieve this, a new data set of microtextured test samples is created. The different geometric variables that define a microtexture are in the range of values studied. The total number of new microtextured surfaces is 6783. In this way, the tests results with the same testing conditions shown in Sect. 2.1 are obtained for each of the different test samples.

According to the friction coefficient data predicted using the Neural Network, it is determined that the optimal design is a circular shape with dimension 1 and 2 equal to 100 μm; texturing density 8%; depth 110 μm and Ra 0.007 μm. The sum of x (from Eq. 2) is equal to 7. Figure 1 compares the results of a series of six predictions obtained for the optimal sample with an untextured sample. This graph shows that the friction

values predicted by the Neural Network are reduced with respect to the untextured test sample, in all SRR conditions for a 20 N load. Also, the texturing effect is greater at low speeds, where theoretically the presence of textures should lead to more favorable lubrication conditions.
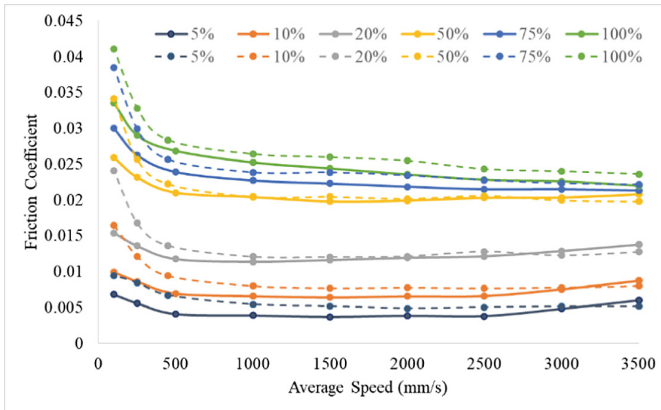
Fig. 1. Comparison between the Stribeck curves for optimal design (solid line) and an untextured sample (dashed line) at different SRR, load of 20 N and temperature of 40 ℃

The results show that the texturing density and geometry predictions follow the trend of other empirical studies [1, 6]. It seems logical that greater depths allow a greater friction reduction, since the microtextures act as lubricant reservoirs. However, there is no overall optimal value. Rosekranz et al. [14] obtained that the optimal depth was between 25 and 50 µm. While Echávarri et al. [1] have concluded that the optimal depth for elliptical textures is around 78 µm, increasing the friction drop as texture depth increases. Therefore, tests must be performed to verify this effect.

4   Conclusions

This study has shown the use of Artificial Intelligence algorithms for predicting the friction coefficient in lubricated contacts with microtextured surfaces.

The architecture of the Neural Network is formed with one hidden layer of 64 neurons. The predictions can be obtained on any computer in a few seconds. This gives to the Neural Network a notable advantage over complex numerical simulations.

The predictions made by the Neural Network on the friction coefficient show a Stribeck curve with a similar shape to the experimental data, demonstrating that the network captures the texturing effect on the Stribeck curve. Furthermore, if we compare all the Stribeck curves of the textured test sample in Fig. 1 with the untextured sample, they show an improvement in friction. Finally, it is worth mentioning that the network can accurately predict the influence of the slide-to-roll ratio, allowing the results to be generalized for other slide-to-roll ratio values within the studied range.

In the future, the authors will compare the results of the Neural Network prediction with experimentation to verify the friction reduction.

References

1. Echávarri, J., de la Guerra, E., Bellón, I., Chacón, E.: Optimizing the design of textured surfaces for reducing lubricated friction coefficient. Lubr. Sci. **29**(3), 183–199 (2017)
2. Gohar, R., Rahnejat, H.: Fundamentals of Tribology, 3rd edn. World Scientific Publishing Europe (2019)
3. Kovalchenko, A., Ajayi, O., Erdemir, A., Fenske, G., Etsion, I.: The effect of laser surface texturing on transitions in lubrication regimes during unidirectional sliding contact. Tribol. Int. **38**, 219–225 (2005)
4. Gachot, C., Rosenkranz, A., Hsu, S.M., Costa, H.L.: A critical assessment of surface texturing for friction and wear improvement. Wear **372–373**, 21–41 (2017)
5. Xu, Y., et al.: Characterization of the tribological behavior of the textured steel surfaces fabricated by photolithographic etching. Tribol. Lett. **66**, 55 (2018)
6. Wakuda, M., Yamauchi, Y., Kanzaki, S., Yasuda, Y.: Effect of surface texturing on friction reduction between ceramic and steel materials under lubricated sliding contact. Wear **254**(3), 356–363 (2003)
7. Predescu, A., Pascovici, M.D., et al.: Friction evaluation of lubricated laser-textured surfaces. Lubr. Sci. **22**(10), 431–442 (2010)
8. Ronen, A., Etsion, I., Kligerman, Y.: Friction-reducing surface-texturing in reciprocating automotive components. Tribol. Trans. **44**, 359–366 (2001)
9. Marian, M., Grützmacher, P., Rosenkranz, A., Tremmel, S., Mücklich, F., Wartzack, S.: Designing surface textures for EHL point-contacts - transient 3D simulations, meta-modeling and experimental validation. Tribol. Int. **137**, 152–163 (2019)
10. Marian, M., Tremmel, S.: Current trends and applications of machine learning in tribology—a review. Lubricants **9**(9), 86 (2021)
11. Echávarri, J., et al.: Artificial neural network approach to predict the lubricated friction coefficient. Lubr. Sci. **26**, 141–162 (2014)
12. García Moltó, J.J.: Inteligencia artificial aplicada al análisis tribológico de texturizados superficiales con Python. Bachelor thesis, Universidad Politécnica de Madrid (2021)
13. Bobadilla, J.: Machine Learning y Deep Learning: Usando Python, Scikit y Keras. Ra-Ma Editorial (2021). 9789587921465
14. Rosenkranz, A., Szurdak, A., Garchot, C., Hirt, G., Mücklich, F.: Friction reduction under mixed and full film EHL induced by hot micro-coined surface patterns. Tribol. Int. **95**, 290–297 (2016)

Mechatronic Design of a New Fluid Pivot Journal Bearing

Jorge González Salazar$^{(\boxtimes)}$ and Matías Reumay San-Martín

Department of Mechanical Engineering, Universidad de La Frontera, Francisco Salazar 01145, 4811230 Temuco, Chile
`jorge.gonzalez@ufrontera.cl`

Abstract. This work introduces a new sort of mechatronic hydrodynamic journal bearing for controlling vibrations in rotating machinery. This mechatronic design aims at improving an increasingly demanded bearing. The new mechatronic fluid pivot journal bearing is built upon a tilting pad journal bearing with a spherical pivot modified to inject pressurized oil into the pivot-pad gap. It is pursued that the bearing properties can be affected via controlling the pivot behaviour. The initial concept is presented followed by the design of each subsystem. An isothermal model is utilized. Results show a lab-size bearing ready for being experimentally validated. It is concluded that the proposed design poses a solution for common problems of hertzian contact based pivot hydrodynamic bearings.

Keywords: Hydrodynamic bearings · Active bearings · Mechatronics

1 Introduction

The Tilting Pad Journal Bearings (TPJBs) [1] are fundamental machine elements for load supporting in rotating machinery with good performance under extreme operational conditions of load and rotational speed. However, the steadily demanding operational conditions deplete the bearing capability of dissipating energy. Incorporating elements of mechatronics such as vibration sensors, hydraulic servo valves, control systems and laws to inject lubricant in a controlled way, has been proposed as a solution to tackle high vibration amplitudes by acting directly over the bearing behaviour and expand the machine operational limits. Santos [2] reviews trends in fluid film bearings linked to mechatronic redesign. In [3] the author aims at adding flexibility to the pivot point of a TPJB via membrane chambers. In [4] the same author presents the active lubrication, the controlled injection of high-pressure lubricant to the shaft load supporting fluid film through a centered bore at the pad. Active lubrication is modelled through a thermo-elasto-hydrodynamic approach based on the modified Reynolds equation. More recently, Varela *et al.* [5] proposed and studied theoretically and experimentally a mechatronic version of a Leading Edge Groove TPJB, obtaining good results in terms of its applicability. TPJBs can feature different types of pivots such as rocker, spherical, flexible, and fluid. Authors incorporate the pivot flexibility determined by the hertzian contact theory

[6] by assuming a pad radial movement as a new degree of freedom [7]. It is demonstrated that the TPJBs behaviour is highly affected by the pivot design [8], specially at demanding operational conditions where the pivot stiffness becomes larger than the one of fluid film, therefore decreasing the capability to dissipate energy.

1.1 The Mechatronic Fluid Pivot Journal Bearing

This work proposes a new design that focuses on the fluid pivot dynamics. The proposed design is inspired in the granite fountain [9] to incorporate a lubricated mechanism at pivot able to support a high load with small amount of lubricant flow. It is a mechatronic approach of a TPJB with a spherical pivot to support the pad [10]. This spherical pivot has been modified into an injector to provide, in a controlled way, high pressure lubricant in between surfaces of the pivot and pad seat. In this way, a fluid pivot with controllable lubricant injection is obtained. The proposed bearing design aims at becoming a mechatronic alternative to improve the pivot dynamics. As results of this work, the conceptual design and the design of a first mechatronic Fluid Pivot Journal Bearing (FPJB) prototype are presented. In the state-of-the-art review a FPJB was found [11]. However, it can be considered as non-mechatronic bearing.

2 Bearing Design

2.1 Bearing Fundamentals

The bearing concept surges from the granite ball fountains observations, also known as *ball fountain* [9], in which a thin fluid layer of water allows it to develop a hydrostatic pressure distribution able to support a high load, the granite ball weight. The same principle can be imposed at the pivot-pad socket gap aiming at this extra source of lubricant can: 1) to avoid the hertzian contact between surfaces and to remove the friction resistant moment, 2) to provide an additional source of damping and 3) to endow the pivot dynamic properties with the possibility of being controlled. A first isothermal model is considered although the literature establishes a thermo-elasto-hydrodynamic model to properly describe the phenomena in tilting pad journal bearings [12].

2.2 Bearing Design

The standard recommendations for designing hydrodynamic bearings were attended besides further considerations from a mechatronics viewpoint.

Design Parameters. a) Standardization: optimized and standardized sizes to reduce space and cost of production are considered. b) Lubrication: immersion lubrication is considered with an ISO VG22 lubricant. c) Material: bronze is utilized instead of babbitt, fulfilling the same fuse function to protect the shaft in case of surfaces contact. d) Specific Load: it is necessary to avoid low and high values due to instability and heat transfer and babbitt fatigue problems. For the bearing is approximately 1 MPa. e) Tangential Shaft Surface Velocity: it increases with the shaft diameter and shaft rotational speed and for the bearing is approximately 52 m/s. It is a critical design parameter because it

can develop a turbulent flow. f) L/D ratio: it is defined as 1 to be utilized in the available test rigs having lower specific load, hence lower stiffness, and good damping properties. g) Clearance: the narrowed the tolerances, the higher the cost of producing it. In this case a value of 1,1 mils per inch in diameter is selected. h) Pivots: a partial contact of a spherical pivot with the pad socket is utilized in this design.

Mechatronic Design Parameters. They are considered as: i) Actuator. Two electrohydraulic servo valves for injecting high pressurized lubricant to provide a plane control force. ii) Sensors. Displacement sensors for measuring the shaft positioning and feedback the control laws. iii) Injector. An injector orifice in the pivot center to create a fluid film between the pivot and pad socket surfaces. The Table 1 summarizes the main design parameters of the mechatronic fluid pivot journal bearing.

Table 1. Design parameters of mechatronic FPJB.

Geometrical parameters			Geometrical parameters		
R_j	Shaft radius	49.89 [mm]	R_{piv}	Pivot radius	20 [mm]
n	Pad number	4	r_{max}	Pivot Insertion	5 [mm]
R_p	Pad radius	50 [mm]	m_p	Preload	$0.2 < m_p \leq 0.8$
d	Pad thickness	17 [mm]	Operational Parameters		
β_o	Pad arc	60 °	Ω	Max. Rotational speed	10.000 rpm
L/D	Lengh/diam. Ratio	1	W	Max. Load	10 kN
C_p	Pad radial clearance	0.11 [mm]	μ	Lub. Viscosity	ISO VG 22
α	Pad offset	50%	Mechatronic parameters		
X_s	Pivot radial clearance	0.1 [mm]	I_d	Injector Diameter	3–5 [mm]
				Servovalves number	2

2.3 Design Stages: A System Approach

The hydrodynamic bearing is designed under a constructive approach which allows unique functional subsystems to be identified. This implies that the system is compounded by a minimum number of pieces easily of machining and installing in the laboratory test rigs. Furthermore, it is also flexible as the pieces shall be adjustable and interchangeable to study additional configurations of the bearing. The design stage considered are: 1) Pivot system: it is compounded by the pad and the spherical pivot. Pivots are installed in an oil distributor ring. The pivots can be adjusted to change the pad-pivot clearance. 2) Oil distributor system: It comprises the oil supply channel from servo valves to the spherical pivots mainly compounded by a distributor ring. The return lines are also part of the system. 3) Sealing ring: It is meant for sealing the distribution ring to avoid leakages. 4) Housing and accessories: It comprises the protecting housing,

oil deposit, servo valve mounting block, seals, bolts and foundation bolts. The housing is considered stiff, and it allows the simple lubricant recovering. Sensors mounting structures are also considered.

3   Results

3.1   The Mechatronic Fluid Pivot Journal Bearing

The Fig. 1 a) and b) show the designed bearing assembled and exploited respectively. A total weight of 109 kg is estimated with the CAD software considering bronze as pad material and steel for other pieces. Geometrical parameters are stablished in Table 1. Metric bolts between M3 and M20 are utilized. Seals are used in caps, servo valve blocks and pivots. Two radial shaft seals are also considered to minimize leakages between shaft and bearing. The Table 2 summarizes the main bearing components.

The following characteristics are highlighted for the proposed mechatronic FPJB: 1) It allows operating the bearing in load-between-pads and load-on-pads configurations. 2) It allows adjusting the pad-pivot clearance due to the type of o-ring utilized, which can be deformed up to 25% of its original size. This affects the whole bearing clearance. 3) Simple and flexible oil and heat extraction thanks to its lower oil collector with two oil outlets. The collector volume is calculated based on the oil flow rate. 4) It allows bearing alignment thanks to ovals holes for mounting bolts. 5) The insertion percentage of the spherical pivot in the pad socket is 25%. 6) It allows an actuating active control force in two perpendicular directions. 7) The injected oil flow, by the nozzle in the pivot, reaches the pad socket or seat. It is expected that the bottom pads also feature immersion lubrication. 8) A high-pressure pump is needed to supply the lubricant.
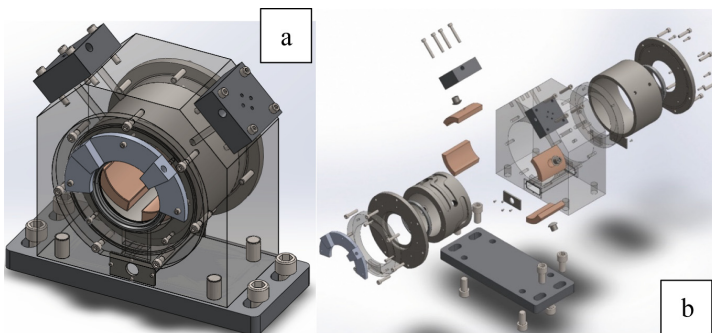
Fig. 1.   Mechatronic Fluid Pivot Journal Bearing. **a)** Assembled. **b)** Exploited.

Table 2. Components List of the Mechatronic FPJB.

N°	Element	Function
1	4 pads + spherical pivots	To Support the load
2	1 oil distributor	To inject fluid towards the pivot nozzles
3	1 housing	External compartment of the bearing, it contains the pieces belong to bearing and shaft
4	1 opened collector cap	It belongs to the lower reservoir of the bearing; it has the bolt holes and the hole for connecting the flow line to the high-pressure pump
5	1 pair of sensors support	To fix the displacement sensors
6	2 servovalves bases	To fix the servovalves to the housing

3.2   Bearing Simulations

The simulations are performed by solving the isothermal model with the finite difference method. The correct implementation and convergence study of the method has been validated in cylindrical journal bearings and TPJBs found in literature. Afterwards, the method is adapted to the mechatronic FPJB. It is simulated with data of Table 1 and with the operational conditions reported in the graph legends.

Figures 2a) and 2b) depict the results for the eccentricity and pad tilt. As the rotational speed increases, the eccentricity decreases. Besides, there is lower eccentricity at higher thickness h_{pi} for a fixed rotational speed. Conversely, occur with the load W. For the case of pad tilt, it can be seen in Fig. 2b) that as the rotational speed increases, the pad tilt also decreases, as in the previous case.
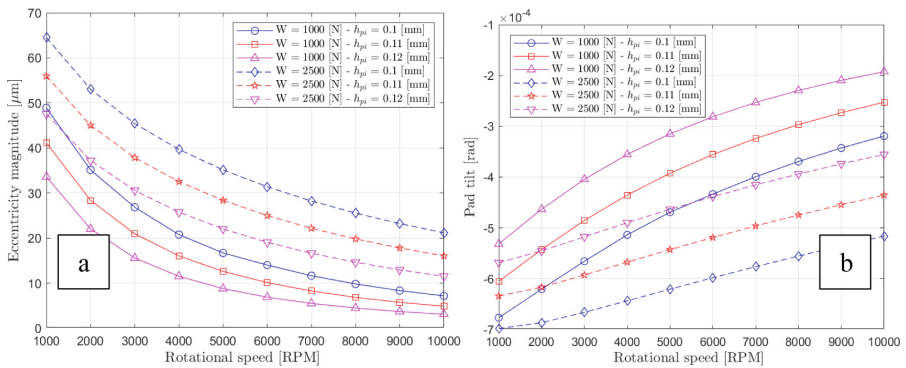
Fig. 2. a) Eccentricity v/s rotational speed, b) Pad tilt v/s rotational speed.

Figure 3a) depicts the hydrodynamic pressure distributions at the Shaft-Pad surface and Fig. 3b) depicts the hydrostatic pressure distribution at the Pad-Pivot surface. The difference in magnitudes between them is mainly because the surfaces are different in

size. By comparing Figs. 3a) and 3b), it can be observed that there is some symmetry in the pressure fields because a constant hydrostatic thickness h_{pi} is considered.
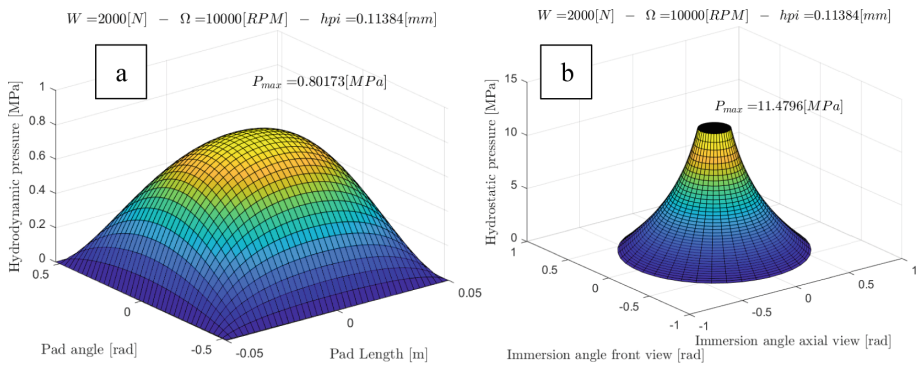
Fig. 3. a) Hydrodynamic and b) hydrostatic pressure distributions.

4 Conclusions

The present work has presented a prototype of a new design of fluid pivot journal bearing with a mechatronic approach, the mechatronic FPJB. This approach is applied aiming at influencing the bearing properties by means of controlling the physics that dominates the modified spherical pivot behaviour for injecting lubricant behind of each pad. The proposed design incorporates some industrial aspects, and it can be incorporated into test rigs for further experimental tests. An isothermal model is used to simulate the mechatronic FPJB. It is expected that this bearing can provide an extra and controllable source of damping when compared with Hertzian contact pivot bearings.

References

1. Nicholas, J.C.: Tilting pad bearing design. In: Proceeding Twenty-Third Turbomachinery. Symposium, pp. 179–194 (1994)
2. Santos, I.F.: Controllable sliding bearings and controllable lubrication principles-an overview. Lubricants **6**(1), 1–16 (2018)
3. Santos, I.F.: Design and evaluation of two types of active tilting pad journal bearing. In: Burrows, C.R., Keogh, P.S. (eds.) The Active Control of Vibration, pp. 79–87. Mechanical Engineering Publications Limited, London (1994)

4. Santos, I.F., Russo, F.H.: Tilting-pad journal bearings with electronic radial oil injection. J. Tribol. **120**(3), 583–594 (1998)

5. Varela, A.C., Santos, I.F., Salazar, J.G., Salazar, C.P.: Experimental and theoretical study of an actively lubricated LEG tilting pad bearing. In: 13th International Conference on Dynamics of Rotating Machinery, pp. 244–259. Technical University of Denmark (2019)

6. Kirk, R.G., Reedy, S.W.: Evaluation of pivot stiffness for typical tilting-pad journal bearing. J. Vib. Acoust. Trans. ASME **110**(2), 165–171 (1988)

7. Rouch, K.E.: Dynamics of pivoted-pad journal bearings, including pad translation and rotation effects. ASLE Trans. **26**(1), 102–109 (1983)

8. Mehdi, S.M., Jang, K.E., Kim, T.H.: Effects of pivot design on performance of tilting pad journal bearings. Tribol. Int. **119**(1), 175–189 (2018)

9. Snoeijer, J.H., Vander Weele, K.: Physics of the granite sphere fountain. Am. J. Phys. **82**(11), 1029–1039 (2014)

10. Ciulli, E., Forte, P., Antonelli, F., Minelli, R., Panara, D.: Tilting pad journal bearing ball and socket pivots experimental determination of stiffness. Machines **10**(81), 201–216 (2022)

11. Nelson, D.V., Hollingsworth, L.W.: The fluid pivot journal bearing. J. Lubr. Technol. **99**(1), 122–127 (1977)

12. Monmousseau, P., Fillon, M., Frêne, J.: Transient thermoelastohydrodynamic study of tilting-pad journal bearings - comparison between experimental data and theoretical results. J. Tribol. **119**(3), 401–407 (1997)

Autonomous Navigation for an Intelligent Sailboat - Sensailor

Marcelo Fajardo-Pruna[1]([✉]) [iD], Daniela Sanchez-Orozco[1] [iD], Karen Torres-Medina[1] [iD], Luis Lopez-Estrada[2] [iD], Christian Tutiven[1] [iD], and Yolanda Vidal[3] [iD]

[1] Escuela Superior Politécnica del Litoral, ESPOL, Guayaquil, Ecuador
`mrfajard@espol.edu.ec`
[2] Universidad Politécnica de Madrid, Madrid, Spain
[3] Universitat Politécnica de Catalunya, Barcelona, Spain

Abstract. This article presents the development of an autonomous navigation system for the intelligent sailboat Sensailor. This vehicle will be equipped with a Lidar and a camera for obstacle recognition. The recollected data will allow the sailboat to register the obstacle coordinates and determine the zones for safe navigation. Based on that, the intelligent system will apply AI algorithms for path planning, in order to get the shortest safe trajectory. This way, it will be guaranteed that the Sensailor can translate from an initial to a target position while optimizing time and resources.

Keywords: Self-manned vehicles · autonomous sailboat · path planning · robotics

1 Introduction

The Sensailor is an unmanned surface vehicle, originally developed by the Polytechnic University of Catalonia [1]. This investigative work has as main objective the development of a more robust navigation system. To fulfill this, a NVIDIA Jetson Nano embedded system will be used to obtain data from a Lidar sensor and a camera for obstacle recognition. Then, the same CPU will be able to process the information and generate new trajectories to be follow by the controller system. This will increase the Sensailor versatility, allowing it to perform in different unknown environments and generating new feasible trajectories in real time.

2 Methodology

2.1 Autonomous Mapping and Localization

The autonomous sailboat will move in a highly changing environment. It is needed to ensure the integrity of the unmanned vehicle by implementing an estimation of its position and orientation, as well as mapping its surroundings. Multiple sensors are reinforced, information is collected, merging the data obtained from a camera with a Lidar

point cloud. In the first instance, a layer is created to preprocess the filtering images and the filter of the LIDAR point cloud. Therefore, to improve the effectiveness of obstacle detection, a list of steps has been stipulated in Fig. 1 [1].
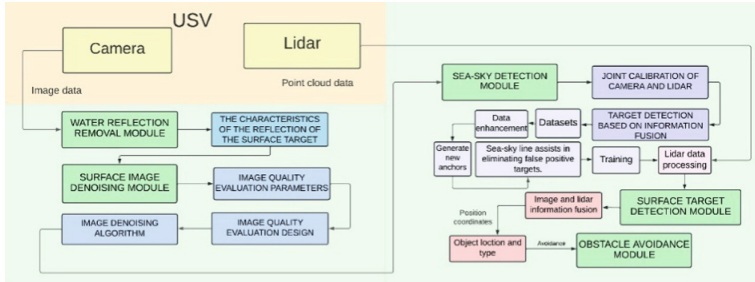
Fig. 1. Module diagram for obstacles avoidance

The first stage is eliminating the reflection generated on the surface of water since it interferes when detecting and tracking moving objects on the surface. Therefore, the input image turns into a grayscale, and the mean threshold function [2] converts it into a binary image Fig. 2 (a–b); consequently, the 9-square grid method is applied to detect the outline. If a difference of 8 pixels does not exist near a pixel, a contour is created.

(a)   (b)   (c)   (d)   (e)
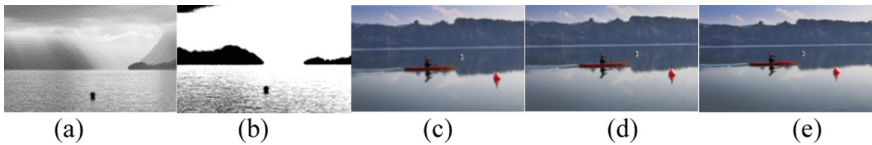
Fig. 2. a) Grayscale image b) Binary image. c) Original image. d) Image with noise. e) Image with Gaussian filter.

The existing noise interference in the images taken by the USV also affects the detection of obstacles. If an image has poor quality, a denoising processing is performed, Fig. 2 (c–e), otherwise this step is omitted. To determine the quality of the image techniques such as MSE (Mean Square Error), PSNR (Peak Signal to Noise Ratio), and SSIM (Structured Similarity Indexing Method) are used. Some results are in Fig. 3 (a–e). In addition, if it is necessary to remove the noise due to an unacceptable distortion, the BM3D (Block-matching and 3D filtering) algorithm is applied.

The Watershed algorithm is applied to segment complex images by detecting contours and finding overlapping objects within the image. For the detection of the sea sky, the Otsu method [3] is included, calculating the threshold to decrease dispersion in each segment, but increasing it when contrasted with others (Fig. 4). In contrast, by using the Hough transform, possible horizons are extracted, and a single horizon is chosen through probabilistic intervals [4].

It was decided to merge the high-quality images of the camera with the Lidar point cloud. The camera obtains high resolution, and the Lidar gets depth data more accurate.

(a)   (b)   (c)   (d)   (e)
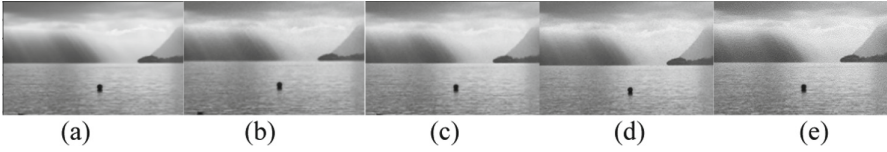
Fig. 3. a) Original image. b) Impulsive Noise with MSE: 10590 and PSNR: 18.11. c) Gaussian noise. MSE: 619.06 and PSNR: 20:21 d) Impulsive noise suppression with MSE:279.18 and PSNR: 23.67 e) Noise suppression with Gaussian filter. MSE: 238.15 and PSNR: 24.36.

Fig. 4. Sky and sea line identification.

The relationship between the coordinates of the arbitrary world and the coordinate system [5], for the image pixels, is estimated by taking the center of the lens as the system origin. The "X" axis, and the y-axis as parallel to the opposite sides of the phase. Finally, the "Z" axis, which represents the optical axis of the lens, is perpendicular to the image plane as shown in Eq. (1).

$$
Z_c \begin{bmatrix} x \\ y \\ 1 \end{bmatrix} = K \begin{bmatrix} x_c \\ y_c \\ z_c \end{bmatrix} = \begin{bmatrix} f_x & 0 & c_x \\ 0 & f_y & c_y \\ 0 & 0 & 1 \end{bmatrix} \begin{bmatrix} x_c \\ y_c \\ z_c \end{bmatrix} = \begin{bmatrix} f_x & 0 & c_x \\ 0 & f_y & c_y \\ 0 & 0 & 1 \end{bmatrix} \left(\begin{bmatrix} R_{11} & R_{12} & R_{13} \\ R_{21} & R_{22} & R_{23} \\ R_{31} & R_{32} & R_{33} \end{bmatrix} \begin{bmatrix} X_w \\ Y_w \\ Z_w \end{bmatrix} + \begin{bmatrix} t_x \\ t_y \\ t_z \end{bmatrix} \right)
$$
(1)

On the one hand, the image data from the camera is represented by a three-dimensional lattice cloud made by Lidar [6], for which a transformation matrix, Eq. (2), is created that assigns 3D points to 2D points.

$$
\begin{pmatrix} u \\ v \\ 1 \end{pmatrix} = \begin{pmatrix} f_u & 0 & u_0 \\ 0 & f_v & v_0 \\ 0 & 0 & 1 \end{pmatrix} \begin{pmatrix} R & t \\ 0 & 1 \end{pmatrix} \begin{pmatrix} x \\ y \\ z \\ 1 \end{pmatrix} = \begin{pmatrix} m_{11} & m_{12} & m_{13} & m_{14} \\ m_{21} & m_{22} & m_{23} & m_{24} \\ m_{31} & m_{32} & m_{33} & m_{34} \\ m_{41} & m_{42} & m_{43} & m_{44} \end{pmatrix}
$$
(2)

Obstacles were detected through YOLOV3 following certain rules. Some areas in the image are selected, labeling those regions according to their position. The model uses a convolutional neural network that extracts data from the characteristic image by predicting the location and category according to the neural network model. It is contrasted with the label and the loss function is obtained by evaluating the deviation between the real scenario and the one predicted based on what the network learned (Fig. 4). The point cloud obtained from Lidar is continuously processed, obtaining the point cloud cluster that can detect the obstacle (Fig. 5).

Considering that weather conditions generate dispersion and interference points in the Lidar point cloud, a conditional elimination filter [7] is used to analyze the neighborhood between each point and calculate the Euclidean distance [8]. If a point has very few neighbors, it is considered atypical interference.

Fig. 5. Obstacle recognition with YoloV3.

Fusion of camera and lidar data occurs by projecting the target point cloud cluster and image bounding boxes, calculating two-dimensional bounding boxes, and joining the information from both.

$$J_A = J_U + \frac{\left[L * sen\left(\theta * \frac{\pi}{180}\right)\right]}{\left[111 * \cos\left(W_U * \theta * \frac{\pi}{180}\right)\right]} \qquad W_A = W_U + \frac{\left[L * cos\left(\theta * \frac{\pi}{180}\right)\right]}{[111]} \qquad (3)$$

The USV can detect obstacles with its distance and angle direction relative to the autonomous sailboat. While, through the electronic compass and inertial navigation; the trajectory latitude, longitude, and angle are obtained. With Eq. (3), the longitude "J" and latitude "W" of the obstacle is found, being "U" the autonomous sailboat and "A" the obstacle, considering that the latitude differs by a degree every 111 km.

2.2 Planification

The workspace is discretized to be represented by a matrix where the cell size guarantees that the sailboat can always fit inside a cell. The coordinates of the obstacles are redefined based on the equivalent cell in the matrix. The available spaces within the matrix where the sailboat can move are called safe zones. On the other hand, non-safe zones are those that have an obstacle or a portion of it inside the cell, or the limits of the workspace. To guarantee a safe navigation of the sailboat, the norms stipulated in the Convention on the International Regulations for Preventing Collisions at Sea (COLREGs), must be considered [9].

It is intended to optimize the trajectories as the shortest safe path. Special attention must be paid to the redundancy of movements, preventing loops or going through the same segment several times without justification. For this, it was decided to use a combination of two trajectory planning algorithms, as shown in Fig. 6.

Fig. 6. Trajectory Planning General Algorithm

The intelligent algorithm A* evaluates the array by classifying its cells as occupied or free. For this, an admissible heuristic function is taken as a reference, considering the

best possible scenario. This corresponds to the absence of obstacles in which the motion can be carried out by a single straight line. The heuristic function h is the Euclidean distance between the evaluated point and the final point. Each cell has an associated g_i value corresponding to the number of steps that must be taken from the cell of origin to it. Adding both parameters determine the f_i cost of each cell. The algorithm will choose the cell with the lowest cost to update its current position. If the trajectory reaches a c_i cell with all its paths blocked, the algorithm returns to the previous position c_{i-1}, eliminates the option of moving to c_i cell, and selects the adjacent cell with the second lowest cost. These actions are repeated until the program finds a path that reaches the destination position through the cells with the lowest possible cost [10] (Fig. 7).
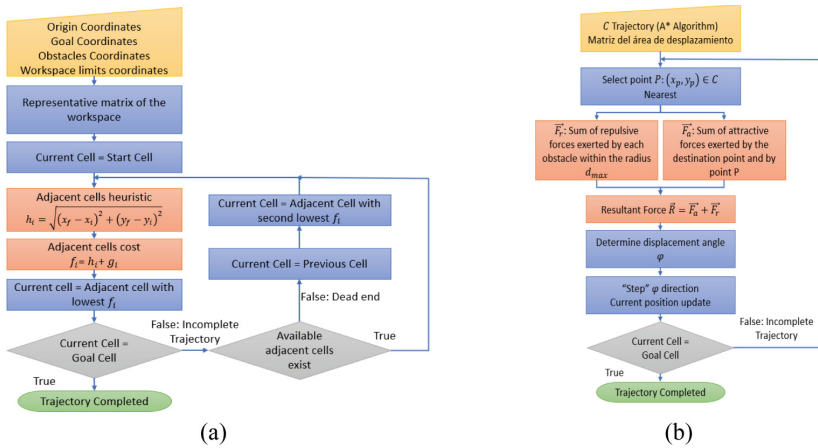
Fig. 7. a) A* algorithm Flowchart. b) Potential Fields algorithm Flowchart.

Since the system requires constant updating of the sampled space, the trajectory generation system is complemented with an algorithm based on potential fields. Unlike the A* algorithm, it can be implemented in real time, constantly updating the trajectory according to the motion of the obstacles. The direction of movement of the vehicle is established by the direction of the force resulting from the sum of the attraction and repulsion forces [11]. This way, the final trajectory followed by the USV is very close to the optimal route generated by the A* algorithm. This algorithm is guaranteed to work efficiently updating the trajectory in real time as required (Fig. 8).
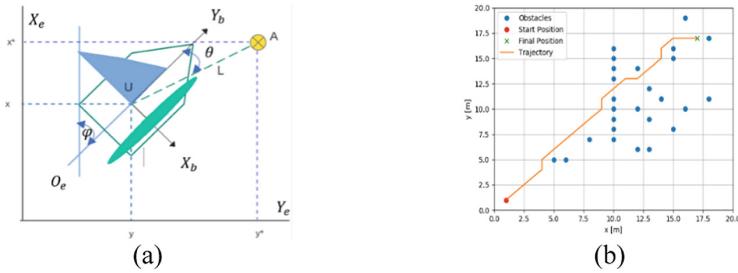
Fig. 8. a) Obstacle coordinate system with respect to the USV. b) Generated Trajectory Example.

3 Conclusions

In this research, it is demonstrated the solution to the autonomous navigation of a Sailboat. It was possible to detect obstacles by segmenting and labeling images. For the sailboat to be able to perceive any object close to it, the image quality has been corrected and noise has been reduced. Fast response was gotten when implementing Yolo (up to 30 FPS) by tagging obstacles in real-time. By having the data on the location of the obstacle, the sailboat automatically traces an obstacle avoidance route. First, it uses the intelligent search algorithm A* to generate the shortest safe path. Additionally, for navigation in real-time, the algorithm of potential fields was complimented. It was assumed that the GPS obtained correct coordinates without error. Therefore, in future research, a Kalman filter could be added to treat the location of the USV.

References

1. Moreno-Ortiz, A., et al.: Modelling of an intelligent control strategy for an autonomous Sailboat – SenSailor. In: 2022 5th International Conference on Advanced Systems and Emergent Technologies (IC_ASET), Hammamet, Tunisia, pp. 34–38 (2022). https://doi.org/10.1109/IC_ASET53395.2022.9765928
2. Zhang, W., et al.: Research on unmanned surface vehicles environment perception based on the fusion of vision and lidar. IEEE Access **9**, 63107–63121 (2021). https://doi.org/10.1109/ACCESS.2021.3057863
3. Kim, H., et al.: Vision-based real-time obstacle segmentation algorithm for autonomous surface vehicle. IEEE Access **7**, 179420–179428 (2019). https://doi.org/10.1109/ACCESS.2019.2959312
4. Kristan, M., Kenk, V.S., Kovačič, S., Perš, J.: Fast image-based obstacle detection from unmanned surface vehicles. IEEE Trans. Cybern. **46**(3), 641–654 (2016). https://doi.org/10.1109/TCYB.2015.2412251
5. Liang, D., Liang, Y.: Horizon detection from electro-optical sensors under maritime environment. IEEE Trans. Instrum. Meas. **69**(1), 45–53 (2020). https://doi.org/10.1109/TIM.2019.2893008
6. Ren, J., Zhang, J., Cui, Y.: Autonomous obstacle avoidance algorithm for unmanned surface vehicles based on an improved velocity obstacle method. ISPRS Int. J. Geo-Inf. **10**(9) (2021). https://doi.org/10.3390/ijgi10090618
7. Wu, P., et al.: Autonomous obstacle avoidance of an unmanned surface vehicle based on cooperative manoeuvring. Ind. Robot. **44**(1), 64–74 (2017). https://doi.org/10.1108/IR-04-2016-0127

8. Muhovic, J., Mandeljc, R., Bovcon, B., Kristan, M., Pers, J.: Obstacle tracking for unmanned surface vessels using 3-D point cloud. IEEE J. Oceanic Eng. **45**(3), 786–798 (2020). https://doi.org/10.1109/JOE.2019.2909507
9. Polvara, R., et al.: Obstacle avoidance approaches for autonomous navigation of unmanned surface vehicles. J. Navig. **71**(1), 241–256 (2018). https://doi.org/10.1017/S0373463317000753
10. Benjamin, M.R., Curcio, J.A.: COLREGS-based navigation of autonomous marine vehicles. In: 2004 IEEE/OES Autonomous Underwater Vehicles, pp. 32–39 (2004). https://doi.org/10.1109/AUV.2004.1431190
11. Ju, C., Luo, Q., Yan, X.: Path planning using artificial potential field method and a-star fusion algorithm. In: Global Reliability and Prognostics and Health Management, PHM-Shanghai (2020). https://doi.org/10.1109/PHM-SHANGHAI49105.2020.9280929

Author Index